UNIVERSITY OF SOUTHAMPTON

FACULTY OF SCIENCE, ENGINEERING AND MATHEMATICS

SCHOOL OF OCEAN AND EARTH SCIENCES

MANTLE SOURCE COMPOSITION BENEATH THE MID-ATLANTIC RIDGE: CONTROLS ON THE DEVELOPMENT OF E-MORB SEGMENTS AND OCEANIC CORE COMPLEXES

BY SAMANTHA CLARE WILSON

THESIS FOR THE DEGREE OF DOCTOR OF PHILOSOPHY

OCTOBER 2010

DEDICATION

To my family, who are always encouraging, enthusiastic, and supportive, and from whom I inherited my interest in the natural world, and also to Michael, for making ‘writing up’ a great time.

Graduate School of the National Oceanography Centre, Southampton

This PhD dissertation by Samantha Clare Wilson was produced under the supervision of the following persons:

Supervisors:

Dr. Bramley J. Murton

Dr. Rex N. Taylor

Chair of Advisory Panel:

Prof. Damon A. Teagle

UNIVERSITY OF SOUTHAMPTON

ABSTRACT

FACULTY OF ENGINEERING, SCIENCE AND MATHEMATICS

SCHOOL OF OCEAN AND EARTH SCIENCES

Doctor of Philosophy

MANTLE SOURCE COMPOSITION BENEATH THE MID-ATLANTIC RIDGE: CONTROLS ON THE DEVELOPMENT OF E-MORB SEGMENTS AND OCEANIC CORE COMPLEXES

By Samantha Clare Wilson

The thickness and continuity of volcanic cover at slow-spreading ridges is variable. Magmatically 'robust' regions are interspersed with areas which experience little volcanism. Near the Fifteen-Twenty Fracture Zone (FTFZ), (MAR), volcanism appears exceptionally limited. Here, spreading at numerous sites is instead accommodated by extension on low-angle detachment faults, exposing peridotite to form oceanic core complexes (OCCs). Little is known about the mechanisms controlling the transition between spreading states. This study investigates these mechanisms in detail (MAR, 12º6'N-14°N).

Basalts around the FTFZ are E-MORBs with a HIMU-FOZO flavour. There is no evidence that melt production is currently lower at OCC spreading sites than the surrounding magmatic areas. The geochemistry of dykes (OCC surface, 13º19'N,-44º95W) shows that melt here is diverted along the detachment fault, resulting in reduced volcanism in the axis.

The mantle source in this region was extensively depleted during a previous melting episode(s). This study finds that the source was also variably veined with refertilising material of HIMU-FOZO character. Basalts erupted immediately prior to OCC formation, and now located off-axis, (13º19'N,-44º95W) are geochemically bimodal, and different to the on-axis melts. Trace element and geochemical modelling data shows that 'M1' (LREE & volatile-rich, CPX-bearing E-MORBs) are high-pressure, garnet-phase, low melt fractions, whilst 'M2' (less enriched, flatter REE profiles) are low melt fractions formed by spinel-phase melting.

In areas of *exceptional* bulk source depletion, melt production is limited by the geochemistry of the source.' M1' basalts result from rapid melting and extraction of a small volume of enriched vein material. This locally cools and dehydrates the source. Low melt fractions 'M2' are then generated from this depleted source. Due to the lack of fusible components, melt production remains insufficient to sustain magmatic spreading, and an OCC forms. Thus, periods of low melt production, resulting directly from mantle compositional characteristics, drive the transition from magmatic to 'fault-dominated' spreading.

TABLE OF CONTENTS

LIST OF FIGURES

by a fault line close to the axis. In active OCCs, this fault line is very sharp, whereas in extinct structures it may be overlain by sediment or volcanics. The core complex dome consists of uplifted and heavily serpentinised ultramafic material overlain by talus and rider blocks dragged from the hanging wall.

Figure 7: Ocean ridge crustal accretion models. (A) Typical Penrose model for fast-spreading, based upon the interpretations of the Oman Ophiolite. (B) Modified Penrose model for slow-spreading crust reflecting the abundance of gabbro and peridotite sampled at transforms, (C) model for the anomalous 14-16°N region of the MAR. After Dick *et al*. (2006).

Figure 8: Illustration of the process whereby slip on a steep normal fault (a) rotates out to a shallower angle, exposing peridotite on the core complex surface (b). The detachment may be severed by the development of a later high angle fault (c). From Smith *et al*. (2006).

Figure 9: Slip on a steep normal fault in the valley wall is aided by seafloor weathering processes and serpentinisation, which act to weaken the fault plane, making it more prone to slip. This process may be especially significant where melt supply is low, and normal valley wall faults extend to accommodate spreading.

Figure 10: Distribution of well-known hydrothermal vent sites along the MAR, 10-50°N. Also shown are the positions of major fracture zones and the Azores Plateau. After Baker *et al*. (1995).

Figure 11: Correlations in the central MAR between seismicity, asymmetric spreading, and the development of hydrothermal vent sites. Hydrothermal sites almost exclusively occur in asymmetrically spreading crust. From Escartín *et al*. (2008).

Figure 12: The sinusoidal shape of the central MAR, the position and extent of the major fracture zones, and the relationship of the MAR with the Azores hotspot and associated plateau. Global position inset.

Figure 13: La/Sm vs. latitude data for the Mid-Atlantic Ridge 5°S-65°N. High La/Sm ratios are seen at the Azores Hotspot (~30-40°N), but rapidly drop away to N-MORB values south of ~30°N. This suggests that significant plume influence on trace element geochemistry does not extend south of this position. Data sources – PetDB, this study.

Figure 14: The morphology of the MAR between the FTFZ and Marathon FZ is highly variable. Black stars indicate the distribution of structures identified as OCCs (Smith *et al*. 2006, 2008).

Figure 15: Bathymetry data showing highly variable ridge flank morphology and numerous non-transform offsets in the axial valley between 15°20'N and 12°60'N. After Smith *et al*. (2008).

Figure 16: Variations in axial seismicity between 12°60'N and 15°2'N. Typically on the northern MAR, seismicity extends for 15-20km either side of the axis. However, between 13°N-14°N a parallel band of seismicity is clearly visible ~70km off axis. Smith *et al*. (2008).

Figure 17: The approximate positions of ridges and troughs in the FTFZ region of the MAR. Also shown is the position of the region of off-axis seismicity, taken from Smith *et al.* (2008).

Figure 18: Enrichment zones on the MAR. Some of these, such as Iceland and the Azores, are associated with elevated crust and geophysical signatures such as negative RMBA. The geochemical enrichment at these sites is recognised as originating from mantle plumes. Enrichment zones also occur at 45°N and near the FTFZ, but there is no clear gravimetric or bathymetric evidence to suggest the presence of a mantle plume at these sites. Geochemical data normalised to chondrite. From Bougault *et al.* (1988).

Figure 19: Locations of ODP Leg 209 drilling sites either side of the FTFZ. From Garces and Gee, (2007).

Figure 20: Oceanic core complex developmental stages, as described by MacLeod *et al.* (2009). (a) Normal slow-spreading ridge. (b) Reduction in melt supply – spreading transfers to a normal valley wall fault off-axis. (c) Continued spreading on the rotated fault exhumes mantle material onto the seafloor, forming a core complex. The fault line is migrated back toward the original axis position. (d) The fault axis migrates back in line with the magmatic axis. Renewed magmatism cuts through the fault line, and normal magmatic spreading resumes. From MacLeod *et al*. (2009).

Figure 21: Bathymetry from the JC007 cruise, showing the area between 12°60'N-14°N. The four oceanic core complexes identified by Smith et al. (2006) are highlighted in red.

Figure 22: A) Key structural features of the 13°19'N oceanic core complex, including the breakaway ridges, corrugated dome, fault line and inward propagating neovolcanic zones. B) Corresponding TOBI sidescan-sonar imagery. From MacLeod *et al.* (2009).

Figure 23: Combined TOBI and bathymetry image produced by the 3D visualisation software package Fledermaus®. Image view is facing west, along the axis-normal length of the core-complex at 13°19N. In the foreground, hummocky neovolcanic terrain propagates toward the sharp, brightly reflective fault surface. On the core complex dome, corrugations are clearly visible. Beyond the dome, back-tilted volcanic blocks mark the breakaway ridge, which is approximately axis-parallel. MacLeod *et al.* (2009).

Figure 24: ArcGIS processed EM-120 bathymetry map showing the location of dredge sites, the major lithologies recovered, and their geographic distribution. Symbols as follows: red circles - basalt, green circles - peridotite, orange triangles - peridotite and basalt.

Figure 25: Schematic diagram of the internal layout of a magnetic sector thermal ionisation mass spectrometer, showing the different paths taken by heavy and light isotopes to the detectors. Rex Taylor, pers. comm.

Figure 26: Modern TIMS filaments. The sketch shows a single filament (a), and also the correct alignment of a triple filament setup (b). Sample is loaded neatly onto the centre of the ribbon to achieve efficient ionisation.

Figure 27: Examples of hand specimens from the 12°6'N-14°N region. These rocks show common basalt features such as glassy layers, vesicles and alteration features. Clockwise from left to right: 1. Pillow basalt with fresh glass (from axis). 2. Moderately altered pillow basalt with vesicles and discoloured alteration rim (breakaway). 3. Fresh, plagioclase-phyric pillow basalt without glass (breakaway). 4. Altered, recrystallised pillow basalt with thick vein (talus). 5. Extensively recrystallised greenstone pillow basalt with cross-cutting veins (hydrothermal toe talus). 6. Pillow basalt with devitrified glass and a thick oxide coating (breakaway).

Figure 28: Photomicrographs of on-axis basalts from 12°6'-14°N showing large anhedral to subhedral plagioclase crystals with prominent twinning. Blebs, cracks and other structural irregularities indicative of disequilibrium are common in these crystals.

Figure 29: Photomicrographs (taken with crossed polars) of off-axis basalts from 13°19'N. Bottom: Cluster of irregularly shaped plagioclase and olivine crystals, interspersed with smaller olivine and (?) pyroxene crystals within a matrix of basaltic glass and fine (<1mm) plagioclase. Top: Cluster with larger, more well-developed crystals.

Figure 30a,b: Photomicrographs taken with crossed polars and plane polarised light (top right, second row right) of off-axis basalts from 13°19'N. Highly irregularly shaped olivine crystals are found in many samples from the OCC. These crystals range from radially clustered to individual, lath-like examples. Some of these are complex dendritic, open and/or closed 'Hopper' crystals, with large voids in the crystal centres. The crystals are typically ~1mm in size, though, occasionally, lath-like examples reach 3mm in length.

Figure 31: Photomicrographs (taken with crossed polars) of off-axis basalts from 13°19'N. Augite crystals are large (~3-5mm) and subhedral, displaying strong evidence of chemical disequilibrium in the form of indistinct crystal boundaries, blebs, cracks and other defects They are surrounded by fine (<1mm-2mm) laths of plagioclase. The augite crystals are simply twinned, and sector zoning is observed in some examples.

Figure 32: Bathymetry map showing the estimated position of the ridge axis (black line) overlaid by the positions of dredges sampling on-axis material (red markers). Black markers denote dredges in off-axis positions and will be considered separately. Off-axis sites are defined as those where *in situ* material is sampled from outside the axial zone. Talus material from core complex domes is considered to have originated in the axis, before being dragged over the fault surface, and therefore sites sampling talus are included in the 'on-axis' site category.

Figure 33: Major element plots showing the composition of basalts from this study (black markers) relative to the N-MORB average (yellow diamond). Average N-MORB value from the data of Hoffmann (1988). Error bars lie beneath the display markers.

Figure 34: Ternary discrimination diagram for basalt (after Meschede, 1986). The diagram shows that rocks from this study (black markers) extend from N-MORB

to E-MORB in composition, and that some samples have higher Zr and Nb than is expected even for E-MORB.

Figure 35: REE plot showing that on-axis data from 12°60'-14°N (blue) extend from N-MORB-like profiles to LREE enriched E-MORB compositions. Average N-MORB (black dashes) and average global MORB (black) and E-MORB (red) compositions for the Atlantic region and worldwide are shown for comparison. See legend for data sources.

Figure 36: Regression lines on trace element ratio vs. latitude plots show that there is a general transition from LREE enriched compositions at the 14°N 'enrichment anomaly' (as described by Hémond *et al*., 2006) to less enriched signatures near the Marathon fracture zone at 12°60'N.

Figure 37: ArcGIS processed bathymetry map overlaid with markers to show sample sites characterised as 'on-axis magmatic spreading', 'on-axis core complex spreading' and 'off-axis' sites. Samples from on-axis at OCC sites are shown in blue, magmatic on-axis samples are shown in red, and off-axis sites are black.

Figure 38: Major element concentration (wt %) plots. On-axis magmatic samples are represented by red triangular markers and on-axis OCC samples by blue square markers. Arrows indicate the direction of fractional crystallisation in both plagioclase-accumulated (blue) and non-plagioclase-accumulated (orange) basalt groups.

Figure 39: Major element concentration data (wt%), including insets to show trends more clearly. Data is overlaid with arrows to show geochemical trends. Blue arrows indicate plagioclase accumulation, whilst fractionation in the absence of plagioclase accumulation is shown in orange. The concentrations of pure mineral compositions (see Table 11) are indicated by symbols. Plagioclase compositions are denoted by a blue square, clinopyroxene by a green oval, and olivine by a green triangle.

Figure 40: Al_2O_3 vs. percentage of plagioclase in basalt samples from 12°6'-14°N. The red arrow shows the trend in increasing Al_2O_3 with percentage of plagioclase phenocrysts in the sample. The arrow on the dashed regression line points toward the composition of pure plagioclase, as denoted by the blue square symbol. High Al_2O_3 samples at 0% are likely to result from consumption of accumulated plagioclase by the melt.

Figure 41: Major element concentration data show the geochemistry of oceanic core complex (blue squares) and magmatic (red triangles) basalt from 12°60'-14°N, as well as dolerite dyke samples (yellow) from the core complex toe at 13°19'N.

Figure 42: Rare Earth Element (REE) data for magmatic (red) and core complex (blue) basalt samples from 12°60'-14°N. The plots show that basalts from each group extend from N-MORB-like to LREE enriched E-MORB in character.

Figure 43: Trace element ratio plots show data for magmatic (red) and core complex (blue) basalt samples. Both groups extend from N-MORB to E-MORB in character, and occupy very similar areas of compositional space.

Figure 44: Simplified sketch map of the 13°19'N core complex, showing the location of all nearby dredge sites. Neovolcanic zones are shown in black, and the axial valley floor in grey. The ~5x vertically exaggerated cross-section runs through the centre of the core complex, and shows the point at which exhumed peridotite and basalt talus meet back-tilted *in situ* volcanic seafloor.

Figure 45: sketch map of the 13°19'N core complex, showing the location of all dredge sites. The sketch map is rotated to better show the features at the core complex toe. Off-axis sites where rocks are thought to *be in situ* are labelled in green. On-axis volcanic seafloor sites are shown in red. Dredge sites shown in blue retrieved a mixture of serpentinised peridotite and basalt. The basalt from these sites is interpreted as talus broken up from the axis in the vicinity of D13 and dragged over the core complex dome by the action of the fault.

Figure 46: Major element plots show that off-axis (green markers) samples have bimodal compositions, extending from N-MORB-like compositions to highly enriched E-MORB compositions. These E-MORBs are substantially more enriched than the on-axis samples examined earlier (black markers). Red circles highlight the bimodality of the off-axis sites (see K, P, Ti, Na).

Figure 47: Major element plots show data from dredges D05 (green), D06 (red) and D12 (purple), as well as on-axis data for comparison (black). Each dredge contains both enriched and depleted samples.

Figure 48: REE data show the bimodality of off-axis basalts. Group M1 (pink) are characterised by extremely LREE-enriched basalts with steep REE profiles. M2 (yellow) have N-MORB like, flat, or slightly LREE-enriched profiles. Shown for comparison are on-axis samples (blue) typical N-MORB (dashed black, Sun and McDonough, 1989) and E-MORB (solid black, Donnelly *et al*., 2004) compositions.

Figure 49: Major element data shows that on-axis (black) and M2 (yellow) data lie on both plagioclase accumulation (blue arrow) and non-plagioclase-accumulation (orange arrow) trends, but M1 (pink) basalts only lie on the non-plagioclase-accumulation trend.

Figure 50: Trace element plots illustrate the bimodality of M1 and M2 compositional groups. Group M1 (pink) is highly enriched, and group M2 (yellow) more N-MORB like. There is a significant compositional gap between the groups. On-axis data (black) are shown for comparison.

Figure 51: Trace element ratios vs. latitude (this study). The plots show that on the whole, enrichment decays from 14°N - 12°60'N. However, at 13°19'N, the compositional range is much greater than at any other location, and the enriched and depleted end-members of the local array are both found here.

Figure 52: Trace element and ratio plots show the bimodal compositions of off-axis basalt groups M1 (pink) and M2 (yellow). On-axis data (black) for comparison. M1 basalts have high Dy/Yb, low Yb/Lu and high La/Yb relative to the general ridge trend. M2 data conforms to the on-axis ridge trend, but lies at the depleted end of the array.

Figure 53: H_2O (FTIR) vs. major element concentration data for basaltic glass from M1 (yellow), M2 (pink) and on-axis samples (black). The data shows the bimodality of groups M1 and M2. M1 samples extend to higher concentrations of H_2O than M2 rocks. Ce vs. Nd data is shown for comparison, as Ce and H_2O behave similarly in basalt.

Figure 54: Regional Element [8] data against latitude for the MAR (black, PetDB MORB data). Ti[8] values for the 12°60'-14°N segment (green) have a substantially greater range than anywhere else on the ridge. P [8] and K [8] extend to higher concentrations at 12°60'-14°N than the rest of the central MAR, whilst Na [8] values are typically lower.

Figure 55: Trace element data against latitude for the MAR (black-PetDB MORB data). Nb, Nd, Zr and Ce values for the 12°60'-14°N area (green) extend to substantially higher and lower values than anywhere else on the central MAR . Y and Yb values are lower than average for the region.

Figure 56: Pb $^{208}Pb/^{204}Pb$ vs. $^{206}Pb/^{204}Pb$ Atlantic data (PetDB MORB, 5°S-89°N, blue) form an array which follows the NHRL (northern hemisphere reference line). Also shown is on-axis data from 12°60'-14°N (black), as well as off-axis M1 (pink), and M2 (yellow) basalts. M1 basalts lie at the radiogenic end of the local isotopic array, whilst M2 occupy the unradiogenic end. M1 and M2 basalts also lie on different compositional vectors to the on-axis samples, as shown in Δ7/4 and Δ8/4 plots. M1 basalts extend towards low Δ8/4, and project outside the Atlantic MORB array. Error is displayed by a red marker.

Figure 57: $^{206}Pb/^{204}Pb$, $^{143}Nd/^{144}Nd$ and $^{87}Sr/^{86}Sr$ isotope ratios for on-axis data (black), and off-axis M1 (pink) and M2 (yellow) basalts. The data is shown in relation to the Atlantic data array (PetDB MORB data, 55°S-89°N, blue). M1 basalts have a very steep $^{87}Sr/^{86}Sr$ vs. $^{143}Nd/^{144}Nd$ trend, which substantially differs from the gradient of the Atlantic MORB trend.

Figure 58: Variations of $^{87}Sr/^{86}Sr$, $^{143}Nd/^{144}Nd$ and $^{206}Pb/^{204}Pb$ isotope ratios with latitude in the Atlantic. Regional data (PetDB MORB, black) shows that there is substantial variation throughout the central MAR region. 0-5°N and 30-35°N are characterised by high $^{87}Sr/^{86}Sr$ and $^{206}Pb/^{204}Pb$ ratios, and low values of $^{143}Nd/^{144}Nd$. The N-MORB region between 17°10'N (marked by red line) and 22°N is characterised by low $^{87}Sr/^{86}Sr$ and $^{206}Pb/^{204}Pb$ ratios, and high values of $^{143}Nd/^{144}Nd$. Samples from 12°60'N– 14°N extend to very high $^{87}Sr/^{86}Sr$ and low $^{143}Nd/^{144}Nd$ values, with $^{206}Pb/^{204}Pb$ values higher than 17°10'N, but lower than those at 0-5°N.

Figure 59: Trace element data illustrating the geochemical variations across the dome of the 13°19'N core complex. M1 (yellow) and M2 basalts (pink) are bimodal, bracketing the composition of basaltic talus (orange) and on-axis basalts from 12°60'-14°N (blue). The sketch map (bottom) illustrates the geographic features with which the data correlates.

Figure 60: Trace element ratio data illustrating the geochemical variations across the dome of the 13°19'N core complex. M1 (yellow) and M2 (pink) basalts are bimodal, bracketing the composition of basaltic talus (orange) and on-axis basalts from 12°60'-14°N (blue).

Figure 61: Thin-section sketch (10x magnification) to illustrate key textural features of large (~2-8mm), rounded plagioclase phenocrysts in on-axis basalt samples from 12°6'-14°N. The brownish cast (when viewed with crossed polars) results from the thickness of the section.

Figure 62: Thin section sketches (20x magnification) to illustrate the textural features and associations of radial plagioclase and olivine crystal clusters in rock samples from the 13°19'N OCC.

Figure 63: Thin section sketch (10x magnification) illustrating the key textural features and associations of rounded, simply twinned clinopyroxene crystals found in basalts from dredges D05 and D10, 13°19'N.

Figure 64: Trace element ratio vs. isotope data for basalts from 12°6'-14°N. On-axis OCC spreading sites (blue) and magmatic spreading (red) sites are shown.

Figure 65. Summary of mantle convection models. 1) Whole mantle convection: plates break through the transition zone. 2) Layered mantle convection: plates are confined to the upper mantle. 3) Whole mantle convection with deep blobs of primordial mantle. 4) Layered mantle convection with a deep layer of primordial mantle. 5) Whole mantle convection with plate depletion at subduction zone. From Albarède and van der Hilst (1999).

Figure 66: In the $^{208}Pb/^{204}Pb$ vs. $^{206}Pb/^{204}Pb$ plot, the 12°60'N-14°N on-axis array (black) lies parallel to the NHRL (Northern Hemisphere Reference Line, red broken line). The triangular array formed by Atlantic PetDB MORB data is shown in blue. The on-axis array appears to primarily represent mixing between DMM and FOZO. Displacement off the trend to higher $^{206}Pb/^{204}Pb$ values is seen for off-axis M1 (pink) and to a lesser extent for M2 (yellow) basalts, and appears to represent three-component mixing between DMM-HIMU-FOZO. Note that for M1, n=6, sample markers overlap. Mixing between DMM and a higher proportion of HIMU-FOZO is shown by the solid blue line. Errors for the data from this study (M1, M2, on-axis) are shown by red marker.

Figure 67: $^{206}Pb/^{204}Pb$ vs. $^{87}Sr/^{86}Sr$ isotope data for the Atlantic (blue, PetDB MORB data), on-axis rocks from 12°60'-14°N (black) and off-axis M1 (pink) and M2 (yellow) basalts. M1, M2 and on-axis rocks define mixing between primarily DMM-HIMU-FOZO, with M1 and M2 group basalts trending toward mixing with a greater proportion of HIMU. The translucent green oval shows the position of the FOZO array with greater precision than the label.

Figure 68: $^{143}Nd/^{144}Nd$ vs. $^{206}Pb/^{204}Pb$ isotope data for the Atlantic (PetDB, MORB blue), on-axis samples from 12°60'-14°N (black), and off-axis M1 (pink) and M2 (yellow) basalts define mixing between primarily DMM-HIMU-FOZO. The translucent green oval shows the position of the FOZO array with greater precision than the label.

Figure 69: $^{143}Nd/^{144}Nd$ vs. $^{87}Sr/^{86}Sr$ data (Atlantic PetDB MORB data –blue, on-axis 12°60'N-14°N - black, off-axis M2 - yellow, M1 - pink) separates the HIMU and FOZO end-members spatially from EMI and EMII, showing that FOZO and HIMU are the enriched end-member components contributing to the 12°60'N-14°N array, and that M1 forms primarily from mixing between HIMU and

FOZO.The translucent green oval shows the position of the FOZO end-member with greater precision than the label.

Figure 70: $^{207}Pb/^{204}Pb$ vs. $^{206}Pb/^{204}Pb$ isotope data for the Atlantic (PetDB MORB, blue), on-axis samples from 12°6'-14°N (black), and off-axis M1 (pink) and M2 (yellow) basalts define mixing between primarily DMM-HIMU-FOZO. The translucent green oval shows the position of the FOZO array with greater precision than the label.

Figure 71: Δ7/4 and Δ8/4 plots for Atlantic (PetDB MORB, blue), on-axis 12°6'N-14°N (black), and off-axis basalts M2 (yellow) and M1 (pink) show a trend toward HIMU for M1 and M2 basalts. This trend is most clearly illustrated by the Δ8/4 vs. $^{206}Pb/^{204}Pb$, where M1 basalts extend to very low values of Δ8/4 (~-40). The translucent green oval shows the position of the FOZO array with greater precision than the label.

Figure 72: Trace element ratio data for on-axis (black), and off-axis M2 (yellow) and M1 (pink) basalts. This trace element ratio data is fractionation and melt fraction independent, and shows that M1 rocks form from an enriched HIMU source, whilst on-axis and M2 rocks form from more depleted bulk sources. For the sources component field positions, refer to Table 13.

Figure 73: Trace element ratio data for on-axis (black) and off-axis M2 (yellow) and M1 (pink) basalts. HIMU sources are enriched in Th relative to Pb, without an accompanying increase in Rb/Sr. M1 basalts trend toward high Th/Pb values, but have Rb/Sr values which lie within the on-axis array.

Figure 74: Isotope ratio vs. trace element ratio plots show that off-axis M1 (pink) basalts are the most enriched in terms of source, whilst M2 (yellow) basalts are some of the most depleted (enriched here referring to radiogenic Sr and Pb, and unradiogenic Nd isotopes). The on-axis array from 12°6'-14°N (black) occupies the centre of the compositional array.

Figure 75: REE plot showing mantle end-member inputs for modelling. HIMU (green) composition is that of Hannigan *et al*., (2001). Enriched (pale brown), depleted (dark brown) and average DMM (medium brown) compositions are from Workman and Hart (2004).

Figure 76: REE plot to illustrate bulk compositions calculated from mixing between Av. DMM (Workman and Hart (2004), and HIMU (Hannigan *et al,*. (2001) end-members.

Figure 77: REE plot to illustrate bulk compositions calculated from mixing between Enr. DMM (Workman and Hart (2004), and HIMU (Hannigan *et al*., (2001) end-members.

Figure 78: REE plot to illustrate bulk compositions calculated from mixing between Dep. DMM (Workman and Hart (2004), and HIMU (Hannigan *et al*., (2001) end-members.

Figure 79: Compositions of real rocks from on-axis (12°60'-14°N – AXD and AXE), and off-axis (13°19'N, M1D, M1E, M2D and M2E). These samples represent the compositional end-members of the three basalt groups. These

compositions are colour coded, blue for on-axis rocks, yellow for M2, and pink for M1. The two compositions in each colour represent the enriched (E) and depleted (D) ends of the compositional spectrum for each basalt type in the ~15°N region.Their compositions will be reproduced by the model in order to calculate melting conditions at 12°60'-14°N. Compositions of DMM (brown colours, Workman and Hart, 2004), and HIMU (Green; Hannigan *et al*., 2001) are shown for comparison.

Figure 80: Modelled compositions (dotted lines) matching on-axis real rock samples AXD and AXE (solid blue lines). Also shown are HIMU in green (Hannigan et al., 2001) and Average DMM in black (Workman and Hart, 2004). The dotted lines illustrate the model compositions most closely matching those of the natural rocks. The models match the compositions closely, though the LREE end of the modelled AXD equivalent is too depleted to match the natural rock.

Figure 81: Modelled compositions (dotted lines) matching off-axis real rock samples M2D and M2E (solid yellow lines). Also shown are HIMU (Hannigan et al., 2001) and Average DMM (Workman and Hart, 2004). The dotted lines illustrate the model compositions most closely matching those of the natural rocks. The models reproduce the compositions well.

Figure 82: Modelled compositions (dotted lines) matching off-axis real rock samples M1D and M1E (solid red lines). Also shown are HIMU (Hannigan et al., 2001) and Average DMM (Workman and Hart, 2004). The dotted lines illustrate the model compositions most closely matching those of the natural rocks. The models do not reproduce the compositions well, especially at the M- and HREE end of the compositional spectrum.

Figure 83: Diagram to show the natural composition of M1E (red), and the modelled composition (yellow dashed), resulting from the model inversion. The new bulk composition (purple) obtained is shown. Also shown are HIMU (Hannigan et al., 2001) and Average DMM (Workman and Hart, 2004).

Figure 84: Diagram to show the natural composition of M1E (red), and the modelled composition (yellow dashed), resulting from the input of the new bulk composition (purple). Also shown are HIMU (Hannigan et al., 2001) and Average DMM (Workman and Hart, 2004). The diagram shows that the model composition now closely resembles the natural composition, representing a substantial improvement over the initial model output.

Figure 85: Enrichment zones and their correlation with bathymetric highs at sites such as the Iceland and Azores hotspots. An enrichment zone is also seen at the FTFZ, despite the lack of gravimetric or bathymetric evidence to suggest the influence of a mantle hotspot here. After Bougault *et al*. (1988), data from PetDB (black) and this study (red).

Figure 86: Geochemical characteristics of MAR basalts (0-50°N). A red line denotes the position of the geochemical limit at 17°1'N. After Dosso (1993). Data from PetDB (black) and this study (red).

Figure 87: Variations in trace element ratios with latitude on the MAR (5°S-60°N). Data from PetDB (black) and this study (red).

Figure 88: Variations in $^{206}Pb/^{204}Pb$, $87^{Sr}/^{86}Sr$ and $^{143}Nd/^{144}Nd$ data with latitude on the MAR (5°S-60°N). Data from PetDB (black) and this study (red).

Figure 89: Rose diagrams generated by the qualitative data from Table 24. The diagram shows that the 15°2'-12°60'N shape is similar to that of the Azores, but shares somewhat fewer characteristics with the other shapes. The bottom circle acts as a key, showing the positions of different scores and geochemical attributes.

Figure 90: Overlaid rose diagrams are used to compare the sites directly. In each case, 12°60'N-15°20'N data are overlaid with the data from another site. In this way, 12°60'N -15°20'N data which are not matched shows through as blue, data from the overlapping locality which is not matched is orange, but overlap (where the data is the same) is brown. Hence, when 12°60'N-15°20'N is overlaid with 12°60'N -15°20'N data, the whole shape is brown. The best match to the 12°60'N -15°20'N data is the Azores data.

Figure 91: Major element, trace element and isotopic data for basalt enrichment zones on the MAR. 12°60'-15°20' data from this study and PetDB. All other data from PetDB. RR= Reykjanes Ridge. The data show that the 12º60'-15º20'N area is geochemically most similar to the Azores.

Figure 92: Trace element ratio data for enrichment zones on the MAR. 12°60'-15°20' data from this study and PetDB. All other data from PetDB. Data for each region is shown where available. Once again, the 12º60'-15º20'N area is geochemically most similar to the Azores.

Figure 93: K/Ba vs. La/Sm data for enrichment zones on the MAR. 12°6'-15°2' data from this study and PetDB. All other data from PetDB. Data for each region is shown where available. Once again, the 12º60'-15º20'N area is geochemically most similar to the Azores.

Figure 94: ΔNb plot for the discrimination of MORB and OIB, as described by Fitton (2007). The plot shows 12°6'N-14°N on-axis (black), M1 (pink) and M2 (yellow) data. All data lie above the 'ΔNb=0' line (the lower line on the diagram), and are therefore in the OIB range

Figure 95: ΔNb plot for the discrimination of MORB and OIB, as described by Fitton *et al*., (1997) and Fitton (2007). 12°60'-15°20' data and Azores data lie within the OIB range. 17°1'-22°N data and 23°N data (yellow group) fall below the ΔNb=0 line (the lower line on the diagram) in the N-MORB range. The Iceland data array includes data for the Reykjanes Ridge, and crosses the ΔNb=0 line from OIB into N-MORB south of Iceland on the Reykjanes Ridge, where the hotspot ceases to interact with the ridge. 12°60'-15°20' data from this study and PetDB. All other data from PetDB. There is no data available for 45°N or 1°S-2°N.

Figure 96: ΔNb vs. latitude plot for the discrimination of MORB and OIB. The plot shows data fom PetDB and this study.

LIST OF TABLES

Table 7: 2σ standard deviations for ICPMS precision (this study) are typically 5-6%. Average U, Th, Ta and Nb values are higher, due to poor repeatability on BIR-1 in some runs. Average 2σ SD values as quoted here are applied to the data in this thesis.

Table 8: Percentage errors for ICPMS accuracy in this study, as calculated from average values for analysed SRMS. Errors are typically 1-6%, though some higher errors are reported for individual SRMs, particularly BIR-1.

Table 9: Reproducibility data for the NBS 981 standard at NOC, 2004-present. n=62.

Table 10: SEM precision data for major elements (this study). Precision is 2-4% for Fe, Ca, Si, Al and Mg oxides, which is sufficient for use in stoichiometric calculations. Reproducibility of Na, Ti and Cr is very poor.

Table 11: Clinopyroxene compositions obtained from SEM spot analysis of individual crystals from the 13°19'N OCC provide an estimate of the compositions of clinopyroxene at the site.

Table 12: The relationship of the data array from this study to average N-MORB values, as given by Hoffmann (1988).

Table 13: Normalised average mineral compositions calculated from SEM analyses of crystals in basalt from 12°60'-14°N. Symbols are used in Figure 45 to show the positions of these mineral compositions.

Table 14: DMM isotope values from Su and Langmuir (2003), HIMU, EMI and EMII isotope values, from Rollinson (1993) p233-236, FOZO data from Hauri *et al*. (1994) and Stracke *et al*. (2005).

Table 15: Trace element ratio concentration data for a range of incompatible trace element pairs, showing average values for basalts with a variety of source characteristics. Data from Hart *et al*. (1992), Armienti and Gasperini (2007), this study.

Table 16: Raw compositions of input sources. Modelled HIMU composition from Hannigan *et al*. (2001). Enriched, depleted and average DMM are from Workman and Hart, (2004). Tm data for DMM are unavailable, and so data (red, italicised) are interpolated and included to allow plotting of data on logarithmic REE plots.

Table 17: Bulk compositions calculated from mixing between Av. DMM (Workman and Hart (2004), and HIMU (Hannigan *et al*., (2001) end-members.

Table 18: Bulk compositions calculated from mixing between Enr. DMM (Workman and Hart (2004), and HIMU (Hannigan *et al*., (2001) end-members.

Table 19: Bulk compositions calculated from mixing between Dep. DMM (Workman and Hart (2004), and HIMU (Hannigan *et al*., (2001) end-members.

Table 20: Simplified garnet-phase and spinel-phase assemblages and mineral proportions for the mantle source. From McKenzie and O'Nions (1991).

Table 21: The proportions of melting in the spinel- and garnet phase melting fields applied in the model.

Table 22: Compositions of real rocks from on-axis (12°60'-14°N), and off-axis (13°19'N, M1 and M2). These samples represent the compositional end-members of the three basalt group. Their compositions will be reproduced by the model in order to calculate melting conditions at 12°60'-14°N.

Table 23: Example data to illustrate the working model. A real composition (M2D) is shown alongside three modelled iterations (melt fractions 9.8-10%), as well as the misfit function data for these three iterations. A lower RMS misfit indicates less deviation from the natural data.

Table 24: Table outcome data, showing the best model outcomes for each of the three source models. The table also shows the percentage of HIMU contributing to the melt composition, the percentage of garnet melting contributing to the composition, the melt fraction of the melt, and the goodness of fit value for each outcome. Outcomes from Depleted DMM and Average DMM produce better goodness of fit data than Enriched DMM combinations.

Table 25: The composition of the modelled modified bulk source, calculated by force-fitting the model to reproduce the composition of the real rock 'M1E'.

Table 26: Qualitative illustration of the variation in a range of geochemical characteristics between different enrichment zones on the MAR. Cell colours are used to denote variations from the average value. Data used to obtain averages is PetDB data for basalt 5°S-60°N on the MAR. See colour key for details.

DECLARATION OF AUTHORSHIP

I, Samantha Clare Wilson, declare that the thesis entitled '**MANTLE SOURCE COMPOSITION BENEATH THE MID-ATLANTIC RIDGE: CONTROLS ON THE DEVELOPMENT OF E-MORB SEGMENTS AND OCEANIC CORE COMPLEXES**' and the work presented in the thesis are both my own, and have been generated by me as the result of my own original research. I confirm that:

- this work was done wholly or mainly while in candidature for a research degree at this University;
- where any part of this thesis has previously been submitted for a degree or any other qualification at this University or any other institution, this has been clearly stated;
- where I have consulted the published work of others, this is always clearly attributed;
- where I have quoted from the work of others, the source is always given. With the exception of such quotations, this thesis is entirely my own work;
- I have acknowledged all main sources of help;
- where the thesis is based on work done by myself jointly with others, I have made clear exactly what was done by others and what I have contributed myself;
- none of this work has been published before submission

Signed:  **Date:** 29/10/10

ACKNOWLEDGEMENTS

I would like to thank my supervisory panel, Bramley Murton, Rex Taylor and Damon Teagle for their support and patience, and for providing me with the opportunity to write this work in the first place.

I'd also like to thank Henry Dick for sharing his wealth of knowledge on mantle peridotites, ophiolites and oceanic core complexes, and for allowing me to stay in his wonderful home whilst visiting WHOI.

Thanks also to Matt Cooper, Ian Croudace, Loraine Foley, Tina Hayes, Laura Hepburn, Andy Milton and Ross Williams for laboratory support, and to Tim Le Bas for help when learning ArcGIS.

All JC007 bathymetry presented in this thesis was post-processed by Tim Le Bas, NOCS.

A special thanks goes to Bob Jones and John Ford for producing thin-sections and FTIR wafers rapidly and superbly.

This work was funded by NERC.

CHAPTER ONE – INTRODUCTION AND GEOLOGICAL CONCEPTS

This chapter discusses the concepts and hypotheses that form the basis of this thesis. It introduces the geology of the mid-ocean ridge (MOR) system, and provides a literature review of the current state of knowledge of MOR processes.

1.1 – INTRODUCTION

At mid-ocean ridges, melt is produced as tectonic plates move apart, decompressing the mantle beneath. The resulting mafic material is accreted to the separating plates, forming new oceanic crust.

Geological observations reveal that the ridges are not continuous. They are segmented by 'numerous rigid and non-rigid discontinuities' (MacDonald *et al*., 1991). Tectonic segmentation occurs at several scales that overlap or form a continuum (Batiza, 1996). By convention, segmentation is described hierarchically, according to the method of Macdonald *et al.* (1988). The first level of segmentation (1st order) occurs where the ridges are offset laterally by large transform faults. Ridge segments bounded by transform faults may be further segmented by non-transform (2nd order) offsets (NTOs), whereby the ridge axis is laterally offset without the presence of significant transform faulting (Sempéré *et al*., 1993). Segmentation also takes place on a finer geographic scale, in the form of (3rd and 4th order) small offsets (jogs) in axial valleys and neovolcanic zones.

Ridge spreading rates are variable, and usually categorised as fast, medium or slow. In general, fast-spreading ridges have full spreading rates >100 mm/yr, medium spreading ridges between 100 and 55 mm/yr and slow spreading ridges 55 to 20 mm/yr.

Ridge morphology is thought to be partially dependent on spreading rate; fast- and slow-spreading ridges have substantially different morphology. Slow-

spreading ridges typically have 1-2km deep axial valleys, whereas fast-spreading ridges form axial highs (Ito and Behn, 2008).

Geophysical and morphological observations suggest that upwelling mantle is focused toward the centre of (1st order) ridge segments, and therefore these areas are magmatically robust (Whitehead *et al*., 1984; Lin *et al*., 1990; Cannat *et al*., 1995). At segment ends, mantle focusing away from the area leads to reduced magmatism. Here, cooling related to the proximity of a transform fault affects the thermal structure of the upper mantle beneath the segment. Microseismicity studies show that the depth of earthquake activity increases from the segment centre to the segment ends, indicating that the depth of the cold brittle zone is greater in distal areas (Gac *et al*., 2003).

On slow-spreading ridges such as the Mid-Atlantic Ridge (MAR), mantle peridotites are recovered from inside-corner bathymetric highs (adjacent to ridge-transform intersections).

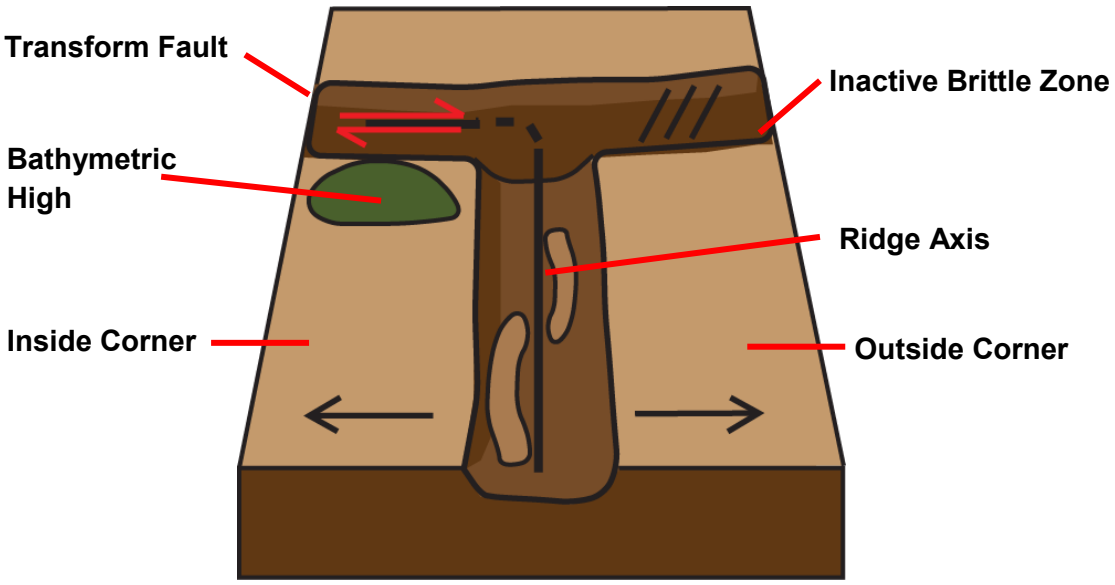

Figure 1: Diagram to show the occurrence of bathymetric highs on inside corners of slow-spreading ridge segments. After Severinghaus and MacDonald (1988).

Peridotite is exposed in these cold, brittle regions by exhumation on shallow detachment faults (e.g. Cannat *et al*., 1997). As these faults evolve, structures known as oceanic core complexes (OCCs) are formed. OCCs consist of a

domed, corrugated massif, formed from exhumed lower crustal and upper mantle rocks, bounded by a shallow detachment fault. They are reported at many inside-corner sites globally (e.g. Atlantis Massif, Kane Megamullion, Atlantis Bank, Fuji Dome).

Whilst the phenomenon of detachment-fault-related spreading is well described (e.g. Cannat, 1993; Cann *et al*., 1997), little is known about the mechanisms that control the transition between magmatic and 'fault-dominated' spreading states. OCC development is considered by many (e.g. Karson, 1990; Tucholke and Lin, 1994; Tucholke *et al*., 1998; Escartín *et al*., 2003) to be related to periods of amagmatism (low/no melt provision). Therefore, their formation at segment-end inside corners, far from the locus of mantle focusing, is explicable.

Recently, however, OCCs have been identified in segment-centre positions on the MAR (12º60'N-15º20'N) between the Fifteen-Twenty (FTFZ) and Marathon Fracture Zones (Smith *et al*., 2006). No conventional intra-segment mantle focusing model can be applied to explain their formation here.

This thesis investigates the cause of segment-centre OCC formation between 12º60'N-14°N. This segment is unusual in that the ridge topography is irregular and chaotic in comparison to that of surrounding segments (Smith *et al*., 2006). The thickness and continuity of volcanic cover is highly variable. At numerous sites, corrugated, axis-normal OCC domes mark positions where ridge spreading is taken up via movement on low-angle detachment faults (MacLeod *et al*., 2002; Smith *et al*., 2006). At these sites, evidence for axial volcanism is scarce. However, the OCCs are interspersed on a 10-20km scale with magmatic areas where classic slow-spreading ridge morphology is observed.

It has been noted (Dosso *et al*., 1991; Hémond *et al.*, 2006) that the 12º60'N-14°N area produces enriched basalt (E-MORB). Abundant E-MORB signatures are commonly taken to indicate plume influence, and are associated with high melt production and thick crust. Clearly, the 12º60'N-14°N area does not conform to these criteria. The origin of E-MORB signatures here is another characteristic of the segment which is not yet fully understood.

A lack of neovolcanic terrain in the axis at OCCs suggests that faulting accommodates the majority of the spreading at these sites, and that magmatism is inactive, or greatly reduced. A reduction in melt supply may therefore cause (or contribute to) the development of OCCs.

There are a number of possible reasons for reduced melt supply at OCCs. Some of these relate to *production* of melt in the mantle, and others to its *provision* at the ridge. Variations in mantle composition, including hydration, and changes in mantle temperature could both affect the amount of melt produced. Changes in 'crustal plumbing' due to localised tectonic differences beneath the axis may dictate low melt delivery to some regions of the ridge.

It is also possible that a form of fine scale mantle focusing operates beneath the 12º6'N-14°N area, limiting melt provision to OCC sites. The length scales at which mantle focusing varies are not well constrained. Extremely localised melt focusing variations could explain fluctuations in melt supply on a limited geographic scale. In this model, mantle is focused away from core complex sites in the same way as it is focused away from 1st order segment ends, creating 'inside corner' conditions thought to be conducive to OCC formation.

This study addresses these hypotheses using major element (XRF), trace element (ICPMS), H_2O content (FTIR) and isotopic (TIMS) analyses, combined with petrological data, geochemical modelling and structural evidence (TOBI imagery/bathymetry). The key aim is to identify the causes of apparent magma starvation at the OCCs, and investigate how this relates to their formation.

Melt fractions, trace elements, incompatible TE ratios and Pb, Sr and Nd isotope data will be examined to constrain mantle source composition. Isotope data and the ratios of very incompatible trace elements to moderately incompatible trace elements will be used to distinguish genuine source enrichments from those arising as a function of variable melt fraction. Trace element enrichments arising from source composition correlate with source isotopic characteristics. This allows them to be distinguished from enrichments arising from melt fraction. Mantle temperature changes will be assessed by considering variations in the depth of melting alongside source geochemistry. If a distinct geochemical signature for OCC sites is not identified, the development of segment centre

OCCs may be attributable to melt provision related hypotheses (mantle focusing and/or crustal plumbing effects).

Major element, trace element and isotopic data for 12°6'N-14°N will be compared to data for the surrounding central MAR. Thus the relationship between source composition, extent of melting, E-MORB production, ridge morphology and volcanism can be explored. This will allow characteristics specific to the 12°60'N-14°N area, which may contribute to its unusual morphology and geochemistry, to be identified.

SUMMARY OF AIMS

1) Use geochemical, petrological and structural data to identify the cause of OCC development in the central parts of the 12º60'-15º20'N segment of the MAR, by distinguishing between the following hypotheses:

    - OCCs form as a result of compositional/temperature/hydration variations within the underlying mantle. Variations must exist as small (~15-20km across) 'blobs' in the mantle, as this is the typical spacing of OCCs at the surface.

    - OCCs form as a result of unusually fine scale mantle focusing. Core complexes may occur at the distal edges of 3D mantle upwellings, whereas magmatic areas lie above the centres. This implies mantle upwelling with a spacing of ~15-20km, as this is the typical spacing of OCCs at the surface.

    - OCCs form as a result of tectonic characteristics in the underlying crust. Melt is produced beneath OCCs, but is unable to reach the surface. Melt may freeze into the crust as gabbro, or travel along axis away from OCC sites in dykes.

2) Use geochemical and petrological data for 12º60'-15º20'N and the surrounding MAR to explain the occurrence of a 'plume-like' E-MORB geochemical anomaly in a segment where magmatism appears limited.

3) Produce a model that provides an explanation for the coexistence of OCCs and the E-MORB geochemical anomaly at 12º60'-15º20'N.

1.2 - THE MID-OCEAN RIDGES

1.2.1- Introduction to the Mid-Ocean Ridges

Mid-ocean ridges are constructive tectonic plate boundaries, where hot, decompressing mantle upwells to 'fill the gap' as tectonic plates pull apart. The resulting melts cool and accrete to the separating plates, forming new seafloor. The Earth's MOR system hosts ~80 percent of global volcanism (Elliott, 2002), and contributes major fluxes of heat, volatiles and metals to the oceans (Kennish and Lutz, 1992). Ridges host a range of geological processes, both igneous and tectonic (Harrison, 1974; Harrison and Ball, 1973; Forsyth, 1977; Harrison and Stieltjes, 1976; Cordery and Morgan, 1992; Gràcia and Escartín, 1999).

Although first-order processes are well understood, there are some aspects of ridge behaviour about which questions remain. For example, the mechanism(s) that cause low-angle detachment faulting (common on slow-spreading ridges) are not fully understood.

1.2.2 - Mid-Ocean Ridges - Morphology and Spreading Rates

MORs are linear chains elevated 2-3km above the surrounding abyssal plain (Gràcia and Escartín, 1999), as a result of thermal uplift due to mantle convection (MacDonald *et al*., 1991). Spreading rates are traditionally described as varying from > 80-100 mm/yr in fast-spreading ridges to <20 mm/yr in slow-spreading ridges (Blondel and Murton, 1997). Variations in spreading rate are accompanied by substantial morphological and tectonic differences (Chen and Morgan, 1990a, b; Lizerralde *et al*., 2004).

Fast-spreading ridges are characterised by axial highs (~400m), sometimes with small linear depressions at their crests, no more than 100m in width (Dick *et al*., 2003). They have long, straight ridge sections (>100km) with small lateral offsets or large scale fracture zones (Gràcia and Escartín, 1999). Rift mountain topography is minimal (Phipps-Morgan *et al*., 1987) and point-source seamount volcanoes and sheet flows are common. Tectonics produces a dense population of small-throw fault scarps that face both into and away from the ridge axis (Carbotte and MacDonald, 1990). Abyssal hill topography is less pronounced than at slow-spreading ridges, and faulting is less prominent (Menard, 1967; Sleep and Rosendahl, 1976; Mutter and Karson, 1992; Gràcia and Escartín, 1999).

Slow-spreading ridges are dominated by composite volcanoes, hummocky volcanic ridges and pillow lavas. The relief is highly variable, with rough, elevated rift-mountain topography, and deep axial rift valleys (>1km high) bounded by high, steeply sloped, inward-facing normal faults (Phipps-Morgan *et al*., 1987; Carbotte and Macdonald 1990; Shaw and Lin, 1993; Gràcia and Escartín, 1999). ‘Intermediate’ spreading ridges are composed of alternating sections which have either slow- or fast-spreading ridge morphology (Dick *et al*., 2003).

MORs are divided into segments (Schouten *et al*., 1985) delineated by numerous rigid and non-rigid discontinuities (MacDonald *et al*., 1991). Segments develop near-perpendicularly to the direction of least compressive stress, and orthogonal to the spreading direction. Tectonic segmentation occurs at several scales

(Allerton *et al*., 1993) that overlap or form a continuum (Batiza, 1996). Segments are categorised by scale and type, as described by MacDonald *et al*. (1991).

The first level of segmentation (first-order) occurs where ridges are offset laterally by large transform faults (Batiza, 1996). Segments bounded by transform faults may be further divided by non-transform (second-order) offsets (NTOs), whereby the ridge axis is laterally offset without significant transform faulting (Sempéré *et al*., 1993). Second-order discontinuities range in length from less than 10km to ~30km and vary in age offset from 0.5 to approximately 2.0Myr (Grindlay *et al*., 1990). Like transform fault boundaries, they have distinctive morphology in both on- and off-axis discordant zones. They are more clearly defined than segments on a finer geographic scale (Grindlay *et al*., 1990) which are known as third- or fourth-order discontinuities, or 'jogs', and manifest as small offsets in axial valleys and neovolcanic zones.

The length, frequency and morphology of ridge segments each vary with spreading rate. Figure 2 illustrates the differences between segment morphology at slow-spreading and fast-spreading centres.

Crustal thickness correlated ridge segmentation data shows that at the slow-spreading MAR, first-order segments range in length between ~15 and 100km (Lin *et al*., 1990; Gac *et al*., 2003), with an average value of ~40km (Gràcia and Escartín, 1999). On fast-spreading ridges such as the East Pacific Rise (EPR), segmentation is much less frequent (Magde and Sparks, 1997) and therefore first-order segments are typically longer.

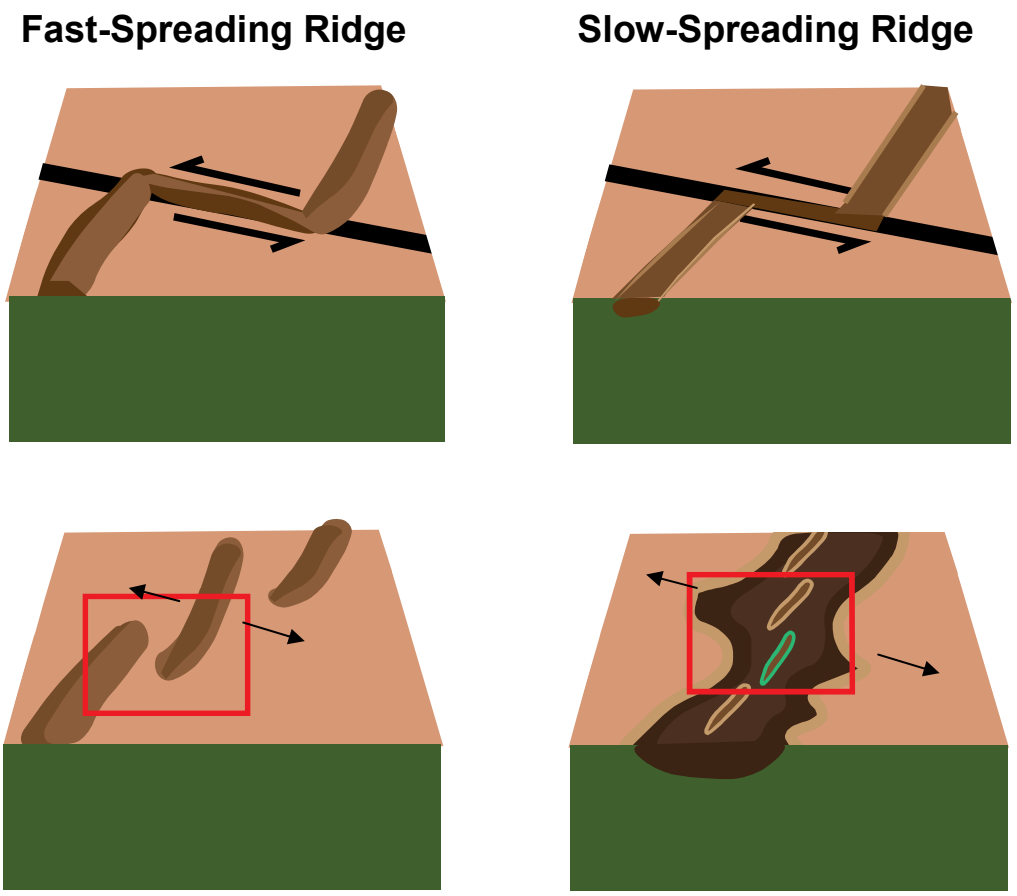

Figure 2: Mid-Ocean Ridge segments are classified according to morphology, length and longevity. First-order discontinuities (a) are transform faults, which offset the ridge axis by ~40 km and are usually long lived. Second-order discontinuities (b) are usually large overlapping spreading centres, which are well defined.

The tectonics of axial valley faulting is thought to be a significant contributor to the morphology of slow-spreading ridge segments. Thibaud *et al*. (1998) find that

the morphology of segments characterised by rough seafloor topography, deep, well-defined axial valleys and short segment length (such as 12°60'N-14°N) is *primarily* controlled by tectonic rift valley formation.

Qin and Buck (2005) present evidence for controls on maximum rift valley relief, which they argue is determined by the competition between isostasy and lithospheric geometry. If the axial lithosphere is much thinner than the flanking lithosphere, isostatic force will break outward dipping faults on the axis, stopping the deepening of the rift valley (axial failure mode). Conversely, if the thickness of axial lithosphere is close to that of the flanks, flexural bending will break new faults on the flanks (flanking failure mode), also stopping the rift valley from deepening (Qin and Buck, 2005, see Figure 3).

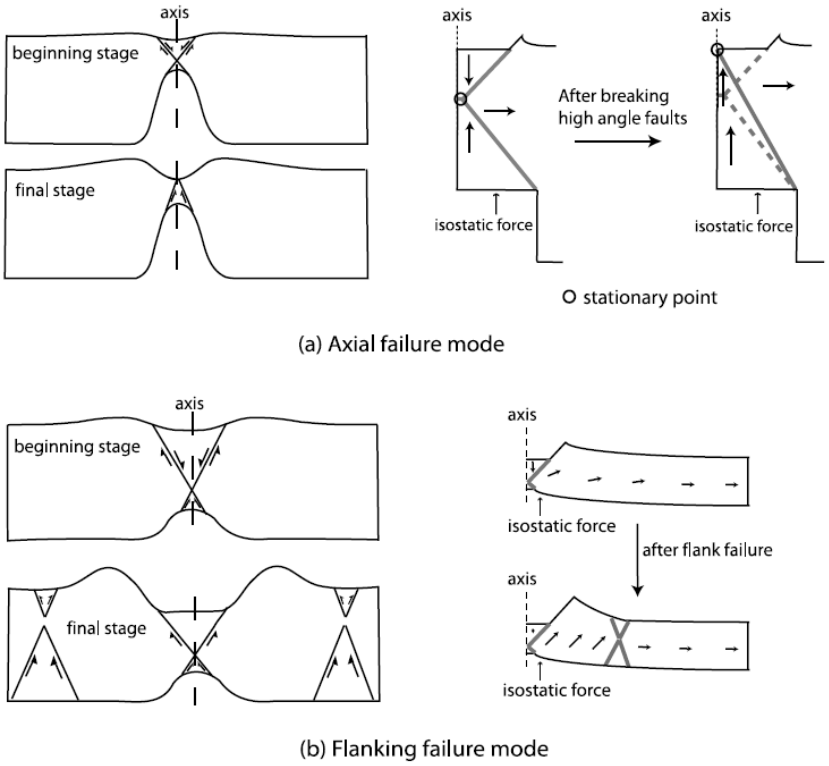

Figure 3: Models from Qin and Buck (2005) to show failure modes produced by their model. Arrows indicate the motion of the blocks. (a) Axialfailure mode. Two inward dipping normal faults cut the center of the axial lithosphere at the beginning stage and create the axial valley and flanking shoulders. The isostatic restoring force resists the downslide of the upper triangle and pushes up the stationary point (right). At the final stage the isostatic force pushes the stationary point onto the surface by breaking high-angle outward dipping faults, which stops the valley deepening. Dashed lines in Figure 4a (right) indicate inactive faults. (b) Flanking failure mode. Inward dipping faults form at the beginning stage the same as Figure 4a. With increasing extension, the flanks fail by bending at the

position where the curvature is the maximum. The flexural wavelength decreases with increasing extension and the flanking uplifts are limited to this wavelength (right). When the flanks completely fail, the wavelength gets to its minimum and rift valley reaches its maximum depth. From Qin and Buck, (2005).

Three dimensional temperature and rheology models have been used to investigate the effects of crustal thickness and ridge segmentation on the underlying lithospheric structure. At slow-spreading ridges, focused mantle upwelling causes substantial variations in crustal thickness and temperature along axis. This results in a weak zone in the lower crust that decouples brittle upper crust from upper mantle. In contrast, fast-spreading ridge segments with little crustal thickness variation are uniformly weak along axis (Shaw and Lin, 1996). The dependence of lithospheric structure on spreading rate explains the first order observations of large, widely spaced faults at slow-spreading ridges and small, closely spaced faults at fast-spreading ridges (e.g., Searle and Laughton, 1981). The development of low-angle detachment faults, and related exhumation of peridotite, has been reported from many slow-spreading ridge segment ends. This suggests that low-angle faulting also plays a substantial role in the development of slow-spreading ridge morphology.

Although morphology is strongly dependant on spreading rate, rapid morphological changes along intermediate spreading ridges indicate that it also depends on other factors such as melt supply (Sempéré *et al*., 1997), as well as the geometry of the ridge and the thermal structure and composition of the underlying mantle (Dick *et al*., 2003).

1.2.3 – Mid-Ocean Ridges- Crustal Thickness and Thermal Structure

Mantle temperature and spreading rate are considered to be the two fundamental variables that determine the extent of mantle melting and crustal production at MORs (McKenzie and Bickle, 1988; Niu *et al*., 2001).

Seismic and gravity data indicate that the average thickness of oceanic crust is ~6km. This is fairly constant at intermediate- and fast-spreading ridges, but

variable in slow-spreading ridges (Cannat, 1996). At very low spreading rates seismic crustal thickness is predominantly dependent on spreading rate, with ridges producing thinner crust at rates of <20mm/yr (White *et al*., 2001)

At fast-spreading ridges, crustal thickness remains similar for large distances along the ridge (Fox *et al*., 1984; MacDonald *et al*., 1988). A lack of peridotite outcrops suggests that the crust is fully igneous in composition (Gràcia and Escartín, 1999). Conversely, crustal thickness variations from segment centres at the MAR (shown by negative Residual Mantle Bouguer Anomalies - (RMBA)), indicate that crustal thickness varies on individual segments by as much as 4km (Magde and Sparks, 1997).

Magmatism at fast-spreading ridges is fed by two-dimensional, sheet-like mantle upwelling (Lin and Phipps-Morgan, 1992; Gràcia and Escartín, 1999). Magmatism takes place along the length of the segment. The effects of ridge transform offsets on the thermal regime are less substantial than in slow spreading, where the thermal structure is thought to reflect focused upwelling. Here, the hottest region and thickest crust are at the segment centre, whilst colder areas with a thinner crust are found at segment ends (Whitehead *et al*., 1984; Lin *et al*., 1990; Cannat *et al*., 1995). Large negative RMBAs suggest that the crust is thickest (and hottest) at segment centres, which in turn suggests melt focusing beneath (Lin *et al*., 1990). Microseismicity data show that the depth of earthquake activity increases from the segment centre to the segment ends, indicating that the depth of the brittle zone is greater in distal areas (Gac *et al*., 2003).

The temperature field of a ridge segment is affected by the thermal and mechanical effects of offsets. Heat is thought to be conducted through transform faults and away from the segment. This cooling effect reduces melt production, and thus thinner crust is produced at the segment ends (Fox *et al*., 1980). Seismic investigations also show that crust thins progressively from the segment centre to the segment ends. This indicates lower crustal production at segment ends, therefore implying that less melt is available. Calculations by Neuman and Forsyth (1993) suggest that the cooling effect of proximity to a ridge offset should deepen the 750°C isotherm (less than 3km for 30km offset, but over 8km for

100km offset). They also predict that the 750°C isotherm deepens significantly as the magma supply is reduced. This effect is of the same order of magnitude as that caused by the offsets (if the melt supply decreases from enough magma to form a 6km thick magmatic layer, to enough to form a 5km layer). At slower spreading rates, the thermal effects of ridge offsets are much more dramatic than at faster ridges (Neuman and Forsyth, 1993).

On the MAR, crustal thickness varies by ~1-4km, on a scale of a few tens to hundreds of kilometres, with the thinnest crust correlating with discontinuities in the ridge axis (Cannat *et al*., 1995). Crustal thickness varies with changes in morphology and faulting patterns, which reflect the properties of the lithosphere beneath. Areas with thin overlying crust display the seismic and morphological characteristics associated with a cold, thick underlying lithosphere. In these areas, the axial lithosphere is probably thicker than the crustal layer. (Cannat, 1996).

Spreading rate is thought to influence the degree of lithospheric cooling under the ridge axis (Gràcia and Escartín, 1999). Mantle flow models suggest that at low spreading rates, conductive cooling at the top of the mantle column decreases melt production. Mantle upwelling slowly 'feels the effect' of conductive cooling from the top of the melt column earlier in its melting history than mantle upwelling quickly, leading to reduced melt production at slow-spreading ridges (Robinson *et al*., 2001; Dick *et al*., 2003). Minor changes in melt supply, ridge geometry or mantle composition then have a substantial effect on ridge morphology (Niu and Hékinian, 1997; Dick *et al*., 2003).

Studies of MAR segments with the same mantle potential temperature and spreading rate show that these are not the only two factors upon which crustal production and extent of melting relies. Whilst some segments have thick crust and axial topographic highs, others have thin, weak crust and deep axial valleys. Analyses show that source geochemistry is the additional variable which controls melt production, crustal thickness and axial morphology at these segments (Niu *et al*., 2001).

1.2.4 – Mid-Ocean Ridges - Mantle Flow and Melting

Magmatism at MORs is fed by melt extracted from the upwelling mantle. Melt aggregates in the upper mantle, held in magma chambers prior to eruption (Whitehead *et al*., 1984).

Two end-member models exist to describe the upwelling of mantle beneath mid-ocean ridges. The first is a 2-Dimensional model, whereby upwelling mantle forms a sheet-like structure beneath the ridge. Mantle corner flow is followed by horizontal flow perpendicular to the ridge axis. The second describes 3D upwelling, whereby mantle is focused toward the segment centre in a cone-like 'diapir', and travels radially away post corner flow. These models are summarised in Figure 4.

The 3D model is applied at slow-spreading ridges, where the heterogeneous distribution and abundance of basalt and peridotite across segments implies a melt-rich segment centre and a cold, melt-starved segment end. This model is supported by crustal thickness variations along slow-spreading segments, as discussed above (Fox *et al*., 1980; Choblet and Parmentier, 2000; Gac *et al*., 2003). Whilst the 2D model implies that upwelling occurs as a 'passive' response to spreading, the 3D model requires an element of active, buoyant upwelling of mantle underneath the ridge. This raises questions about the scale of upwelling diapirs, and the geographic spacing between them, which may define the length scale of ridge segmentation.

Laboratory flow experiments on 2D vs. 3D models suggest that the pattern of segment scale convection is a function of spreading rate and Rayleigh number. 2D 'passive upwelling' is found at low Rayleigh numbers and high spreading rates, suggesting that 3D 'buoyant upwelling' is only applicable at slow-spreading ridges (Kincaid *et al*., 1996). Tank experiments using water-glycerine mixtures show that gravitational instabilities develop as widely spaced, diapir-like bodies (Whitehead *et al*., 1984). Plagioclase peridotites from the SWIR are thought to have been depleted by on-axis melting, and subsequently refertilised by low-

degree melt impregnation, supporting a 3D interpretation of mantle melting and upwelling (Warren *et al*., 2002).

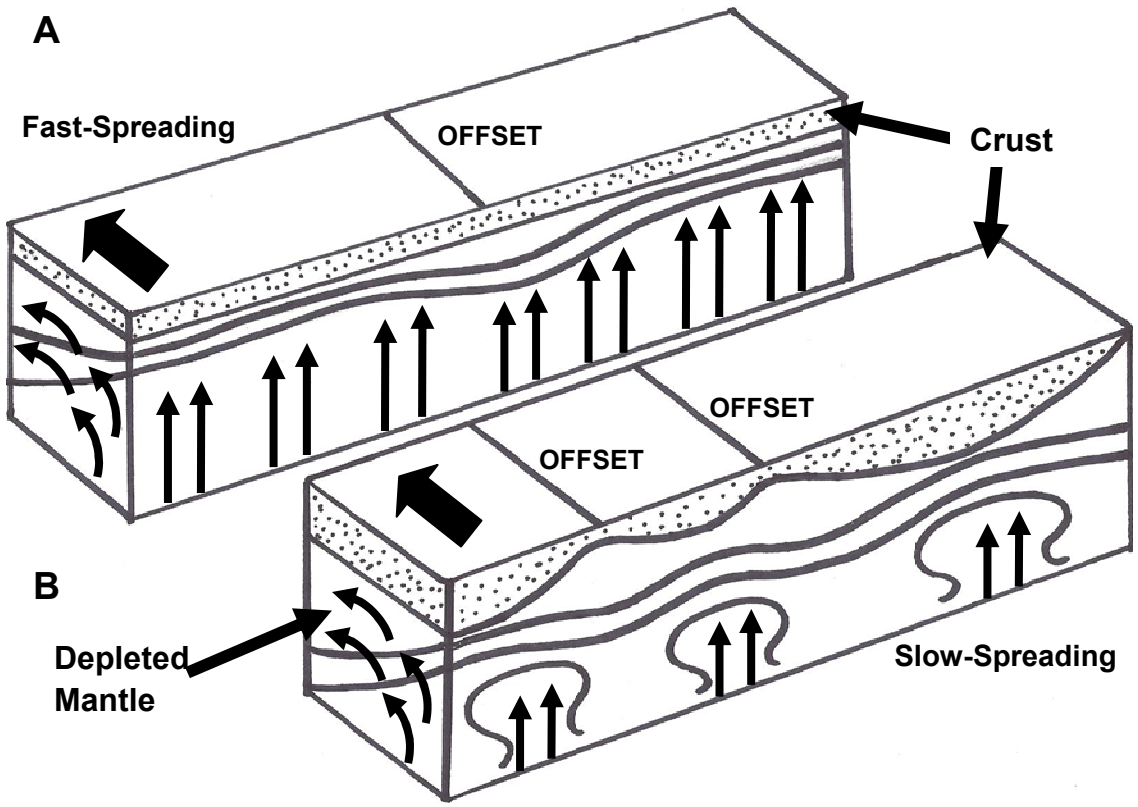

Figure 4: Along-axis block diagrams illustrating the differences between A) 2D (fast-spreading, sheet-like), and B) 3D (diapiric, slow-spreading) upwelling models. Heavy black arrows indicate the direction of spreading. Narrow black arrows show the nature of mantle upwelling in each model. After Gràcia and Escartin, (1999).

Numerical models identify conditions under which 3D upwelling can be considered a mechanism for magmatic segmentation at slow-spreading ridges. Smaller segmentation wavelengths (~40-70km) occur if the buoyant region is thinner; the thickness is primarily controlled by the temperature interval between the wet and dry solidii (Choblet and Parmentier, 2000). 3D upwelling models easily generate the 4km intra-segment thickness variations implied from RMBA analyses if combined with 3D melt migration. This increases crustal thickness all along segments, regardless of the wavelength of buoyant upwelling. This model

does not, however, predict the development of segment centre diapirs (Magde and Sparks, 1997).

Compositional data from MORB and abyssal peridotite suggest that the mantle beneath mid-ocean ridges typically melts by ~10-22% (Niu, 1997). Mantle temperature (Klein and Langmuir, 1987; McKenzie and Bickle, 1988) and composition (Asimow and Langmuir, 2003) are thought to have significant effects on the extent of partial melting. Modelling in the CMASN system (a system for modelling chemical and mineralogical behaviour of rocks via the use of an artificial composition - CaO, MgO, Al_2O_3, SiO_2 and Na_2O) suggests that total fractional melting in the plagioclase-spinel lherzolite transition zone is ~24%, which is adequate to produce the oceanic crust. The residual mineral proportions from this calculation closely match those of average abyssal peridotites (Presnall *et al*., 2002).

The conditions under which melting begins are dependent upon the composition, density and temperature of the mantle beneath the ridge. Niu and O'Hara (2008) suggest that dense, fertile mantle gives rise to deeper ridges relative to less dense fertile (more refactory) mantle. In this scenario the rate and magnitude of upwelling is weak. Conductive cooling retards melting at a greater depth than for shallow ridges, giving rise to a short melting interval. This may generate thinner crust than less dense fertile mantle beneath shallow ridges.

The mantle compositional variations required to explain global ridge depth and chemistry require a deep (~transition zone) isostatic compensation depth, suggesting that although ridges are shallow structures, melt production is partly controlled by deep processes in the mantle (Niu and O'Hara, 2008). Some suggest that significant partial melting typically begins at 120-60km depth (Klein and Langmuir, 1987; McKenzie and Bickle, 1988). However, Shen and Forsyth (1995) argue that melting beneath normal ridges commences in the spinel-garnet transition zone (about 60-70 km depth). This indicates much lower potential temperatures than suggested by earlier studies such as Klein and Langmuir (1987), the differences arising from the treatment of the $Fe_{[8]}$ parameter when correcting for source heterogeneity and fractionation (Shen and Forsyth, 1995). The MELT seismic tomography experiment across the EPR shows that the

largest amount of melt is found at ~30km depth, whilst deeper regions host less melt (Forsyth *et al*., 2000).

Petrological analyses of MORB (olivine + plagioclase + augite) show that crystallisation takes place in a pressure range 1atm-1GPa. MORB from fast-spreading ridges partially crystallises in the crust at segment centres, and in the crust and mantle at segment ends. MORB from slow-spreading ridges shows substantial partial crystallisation in the mantle, consistent with conductive cooling of the melt column (Herzberg, 2004).

The FAIM seismic refraction experiment, conducted in the western Mid-Atlantic, finds that at slow spreading rates, gabbro may be preferentially frozen into the crust (Lizzeralde *et al*., 2004). Analysis of the amount of gabbro stored shows that it is sufficient to account for a ~1.5km increase in crustal thickness in the areas studied, suggesting that changes in spreading rate may affect melt extraction processes, rather than melt production (Lizzeralde *et al*., 2004). The geochemistry of gabbros from the very slow-spreading SWIR shows that these rocks are mixtures of cumulate crystals and a significant proportion of basalt. This shows that they cannot be simply described as resulting from trapped melt frozen into the crust, but may originate from interstitial melt migrating through a crystal mush (Coogan *et al*., 2000). It may therefore be an oversimplification to assume that gabbro bodies on slow-spreading ridges are formed simply by melt lenses freezing into the crust.

Melt extraction is thought to be efficient, but exactly how it occurs is still a topic for debate. Some suggest that melt segregates into dunite channels (Kelemen *et al*., 1995a, 1995b), stripping out pyroxene and precipitating olivine as it travels through peridotite. Typical N-MORB is in chemical disequilibrium with harzburgite, and this model could explain this. Examinations of dunite channels in ophiolites have been used to infer melt focusing through these regions (e.g.: Hirschmann, 1995; Kelemen *et al*., 2000; Müntener and Piccardo, 2003; Sundberg *et al*., 2009). Observations of melt focusing in dunite channels have also been made at OCCs (i.e. Dick *et al*., 2008). However, some authors have argued that melt predominantly travels through the mantle by creep along grain boundaries (e.g. Dijkstra *et al*., 2003). Evidence of this process is seen in relict

peridotite, in the form of interstitial material and blebs (clinopyroxene/plagioclase), interpreted as trapped percolating melt (e.g. Rampone *et al*., 1997; Seyler *et al*., 2001).

U-series studies have proven crucial for understanding the nature of mantle melting and melt extraction (Stracke *et al*., 2006). Melt fraction and extraction rates directly control the composition of MOR basalts in terms of U-series nuclides (Richardson and McKenzie, 1994). U-Th-Pa-Ra systematics in MORB suggests melt flow rates too high to be explained by compaction-driven melt extraction (Connelly *et al*., 2009). Evidence from geochemical studies at Theistareykir, Iceland, provides strong support for the hypothesis that melt flow is channelled at ridges (Stracke *et al*., 2006). This study shows that U-Th-Pa-Ra systematics in MORB can be explained by models without chemical equilibrium between melt and solid, when variations in residual porosity, upwelling rate and melt velocity are properly accounted for.

It is likely that beneath MORs both processes are active to some degree, and work in conjunction to transport melt through the upwelling mantle to the surface.

1.2.5 - Mid-Ocean Ridges - Lithologies

The most common lithologies recovered from the mid-ocean ridges are basalts and basaltic glass, dolerites, gabbros and relict peridotites.

Basalt and glass are formed by eruption of lava at the ridge axis, and are found throughout a ridge segment. Basaltic glass is formed by quenching of melt on contact with seawater, and is amorphous, as it cools too rapidly for significant segregation of crystal phases from the melt.

Gabbros are formed by melt frozen into the lithosphere as lenses and magma chambers. Dolerites are emplaced as dykes, both individual and as part of the sheeted dyke complex, throughout ridge axes. Peridotite and gabbro are most frequently recovered on distal parts of ridge segments, where material from deep within in the lithosphere is exposed by faulting near to ridge transform offsets.

Peridotite is thought to be the material remaining after the mantle melting process. Its mineralogy is variable and dependant on original composition and alteration processes.

Minor lithologies such as authigenic carbonates and red jasper are formed at hydrothermal sites, along with associated sulphides. Their distribution is localised around sources of heat and fluid flux, which drive the hydrothermal activity.

1.2.6 – The Geochemistry of Mid-Ocean Ridge Basalt (MORB)

Basalts are rich in MgO and CaO and low in SiO_2 and Na_2O plus K_2O relative to most common igneous rocks.

Average Composition of N-MORB (Wt %)	
SiO_2	50.45
TiO_2	1.615
Al_2O_3	15.255
FeO	10.426
MnO	0.19
MgO	7.576
CaO	11.303
Na_2O	2.679
K_2O	0.106
P_2O_5	0.12

Table 1: Typical N-MORB composition, from Hart et al, 1999.

Normal MORBs (N-MORB) are tholeiites low in total alkalis and in incompatible trace elements. They have relatively flat REE patterns when normalised to chondritic values. Although MORB compositions are distinctive relative to average compositions of basalts erupted in other environments, they are not uniform (Hofmann, 2003).

The majority of MORBs are depleted in highly incompatible elements and radiogenic isotopes such as ^{87}Sr and ^{206}Pb. In contrast, enriched-MORB (E-MORB) is relatively enriched in these (Donnelly, 2002). Depleted MORB (D-MORB) compositions are depleted relative to MORB. Axial basalts from fast-spreading ridges are typically N-MORB with lower Na and higher Fe, whereas on slow-spreading ridges E-MORB compositions are also commonly found. High Na may reflect small degrees of mantle melting, whilst high Fe may be an indicator of deep mantle melting (Dick *et al*., 2003).

MORB compositions are a continuum. However, the concept of D-, N, and E-MORB is useful for comparing different compositional regimes (Hofmann and Hémond, 2006). The wide variety of compositions seen in MORB can be explained by several factors. The first is the composition of the mantle source, which may vary from geochemically depleted to enriched. Parameters such as K_2O/TiO_2 can be used as an indicator of the enrichment of the mantle source (Shen and Forsyth, 1995). Mantle compositional heterogeneities may arise from inclusion of subducted oceanic crust, oceanic island material (OIB input- see Hémond *et al*., 2006) or subducted sediment. They may also arise from previous episodes of melting, refertilisation or metasomatism (metasomatism, see Sun and Hanson, 1975). These mechanisms alter the chemistry of the mantle source, and therefore have a substantial effect upon the composition of the MORB they produce.

E-MORB can form as a result of melting heterogeneous mantle. Donnelly *et al.,* (2004) present data from the MAR south of the Kane FZ, where a small proportion of basalts have E-MORB signatures. Using trace element and isotope systematics, the authors show that this E-MORB is generated by early melting during subduction (where mantle material is mixed with low-degree crustal melts) followed by a later melting stage beneath the MOR.

Whilst basalt initially acquires its chemical characteristics from the source, its geochemistry is also influenced by a number of other factors (Rubin *et al*., 2009). The composition of basalt is strongly dependent upon melt fraction. As incompatible elements in the mantle enter the melt more readily than compatible elements, they are preferentially removed during the earliest phases of melting. If the melt fraction is low, these elements are proportionally more significant in the resulting melt than if the melt fraction is high. Therefore, low melt fraction melting of a depleted mantle source can generate E-MORB compositions with LREE enrichment, whereas high melt fraction melting of a LREE enriched source can produce compositions closer to N-MORB.

The thermal regime beneath the ridge determines when the melting path begins and ends. The length of the melt path, as well as the depth at which it begins and ends, are important controls on melt fraction and on the resulting basalt composition. For example, a short melt path that starts deep and does not persist long after the garnet-spinel transition will have a small melt fraction, and chemistry which reflects the high percentage of the melt derived from garnet-phase mantle. If the same starting melt follows a long melt path to shallower depths in the spinel field, a higher melt fraction results. This melt will have a composition much more reflective of spinel chemistry because the garnet component (though still included) is now less proportionally significant.

Variations in the final depth of melting may be due to cooling near the surface, effects of nearby transform faults, and the local importance of dynamic upwelling (Shen and Forsyth, 1995). Models have shown that lithospheric thickness also controls the extent of partial melting. Seamounts on old ocean floor (thick lithosphere) generate small amounts of partial melting, whereas those on younger, thinner lithosphere generate higher degrees of partial melting. At low degrees of partial melting, incompatible components are more compositionally significant, and basalt compositions are more enriched (Ito and Mahoney, 2005.) At MORs, the cold, thick lithosphere beneath slow-spreading ridges may generate E-MORB by the same mechanism. If melting is also suppressed by conductive cooling of the melt column, this further affects the amount of melt produced (Robinson *et al*., 2001; Dick *et al*., 2003). Recent studies suggest that

regional mantle heterogeneity is generally preserved in MORB most clearly where the melt supply is low (Rubin *et al*., 2009).

Axial MORB chemistry has long been correlated with ridge depth (Klein and Langmuir, 1987). Originally these studies were based upon the parameters Na[8] and Fe[8], Na and Fe concentrations normalised along liquid lines of descent (LLD) to MgO =8wt %; Na[8] correlating with extent, and Fe[8] with depth of melting (Klein and Langmuir, 1987, 1989; Langmuir *et al*., 1992). Niu and O'Hara (2008) argue that these parameters are unreliable, preferring to correct to Mg# =0.72, as this maybetter represent equilibrium with mantle conditions. Shen and Forsyth, (1995) show that regional averages of Fe[8] are strongly dependent on enrichment, suggesting that if Fe[8] is used to infer depth of melting, corrections for the compositional heterogeneity of the source are required, as well as for the complex effects of fractionation.

Niu and O'Hara (2008) suggest that the dense, fertile nature of mantle beneath deep ridges restricts the amplitude and rate of upwelling and reduces decompression melting. Conductive cooling becomes significant, and melt is restricted to a deep level. The melting column is therefore short, and melt production is low, generating thin crust. In contrast, the fertile (more refractory) mantle at shallow ridges generates greater degrees of melt (Niu and O'Hara, 2008), and melting starts at greater depths (Salters, 1996). The findings of Niu and O'Hara (2008) are supported by the fact that some of the world's deepest ridge (Australian-Antarctic Discordance, Mid-Cayman Rise) have significant garnet signatures in their basalts, indicative of short, deep upwelling paths (Salters, 1996).

Once melt is generated, physical processes further alter its chemistry. Small 'packets' of melt rise through the mantle, each possessing distinct chemical compositions, which are representative of heterogeneous sources and varied melt fractions. As they migrate toward the surface, they assimilate material and amalgamate with other melts. Therefore, when the melts reach the surface, they are substantially modified. The compositions of the resultant basalts are averages of the source chemistry, and small, localised chemical heterogeneities

in the underlying mantle are ‘smoothed out’. Isotopic patterns in basalts can be used to infer the compositions of separate geochemical sources.

Fractional crystallisation involves the removal and segregation from a melt of successive crystallising mineral phases, so that rocks formed at different levels of fractional crystallisation represent a ‘liquid line of descent’ (Bowen, 1928). The process preferentially removes some elements from the melt and into the solid phase, and therefore changes the composition of the melt remaining, relatively enriching it in elements incompatible in the solid phase. Fractional crystallisation in magmatic systems is complex, because variations in source composition and PT conditions have dramatic effects on the evolution of the melt. For example, in some dehydrated compositions at high pressure, crystallisation of orthopyroxene is favoured, whereas in wet melt, olivine crystallises.

Fractional crystallisation is commonly the cause of trends seen on compositional diagrams for MORB. These trends can be indistinguishable from those produced by variations in partial melting (see Rollinson, 1993). Distinguishing between these processes is important in geochemistry, and there are a number of ways to identify the effects of fractional crystallisation, such as calculating the Mg/Fe ratio. This is useful as an index of fractional crystallisation in melts, as Mg-Fe ratios change rapidly in the first stages of crystallisation, due to the high Mg/Fe of the crystallising ferromagnesian minerals relative to the host melt (Roeder and Emslie, 1970). Trace element ratios, incorporating incompatible elements such as Zr, Nb and Y, are changed little by secondary processes such as crystal fractionation (Peirce and Cann, 1973) due to the similarity of distribution coefficients between the trace elements (see distribution coefficients, e.g. Nash and Crecraft, 1985; Hart and Dunn, 1993). Therefore, strong variations in incompatible trace element ratios are likely to reflect variations in source composition or melt fraction, rather than variations in the amount of fractional crystallisation.

Mantle plumes are thought to form from enriched mantle sources, and are arguably responsible for generating enriched ocean island basalts (OIBs) worldwide. Many instances are described of plume material ‘interacting’ with MORs, creating E-MORB regions. Examples of this behaviour are the interaction

of the Iceland plume with the MAR on the Reykjanes ridge (Murton *et al*., 2002), and the interaction of the Reunion hotspot with the neighbouring Central Indian Ridge (Nauret *et al*., 2006).

The Reykjanes ridge is characterised by 'V' shaped ridges thought to originate from the physical interaction of plume magmas with the ridge structure (e.g. White *et al.,* 1995; Ito, 2001, Murton *et al*., 2002). Geochemical evidence for plume-ridge interaction is also seen. Incompatible element concentrations and crustal thickness increase northward to the intersection of the MAR with Iceland, and Nd and Sr isotope systematics reveal melting and mixing within a southward thinning mantle wedge beneath the Reykjanes ridge (Murton *et al*., 2002).

At the Central Indian Ridge (CIR) between the Rodriguez Triple Junction and the Marie Celeste Fracture Zone, basalts tend toward higher incompatible element concentrations northward, corresponding with increasing H_2O/TiO_2 and Dy/Yb ratios. The geochemistry of these rocks is interpreted to fall on a mixing line between N-MORB and Réunion hotspot lavas, and therefore it is determined that the Réunion hotspot is the source of hydrated and enriched material in this region of the ridge (Murton *et al*., 2005).

Whilst plume-ridge interaction may provide an explanation for the generation of some E-MORBs, it is likely to be inappropriate for isolated E-MORBs in regions where no geophysical evidence for the presence of a plume is found.

1.2.7 - The Alteration of MORB

Basalt recovered from mid-ocean ridge axes is typically young and largely chemically unaltered post-eruption. However, basalt exposed on the seafloor and in the crust beneath it is subject to low temperature alteration by interaction with seawater (low temperature), and also to alteration by exposure to fluids from high temperature hydrothermal sites (Gillis *et al*., 1993).

Early palaeomagnetic studies (Vine and Matthews, 1963) showed that basalts increase in age with distance from the axis. Off-axis samples may, therefore,

have suffered more alteration. Glass on older basalt pillows is commonly devitrified and coated with manganese crust deposits, the thickness of which positively correlate with the extent of devitrification (Hekinian and Hoffert, 1975).

Hydrothermal alteration is geographically limited to near-axis areas where hot fluids driven by magmatism and intrusions are focused. Low-temperature alteration by seawater takes place wherever water and rock interact. During alteration, the geochemistry and mineralogy of basalt can be substantially modified. It is important to understand these processes, and their potential implications, when interpreting geochemical and petrological data from MORB (Sun and McDonough, 1989).

Alteration of crustal material is also of geochemical interest because modification of crustal material during alteration processes may have significant influence on the future generation of heterogeneous mantle sources. For example, studies from a number of ridge localities suggest that Pb is concentrated in 'greenstones' during the hydrothermal alteration process. Pb depletion of the surrounding material may be such that, once subducted, this material can generate the HIMU (high μ) mantle source (see Muhe *et al*., 1997).

For basalt in the crust but not directly exposed to the surface, the level of alteration is dependent upon the permeability of the crust. Lister (1972, 1974) proposed two mechanisms for circulation of seawater through the crust, the first being hot, active fluid cells driven by heat from axial magma lenses or cooling plutons, and the second being controlled by contraction of rocks as they move off axis and cool. Rocks may also come into contact with seawater due to the action of faults, which provide conduits for fluids to pass through the crust.

During low temperature alteration, the main geochemical processes are hydration of minerals, formation of oxides, and alkali fixation. During hydration of basalts or basaltic glass to palagonite K, Ti, Al, Fe, Mn, P and H_2O are gained and Si, Mn, Mg, Ca and Na are lost (Bu *et al*., 2008). $^{87}Sr/^{86}Sr$ ratios increase during seafloor weathering (Spooner, 1976). The rate and extent of replacement of volcanic glass by palagonite is dependent on a variety of factors, including temperature, time, structure of the primary material, surface area of the primary material and growth rate of the secondary phases (see Stroncik and Schminke, 2002). As off-

axis basalts are older and have been exposed to seawater for longer than newly erupted basalts, the amount of glass remaining may have been substantially reduced.

The chemical mobility of trace elements during low temperature hydrothermal alteration is a topic of some debate. Some studies suggest that REE are highly stable during alteration (Jochum and Verma, 1996), whilst others suggest they are highly mobile (Verma, 1992). Leaching of active components can lead to relative enrichment of REE, and precipitation of REE-rich ferromanganese oxides can also increase REE content and alter the proportions of LREE and HREE present (Bu *et al*., 2008). It is generally agreed that the alkalis and Ba, Sr, and U are strongly mobile (Teagle *et al*., 1996; Krolikowska-Ciaglo *et al*., 2007), as altered glass and samples from basalt margins have the high concentrations of these elements when compared with fresh N-MORB glasses.

In high-temperature alteration, mineralogical changes take place as basalt reacts. Igneous mineralogy is replaced with greenschist-facies phases such as albite, chlorite, epidote and actinolite, along with associated quartz and sulphides (Humphris and Thompson, 1977). Typically, MgO and H_2O are gained, and CaO and SiO_2 are lost, along with Cu and Sr, though Cu is commonly precipitated in veins (Humphris, 1976). In experimental 'seawater-dominated' systems at 300°C, nearly all of the Na, Ca, Cu, Zn, and CO_2 and most of the K, Ba, Sr, and Mn were leached from the silicates. H_2S, Al, Si, and possibly Co were also significantly mobilized, whereas V, Cr, and Ni were not (Seyfried and Mottl, 1982). Hajash and Archer (1980) suggest that the extent of chemical exchange in these systems is strongly dependent on temperature and the water/rock ratio. Model reactions between seawater and basalt at low water/rock ratios can be considered to consist of two exchanges: Mg for Ca, and Na for Ca (Mottl and Holland, 1978).

Studies of hydrothermal alteration at the Galapagos Fossil Hydrothermal Field show that REE are relatively immobile, and that Sr isotope ratios increase with alteration. The rocks here show complex zonation of alteration which is interpreted as representing alteration by a mixture of low temperature seawater

and hotter hydrothermal fluids (Ridley *et al*., 1994). It is likely that many basalts have experienced both high temperature and low temperature alteration.

1.2.8- Seafloor Distribution of Mantle Peridotites

Dredging and IODP drilling has revealed that abyssal peridotites are abundant on the seafloor at slow-spreading ridges. The majority of these are reported from areas near to segment ends and fracture zones (Melson and Thompson, 1971; Cannat and Seyler, 1995; Escartín *et al*., 2003). Mantle upwelling models suggest that the centres of ridge segments are hot and magmatically active, whereas distal parts tend to be colder and the geotherm deeper, with the brittle region extending further into the lithosphere (Figure 5).

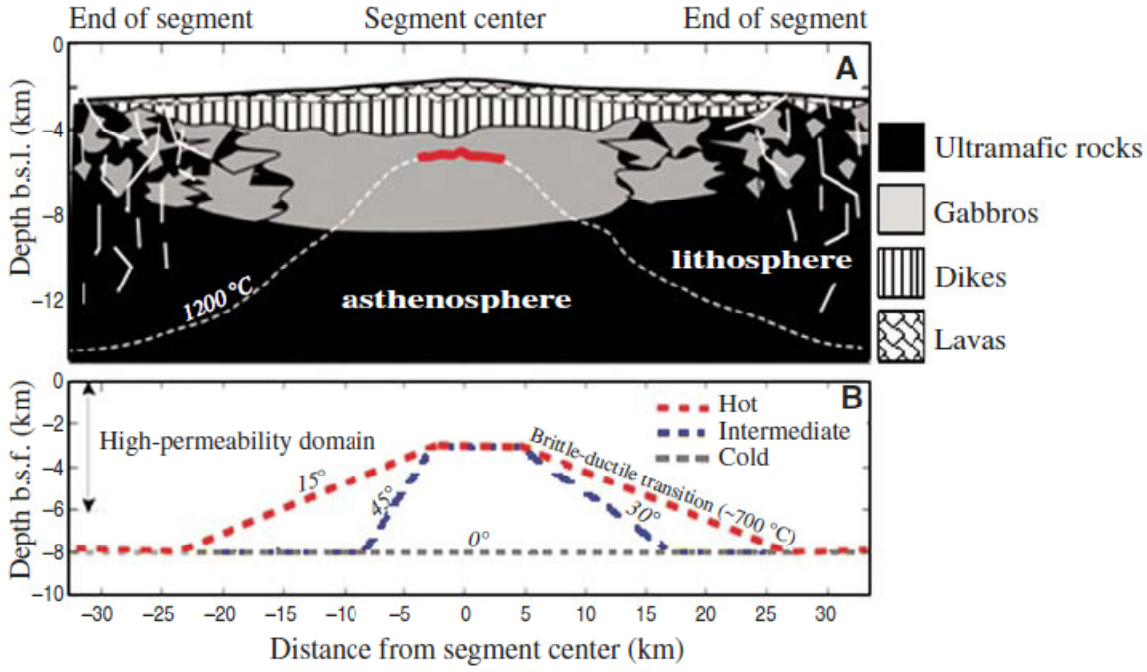

Figure 5. Possible along-axis thermal structure of Mid-Atlantic Ridge segment. A) 1200 °C isotherm (melt liquidus and base of lithospheric mantle) sketched for hot axial regime end-member configuration with central melt lens (red line) in the crust. Bsl - .below sea level. B) Along-axis geometry of brittle-ductile transition (700 °C) for three possible thermal structures, from hot (crustal melt lens and broad central thermal anomaly), to intermediate (crustal melt lens and narrow central thermal anomaly), and cold (no crustal melt lens, no central thermal anomaly). These three geometries determine range of isotherm slopes and of

aspect ratios (R) tested in the hydrothermal circulation models: up to 15° for R = 6 in the hot end member, up to 30° or 45°, respectively, for R = 3 or 2/3 in the intermediate case, and zero (flat isotherm) in the cold end member. b.s.f. - below seafloor. From Fontaine *et al*., 2008.

The thermal structure and tectonics of segment ends may explain the exposure of peridotite on the seafloor here. However, exposure of peridotite by faulting is not restricted exclusively to segment ends (Cannat *et al*., 1997). Upper mantle material is also found away from transform fault scarps along the MAR (Juteau *et al*., 1990). Peridotite exhumation in central parts of segments has been reported on domed topographic highs on or near the ridge axis, associated with low-angle detachment faults (e.g.: Tucholke *et al*., 1998; Karson, 1999; Blackman *et al*., 2002; Smith *et al*., 2006). Based on peridotite recovery from DSDP and ODP Legs on the MAR, Juteau *et al*. (1990) conclude that tectonic exhumation of peridotite to the seafloor away from transform zones may be a routine part of ridge behaviour.

CHAPTER TWO - OCEANIC CORE COMPLEXES

The 12°60'N-15'20°N region of the slow-spreading MAR is an 'amagmatic' section of the ridge. It is unusual in terms of morphology, having thin crust and highly irregular topography punctuated by the domed, corrugated surfaces of OCCs (Smith *et al*., 2006).

The existence of OCCs, also known as 'megamullions' in reference to their domal structure (Tuckolke *et al*., 1998), is well documented at near-axis segment-end sites on many slow-spreading ridge segments (Cann *et al*., 1997; Escartín *et al*., 2008). OCCs are characterised by a dome composed of crustal and upper mantle rocks, exposed by a shallow, large-offset detachment fault. The point at which the fault initiates is known as the 'breakaway', and is marked by a ridge-parallel, linear feature. The dome is covered with axis-normal corrugations lying parallel to the offset direction. The side of the detachment fault nearest the axis is known as the 'termination'. Here the fault is inferred to dip below the axis.

The connection between detachment faulting and the formation of oceanic crust at ridge-transform intersections was first recognised 30 years ago (see Dick, 1981). Since, numerous geophysical and sampling campaigns, including deep drilling, have examined the structures in increasing levels of detail (e.g. Karson *et al*., 1990; Tucholke and Lin, 1994; Cann *et al*., 1997; Smith *et al*., 2006, 2008; MacLeod *et al*., 2009). The term 'oceanic core complex' was first used by Karson and Lawrence (1997) to describe exposures of gabbroic and ultramafic rock at the seafloor on crustal detachments. The term was more recently redefined to include all structural blocks between the breakaway and hanging wall blocks on the ridge axis side of the termination (Blackman *et al*. 2002, 2009).

Many questions have been raised about OCC formation, the mechanisms involved in their development, and their relevance in terms of the broader fields of crustal architecture and plate tectonics. This chapter examines the nature and origin of OCCs, exploring theories on their formation, development, evolution and termination. It also attempts to assess the importance of detachment faulting as a tectonic process contributing to the formation of slow-spreading ridges.

2.1- AMAGMATIC SPREADING

Amagmatic spreading refers to separation of the plates in slow-spreading settings, where melt supply is very low (or non-existent), preventing normal spreading from taking place (i.e.: Sauter *et al*., 2004; Cannat *et al*., 2008; Tremblay *et al*., 2009; Cipriani *et al*., 2009). Topographic, lithological and geophysical data indicate that ridge spreading in amagmatic areas is accommodated by movement along low-angle detachment faults (e.g. Smith *et al*., 2006). Amagmatic spreading is defined formally as 'spreading on an area of the ridge where magmatic spreading (M) ≤ tectonic spreading (T) (Buck *et al*., 2005; Tucholke *et al*., 2008).

2.2 - THE GEOLOGICAL CHARACTERISTICS OF AMAGMATIC REGIONS

Amagmatic spreading is thought to involve a complex alternation of magmatic and amagmatic periods, controlled by the episodic nature of melt supply. During amagmatic periods, faulting may be a highly important mechanism for the accommodation of plate spreading. The interplay of low-angle detachments and high-angle normal faults locally leads to the exhumation of lower crust and upper mantle peridotites to the seafloor, forming OCCs (Tremblay *et al*., 2009).

Amagmatic brittle extension appears to take place on only one side of the ridge axis. This leads to the formation of a domed mullion on one ridge flank, and a more morphologically 'normal' area on the other (Escartín *et al*., 2008). The overall topography is therefore asymmetric about the axial valley, and the pattern of axial highs and troughs familiar for magmatic spreading is not found (Cannat *et al*., 1995). It is not clear how much spreading is taken up by each flank of the ridge in this scenario. The temporal extents of OCCs are commonly estimated by assuming extension at the half spreading rate. Correlations between asymmetrical spreading regions, hydrothermal activity and seismicity have been

identified (Escartín *et al*., 2008) suggesting that these fault systems may focus hydrothermal fluids.

Amagmatic behaviour is common at segment ends, though ocasionally segment centres behave amagmatically (see ~15°N region, as described by Smith *et al*., 2006). They appear to share key geological characteristics with segment ends, such as asymmetric topography and sporadic melt supply. Amagmatic areas have rugged topography, and irregular faulting patterns. They typically have deep axial valleys, indicative of a thick underlying lithosphere (Cannat, 1993). This suggests that the brittle deformation zone extends to greater depth here than at typical segment centres.

In accordance with 3D mantle upwelling models, melt provision at slow-spreading ridges is thought to be reduced close to ridge-transform intersections, as melt is actively focused toward segment centres (see Gràcia and Escartín, 1999). The thick lithosphere at segment ends is likely to prevent the development of long-lived crustal magma chambers, and so melt will freeze in small dykes and gabbroic sills, reducing the amount of surface magmatism. The proportion of gabbroic material (representing melt lenses and magma chambers) varies between OCCs. This observation has led to substantial debate about the availability of melt in amagmatic regions.

The ‘plumbing system’ beneath amagmatic areas is likely to consist of small, isolated melt lenses negotiating a thick, cold lithosphere. Therefore, part of the lower crust in such regions is likely to be made up from gabbros frozen in rather than melts erupted. This means that lithospheric thickness is not necessarily an accurate indicator of total melt production (e.g. Cannat, 1996; Schouten *et al.,* 2010). A lack of surface volcanism does not, therefore, necessarily indicate complete amagmatism.

Mantle melting in amagmatic areas may be suppressed by enhanced conductive cooling of the upwelling mantle (Dick *et al*., 2003), facilitated by seawater travelling through fault systems. This would be especially significant in an area with a thick lithosphere and a deep brittle zone.

As a result of the processes described above, the crust generated in amagmatic areas is anomalously thin, and volcanism is infrequent (Tucholke and Lin, 1994).

2.3 – THE GLOBAL DISTRIBUTION OF OCEANIC CORE COMPLEXES

OCCs are common at spreading rates ranging from 14 to 75 mm/yr (Tucholke *et al*., 2008). This suggests that they are part of a significant tectonic mechanism at slow-spreading ridges (Morris *et al*., 2009, MacLeod *et al*., 2009).

OCCs have been reported on the MAR, the Southwest Indian Ridge (SWIR) and the Central Indian Ridge (CIR). Specific OCCs such as Atlantic Massif (MAR), Atlantis Bank (SWIR), Fuji Dome (SWIR) and Kane Megamullion (MAR) have been the focus of detailed geophysical, lithological, geochemical and tectonic studies (including ODP and IODP drilling). A summary of known OCC sites around the world is presented in Table 2.

Studies identifying OCC corrugated domes

General Location Name	**Reference**
MAR 30ºN: Atlantis Massif, SOCC, WOCC	Cann *et al*. (1997)
MAR 22ºN-27ºN: Dante's Domes, Kane OCC	Tucholke et al. (1998)
Rodriguez Triple Junction, CIR	Mitchell et al. (1998)
Chile Rise	Martinez et al. (1998)
Australian-Antarctic Discordance (1)	Christie et al. (1998
SWIR: Atlantis Bank	Dick and Others (2000)
Philippine Sea: Godzilla Megamullion	Ohara et al. (2001)
MAR 5ºS	Reston et al. (2002)
MAR 36º40'N: Saldanha Massif	Miranda et al. (2002)
SWIR: FUJI Dome	Searle et al. (2003)
MAR 14º-16ºN: includes 15º45'N OCC	Fujiwara et al. (2003), MacLeod et al (2002)

Australian-Antarctic Discordance (several)	Okino et al. (2004)
CIR 5º15'S: Vityaz Megamullion	Drolia and DeMets (2005)
MAR 13ºN	Smith et al. (2006)
SWIR 61º-65ºE (several)	Sauter et al. (2008)

Table 2: A list of studies describing OCCs from a variety of sites on mid-ocean ridges worldwide. After Blackman *et al*. (2009).

The majority of OCCs occur as topographic 'highs' found in the inside corners of ridge-transform intersections (Dick *et al*., 1981; Ranero *et al*., 1999; Reston *et al*., 2002; Searle *et al*., 2003; van Wijk and Blackman, 2005, 2008). These areas are thought to be conducive to the formation of OCCs, as melt supply is low, the crust is thin, and the lithosphere is cold and thick in regions adjacent to ridge-transform offsets.

Some OCCs are reported from mid-segment positions along the MAR (see Smith *et al*., 2006, 2008; Dannowski *et al*., 2008). Topography, axial morphology and geophysics in these areas suggest that they share key geological characteristics such as thick lithosphere and low melt supply with their segment-end counterparts. These are thought to be determining factors in the onset of detachment fault development.

OCCs are not usually reported from fast-spreading ridges, probably as magmatism here is too robust to allow or require their formation. However, the Parece Vela Megamullion (also known as the Godzilla Megamullion) is an exception to this rule, occurring in an intermediate-fast spreading ridge setting, in an extinct backarc basin in the Philippine Sea (Ohara *et al*., 2007). The large OCCs on the Australia–Antarctic Discordance (AAD), which lies on the SWIR, also formed at intermediate spreading rates (Okino *et al*., 2004).

2.4 - OCCURRENCE OF OCCS IN THE ATLANTIC OCEAN

The existence of OCCs was first confirmed in the Atlantic by Cann *et al*., (1997), in a study describing three core complexes along the Atlantis fracture Zone (~30°N). Tucholke *et al*. (1998) reported 17 megamullion structures, identified on the basis of RMBA analyses and direct sampling. Smith *et al*., (2006, 2008) identify up to 45 separate complexes between 13°-15°N alone. Further evidence of OCCs has been reported in the (~26°N) TAG segment (Tivey *et al*., 2003).

Several of these OCCs have been studied in detail, such as the Kane Megamullion (Dick *et al*., 2008), Dante's Dome (Tucholke *et al*., 2001), complexes between 12°60'-14°N (MacLeod *et al*., 2009, this study), 15°45'N (Escartín *et al*., 1999; MacLeod *et al*., 2002) and 5°S (Reston *et al*., 2002).

Kane megamullion (23°40'N and 22°30'N - MARK area) has a geographic extent of ~23km by 40km (Williams *et al*., 2006) and was formed at the axis adjacent to Kane Fracture Zone between 2.1 and 3.3Ma (Xu *et al*., 2009) by asymmetric spreading during the last 3-4Ma (Schultz *et al*., 1988). The OCC consists of the Babel, Abel, Cain, Adam and Eve domes, rising to >1km above the seafloor, the largest of which are the central Cain and Abel domes (Dick *et al*., 2008).

The complex and its surrounds have been the focus of bathymetric mapping (Pockalny *et al*., 1988), sonar (Gao, 1997; Gao *et al*., 1998) submersible and direct sampling campaigns (e.g. Karson and Dick, 1983; Karson and Brown, 1988; Mével *et al*., 1991; Auzende *et al*., 1994; Dick *et al*., 2008), as well as ODP drilling Legs 109 (Shipboard Scientific Party, 1988) and 153 (Cannat *et al*., 1995).

Seismic refraction experiments have been carried out (e.g. Canales *et al*., 2000, Xu *et al*., 2009). Seismic tomography models indicate that lithologies vary from gabbroic intrusions, serpentinised peridotites and basalts on a ≤10km scale. Gabbros are especially found close to the termination (Xu *et al*., 2009).

The inside corner near the Atlantis Transform hosts 3 massifs, 10-15km across, rising to depths shallower than 2000m (Blackman *et al*., 1998). These massifs are characteristic of OCCs (Blackman *et al*., 2002) and similar to those found at

Kane Megamullion (Cannat *et al*., 1997). The Atlantis Massif has been the subject of detailed study, both in terms of mapping (Blackman *et al*., 2002, Karson *et al*., 2006) and drilling (Blackman *et al*., 2006). Multibeam and sidescan-sonar mapping has revealed the structural details of these massifs (Blackman *et al*., 1998). Atlantis Massif was formed within the past ~2Ma. Submersible and camera imagery indicates that a series of faults, not a single detachment, were involved in the uplift of the complex (Blackman *et al*., 2002). Multichannel seismic data suggests that Atlantis Massif formed by sequential slip on two different detachment faults that merged at depth, with breakaways as little as 2 km apart (Canales *et al*., 2004).

IODP drilling expeditions 304 and 305 (Hole U1309D) recovered gabbroic and minor ultramafic rocks (Zhao and Tominaga, 2009). The Atlantis Massif also hosts a large, low-temperature seawater dominated hydrothermal system, known as the Lost City Hydrothermal Vent Field, where serpentinisation of ultramafics took place predominantly in the temperature range 150-200°C (Boschi *et al*., 2008).

The region adjacent to the 5°S Fracture Zone is morphologically unusual, in that both the inside corner and the outside corner of the ridge-transform intersection host corrugated massifs. The outside corner massif is thought to have formed by rifting of an inside corner OCC during a ridge jump. Sampling of the inside corner massif recovered gabbros and serpentinised peridotite (Reston *et al*., 2002).

2.5 - OCCS IN THE INDIAN OCEAN

OCCs have been reported at several sites in the Indian Ocean, for example 5°S (Drolia and DeMets, 2005) 25°15'S (Mitchell *et al*., 1998) 126°E (Christie *et al*., 1998, Okino *et al*., 2004). Atlantis Bank (~57°E) was the focus of a deep drilling expedition (Dick *et al*., 1991) and Fuji Dome (64°E) was the subject of a detailed geophysical study (Searle *et al*., 2003).

Atlantis Bank is an uplifted OCC located on the eastern side of the Atlantis II Fracture Zone, SWIR, which rises >3km above surrounding seafloor of the same age (Baines *et al*., 2003). It is ~11 million years old, ~5km wide, 10km long in the direction of spreading and ~700m below sea level (Allerton and Tivey, 2001). The OCC has been the focus of dredging, submersible surveys and drilling at ODP site 735B. Sampling indicates that the complex exposes primarily lower crustal rocks, with drilling producing gabbroic cores (Dick *et al*., 1999). Models suggest that flexural uplift during detachment faulting is able to account for a third of the anomalous height of the complex. Flexure of nearby transform-parallel normal faulting is thought to account for the remainder (Baines *et al*., 2003).

Fuji Dome, imaged by Searle *et al*., (2003), during a bathymetric, geophysical and TOBI submersible survey, is an inside corner high OCC thought to have been active from 1.95Ma for ~1Ma during a period of reduced magmatic accretion and asymmetrical spreading.

2.6 - INTERMEDIATE-FAST SPREADING OCCS IN THE PHILIPPINE SEA

Godzilla Megamullion, in the Parece Vela basin, is the largest OCC yet discovered (Ohara *et al*., 2001; Ohara *et al*., 2007), being 10 times greater in size than OCCs on the MAR, and representing an estimated maximum of 3.6Myr of spreading (Ohara *et al*., 2003). This megamullion, like those on the AAD, is unusual, having formed in an intermediate spreading setting (Ohara *et al*., 2007), with an estimated spreading rate of 8.8–7.0 cm/yr full-rate (Ohara *et al*., 2003). The seafloor in this region is characterised by irregular topography (Okino *et al*., 1998) indicative of a weak magma supply (Ohara *et al*., 2001, 2003), suggesting that the area is ‘amagmatic’ and conducive to the development of OCCs.

The Godzilla Megamullion is morphologically and geophysically similar to OCCs in the Atlantic. Seismic studies show that a strong reflector observed below Godzilla is similar to the geophysical signatures beneath Atlantis Massif (Ohara *et al*., 2007).

The megamullion has been the focus of a number of research cruises in recent years. These expeditions included the dredging cruise KR03-01, submersible dive cruise YK04-05-Leg 4, and seismic studies by the Japanese government for the 'Law of the Sea' project. An IODP site survey was conducted (August-September 2007) as a two-Leg cruise (KH07-2-Leg 2 and 4) of R/V Hakuho in the Parece Vela Basin. Microstructural and petrological analysis of gabbros from the Godzilla Megamullion reveal the development of a ductile shear zone in the lower crust, thought to represent the surface of a detachment fault (Harigane *et al*., 2008). Examination of the domal morphology of this OCC suggests that it may have evolved through multiple detachment events (Ohara *et al*., 2007).

Irregular terrain with isolated corrugated topographic highs, reminiscent of OCC-forming areas on the MAR (e.g. Smith *et al*., 2006, 2008) may indicate that the Parce Vela basin also hosts other OCCs. Ohara *et al*., (2007) report three further detachment faulting episodes in the region, two exposing gabbroic cores, and the third exhuming only shallow crust.

2.7 - A SUMMARY MODEL OF OCEANIC CORE COMPLEX DEVELOPMENT

Slow-spreading ridge segments undergo amagmatic phases, where plate separation is accommodated by faulting, rather than by magmatic accretion (Cannat, 1993, Cannat *et al*., 2008, Tremblay *et al*., 2009, Cipriani *et al*., 2009). Because of their geographic association with amagmatic spreading crust, especially at ridge-transform intersection inside corners (e.g. Kane Megamullion, Atlantis Massif) it is thought that OCCs form as a response to periodic reductions in magma supply (see Tucholke and Lin, 1994, Escartín *et al*., 2008, Smith *et al*., 2006, 2008). In amagmatic periods, spreading is accommodated on low-angle detachment faults (Tucholke *et al*., 1998). Recent studies, however, have cited the presence of large amounts of gabbro in OCC domes (e.g. Kane Megamullion, Atlantis Massif) as evidence to suggest that melt supply is not reduced during OCC formation (Dick *et al*., 2000; MacLeod *et al*., 2002; Reston *et al*., 2002; Escartín *et al*., 2003; Blackman *et al*., 2006). The relationship between melt

supply and OCC formation remains a matter of some debate, and is discussed in detail later in this chapter.

OCC domes, sitting ~1-2km above the surrounding seafloor (Blackman *et al*., 2009), are interpreted to represent the uplifted, rotated shallow footwall blocks of very large offset, low-angle faults (Tucholke *et al*., 1998), which exhume lower crust and mantle rocks onto the seafloor (Blackman et al., 2009; MacLeod *et al*., 2009). The typical morphology of an OCC is illustrated in Figure 6.

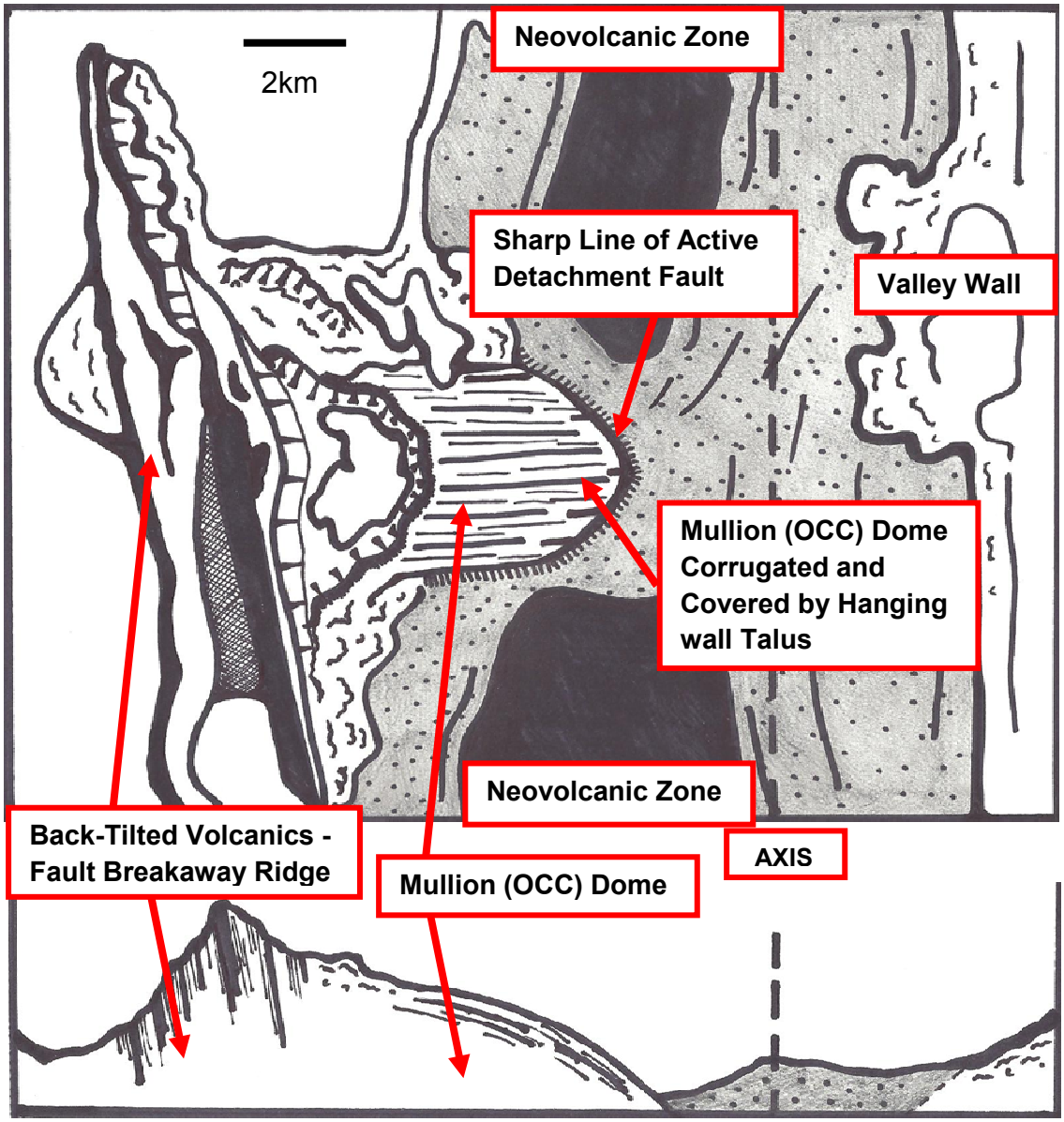

Figure 6: Sketch map and ~5x vertically exaggerated cross-section of the OCC at 13°19'N on the MAR. The diagram illustrates the morphological characteristics of a typical oceanic core complex. The structure is bounded at its older edge by a breakaway ridge consisting of back tilted volcanic crust, and at its younger edge by a fault line close to the axis. In active OCCs, this fault line is very sharp, whereas in extinct structures it may be overlain by sediment or volcanics. The core complex dome consists of uplifted and heavily serpentinised ultramafic material overlain by talus and rider blocks dragged from the hanging wall.

The mullion structures are marked by pronounced axis-perpendicular corrugations or striae, which are parallel to the direction of fault displacement. Volcanic blocks and debris overlying the dome are inferred to be hanging wall or rider blocks (Blackman *et al*., 2009).

A ridge-parallel 'breakaway' zone shows where the detachment fault initiates. With continued slip, more of the detachment becomes exposed at the seafloor, and it extends toward the spreading axis from the breakaway, occasionally obscured by hanging wall blocks.

Once spreading is accommodated by a fault, it may be more energetically favourable to maintain spreading on this fault than to switch to another fault in the rift valley. Therefore, spreading may continue on the original fault for some time (Tucholke *et al*., 1998).

Continued slip on a detachment fault may be aided by the formation of serpentine and/or talc in exposed lithologies, localising strain along the fault plane (Boschi *et al*., 2006; MacLeod *et al*., 2009). Sonar images of corrugated surfaces at the MAR (~30°N) show that detachment faults are shallower than predicted by faulting models. This may be due to the lubricating effects of serpentinised peridotite on the fault surface (Cann *et al*., 1997). The role of alteration assemblages in fault behaviour is the subject of a later section.

One of the key debates on OCC formation is whether the detachment faults form and slip at low angles, or whether they are rotated from an original high angle, after a large offset (see Lavier *et al*., 1999). They may originate as steep valley wall faults and then shallow out as they enter mechanically weak, partially serpentinised peridotite below the crust. Shallowing may result from flexural unloading, causing the fault to rotate on its hinge, and flatten out as it emerges (Smith *et al*., 2006). As the fault surface is exposed, flexural unloading of the peridotite causes it to bow upward, forming the domed shape we observe at the seafloor. Volume expansion of peridotite as it serpentinises may contribute to this effect. The high-angle vs. low-angle fault origin debate will be addressed in detail in sections 2.11 - 2.13.

Active detachment faults cut through all previous geological structures. The sharpness of these fault boundaries poses questions about how they propagate once slip is localised onto them. There is evidence that detachment faulting involves subcritical propagation of fractures along crustal-scale shear zones as they pass through the ductile-brittle transition (Lister, 1999).

The lifetime of detachments (the time that they are the main locus of spreading on their side of the axis) is thought to be ~1-3Ma (Escartín *et al*., 2008, Tucholke *et al*., 2008). Gravity and morphological data suggest that detachment faulting is relatively long-lived in crust spreading at <25-30mm/yr, whereas at higher rates it will be intermittent. Above ~40mm/yr it is unlikely to occur (Tucholke and Lin, 1994). It is thought that detachments are terminated when magmatic accretion at the axis re-emerges as the dominant mechanism of plate spreading (MacLeod *et al*., 2009).

As OCCs are found in amagmatic settings, a connection between reduced melt supply and their formation is established. However, until recently, little was understood about fault initiation, strain localisation, uplift, extent of magmatism during active faulting, and how faults are terminated prior to the resumption of normal magmatic spreading (Escartín *et al*., 2004; MacLeod *et al*., 2009). Also, it is not known why certain faults develop large offsets, taking up significant amounts of plate extension, whilst other nearby faults do not.

2.8 – THE SUBAERIAL ANALOGUES OF OCCS

OCCs are similar in scale and structure to metamorphic core complexes (Tucholke *et al*., 1998). The domal highs, with their 10–20km extent, relative smoothness of the capping seafloor, and 1–2km of relief, were recognized by Tucholke *et al*., (1997) as similar to the ‘turtleback’ morphology observed at some metamorphic core complexes in the Basin and Range (Blackman *et al*., 2009). The similarities may also extend to formation processes; both types of structure feature low-angle faults, the formation and propagation of which are a subject of intense debate.

The study of OCCs has been complemented by examination of many structurally analogous metamorphic core complexes (e.g. Reynolds and Lister, 1987, Scott and Lister, 1992). Comparisons have also been made with ophiolites (for example the Canadian Appalachian and Albanian Dinaride ophiolite belts), which are interpreted to contain fossilised OCCs (e.g. Tremblay *et al*., 2009). The lithological and structural characteristics of these ophiolites are consistent with asymmetrical oceanic extension and upper crust and mantle exhumation.

It has been argued that OCC-like detachment structures are found in the Limassol Forest area of the Troodos ophiolite, Cyprus. Here, core complexes of mantle peridotite are shown to have been exposed at the seafloor, or to have been covered by overlapping crustal blocks, separated from the peridotite core and from each other by low-angle extensional faults. These structures are interpreted to have resulted from crustal construction in an inside-corner area of an oceanic spreading centre (Cann *et al.,* 2001).

However, the use of ophiolites to model OCC processes must be approached cautiously. It is arguable whether ophiolites represent true oceanic crust. They may be more representative of small aborted oceans or marginal basins, within which geological conditions differ from those at mature spreading centres (Auzende *et al*., 1989).

2.9 - OCCS AND THE NATURE OF THE CRUST

Hess (1962) argued that oceanic crust is composed of serpentinised mantle peridotite, but this assertion was not supported by contemporary field observations. Extensive sampling of MORB and detailed examination of Ophiolites led to the development of the 1972 Penrose model for the structure of ocean crust. This simple layered model consists of basalts (pillow lavas) underlain by dykes and substantial gabbro (the crystallised product of melt in the crust), then upper mantle peridotite (Anonymous, 1972). This model was supported by available seismic data (e.g. Bonatti *et al*., 1971).

The formation of a model for the structure of the crust based on ophiolite data caused substantial debate. Geochemical, geophysical, structural and tectonic data from ophiolites are complex, suggesting various tectonic settings for their origin (Dilek and Newcomb, 2003). Interpretation is difficult as their provenance is uncertain, and their geology can be substantially modified by tectonics and overprinting during the processes which expose them at the surface (Malpas and Robinson, 1997). Whilst ophiolites were originally interpreted as forming in true MOR environments, petrological evidence shows that they have 'arc-like' geochemistry (e.g. Shervais and Kimbrough, 1985; Menzies *et al*., 1980; Pearce, 1991). Some cite this as conclusive evidence that ophiolites are not simply 'normal' oceanic crust. Others argue that the geochemical anomalies could arise from complex mantle component mixing effects, and that structural evidence for a MOR origin is compelling (Gass 1968; Moores *et al*., 2000).

Lagabrielle and Cannat (1990) argue that the association of slow-spreading crust with segment centre OCC massifs (MAR) is replicated in the ophiolites of the western Alps and the Ligurian ophiolites of the Apennines. They therefore suggest that models describing ophiolite complexes as anomalous 'aborted ocean' settings should be reappraised. With the advent of improved geophysical and sampling techniques, the attention of those attempting to verify the Penrose model shifted from ophiolites to the oceans.

The lower crust and upper mantle material exposed in fracture zones initially lent support to the Penrose model. However, it unlikely that this material is representative of the original stratigraphy of the crust, as it has been substantially disrupted by faulting (Francheteau *et al*., 1976). It is recognised that models of crustal architecture and geology based upon analysis of transform zones may not be representative of the whole oceanic crust, as these areas have anomalously thin crust, arising from segment-end amagmatism.

However, the discovery of mantle peridotite and lower crustal lithologies on the seafloor at OCCs provides a unique set of 'tectonic windows' (Dick 1989), through which the structure of the lower crust can be examined. Figure 7 summarises the typical Penrose model for fast-spreading, based upon interpretations of the Oman Ophiolite. Also shown are modifications proposed on

the basis of studies of different regions of the MAR. Material unroofed at OCCs is brought to the surface by detachment faulting, and it is not known whether it is truly representative of the structure of the crust beneath. Deep drilling at three OCC sites (MAR) shows that the footwalls are relatively intact, not pervasively deformed. This provides an opportunity to examine a section of the crust that is usually overlain by a thick layer of upper crustal rocks (Blackman *et al*., 2009). Detailed geophysics and sampling suggests a much more complex crustal structure than that proposed by the Penrose model.

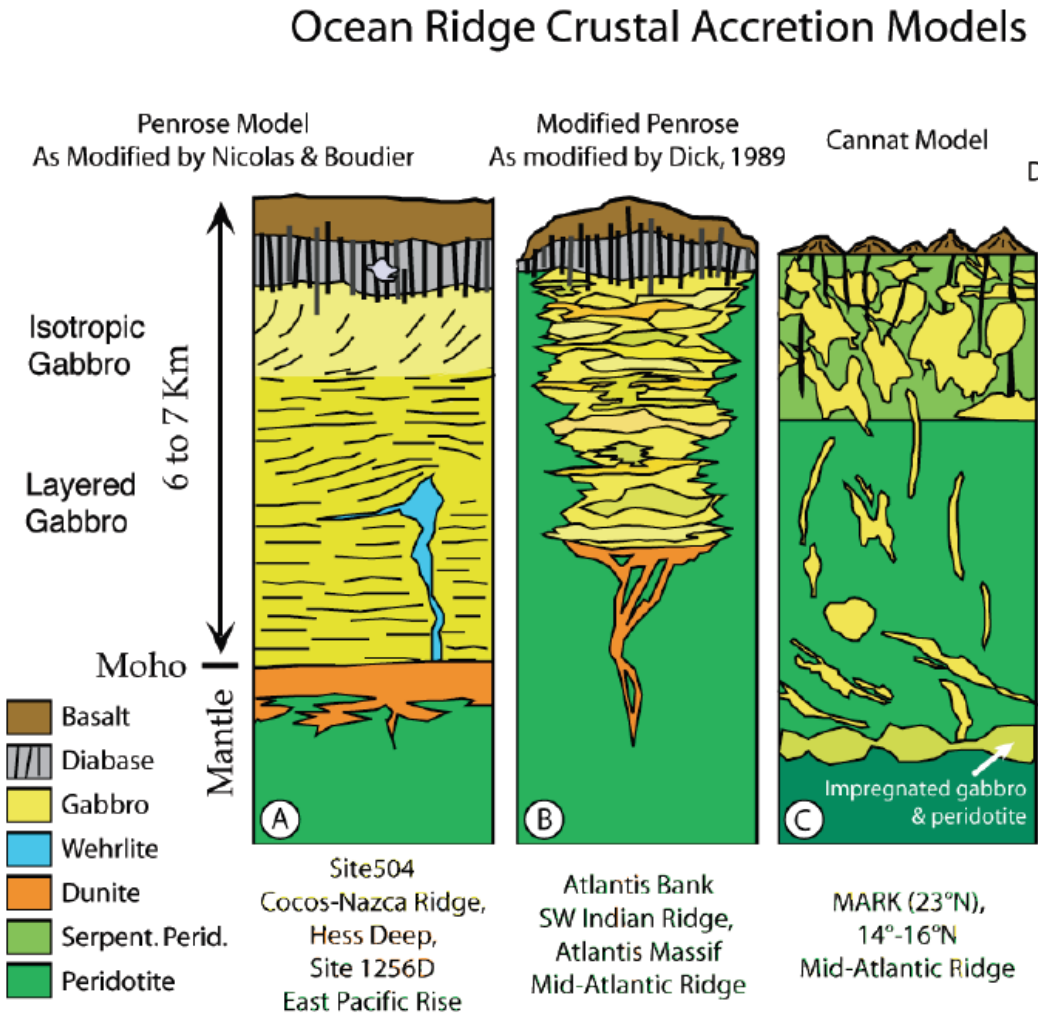

Figure 7: Ocean ridge crustal accretion models. (A) Typical Penrose model for fast-spreading, based upon the interpretations of the Oman Ophiolite. (B) Modified Penrose model for slow-spreading crust reflecting the abundance of gabbro and peridotite sampled at transforms, (C) model for the anomalous 14-16°N region of the MAR. After Dick *et al*. (2006).

Layered gabbros in ophiolites were once considered to be the product of crystallisation in large (~30km wide, 3-6km deep) magma chambers. However, the existence of such large magma chambers is not supported by geophysical evidence (Quick and Denlinger, 1993), especially in slow-spreading environments, where long-lived, steady-state magma chambers are unlikely to form (Sinton and Detrick, 1992). Whilst the Penrose model may apply at fast-spreading ridges (see Dilek and Newcomb, 2003), seismic tomography, surface sampling and deep-drilling campaigns have shown that the amount and distribution of gabbro varies substantially in slow-spreading ridge segments, and between individual OCCs. Gabbro possesses a wide range of compositions reflecting mechanical as well as chemical processes beneath the ridge. Understanding its distribution and composition at OCCs could prove critical, not only for understanding the relationship between OCCs and magmatism, but also for producing accurate models of the structure of slow-spreading crust.

The proportions of lithologies recovered at OCCs are highly variable. Deep-drilling reveals large amounts of gabbro, exceeding 95% in the upper parts of some complexes. Drilling campaigns at 15°45'N MAR (200m, Keleman *et al*., 2004), Atlantis Massif, 30°N (1415m, Blackman *et al*., 2006) and Atlantis Bank, SWIR (1500m, Natland and Dick, 2002; Dick *et al*., 1999) have all recovered serpentinised peridotite and gabbro, with gabbro dominating the sequence. Seafloor sampling of OCCs typically recovers large amounts of serpentinised peridotite, with ~70:30 peridotite to gabbro ratio (Blackman *et al*., 2009). It is not known whether these proportions are representative of the whole OCC (Xu *et al*., 2009). The ratio could be biased by intrusion of serpentine along faults which are now exposed (Blackman *et al*., 2009).

If models correlating OCC development with reduced magmatism are correct, then we would expect crust in these regions to be thin. Seismic velocity profiles of the subsurface at OCCs are used to examine whether crustal thickness conforms to the traditional Penrose ophiolite model (as seen in normal oceanic crust, e.g. White *et al*., 1992), or more closely resembles the modified Penrose models of Dick (1989), or the gabbro 'plum' model proposed by Cannat (1993, 1997). It must be noted, however, that correlations of lithology with seismic velocity are open to interpretation (partially serpentinised peridotite and gabbro

are difficult to distinguish); and that alteration and brittle deformation can also substantially affect these values.

Early seismic studies at Atlantis Bank (SWIR), and TAG (MAR) showed that crustal structure on the OCC contrasts strongly with that in the surrounding crust (Muller *et al*., 1997, 2000; Canales *et al*., 2007 respectively), and that OCC domes are dominated by high velocity regions.

More recently, using large-offset multichannel seismic data, Canales *et al*., (2008) derived 2D seismic tomography models for three OCC sites on the MAR (Atlantis Massif, Kane Megamullion and Dante's Domes). Their findings report many good correlations between velocity structure and lithology, as documented by sampling and seafloor morphology. However, this is not the case at Atlantis Massif. Here, anomalously high seismic velocity regions are commonly present near fault terminations (Canales *et al*., 2008). High velocity regions also underlie the dome. IODP drilling of Atlantis Massif (Hole U1309D) core returned 97.8% gabbro in the top of the core (Dick *et al*., 2006), which do not correlate with the high velocities found by seismic studies. The same correlation is seen in Hole 735B at Atlantis Bank. This may suggest that high velocity regions on other OCCs also represent large gabbro bodies.

Since basalt on OCCs is thought to be talus underlain by lower crustal and upper mantle rocks, it seems unlikely that the complexes consist of normal basaltic crust. None of the gabbros appears more altered or fractured than the others, and so these processes are unlikely to be responsible for seismic variation between the domes. The recovery of large amounts of serpentinised peridotite on detachment fault surfaces and the presence of hydrothermal systems, which are thought to be driven by serpentinisation, suggests that the gabbro bodies are surrounded by serpentinised peridotite (Blackman *et al*., 2009).

Although the upper parts of OCCs have been relatively well explored by geophysics and drilling, the deeper parts are less well studied. Seismic velocities are consistent with either gabbro or serpentinised peridotite, highlighting the difficulty of relying upon seismic data to infer crustal composition in the absence of ground-truthing.

Dick *et al*., (2006) cite the gabbroic composition of the Atlantis Massif (MAR) as evidence to modify the Penrose model for slow-spreading ridge segments. The modified model supports the theory of segment centre melt focusing. Gabbros in this model taper out toward segment ends, giving way to peridotite overlain by thin basaltic crust (Dick, 1989; Dick *et al*., 2006).

Hole 735B (Atlantis Bank) and Hole U1309D (Atlantis Massif) are substantially different to each other. Both holes reveal structural complexity in the crust which exceeds that predicted by the Penrose model, however, variations in geochemistry and deformation throughout the holes indicate that even within slow spreading environments, crustal structure and chemistry is much more variable than previously thought. Seismic tomography at Kane Megamullion may suggest lithological variations between gabbro, serpentinised peridotite and basalt on a ≤10km scale, with gabbro becoming increasingly more significant toward the fault termination. This distribution also indicates a substantial departure from the Penrose model (Xu *et al*., 2009).

Sampling around 15°N on the MAR, including deep drilling on ODP Leg 209, reveals serpentinised peridotite intruded by ~40% gabbros, and overlain by thin basaltic crust and dykes (Kelemen *et al*., 2004). This suggests that the crust here contains substantially less gabbro and dykes than predicted by the Penrose model (Cannat 1997). Surface sampling of OCCs between 12°6'-14°N on the MAR recovered >3% gabbro. Dredges contained serpentinised peridotite and overlying basaltic talus material. Gabbro may be a much less substantial crustal constituent here.

Deep drilling and surface sampling of OCCs shows that whilst the Penrose model may be applicable to fast-spreading settings, it cannot explain the crustal complexity at slow-spreading ridges. Modified Penrose models appear to be locally applicable at Atlantis Massif and Atlantis Bank, but do not apply near 15°N, where gabbro much less significant. The crust at slow-spreading centres is clearly complex and highly variable.

2.10 - THE MORPHOLOGICAL AND STRUCTURAL CHARACTERISTICS OF OCCS

Initially, OCC studies relied heavily upon analogy with metamorphic core complexes and ophiolites. More recently, numerous geophysical techniques have been applied to better understand the subsurface structure and properties of *in situ* OCCs. Sonar data, gravity, magnetics, borehole geophysics and seismic studies (earthquake monitoring and seismic imaging) have all been applied.

Levels of seismicity in regions associated with OCC formation are high (Smith *et al*., 2003). The main seismic activity associated with OCCs takes place within the region ~15km from the magmatic axis (Smith *et al*., 2008). Hydroacoustic monitoring has been carried out in a number of regions where OCC formation is documented. Measurements from an ocean bottom array on the MAR (adjacent to the 5°S Fracture Zone) recorded a total of 148 well-constrained events, concentrated within the western half of the median valley. This seismicity suggests an asymmetric tectonic regime (Tilmann *et al*., 2004).

Seismic refraction data from the TAG segment, 26°N, MAR, recorded 19,232 microearthquakes, defining a ~15km long, dome shaped detachment fault, which extends to depths of >7km, dipping at ~70°. Modelling indicates that the fault shallows to a dip of 20±5° as it rolls over, and that it becomes aseismic at ~3km depth (DeMartin *et al*., 2007).

Reston *et al*. (2004) present pre-stack depth migration imagery from the Central Atlantic, which documents the scale and geometry of normal faulting in oceanic crust formed over 25 Myr. at a half-spreading rate of less than 10 mm yr^{-1}. The data reveal normal faulting (dips > 35°), gently dipping segment centre detachment faults, and gently dipping, large offset (~10km heave) faults rooted in deep crust beneath domal highs at ridge-transform intersections. These features are interpreted as fossilised examples of the long-lived detachment faults found beneath the modern spreading axis.

Sonar mapping of OCCs has been accomplished using hull-mounted (echo-sounders and multibeam) or deep-towed (sidescan) systems (e.g. Searle *et al*.,

2003; MacLeod *et al*., 2009), which obtain swaths of data via beam-forming an acoustic signal of essentially a single frequency (Blackman *et al*., 2009).

Key OCC features such as shallow, corrugated domes are identified in backscatter images via analysis of slope/roughness variation and its correlation with seafloor type, as inferred from backscatter pattern (Blackman *et al*., 2009). In some cases, unit contacts and fault lines are exceptionally clear, although talus fall and local sediment cover obscures these features on older OCCs (see TOBI data, MacLeod *et al*., 2009).

OCCs are characterised by a number of key morphological features, including a corrugated dome and a ridge-parallel breakaway fault. Application of sonar imaging has allowed many examples of these features to be examined in detail. The distance between the breakaway and the termination, the height of the dome, and the angle of tilted blocks all provide details of the lifespan of the OCC and the amount of uplift and rotation on the fault. The palaeo-top of individual rotated blocks on the faults can be identified by volcanic features on one side of tilted surfaces (Blackman *et al*., 2009).

High quality bathymetry and sidescan-sonar data have been combined to image OCCs and their surrounds in detail. MacLeod *et al*. (2009) used EM120 bathymetry and TOBI sidescan-sonar to image the segment-centre region between 12°60’N and 14°N (MAR). Highly detailed imagery reveals OCCs at different life stages. Off-axis, heavily sedimented OCCs are found near regions of robust axial magmatism, whilst active structures with clear, sharp fault lines root in regions where little volcanism is evident.

Cann *et al*. (1997) combined high-resolution bathymetry with TOBI sidescan sonar to image the 30°N region of the MAR, providing data on the (typically) ridge-perpendicular OCC corrugations. The scale of corrugations on domal complex highs was identified as varying from km to ~100m scales, both in wavelength and amplitude (Tucholke *et al*., 1998). Images of slickensides on the OCC at 15°45’N confirm fault movement parallel to the larger-scale corrugations (MacLeod *et al*., 2002). Theories explaining the formation of corrugations on exposed fault surfaces are numerous. It has been suggested that corrugations on subaerial core complexes are produced by folding after exposure (Spencer,

1982; Yin, 1991), or by development of drainage networks on the fault surface (Spencer, 2000). Other studies describe corrugation formation during faulting (Davis and Lister, 1988).

Basaltic rubble from OCC domes is interpreted as talus dragged onto the footwall by hanging wall displacement (Tucholke *et al*., 2001). The relationship of the talus to the corrugations is not clear. Talus has been imaged on Atlantis Massif (Blackman *et al*., 2002) and on complexes at 13°19'N and 13°30'N (this study). Greenschist metamorphism of basaltic rubble from Atlantis Massif may suggest that the material originated from the underside of the hanging wall (Searle *et al*., 2003). The association of highly altered pillow basalt from the corrugated surface at 13°19'N with serpentine and pyrite-, chalcopyrite- and sulphide-bearing talc clay may indicate that alteration results from focusing of (300-400°C) hydrothermal fluids on detachment fault planes.

Magnetic anomalies show variations in the amount of spreading either side of the axis, allowing areas of asymmetric spreading to be identified. Betwwen 14°-16°N (MAR), magnetic anomalies are much more variable than in areas where OCCs are not found (Fujiwara *et al*., 2003).

Analysis of palaeomagnetic direction data from IODP site U1309 (Atlantis Massif) shows rotation of the footwall by up to 50°, and suggests that the original fault orientation was steep, shallowing out later (Zhao and Tominaga, 2009). Re-orientated palaeomagnetic data in drill-core samples from Atlantis Massif is consistent with this, indicating a 46±6° anticlockwise rotation of the footwall (Morris *et al*., 2009). Anomalous magnetic remnance inclinations in ODP Leg 209 cores indicate substantial tectonic rotation below Curie temperature in this region (Schroeder *et al*., 2007). Palaeomagnetic data from the FTFZ also shows detachment fault rotations ranging between 50° and 80° (Garcés and Gee, 2007).

Gravity surveys identify lithologies below the seafloor on the basis of density differences. There are substantial differences in the densities of the main lithologies associated with OCC formation, basalt (2400-2700kgm^{-3}) gabbro (2900kgm^{-3}) and peridotite (3300kgm^{-3}). Average densities can be substantially affected by alteration. For example, peridotite density can be reduced to as low as 2600kgm^{-3} by pervasive serpentinisation (e.g. Miller and Christiansen, 1997).

Some OCCs have gravity anomalies consistent with low-density regions that have been fractured and pervasively serpentinised. The rough, corrugated topography associated with these features has the appearance of series of ridge-parallel fractures consistent with tectonic disturbance (Cannat *et al*., 1995).

Segment-end OCCs return gravity highs (Tucholke and Lin, 1994; Cannat *et al*., 1995; Tivey *et al*., 1998) when compared to the surrounding volcanic material (Searle *et al*., 2003). High RMBA 'bulls eyes' coincide with OCC domes (Tucholke *et al*., 1998; Fujiwara *et al*., 2003). The highest values are recorded near the termination of Fuji Dome and Atlantis Massif (Blackman *et al*., 2009).

Gravity surveys suggest that OCCs form in areas of thin crust, whereas the crustal thickness on the opposite flanks (outside-corner) is normal (Tivey *et al*., 1998). Density variations between OCC domes and the surrounding seafloor are consistent with variations between volcanic seafloor and gabbro, and also between basalt with gabbro intrusions and serpentinised peridotite.

Geophysical studies have revealed many details of the structure and formation history of OCCs. Blackman *et al.* (2009) argue that the three-dimensional nature of OCCs must be taken into consideration to improve gravity surveys, as 2D models assume certain geographic continuity of units, which may not be representative of their true extent beneath the surface. Additionally, they reiterate the importance of extending geophysical surveys to the terrain surrounding OCCs, in order that models of formation and development may be understood in a wider context.

2.11 - THE ORIGIN OF OCEANIC DETACHMENTS - HIGH-ANGLE VS. LOW-ANGLE FAULTING

Abyssal hill bounding normal faults are the most common tectonic feature on Earth (Buck *et al*., 2005). Graben faults globally show a large range of offsets, from microscopic slip to offsets of ~10km on metamorphic core complexes (Lavier *et al*., 2000, and references therein).

On slow-spreading ridges, normal faults are more planar toward the segment centre than at the ends (Sempéré *et al*., 1993). Fault spacing and offset increase towards segment ends, perhaps due to changes in lithospheric thickness.

Flexural unbending of the plate as it moves away from the axis forms the faults seen at fast-spreading ridges. However, at slow-spreading ridges, fault offset and dip is thought to be controlled by plate stretching, and its relationship with dyke intrusion (Buck *et al*., 2005). Faults with offsets smaller than the thickness of the brittle layer are common in rifts, generally dipping steeply at ~45° (Jackson, 1987). However, many shallower (<30°), large-offset faults have been observed (i.e. Cann *et al*., 1997, Tucholke *et al*., 1998).

For the last 30 years, researchers have suggested that upper mantle and lower crustal lithologies are exposed on the seafloor by large offset, low-angle detachment faults (e.g. Dick *et al*., 1981; Karson and Dick, 1983; Karson, 1990). Early models invoked detachment faults as a mechanism for transporting peridotite to the seafloor at inside corner highs (Michael and Bonatti, 1985, McKenzie and Bickle, 1988). The first direct evidence for the existence of such structures in the oceans was provided by Cann *et al*. (1997), in a study presenting sonar images of megamullions, and showing that their surfaces are planar, corrugated and orientated perpendicular to the ridge axis. Although the features did indeed resemble detachment faults, they were shallower than previously predicted. This shallowing is attributed to the mechanical effects of serpentinised peridotite, which may serve to lubricate the fault surface.

The existence of low-angle oceanic detachment faults has been corroborated by evidence from ophiolites (MacLeod, 1990; Tremblay *et al*., 2009), and further confirmed by sampling of highly strained fault rocks (serpentinised mylonites) from the corrugated surfaces of OCCs (MacLeod *et al*., 2002; Escartín *et al*., 2003; Boschi *et al*., 2006).

Low-angle detachment faults are certainly observed on the seafloor today (see Cann *et al*., 1997, Tucholke *et al*., 1998 and numerous subsequent studies). Many argue that they form at low angles (e.g. Davis and Lister, 1988; Wernicke, 1995). However, there is evidence to suggest that these faults are not shallow when they initiate, beginning their lives as steep normal faults (MacLeod *et al*.,

2009). The resolution of this debate is fundamental to the understanding of the OCC formation.

2.12 - EVIDENCE FOR A LOW-ANGLE ORIGIN FOR OCC DETACHMENTS

Structural analyses of low-angle faults bounding metamorphic core complexes in the South Western U.S. have been used to argue that a high-angle origin for shallow detachments is unlikely. Scott and Lister (1992) argue that if the direction of highest compressive stress is vertical during extension, the formation of low-angle detachment faults is mechanically difficult.

Simple-shear models envision the development of low-angle normal faults with dips less than 30° (Wernicke *et al*., 1985). The initial models have been substantially modified to accommodate field observations such as arching of low-angle faults (Reynolds and Lister, 1990) and occurrence of detachment fault sequences (Lister and Davis, 1989). The simple shear model is at odds with the Mohr-Coulomb theory of faulting (Hubbert 1951) and Andersonian faulting theory (Anderson, 1951). It also fails to reconcile seismic evidence on the focal mechanisms of faults (Jackson and White, 1989). The simple shear development of detachment faults has not been physically demonstrated by modelling (Gartrell, 1997).

Those who favour low-angle origins argue that the rotated block and secondary fault sequence envisioned by the models of Buck (1988) and of Wernicke and Axen (1988) is not seen in field observations of subaerial detachments. Davis and Lister (1988) cite the example of the Whipple detachment, California, which cuts high-angle faults above and below. They argue that this fault may be the youngest in a progressive detachment sequence. This is a model which is consistent with field observations at other subaerial detachments, such as the Rawhide fault (Scott and Lister, 1992).

Some subaerial detachment faults may be inconsistent with models for high-angle origins i.e. Chemehuevi (John and Foster, 1993); and Buckskin-Rawhide,

(Scott and Lister, 1992) where authors suggest detachment formation angles of 25-30° (Scott and Lister, 1995). The model of Gartrell (1997) suggests that boudinage of a strong layer may provide a mechanism for low-angle detachment fault origin.

The mathematical model of Zheng (1992) uses the 'maximum effective moment criterion' to examine formation of low-angle detachment faults. Results suggest that upward propagation of the synthetic extensional crenulation cleavage through mid-crustal domains of mylonitisation by strain localisation is an effective mechanism for the formation of low-angle detachments.

2.13 - EVIDENCE FOR A HIGH-ANGLE ORIGIN OF OCC DETACHMENTS

It is important to note that, by definition, a fault which starts at a high angle and shallows out later is not strictly a detachment fault. Lister (2004) defines detachment faults as 'forming at gently dipping even sub-horizontal orientations as the result of sub-critical failure in ductile shear zones as they begin to pass through the ductile-brittle transition'. However, the shallowly dipping faults bounding OCCs are referred to as 'detachment faults' by authors promoting both shallow and steep origin models.

High-angle fault origin models describe a mechanism whereby faults start out steep and gradually shallow out to the angles observed today. Flexural unloading and rebound of the footwall during stretching can cause the upper part of the fault to rotate on its hinge, shallowing as it emerges to acquire 'anti-listric' geometry. These models are collectively known as 'rolling-hinge' models, and have been proposed by many (for example: Lavier *et al*., 1999; Buck *et al*., 2005; Tucholke *et al*., 2008). Figure 8 illustrates OCC development according to a rolling hinge model.

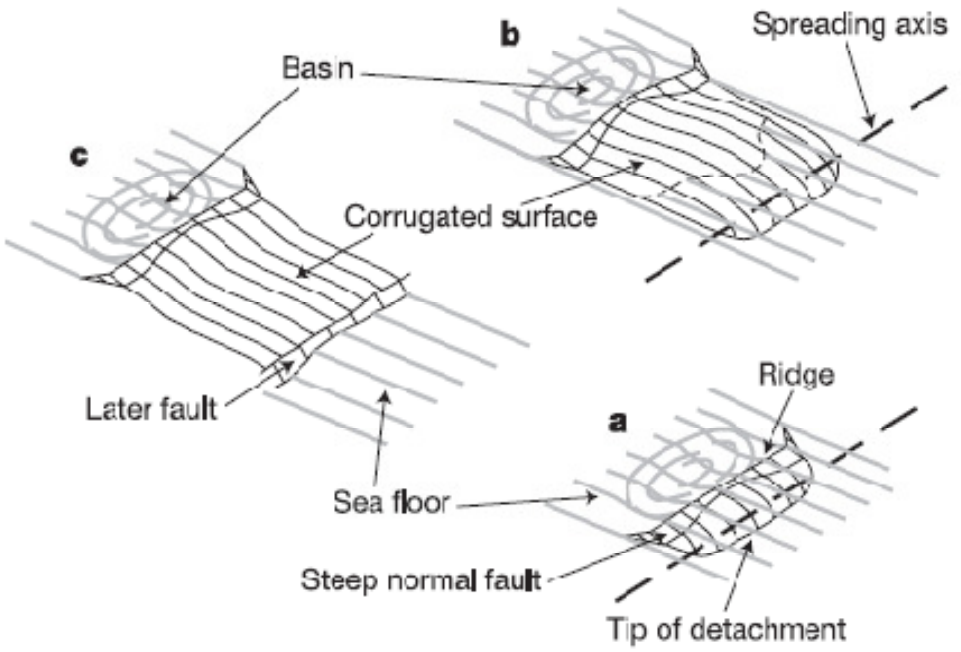

Figure 8: Illustration of the process whereby slip on a steep normal fault (a) rotates out to a shallower angle, exposing peridotite on the core complex surface (b). The detachment may be severed by the development of a later high angle fault (c). From Smith *et al*. (2006).

In rotated normal fault models, (Buck, 1988, Wernicke and Axen, 1988) faults rotate and flatten until cut off by a new fault in the hanging wall (Brun *et al*., 1994). When slip on such a fault becomes mechanically difficult, some models invoke high-angle secondary faults cutting into the hanging wall above the primary fault toe, as a method of redistributing stress. This creates a sequence of rotated blocks lying on top of the main active fault, with the least tilted blocks closest to the youngest secondary faults (Buck, 1988; Wernicke and Axen, 1988). Tilted-block models are a little different, (Angelier and Colletta, 1983, Davis, 1983) describing situations where steep normal faults separating large blocks are able to rotate to low angles (Brun *et al*., 1994).

Data on global fault focal mechanisms shows that only a small proportion of faults have a dip of less than 30°. Andersonian fault mechanics (Anderson, 1951) predicts that normal faults dipping at less than 45° cannot slip (Wernicke, 1995).

Formation of low-angle normal faults, according to this theory, requires the principal stress axes in the brittle upper crust to be significantly inclined with respect to the Earth's surface (Zheng, 2002) necessitating substantial shear stress in the vertical plane (Westaway, 1999).

Mechanical modelling suggests that loading conditions can alter the principal stress orientations in faults to configurations consistent with those in low-angle detachment faults. Elastic models with shear traction applied to the upper-crustal brittle layer were proposed as a possible cause for inclined principal stress axes (Yin, 1989). However, coulomb failure analysis claims that limits on shear traction of ~100Pa preclude its possibility as a mechanism for initiating detachment faulting. Coulomb failure does not reproduce frictional slip on low-angle surfaces at geologically plausible pore pressures, boundary pressures, or rock strengths. All models tested by Wills and Buck (1997) require unrealistically high tensile stresses in the upper 5km of the crust, and suggest that failure will begin on high-angle faults, before low-angle faults have a chance to develop. Subsequently, modelling has indicated that it is possible to generate stress fields in suitable orientations for detachment faulting, but only at extreme stress conditions, such as those generated during subduction (Westaway, 1999).

By reconstructing the original dip of rotated fault blocks at the breakaway of faults from the MAR, MacLeod *et al*. (2009) argue that the detachments started out as normal faults. Assuming the now outward-tilted volcanic slopes were initially horizontal, the original dip of the faults prior to tilting is given by the sum of the present-day dip of the volcanic surface associated with each fault scarp and of the scarp itself. The original dip of non-OCC faults on the surrounding ridge flank is 65°±12°, and the same angle, 65°±10°, is found for the faults on the opposite flank. The calculated average initial dip for the OCC detachment headwalls is 61°±12°, which is similar to normal faults on both flanks of the ridge axis.

Lab experiments use homogeneous sand layers over a layer of ductile silicone to model the development of detachments in metamorphic core complexes in a brittle-ductile crust (Brun *et al*., 1994). Results indicate that the rise of a domal core complex requires shear to be localised around a 'soft inclusion' in a laterally inhomogeneous ductile layer. The authors suggest that this soft heterogeneity

could, in nature, represent partially molten rocks at the brittle-ductile transition. All faults produced by this modelling method start at high angles, and rotate to lower dips during extension (Brun *et al*., 1994). However, Scott *et al*. (1995) argue that the rheological properties of the soft heterogeneity would have to remain constant throughout uplift of the complex, and that this is unrealistic. They conclude that the model of Brun *et al.* (1994) is insufficient, both on the basis of the rheological argument above, and because the model fails to accurately reproduce the formation of subhorizontal shear zones, and denudation of the lower plate.

Analysis of palaeomagnetic direction data from IODP site U1309 at Atlantis Massif shows rotation of the footwall by up to 50°, and suggests that the original fault orientation was steep, and that it shallowed out later (Zhao and Tominaga, 2009). Re-orientated palaeomagnetic data in drill core samples from Atlantis Massif agree, indicating a 46±6° anticlockwise rotation of the footwall (Morris *et al*., 2009) providing strong support for flexural rolling hinge models whereby faults start out dipping steeply, subsequently rotating to shallower dips.

Though many studies have proposed low-angle origins for detachment faults bounding subaerial core complexes, there is substantial evidence to suggest that submarine detachments, at least, must form from the rotation of a steep normal fault to a shallower angle. Rolling-hinge models best reconcile the features of core complexes with geophysical evidence such as the occurrence of earthquakes at depth beneath OCCs, and palaeomagnetic data which shows that material within mullions has been substantially tectonically rotated.

2.14 - SERPENTINISATION, FLUID FLOW AND FAULTING AT OCEANIC CORE COMPLEXES

OCCs are formed in the cooling lithosphere. Over time, shallow processes and weathering become more significant contributors to the evolution of the mullion structure (Blackman *et al*., 2009). This suggests that the mechanical properties of alteration minerals, microscale fracturing and the flow of hydrothermal fluids

through fault planes may be vital factors in promoting long-lived exhumation of lower crustal and upper mantle lithologies.

Detachments are not typically associated with fault gouge or vastly disrupted breccia, and are 'knife-sharp', cutting cleanly through all previously formed structures. There is evidence that detachment faults propagate by subcritical fracturing, particularly at the microscale (Lister, 2004). Microseismicity studies suggest that microearthquakes indicating movement on low-angle faults are induced by fluid overpressure along the fault plane, which causes small ruptures (Collettini and Holdsworth, 2004).

Serpentinite is formed at MORs when mantle peridotite is exposed to seawater, and olivine and pyroxene are metamorphosed and hydrated. Olivine reacts to form serpentine, brucite and magnetite (<250°C), whilst pyroxene reacts to form talc and tremolite (>350-400°C) (Bach *et al*., 2004). These results are consistent with observed styles of rock-seawater reaction at hydrothermal vent fields. At OCCs, unroofed peridotite is extensively serpentinised along the fault zone. The thickness of serpentinite on the domes is unknown. Assuming that the steep slopes surrounding OCCs provide a cross-section through their structure, serpentinites may extend to depths of at least several hundred meters. However, deep-drilling at OCCs has recovered gabbroic sequences with virtually no serpentinised peridotite (Ildefoinse *et al*., 2007) despite the fact that relatively fresh peridotite is preserved immediately beneath. This suggests that in the localised zone where fault shear is extreme, and where serpentinisation is almost 100% complete, the mechanical strength of serpentine influences the ease of slip along the fault.

Rock deformation experiments show that serpentinisation has a dramatic effect on the strength of peridotite. At 10-15% serpentinisation, the strength of the lithosphere is reduced by ~30% (Tucholke *et al*., 1997), and talc, found in abundance on the OCCs at 13°19′N and 13°30′N (this study), and also at Atlantis Massif (Karson *et al*., 2006) is considerably weaker, possessing only 20% of the mechanical strength of (Lizardite) serpentine (Escartín *et al*., 2008). Talc and minor serpentine recovered from the OCC at 13'19N have the appearance and mechanical properties of soft clay or putty, and contain numerous euhedral pyrite

and chalcopyrite crystals, which lends support to a theory of intense hydrothermal processing.

Results from flexural models indicate that if serpentinisation is focused in the brittle zone strain localisation increases, providing a possible explanation for the development of very long fault throws. This finding is supported by the observation that at magmatic segment centres, where serpentinisation is minimal, normal faults are closely spaced with short throws. At segment ends (where peridotite is exposed, the brittle zone is deep and serpentinisation is widespread) faults are much more widely spaced, with substantially longer throws (Escartín *et al*., 1997).

MacLeod *et al*. (2009) show that OCC detachments at the MAR (12°6'-14°N) initiated as normal faults at steep angles (~65°), and shallowed out later. Whilst the majority of normal faults become inactive as they are displaced away from the ridge by spreading, some faults shallow out, developing offsets nearly three times as large as those of other faults in the area. Since all of the normal faults share a common formation history, large offsets must be triggered by different conditions on specific faults. MacLeod *et al.* (2009) attribute the development of large offsets to weakening of the fault plane during serpentinisation and hydration. This effect may become significant when the magma supply is locally diminished. In this scenario, as a normal fault extends to accommodate spreading, the crust is thinned, and mantle lithologies beneath are exposed to seawater and hydrothermal fluids, promoting serpentinisation, and lubricating the fault plane. This process is summarised in Figure 9.

There is increasing physical evidence for a correlation between the occurrence of vent fields and low-angle detachment faults on slow and ultraslow spreading ridges (Tivey *et al*., 2003; German and Lin, 2004; DeMartin *et al*., 2007). Black smoker fluids are thought to result from seawater-derived fluid that is discharged vertically from the crust (~1-3km depth). However, trace element and Sr and O isotope data from the OCC at 15°45', MAR, indicates that fluids at 300-400°C were intensely focused along the detachment, and the surrounding rocks underwent extreme alteration by hydrothermal fluids (McCaig *et al*., 2007). In this model, the heat driving hydrothermal circulation is sourced from gabbro bodies

cooling beneath the OCC dome. Intense fluid focusing could aid fault propagation by weakening, altering and serpentinising the rocks along the fault plane. Micro-earthquake seismicity data and modelling at the TAG vent field suggests that hydrothermal fluids exploit the detachment fault to extract heat from near to the crust-mantle interface (DeMartin *et al*., 2007).

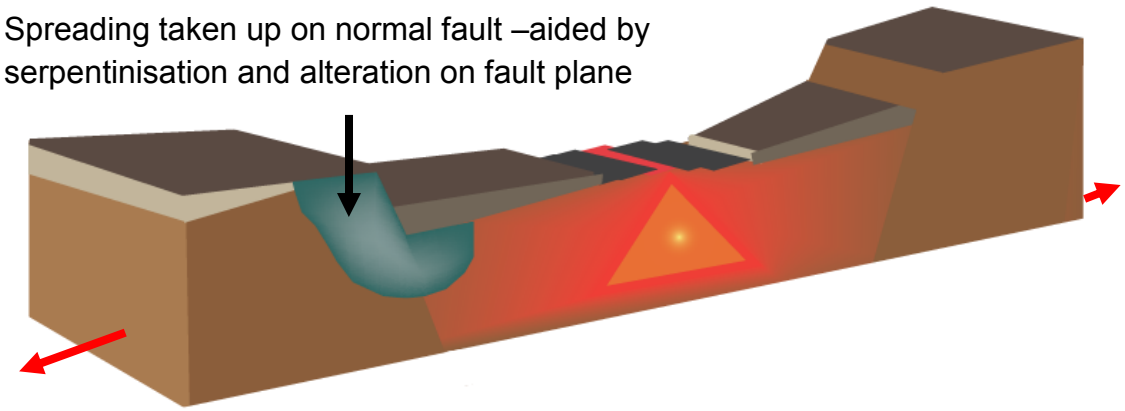

Figure 9: Slip on a steep normal fault in the valley wall is aided by seafloor weathering processes and serpentinisation, which act to weaken the fault plane, making it more prone to slip. This process may be especially significant where melt supply is low, and normal valley wall faults extend to accommodate spreading.

Talc is one of the weakest fault zone minerals. Friction experiments on fault gouge indicate that talc heated to 100-400°C is consistently weaker than at room temperature. Talc has a stability field ranging from surficial to eclogite facies conditions, and exhibits velocity-strengthening behaviour, i.e. its strength increases with increasing shear rate (Moore *et al*., 2008). Talc is therefore both stable and mechanically weak at detachment fault conditions. The conditions for its formation via hydration of pyroxene also prevail in detachment fault zones. Talc formation may be an important fault weakening process at detachment faults, and its velocity strengthening behaviour may contribute to stabilisation of the slow, creeping slip on oceanic detachments (Moore *et al*., 2008).

2.15 - MAGMATISM AND ACTIVE FAULTING

Whilst the geographic association of OCCs with amagmatic crust is well established, the role of melt provision and supply in the formation of OCCs is not well understood. Amagmatic areas have highly variable crustal thicknesses. It is thought that they experience periods of magmatic quiescence and tectonic spreading, interspersed with periods of normal spreading. OCCs form where crust is thin, surface volcanism is sporadic and peridotite is exposed on the seafloor. This observation suggests that detachment faulting initiates as a mechanism to accommodate plate spreading during an amagmatic episode (e.g. Karson, 1990; Tucholke and Lin, 1994; Tucholke *et al*., 1998; Escartín *et al*., 2003).

On the Knipovich Ridge (northernmost MAR), interpretation of magnetic anomalies indicates that normal gabbroic crust is formed during periods of spreading at ~8mm/yr. At ~5.5mm/yr the ridge becomes amagmatic. Upper mantle material is serpentinised, and subsequently exposed on the seafloor (Kandilarov *et al*., 2008).

Analysis of peridotite geochemistry and fabrics at the Vema Lithospheric Section (VLS- EMAR segment, MAR) suggests that spreading has been symmetrical throughout most of the mid-history of the region. However, during a time interval of ~1.4Ma, strongly deformed peridotite Mylonites were formed. Geochemistry of these rocks suggests that they experienced a relatively low degree of melting (Cipriani *et al*., 2009).

OCC development between 12°60'N to 14°N is associated with suppression of magmatism on a $10^{\wedge 6}$ time scale and a 20-30km along axis length scale (MacLeod *et al*., 2009). Opposite the active 13°19′N and 13°30′N OCCs, neovolcanic zones are reduced or absent. TOBI backscatter images and estimates of sedimentation rates in the axis show that the axial valley here has been volcanically inactive for a similar length of time as the OCCs have been active. However, magmatism may persist throughout the period when an OCC is active (Dick *et al*., 2000, MacLeod *et al*., 2002, Reston *et al*., 2002, Escartín *et*

al., 2003, Blackman *et al*., 2006). The occurrence of gabbro at OCCs (e.g. Kane Megamullion, Atlantis Bank, Atlantis Massif) may suggest that magmatism is moderate during OCC formation (Cannat *et al*., 1997; Karson, 1999; MacLeod *et al*., 2003; Ildefoinse *et al*., 2007; Kelemen *et al*., 2007).

Numerical models simulating fault development suggest that OCCs are best reproduced during normal levels of magma supply (Buck *et al*., 2005). Ildefoinse *et al.* (2007) suggest that OCCs develop as a result of the rheological differences between gabbro and surrounding serpentinised peridotite. Intrusion of a gabbro body into peridotite causes strain localisation around the pluton margins, eventually resulting in an uplifted structure with a gabbro core surrounded by highly deformed serpentinite. The presence of large gabbroic plutons requires that OCCs form during periods of normal melt production.

Similarly, Xu *et al.* (2009) suggest that gabbros emplaced at Kane Megamullion may have been instrumental in its formation via strain localisation in a weak zone around the gabbro body, which promoted the initiation of the fault. If gabbro mush focuses strain in these localities, the gabbros should exhibit extensive and widespread plastic deformation. Deformation textures in gabbro from Atlantis Massif indicate that high-temperature (>500°C) strain occurred via crystal-plastic flow and diffusive mass transfer, but that strain is partitioned into peridotite at low temperature (Schroeder and John, 2004). Textures in gabbroic rocks from this site are highly variable, however (Godard *et al*., 2009).

Gabbro strain localisation models are not supported by observations on the MAR between 12°60'N and 14°N, where sampling recovered virtually no gabbro. Therefore, gabbro may not necessarily be a constituent of all OCC domes, and melt provision here may be low. However, it should be noted that sampling of these OCCs by surface dredging only may have failed to reproduce the proportions of lithologies in the subsurface.

The numerical models of Buck *et al*. (2005) and Tucholke *et al*. (2008), in which amagmatic spreading generates new crust at approximately half the spreading rate, successfully reproduce typical OCC geometry for intermediate magma supply. This observation is broadly in agreement with the findings of MacLeod *et al.* (2009), who report a magma supply of M= 0.63±0.05 at OCCs.

Tucholke *et al.* (2008) present modelling and geological data indicating that ~30-50% of extension is accommodated by magmatic spreading during OCC development. Significant magmatic accretion takes place in the detachment footwalls. They argue that the irregular magmatism associated with reduced melt provision may focus unevenly beneath the axis. This results in an uneven brittle-plastic transition in the zone where detachment faults root, and may explain the corrugated topography of OCC domes.

Some argue that robust magmatism is capable of generating conditions suitable for OCC development. Parsons and Thompson (1993) suggest that in metamorphic core complexes, mid-crustal inflation due to magmatism may be a sufficient to rotate the principal stress axes into orientations favourable for development of slip on low-angle detachment faults. The 3D thermo-mechanical modelling of van Wijk and Blackman (2005) investigates the orientation and magnitude of stress fields at ridge-transform discontinuities. During simulated magmatic episodes, high stress amplitudes are not found at inside corner highs, and thus the formation of OCCs is unlikely at this time.

Magmatism may be key in controlling the cessation of detachment faulting. Near 14°N on the MAR, an off-axis, heavily sedimented OCC sits alongside an active neovolcanic valley, where fresh pillow basalts were sampled. Recently, the axis here experienced a switch in the locus of spreading from detachment fault slip, to normal axial magmatism. Tucholke *et al.* (1998) suggest that detachment faults are terminated when magmatism becomes robust enough to reach the segment end, weakening the axial lithosphere and promoting inward fault jumps there.

Sidescan sonar imagery shows triangular neovolcanic zones cutting across the active toe of the OCC at 13°19'N. MacLeod *et al*. (2009) argue that termination occurs when axial magmatism cuts across the fault axis, returning the locus of spreading to the ridge. The factors controlling the resumption of magmatism are not understood, though changes in mantle geochemistry, mantle focusing or crustal plumbing are possible causes. Undoubtedly OCCs form in areas characterised by thin crust and limited volcanism. However, there is strong evidence to suggest that melt supply during these 'amagmatic' episodes is normal.

The relationship between magmatism and tectonic spreading remain unclear, and the connections between magma supply and detachment faulting require further study. The development of OCCs in both segment-end and segment-centre positions suggests that the balance of tectonic and magmatic forces is critical in creating favourable formation conditions (Buck *et al*., 2005). Conflicting evidence on the basis of gabbro recovery from different OCCs (plentiful gabbro at Atlantis Bank, Atlantis Massif, Kane Megamullion, versus little gabbro at ~15°N) may be an artefact of sampling bias. Conversely, it may indicate that the OCCs are compositional/morphological end-members, as indicated by the application of modified Penrose (Dick, 1989) and Plum pudding (Cannat, 1997) crustal models at these sites respectively. The interplay between tectonism and magmatism, if better understood, could provide vital constraints on OCC formation and development (Blackman *et al*., 1998).

2.16 - HYDROTHERMAL ACTIVITY AND DETACHMENT FAULTING

Many segments in the central MAR host hydrothermal vent sites (Figure 10). The majority of those between 12.5°N-35°N are found in asymmetrically spreading segments, in the vicinity of active detachment faults (Escartín *et al*., 2008).

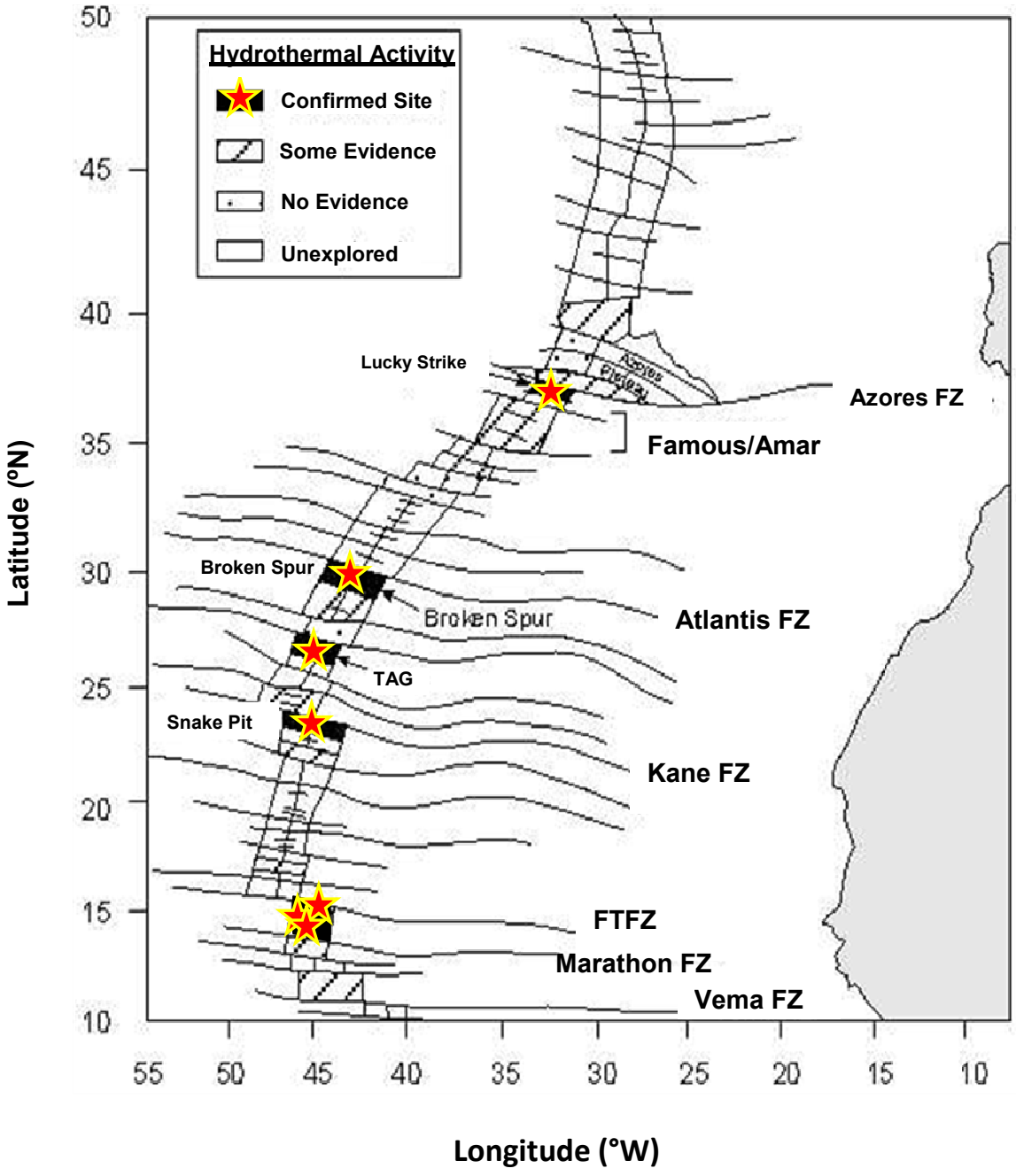

Figure 10: Distribution of well-known hydrothermal vent sites along the MAR, 10-50°N. Also shown are the positions of major fracture zones and the Azores Plateau. After Baker *et al*. (1995).

Correlations between asymmetric spreading and hydrothermal activity on the MAR (Figure 11) have been described (Escartín *et al*., 2008). Evidence for high-temperature fluid circulation along detachment faults suggests that peridotite-hosted hydrothermal activity may be closely linked with the development of shallow detachment faults on the MAR (Boschi *et al*., 2006; McCaig *et al*., 2007).

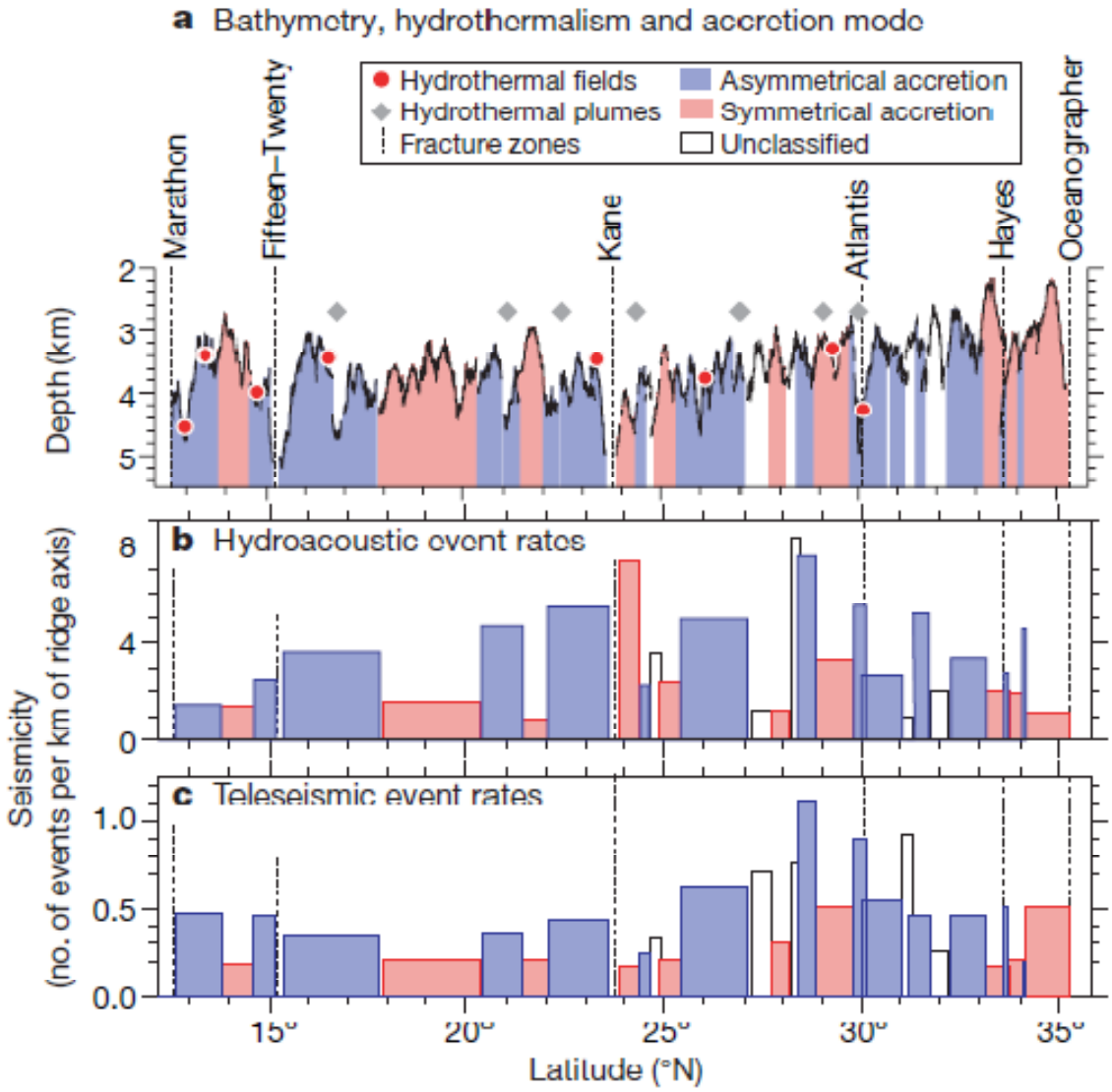

Figure 11: Correlations in the central MAR between seismicity, asymmetric spreading, and the development of hydrothermal vent sites. Hydrothermal sites almost exclusively occur in asymmetrically spreading crust. From Escartín *et al*. (2008).

Hydrothermal sites operate at a variety of temperatures. Some hot vents are hosted in ultramafic rocks (e.g. Rainbow), others are cooler (Lost City) (McCaig *et al*., 2007). To date, few ultramafic-hosted hydrothermal systems have been discovered (Petersen *et al*., 2009). In the central MAR a number of sites have been studied in depth.

The Broken Spur field (~29°N) is sulphide dominated and contains abundant pyrrhotite (Rusakov, 2007). The TAG hydrothermal vent field (26°10'N) is underlain by lower crustal gabbros and serpentinised peridotites at depths as shallow as 1km (Canales *et al*., 2007), and is located on a detachment fault (Tivey *et al*., 2003). Canales *et al.* (2007) argue that the primary heat source for the TAG is an underlying magma chamber.

The Snake Pit hydrothermal site (23°22'N), ~30km south of the Kane transform, consists of basalt hosted, active, hot (~350°C) black smoker vents and sulphide chimney mounds with cold seeps (~226°C) surrounded by a thick layer of hydrothermal sediment (Karson and Brown, 1988).

Hydrothermal processes in the region around the FTFZ have been reported (e.g. Simonov and Milosnov, 1996, Alt *et al*., 2007). Hydrothermal temperatures are thought to extend from 230-250°C to >350°C. Simonov and Milosnov (1996) suggest that the composition of the hydrothermal fluids indicates that both seawater and magma derived fluids are present, and argue that high salinity indicates a magma chamber source. Alt *et al.* (2007) report high temperature hydrothermal fluids derived from interaction with gabbro at depth.

On the basis of extreme isotopic alteration, McCaig *et al.* (2007) show that black smoker fluids at 300-400°C were focused along the detachment of the OCC at 15°45'N. Talc-tremolite-chlorite schist development in the fault zone results from fluid exchange between mafic and ultramafic rocks, with equilibrium fluids being representative of an ultramafic hosted site. The detachment fault represents a major pathway for fluids through the crust, as evidenced by extremely low $d^{18}O$ of altered plagiogranite veins (Jöns *et al*., 2009). Ultramafic-hosted hydrothermal activity at the intersection of the FTFZ with the MAR near 15°45'N is characterised by high Methane to Mn ratios. These contrast with ratios found in black-smoker type hydrothermal fluids hosted in mafic rocks at segment centres

(Rona *et al*., 1992). High methane values are thought to result from ongoing serpentinisation reactions within exposed ultramafics (Charlou *et al*., 1998).

The Logatchev Field (~15°N) consists of six active vent sites and, like the Rainbow site, is known to be influenced by ultramafics. The hydrothermal fluids are depleted in boron compared to seawater, and have lower lithium than basaltic systems. Their signature is characteristic of fluids related to serpentinisation processes in the reaction zone, though interaction with gabbro is also thought likely (Schmidt *et al*., 2007; Petersen *et al*., 2009). Analyses of host rocks at Logatchev reveal that whilst harzburgites and dunites are heavily serpentinised, gabbros are relatively fresh. This shows that alteration processes are a combination of serpentinisation, melt/rock interaction of serpentinites and mafic intrusions, and low-temperature seafloor weathering (Augustin *et al*., 2008).

The Ashadze hydrothermal vent field, hosted in the ultramafic complex at 13°02'N, comprises two active vent fields located at two different levels on the western wall of the axial valley near 13°N. The Ashadze 1 and 2 sites, 5 km apart, are respectively 4 km and 9 km off-axis (Ondreas *et al*., 2007). Sulphide chimney fragments, ore assemblages, sulphide breccias and mineralised peridotite samples have been recovered from these sites (Mosgova *et al*., 2008).

Inactive hydrothermal sites are reported on the western, northern and eastern slopes of the 13°30'N OCC. Iron and copper-zinc sulphide hydrothermal deposits record evidence of fluid interaction with peridotite and basalt (Beltenev *et al*., 2007). Active or recently active hydrothermal activity is also reported on the OCC at 13°19N, where chimney sulphides and mineralised talc mud were recovered by dredging (MacLeod *et al*., 2009).

CHAPTER THREE – GEOLOGY OF THE CENTRAL MAR REGION

The primary study area for this work is on the MAR south of the Fifteen-Twenty Fracture Zone (FTFZ), from 14°N to the Marathon Fracture Zone at ~12°60'N. This chapter provides a detailed introduction to the morphological, structural, lithological and geochemical characteristics of this segment, and of the surrounding central MAR.

3.1- REGIONAL TECTONICS AND MORPHOLOGY OF THE CENTRAL MAR

The central North Atlantic (~9° to 35°N) was formed by the separation of North America and Africa. To the north it is bounded by the Eurasia-Africa (EURA-AFRC) or Azores-Gibraltar Plate Boundary and the Pico Fracture Zone, to the south by the North America-South America (NOAM-SOAM) Plate Boundary (Collette and Roest, 1992).

The slow-spreading MAR (~15mm/yr half-rate) is marked by a 1.5–3km deep axial rift valley (Bohnenstiehl *et al*., 2003) with a valley floor 4-15km across. Near-bottom surveys show that much of the valley floor has experienced recent volcanism (Bohnenstiehl *et al*., 2003). The ridge is sinusoidal in shape and densely populated by fracture zones, which are typically more elongate in extent to the east than to the west (Figure 12).

Segments between the major fracture zones (Atlantis FZ, Kane FZ, FTFZ and Vema FZ) are frequently bounded by non-transform offsets. Many have asymmetric spreading areas (i.e. Rona *et al.*, 1976; MacDonald, 1977; Allerton *et al*., 2000; Smith *et al*., 2006; Escartín *et al*., 2008) where mantle peridotite is unroofed along detachment faults (Dick, 1989; Cannat *et al*., 1995; Cannat, 1996; Escartín and Cannat, 1999; Smith *et al*., 2006). Asymmetric spreading has been a feature of MAR behaviour throughout its history (Bird *et al*., 2007).

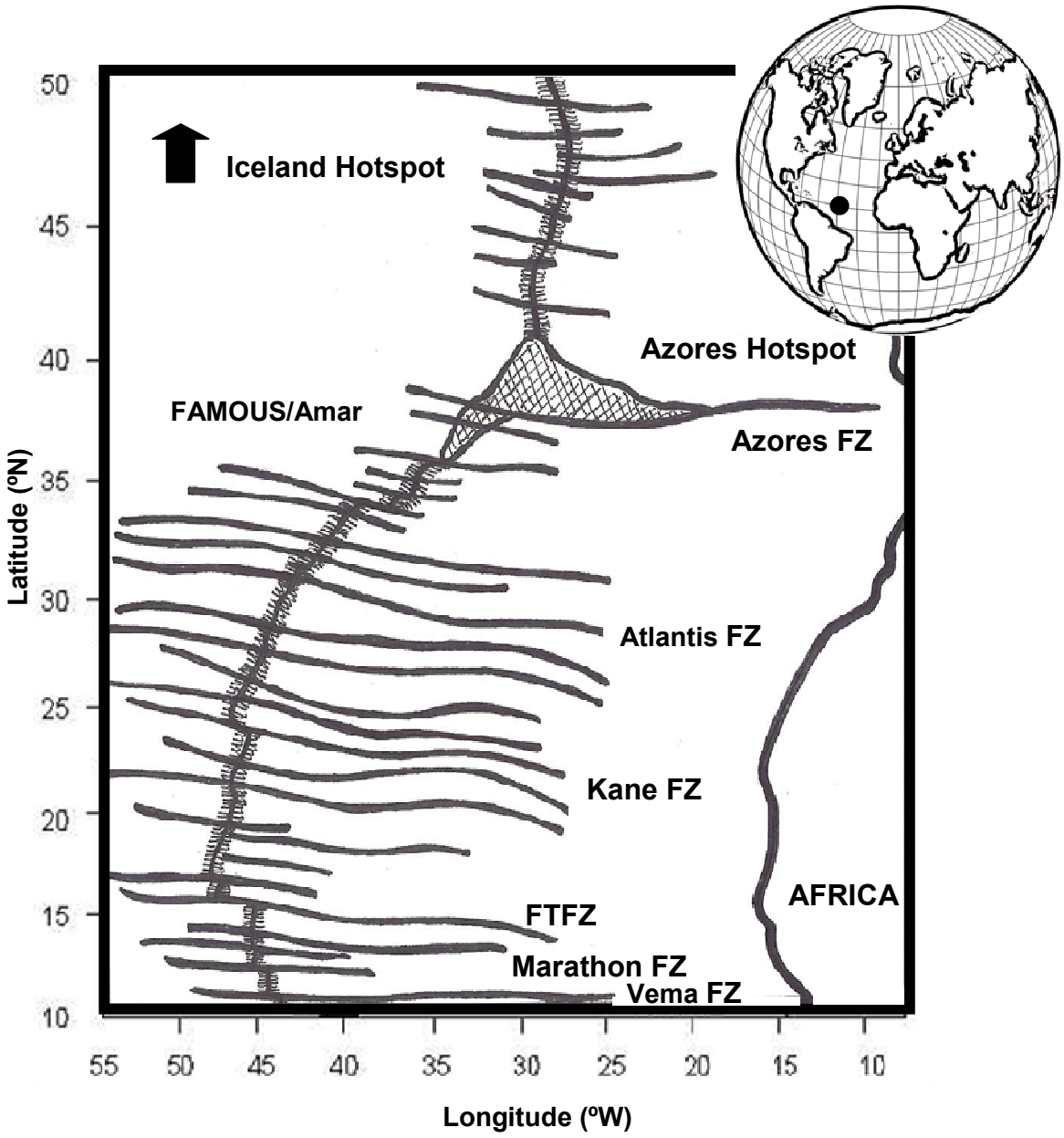

Figure 12: The sinusoidal shape of the central MAR, the position and extent of the major fracture zones, and the relationship of the MAR with the Azores hotspot and associated plateau. Global position inset.

In the north, the ridge interacts with the Azores hotspot (39°N), becoming shallower and broader (Bohnenstiehl *et al*., 2003). This interaction is visible in the form of a plateau to the east of the MAR, forming the Azores Island chain. Seismic tomography centres the hotspot low-velocity anomaly on 38.5°N, 28.5°W (Yang *et al*., 2006).

Average crustal thickness immediately north of the Azores plateau is close to the 6km global average for ocean crust. Plume influence on ridge accretion here is thought to have been very limited in recent time (Maia *et al*., 2007). V-shaped, east-west orientated bathymetric features and geochemical gradients are observed along the MAR south of the Azores. It is suggested that Azores plume material flows southward along the ridge (Schilling, 1973; White and Schilling, 1978). East-west asymmetry of bathymetric highs, reported as far south as 27°N (Thibaud *et al*., 1998) may reflect the surface effects of sub-lithospheric plume flow (Yang *et al*., 2006). However, MORB trace element compositions suggest no strong plume influence south of ~30°N (Figure 13).

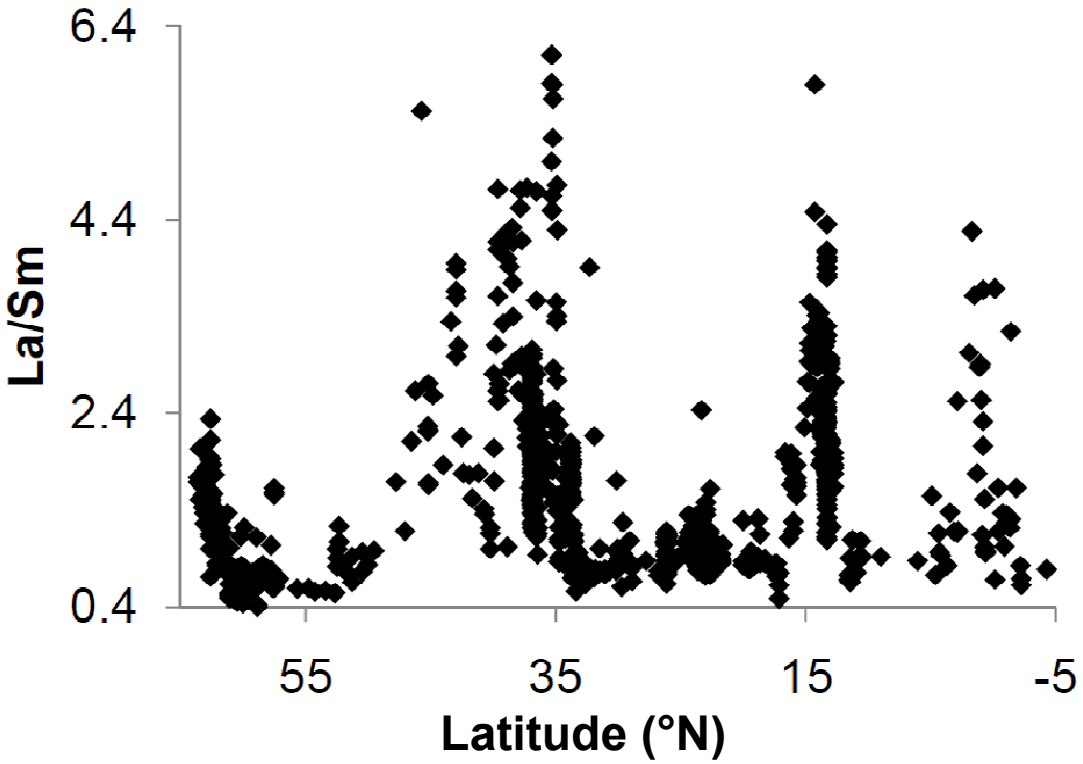

Figure 13: La/Sm vs. latitude data for the Mid-Atlantic Ridge 5°S-65°N. High La/Sm ratios are seen at the Azores Hotspot (~30-40°N), but rapidly drop away to N-MORB values south of ~30°N. This suggests that significant plume influence on trace element geochemistry does not extend south of this position. Data sources – PetDB, this study.

Ultramafic exposures, asymmetric spreading and OCCs are common on the central Mid-Atlantic ridge. The Vema FZ (9°-11°N) left-laterally offsets the MAR by ~320km and hosts serpentinised peridotite, gabbro, dolerite and basalt exposures (Auzende *et al*., 1989). Adjacent segments are typically floored by

MORB (Melson and Thompson, 1971). It is suggested that the Vema Lithospheric section, exposed on the south wall of the Vema transform, formed during a period of amagmatic spreading corresponding to a thermal minimum of the local sub-ridge mantle at crustal ages from 16.8 to 18.2 Ma (Cipriani *et al*., 2009). Bonatti *et al.* (2003) use crustal thickness estimates and chemistry of peridotite from the region to show that mantle upwelling and melting beneath the MAR operates in dynamic pulses, creating crustal thickness variations on a 3-4Myr timescale.

Ultramafic exposures are also well documented at the Atlantis (~30°N) and Kane (~23°N) Fracture zones, where OCCs are found at ridge-transform intersection inside-corner highs, and at 15°45'N.

Between the FTFZ and Marathon Fracture Zone, OCCs are common (Figure 14), and not limited to inside corner highs adjacent to major transforms (Gràcia and Escartín, 1999; Smith *et al*., 2006, 2008).

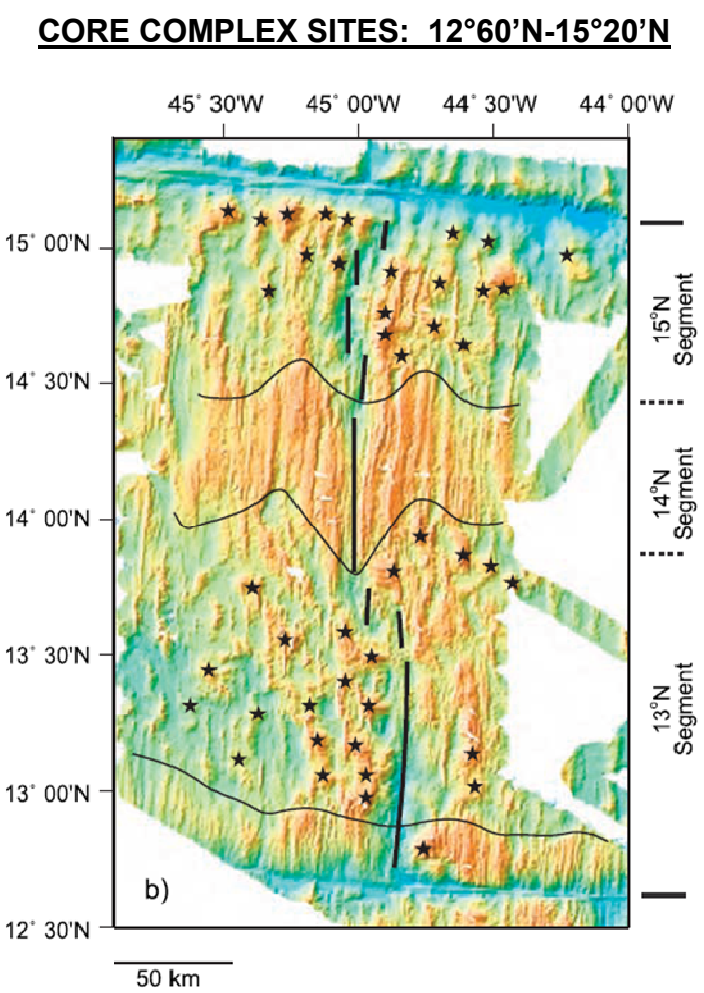

Figure 14: The morphology of the MAR between the FTFZ and Marathon FZ is highly variable. Black stars indicate the distribution of structures identified as OCCs (Smith *et al*. 2006, 2008).

The FTFZ offsets the MAR >195 km in a sinistral sense (Roest and Collette, 1986). It has a broad valley and is oriented 94°–98°E (Fujiwara *et al*., 2003). North of the FTFZ, the axial valley has linear morphology, whereas to the south

the axial valley is formed by a series of en-echelon axial deeps (8-18km in length) and short axial ridges (Gràcia and Escartín, 1999). The southern half of the segment (12°60'N-14°N) is broken by a non-transform discontinuity offsetting the neovolcanic axis by ~7.5km sinistrally (MacLeod *et al*., 2009). The morphology of the axial valley is shown in Figure 15.

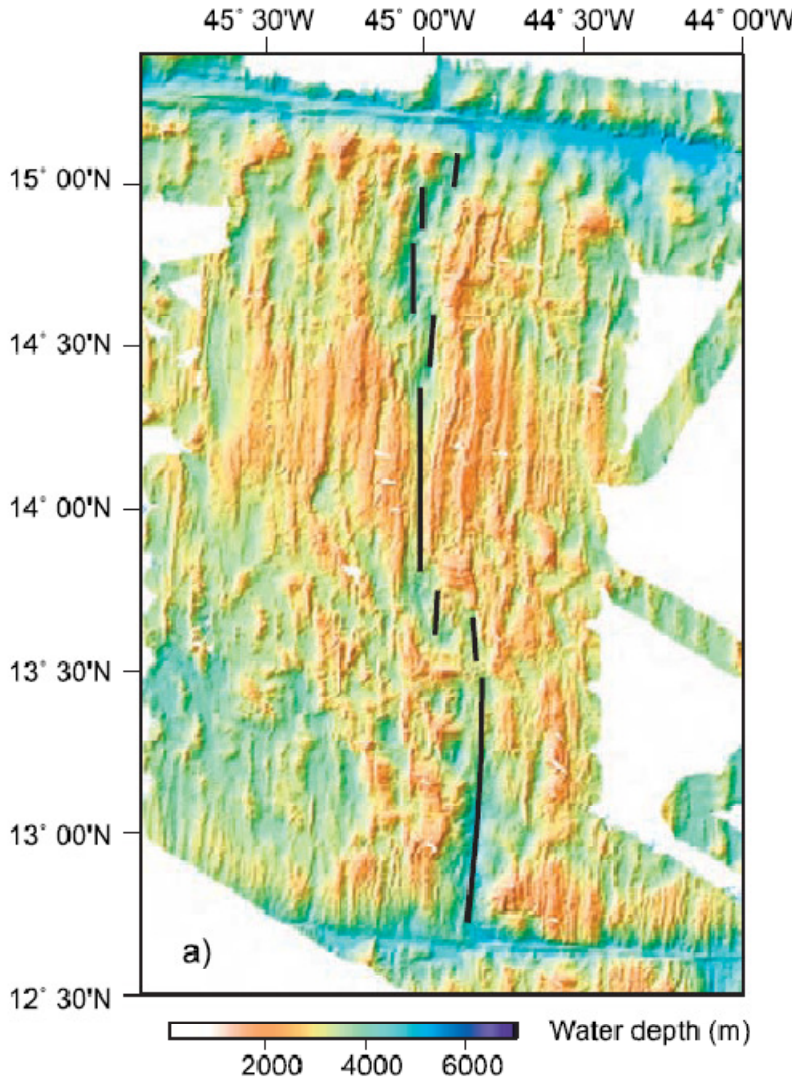

Figure 15: Bathymetry data showing highly variable ridge flank morphology and numerous non-transform offsets in the axial valley between 15°20'N and 12°60'N. After Smith *et al*. (2008).

The segment centre (14°N) is characterised by ridge-parallel abyssal hill topography and negative RMBA (Fujiwara *et al*., 2003) typical of magmatic spreading ridges.

However, north and south of 14°N the crust is thin or absent (Escartín and Cannat, 1999, Fujiwara *et al*., 2003). Areas where peridotite is exposed on the seafloor have positive RMBA, indicating high-density regions within the magmatic crust (Fujiwara *et al*., 2003). Here, ridge-parallel faulting is replaced by rugged terrain with short fault scarps (Cannat *et al*., 1997). The topography is highly variable, with deep axial valleys flanked by segment centre OCCs (Smith *et al*., 2006).

The MAR in the vicinity of the FTFZ has been sampled by numerous dredge and submersible studies (Cannat *et al*., 1992; Cannat *et al*., 1997), as well as ODP drilling (Escartín *et al*., 2003; Garcés and Gee, 2007; MacLeod *et al*., 2002). Outcrops of lower crustal and mantle rocks are extensive on both flanks of the axial valley over an unusually long (along-axis) distance. This indicates a high ratio of tectonic to magmatic extension (Fujiwara *et al*., 2003). The width of the neovolcanic zone (identified by sonar backscatter imaging) is highly variable between 12°60'N-15°20'N, extending from zero at active OCCs (13°19'N, 13°30'N) to 8-10km in magmatically robust areas, and at the inactive 13°48'N complex (MacLeod *et al*., 2009).

Evidence for the availability of melt is contradictory. The abundant peridotite exposures and OCCs, combined with thin crust and a lack of fresh volcanics in the axis (MacLeod *et al.*, 2009), imply low melt supply. However, 'hotspot-like' E-MORB geochemistry (Dosso *et al*., 1991) and normal ridge topography at 14°N suggest a strong melt supply, and perhaps a fertile mantle source (Fujiwara *et al*., 2003).

3.2 - OFF-AXIS SEISMICITY, RIDGES AND TROUGHS IN THE 15°N REGION

Studies on the central MAR reveal off-axis seismicity south of the FTFZ (Figure 16).

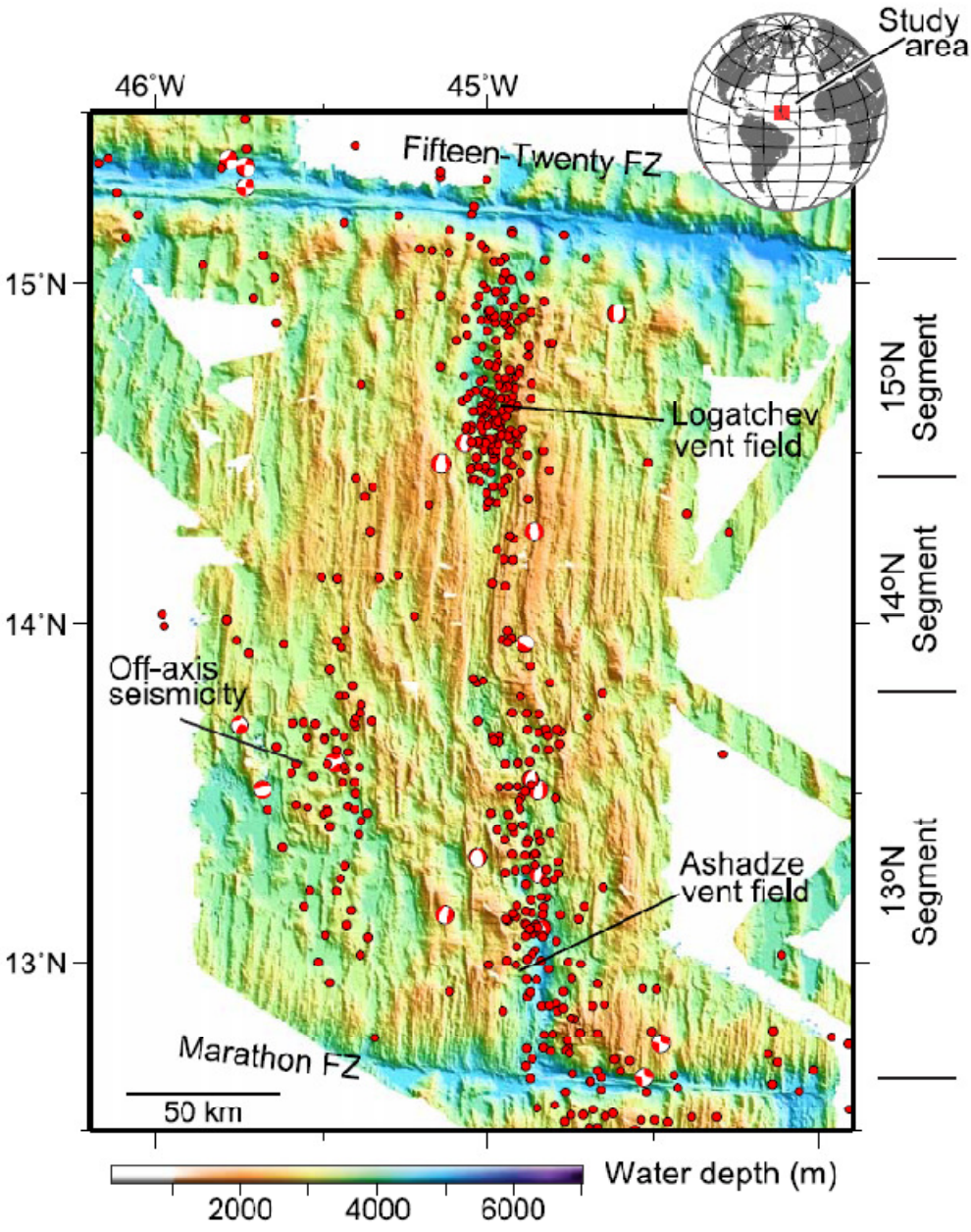

Figure 16: Variations in axial seismicity between 12°60'N and 15°2'N. Typically on the northern MAR, seismicity extends for 15-20km either side of the axis. However, between 13°N-14°N a parallel band of seismicity is clearly visible ~70km off axis. Smith *et al*. (2008).

Hydroacoustic monitoring (15-35°N) shows that the seismically active zone normally extends for ~15-20km either side of the axis (Smith *et al*., 2002, 2003). Seismicity is not usually considered to be important in ridge evolution beyond this seismic zone (Smith *et al*., 2003). However, between 13-14°N a ridge-parallel band of off-axis seismicity is found~70km west of the ridge axis (Smith *et al*., 2002). It is thought that this seismicity arises from unusual plate stresses, or as a result of the initiation of a ridge jump within the area (Smith *et al*., 2002). Roest and Collette (1986) describe leaking of the FTFZ transform, interpreted as the result of a recent change in spreading direction in the area, perhaps associated with the development of a North America-South America-Africa (NOAM-SOAM-AFRC) triple point.

There has been substantial argument over the precise position of this triple junction. Many agree that the NOAM-SOAM boundary is currently situated between 10° and 20°N (Minster and Jordan, 1978; Roest and Collette 1986; Muller and Smith, 1993). Vogt and Perry (1981) and Le Douaran and Francheteau (1981) suggest that the plate boundary is near ~13°N. Collette and Roest (1992) and Gràcia and Escartín (1999) argue that the present NOAM-SOAM-AFRC triple junction is situated just north of the FTFZ. It may have occupied this position since 67 Ma (Muller and Smith, 1993), having migrated northward from the Marathon FZ (10°N) to 14°N-16°N (Gràcia and Escartín, 1999).

The inferred presence of the triple-point is based upon several features of the ridge, and of the FTFZ itself. The FTFZ and Vema FZ are both ‘leaky transforms’ suggesting a relatively recent change in spreading direction. North of 17°50’N, fracture zone trending directions conform to the modern spreading direction of the northern central Atlantic, whereas the Marathon FZ, Mercurius FZ and Vema FZ trend differently (Collette and Roest, 1992). The broad morphology of the transform valleys may also result from changes in spreading direction (Fujiwara *et al*., 2003).

OCCs either side of the second segment north of the FTFZ, one in 5Ma crust, and one in 2-3Ma crust, have been cited as evidence of a westward ridge jump that transferred OCC material to the eastern ridge flank (Fujiwara *et al*., 2003).

A series of ridges and troughs are found in the vicinity of the FTFZ: the Barracuda Ridge and Trough, the Tiburon Ridge east of the Lesser Antilles Arc, the Researcher Ridge and Trough, and Royal Trough west of the FTFZ (Figure 16). The Barracuda Ridge has been identified as part of the FTFZ, whilst the Researcher Ridge and Trough and the Royal Trough form a volcano-tectonic complex with an extensional character. The ridges and troughs have a general 100° strike and may indicate differential north-south movement between areas to the north and the south of the features (Roest and Collette, 1986).

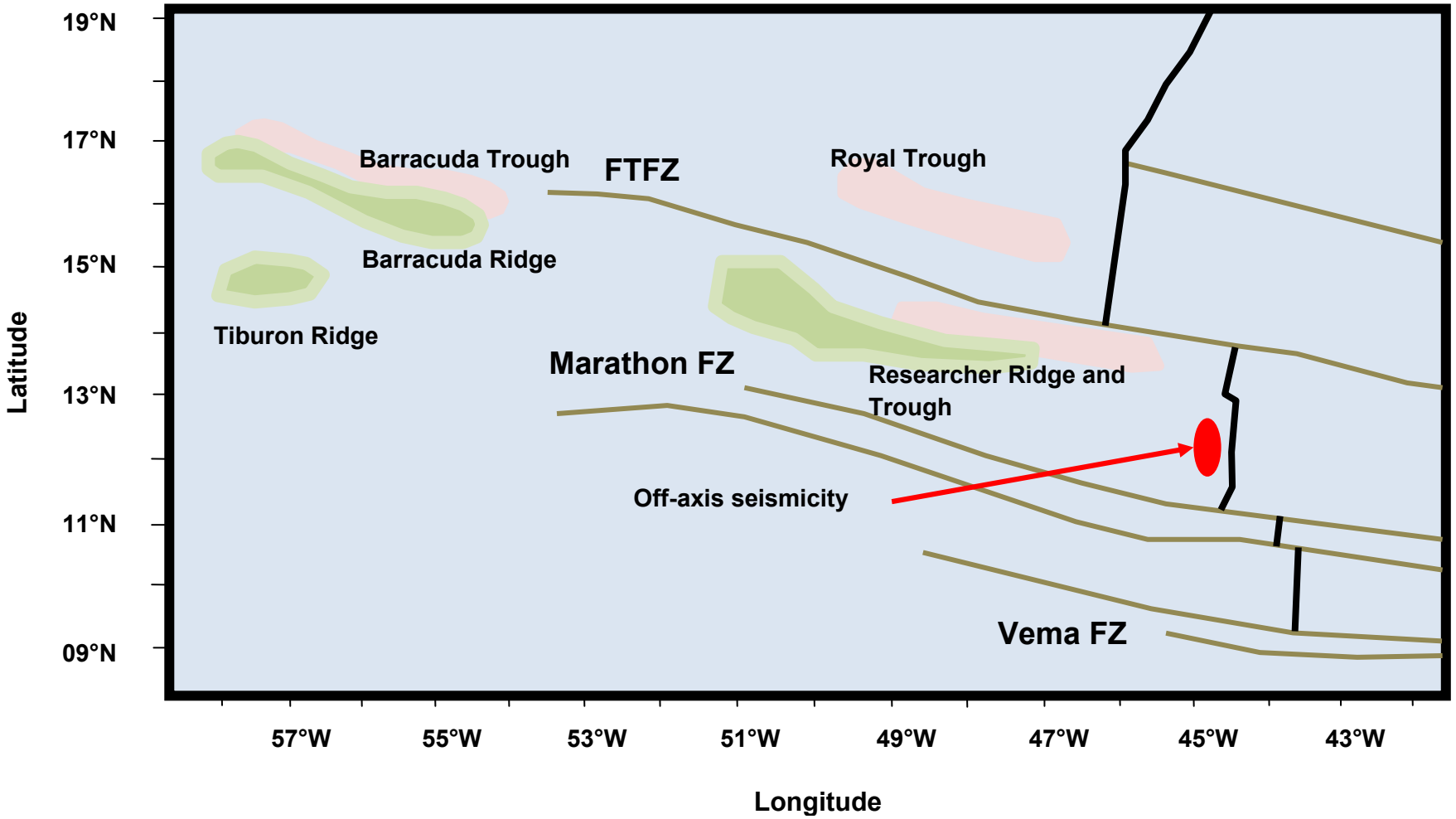

Figure 17: The approximate positions of ridges and troughs in the FTFZ region of the MAR. Also shown is the position of the region of off-axis seismicity, taken from Smith *et al.* (2008).

These ridges and troughs share a common alignment, and may result from unusual tectonic stresses around the FTFZ caused by the presence of the proposed NOAM-SOAM-AFRC plate boundary. Forty years ago, it was suggested that the Barracuda Ridge and Trough mark the position of the intersection of the NOAM-SOAM plate boundary with the Caribbean (Bowin, 1976).

Plate reconstructions indicate that the FTFZ and surrounds experienced a period of transtension in the Cretaceous, followed by a period of transpression in the Tertiary, south of the FTFZ. Modelling by Muller and Smith (1993) indicates that the Moho is uplifted over short wavelengths here, and that crustal thinning related to this uplift may be responsible for the observed crustal deformation.

3.3 - MORB GEOCHEMISTRY ALONG THE MAR (5°S-70°N)

Basalts between 10°-24°N reportedly form from the most depleted mantle source in the north Atlantic. A geochemical gradient exists from 10°-17°N, with limit occurring at ~17°10°N. This trend is apparently unaffected by the FTFZ (Dosso *et al*., 1993) and is not obviously related to any structural feature. Basalts north of the limit have homogeneous N-MORB compositions. South of the limit, basalt compositions are highly variable, ranging from D- to E-MORB. LREE enriched E-MORB is common south of 17°10°N. A ‘hotspot-like’ geochemical enrichment anomaly occurs, centred on 14°N and extending at least 300km along the strike of the rift valley. It generates E-MORB up to 40 times more enriched in highly incompatible elements than N-MORB on nearby segments (Bougault *et al*., 1988). Basalt has been recovered along the median valley in the vicinity of 14°N. Geochemistry progressively changes to slightly E- or N-MORB to the south, approaching the Marathon FZ.

Anomalous zones of geochemical enrichment exist throughout the central MAR. Some of these correlate with major elevations of zero-age crust (Figure 18), and negative RMBA, and are recognised as hotspots such as the Azores and Iceland. Others are found in areas without ridge-centred gravity anomalies or substantial crustal elevations (Bougault *et al*., 1988).

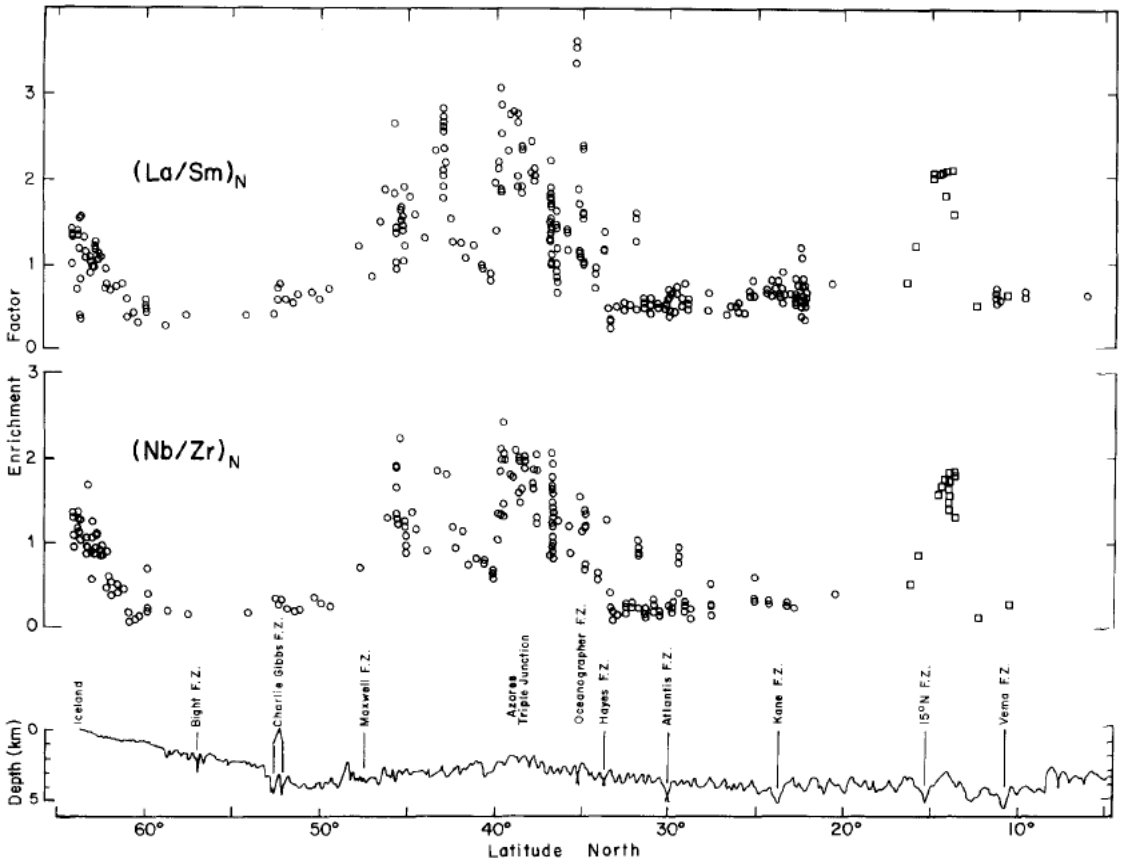

Figure 18: Enrichment zones on the MAR. Some of these, such as Iceland and the Azores, are associated with elevated crust and geophysical signatures such as negative RMBA. The geochemical enrichment at these sites is recognised as originating from mantle plumes. Enrichment zones also occur at 45°N and near the FTFZ, but there is no clear gravimetric or bathymetric evidence to suggest the presence of a mantle plume at these sites. Geochemical data normalised to chondrite. From Bougault *et al.* (1988).

Melts from 29°-34°N are formed from a source with homogeneous volatile composition, and are not strongly fractionated. Melts from 12°-18°N however, are thought to have distinct mantle sources, perhaps originating from a geochemically heterogeneous plume (Silantyev *et al*., 2008). Mantle source

variations at the segment scale or smaller are favoured to explain geochemical signatures in the region (Dosso *et al*., 1993).

On the central MAR geochemistry varies from N-MORB to E-MORB, differing between segments. The mantle beneath 5°N-15°N is reported to have HIMU (high U/Pb) character (Dosso *et al.*, 1991, Schilling *et al.*, 1994, Hannigan *et al.*, 2001). This source is normally associated with ocean islands such as St Helena (see Chaffey *et al*., 1989) and suggests a more complex mantle origin than that usually envisioned for MORB (Dosso *et al.*, 1991). Schilling *et al*. (1994) identified two distinct geochemical zones between 7°S-5°N. They suggest that the north of this area, with strong HIMU signatures, interacts with the Sierra Leone Plume. Less pronounced HIMU signatures in the south are interpreted to result from passive sampling of 'Pb-rich lumps' in the mantle, perhaps originating from the dispersion of the St Helena or Ascension mantle plumes (Schilling *et al.*, 1994). Dosso *et al*. (1991) invoke the presence of an 'incipient, ridge centred plume' to explain geochemical and bathymetric anomalies at 14°N.

Basalt enrichment between 14°N-15°N may be similar to that at 2°N-1°S (Suschevskeya *et al*., 2002). Enriched melts from both regions are noted for their high $^{206}Pb/^{204}Pb$ (20.0), $^{207}Pb/^{204}Pb$ (15.6), $^{208}Pb/^{204}Pb$ (39.5), and $^{87}Sr/^{86}Sr$ (0.7030) at a $^{143}Nd/^{144}Nd$ ratio as low as 0.5128. They also have high Na for MORB and have been compared to the alkaline magmas of the Cameroon Line. Mantle heterogeneities in the region may arise from metasomatism of the mantle and capture of enriched melts early in the history of the Atlantic Ocean (Suschevskeya *et al*., 2002). The mantle is moderately depleted between 12°-13°N, and highly depleted at 2°-3°N and 14°-15°N. Strongly depleted regions correlate with LREE enrichment and, arguably, with zero age topographic highs. These characteristics have been attributed to a mantle thermal plume or metasomatized H_2O rich mantle domains. These cause enhanced melting, providing a source for basalt enrichment, and may be relics of an originally subcontinental mantle (Bonatti 1992). Enrichment may also arise through recycling of alkali basalts found on oceanic islands and seamounts (Hémond *et al*., 2006).

Skolotnev *et al.* (1999) report a correlation (12°10'N-15°20'N) between enriched basalts and segment centres with elevated lithospheric permeability. They describe cyclic volcanism with 2-2.5 Myr periodicity, during which basalt compositions vary from depleted to enriched. Enriched basalts are derived at ages ~25Ma, and are contemporaneous with the formation of the Researcher ridge. Low Si, high K_2O, TiO_2, P_2O_5, L- and MREE basalts, and low-Si depleted basalt are found outside the rift valley. They argue that these basalts are formed by fractionation in large intermediate magma chambers, and attribute their unusual geochemistry to association with a mantle plume.

Segments in the central MAR exhibit a number of unusual geochemical characteristics, which have been attributed by many to plumes. However, geophysical and topographic evidence for a plume in the region is lacking. Although Dosso *et al*. (1991) report a bathymetric anomaly at 14°N, attributing this to a plume, the magnitude of the bathymetric change is very limited in comparison to the plateaux, islands and thick crust produced at other hotspots such as the Azores.

3.4 - CRUSTAL STRUCTURE AND ULTRAMAFICS IN THE CENTRAL MAR

The central MAR hosts a large number of OCCs (see Escartín and Cannat, 1999; MacLeod *et al*., 2002; Casey *et al*., 2008; MacLeod *et al.*, 2009). Many sites, such as Kane Megamullion (23°40'N), the MARK area (22°30'N), Atlantis Massif (30°N) and the TAG segment (~26°N) are found at ridge-transforms, on 'inside corner highs'. A mid-segment OCC is reported at 22°15'N (Dannowski *et al*., 2008). Between the FTFZ and the Marathon Fracture Zone, Smith *et al.* (2006, 2008) identify as many as 45 separate segment-centre complexes. Sampling reveals that peridotite outcrops are common here, both in the median valley and its surrounds.

Gabbros and other plutonic rocks are widespread in the intersection between the MAR and the FTFZ, and are thought to form from heterogeneous mantle sources (Silantyev, 1998). Peridotite recovered from the intersection between the FTFZ

and the MAR is extremely depleted in incompatible elements, having experienced more than 25% partial melting. Enriched basalts are abundant here (Perfilev *et al*., 1996). Some peridotites (13°N) contain strongly incompatible element depleted pyroxene, whilst others show enrichments and veining, evidence of interaction with melt (Pertsev *et al*., 2009).

Mantle focusing theory predicts that beneath slow-spreading ridges mantle upwelling is focused toward segment centres, though it is not known on what geographic scales this upwelling operates. Thin crust and ultramafic exposures between 12°N-14°N suggest that the melt supply is low. However, thick crust, enriched compositions and robust volcanism at 14°N suggest the opposite. Focused mantle upwelling on a short geographic scale could explain these localised variations. ODP Leg 209 set out to constrain mantle upwelling and focusing mechanisms by analysing peridotite samples from a series of drill holes along the ridge segments either side of the FTFZ (Bach *et al*., 2004; Kelemen *et al*., 2004; Kelemen *et al*., 2007). Eight sites were drilled successfully (Figure 19), recovering ~354 metres of residual mantle peridotite intruded by gabbroic rocks, which account for up to 25% of the recovered material.

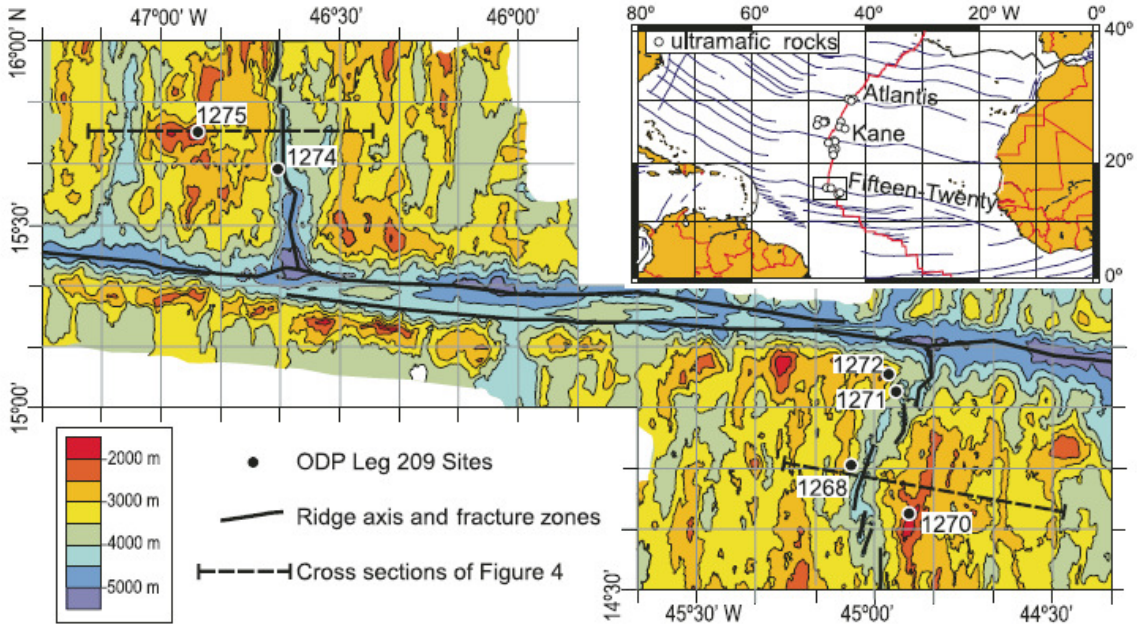

Figure 19: Locations of ODP Leg 209 drilling sites either side of the FTFZ. From Garces and Gee, (2007).

Analyses of drilled samples provided no clear evidence of mantle focusing toward the segment centre (Miller *et al*., 2004), though variations may have been overlooked if they exist on a smaller scale than the sampling resolution of ~25km. The presence of brucite at two sites suggests that, prior to alteration, these rocks were olivine rich peridotites (<90% olivine), known as dunites. This may indicate mantle focusing, as dunite is commonly cited as evidence of channelized mantle flow (e.g. Kelemen *et al*., 1995a).

A high proportion of the gabbroic intrusions (Leg 209) do not represent cumulates that yielded basalts. Rather, they accumulated and cooled in the lithosphere without erupting. Hence, relatively primitive gabbroic cumulates are distributed at depth in the crust here (Miller *et al*., 2004).

Serpentinised harzburgite was recovered from Site 1272A and Site 1274A along with a small amount of dunite. Though highly serpentinised, these rocks preserve relics of primary phases: olivine≥ orthopyroxene≥ clinopyroxene (Vils *et al*., 2009). The primary composition of the mantle rocks at the two sites differ slightly; this is reflected in the REE patterns of whole rock samples (Godard *et al*., 2008), but at both sites the peridotites appear to have experienced high levels of melt extraction (Seyler *et al*., 2007; Godard *et al*., 2008; Suhr *et al*., 2008). These peridotites represent the most refractory (extensively melted) compositions ever sampled at a slow-spreading ridge (Godard *et al*., 2005). They lack residual clinopyroxene, but have olivine Mg# up to 0.92 and spinel Cr# (~0.5), indicating high degrees of partial melting (Seyler *et al*., 2007). In general, peridotites from just south of the FTFZ are the most refractory on the MAR (Dosso *et al*., 1993).

Abyssal peridotites are typically lherzolitic in composition. However, melt-percolation dominated microstructures in samples from site 1274A suggest a harzburgitic host for these rocks, indicating a previous depletion event in this region (Suhr *et al*., 2008). Seyler *et al.* (2007) suggest that the ultra-refractory compositions at Hole 1274A formed as a result of previous partial melting of the mantle, followed by melt-rock reaction and refertilisation, before upwelling and remelting at the ridge. The ultra-depleted compositions resulted from melt re-equilibration with residual harzburgites. Beryllium, lithium and boron concentrations, along with textural observations and major element compositions

obtained from microprobe analysis of 1272A and 1274A peridotites suggest that they reacted with a mafic silicate melt prior to serpentinisation (Vils *et al*., 2008).

Amphibole thermometry data from small-scale plagiogranite melt impregnations suggests that these rocks formed by hydrous partial melting of gabbroic intrusions in an oceanic detachment fault (Jöns *et al*., 2009). This process is predicted by experiments (see Koepke *et al*., 2004) and by textural studies (Koepke *et al*., 2005). Jöns *et al*. (2009) argue that fluids (either magmatically or seawater derived), hydrate the crust along the detachment, and, at high temperatures, are sufficient to lower the solidus of gabbro, facilitating partial melting.

At 15°45'N (ODP Leg 209, sites 1275B and 1275D) Silantyev *et al.* (2008) invoke the presence of a large steady-state magma chamber for the production of melt parental to gabbroic rocks in the OCC. Using Nd and Sr isotope systematics, two melt sources are suggested for the formation of the plutonic rocks, a depleted source forming the gabbro and diabase, and an enriched source from which trondhjemites were derived (Silantyev *et al*., 2008). The lithologies recovered, and their relative abundances, indicate that a modified Penrose model (see Dick, 1989) best describes the structure of the crust at this locality.

Four mid-segment OCCs, originally identified by Smith *et al*. (2006), occupy the region between 12°60'N-14°N (Figure 21). They are located at 13° 48'N, 13° 30'N, 13° 19'N and 13° 02N'. They vary in terms of their distance from the axis, sedimentation levels and their relationship with adjacent neovolcanic zones. These variations are thought to result from each massif representing a different stage of the OCC life cycle (MacLeod *et al*., 2009, see Figure 20.)

Stage 'a' shows a section of slow-spreading ridge, with a volcanic valley receiving an average melt supply, bounded on either side by normal valley wall faults. In 'b' the cross-section reveals a reduction in melt supply at the axis. As a result of insufficient melt supply, spreading switches from the magmatic axis to a valley wall fault, shifting the effective position of the spreading axis out into the valley wall. In 'c' continued spreading on the rotated fault exhumes mantle material, forming an OCC dome. The effective position of the spreading axis is migrated back toward its original position. With continued development of the

OCC (d) the fault axis is migrated back in line with the magmatic axis. Renewed magmatism at this stage cuts through the fault line rooted in the axis. In time, the fault is completely cut off, and normal magmatic spreading resumes. The OCC is then inactive. Hydrothermal activity ceases, and the complex moves off axis as spreading continues. Over time, fault line becomes obscured by subsequent lava flows and sediment cover.

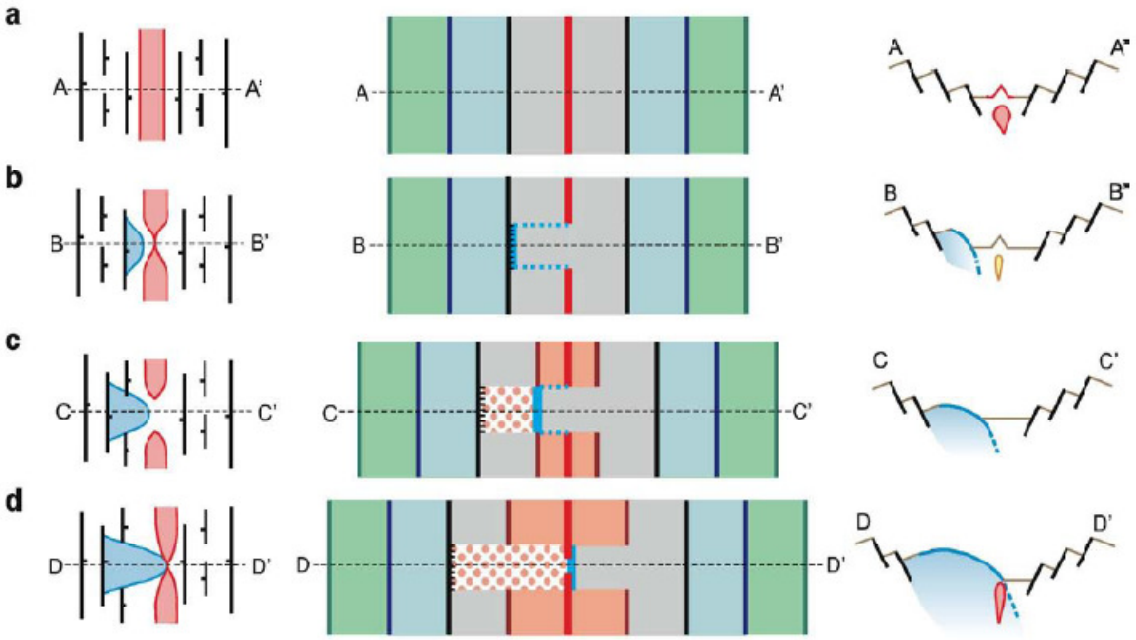

Figure 20: Oceanic core complex developmental stages, as described by MacLeod *et al.* (2009). (a) Normal slow-spreading ridge. (b) Reduction in melt supply – spreading transfers to a normal valley wall fault off-axis. (c) Continued spreading on the rotated fault exhumes mantle material onto the seafloor, forming a core complex. The fault line is migrated back toward the original axis position. (d) The fault axis migrates back in line with the magmatic axis. Renewed magmatism cuts through the fault line, and normal magmatic spreading resumes. From MacLeod *et al*. (2009).

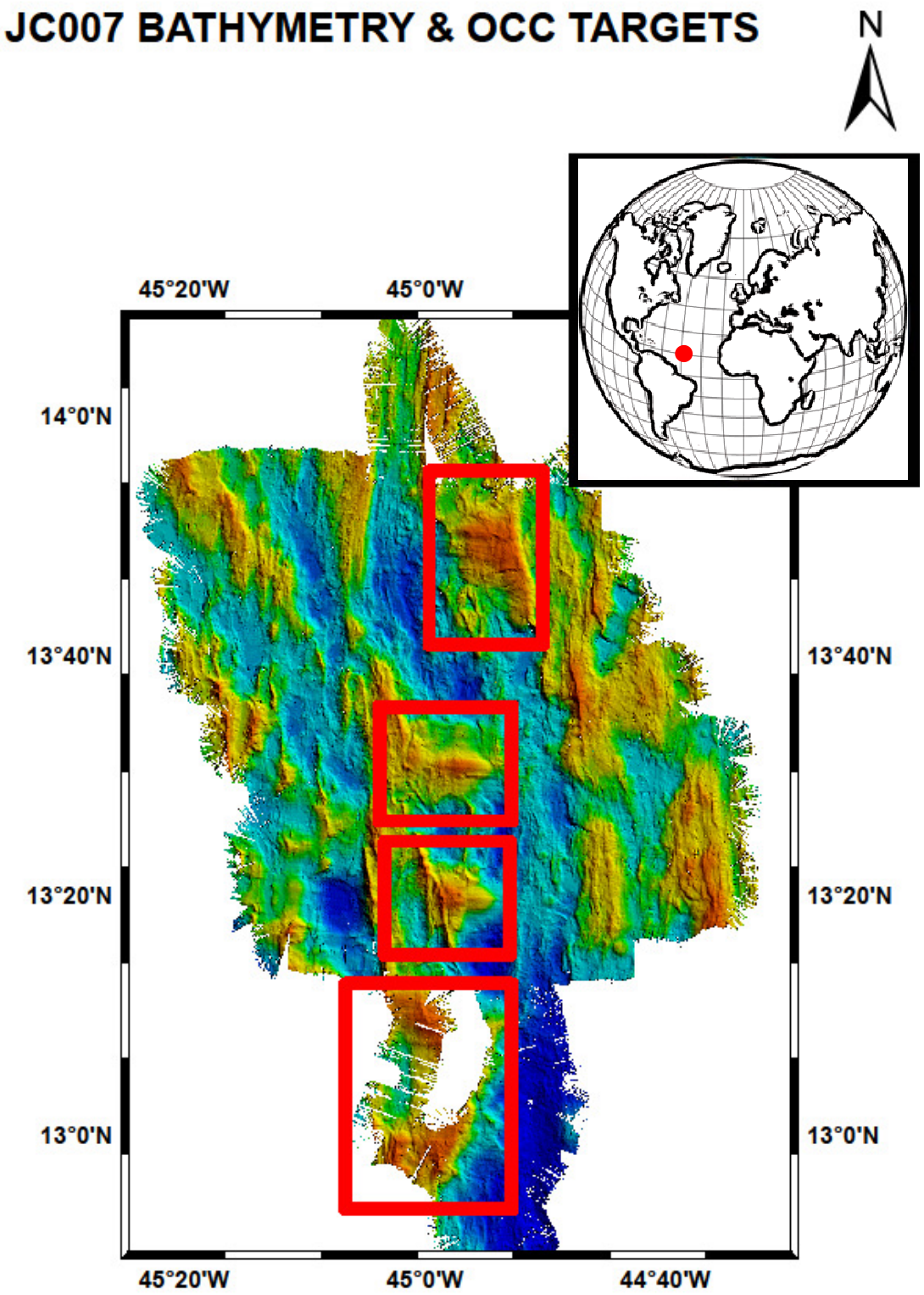

Figure 21: Bathymetry from the JC007 cruise, showing the area between 12°60'N-14°N. The four oceanic core complexes identified by Smith et al. (2006) are highlighted in red.

3.5 - THE 13°19'N CORE COMPLEX

The 13°19'N OCC is 11km across at its widest point, narrowing to <1km at the toe. The fault has a horizontal component of displacement of 9km, extending in the west to a clear, pronounced fault scarp dipping at 32°E. The structure is composed of a smooth, axis-perpendicular-corrugated dome, elongated in the axial spreading direction, and a topographically rougher, more elevated region to the west. This region, known as the breakaway, is a ridge with a western flank consisting of tilted volcanic seafloor. The geometry of the breakaway implies a crustal thickness of 2.5 - 3.2km prior to OCC development. Together these features make up the footwall of the detachment fault. The main features of the OCC and its surrounds are shown in Figure 22 (MacLeod *et al*., 2009). A lack of sedimentation, combined with the sharpness of the fault boundary, strongly indicate that the fault is currently active. These details are shown in TOBI/Fledermaus imagery of the active fault surface (Figure 23).

The dome consists of highly serpentinised peridotite and talc schist covered with basaltic talus. At the fault toe, hydrothermal sulphide chimney pieces, mineralised talc mud, greenschist-facies dolerite dykes and altered pillow basalts were recovered. Gabbro represented only ~2% by weight of recovered material. This suggests that the crust underlying the 12°60'N-14°N region does not closely resemble the gabbro 'plum-pudding' model invoked by Cannat (1993, 1997), where we would expect to find gabbro bodies embedded within the peridotite being exhumed. At the fault breakaway, basalts dominate and peridotite is absent. Figure 25 summarises sampling locations and the lithologies recovered.

In the axial valley on the hanging wall, 3-4km of sedimented and fractured volcanic seafloor immediately opposite the fault gives way to neovolcanic terrain to the immediate north and south, forming triangular zones characterised by hummocky, young volcanic terrain. These neovolcanic zones are thought to propagate inward to intercept the fault line, ultimately leading to fault termination and resumption of magmatic spreading (MacLeod *et al*., 2009).

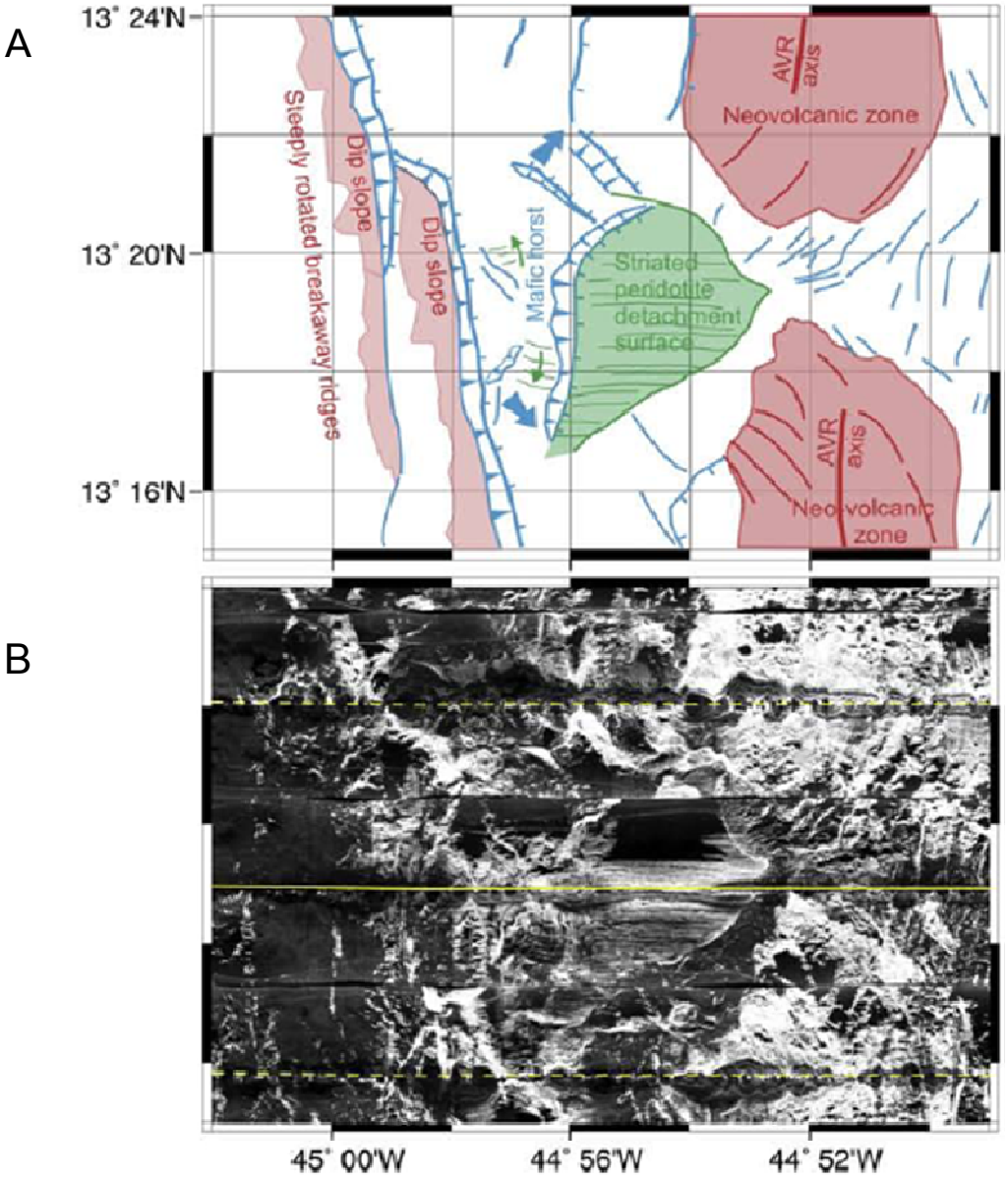

Figure 22: A) Key structural features of the 13°19'N oceanic core complex, including the breakaway ridges, corrugated dome, fault line and inward propagating neovolcanic zones. B) Corresponding TOBI sidescan-sonar imagery. From MacLeod *et al.* (2009).

Figure 23: Combined TOBI and bathymetry image produced by the 3D visualisation software package Fledermaus®. Image view is facing west, along the axis-normal length of the core-complex at 13°19N. In the foreground, hummocky neovolcanic terrain propagates toward the sharp, brightly reflective fault surface. On the core complex dome, corrugations are clearly visible. Beyond the dome, back-tilted volcanic blocks mark the breakaway ridge, which is approximately axis-parallel. MacLeod *et al.* (2009).

3.6 - 13°30'N, 13°48'N AND 13°02'N CORE COMPLEXES

The 13°30'N OCC is similar to the 13°19'N OCC in terms of morphology and position relative to the axis. Only the toe of the OCC was dredged, but more extensive sampling by Beltenev *et al.* (2007) confirms that the site is composed of serpentinised peridotites associated with moderately altered basalts and greenschist-facies metabasites intruded by plagiogranite. Gabbro occurs infrequently (~2-3%). Diabase dykes intruded into the lower part of the footwall indicate syn- to post-uplift magmatic intrusion (MacLeod *et al*., 2009). Sulphide edifices indicate recent hydrothermal activity at the site.

The OCC at 13°48'N lies on the eastern side of the axis, above the axial discontinuity at 13°36'N. The complex is set back from the neovolcanic axis, and is substantially more faulted and sedimented than the others. The near-axis fault boundary (termination) is much less clearly defined. The complex consists of a corrugated domal footwall and steeply back-tilted breakaway ridge, though the dome is flatter than the other OCCs described here, dipping from 15° at the toe to 0° at the summit (MacLeod *et al*., 2009).

The 13°02'N OCC was not extensively sampled. Small amounts of peridotite recovered from the slopes below the OCC have similar compositions and extents of serpentinisation to those from the other sites.

The 13°19'N and 13°30'N OCCs are currently active (Figure 21, stages c-d), and are rooted in the magmatic axis. The morphology and extent of neovolcanic zones shows that volcanism is resuming, following a period of quiescence. The OCCs are in the process of being 'cut off' by volcanism. The axis at 13°30'N contains an almost continuous neovolcanic zone. This suggests that this site has nearly returned to magmatic spreading (stage d). The neovolcanic zone at 13°19'N forms discrete triangular areas either side of the complex, suggesting that a substantial component of spreading is still accommodated by the detachment fault (stage c). These areas of the ridge are considered to be transitional between fault-driven and magmatic spreading.

The 13°48'N OCC is off-axis and heavily sedimented, suggesting that it has been exposed on the surface for some time. Peridotite recovered here is

extensively serpentinised. TOBI imagery shows that magmatism has resumed in the axis. The complex is classified as ‘dead’, because the fault is no longer tectonically involved in axial spreading. Effectively, the ridge has returned to stage ‘a’.

It is not known whether the detachment fault of the 13°02’N complex is active, but the OCC hosts the large Ashadze hydrothermal vent field, indicating that heat and fluid flow persist beneath the complex.

CHAPTER FOUR – SAMPLING, STUDY HYPOTHESES AND AIMS

Here, project aims are comprehensively discussed, and sampling strategies employed during the RRS James Cook cruise JC007 (12°60'N-14°N, MAR - March-April 2007) are described.

4.1 - AIMS OF THIS STUDY

The 12°60'N-14°N region of the MAR is characterised by unusual topography, thin crust and segment-centre OCC development, all of which suggest a poor melt supply. However, E-MORB signatures, thick crust and normal, ridge-parallel topography at 14°N is indicative of a good melt supply, and, arguably, enriched mantle source material. This study aims to examine the on- and off-axis geochemistry of basalt in order to constrain models of melt supply. Major element, trace element and isotopic data for 12°60'-14°N will be compared to MORB data for the wider central MAR, to identify regional trends which may explain the unusual morphological and geochemical characteristics of the segment.

OCCs form in amagmatic areas, where melt supply is low, and are thought to terminate as a result of the onset of renewed magmatism. Basalts from off-axis along the length of the 13°19'N OCC provide a uniquely comprehensive dataset for a mid-segment core complex. This study will examine the evolution of basalt compositions throughout the lifetime of the OCC in order to determine whether mantle composition and/or melt supply assert any control on OCC formation.

Between 12°60'N-15°20'N, amagmatic areas are interspersed with normal spreading areas on a 15-25km scale. Fine-scale mantle focusing could explain such variations in melt supply. At slow-spreading ridges, 3D mantle upwelling is focused to segment centres, which therefore receive a good melt supply. Their crust is typically thicker than that at segment ends, and magmatism is regular and ongoing.

At segment ends, on the distal edge of the radial upwelling mantle column, the crust is thin. Faulting and unroofing of ultramafic material are common processes here. Melt focusing variations are identifiable in gravity data, as gravity low 'bull's-eyes' coincide with areas of enhanced upwelling. The focusing of melt toward the centre of a ridge segment affects the thermal structure and therefore also the mechanical properties of the lithosphere. The centre of the segment is hotter with a thinner lithosphere, whereas the lithosphere is thicker at the cold segment ends, and hence the brittle deformation zone extends to greater depths. It is thought that in these cold, brittle zones, a significant amount of plate separation may be accommodated by faulting.

Despite the existence of well established melt focusing models, there is little agreement on the scales at which they operate. In regions such as 12°60'N-15°20'N, melt focusing may operate on a fine scale, creating mid-segment variations in lithospheric thickness, melt supply and crustal properties. This could produce local segment-centre conditions favourable for the OCC formation.

An alternative hypothesis of this thesis is that of mantle compositional or temperature control on OCC formation. It is postulated that the mantle produces less melt at OCCs than at magmatic sites. Changes in mantle source composition, hydration and/or temperature could produce variable melt fractions, resulting in localised changes in melt supply along axis. It is also possible that 'crustal plumbing' could be preventing a percentage of the melt produced from reaching the ridge axis at OCC sites. Therefore the parameters controlling magmatic vs. fault-driven spreading may be structural, not geochemical.

There are three primary hypotheses:

1. Sub-segment scale variations in mantle focusing create localised areas of cold, thick lithosphere, deep brittle zones and enhanced cooling. In these areas, melt supply is low and conditions are favourable for the formation of OCCs.
2. Variations in melt supply along the segment arise from changes in characteristics of the mantle, such as temperature or composition, which control the extent of melting. OCCs correlate with areas where melt fraction is low.

3. The mantle melts to a similar degree underneath magmatic and OCC areas, but that the physical structure of the ridge at the crustal level prevents the delivery of much melt to OCCs.

This study aims to use geochemical and petrological data, combined with structural evidence from TOBI imagery and bathymetry, to test these hypotheses.

If mantle composition is responsible for low melt supply at OCC sites, basalts here will have geochemical signatures indicative of low melt production (low melt fraction, F). Low F basalts are typically enriched in incompatible major and trace elements, as these are first to enter the melt at the onset of melting. Higher F basalts have less enriched signatures, as highly incompatible elements are 'diluted' by the presence of compatible elements, which enter the melt at higher degrees of melting. Trace elements, incompatible trace element ratios and isotopes provide details of source composition. Isotope data and the ratios of very incompatible trace elements to moderately incompatible trace elements can be examined to distinguish genuine source enrichments from those arising as a function of variable F. Enrichments inherited from the source correlate with source isotopic characteristics, whereas enrichments resulting purely from low melt fraction do not. If F is similar at OCC and magmatic sites, a crustal plumbing hypothesis will be the more likely cause for melt supply variations.

4.2 - SAMPLING OF THE 12°60'N-14°N CORE COMPLEXES

During the RRS James Cook cruise 'JC007', the four OCCs, and the ridge axis between them, were imaged by Multibeam (Simrad EM120), and TOBI sidescan-sonar. The TOBI survey covered a 70km stretch of the ridge axis, and was composed of 13 ridge-parallel survey lines. TOBI data were draped over gridded bathymetry using Fledermaus® 3D visualisation software. Geochemical samples were recovered by dredging at 30 stations (Figure 23, Table 3), with good geographic coverage from the segment centre at 14°N to the intersection of the axis with the Marathon FZ. Dredge site selection was informed by EM-120

multibeam bathymetry data and TOBI imagery produced and processed during the cruise.

On-axis sites were selected to recover fresh volcanic samples from active neovolcanic zones, whilst off-axis dredges targeted OCCs. Dredge tracks were selected to run up fault scarps in order to maximise recovery of exposed lithologies whilst avoiding overlying sediment, which is likely to collect at the base of scarps and on level surfaces. Peridotite and basaltic talus were recovered on the OCC domes, as well as from the nearby axis. Minor gabbro, dolerite and hydrothermal lithologies were also recovered. Sampling of the breakaway at 13°19'N recovered basalt only. Fresh pillow basalt, sheet flow pieces and glass were recovered from neovolcanic zones along the ridge axis.

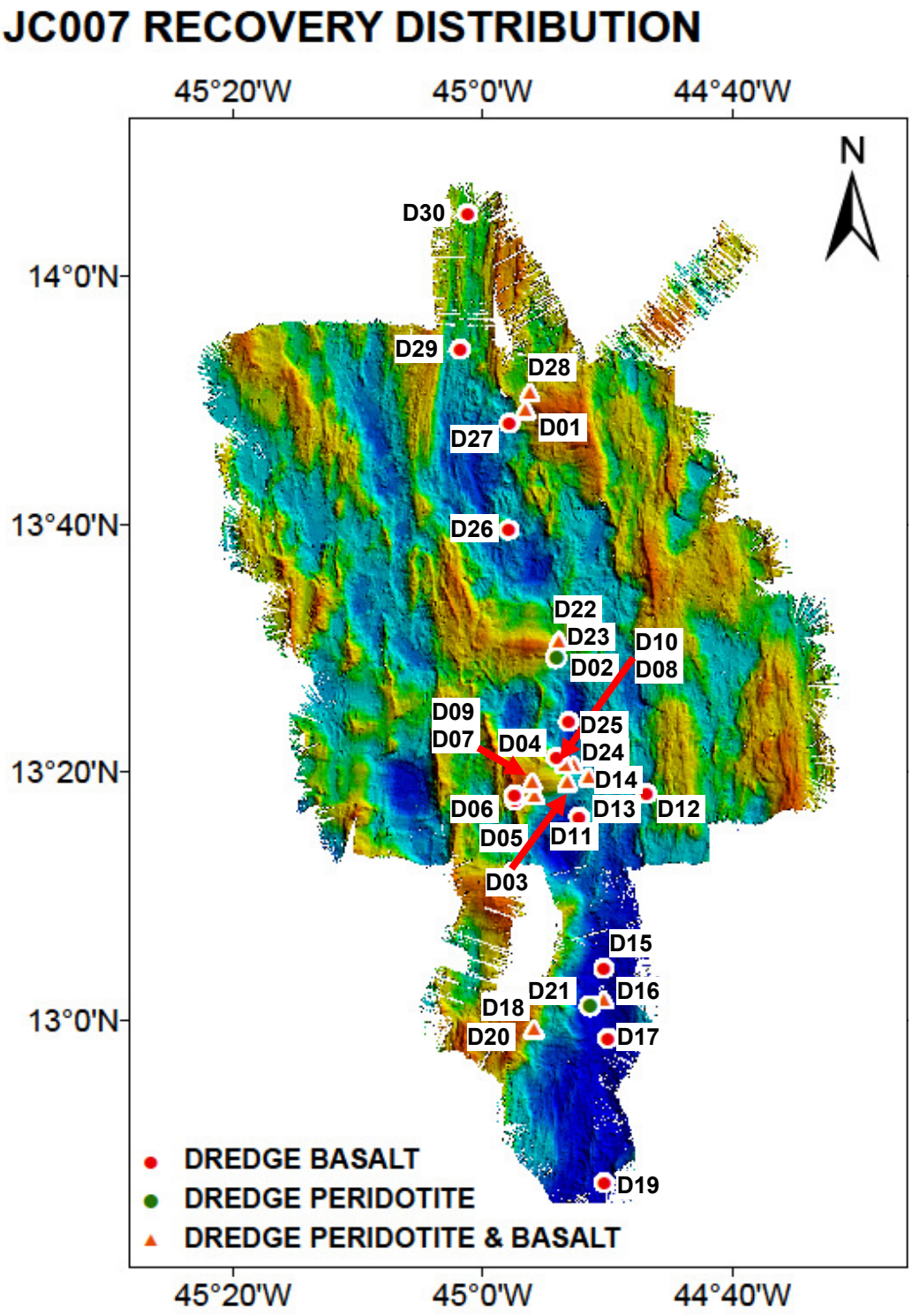

Figure 24: ArcGIS processed EM-120 bathymetry map showing the location of dredge sites, the major lithologies recovered, and their geographic distribution. Symbols as follows: red circles - basalt, green circles - peridotite, orange triangles - peridotite and basalt.

Table 3: Dredge Track Start Points, JC007 Cruise

Dredge	Latitude (Dec.)	Longitude (Dec.)	Depth (m)	Dredge Location
D01	13.8198	44.9432	2932	Core Complex Toe
D02	13.4872	44.9023	3172	Core Complex Toe
D03	13.3042	44.8948	3324	Core Complex Flank
D04	13.3567	44.9185	2975	OCC Block NE
D05	13.2962	44.9575	2612	OCC Breakaway S Flank
D06	13.3033	44.9583	2526	OCC Breakaway W
D07	13.3007	44.9312	2962	OCC SE Flank
D08	13.3427	44.8790	3450	Axis N of OCC
D09	13.3192	44.9343	2354	OCC E Dome
D10	13.3428	44.8903	3187	OCC Dome N
D11	13.2732	44.8718	3740	Axis S of OCC
D12	13.3045	44.7822	3457	Axial Valley Wall
D13	13.3188	44.8871	3196	Toe OCC
D14	13.3257	44.8592	3500	Axial Terrain E of OCC
D15	13.0697	44.0888	4496	Axis
D16	13.0270	44.8388	4820	Axial Valley Floor/Wall E
D17	*12.9753*	*44.8335*	*4610*	*Axial Valley Floor*
D18	*12.9602*	*44.9378*	*3343*	*W Wall Ashadze*
D19	12.7808	44.8385	4094	Axis N of Marathon FZ
D20	12.9863	44.9318	2866	W Wall Ashadze
D21	13.0185	44.8572	4357	W Valley Wall
D22	*13.5157*	*44.9022*	*2949*	*OCC Toe*
D23	13.5097	44.8988	2854	OCC Toe
D24	13.3532	44.9023	3011	Axis N of OCC
D25	13.4010	44.8855	3857	Axis Between OCCs
D26	13.6595	44.9660	3496	Axis Between OCCs
D27	13.8030	44.9647	3164	Terrace below OCC
D28	13.8430	44.9378	2768	OCC Flank
D29	13.9025	45.0305	3181	Axis N of OCC
D30	14.0853	45.0207	2970	Axis Centre 14N

Table 3: Dredge track starting locations, depths, and short dredge site descriptions for JC007 Cruise. Empty or aborted dredges are *italicised.*

The sampling strategy involved extensive dredging of OCC sites, associated neovolcanic zones, and magmatically spreading volcanic terrain. OCCs proved to be variably sedimented as well as covered with basalt talus. Extensive sampling coverage was achieved on the young, active OCC at 13°19'N, providing a sample time series from before OCC initiation to the present day.

CHAPTER FIVE- ANALYTICAL METHODS

This chapter details the procedures for selecting and preparing samples for analysis, and provides details of analytical methods used.

All geochemical techniques are subject to interferences, instrument drift and other errors resulting from aspects of chemical behaviour, sample preparation and machine setup. These effects are overcome by the implementation of rigorous laboratory procedures, combined with the application of calibrations using standard reference materials (SRMs). Errors for each of the analytical techniques are also quantified in this chapter, while details of the sources of the recommended/preferred values for SRMs used are reproduced in Appendix 1. The techniques used in this study include:

- Crystal imaging and identification by Optical Microscopy and Scanning Electron Microscopy (SEM).
- Major element analyses of whole rock samples by Wavelength Dispersive X-Ray Fluorescence Spectrometry (WD-XRF- Phillips Magix Pro).
- Trace element analyses by Inductively Coupled Plasma Mass Spectrometry (ICP-MS - Thermo X-Series)
- Pb, Nd and Sr isotope ratios by Thermal Ionisation Mass Spectrometry (TIMS - VG Sector 54).
- Glass volatile contents by Fourier Transform Infra-Red Spectroscopy (FTIR – Nicolet FTIR Bench), and post-processed using ‘Omnic’ peak analysis software.

These data were collected at the National Oceanography Centre, Southampton (NOCS).

5.1 – SAMPLE SELECTION AND PREPARATION

5.1.1 - Selection of Analytical Samples from Dredge Hauls

A dredge haul represents material collected from along a track that can vary from a few 100m to a few 1000m in length. The precision of a given sample's location is limited to the length of sea-bed contact for the dredge deployment. The amalgamated material from along a dredge track must be sorted logically. Sorting by lithology is the first stage. Further sorting may then be applied on the basis of mineralogy, texture, and alteration.

In the case of basalt and glass, a number of criteria are used to distinguish basalts of different origins. Firstly, sheet flows can be separated from pillow basalts by morphology. Pillow basalt fragments have radial morphology, with large feldspar crystals commonly concentrated in the glassy layers near the surface. Small, rapidly cooled, extremely glassy billow basalts have thick concentric layers of glass on their outside surfaces, which peel away from each other with ease. Sheet flows have flat, layered morphology. Basalts can also be divided on the basis of modal phase proportions and vesicularity. They can be variably plagioclase-, olivine- and pyroxene-phyric, or may be aphyric.

Alteration levels, the thickness and freshness of glass layers, and the thickness of manganese crust accumulations can be used to separate basalts of different relative ages. Young pillow basalts commonly exhibit little alteration, and have thick, fresh, glassy layers, free from Mn-crust and devitrification. Older pillow basalts progressively lose their glassy layers. Devitrified glass, extensive alteration and thick manganese crusts are indicators of basalts that have spent a substantial amount of time on the seafloor.

5.1.2 - Selection of Analytical Samples- Alteration

Basalts on the seafloor undergo alteration processes as a result of interaction with seawater and hydrothermal fluids. With age, glassy layers devitrify and become coated in manganese oxide crusts. These processes can lead to significant geochemical changes. When analysing basalt for primary chemistry, it is important to recognise and avoid material which has experienced alteration.

Altered basalts with greenschist-facies mineralogy (greenstones) take on their characteristic colour, indicative of alteration to chlorite and/or epidote dominated assemblages, with clays, albite, actinolite and quartz (Mottl, 1983) at temperatures ~200-300°C (see. Tomasson and Kristmannsdottir, 1972; Stakes *et al*., 1984; Shau and Peacor, 1992). Basalts that have experienced low temperature reactions with seawater typically develop pale margins, and may be softened and clay-like when cut with a diamond saw. Experimental data from Seyfried and Bischoff (1979) shows that at 150°C, seawater interaction with basalt results in alteration to iron-rich saponite (smectite clay). Veining, filled vesicles and grainy recrystallisation textures are also indicators of alteration.

Devitrified glass develops ‘milky’ or ‘dusty’ areas, which may take the form of radial ‘snowflake’ patterns. Glass also becomes coated with manganese-iron oxides, forming dark crusts which commonly take on a red-orange colouration. Fresh faces of manganese crust are extremely hard to distinguish from volcanic glass, even by microscopy. Manganese-iron oxide is rich in an array of trace elements including Ni, Cu, Co, Ba, Sn and Pb (De Carlo *et al*., 1987 and references therein). Inclusion of any of this material in an analytical sample of basalt will substantially affect its trace element composition. This is especially critical in the case of Pb isotope analysis, as Pb is a constituent of Mn-Fe oxides.

Careful examination of hand specimens and thin-sections is the primary method of selecting fresh basalt and glass. Fresh material can be physically separated by a number of means. Altered rims or veins are effectively removed by use of a diamond saw, though sampling bias must be avoided. For example, removal of

an aphyric outer layer from an otherwise olivine-phyric sample would lead to a misleading over-representation of olivine in a bulk rock analysis.

5.1.3 - Sample Preparation - Crushing, Cleaning, Picking and Powdering

Following selection and isolation of fresh material, basalt chosen for major element, trace element and isotopic analysis is crushed to facilitate examination of the fragments under an incidental light microscope. Crushing is carried out using a manually operated fly press, with the rock sample placed inside tough plastic bags to prevent contact with the pressing plates, and associated contamination. Once crushing is complete, samples are sieved in a Teflon sieve stack. The 0.5mm-1.0mm fraction is recovered for analysis. This crushed fraction is washed using ultra-pure water in an ultrasonic bath to remove powdered rock, adhered clay minerals and plastic fragments from the crushing bags. Ultrasonic washing is repeated until the water runs clear. The sample is then dried overnight at ~70-80°C.

Clean, dried chips are manually picked under the microscope to ensure that the analytical fraction only contains the desired material (whole rock/glassy material/phenocrysts). This process involves selection of individual pieces of fresh material, and rejection of undesirable contaminants such as altered material, Mn-Fe oxide crust, organisms, devitrified glass and phenocrysts which are not desired.

Trace contaminants may remain even in thoroughly picked samples. These are commonly sufficient to affect the results of sensitive Sr or Pb isotopic analysis. To remove trace contaminants, samples are acid leached. This involves heating rock chips in 6M HCl to 130°C in a sealed Teflon vessel for up to 3 hours, depending on the level of contamination suspected. The rock chips are rinsed repeatedly to remove any traces of the leachate. Acid leaching is not necessary for major and trace element determination by XRF and ICPMS. In these cases, picked chips are prepared by milling them to a 10 micron powder in a stainless steel rotary

iron mill. This homogenises the sample and provides sufficient surface area for rapid and effective acid digestion.

5.2 - SOURCES OF ERROR IN GEOCHEMICAL ANALYSIS

There are a number of types of error that can be introduced into geochemical analyses. Some result from physical contamination of samples during preparation processes or analysis. This results in the outcome, (e.g. a measured composition), being different from the actual composition of the sample. Errors can also be introduced by 'human error', by the limitations of analytical techniques, or by data processing methods. Only when a robust confidence interval is established for a data-point, can it be legitimately compared to other data.

5.2.1 - Physical Contamination of Rock Samples

Physical contamination of samples is especially likely when crushing and powdering rock. During these processes, rock samples come into physical contact with a variety of equipment. Material may be transferred from one sample to another, or contamination may arise from addition of material from the apparatus itself. Crushing apparatus are typically made from low-contamination materials, designed for purpose. However, addition of some elements, such as Nb, can still occur, even in the 'ultra-clean' crushing media, such as agate (Jochum *et al*., 1990). The various low-contamination metals used can introduce W, Co, Ta, Sc, Cr, Fe, Cu, Mn, Zn and Ni to a sample (Rollinson, 1993).

Cross-contamination is avoided by implementing thorough cleaning procedures. These are preformed before and after handling samples to ensure that no material is transferred between them. Vacuuming and scrubbing of crushing and milling equipment, followed by thorough cleaning with ultrapure water serve to

minimise unwanted material transfer. Samples are wrapped in strong plastic during crushing to avoid contact with the metal parts of the apparatus. Plastic fragments are easily separated later during washing and picking. Thorough cleaning of mill equipment using iron-free sand is recommended to minimise cross-contamination.

Physical contamination can be introduced into samples by use of impure or contaminated laboratory reagents. For sensitive procedures such as trace element and isotope analysis, ultra-pure reagents are used. Where acid concentrations are critical to the procedure, titrations are performed accurately. Laboratory contamination levels are monitored by the inclusion of procedural blanks in each sample run.

5.3 - ANALYTICAL TECHNIQUES - XRF (X-Ray Fluorescence Spectroscopy)

XRF has been a standard analytical technique for the measurement of major elements (Na, Mg, Al, Si, P, K, Ca, Ti and Fe) and trace elements (Zr, Ba, Y, Cu, Cr, Ni etc.) in rocks since the 1960s (Potts, 1992). Preparation of samples for major element analysis by this technique is rapid and straightforward. Therefore, the technique is very effective for obtaining large amounts of good quality major element data in a short time frame (Rollinson, 1993).

Major element analysis at the NOC is performed using the ‘Phillips Magix Pro’ Wavelength Dispersive Sequential X-Ray Fluorescence Spectrometer (WD-XRF). Samples run under a vacuum as fused glass discs, handled by an automatic sample changer, accommodating up to 144 samples. The system’s analytical software, ‘Philips SuperQ v4.0’, is used for data collection, calibration and analysis.

5.3.1 - XRF - Background to the Technique

XRF is based upon excitation of a sample by bombardment with X-rays, generated by an X-ray tube operating at a potential of between ~10 and 100kV. Primary X-rays interact with the atoms within the sample, ionising them to generate secondary X-rays, which are characteristic of specific elements. For a discussion of the background to this technique, refer to Potts (1992).

5.3.2 - XRF- Factors Affecting the Selection of Emission Lines

XRF works best with the most intense emission lines available. When selecting spectral lines that are suitable for analysis those from the 1-20keV region are preferred, as these are most efficiently excited and detected by the instrument. Fluorescence yield decreases substantially from the K to M shells. Therefore, Kα transitions are preferentially used for elements Na-Mo, whereas Lα lines are preferred for trace elements such as REE. In the case of major interferences in any of these lines, an alternative line is selected for analysis.

Additionally, the use of inner shell electron transitions minimises effects which arise from electrons interacting with other species, for example by bonding/oxidation, as these interactions involve predominantly outer shell electrons. This means that XRF analyses should be truly elemental, and independent of the oxidation state of the atom (Potts, 1992).

5.3.3 - XRF- Instrument Characteristics

An XRF spectrometer consists of a tube source which produces the X-rays fired at the sample. Secondary X-rays leaving the sample pass through collimators, and are separated by diffraction before being analysed by the detector. In

wavelength dispersive XRF, incoming sample radiation is sorted by the detector on the basis of its wavelength.

The ‘Phillips Magix Pro’ is a sequential spectrometer, meaning that it analyses each element in sequence, pausing between analyses to change the X-ray tube power, diffraction crystal and detector setup. Although machines such as this have long analysis times, their internal setup requires only a short distance between the tube and the crystal; and therefore the maximum possible radiation is detected, and high quality data is obtained.

5.3.4 - XRF- Sample Preparation

Sample preparation for major element analysis involves fusing the powdered, ignited sample into a homogeneous glass disc, as described by Norrish and Hutton (1969). This homogenising method allows for the elimination of matrix and mineralogical effects, which particularly affect light elements such as Si, Na, Mg and Al.

The sample disc is flat in order to keep the geometry of the tube-sample-detector constant. Homogeneity of the bead is important, as microscale heterogeneities at the bead surface lead to poor analytical results. Using borate glass beads is a reliable technique for the homogenisation of rock samples, provided that care is taken during bead production. Lithium tetraborate beads are durable and resist the absorption of water.

To form the beads, fine (10 micron) sample powders are dried overnight at ~110°C to remove non-structural water, and then weighed and ignited in clean ceramic crucibles at 1050°C to remove volatiles. The difference in weight pre- and post-ignition gives the loss on ignition (LOI - see Lechler and Desilets, 1987), which is a measure of the total volatile content of the sample. Glass beads are made by mixing the ignited sample with Li-tetraborate flux in the ratio 5:1 sample to flux, in a clean platinum crucible. The measures 5g flux to 1g sample or 4g flux to 0.8g sample are used for this study. The dry sample and flux powders are

thoroughly stirred to homogenise the powder, minimising the formation of heterogeneous areas of glass. The sample is melted in a muffle furnace at ~1150°C for approximately 10-15 minutes. This time is optimal for allowing thorough melting, whilst minimising reactions between the sample and the platinum vessel.

When thoroughly melted and mixed, the sample is poured into a preheated platinum mould, stirred once again and rapidly cooled. Rapid cooling prevents the development of heterogeneous 'cells'.

5.3.5 - Precision and Accuracy in XRF Data

XRF is a well established technique, the fundamentals of which have not changed dramatically over recent years. Therefore, inter-element and matrix-effect corrections are effectively carried out by the instrument software, and the precision for major element analyses is commonly very high. Precision can be tested by examination of the results of repeat analyses. Instrument accuracy is more variable as it is dependent calibration. However, accuracy can be tested effectively by the use of international reference materials. For a general discussion of precision and accuracy in analytical geochemistry, including factors affecting specific analytical techniques, refer to the discussion by Potts (1992).

Inter-element matrix effects are generally handled effectively by modern software, and thus the limiting factor for producing high quality, precise analytical data by this technique is considered to be inhomogeneity of the analyte (Potts, 1992). Samples that are substantially inhomogeneous will commonly give poor analytical totals (wt % oxide), but small scale inhomogeneity is difficult to detect and mitigate.

Very high or low analytical totals can result from weighing inaccurate proportions of flux to sample or vice versa, and can also result from poor mixing during bead-making, which may lead to heterogeneous composition. These two problems are eliminated by careful weighing and stirring, although small-scale mixing issues

which do not greatly alter the total of the analysis may go undetected, and the same is true for small amounts of instrument drift.

If a low analytical total is obtained (and machine error/poor analytical conditions are ruled out by good in-run reproduction of SRMs), then careful re-melting of the bead before repeating the analysis may eliminate any small compositional heterogeneity. If this approach fails, production of a new bead may serve to eliminate low totals resulting from a human weighing error. If a sample repeatedly gives low totals, the data are likely to be genuine, and probably occur due to a high volatile content resulting from alteration. This can be checked by determining the Loss on Ignition (LOI).

Calibration in XRF is carried out by correcting to published compositions of SRMs. Therefore, the calibration is dependent upon the quality of the compositional data for the SRMs used (Potts, 1992). Whilst confidence in major element SRM compositions is high, the standard values for compositions of trace elements are less well characterised, and so calibrations for trace element analysis are much more difficult. Use of multiple SRMs minimises errors introduced as a result of poorly characterised elements in some SRMs.

Some suggest the use of synthetic standards for calibration and drift monitoring, to eliminate issues arising from uncertainty in the recommended/preferred values of real rock SRMs. Synthesized calibrating standards with chemical reagents are shown to have constitutive properties that are superior to those of rock SRMs. They can ensure the traceability of the analytical procedure and the ‘resultant accuracy and propriety of calibration curves’ (Nakayama and Nakamura, 2008). Despite this, real rock standards produce robust calibrations (i.e. Lozano and Bernal, 2005).

5.3.6 - Precision, Accuracy, Calibration and Correction – This Study

For this study, the international reference materials JB1-A, BIR-1, BHVO-2, and BRR-1 (NOC internal standard), are analysed at the beginning and end of each

block of unknowns. This allows for the identification of any systematic detection drift throughout the analyses.

Beads are analysed in blocks of ~20-30. Processed data are given in weight percent oxide, with a good analysis expected to sum between 98.5-101.5%. Analyses that fall within this range, accompanied by good standard reproducibility, are considered robust. Fe is reported as Fe_2O_3. Precision is assessed by performing repeat analyses of JB-1A, BHVO-2, BIR-1 and the well-characterised NOC internal standard BRR-1 (Table 4).

SiO_2	TiO_2	Al_2O_3	Fe_2O_3	MnO	MgO	CaO	K_2O	Na_2O	P_2O_5
49.82	1.033	14.375	11.88	0.185	8.574	11.954	0.053	1.965	0.087

Table 4: Major element reported values, 1995 (Wt % oxide) for the NOCS internal XRF standard BRR-1 (Basalt). n = 10, Ian Croudace, pers. comm.

In-run precision is typically 0.6%, though precision for light elements (K, Na, and P) is poorer for some SRMs. Precision values are shown in Table 4. Percentage errors (2σ SD) in precision from SRM averages (as quoted in Table 5) are applied to major element analyses in this study.

Accuracy is assessed by comparison of SRM values obtained to recommended or preferred values. Percentage variations in accuracy of SRM data when compared to recommended values are shown in Table 6.

A discrepancy arises in that the USGS quoted value for K_2O for BIR-1 is 0.030, whereas the average K_2O concentration in this study is 0.022, producing a variance of 33%. Reproduction of K_2O for other SRMs used in this study is 2.4%, and so the quoted value for BIR-1 may be unrepresentative of the batch used.

Table 5: XRF SRM Precision Data

SRM		Wt% Total	SiO_2	TiO_2	Al_2O_3	Fe_2O_3	MnO	MgO	CaO	K_2O	Na_2O	P_2O_5
BIR-1	Repeats (n=25)	99.435	47.138	0.947	15.310	11.333	0.176	9.610	13.011	0.022	1.864	0.026
BIR-1	2σ SD (%)	0.3%	0.5%	0.5%	0.5%	0.4%	1.5%	0.3%	0.6%	10.9%	2.2%	16.1%
JB1A	Repeats (n=40)	99.149	52.370	1.280	14.503	8.933	0.150	7.975	9.301	1.474	2.908	0.255
JB1A	2σ SD (%)	0.4%	0.4%	0.5%	0.4%	0.4%	1.2%	1.0%	0.7%	0.9%	6.0%	1.7%
BHVO-2	Repeats (n=29)	99.629	49.370	2.723	13.420	12.265	0.172	7.300	11.283	0.531	2.280	0.266
BHVO-2	2σ SD (%)	0.5%	1.0%	0.6%	0.9%	0.6%	1.4%	0.4%	0.7%	0.8%	1.6%	2.2%
BRR-1	Repeats (n=27)	98.855	49.219	1.015	14.187	11.734	0.191	8.605	11.744	0.053	2.024	0.082
BRR-1	2σ SD (%)	0.5%	0.8%	0.7%	0.6%	0.4%	2.1%	0.6%	1.0%	12.2%	2.2%	6.0%
Average Precision:		**0.5%**	**0.7%**	**0.6%**	**0.6%**	**0.4%**	**1.5%**	**0.6%**	**0.8%**	**6.2%**	**3.0%**	**6.5%**

Table 5: Calculated precision of XRF data (this study). Percentage errors (2σ SD) in precision from SRM averages (**bold**) are applied to the major element data in this study, including dolerite data. In-run precision is typically 0.6%, though precision for light elements (K, Na, and P) is poorer for some SRMs.

Table 6: XRF SRM Accuracy Data

SRM	Data Source	Total (Wt%)	SiO_2	TiO_2	Al_2O_3	Fe_2O_3	MnO	MgO	CaO	K_2O	Na_2O	P_2O_5
BIR-1	Recommended	100.766	47.96	0.96	15.5	11.3	0.175	9.7	13.3	0.03	1.82	0.021
BIR-1	This Study	99.435	47.138	0.947	15.310	11.333	0.176	9.610	13.011	0.022	1.864	0.026
BIR-1	Variance (%)	1.3%	1.7%	1.4%	1.2%	0.3%	0.3%	0.9%	2.2%	**33.5%**	2.3%	18.1%
JB1A	Recommended	98.84	52.41	1.28	14.45	9.05	0.12	7.83	9.31	1.4	2.73	0.26
JB1A	This Study	99.149	52.370	1.280	14.503	8.933	0.150	7.975	9.301	1.474	2.908	0.255
JB1A	Variance (%)	0.3%	0.1%	0.0%	0.4%	1.3%	20.2%	1.8%	0.1%	5.0%	6.1%	2.0%
BHVO-2	Recommended	100.07	49.9	2.73	13.5	12.3	N/A	7.23	11.4	0.52	2.22	0.27
BHVO-2	This Study	99.629	49.370	2.723	13.420	12.265	0.172	7.300	11.283	0.531	2.280	0.266
BHVO-2	Variance (%)	0.4%	1.1%	0.3%	0.6%	0.3%	N/A	1.0%	1.0%	2.1%	2.6%	1.6%
BRR-1	Recommended	99.926	49.82	1.033	14.375	11.88	0.185	8.574	11.954	0.053	1.965	0.087
BRR-1	This Study	98.855	49.219	1.015	14.187	11.734	0.191	8.605	11.744	0.053	2.024	0.082
BRR-1	Variance (%)	1.1%	1.2%	1.8%	1.3%	1.2%	3.2%	0.4%	1.8%	0.1%	2.9%	5.5%
Av. Accuracy:		**0.7%**	**0.8%**	**0.7%**	**0.8%**	**0.9%**	**---**	**1.2%**	**1.0%**	**9.2%**	**4.0%**	**5.8%**

Table 6: Percentage variations in accuracy of XRF SRM data (this study), when compared to recommended values. The USGS quoted value for K_2O for BIR-1 is 0.030, whereas the average K_2O concentration in this study is 0.022, producing a variance of 33% (red). Reproduction of K_2O for other SRMs in this study is 2.4%, and so the quoted value for BIR-1 may be unrepresentative of the SRM batch used in this study.

5.4- ANALYTICAL TECHNIQUES- FTIR (Fourier Transform Infra-Red Spectroscopy)

Analysis of the volatile content of volcanic glass at NOC is carried out using the 'Nicolet FTIR Bench', controlled by 'OMNIC' data collection and processing software.

FTIR is an analytical technique which measures the infrared intensity vs. wavelength of light. FTIR detects the characteristic vibrations of specific chemical functional groups in sample. When IR light interacts with a molecule, chemical bonds will bend or stretch, and specific functional groups respond by adsorbing IR radiation of a specific wavenumber. Hence, the presence of these specific functional groups can be identified by their characteristic adsorbances (Nakamoto, 1997). These characteristic adsorbances remain constant regardless of differences in the molecules they are found in, and are not affected by temperature or pressure.

A Fourier Transform Infrared Spectrometer works by using an interferometer to collect an interferogram of all frequencies requested. The interferogram is formed by splitting the IR beam in two, and sending each beam on slightly different paths, then recombining them, so that the resulting beam contains the interferences between them. The beam then interacts with the sample surface, and specific frequencies are adsorbed by the functional groups present.

This beam now contains a specific series of adsorbance peaks characteristic of the analysed sample. This information is received at the detector and interpreted by the instrument software, using a 'Fourier Transform' to produce a spectrum which can be interpreted.

5.4.1- FTIR Sample Preparation

FTIR is only suitable for detecting volatiles in homogeneous glassy samples. Only fresh glass chips are used. For this study, sample chips ranged between 6mm and 3mm in size. Chips are cleaned in an ultrasonic bath for ~10mins to

remove surface contaminants, set in resin, and polished down on both sides to a thickness of ~200 microns to produce glass wafers. Once these are prepared, they are thoroughly cleaned using methanol. This removes thin layers of wax and resin left over from the grinding process.

Since dissolved water concentrations are dependent on chip thickness, very accurate thickness measurements are required. These are made using a needle micrometer. For large, coherent glass chips there are no difficulties in making thickness measurements. Small chips which remain mounted in resin for ease of handling are hard to measure due to flexure of the resin disc. This effect has been reported by other investigators (Ferreira, 2006), and requires more complex methods of thickness measurement and correction.

5.4.2- Calibration, Corrections and Data Processing

The Nicolet FTIR instrument is not a closed system. The instrument therefore detects contributions from the lab environment, such as atmospheric water vapour (~3500 cm^{-1}, 1630 cm^{-1}) and CO_2 (2350cm^{-1} and 667 cm^{-1}). Analysis of a background spectrum is required for each sample to correct for environmental contributions. The instrument software subtracts the background from the corresponding sample spectrum. The resulting combined spectrum is free of contributions from external sources.

Once spectra are obtained, quantitative measurements of dissolved total H_2O and molecular H_2O are made using the Beer-Lambert law calibration (Ihinger *et al*. (1994).

$$C = (M \times A) / (\rho \times d \times \varepsilon)$$

Where:

C = concentration (weight fraction) of the absorbing species
M = molecular weight of H_2O (18.02)
A = absorbance intensity of the band of interest
ρ = room-temperature density of the basaltic glass (2800 kg/m^3)
d = thickness of the glass chip (path length)

ε = molar absorptivity

Three spectra are recorded per glass chip. Site selections are made on the basis of constant colour and appearance, with glass being free of scratches, vesicles, surface contamination, crystals or any other inhomogeneity. Total dissolved H_2O is measured using the intensity of the broad asymmetric band centred on 3550 cm^{-1}, which corresponds to the fundamental O-H stretching vibration (Nakamoto, 1997).

Using the peak height calculation tool in the OMNIC spectral analysis software, a baseline is set, and peak height calculated for each spectrum. The molar absorptivity for total dissolved water is not strongly compositionally dependent for basaltic compositions and a value of 63 ± 5 l/(mol cm) is used (Ferreira, 2006).

Data for the three spectra are averaged, and standard deviations are calculated for the concentrations obtained.

5.5 - ANALYTICAL TECHNIQUES – ICPMS (Inductively-Coupled Plasma Mass Spectrometry)

ICPMS is a powerful multi-element technique for the rapid analysis of trace elements in geological samples. It is capable of simultaneously analysing a wide range of elements to very low detection limits, using a small amount of sample. The technique is very sensitive for the analysis of many trace elements, including the REE, which fall in the middle of the analysable range of masses. ICPMS has detection limits <10ppt (Nam *et al*., 2008), which relate to the relatively simple mass spectra (Falkner *et al*., 1995; Nam *et al*., 2008) and low backgrounds (Jarvis and Williams, 1993). Trace element concentrations of basalts in this study were measured by solution ICPMS on the ‘Thermo X-Series’ ICP-MS at the NOC.

5.5.1 - ICPMS Sample Preparation

A small amount of 10 micron powdered sample (~0.075g) is digested, following a HF-HNO_3-HCl dissolution procedure, using high purity reagents. Initially, the sample is dissolved in HF-HNO_3 in a Savillex® screw-top Teflon pot, and refluxed on a hotplate at ~130°C for ~24 hours to ensure thorough dissolution. Samples are then dried down, refluxed in HCl, re-dried, and made up to mother solutions (30ml, dilution factor ~420) with 6M HCl. An aliquot of the mother solution is then diluted with 2% HNO_3 to a concentration appropriate for ICPMS analysis (~2000 times dilution of the rock). This 2% HNO_3 contains an In/Re spike, which is used as an internal drift monitor during analysis. A sample of the blank In/Re solution is included in each analysis to monitor solution composition.

Well characterised international standard reference materials (BIR-1, BHVO-2, JB1A, JGB-1, JB-2 and JB3) are prepared using the same procedure, along with a procedural blank used to monitor laboratory contamination levels.

5.5.2 - ICPMS - Instrument Details

The radiofrequency inductively coupled plasma source consists of a plasma torch, which heats the plasma to ~7000K (Falkner *et al*., 1995), causing very efficient mono-atomic ionisation of most elements, which produces an ideal analyte for mass spectrometry. For a discussion of the background to the technique, see Potts (1992).

Solution samples in the In-Re - 2% nitric acid matrix solution are introduced to the instrument by a peristaltic pump and nebuliser (Falkner *et al*., 1995). The sample is carried to the plasma by gas flow, atomised and ionised (Nam *et al*., 2008). The sample introduction system (nebuliser, spray chamber and torch) is of a one-piece construction in the NOC instrument, which ensures accurate and consistent alignment.

The plasma source is connected to a Quadropole ICPMS, an instrument consisting of four rods arranged parallel to the ion beam. These rods are used to control the mass of ions which is passed though the instrument. By rapid, software-controlled adjustment of the voltages on the rods, the instrument can measure each mass which is present in the sample (Falkner *et al*., 1995). The two parts of the instrument are connected by an interface unit which handles the transfer of the ion beam between the plasma and the spectrometer.

Ions are introduced to the spectrometer, where they are separated by their mass to charge ratio (Gray, 1975), and detected by an electron multiplier detector, which detects a cloud of electrons released by the initial impact of an ion, and records this electron cloud as a single pulse, which is digitised and recorded.

5.5.3 - ICPMS- Precision and Accuracy of Data

As ICP spectra are relatively simple and not subject to much interference, selection of mass numbers for ICP analysis is usually based on the most abundant isotope, though there are some background interferences which must be taken into account, such as those generated by Argon ions (Falkner *et al*., 1995), droplets and vaporising particles (Hobbs and Olesik, 1992) and the carrier solution (see Nam *et al*., 2008). Very dilute (~1%) HNO_3 is commonly recommended as the carrier solution, as its spectrum is very close to that of distilled water (Falkner *et al*., 1995). 2% HNO_3 is used as the carrier solution for this study.

Trace impurities in the Argon gas, and traces of metals from the internal environs of the machine (Cu, Ni, and Mo), background impurities in reagents, and photon sensitivity of the detector are also important (Potts, 1992). Interference effects due to the presence of oxides can be significant, especially under wet plasma conditions (Falkner *et al*., 1995), but can be reduced by internal cooling or use of dry plasma (Long and Browner, 1988).

ICPMS data can be affected by the build up of materials within the sampling orifice. Organic and inorganic solids, particularly Al, Si and Zr oxides cause blockages and/or internal contamination effects. These effects can be mitigated by keeping the amount of solid material in sample solutions very low (Jarvis *et al*., 1992). Ensuring a sufficient wash-through time between analyses minimises 'memory effects' arising from the composition of previous samples.

As well as 'spectroscopic' effects, ICPMS is affected by 'non-spectroscopic' matrix interferences. These arise as a result of plasma flow and introduction, and a complex variety of machine setup parameters, including skimmer design (Newman *et al*., 2009), plasma power, ion lens settings and nebuliser flow rate (Vaughan *et al*., 1987). Matrix effects due to space charge effects (mutual repulsion of negatively charged ions as they are forced into a beam) within skimmer cones are also reported for ICPMS (Gillson *et al*., 1988),

In order to obtain robust data, drift in instrument sensitivity with time must be corrected for. This is achieved by the use of an internal standardization procedure, whereby a solution of known concentration is added to each of the samples and standards (In/Re solution in this study). All mass counts for the duration of a block of analyses (typically 20-30 analysed unknowns, plus all standards and blanks in a run) are normalised with respect to this known intensity.

ICPMS calibration is carried out by use of internal and external standards. If external standards are matrix matched and cover the concentration range of interest for each element, calibration by external standards can yield accuracy of 3-8% (Falkner *et al*., 1995). This assumes both the samples and standards are higher than the limit of detection. Internal standards, such as the In/Re solution, are used in ICPMS runs as signal drift monitors. A standard reference material, periodically measured during the procedure, can also be used.

5.5.4 - Precision and Accuracy of ICPMS- This Study

Trace element concentrations are obtained by calibrating isotope count levels to known international standard reference materials BIR-1, JB1A, JGB1, JB-2, JB-3 and BHVO-2. During each analysis, SRMs not included in the calibration are used to cross-check calibration quality.

Contamination effects are monitored by analysis of procedural blanks which accompany all sample runs. Blank subtractions are carried out using the procedural solution blank. Counts for procedural blanks are within error of In/Re solution blanks, indicating that laboratory contamination is negligible.

Precision and accuracy on the instrument is assessed by examining repeat analyses of the SRMs. 2σ standard deviations for precision are typically 5-6%, though average U, Th, Ta and Nb values quoted in Table 7 are higher, due to poor repeatability on BIR-1 in some runs. 2σ SD values as quoted here are applied to the data in this thesis.

Percentage errors for accuracy, as calculated from average values for analysed SRMS compared to recommended values, are typically 1-6%, though some higher errors are reported for individual SRMs, particularly BIR-1. This data can be found in Table 8. Poor repeatability of BIR-1 in both ICPMS and XRF analyses suggests that the BIR-1 source used for this study is contaminated.

Table 7: ICPMS Precision Data

SRM		7Li	45Sc	85Rb	88Sr	89Y	90Zr	93Nb	133Cs	137Ba	139La	140Ce	141Pr	146Nd	147Sm
BHVO-2	Av. (ppm)	4.485	32.826	9.786	396.814	27.372	182.457	17.652	0.102	131.093	15.348	37.889	5.450	24.816	6.185
n=14	% SD (2σ)	6.2%	5.6%	6.4%	5.7%	5.3%	5.4%	3.6%	7.9%	6.0%	5.9%	6.0%	5.4%	5.3%	5.1%
BIR-1	Av. (ppm)	3.117	45.112	0.185	111.321	16.164	15.447	0.780	0.005	7.086	0.596	1.844	0.372	2.352	1.099
n=14	% SD (2σ)	6.1%	5.7%	20.8%	4.5%	5.4%	7.4%	36.3%	12.3%	20.1%	5.8%	7.2%	7.8%	7.6%	6.4%
JB1A	Av. (ppm)	11.322	28.809	41.969	452.950	24.071	146.271	27.114	1.345	520.657	38.736	68.801	7.360	26.884	5.202
n=14	% SD (2σ)	5.7%	4.9%	5.4%	5.3%	4.8%	5.1%	3.0%	5.4%	5.1%	5.3%	5.0%	5.0%	4.9%	5.0%
JB3	Av. (ppm)	7.401	34.934	15.426	412.750	27.348	99.165	2.177	0.965	241.921	8.529	21.527	3.328	15.970	4.321
n=14	% SD (2σ)	5.7%	5.4%	5.6%	5.2%	4.8%	5.0%	10.9%	5.5%	5.2%	5.3%	5.2%	5.0%	4.7%	4.7%
JGB-1	Av. (ppm)	4.655	36.581	6.381	336.750	10.187	29.864	2.490	0.227	65.383	3.597	8.494	1.182	5.387	1.477
n=8	% SD (2σ)	6.3%	6.6%	6.2%	6.2%	6.1%	5.7%	10.0%	6.7%	5.6%	5.9%	6.1%	6.4%	6.5%	6.3%
Average % SD (2σ)		**6.0%**	**5.6%**	**8.9%**	**5.4%**	**5.3%**	**5.7%**	**12.8%**	**7.6%**	**8.4%**	**5.6%**	**5.9%**	**5.9%**	**5.8%**	**5.5%**

SRM		153Eu	157Gd	159Tb	163Dy	165Ho	166Er	169Tm	172Yb	175Lu	178Hf	181Ta	208Pb	232Th	238U
BHVO-2	Av. (ppm)	2.090	6.330	0.950	5.333	0.991	2.527	0.339	2.038	0.286	4.438	1.145	1.773	1.191	0.414
n=14	% SD (2σ)	5.1%	5.3%	5.0%	4.9%	5.2%	5.2%	5.3%	4.9%	5.1%	5.0%	12.5%	4.9%	6.1%	5.0%
BIR-1	Av. (ppm)	0.524	1.842	0.363	2.531	0.567	1.683	0.253	1.683	0.255	0.591	0.059	3.398	0.036	0.010
n=14	% SD (2σ)	5.5%	5.9%	5.3%	5.2%	5.1%	5.1%	4.7%	5.1%	5.1%	5.5%	28.7%	4.9%	46.6%	78.1%
JB1A	Av. (ppm)	1.516	4.825	0.726	4.200	0.824	2.262	0.330	2.147	0.318	3.524	1.789	7.274	9.026	1.640
n=14	% SD (2σ)	4.8%	4.8%	4.6%	4.7%	4.8%	4.9%	4.8%	4.8%	4.6%	4.7%	16.4%	5.3%	5.1%	5.0%
JB3	Av. (ppm)	1.336	4.709	0.751	4.605	0.949	2.677	0.394	2.574	0.388	2.704	0.155	5.743	1.260	0.469
n=14	% SD (2σ)	4.8%	4.5%	4.8%	4.5%	4.8%	5.1%	4.7%	4.1%	4.4%	4.8%	11.0%	5.4%	5.4%	4.7%
JGB-1	Av. (ppm)	0.638	1.678	0.281	1.746	0.365	1.041	0.148	0.961	0.145	0.850	0.138	1.889	0.432	0.097
n=8	% SD (2σ)	6.1%	7.6%	7.1%	7.4%	6.5%	5.8%	8.0%	7.0%	6.8%	5.3%	32.4%	8.4%	7.2%	10.4%
Average % SD (2σ)		**5.2%**	**5.6%**	**5.4%**	**5.4%**	**5.3%**	**5.2%**	**5.5%**	**5.2%**	**5.2%**	**5.1%**	**20.2%**	**5.8%**	**14.0%**	**20.6%**

Table 7: 2σ standard deviations for ICPMS precision (this study) are typically 5-6%. Average U, Th, Ta and Nb values are higher, due to poor repeatability on BIR-1 in some runs. Average 2σ SD values as quoted here are applied to the data in this thesis.

Table 8: ICPMS Accuracy Data

STD (ppm)	7Li	45Sc	85Rb	88Sr	89Y	90Zr	93Nb	133Cs	137Ba	139La	140Ce	141Pr	146Nd	147 Sm
Av. BHVO-2 n=14	4.485	32.826	9.786	396.814	27.372	182.457	17.652	0.102	131.093	15.348	37.889	5.450	24.816	6.185
BHVO-2 Accepted	5	32	9.8	389	26	172	18	None	130	15	38	None	25	6.2
% Variance	11.5%	2.5%	0.1%	2.0%	5.0%	5.7%	2.0%		0.8%	2.3%	0.3%		0.7%	0.2%
Av. BIR-1 n=14	3.117	45.112	0.185	111.321	16.164	15.447	0.780	0.005	7.086	0.596	1.844	0.372	2.352	1.099
BIR1 Accepted	3.6	44	None	110	16	18	0.6	None	7	0.63	1.9	None	2.5	1.1
% Variance	15.5%	2.5%		1.2%	1.0%	16.5%	23.1%		1.2%	5.8%	3.0%		6.3%	0.1%
Av. JB1A n=14	11.322	28.809	41.969	452.950	24.071	146.271	27.114	1.345	520.657	38.736	68.801	7.360	26.884	5.202
JB1A Accepted	10.9	27.9	39.2	442	24	144	26.9	1.31	504	37.6	65.9	None	26	5.07
% Variance	3.7%	3.2%	6.6%	2.4%	0.3%	1.6%	0.8%	2.6%	3.2%	2.9%	4.2%		3.3%	2.5%
Av. JB3 n=14	7.401	34.934	15.426	412.750	27.348	99.165	2.177	0.965	241.921	8.529	21.527	3.328	15.970	4.321
JB3 Accepted	7.21	33.8	15.1	403	26.9	97.8	2.47	0.94	245	8.81	21.5	None	15.6	4.27
% Variance	2.6%	3.2%	2.1%	2.4%	1.6%	1.4%	13.5%	2.6%	1.3%	3.3%	0.1%		2.3%	1.2%
Av. JGB-1 n=8	4.655	36.581	6.381	336.750	10.187	29.864	2.490	0.227	65.383	3.597	8.494	1.182	5.387	1.477
JGB1 Accepted	4.59	35.8	6.87	327	10.4	32.8	3.34	0.26	64.3	3.6	8.17	None	5.47	1.49
% Variance	1.4%	2.1%	7.7%	2.9%	2.1%	9.8%	34.2%	14.5%	1.7%	0.1%	3.8%		1.5%	0.9%
Av. SRM Var.	**6.9%**	**2.7%**	**4.1%**	**2.2%**	**2.0%**	**7.0%**	**14.7%**	**6.6%**	**1.6%**	**2.9%**	**2.3%**	**NONE**	**2.8%**	**1.0%**

STD (ppm)	153Eu	157Gd	159Tb	163Dy	165Ho	166Er	169Tm	172Yb	175Lu	178Hf	181Ta	208Pb	232Th	238U
Av. BHVO-2 n=14	2.090	6.330	0.950	5.333	0.991	2.527	0.339	2.038	0.286	4.438	1.145	1.773	1.191	0.414
BHVO-2 Accepted	None	6.3	0.9	None	1.04	None	None	2	0.28	4.1	1.4	None	1.2	None
% Variance		0.5%	5.3%		5.0%			1.9%	2.2%	7.6%	22.3%		0.8%	
Av. BIR-1 n=14	0.524	1.842	0.363	2.531	0.567	1.683	0.253	1.683	0.255	0.591	0.059	3.398	0.036	0.010
BIR1 Accepted	0.55	1.8	None	4	None	None	None	1.7	0.26	0.6	None	3	None	None
% Variance	4.9%	2.3%		58.1%				1.0%	2.0%	1.6%		11.7%		
Av. JB1A n=14	1.516	4.825	0.726	4.200	0.824	2.262	0.330	2.147	0.318	3.524	1.789	7.274	9.026	1.640
JB1A Accepted	1.46	4.67	0.69	3.99	0.71	None	None	2.1	0.33	3.41	1.93	6.76	9.03	None
% Variance	3.7%	3.2%	4.9%	5.0%	13.9%			2.2%	3.8%	3.2%	7.9%	7.1%	0.0%	
Av. JB3 n=14	1.336	4.709	0.751	4.605	0.949	2.677	0.394	2.574	0.388	2.704	0.155	5.743	1.260	0.469
JB3 Accepted	1.32	4.67	0.73	4.54	0.8	None	None	2.55	0.39	2.67	0.15	5.58	1.27	None
% Variance	1.2%	0.8%	2.8%	1.4%	15.7%			0.9%	0.5%	1.3%	2.9%	2.8%	0.8%	
Av. JGB-1 n=8	0.638	1.678	0.281	1.746	0.365	1.041	0.148	0.961	0.145	0.850	0.138	1.889	0.432	0.097
JGB1 Accepted	0.62	1.61	0.29	1.56	0.33	None	None	1.06	0.15	0.88	0.18	1.92	0.48	None
% Variance	2.8%	4.0%	3.2%	10.7%	9.5%			10.3%	3.2%	3.5%	30.4%	1.6%	11.1%	
Av. SRM Var.	**3.1%**	**2.2%**	**4.0%**	**18.8%**	**11.0%**	**NONE**	**NONE**	**3.3%**	**2.3%**	**3.4%**	**15.9%**	**5.8%**	**3.2%**	**NONE**

Table 8: Percentage errors for ICPMS accuracy in this study, as calculated from average values for analysed SRMS. Errors are typically 1-6%, though some higher errors are reported for individual SRMs, particularly BIR-1.

5.6 - ANALYTICAL TECHNIQUES – TIMS (Thermal Ionisation Mass Spectrometry)

High precision analyses of Sr, Nd and Pb isotope ratios in basalt samples for this study were carried out using two 'VG Sector 54' TIMS instruments at NOC.

The first commercial TIMS instrument became available in 1947 (Yip *et al*., 2008) and TIMS is still recognised as the analytical method of choice for high-precision isotope ratio determination (Woodhead, 2003). TIMS uses thermal ionisation reactions, in which a pure material is loaded onto a metal filament which is heated by a current, causing some of the loaded material to ionise. Ionisation is a function of filament temperature, the work function of the filament substrate (the energy required to remove an electron from the solid surface into vacuum), and the ionisation energy of the element loaded. The relationship between these parameters is described by the Saha-Langmuir equation. A discussion of the derivation and characteristics of this relationship is provided by Dresser (1968).

TIMS is a highly reliable method for the analysis of isotope ratios, producing stable beams for low ionisation energy species such as Sr and Pb. The technique is well established, and the physically stable analytical environment allows for highly precise measurements.

TIMS has lower and more consistent fractionation effects than ICPMS, although it is not efficient in analysing elements with high ionisation energies. Samples must be elementally pure in order to avoid isobaric interference effects and suppression of ionisation off the filament. This means time-consuming column chemistry is needed to isolate the element of interest. However, the high precision data that results is of a quality sufficient to determine fine-scale variations in isotopic systems, such as mantle sources.

The Sector 54 mass spectrometers at NOC have a sample turret suitable for single or triple filaments allowing 20 samples to be measured consecutively without breaking vacuum.

The ion beam leaving the source is separated by mass in a magnetic field. The resulting mass spectrum is analysed by using seven Faraday detectors to provide relative amounts of each isotope. A diagram of the internals of a TIMS instrument is shown in Figure 25.

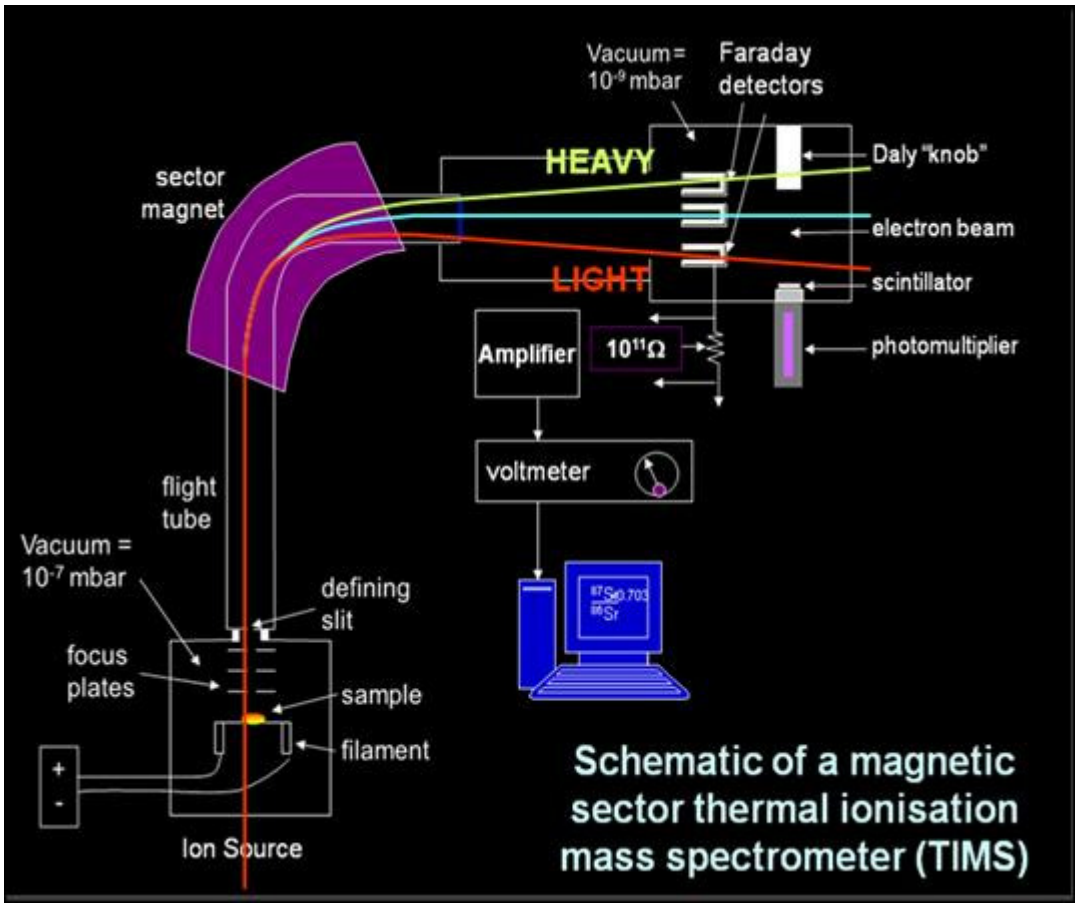

Figure 25: Schematic diagram of the internal layout of a magnetic sector thermal ionisation mass spectrometer, showing the different paths taken by heavy and light isotopes to the detectors. Rex Taylor, pers. comm.

5.6.1 - Sample Preparation for Nd, Sr and Pb Isotope Ratios using TIMS

Pb, Sr, and Nd isotope measurements are made from a single dissolution of the rock. ~0.6g of picked and cleaned basalt or basaltic glass chips are leached in 6m HCl for 1-3 hours at 140°C. This stage is critical as environmental

contamination of non-leached sample powders has been shown to result in $^{206}Pb/^{204}Pb$ being 2% lower than the true sample ratio, and does not only affect low-Pb samples (Thirlwall, 2000).

Each batch of HF-HNO_3 dissolutions is accompanied by a procedural blank, which is used to quantify the amount of Pb contamination introduced into the sample during separation.

5.6.2 - Ion exchange separation of Pb, Sr and Nd.

Ion exchange columns are used to purify samples by isolating the elements of interest from other major and trace elements. The production of near elementally pure samples by column separation permits efficient ionisation of the element, which would not be possible in the presence of other, more abundant elements.

5.6.3 - Separation of Pb on Anion Exchange Columns

Pb separation is carried out using AG1x8 resin, with a column length of ~8mm. Columns are washed with HCl and ELGA water, and then equilibrated by passing 1M HBr prior to sample loading. Samples are taken up in 2ml 1M HBr and centrifuged prior to loading to avoid solids being passed onto the column. Supernatant solution is loaded onto the column and washed on with further passes of HBr. The waste HBr from the column is collected for the Nd and Sr separations. 6M HCl is passed onto the column to release Pb, which is collected in the cleaned Teflon vials. The HCl eluate is then dried and taken up in 1M HBr to be passed through the same column a second time. HBr-HCl based methods for Pb separation are very successful in separating Pb from most other elements, whilst maintaining high yield and low matrix blanks in geological materials. A discussion of the ion-exchange behaviour of Pb and other relevant elements in HBr solutions can be found in the work of Guseva (2005).

5.6.4. - Procedure for Column Separation of Sr

Column waste from the Pb separation procedure, or any other sample mother solution, is subsampled into Teflon to give ~1µg of Sr. This aliquot is passed through columns containing a small amount of Sr-spec. resin (Eichrom). The procedure uses ELGA water and accurately titrated, sub-boiled ultra-pure 3M HNO_3.

5.6.5 - Procedure for Separation of Nd using Cation and Reverse Phase Columns

Nd is isolated from the Pb column waste solution using two sets of columns. First, cation exchange columns (6.5ml Dowex AG50W-X8 200-400mesh) separate Nd from major elements using an aliquot of Pb waste solution containing ~1µg Nd in 2.2M HCl. The eluate is dried before dissolution in 0.15M HCl. The second reverse phase columns separates Nd from other REE by HCl - HDEHP (Bis-(2-Ethylhexyl) Phosphoric Acid) separation.

Further details of column procedures used in this study can be found in the Appendix 2.

5.6.6 - TIMS Filament Preparation and Loading Procedures

Filaments are re-useable steel, electrically-insulated posts between which an appropriate filament ribbon is welded (Figure 26).

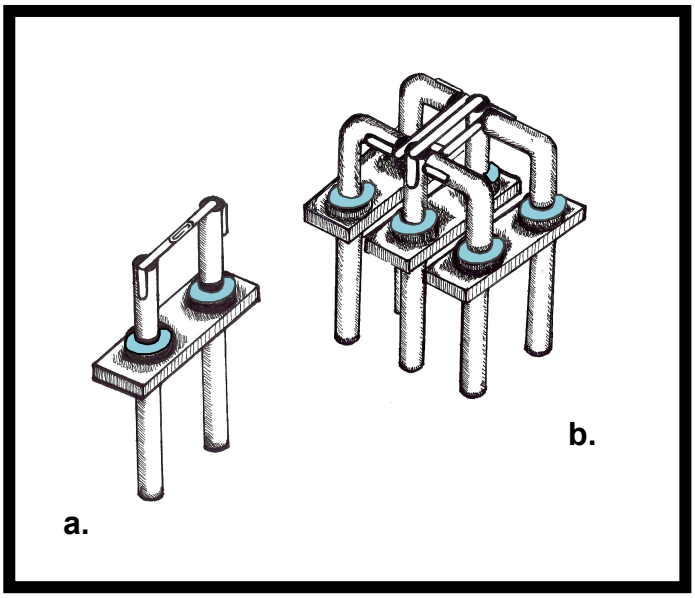

Figure 26: Modern TIMS filaments. The sketch shows a single filament (a), and also the correct alignment of a triple filament setup (b). Sample is loaded neatly onto the centre of the ribbon to achieve efficient ionisation.

Filament posts are abrasively cleaned for >1 hour in 50% H_2O_2 to ensure a clean surface. Filament ribbons are welded between the posts, ensuring a good connection. Zone-refined rhenium ribbon is used for Pb analysis and tantalum for Sr analysis. A Re centre ionising filament with two Ta side sample evaporation filaments in a triple arrangement (see Figure 32) are used for Nd analysis. For details of filament loading procedures, see Appendix 2.

5.6.7 - Precision, Accuracy, Errors and Corrections in (Sr, Nd and Pb) TIMS Data

The acquisition of high quality TIMS isotope ratio data requires a number of procedures and corrections to be applied during analysis. For many elements, stable volatilisation and ionisation take place at different temperatures, and this creates complications for TIMS analysis. For the analysis of Pb, the sample can be loaded within a silica gel, which coats the sample, preventing volatilisation of Pb, so that the filament can be heated to high enough temperatures for

ionisation, without the sample burning off the filament. For details of this method, see (Akishin *et al*., 1957; Cameron *et al*., 1969).

REE also suffer from volatilisation problems. Ingram and Chupka (1953) proposed a multiple filament technique to eliminate this problem. In this method, three filaments per bead are used for each unknown sample. For Nd, two side filaments, composed of Ta, surround a central Re filament. The Ta filaments, upon one of which the Nd sample is loaded, are raised to moderate temperatures corresponding to Nd volatilisation, whilst the central Re filament is taken to higher temperatures, to ionise the sample.

NdO+ ions and single filament methods were originally used to analyse Nd, and continue to be used by some, as they can be more efficient. These methods are commonly carried out using an oxygen bleed valve and/or Si-gel (Thirlwall, 1991), though some have presented methods which use loading media which yields the oxygen in the source, eliminating the need for the bleed valve. These methods have been very successful, yielding stable 2.0–2.5 V beams, and resulting in internal precisions as low as 8 ppm 2σ RSE (Harvey and Baxter, 2009).

Single filament Nd+ analysis can be achieved using Re filaments in the presence of platiniferous carbon to reduce Nd *in situ* at 1350-1550°C, providing a simple single filament approach whereby 50ng Nd yields analytical precision of 0.0022%. This technique benefits from simple loading procedures, and robust loads (Noble *et al*., 1989).

Very high precision (<10 ppm 2σ RSE) Nd measurements by TIMS are possible, though this level of precision commonly requires samples of up to several hundred ng (Harvey and Baxter, 2009). When isotopes are measured by TIMS, mass-dependent fractionation takes place during the ionisation and volatilisation processes on the filament, and data is also affected by the mass-dependent response of Daly detectors (Fletcher, 2007).

Isotope fractionation in mass spectrometry is a process that is not fully understood, but is controlled by evaporation or diffusion processes. To achieve

both a high accuracy and a low uncertainty in mass spectrometric analysis, the magnitude of the fractionation must be well known (Ramebäck *et al*., 2002).

Ionisation and volatilisation require the breaking of chemical bonds, the strengths of which are dependent upon mass. Bonds within lighter isotopes have slightly weaker bonds than heavier isotopes, and therefore the potential energy to break light isotope bonds is lower, and they are more easily broken (Urey, 1947). Thus, when a filament is heated, lighter isotopes are more readily ionised, leading to isotope fractionation in the ratios received at the detector relative to those in the filament salts (White *et al*., 2000).

Further, this effect is not constant throughout the use of a filament. As the filament is heated and the light isotopes are preferentially ionised, the light isotope reservoirs are exhausted more rapidly than the heavier ones, and so the signal received at the detector becomes progressively ‘heavier' over time. This is known as the ‘reservoir effect’, and has a magnitude which is significant. The effect follows a Rayleigh fractionation law, and is corrected for by an internal normalisation procedure in order to achieve an accurate measurement of the isotope ratio (Eberhardt *et al*., 1964).

The linear mass fractionation correction assumes that fractionation is dependent upon mass difference between isotopes, not absolute masses. However, this is an approximation, and for lighter elements, linear models can be improved upon by application of a power law or exponential correction, which takes into account absolute mass difference (Russell, 1979; Hart and Zindler, 1989).

Fractionation effects can only be corrected when two or more isotopes of an element are present in a constant ratio; and unlike Sr and Nd, this is not the case for Pb (Kuritani *et al*., 2006). Since all Pb isotopes except ^{204}Pb form from radioactive decay of U and Th, there is no constant natural ratio in Pb isotopes which can be used to perform an internal normalisation correction (Doucelance and Manhés, 2001).

The application of Si-gel activator in Pb analysis substantially reduces mass fractionation effects (see Akishin *et al*., 1957), but its production is problematic as it is difficult to create Si-gels with a consistent high efficiency. The

physiochemical properties of Si-gel for Pb analysis and may be manipulated to produce more efficient activators (Miyazaki *et al*., 2003).

Filament temperatures during TIMS analysis may affect mass fractionation behaviour. TIMS analyses are shown to obey the typical mass fractionation laws at lower temperatures, but mass fractionation at temperatures >1250°C becomes unpredictable, according to existing laws (Thirlwall, 2000).

Large in-run variations in isotope ratios and corresponding errors between blocks may arise when there is incomplete mixing between the spike and the natural solution on the filament. This was considered by Powell *et al*. (1998) to be a major contributor of error in Pb analysis. However, the large internal errors are produced by the fractionation of a range of isotopic mixtures between the natural and spike, and accuracy of the final fractionation corrected natural value should be unaffected. Precision in this case can be calculated on a block by block basis (Thirlwall, 2000).

^{204}Pb is by far the least abundant naturally occurring isotope of Lead, producing the smallest ion beam. The effects of instrumental errors are thus more significant than for other isotopes, although this is only thought to be a significant source of error on runs where ^{208}Pb beam intensity of 3V for 125 ratios at 5s integration times has not been achieved (Thirlwall, 2000).

Anomalous fractionation behaviour of ^{207}Pb has been shown in the Thirlwall (2000) study, with ratio agreement substantially poorer than internal error for ^{207}Pb/^{206}Pb ratios. The uncertainty propagates through all ratios due to the spike fractionation correction, however, spike and natural errors are opposite in sense, meaning that some internal error cancellation takes place in recalculating natural ratios. The effect is shown to be minimal at optimum Q values.

When analysing elements with at least one isotopic ratio involving no radiogenic isotopes the analyst can select between static and dynamic analytical modes (Lenz and Wednt, 1976). In static mode, each isotope is assigned a collector, and the beam position remains constant throughout the analysis, whereas in dynamic mode each collector receives different masses in a step sequence.

Static analyses are simple and can deal with large mass separations, but amplifier gains and collector efficiencies must be well known. Dynamic collectors have the advantage that neither precise nor accurate amplifier gains/collector efficiencies are necessary, but these analyses are slower because a setting time is required between masses (Ludwig, 1997).

For the analysis of Nd and Sr, appropriate selection of peak vs. background measurement times, peak-jumping modes, and ratios for fractionation normalization will produce the most precise results. Ludwig presents data to indicate that dynamic data for Nd and Sr can be collected without a significant loss of efficiency over static (Ludwig, 1997).

5.6.8 - Pb Double Spike Technique for Fractionation Correction

In some laboratories, external fractionation corrections are applied to Pb data, by application of a correction based on the average fractionation of NIST SRM 981 to each unknown (Doucelance and Manhés, 2001). Conventional corrections for fractionation effects based only on correction to an external standard (e.g. NIST SRMs 981) may be flawed because SRMs have been shown to fractionate substantially differently from natural samples due to impurities in the natural run such as Cd, Zn and organic materials derived from column chromatography (e.g., Woodhead *et al*., 1995; Woodhead and Hergt, 2000). Corrections on the basis of standards also fail to take into account the variability of sample recovery for unknowns, which cannot be assumed to perform as well as SRMS (Fletcher, 2007).

Re-analysis of data published by a number of laboratories prior to 2000 show substantial variations in the reproducibility of conventional Pb data (up to 30x the supposed value), highlighting the dangers of inadequate fractionation corrections and laboratory-based contamination in Pb analysis (Thirlwall, 2000). Double-spike techniques (see Compston and Oversby, 1969) are a more powerful method for the correction of mass-dependent fractionation effects in Pb analysis by TIMS (Fletcher, 2007).

Application of a double-spike technique allows an internal fractionation correction to be applied to Pb analyses (Thirlwall, 2000) by using two separate measurements of spiked and unspiked sample aliquots. Using the double-spike technique, precise and accurate Pb isotopic determinations are routinely made (Woodhead, 1995, Galer, 1999; Thirlwall, 2000, 2002) for relatively large Pb samples (> 10 ng of Pb) by TIMS (Kuritani *et al*., 2006). Most double spikes are produced by using established high-purity ^{207}Pb + ^{204}Pb spikes or ^{202}Pb + ^{205}Pb. (Fletcher, 2007).

Essentially, the spiking technique is based upon the principle of dividing the unknown sample into two aliquots, and introducing a spike to one of these. Lead has four naturally-occurring isotopes: ^{204}Pb (abundance: ~1.4%); ^{206}Pb (~24.1%); ^{207}Pb (~22.1%); and, ^{208}Pb (~52.4%) (Yip *et al*., 2008).The spike should be a substance with a Pb isotopic composition substantially different to that of the unknowns, and containing a high abundance of at least two Pb isotopes which are present as minor isotopic components of the unknown. The exact concentration of the spike need not be known, though its isotopic ratio must be well characterised (Thirlwall, 2000).

A disadvantage of the technique is that the aliquoting of small samples makes the acquisition of high precision data more difficult, by bringing the ^{204}Pb concentration in the sample down toward detection limits. Alternative techniques for the precise analysis of Pb by TIMS have employed variations on column chromatography such as extra column stages to produce ultra pure elemental Pb residues, dramatically improving mass fractionation for the analysis of very small Pb samples (Kuritani and Nakamura, 2002).

Also, the double-spiking technique is only capable of accounting for mass fractionation that occurs after the spike is added, fractionation during sample digestion or separation is not accounted for (Fletcher, 2007).

It is known that isolation methods preceding isotopic analyses can introduce isotopic fractionation, as observed for elements like Fe, Cu and Zn and Cd. This behaviour is not qualitatively identified in Pb (Muynck *et al*., 2007). However, isotopic fractionation during column separation of Pb samples may be a factor contributing error to Pb isotopic analyses.

5.6.9 - Sr, Nd and Pb Analysis – This Study

Strontium measurements are made multi-dynamically with exponential fractionation normalisation to $^{86}Sr/^{88}Sr = 0.1194$ (constant agreed ratio for Earth). The deviation of observed $^{86}Sr/^{88}Sr$ from 0.1194 at each point through the run is divided by the difference between the two masses in order to calculate a fractionation factor per mass unit. $^{87}Sr/^{86}Sr$ determinations typically average 0.710257 ±0.000012 (2sd – n=238) for the NBS-987 standard at NOC. Data is collected over 150 ratios at ^{88}Sr ion beams of ~2-3V. Rb concentrations are monitored, and samples with high Rb (>30 ppm) are treated with caution.

Multi-dynamic $^{143}Nd/^{144}Nd$ measurements are fractionation corrected using $^{146}Nd/^{144}Nd = 0.7219$ (see O'Nions *et al*., 1979) and give $^{143}Nd/^{144}Nd = 0.512110$ ±0.000006 (2sd, n = 24) for the JNdi standard. External precision is +/- 14ppm (2sd) for $^{87}Sr/^{86}Sr$, and ±8ppm (2sd) for $^{143}Nd/^{144}Nd$, both analysed multi-dynamically using exponential fractionation corrections. Nd 144 beams are maintained at 0.5-1.5V, for 150-200 ratios. Samples with low Nd recovery yield stable 0.5V beams that run for up to 200 ratios, but higher voltages are difficult to maintain for a sufficient run time. ^{144}Sm isobaric interference is monitored and corrected for using ^{147}Sm.

For Pb analysis, a target voltage of 2V on ^{208}Pb is maintained where possible, throughout both static and dynamic runs, with internal errors and beam intensity monitored throughout. Isotope ratios are acquired using a multi-dynamic procedure normalising to an initial statically measured $^{208}Pb/^{206}Pb$. The Pb double spike used at NOC, SBL-74, is calibrated relative to NBS982 and produces $^{20x}Pb/^{204}Pb$ ratios reproducible to better than 180ppm. Double spike data is around 10 times more precise than traditional externally fractionation corrected Pb measurements isotope analysis.

An in house procedural blank is produced with each column run of 18 samples, and analysed with the relevant run. In house blank concentrations from 2004-present average 0.09±0.00 ppb.

The NIST standard NBS981 is used to monitor the quality of data and applied corrections. Reproducibility data for NBS981 is presented in Table 9.

	$^{206}Pb/^{204}Pb$	$^{207}Pb/^{204}Pb$	$^{208}Pb/^{204}Pb$
	16.9408	15.4980	36.7220
+/- 2sd	0.0029	0.0031	0.0090
+/- ppm	195	217	249

Table 9: Reproducibility data for the NBS 981 standard at NOC, 2004-present. n=62.

interference from other elements, samples which achieved very few ratios, ran with unstable beams or at unexpectedly high temperatures are repeated using sample remnants from the initial column chemistry, or are re-columned as appropriate.

5.7- ANALYTICAL TECHNIQUES- SEM (Scanning Electron Microscope)

5.7.1 - Use of Quantitative SEM for Rapid Identification of Mineral Compositions

The SEM is a high resolution electron microscope that images a sample by firing a high-energy beam of electrons at the surface. The sample produces secondary and backscatter electrons, and characteristic X-rays that give information on sample surface topography and composition. Secondary (SE) or backscatter electron (BSE) modes are used to image in high resolution. Backscatter electrons given off by a sample are related to atomic number, and therefore the variations in intensity of backscatter are useful in characterising the distribution of elements within a sample.

X-ray emissions in SEM are used to perform rapid compositional analyses of mineral targets selected on a SE image, allowing pinpoint analysis of targets as small as ~10 microns.

The technique is applied to aid in the rapid identification of phenocrysts, as well as to provide specific information on mineral compositions.

5.7.2 - Sources of Error, SEM Calibration and Setup

The SEM is calibrated using a block of known pure elemental standards, and the international basaltic glass standard NIST BIR-1. Major element precision is 2-4% typically, with Na reproducibility at 14%, and Ti at 23% (Table 10). Though precision is poor for some elements, this does not preclude the usage of quantitative SEM for identification of mineral targets by stoichiometric calculations.

NIST BIR1	**Wt %**								
n=99	**FeO**	**MnO**	**Cr_2O_3**	**TiO_2**	**CaO**	**SiO_2**	**Al_2O_3**	**MgO**	**Na_2O**
Average	10.666	0.183	0.104	1.154	13.387	47.602	15.115	9.423	2.041
2 SD	0.326	0.164	0.132	0.263	0.274	0.872	0.380	0.369	0.289
% Var.	3.1	89.8	126.5	22.8	2.0	1.8	2.5	3.9	14.2

Table 10: SEM precision data for major elements (this study). Precision is 2-4% for Fe, Ca, Si, Al and Mg oxides, which is sufficient for use in stoichiometric calculations. Reproducibility of Na, Ti and Cr is very poor.

In order to improve precision in collection of the lighter elements (e.g. Na) which emit fewer characteristic X-rays than heavier elements, sampling times are set to three minutes, as this gives a more stable count level. Each sample is bracketed by the NIST BIR-1 standard, to monitor drift.

Data quality is partially dependent on machine setup. Incorrect focusing of the electron beam prevents collection of the optimal number of counts. This is avoided by performing a re-focus operation between analyses as necessary,

when the SE image is out of focus. This is a subjective approach and perfect focus is not guaranteed.

Changes in beam current have a substantial effect on the number of counts detected, but this can be monitored by returning to the Faraday cup between analyses. Each sample is bracketed by a test of the current on the Faraday Cup, as changes in beam current lead to drift in the number of counts for a given element. If the Faraday cup shows a drift in beam current, then this is adjusted accordingly prior to the next analysis.

Pits and irregularities in the surface of the target can lead to low counts. Careful selection of smooth, heterogeneous, unaltered crystal surfaces minimises these effects. In hydrated minerals low totals are recorded due to the fact that H cations are not detected. Minerals such as serpentine typically report totals of 75-90wt%, and cannot be handled in stoichiometric calculations. Detection of other elements in these minerals is not affected, so mathematical corrections for the ‘missing water’ can be applied.

CHAPTER SIX – BASALT GEOCHEMISTRY

In this chapter, major element, trace element and isotopic data for basalt from 12°60'-14°N on the MAR are presented. Existing data for the central MAR and specifically from the area surrounding the FTFZ are also examined.

6.1 – BASALT PETROLOGY - 12°60'-14°N

On-axis dredges typically recovered pillow basalts, fresh in appearance on cut faces, and possessing fresh to slightly altered glassy rims. They are variably vesicular, and typically contain plagioclase and/or olivine phenocrysts. A small number of sheet flow pieces, characterised by ropy surfaces and a flat morphology, were also found.

In basalts from off-axis sites (13°19'N), glassy rims are altered or absent, reflecting the greater age of the samples. Half spreading rates, assuming plate separation at 25.7 km/Myr (DeMets, 1994) give a maximum age for breakaway ridge basalts of ~1Ma. Basalts from the hanging wall and the back-tilted blocks on the breakaway ridge are thought to be *in situ*. However, basalts from the dome is talus and so age and geographic origin are poorly constrained.

OCC dome talus has undergone varying degrees of alteration (see Figure 27). Some samples appear fresh; some have soft clay rims indicating low-temperature seawater alteration. Others are extensively altered, showing signs of recrystallisation to greenschist facies minerals (chlorite/epidote/actinolite/quartz) and oxides.

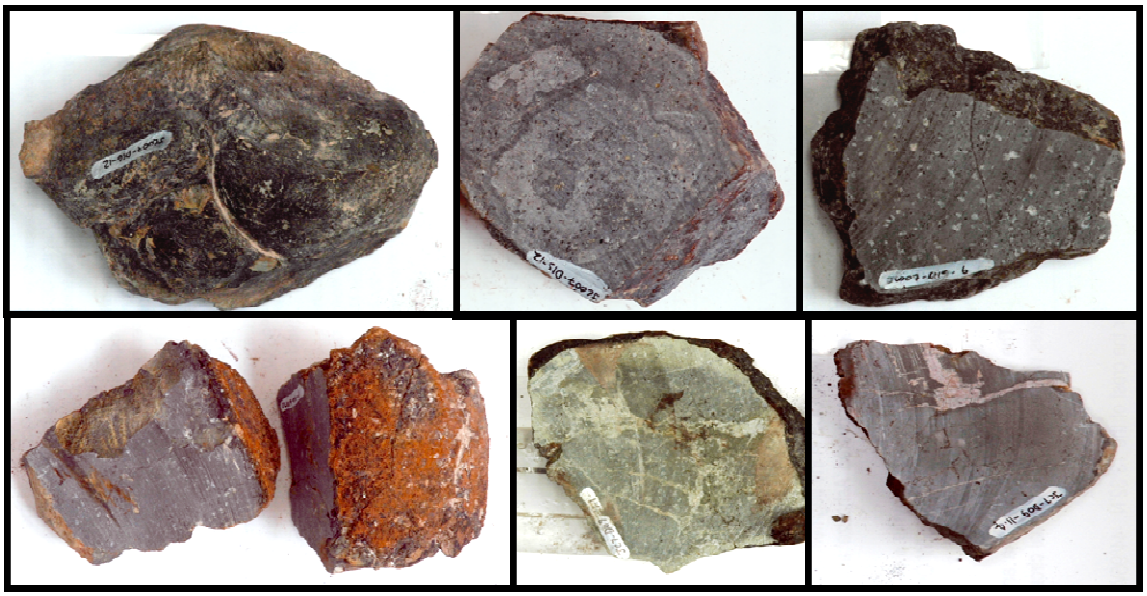

Figure 27: Examples of hand specimens from the 12°6'N-14°N region. These rocks show common basalt features such as glassy layers, vesicles and alteration features. Clockwise from left to right: 1. Pillow basalt with fresh glass (from axis). 2. Moderately altered pillow basalt with vesicles and discoloured alteration rim (breakaway). 3. Fresh, plagioclase-phyric pillow basalt without glass (breakaway). 4. Altered, recrystallised pillow basalt with thick vein (talus). 5. Extensively recrystallised greenstone pillow basalt with cross-cutting veins (hydrothermal toe talus). 6. Pillow basalt with devitrified glass and a thick oxide coating (breakaway).

OCC basalts are typically plagioclase and/or olivine phyric and variably vesicular. Samples from two dredges (D05 and D10) contain clinopyroxene in addition to olivine and plagioclase. Basalts from on-axis neovolcanic zones range from aphyric to plagioclase- and/or olivine-phyric, with vesicularity of 2-10%

6.1.1- Textural Variability in Basalts 12°60'-14°N

Basalts from on-axis display a variety of textures. Some are glassy and aphyric, whilst others contain fine-grained (~1mm) plagioclase and small, subhedral olivine crystals (<1mm). The most common texture is one dominated by large,

euhedral plagioclase phenocrysts (2-8mm) in a fine groundmass, with variable amounts of small olivine and plagioclase crystals (Figure 28).

The large plagioclase crystals found in on axis rocks are anhedral to subhedral in shape. Crystal surfaces are irregular. Structural irregularities indicative of disequilibrium are common.

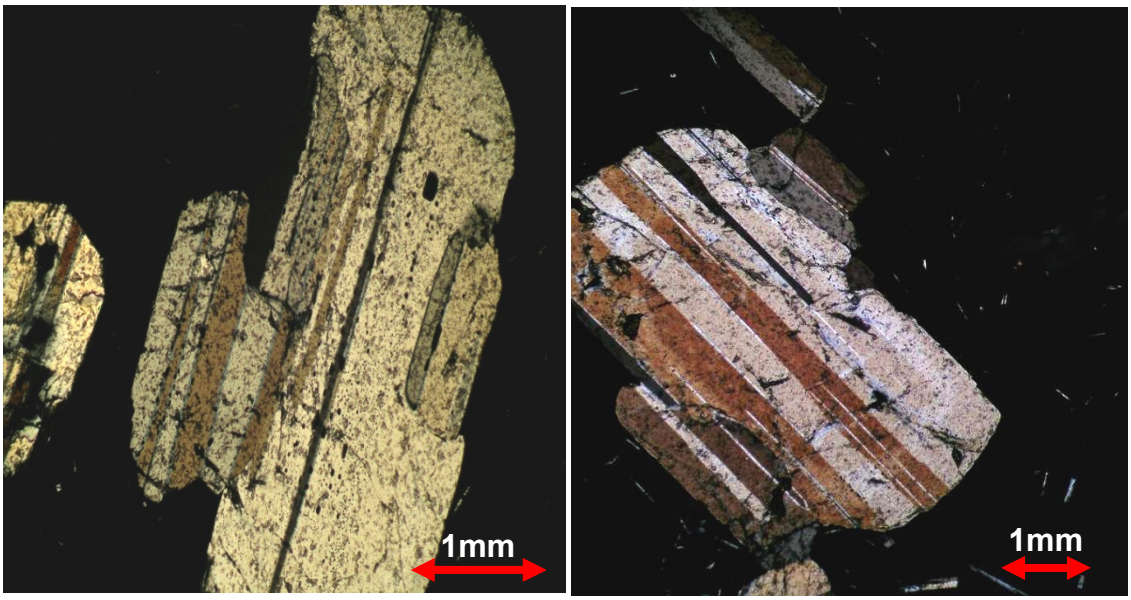

Figure 28: Photomicrographs of on-axis basalts from 12°6'-14°N showing large anhedral to subhedral plagioclase crystals with prominent twinning. Blebs, cracks and other structural irregularities indicative of disequilibrium are common in these crystals.

Some samples from the OCC at 13°19'N have textures containing large plagioclase crystals (~2-8mm typically, 20mm in one example), which show evidence of disequilibrium as seen in on-axis samples. They also contain olivine (<1mm-~2mm) in varying proportions, typically subhedral. However, many OCC samples have textures comprising radial clusters (typically ~2-5mm) of partially-formed plagioclase crystals, interspersed in some cases with <0.5mm olivine crystals. Both olivine and plagioclase crystals in these rocks have highly complex shapes (Figure 29).

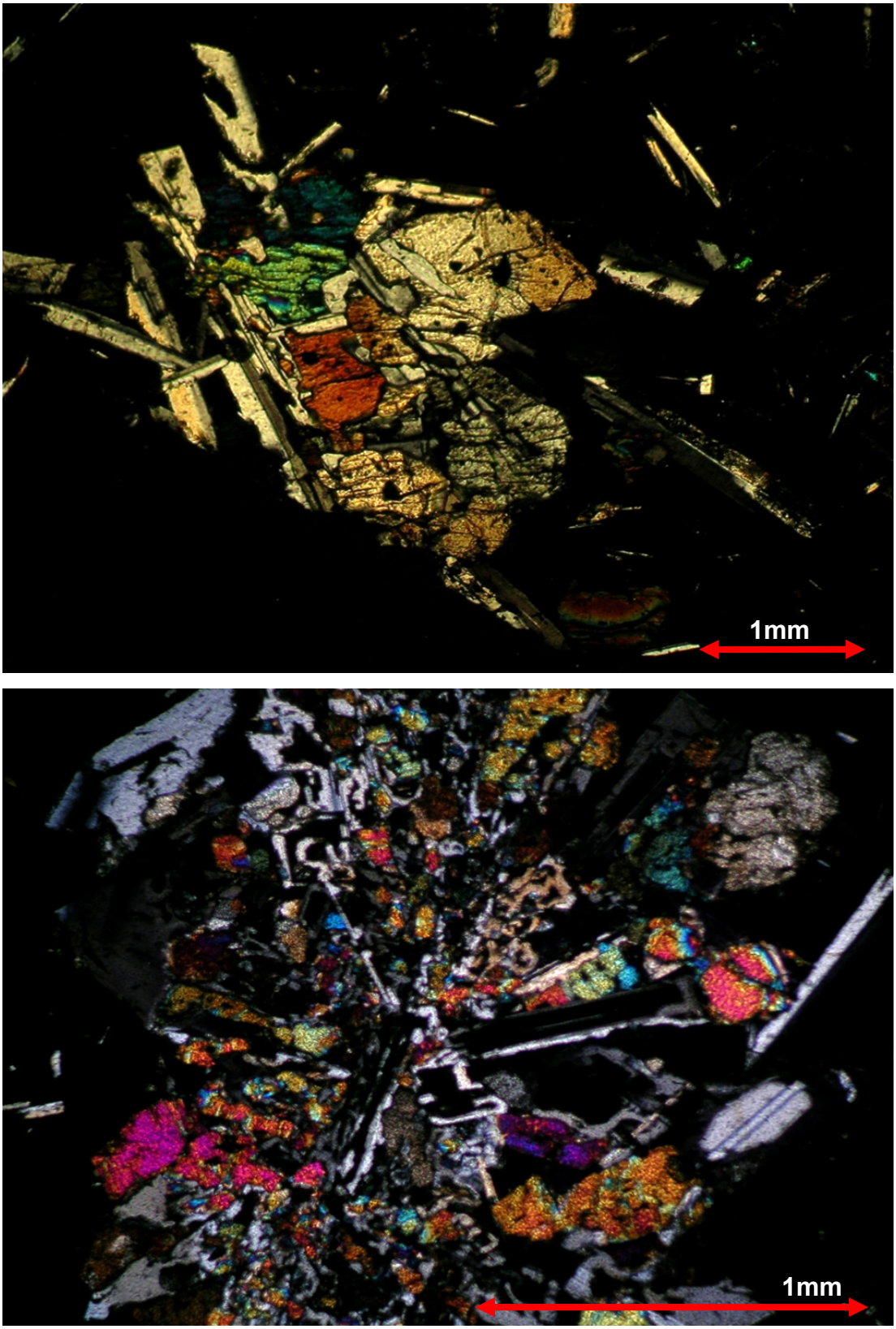

Figure 29: Photomicrographs (taken with crossed polars) of off-axis basalts from 13°19'N. Bottom: Cluster of irregularly shaped plagioclase and olivine crystals, interspersed with smaller olivine and (?) pyroxene crystals within a matrix of basaltic glass and fine (<1mm) plagioclase. Top: Cluster with larger, more well-developed crystals.

The photomicrographs show (1) a cluster of highly irregularly shaped plagioclase and olivine crystals, interspersed with smaller olivine and (?) pyroxene crystals. The radial crystal clusters sit within a matrix of glass and fine (<1mm) plagioclase. Some crystal clusters are more well developed (2) with larger crystals, and distinguishable euhedral crystals.

Highly complex olivine crystals are found in many samples from 13°19'N. Examples are shown in Figure 30 a,b. The crystals range from radial to lath-like and even dendritic in appearance, with large voids in the crystal centres. They are typically ~1mm in size, though, occasionally, lath-like examples reach 3mm.

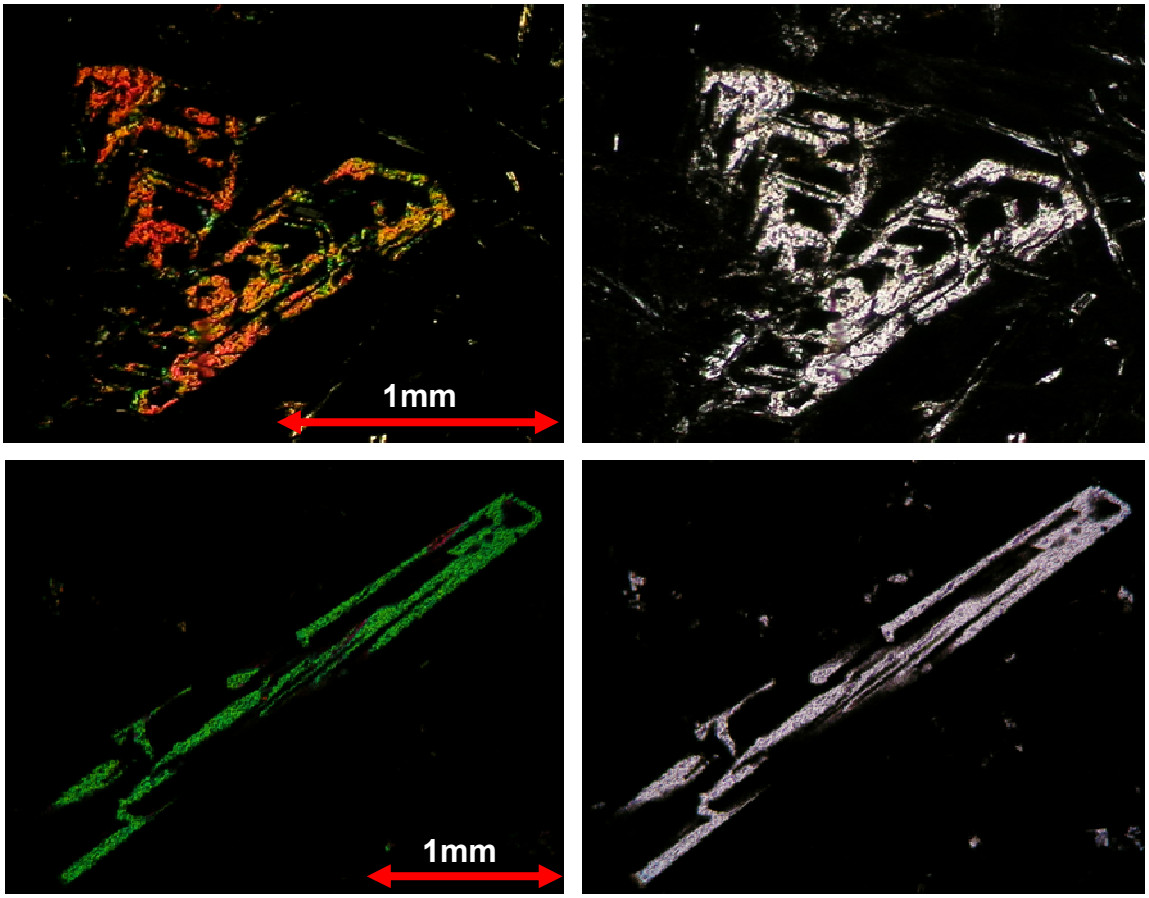

Figure 30a: Photomicrographs taken with crossed polars and plane polarised light (top right, second row right) of off-axis basalts from 13°19'N. Highly irregularly shaped olivine crystals are found in many samples from the OCC. These crystals range from radially clustered to individual, lath-like examples. Some of these are complex dendritic, open and/or closed 'Hopper' crystals, with large voids in the crystal centres. The crystals are typically ~1mm in size, though, occasionally, lath-like examples reach 3mm in length.

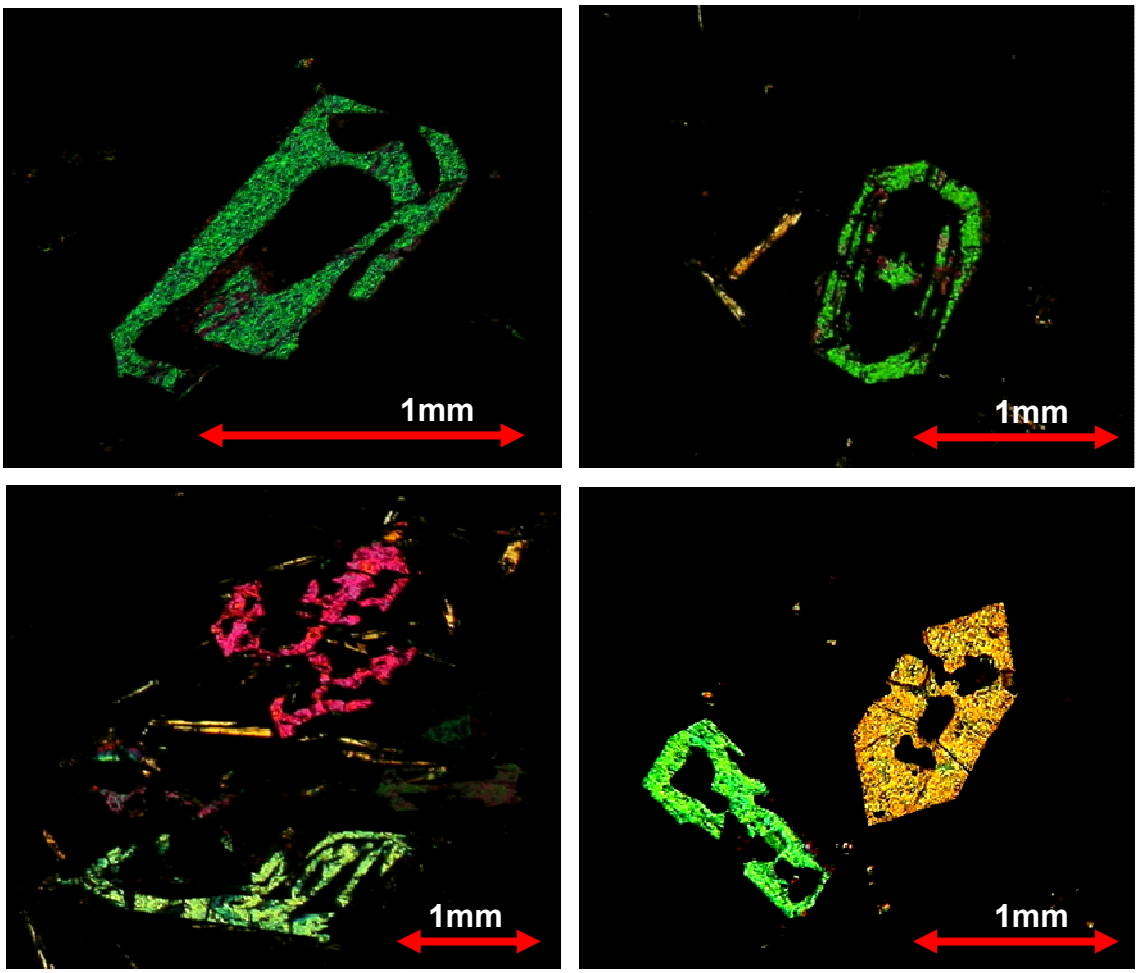

Figure 30b: Photomicrographs taken with crossed polars and plane polarised light (top right, second row right) of off-axis basalts from 13°19'N. Highly irregularly shaped olivine crystals are found in many samples from the OCC. These crystals range from radially clustered to individual, lath-like examples. Some of these are complex dendritic, open and/or closed 'Hopper' crystals, with large voids in the crystal centres. The crystals are typically ~1mm in size, though, occasionally, lath-like examples reach 3mm in length.

Clinopyroxene (augite) crystals, where present, are large (~3-5mm) and subhedral, displaying evidence of chemical disequilibrium in the form of indistinct crystal boundaries, blebs, cracks and other defects (Figure 31). These crystals are surrounded by small (<1mm-2mm) plagioclase, and in some cases complex olivine as described above. The majority of the augites are simply twinned. Sector zoning is also observed in some examples.

Clinopyroxene is only found at 13°19'N, specifically in dredges D05 and D10. Dredge D05 is *in situ*, located on the breakaway ridge, whilst D10 consists of talus from the OCC surface.

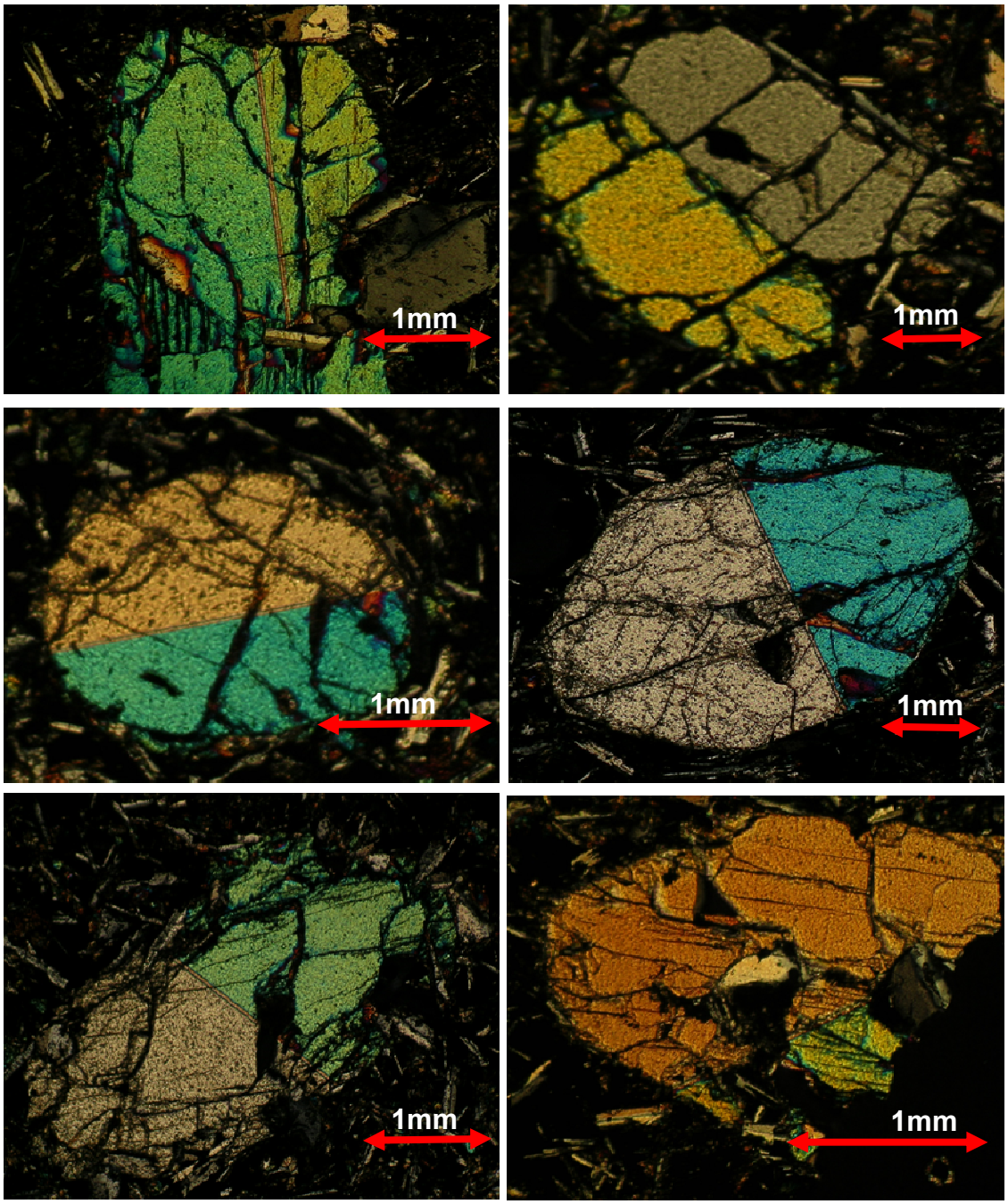

Figure 31: Photomicrographs (taken with crossed polars) of off-axis basalts from 13°19'N. Augite crystals are large (~3-5mm) and subhedral, displaying strong evidence of chemical disequilibrium in the form of indistinct crystal boundaries, blebs, cracks and other defects They are surrounded by fine (<1mm-2mm) laths of plagioclase. The augite crystals are simply twinned, and sector zoning is observed in some examples.

Semi-Quantitative SEM analyses of clinopyroxene crystals are shown in Table 11.

Conc. Wt% Sample #	SiO_2	TiO_2	Al_2O_3	Cr_2O_3	FeO	MgO	CaO	Na_2O	Total
D05-1.4	51.94	0.48	2.63	0.63	6.21	17.94	19.48	0.00	99.57
D10-3	50.59	0.33	3.91	1.11	4.36	17.21	20.61	0.00	98.20
D10-3	50.81	0.40	3.63	1.20	4.08	17.24	21.10	0.00	98.54
D05-11.6	51.38	0.42	3.12	0.70	4.52	17.83	20.19	0.49	98.75
D05-1.2	50.87	0.30	2.65	0.44	5.75	18.12	18.78	0.53	97.73
D05-1.6	52.58	0.17	2.65	0.53	5.20	18.14	19.94	0.62	100.04
D05-1.1	51.53	0.22	3.53	1.11	3.92	17.63	20.75	0.66	99.49

Table 11: Clinopyroxene compositions obtained from SEM spot analysis of individual crystals from the 13°19'N OCC provide an estimate of the compositions of clinopyroxene at the site.

These data provide a positive identification of the pyroxene crystals. However, the data cannot be used to identify specific crystal compositions, as the errors in some elements (especially Na) are very poor.

6.2 - BASALT GEOCHEMISTRY DATA

6.2.1- Along Axis Geochemistry of MORB, 12°60'N-14°N

Basalt from the vicinity of the FTFZ is E-MORB, being enriched in incompatible major and trace elements (Dosso *et al.*, 1991; Hémond, 2006). North of the 17°10'N geochemical limit described by Dosso (1993), the geochemistry tends to more N-MORB-like compositions. Data presented in this study show that basalts from on-axis sites (Figure 32) between 12°60'N-14°N range from nearly N-MORB to E-MORB in composition.

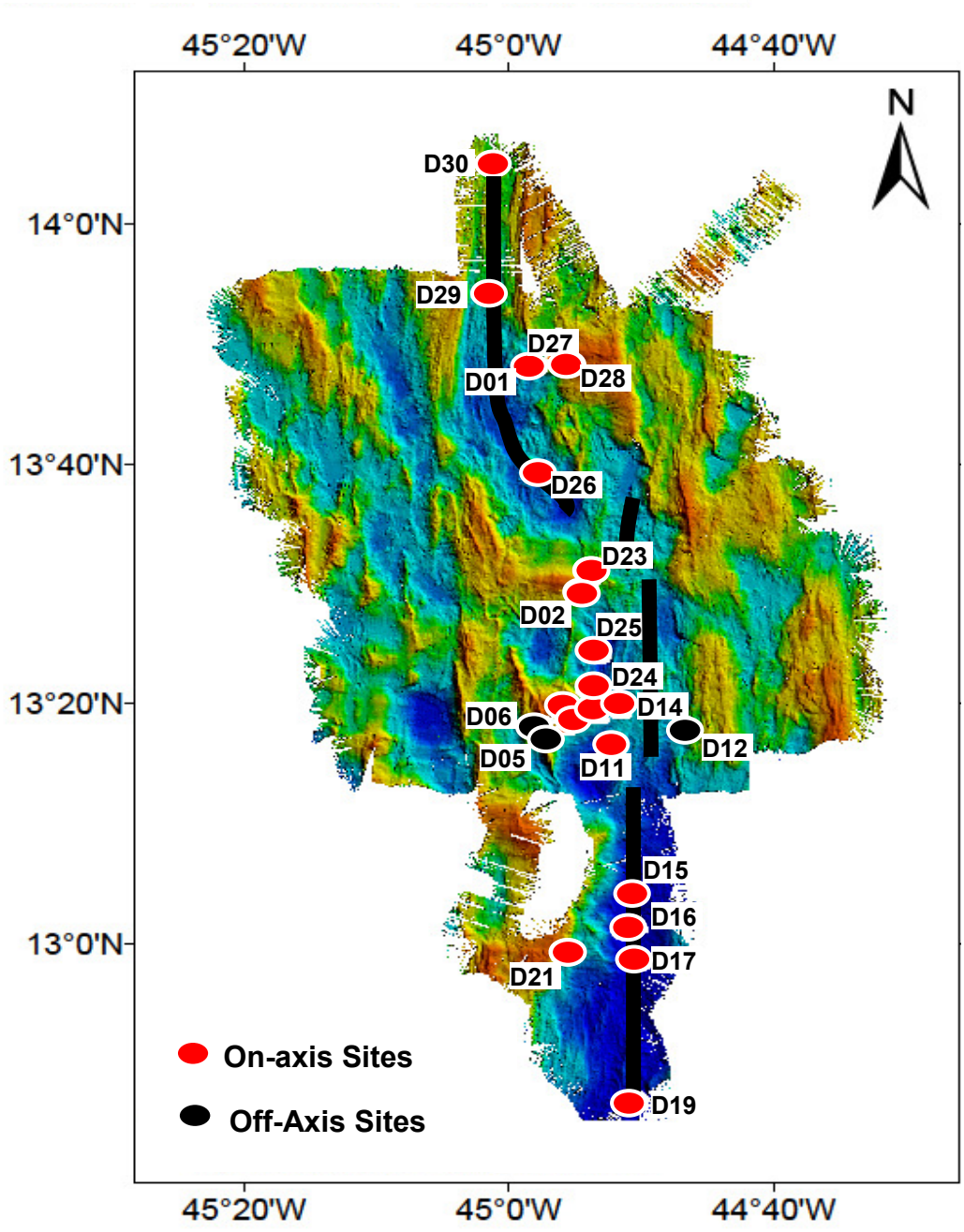

Figure 32: Bathymetry map showing the estimated position of the ridge axis (black line) overlaid by the positions of dredges sampling on-axis material (red markers). Black markers denote dredges in off-axis positions and will be considered separately. Off-axis sites are defined as those where *in situ* material is sampled from outside the axial zone. Talus material from core complex domes is considered to have originated in the axis, before being dragged over the fault surface, and therefore sites sampling talus are included in the 'on-axis' site category.

Rocks from on-axis sites are typically high in incompatible elements K and P relative to N-MORB (see Table 12). Figure 33 shows the relationship of the data array from this study to average N-MORB values, as given by Hoffmann (1988).

	N-MORB (Hoffmann, 1988)	On-Axis 12°60'-14°N
TiO_2	1.615	1.48
Na_2O	2.679	2.54
K_2O	0.106	0.39
P_2O_5	0.12	0.20
MgO	7.58	8.16

Table 12: The relationship of the data array from this study to average N-MORB values, as given by Hoffmann (1988).

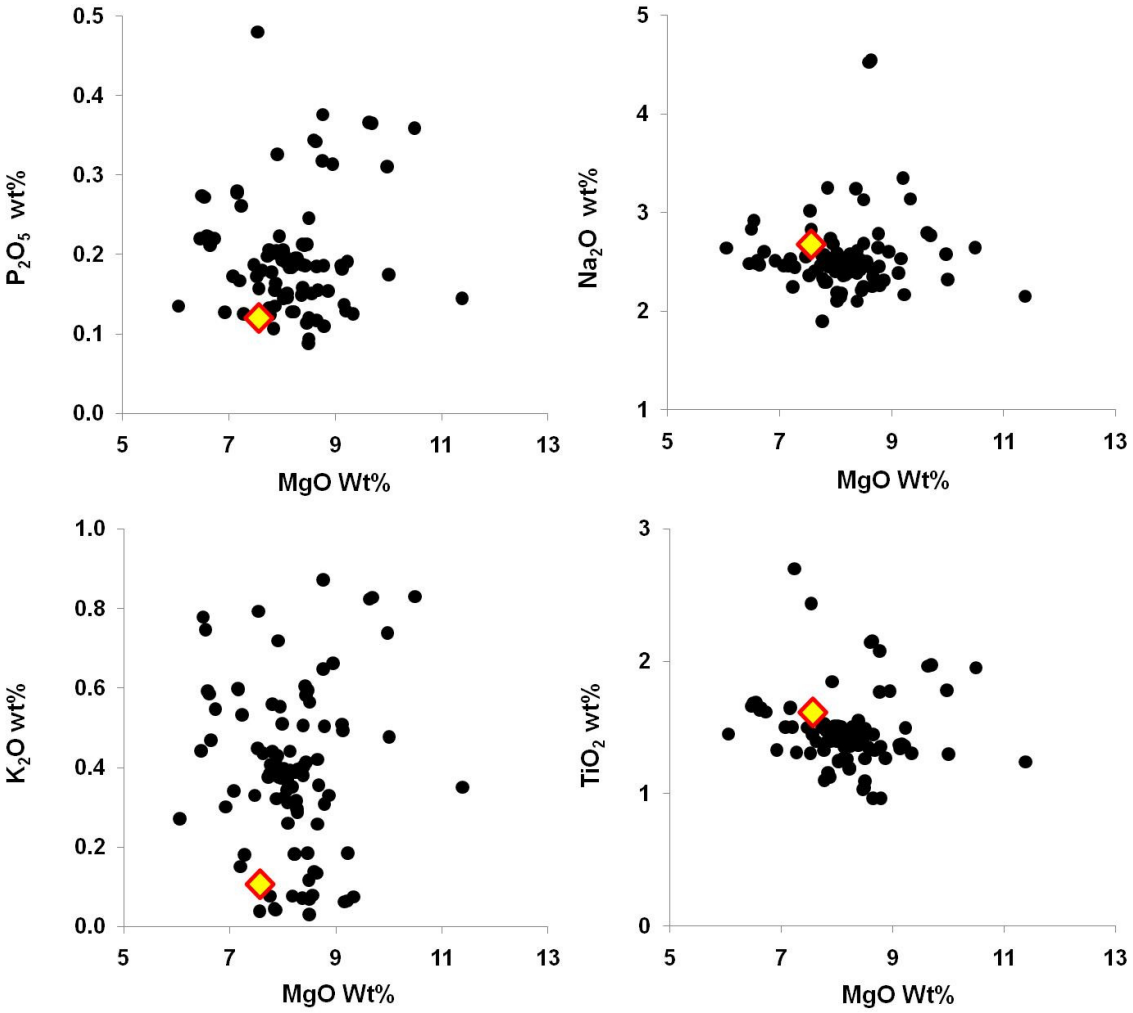

Figure 33: Major element plots showing the composition of basalts from this study (black markers) relative to the N-MORB average (yellow diamond). Average N-MORB value from the data of Hoffmann (1988). Error bars lie beneath the display markers.

Trace element data reveal compositions extending from nearly N-MORB to extremely incompatible element enriched E-MORB. The Zr-Nb-Y discrimination diagram (Figure 34) for basalts (after Meschede, 1986) shows that basalts from the axis between 12°60'N-14°N range from N-MORB to E-MORB in character. Some samples extend to very high (OIB-like) values of Zr and Nb compared to those expected, even for E-MORB.

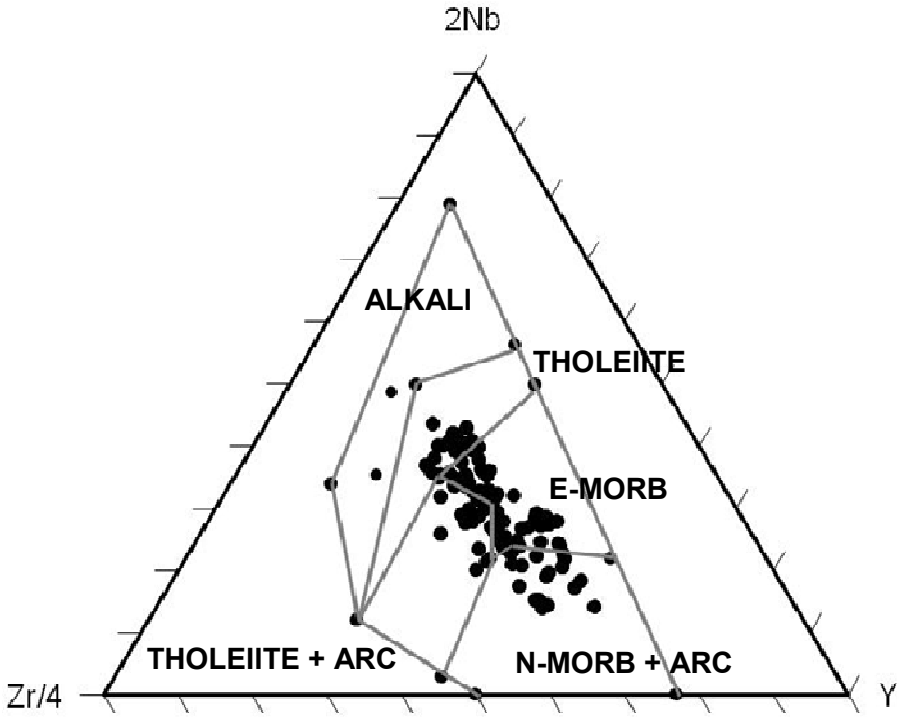

Figure 34: Ternary discrimination diagram for basalt (after Meschede, 1986). The diagram shows that rocks from this study (black markers) extend from N-MORB to E-MORB in composition, and that some samples have higher Zr and Nb than is expected even for E-MORB.

REE data (Figure 35) show that the majority of samples from the ridge axis are enriched in LREE relative to N-MORB and average MORB, with similar, or more highly LREE enriched profiles than the average E-MORB from the nearby MARK area. Some profiles tend toward the more LREE depleted shape of average N-MORB.

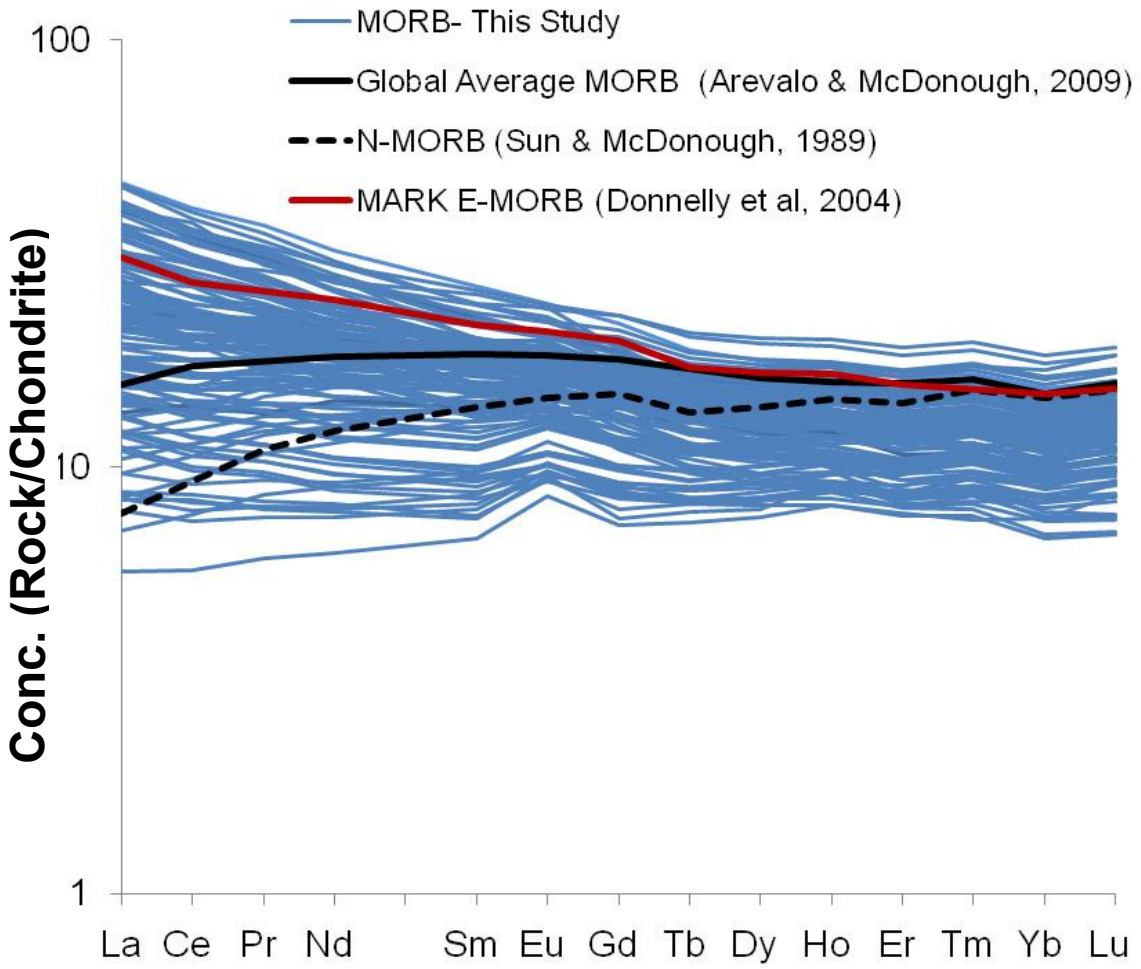

Figure 35: REE plot showing that on-axis data from 12°60'-14°N (blue) extend from N-MORB-like profiles to LREE enriched E-MORB compositions. Average N-MORB (black dashes) and average global MORB (black) and E-MORB (red) compositions for the Atlantic region and worldwide are shown for comparison. See legend for data sources.

6.2.2. - Geographic Relations of On-axis MORB Compositions 12°60'-14°N

Plots of trace element ratio versus latitude (Figure 36) show that there is a broad-scale southward transition from E-MORB to less enriched, more N-MORB like compositions away from the 14°N geochemical 'enrichment anomaly' described by previous studies (see Hémond *et al*., 2006).

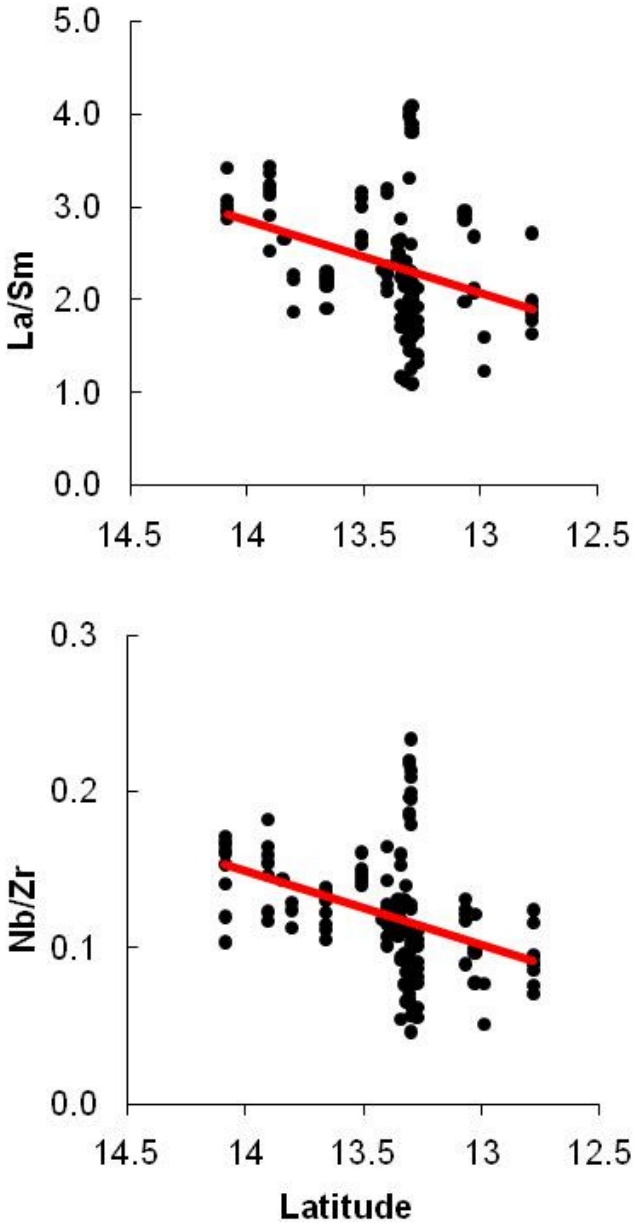

Figure 36: Regression lines on trace element ratio vs. latitude plots show that there is a general transition from LREE enriched compositions at the 14°N 'enrichment anomaly' (as described by Hémond *et al*., 2006) to less enriched signatures near the Marathon fracture zone at 12°60'N.

At certain latitudes, there are large ranges in the trace element ratios, overlying the general southward trend. In order to examine whether these variations correlate with differences in the spreading mechanism, sites along the axis are divided into two categories: on-axis OCC spreading sites, and on-axis magmatic sites. Figure 37 shows the distribution of these sites. Samples are categorised on

the basis of their proximity to the OCCs, and on the nature of the terrain in which they are found.

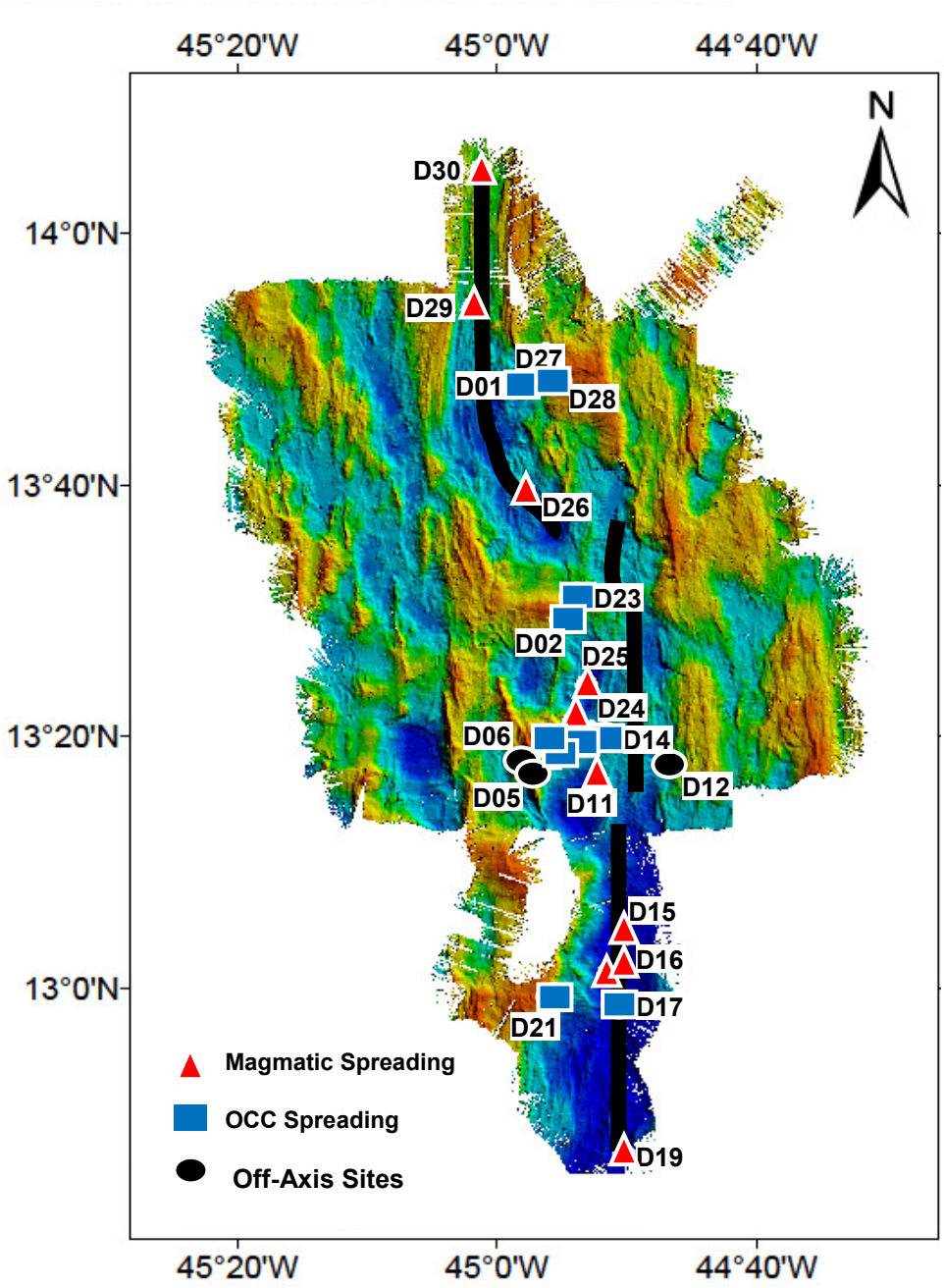

Figure 37: ArcGIS processed bathymetry map overlaid with markers to show sample sites characterised as 'on-axis magmatic spreading', 'on-axis core complex spreading' and 'off-axis' sites. Samples from on-axis at OCC sites are shown in blue, magmatic on-axis samples are shown in red, and off-axis sites are black.

Hummocky volcanic zones in symmetric parts of the axis are considered to be magmatically spreading. Axial seafloor with little evidence of volcanism found close to OCCs is 'OCC spreading'. Major element data (Figure 38) from on-axis samples (OCC and magmatic) indicate that a small number of OCC basalts are more incompatible element enriched than their magmatic counterparts, extending to marginally higher Na_2O, K_2O, P_2O_5 and TiO_2 concentrations.

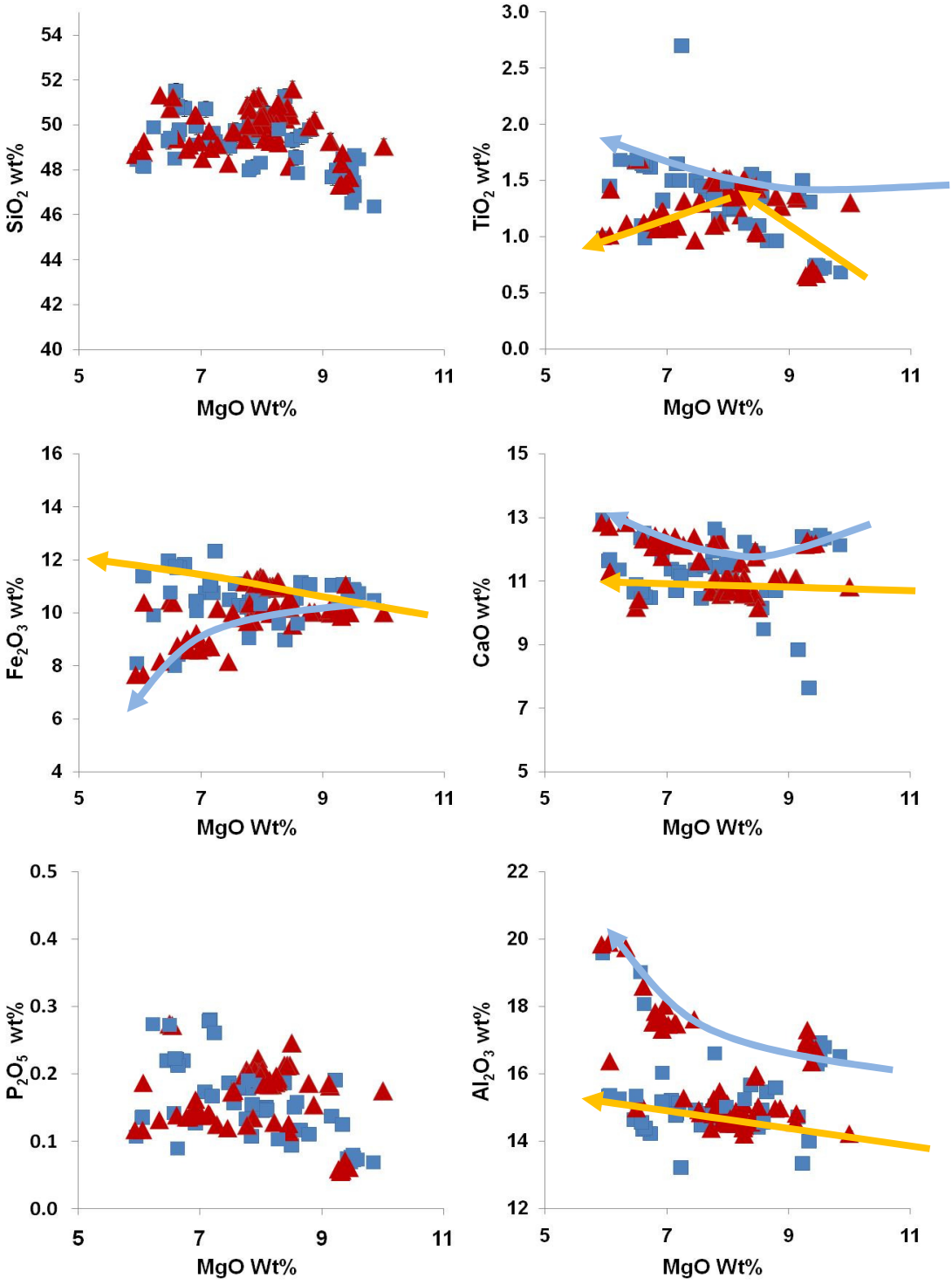

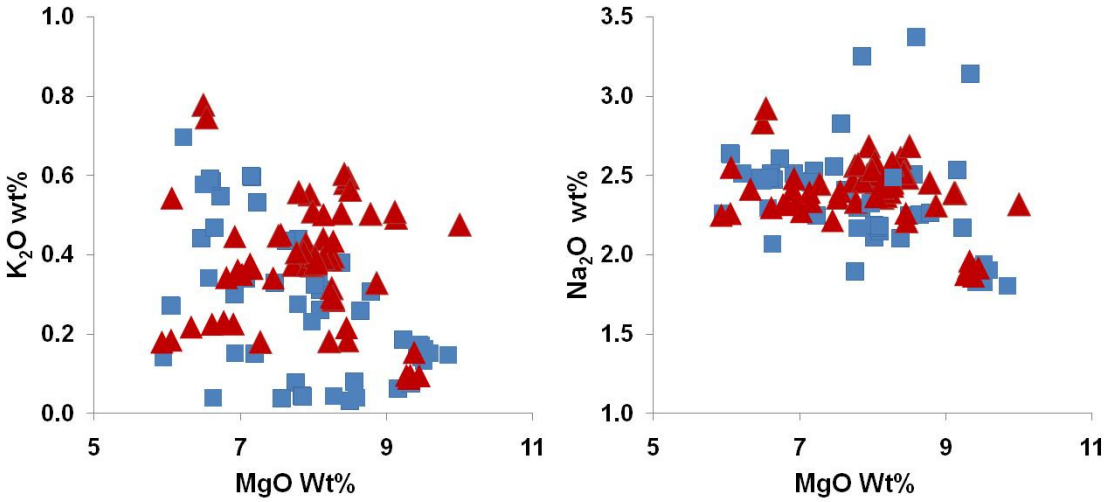

Figure 38: Major element concentration (wt %) plots. On-axis magmatic samples are represented by red triangular markers and on-axis OCC samples by blue square markers. Arrows indicate the direction of fractional crystallisation in both plagioclase-accumulated (blue) and non-plagioclase-accumulated (orange) basalt groups.

The CaO, Al_2O_3 and Fe_2O_3 versus MgO plots in Figure 39 show two divergent trends, both containing OCC and magmatic samples. Trend 1 is characterised by increased TiO_2 vs MgO, Al and Ca well above typical MORB values, but low Fe values, which are indicative of dilution by an excess of plagioclase. Trend 2 exhibits typical MORB values for Ca, Al and Fe. The TiO_2 vs. MgO trend increases, and then rapidly decreases after an inflexion point, likely due to changing Ti behaviour during crystallisation

Plagioclase accumulation trends can be an effect of high pH_2O, which suppresses plagioclase crystallisation (Yoder and Tilley, 1962), leading to enrichment in plagioclase components (Ca and Al) in the melt. Plagioclase crystallisation also affects Fe and other elements not found in plagioclase (i.e. by dilution). The geochemical trends observed cannot be consanguineous, since they start at different positions in TiO_2, Al_2O_3 and CaO vs. MgO.

Figure 38 shows TiO_2, CaO, Al_2O_3 and Fe_2O_3 vs. MgO data, along with arrows projected towards clinopyroxene, olivine and plagioclase compositions taken from average SEM analyses of crystals in basalts from the study area (Table 12).

Mineral	Clinopyroxene n=6 ●	Plagioclase n=47 ■	Olivine n=17 ▲
Conc. Wt %			
SiO_2	49.46	48.01	34.33
TiO_2	0.32	0.03	0.03
Al_2O_3	3.12	31.68	0.18
Fe_2O_3	10.16	1.04	24.28
MnO	0.12	0.03	0.21
MgO	16.97	0.38	40.28
CaO	19.55	16.49	0.27
K_2O	0.01	0.04	0.03
Na_2O	0.28	2.31	0.38
Total	**100.00**	**100.00**	**100.00**

Table 12: Normalised average mineral compositions calculated from SEM analyses of crystals in basalt from 12°6'-14°N. Symbols are used in Figure 45 to show the positions of these mineral compositions.

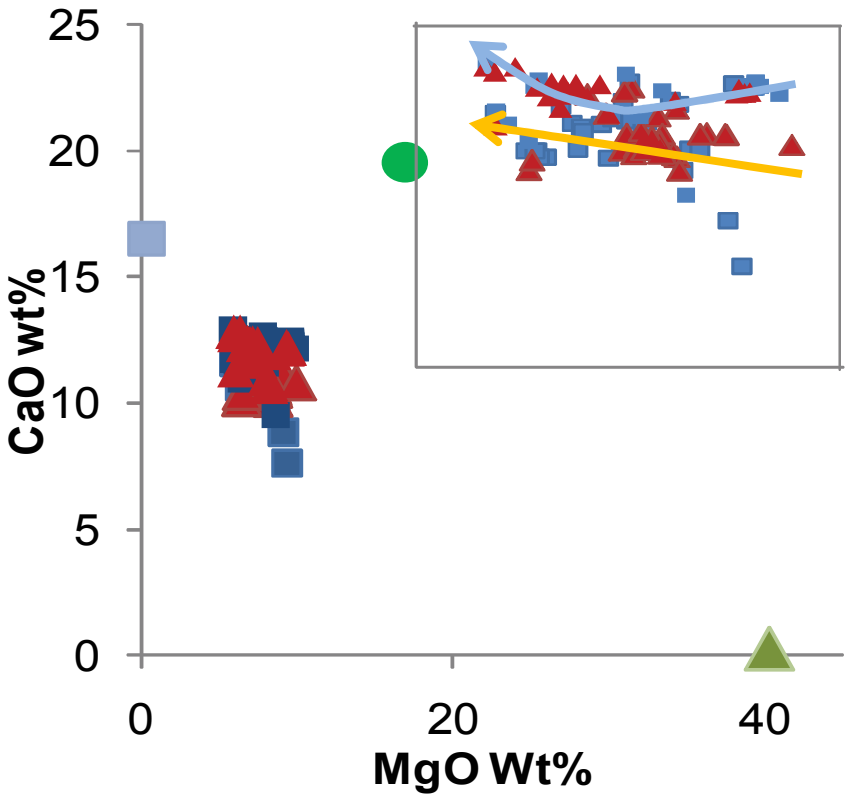

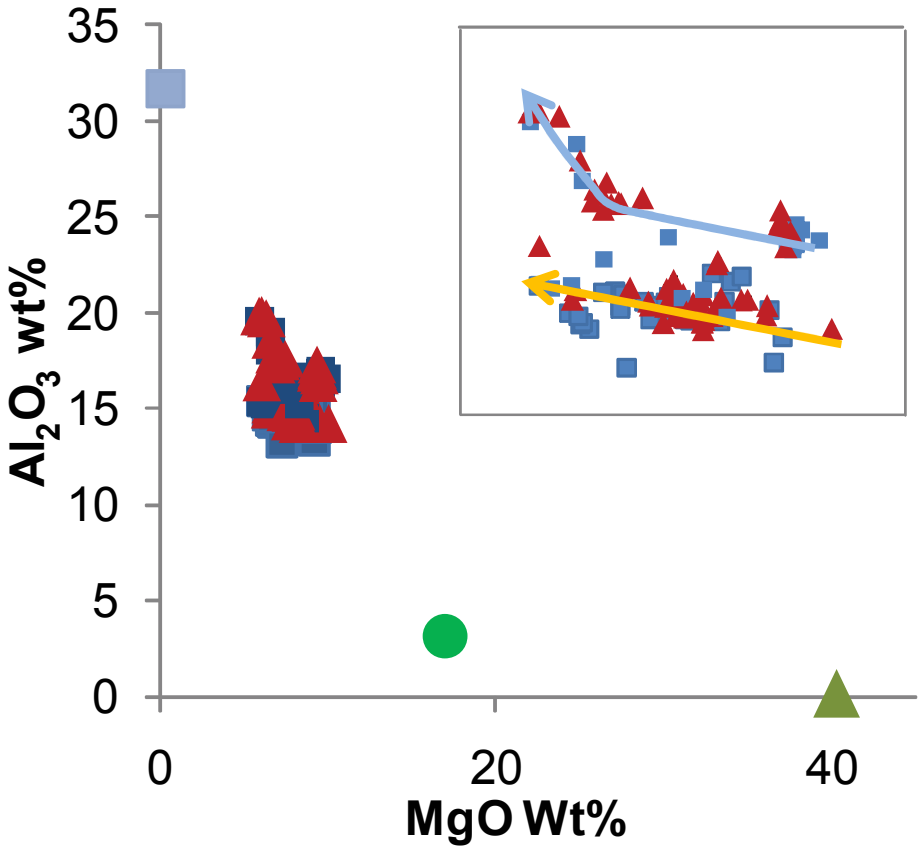
35
30
25
20
15
10
5
0
0
20
40
Al_2O_3 wt%
MgO Wt%

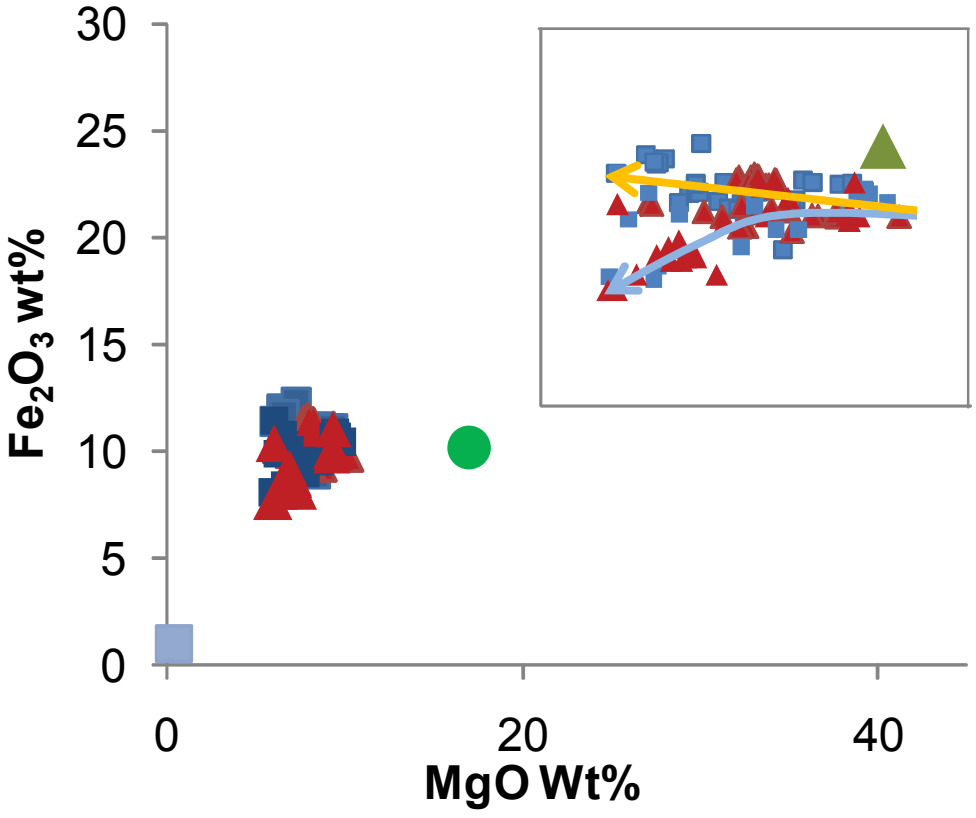
30
25
20
15
10
5
0
0
20
40
Fe_2O_3 wt%
MgO Wt%

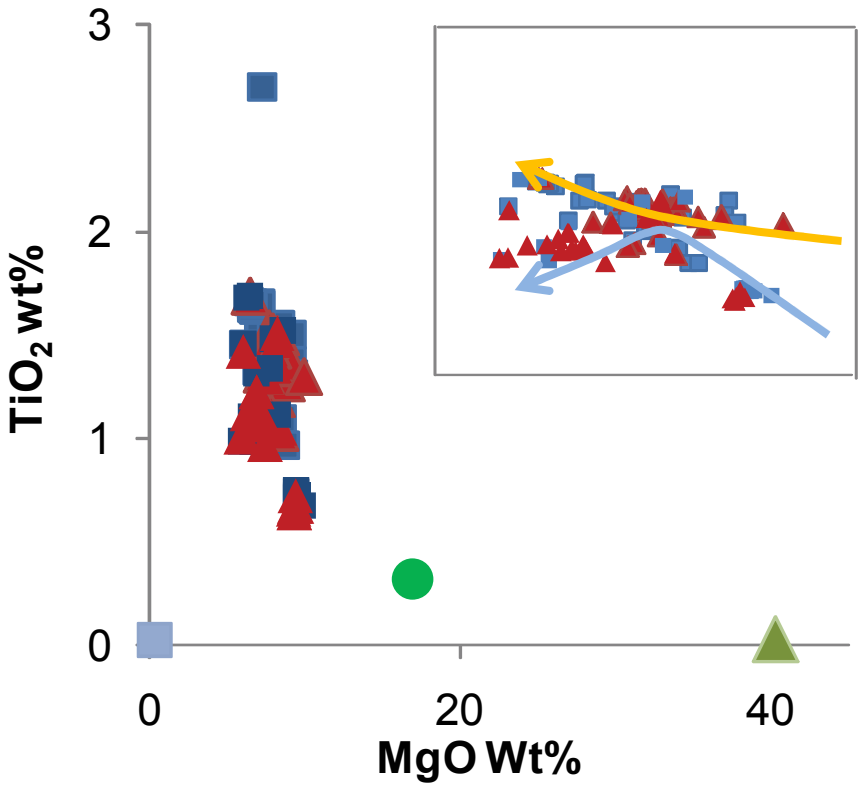

Figure 39: Major element concentration data (wt%), including insets to show trends more clearly. Data is overlaid with arrows to show geochemical trends. Blue arrows indicate plagioclase accumulation, whilst fractionation in the absence of plagioclase accumulation is shown in orange. The concentrations of pure mineral compositions (see Table 11) are indicated by symbols. Plagioclase compositions are denoted by a blue square, clinopyroxene by a green oval, and olivine by a green triangle.

Applying the principles of the 'Lever Rule' (see Cox et al., 1979) to these plots, the second half of the plagioclase accumulation trend (after the compositional inflexion), is unlikely to represent crystalisation from the three phases olivine, clinopyroxene and plagioclase in the system. The trend runs parallel to the polygon defined by ol-cpx-plag, and cannot, therefore, originate from it. However, this only holds if there are no other phases which have not been accounted for.

For all rock samples analysed, the percentages of plagioclase phenocrysts were estimated and plotted against Al_2O_3 concentrations (Figure 40). There appears to be a general increase in Al_2O_3 concentration with percentage of plagioclase in the sample, as we would expect in the case of plagioclase accumulation. This excludes the 30% plagioclase glasses, which all originate from one dredge, and are likely to be naturally highly plagioclase phyric as well as containing

accumulated crystals. However, the approach used in this plot is somewhat flawed. The percentage of phenocrysts present need not correlate positively with Al_2O_3 concentration, because in some cases, accumulated crystals may have been entirely (or partially) consumed by the host melt. This leads to high Al_2O_3 concentrations, but with little or no plagioclase phenocrysts evident.

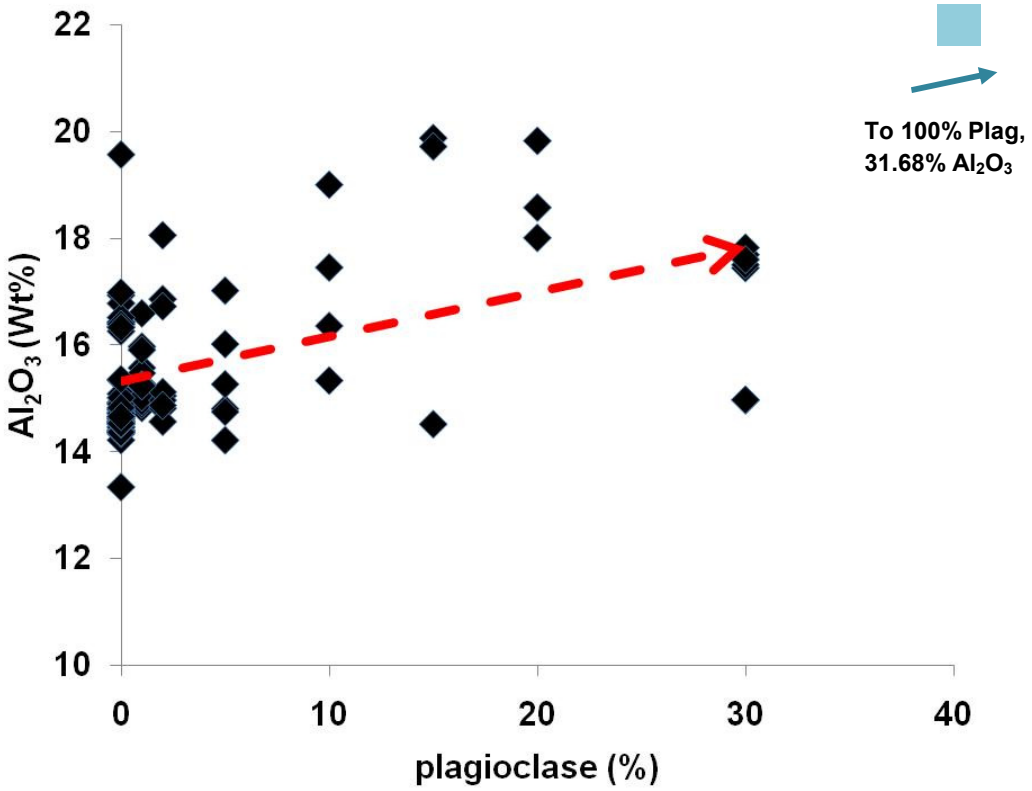

Figure 40: Al_2O_3 vs. percentage of plagioclase in basalt samples from 12°6'-14°N. The red arrow shows the trend in increasing Al_2O_3 with percentage of plagioclase phenocrysts in the sample. The arrow on the dashed regression line points toward the composition of pure plagioclase, as denoted by the blue square symbol. High Al_2O_3 samples at 0% are likely to result from consumption of accumulated plagioclase by the melt.

Escartín *et al.* (2008) used MgO vs. Na_2O, MgO vs. CaO and MgO vs. FeO values from basaltic glass from the central MAR to distinguish between areas of asymmetric spreading and areas of normal magmatic spreading. OCC whole rock data from this study displays marginally higher Na and Fe concentrations than their magmatic counterparts, but the low CaO trend reported by Escartín *et al.* (2008) is not reproduced in these data, and there is no convincing division between the spreading styles in terms of Na and Ca concentration.

Major element data suggests that basalts here have experienced variable amounts of fractionation and plagioclase accumulation. OCC samples appear to lie predominantly on high Fe, low Al and low Ca trends, whilst magmatic samples mostly populate the high Al, high Ca and low Fe trends. This suggests that plagioclase accumulation is a significant process at magmatic sites, but not at OCC sites. Apart from this, there is no clear difference between the geochemistry of basalts recovered from OCCs compared with those from the magmatic sites.

Dolerite dykes, recovered from the toe of the OCC at 13°19'N, are compared with the OCC and on-axis magmatic rocks in Figure 41. The plots illustrate that the dykes fall within the geochemical array defined by the on-axis rocks.

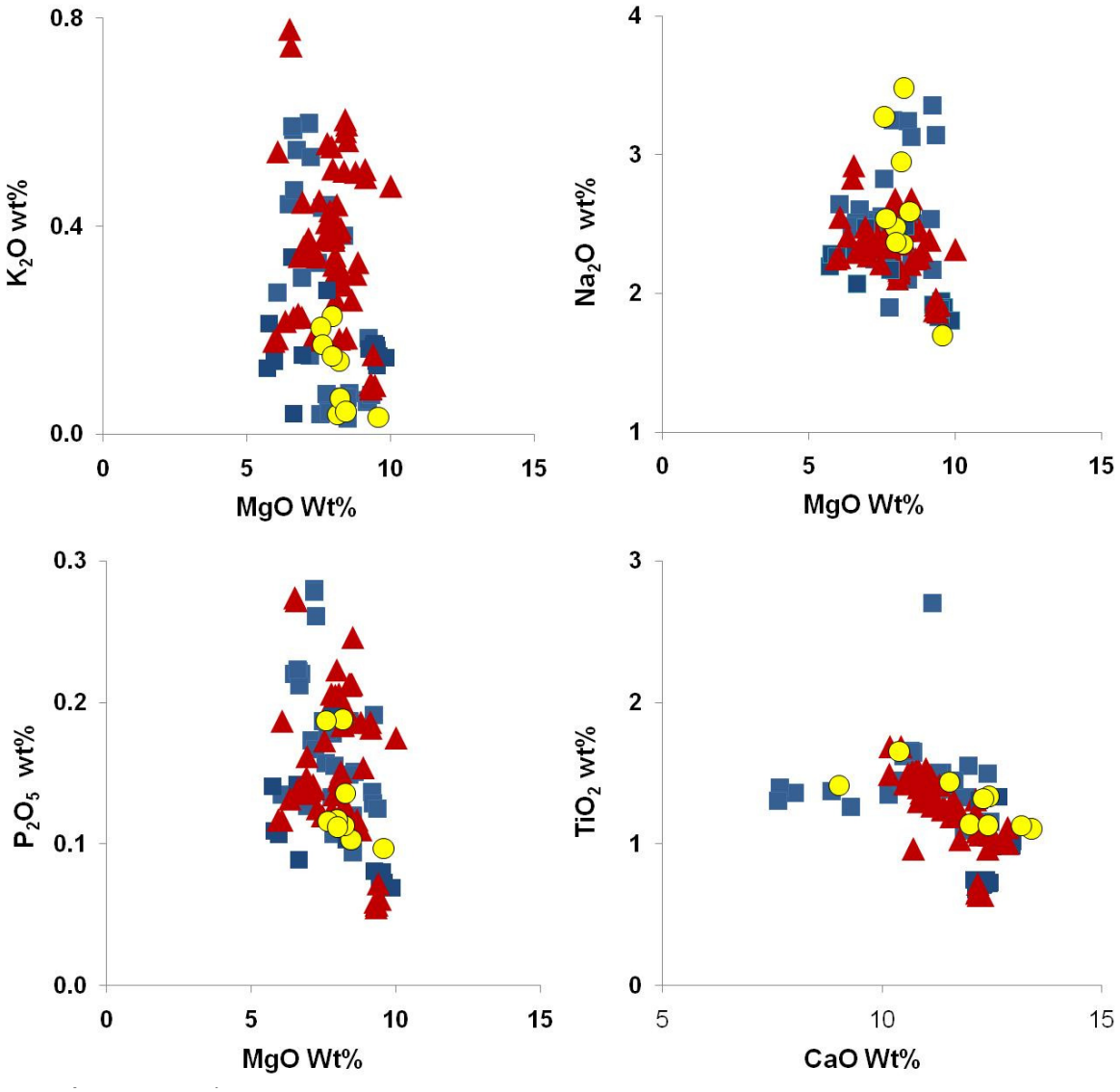

Figure 41: Major element concentration data show the geochemistry of oceanic core complex (blue squares) and magmatic (red triangles) basalt from 12°60'-14°N, as well as dolerite dyke samples (yellow) from the core complex toe at 13°19'N.

REE patterns (Figure 42) indicate that compositions ranging from LREE-elevated E-MORB to N-MORB exist in both magmatic and OCC areas of the axis. There is no simple correlation between levels of LREE enrichment in the axis and spreading style.

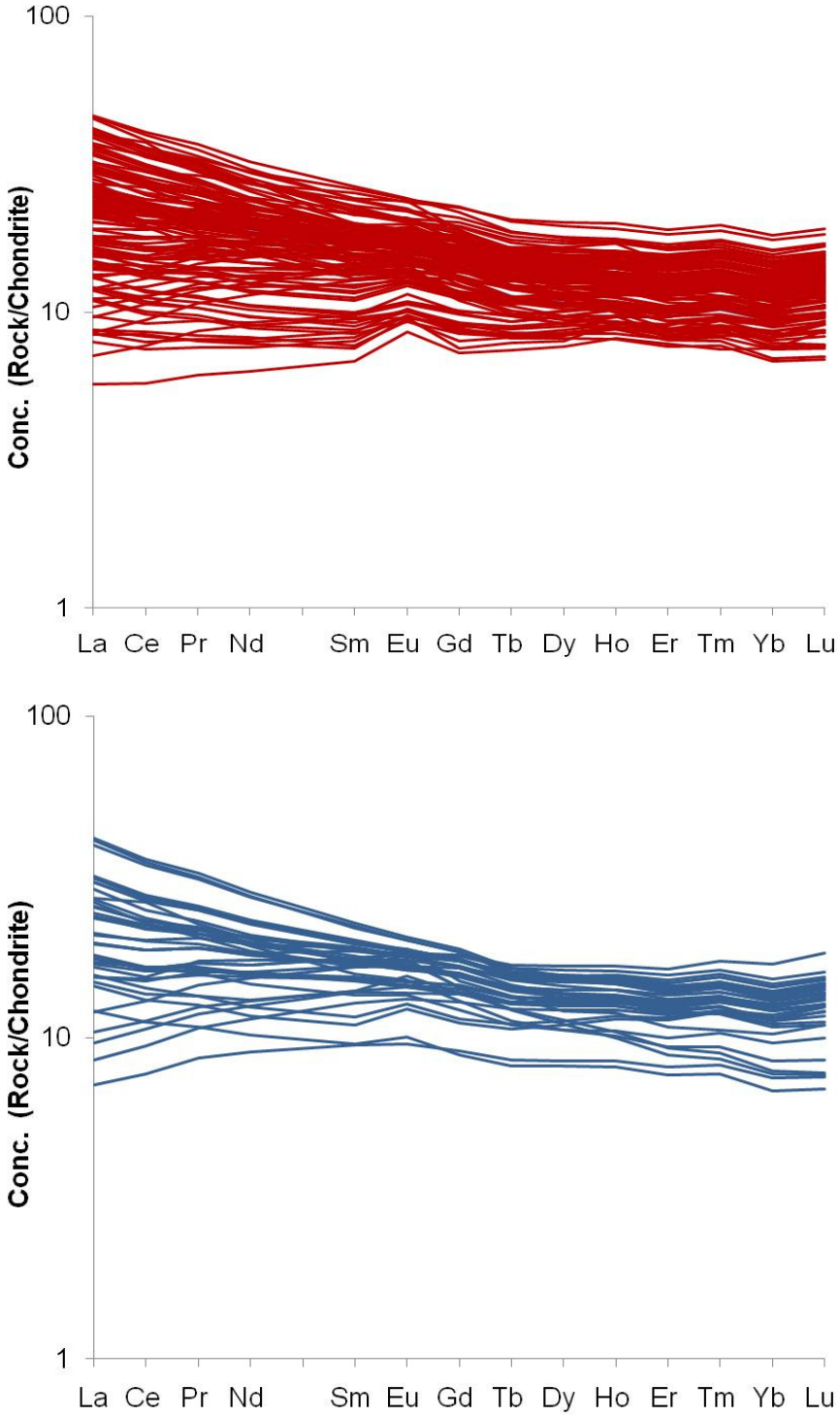

Figure 42: Rare Earth Element (REE) data for magmatic (red) and core complex (blue) basalt samples from 12°60'-14°N. The plots show that basalts from each group extend from N-MORB-like to LREE enriched E-MORB in character.

On trace element ratio plots (Figure 43) magmatic and OCC samples show very similar trends. There are no definitive differences between the major and trace element geochemistry of rocks from active neovolcanic zones, and rocks from the axis opposite OCCs.

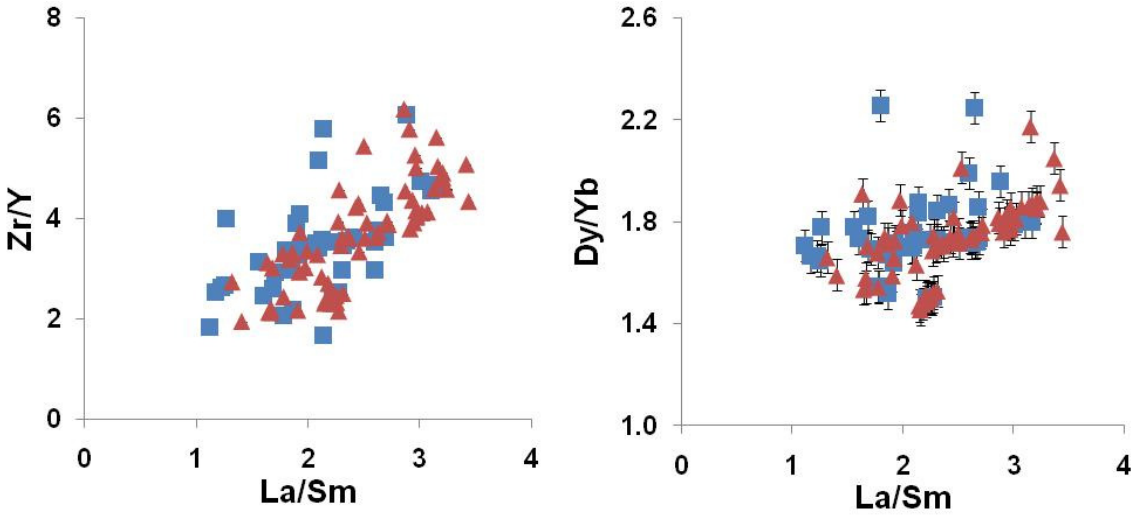

Figure 43: Trace element ratio plots show data for magmatic (red) and core complex (blue) basalt samples. Both groups extend from N-MORB to E-MORB in character, and occupy very similar areas of compositional space.

6.2.3 - Geochemistry of Off-Axis MORB, 13°19'N

The basalts from off-axis at the OCC (13°19N dredges - D05, D06 and D12) were not erupted off-axis. Rather, they are old basalts that were erupted on-axis, and have since moved off-axis. The position of D05 and D06 on the breakaway ridge of the OCC shows that these basalts were erupted prior to the initiation of the OCC. Though the age of these basalts does not necessarily coincide with OCC formation, the compositions of the rocks may be significant in understanding the geochemical behaviour of the ridge immediately prior to formation of the 13°19'N OCC.

These rocks are thought to be *in situ*, unlike talus found elsewhere on the OCC domes (refer to Figure 45). This is because TOBI and bathymetry data shows that the breakaway ridge is formed of back-tilted crustal blocks. These have been rotated, but remain cohesive.

The interpretative map (Figure 44) shows the positions of all dredges on the 13°19'N OCC. The associated cross-section shows the back-tilted basalt blocks of the breakaway ridges, (D05 and D06), and the corrugated core complex dome, as well as the eastern valley wall (normal valley wall fault) rising out of the axis at dredge D12. The cross-section is vertically exaggerated, in order to better illustrate the morphological features of the complex.

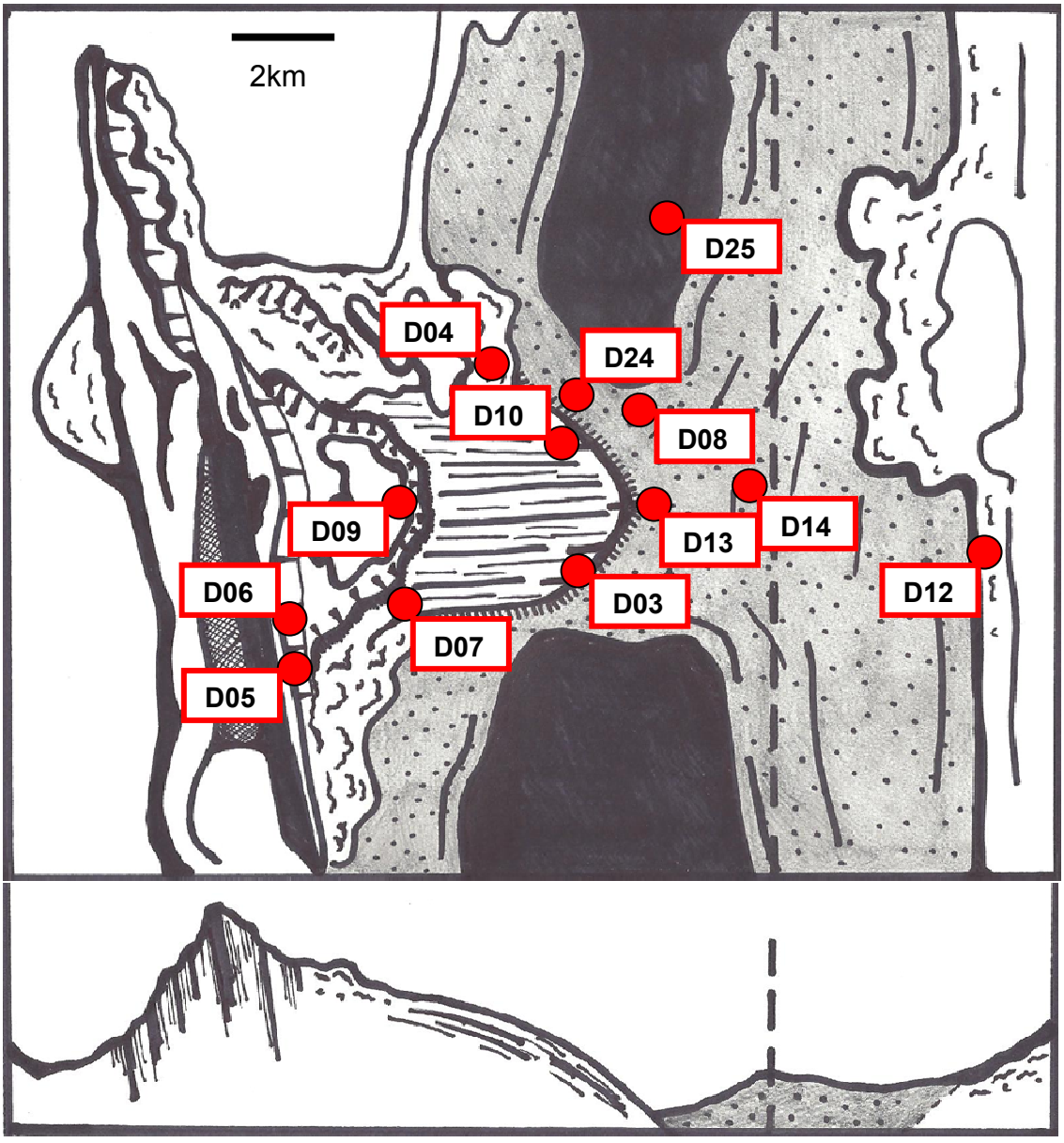

Figure 44: Simplified sketch map of the 13°19'N core complex, showing the location of all nearby dredge sites. Neovolcanic zones are shown in black, and the axial valley floor in grey. The ~5x vertically exaggerated cross-section runs through the centre of the core complex, and shows the point at which exhumed peridotite and basalt talus meet back-tilted *in situ* volcanic seafloor.

A diagrammatic interpretation of the OCC is shown in Figure 45. The back-tilted blocks of the breakaway ridge have been rotated as the fault rolls and shallows, but the rocks have remained as a cohesive unit.

It is not known how much spreading is accommodated on each side of the axis. The eastern valley wall at 13°19'N may accommodate some spreading magmatically, whilst, on the western side, spreading may be completely accommodated on the fault, or, at a 'dying' complex, may be transitional between magmatic and tectonic spreading. Therefore, the ages of the off-axis samples from D12, D05 and D06, and their temporal relationships to each other, are not well constrained. On the basis of half spreading rates, the age of D05 and D06 rocks is estimated to be ~1Ma. This assumes that spreading is shared equally by each side of the axis, but the estimate could be drastically wrong if the balance of spreading at asymmetric zones is skewed significantly to one flank of the ridge. If the core complex accommodated all of the spreading in the axis during its lifetime, the breakaway could be as young as ~0.5Ma. However, the off-axis position of the D12, D05 and D06 dredge sites indicates, (certainly in the case of D05 and D06), that they were erupted prior to OCC initiation.

Figure 44 illustrates how material from the inactive magmatic axis at D13 breaks up along the fault line on the hanging wall side, and is dragged as loose debris over the fault surface. This material is also thought to fall down slump slopes on the OCC surface at sites such as D04 and D08. The distribution of talus across the fault surface is likely to have taken place since the initiation of the fault. Therefore, talus from all over the dome, including the oldest part (D09), is representative of the composition of material from axis. The composition of talus-forming material at the axis may have changed over time during successive volcanic episodes, or the fault may have sampled compositionally diverse layers. However, none of the material on the OCC dome is *in situ*, and so its age and geographic origin cannot be accurately determined.

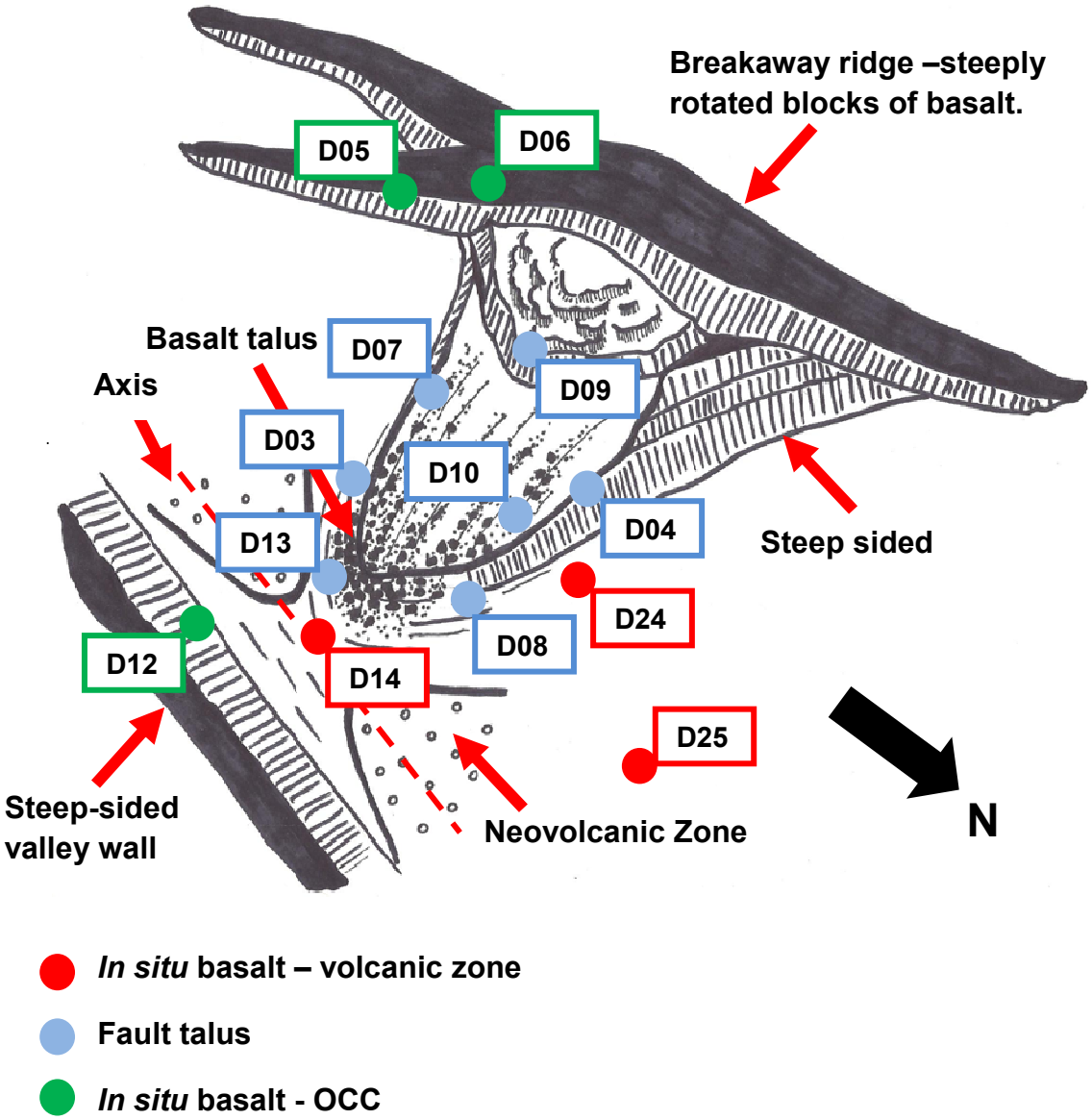

Figure 45: sketch map of the 13°19'N core complex, showing the location of all dredge sites. The sketch map is rotated to better show the features at the core complex toe. Off-axis sites where rocks are thought to *be in situ* are labelled in green. On-axis volcanic seafloor sites are shown in red. Dredge sites shown in blue retrieved a mixture of serpentinised peridotite and basalt. The basalt from these sites is interpreted as talus broken up from the axis in the vicinity of D13 and dragged over the core complex dome by the action of the fault. Label dyke

Extending the geochemical study to include off-axis samples from dredges D05, D06 and D12 reveals that basalts at these sites are geochemically distinct in major and trace element space from other basalts sampled in the segment.

The incompatible major element compositions (Na, K, P and Ti) of a number of the off-axis samples are significantly elevated above those of the basalts in the rest of the segment (Figure 46). It is unlikely that the high K and P values result from alteration, as Ti concentration is consistently high in the same samples. It is clear that the incompatible major element compositions (Ti, P, and K) from these sites are bimodal. They have both N-MORB like compositions which are more depleted than average for the segment, and extremely enriched E-MORB compositions. A significant number of samples appear to be independent of major element trends, including plagioclase fractionation.

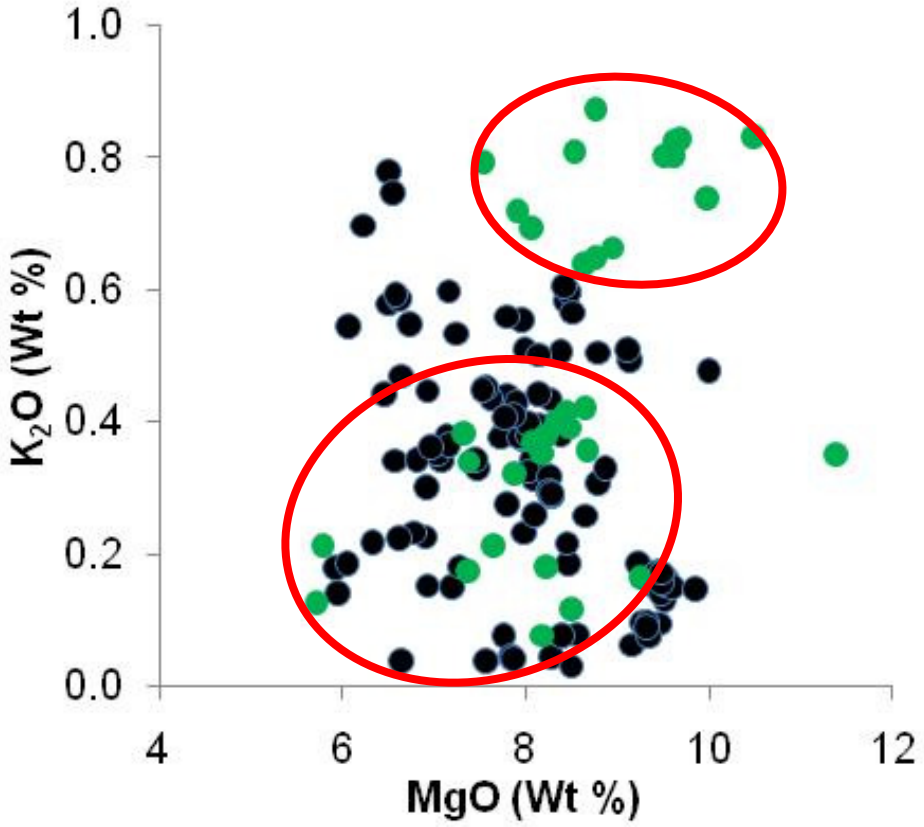

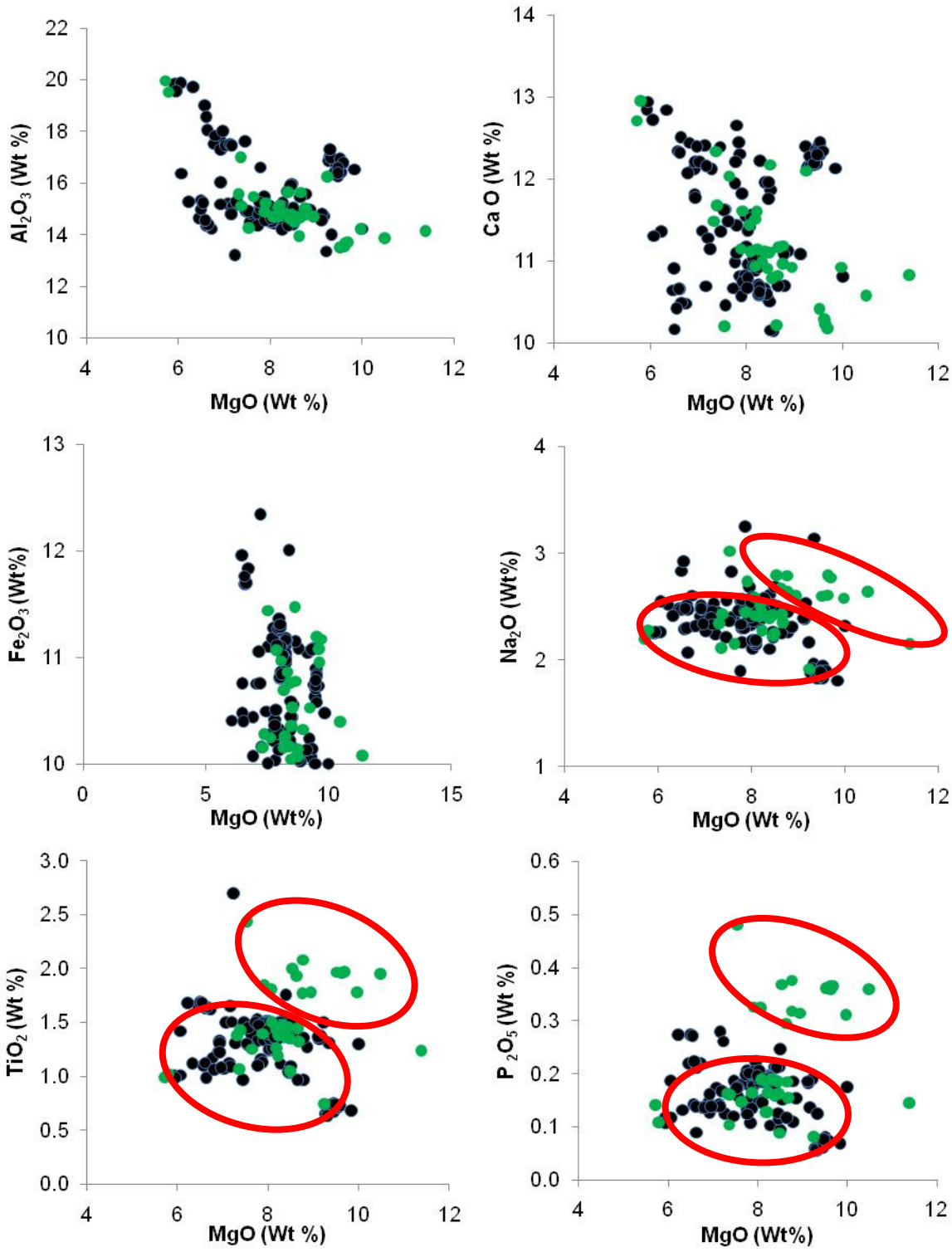

Figure 46: Major element plots show that off-axis (green markers) samples have bimodal compositions, extending from N-MORB-like compositions to highly enriched E-MORB compositions. These E-MORBs are substantially more enriched than the on-axis samples examined earlier (black markers). Red circles highlight the bimodality of the off-axis sites (see K, P, Ti, Na).

The identified compositional groups will henceforth be referred to as M1 (E-MORB) and M2 (~N-MORB). Major and trace element compositions of M1, M2 and on-axis basalts are presented in data tables which can be found in Appendix 3. The derivation of group names relates to the proposed eruption sequence at the core complex. This is discussed in detail in chapter 7.

The major element compositions of the two groups M1 and M2 do not correlate with their geographical distribution either side of the axis, as shown below (Figure 47). Samples from each dredge are present in each compositional group, showing that dredge D12, though geographically separate, has a similar composition to the breakaway sites D05 and D06.

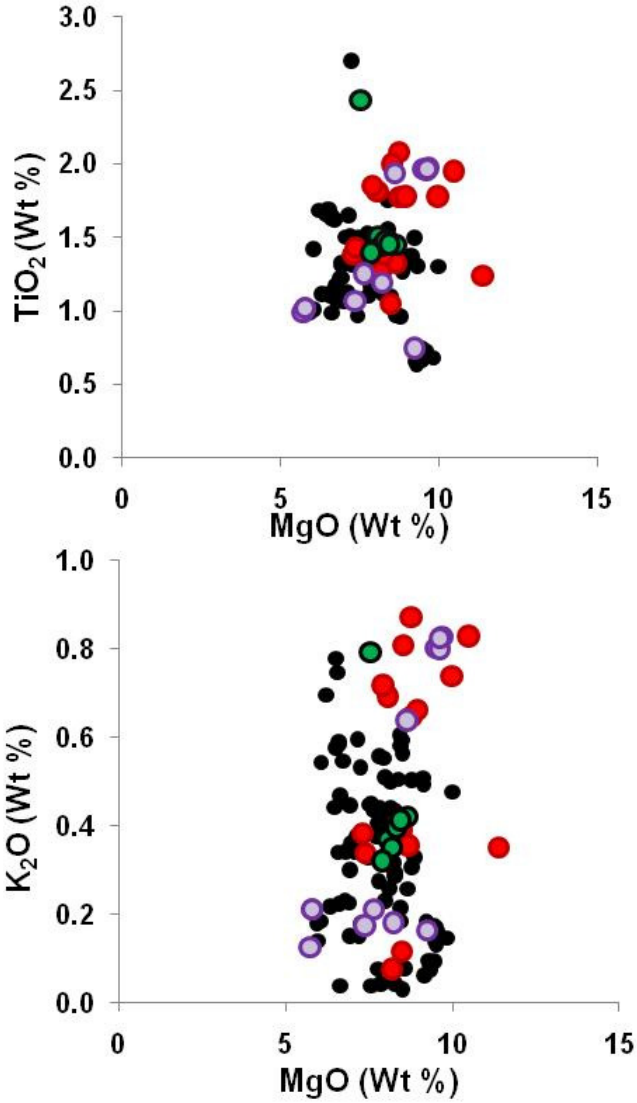

Figure 47: Major element plots show data from dredges D05 (green), D06 (red) and D12 (purple), as well as on-axis data for comparison (black). Each dredge contains both enriched and depleted samples.

The distinct compositions of M1 and M2 off-axis basalts are also reflected in their REE patterns (Figure 48).

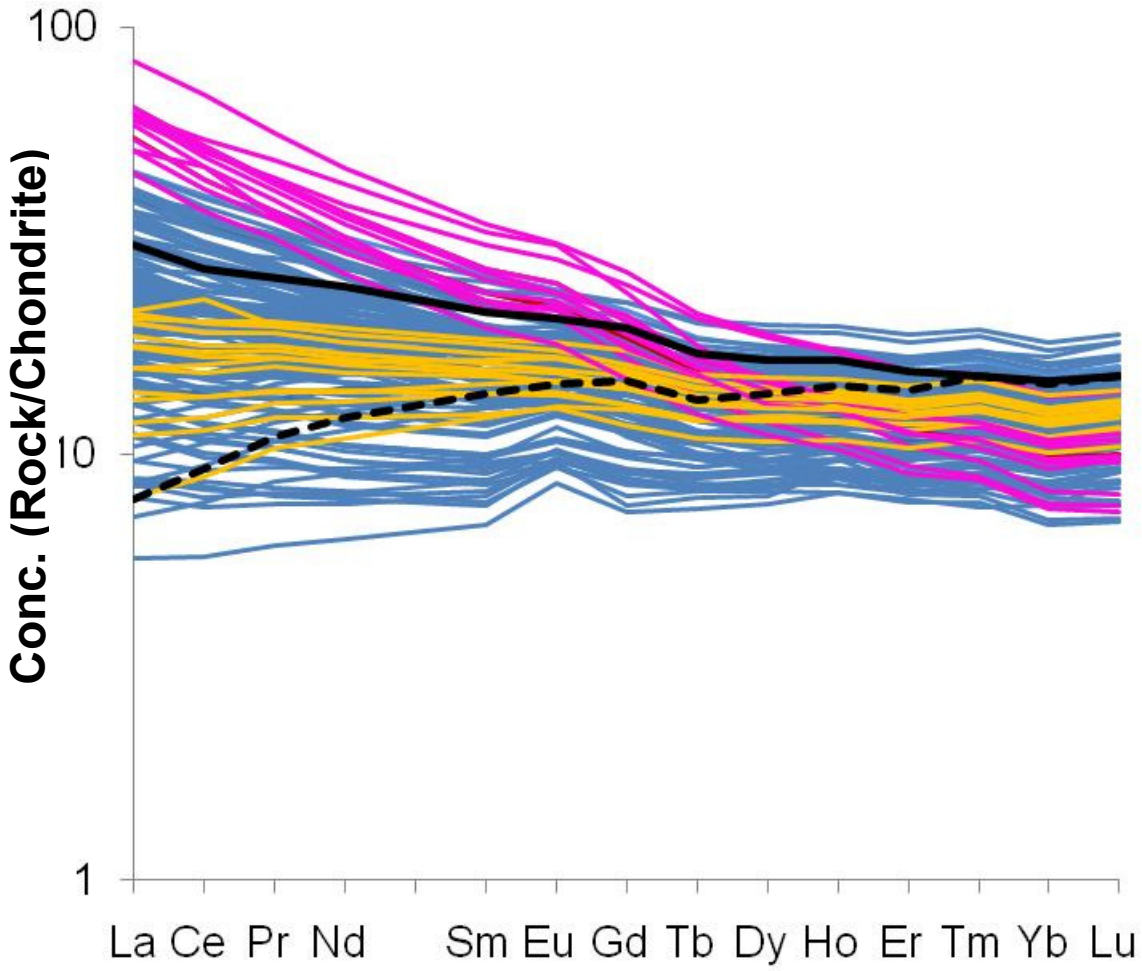

Figure 48: REE data show the bimodality of off-axis basalts. Group M1 (pink) are characterised by extremely LREE-enriched basalts with steep REE profiles. M2 (yellow) have N-MORB like, flat, or slightly LREE-enriched profiles. Shown for comparison are on-axis samples (blue) typical N-MORB (dashed black, Sun and McDonough, 1989) and E-MORB (solid black, Donnelly *et al*., 2004) compositions.

Group M2 have slightly REE-enriched to slightly LREE-depleted profiles which resemble average N-MORB. Conversely, M1 have highly LREE enriched with steeper MREE/HREE patterns than average Atlantic (MARK) E-MORB, suggesting that melting may occur in the garnet facies (i.e. at depths >60km). M1 and M2 extend to compositions more enriched and also more depleted than the typical MORB values of the segment.

Positive Eu anomalies are pronounced in on-axis rocks, and occasionally present in M2 rocks, but absent from M1 samples. This may suggest that plagioclase accumulation affects only M2 and on-axis basalt. This is further confirmed by MgO vs. Al_2O_3 data (Figure 49), which shows that on-axis and M2 data lie on both plagioclase accumulation and non plagioclase accumulation trends, but M1 basalts only lie on the non plagioclase accumulation trend.

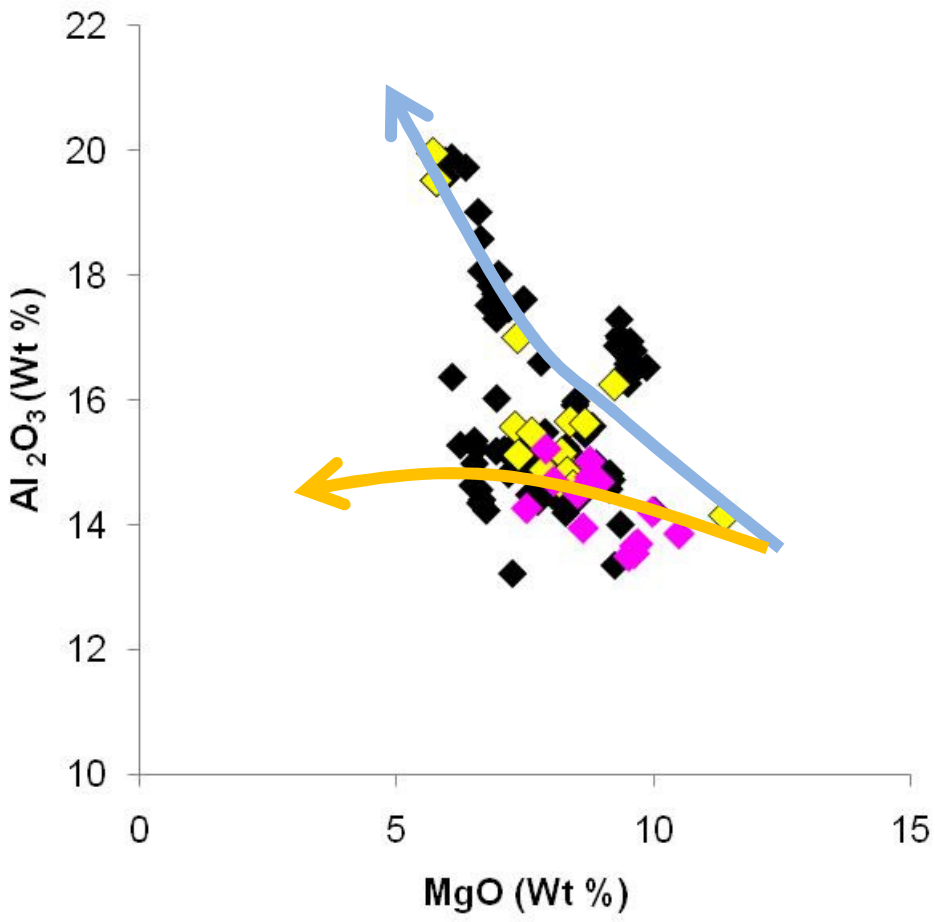

Figure 49: Major element data shows that on-axis (black) and M2 (yellow) data lie on both plagioclase accumulation (blue arrow) and non-plagioclase-accumulation (orange arrow) trends, but M1 (pink) basalts only lie on the non-plagioclase-accumulation trend.

The bimodality of off-axis basalt groups is further illustrated by the trace element plots (Figure 50). Group M1 is extremely enriched in Zr, Nd, Nb, La, Ce and Sm, whereas group M2 has N-MORB like compositions which overlap the depleted end of the on-axis array.

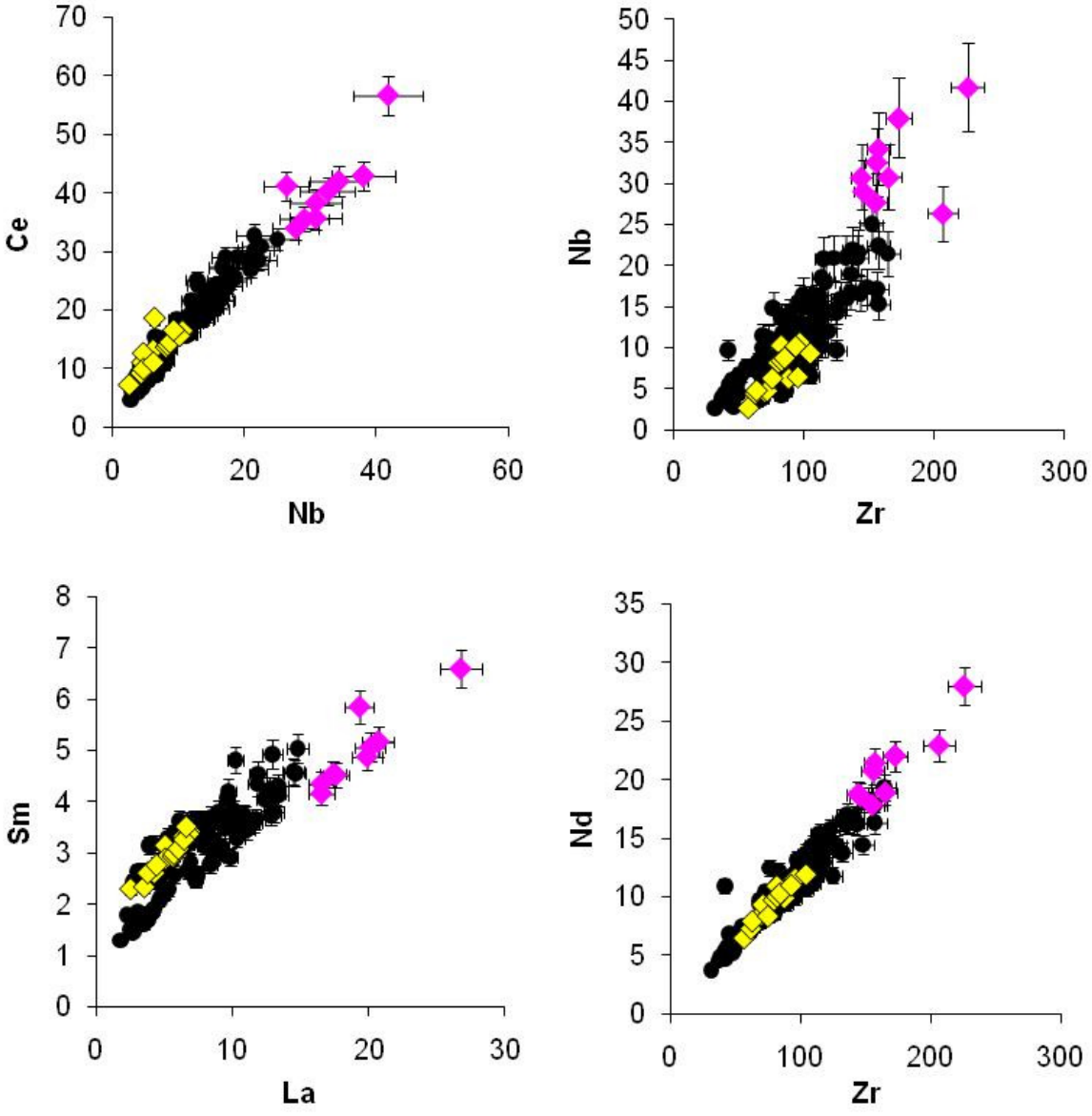

Figure 50: Trace element plots illustrate the bimodality of M1 and M2 compositional groups. Group M1 (pink) is highly enriched, and group M2 (yellow) more N-MORB like. There is a significant compositional gap between the groups. On-axis data (black) are shown for comparison.

Plots of trace element ratios (very incompatible/moderately incompatible elements) against latitude (Figure 51) show that the greatest range in ratio values anywhere in the segment occurs at 13°19'N, where M1 and M2 basalts are found. The plots also indicate that the samples at 13°19'N are significantly more incompatible element enriched than rocks from the previously described 14°N 'enrichment anomaly'.

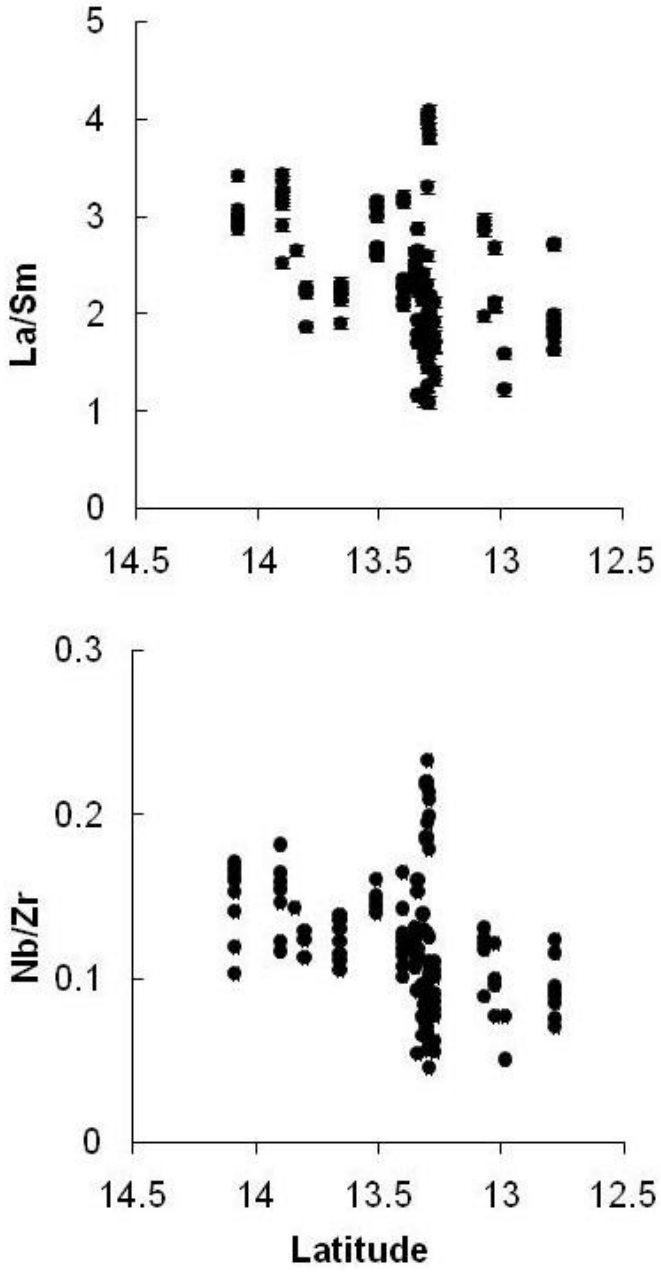

Figure 51: Trace element ratios vs. latitude (this study). The plots show that on the whole, enrichment decays from 14°N - 12°60'N. However, at 13°19'N, the compositional range is much greater than at any other location, and the enriched and depleted end-members of the local array are both found here.

Trace element ratio plots (Figure 52) show the bimodal compositions of groups M1 and M2, and the compositional gap between them, which is filled by the axial rocks. Figure 59 shows that M1 basalts are offset to higher Dy/Yb values, whilst having low Yb/Lu values. M2 values appear to lie on a separate, (lower Dy/Yb) trend. M1 basalts also appear to be displaced in La/Yb space to higher values of La/Yb relative to the general ridge segment trend.

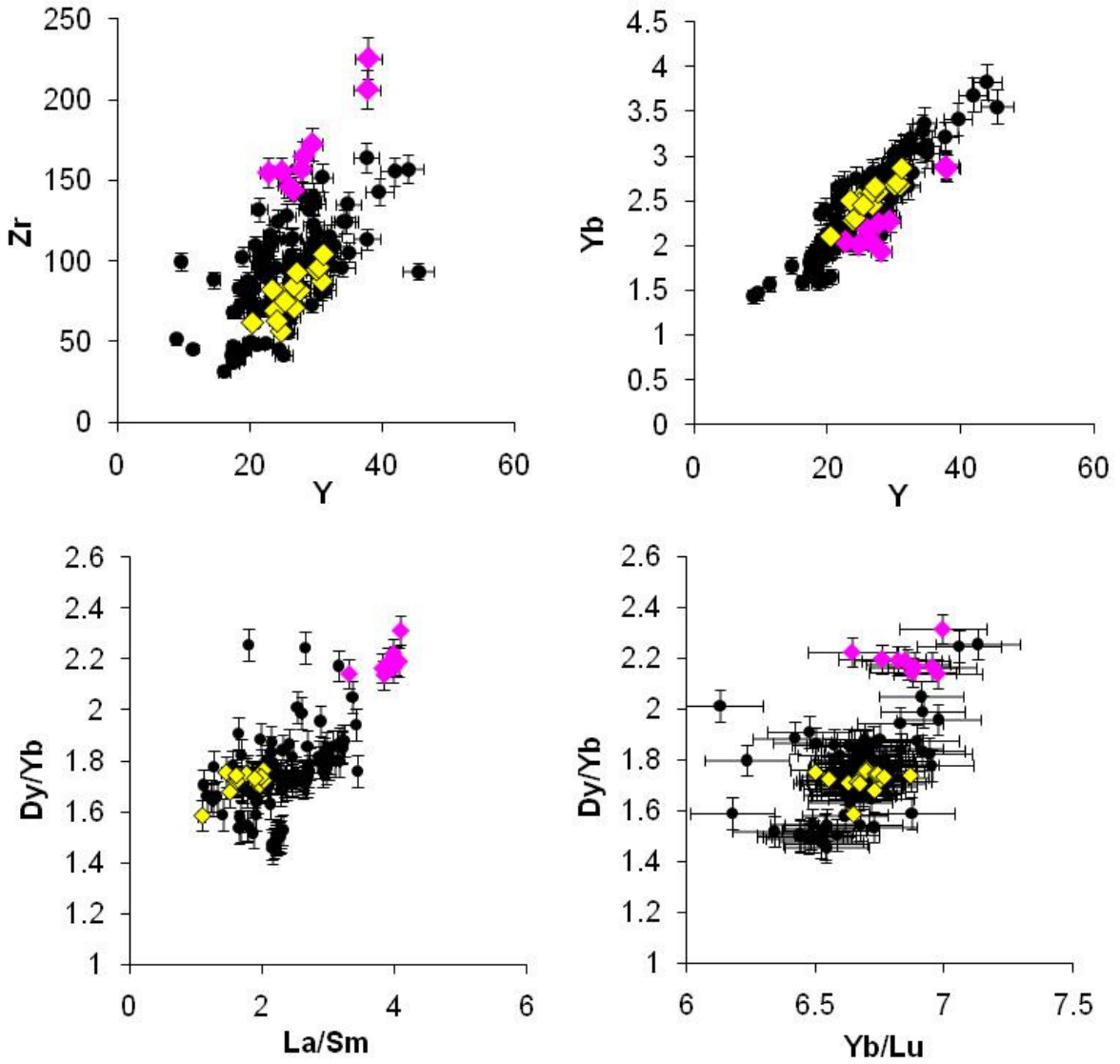

Figure 52: Trace element and ratio plots show the bimodal compositions of off-axis basalt groups M1 (pink) and M2 (yellow). On-axis data (black) for comparison. M1 basalts have high Dy/Yb, low Yb/Lu and high La/Yb relative to the general ridge trend. M2 data conforms to the on-axis ridge trend, but lies at the depleted end of the array.

M1 basalts are enriched in Ce, whereas M2 are low in Ce (Figure 53). The accompanying H_2O data (FTIR) shows the bimodality of the M1 and M2 basalts, and that there is a correlation between high H_2O and high Ce.

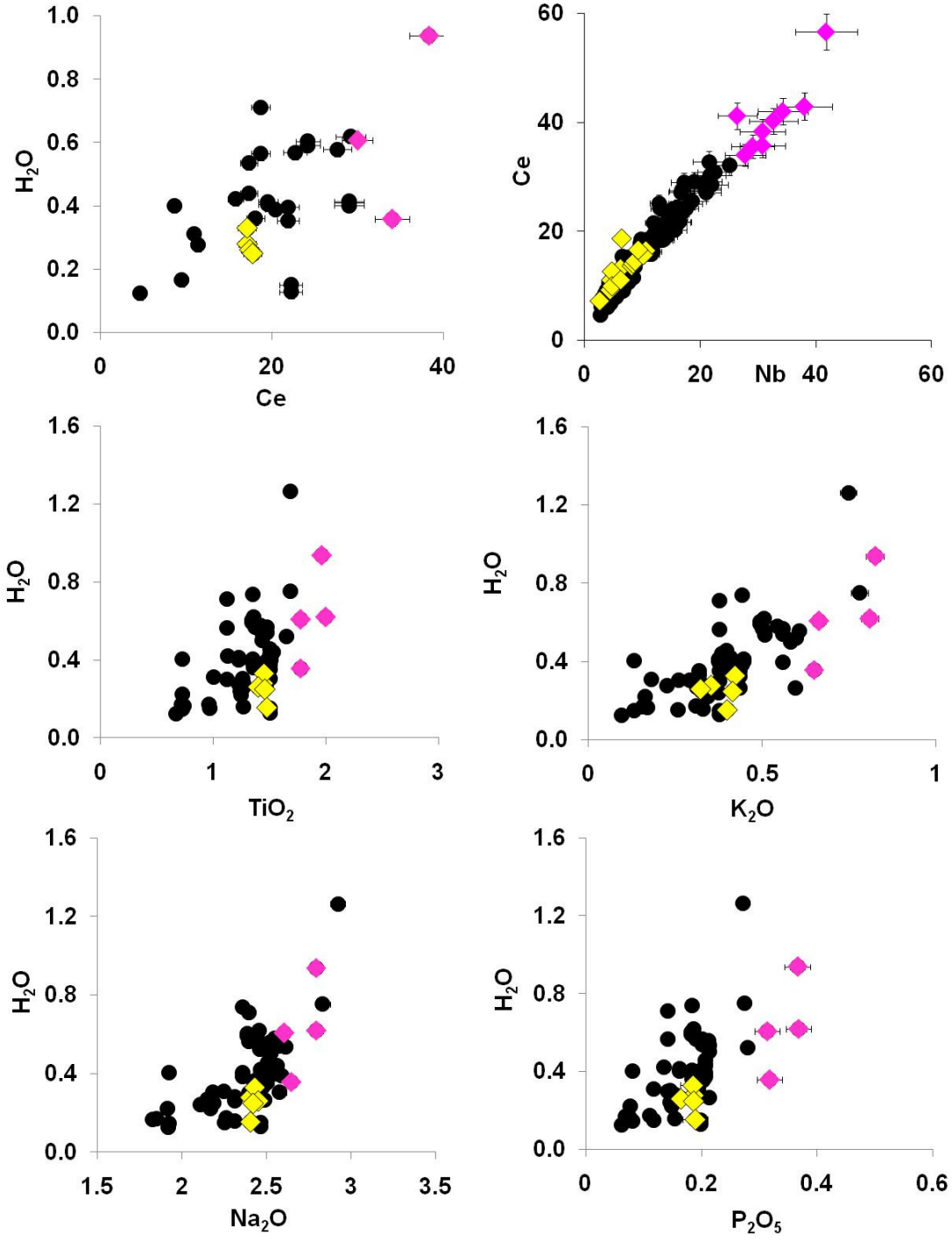

Figure 53: H_2O (FTIR) vs. major element concentration data for basaltic glass from M1 (yellow), M2 (pink) and on-axis samples (black). The data shows the bimodality of groups M1 and M2. M1 samples extend to higher concentrations of H_2O than M2 rocks. Ce vs. Nd data is shown for comparison, as Ce and H_2O behave similarly in basalt.

H_2O and Ce have a very similar degree of incompatibility (Michael, 1995) and hence behave similarly during partial melting and crystal fractionation. Hence, the correlation between H_2O and Ce is likely to reflect a genuine enrichment inherited from the source, indicating that M1 basalts are H_2O-rich relative to on-axis and M2 basalt compositions. Major element vs. H_2O plots confirm that high H_2O also correlates with high Na, Ti, P and K concentrations.

6.2.4 - How do Off-axis Data Compare to the Regional Geochemistry of MORB?

Comparison of incompatible major element [8] values (Figure 54) from this study with data from previous studies (data source-PetDB MORB) shows that the 12°60'-14°N region has highly variable incompatible major element compositions (K, P and Ti values) in comparison with the rest of the central MAR. M1 basalts are some of the most enriched in the whole region, and M2 the most depleted. The rocks from 12°60'-14°N are low in Na[8] (average= 2.39, n=61) in comparison to the central MAR average.

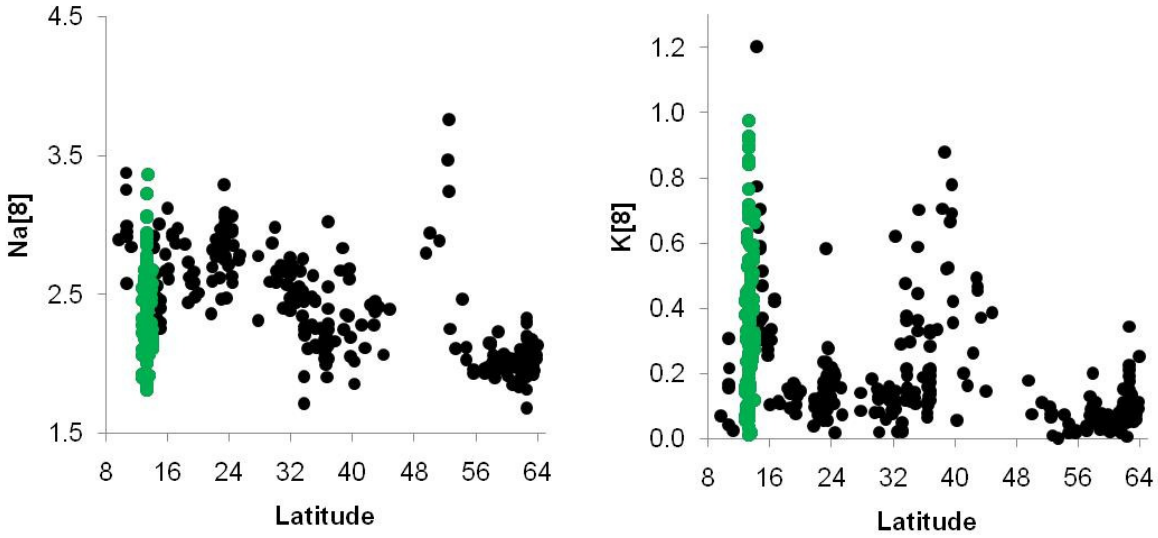

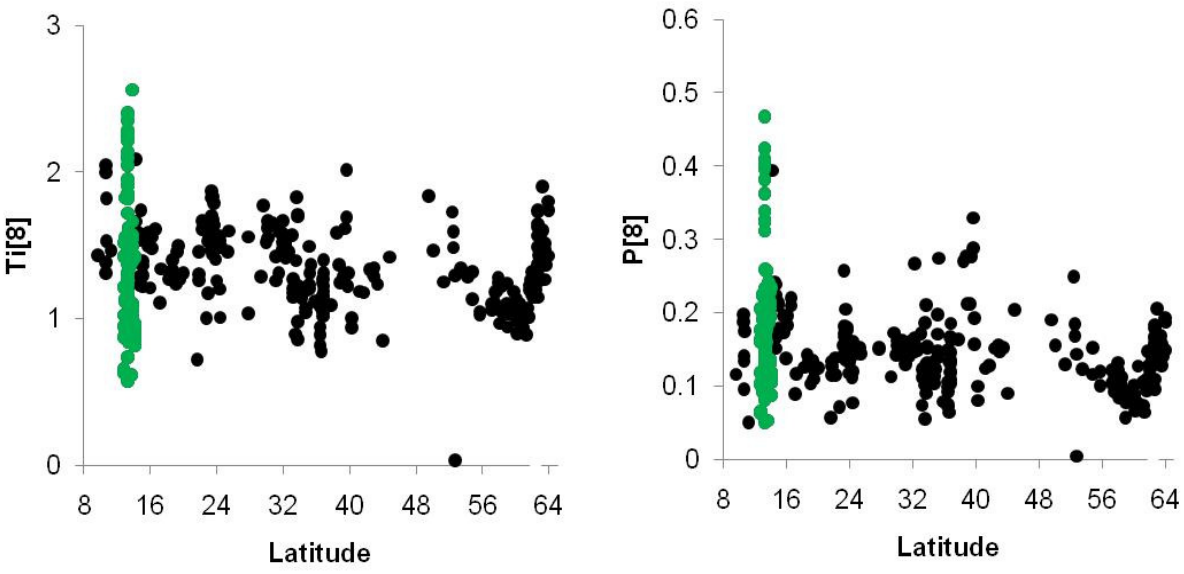

Figure 54: Regional Element [8] data against latitude for the MAR (black, PetDB MORB data). Ti[8] values for the 12°6'-14°N segment (green) have a substantially greater range than anywhere else on the ridge. P [8] and K [8] extend to higher concentrations at 12°6'-14°N than the rest of the central MAR, whilst Na [8] values are typically lower.

Basalts from 12°60'-14°N are the most enriched in the region in elements such as Rb, Sr, Nb, Zr, Nd, Ce, La, Ta, U and Pb (Figure 55). They also have the greatest compositional range in the central MAR. The 12°60'-14°N rocks are characterised by low Y and Yb concentrations, which strongly contrasts with the higher concentrations at 15°20'N and 23°N.

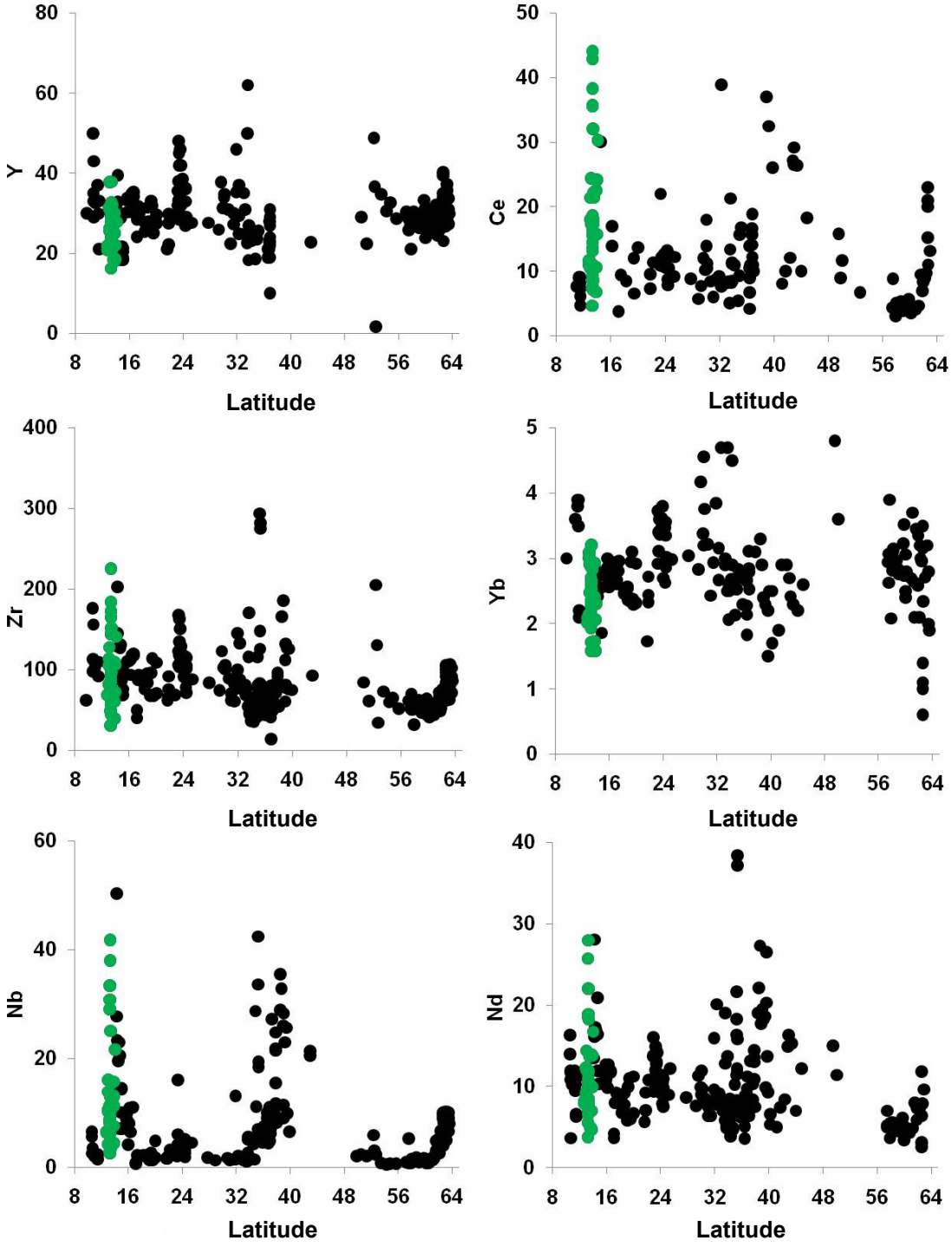

Figure 55: Trace element data against latitude for the MAR (black-PetDB MORB data). Nb, Nd, Zr and Ce values for the 12°6'-14°N area (green) extend to substantially higher and lower values than anywhere else on the central MAR . Y and Yb values are lower than average for the region.

6.2.5 - Isotope Systematics of the Central MAR

Pb isotopes of Atlantic basalts form a $^{208}Pb/^{204}Pb$ vs. $^{206}Pb/^{204}Pb$ array which follows the NHRL (northern hemisphere reference line). This array is shown using Atlantic (5°S-89°N) data from the geochemical database PetDB. Figure 56 shows that the on-axis data from 12°60'N-14°N falls within the Atlantic array. For a full discussion of regional isotope geology and source characteristics, see chapter 7.

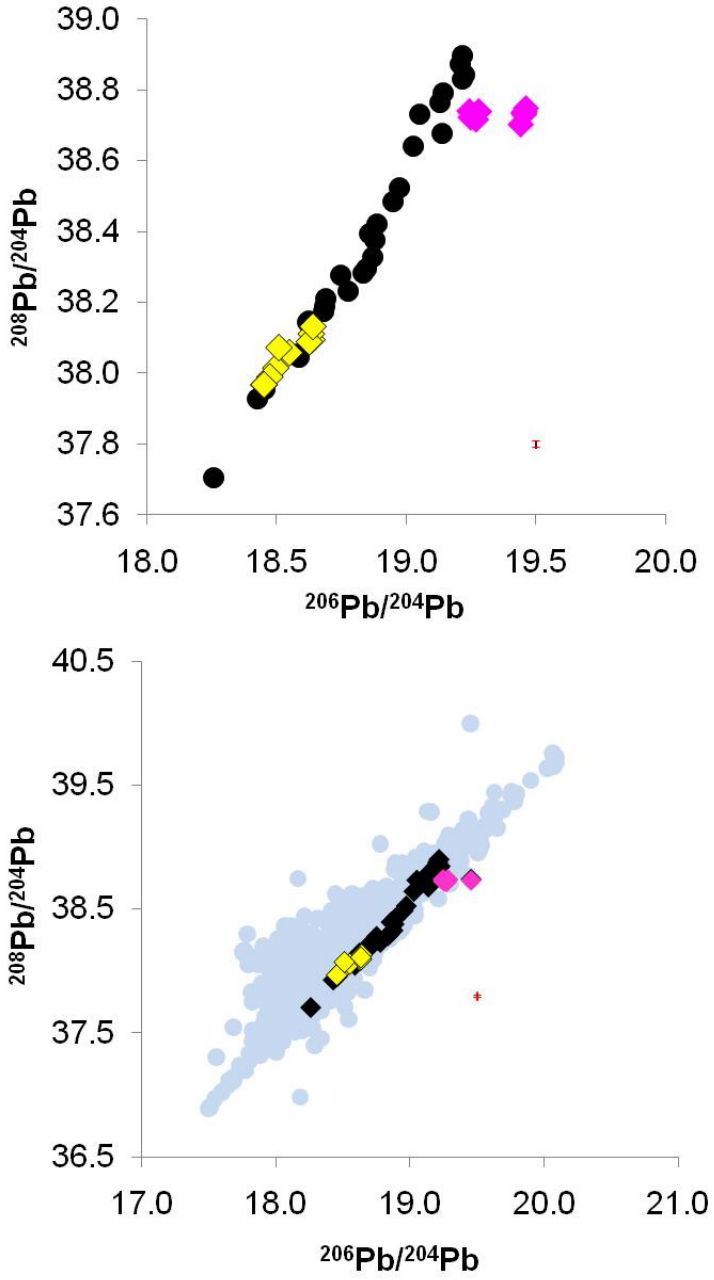

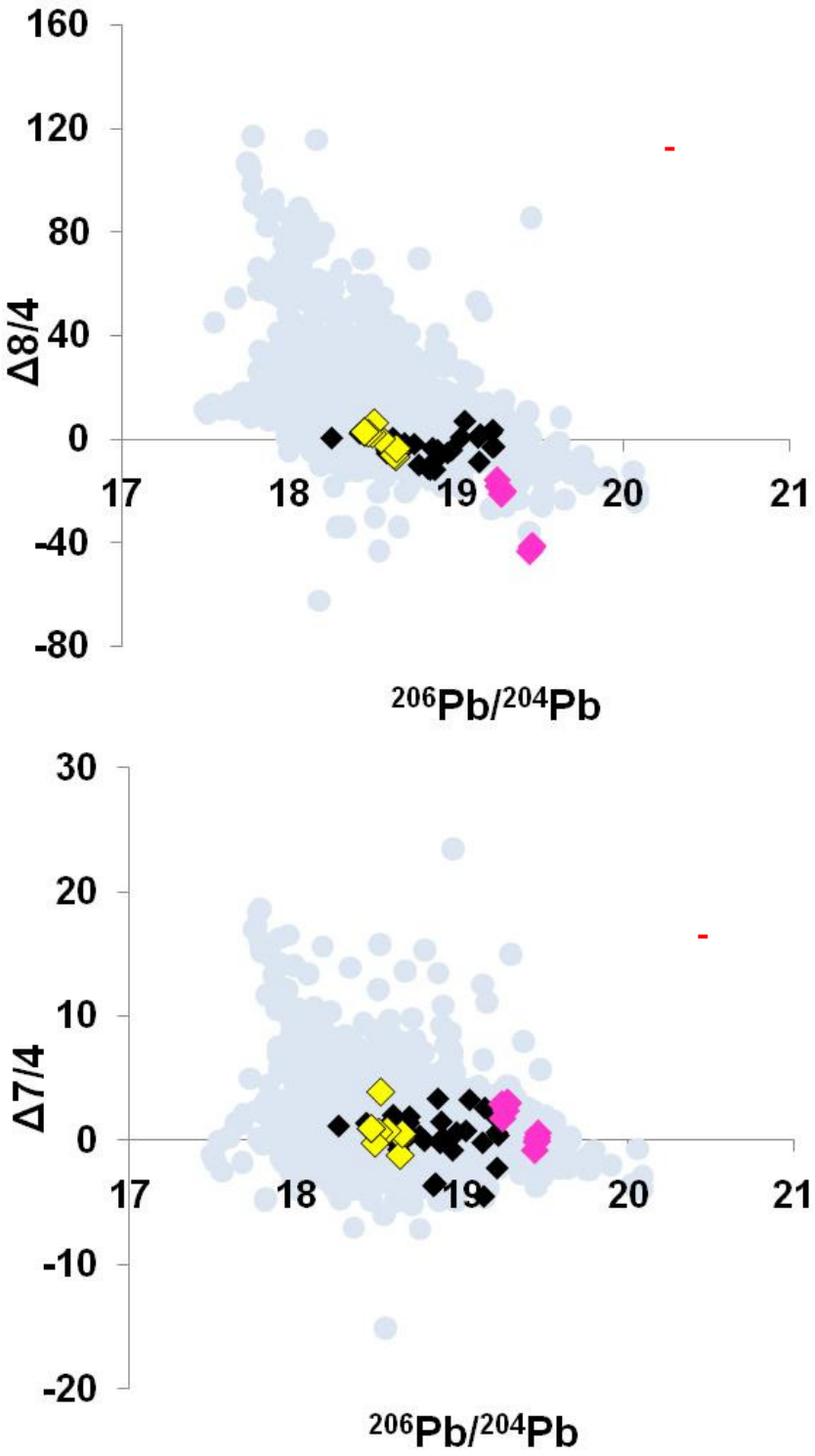

Figure 56: Pb $^{208}Pb/^{204}Pb$ vs. $^{206}Pb/^{204}Pb$ Atlantic data (PetDB MORB, 5°S-89°N, blue) form an array which follows the NHRL (northern hemisphere reference line). Also shown is on-axis data from 12°60'-14°N (black), as well as off-axis M1 (pink), and M2 (yellow) basalts. M1 basalts lie at the radiogenic end of the local isotopic array, whilst M2 occupy the unradiogenic end. M1 and M2 basalts also lie on different compositional vectors to the on-axis samples, as shown in Δ7/4 and Δ8/4 plots. M1 basalts extend towards low Δ8/4, and project outside the Atlantic MORB array. Error is displayed by a red marker.

M2 off-axis basalts lie at the unradiogenic end of the local Pb isotope compositions, but are not untypical values for Atlantic MORB as a whole (data - PetDB). M1 enriched off-axis basalts have more radiogenic $^{206}Pb/^{204}Pb$ than the local on-axis lavas, and lie on a trend extending off the local data array. In addition, M1 basalts extend towards low Δ8/4, and project outside the Atlantic MORB array. Sr and Nd isotope ratios of M1 basalts are also higher than the local array (Figure 57) which is consistent with Atlantic E-MORB compositions. M2 basalts have low $^{87}Sr/^{86}Sr$ and high $^{143}Nd/^{144}Nd$, in line with their depleted trace element characteristics. Once again M1 and M2 bracket local MORB, but are separated by a clear compositional gap.

The local isotopic trends in Pb, Nd and Sr within M1 and M2 basalt groups are different to those of the on-axis array, indicating variations in mantle source contributions between the groups. The data from 12°60'-14°N as a whole define a triangular compositional array, indicating the presence of at least three mantle components contributing to the geochemistry of the basalts.

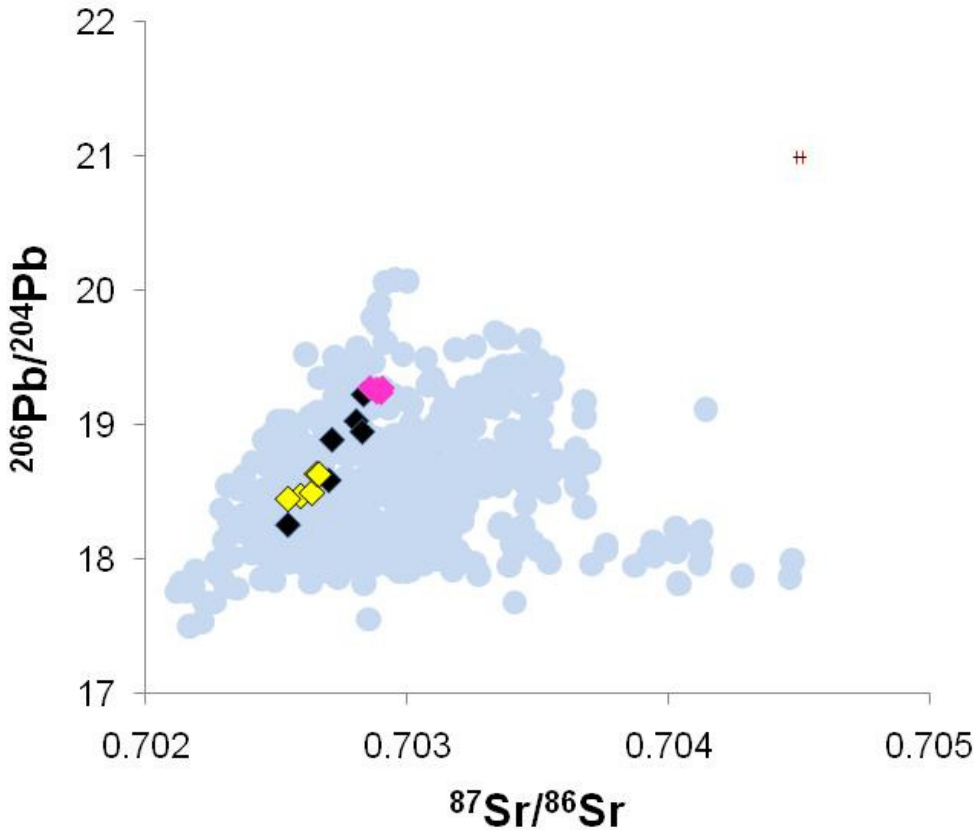

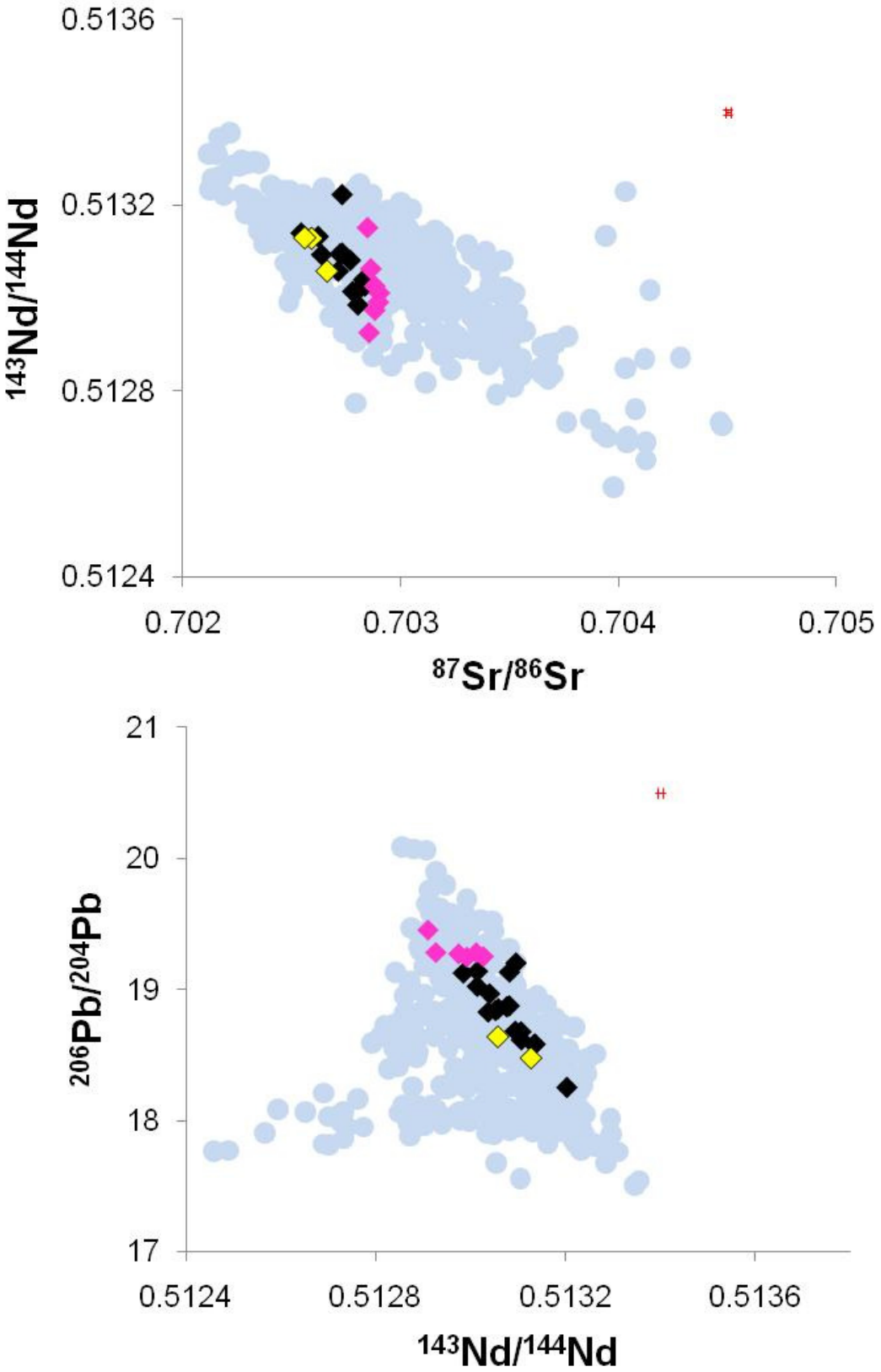

Figure 57: $^{206}Pb/^{204}Pb$, $^{143}Nd/^{144}Nd$ and $^{87}Sr/^{86}Sr$ isotope ratios for on-axis data (black), and off-axis M1 (pink) and M2 (yellow) basalts. The data is shown in relation to the Atlantic data array (PetDB MORB data, 55°S-89°N, blue). M1 basalts have a very steep $^{87}Sr/^{86}Sr$ vs. $^{143}Nd/^{144}Nd$ trend, which substantially differs from the gradient of the Atlantic MORB trend.

Plots of regional isotope data (Figure 58, data from PetDB, 5°S-89°N) show that $^{87}Sr/^{86}Sr$ and $^{206}Pb/^{204}Pb$ isotope ratios between 12°60'N and 14°N are substantially higher than those found north of the 17°10'N geochemical limit proposed by Dosso (1993). The range of Sr and Nd isotope ratios between 12°60'N-14°N closely resembles the range between 0-2°N. $^{206}Pb/^{204}Pb$ ratios between 12°60'N-14°N do not quite extend to the radiogenic values found between 0-5°N, but are still largely higher than 17°10'N -35°N.

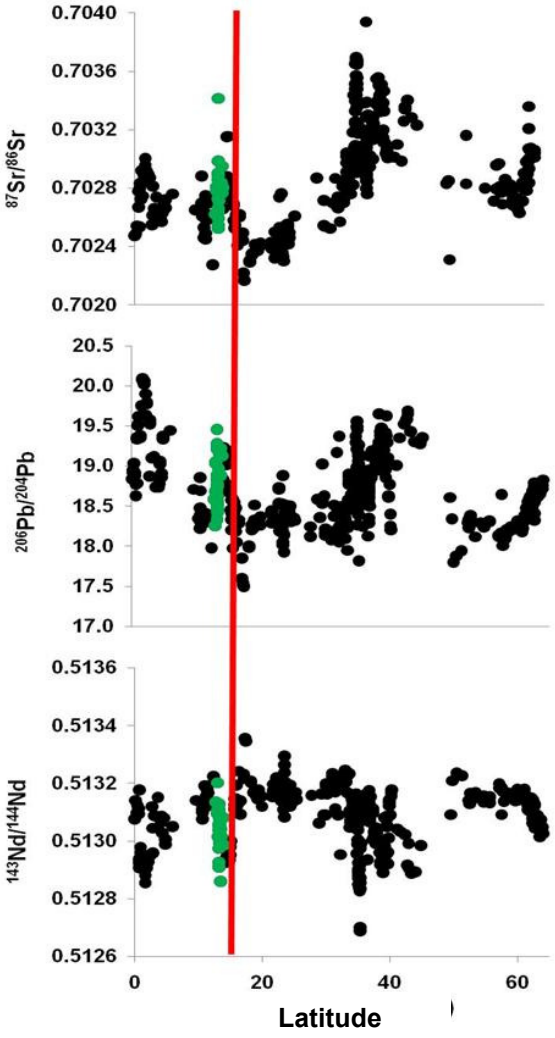

Figure 58: Variations of $^{87}Sr/^{86}Sr$, $^{143}Nd/^{144}Nd$ and $^{206}Pb/^{204}Pb$ isotope ratios with latitude in the Atlantic. Regional data (PetDB MORB, black) shows that there is substantial variation throughout the central MAR region. 0-5°N and 30-35°N are characterised by high $^{87}Sr/^{86}Sr$ and $^{206}Pb/^{204}Pb$ ratios, and low values of $^{143}Nd/^{144}Nd$. The N-MORB region between 17°10'N (marked by red line) and 22°N is characterised by low $^{87}Sr/^{86}Sr$ and $^{206}Pb/^{204}Pb$ ratios, and high values of $^{143}Nd/^{144}Nd$. Samples from 12°60'N– 14°N extend to very high $^{87}Sr/^{86}Sr$ and low $^{143}Nd/^{144}Nd$ values, with $^{206}Pb/^{204}Pb$ values higher than 17°10'N, but lower than those at 0-5°N.

6.2.6 - Chemistry of Basaltic Talus on the 13°19'N OCC

The provenance of basaltic talus on the OCC domes is not well constrained, because the rocks are not *in situ.* Although it is thought that the basalt originates from the axis after breaking off the hanging wall and being dragged over the fault surface, it is not clear from tectonic models or seafloor imagery whether the basalts were erupted prior to, or during faulting. It is possible that basalt layers sampled by the fault may even substantially pre-date the complex, if magmatism in the axis ceased long before slip on the detachment began.

The geochemistry of on- and off-axis basalts at 13°19'N shows that off-axis basalts (pre-dating the OCC) have chemistry different to that of the modern ridge axis. Talus can be compared to these two groups, to determine whether it resembles either, and therefore to further constrain its origins.

Plots of trace elements against longitude (Figure 59) across the 13°19'N OCC illustrate the patterns of enrichment and depletion in groups M1 and M2, which bracket the composition of basaltic talus from the OCC dome. Also plotted are on-axis samples from the ridge. Talus from the OCC dome does not show the same range of chemical variation seen at the off-axis sites, but nor do they mirror the geochemical array on-axis. The data show that the compositions of basaltic talus on the complex dome are very similar to M2. Trace element bivariate and ratio pair plots (Figure 60) also show this relationship clearly.

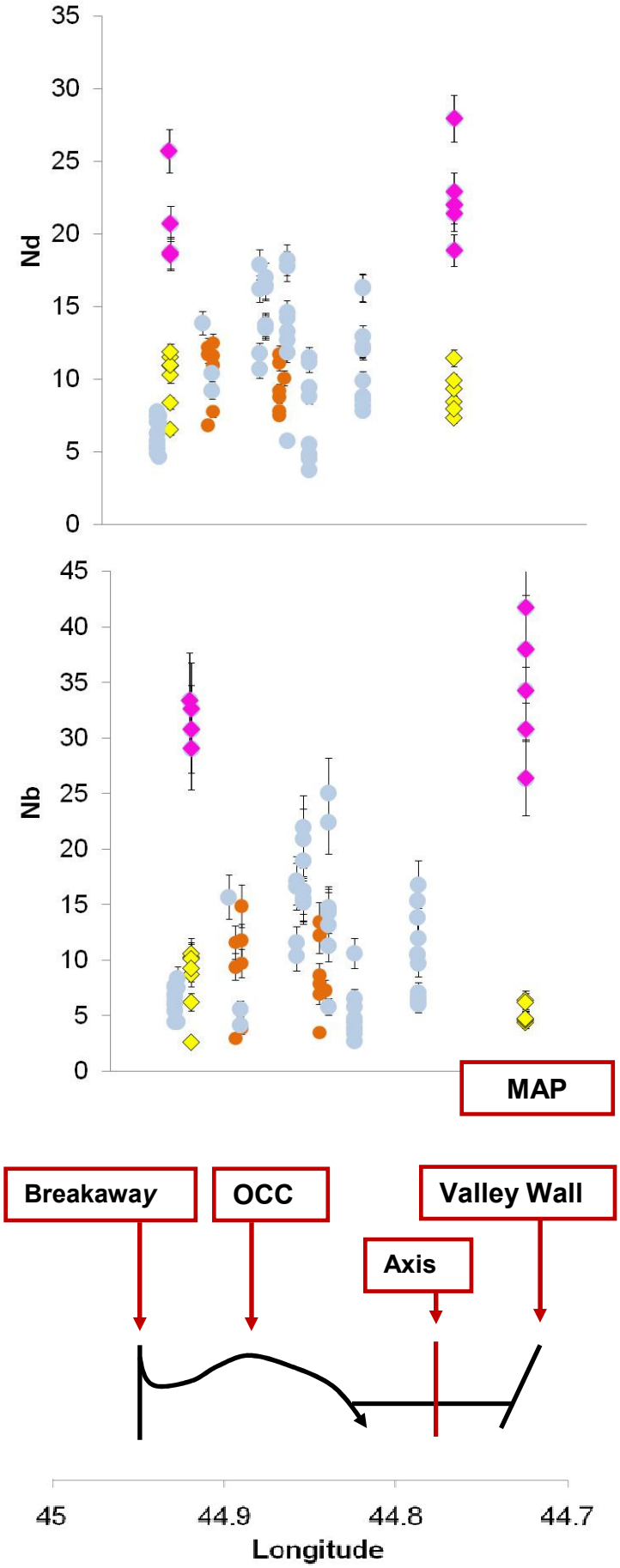
Nd
35
30
25
20
15
10
5
0
Nb
45
40
35
30
25
20
15
10
5
0
MAP
Breakaway
OCC
Valley Wall
Axis
45
44.9
44.8
44.7
Longitude

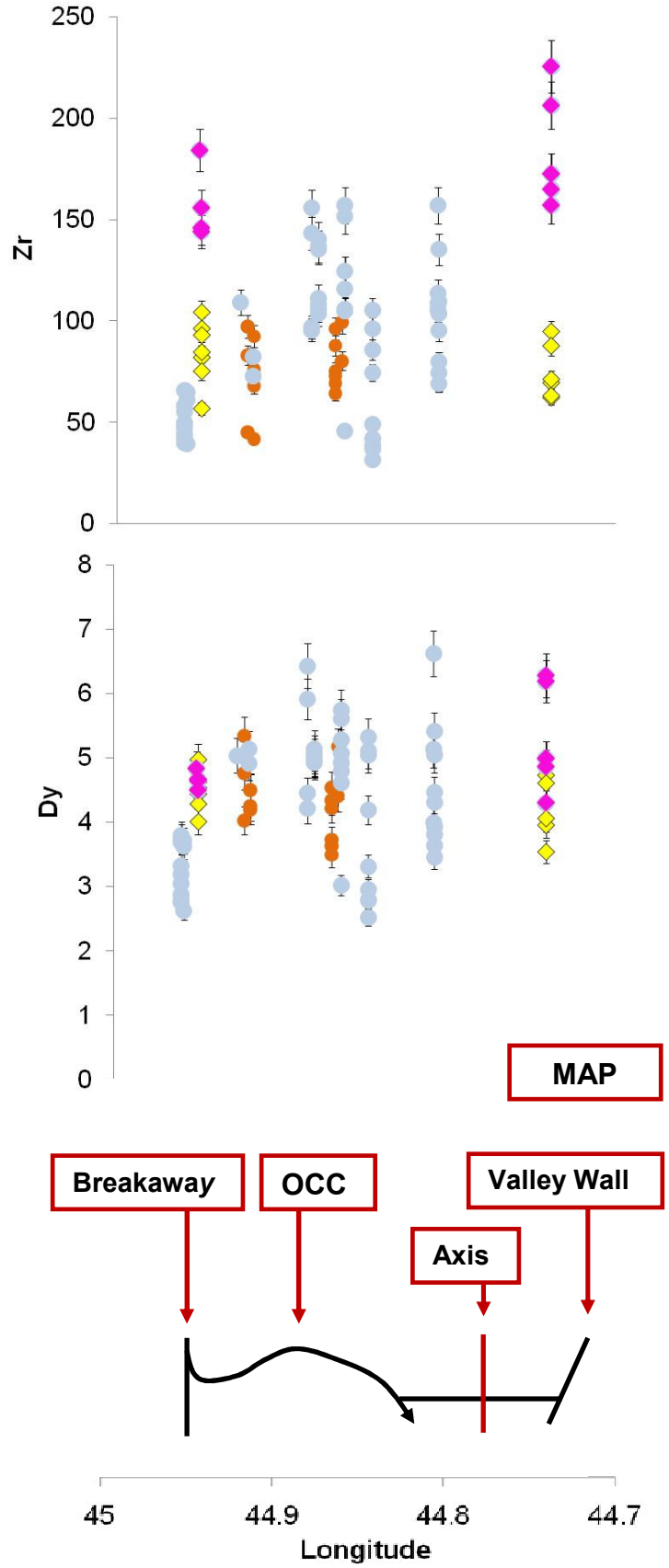

Figure 59: Trace element data illustrating the geochemical variations across the dome of the 13°19'N core complex. M1 (yellow) and M2 basalts (pink) are bimodal, bracketing the composition of basaltic talus (orange) and on-axis basalts from 12°60'-14°N (blue). The sketch map (bottom) illustrates the geographic features with which the data correlates.

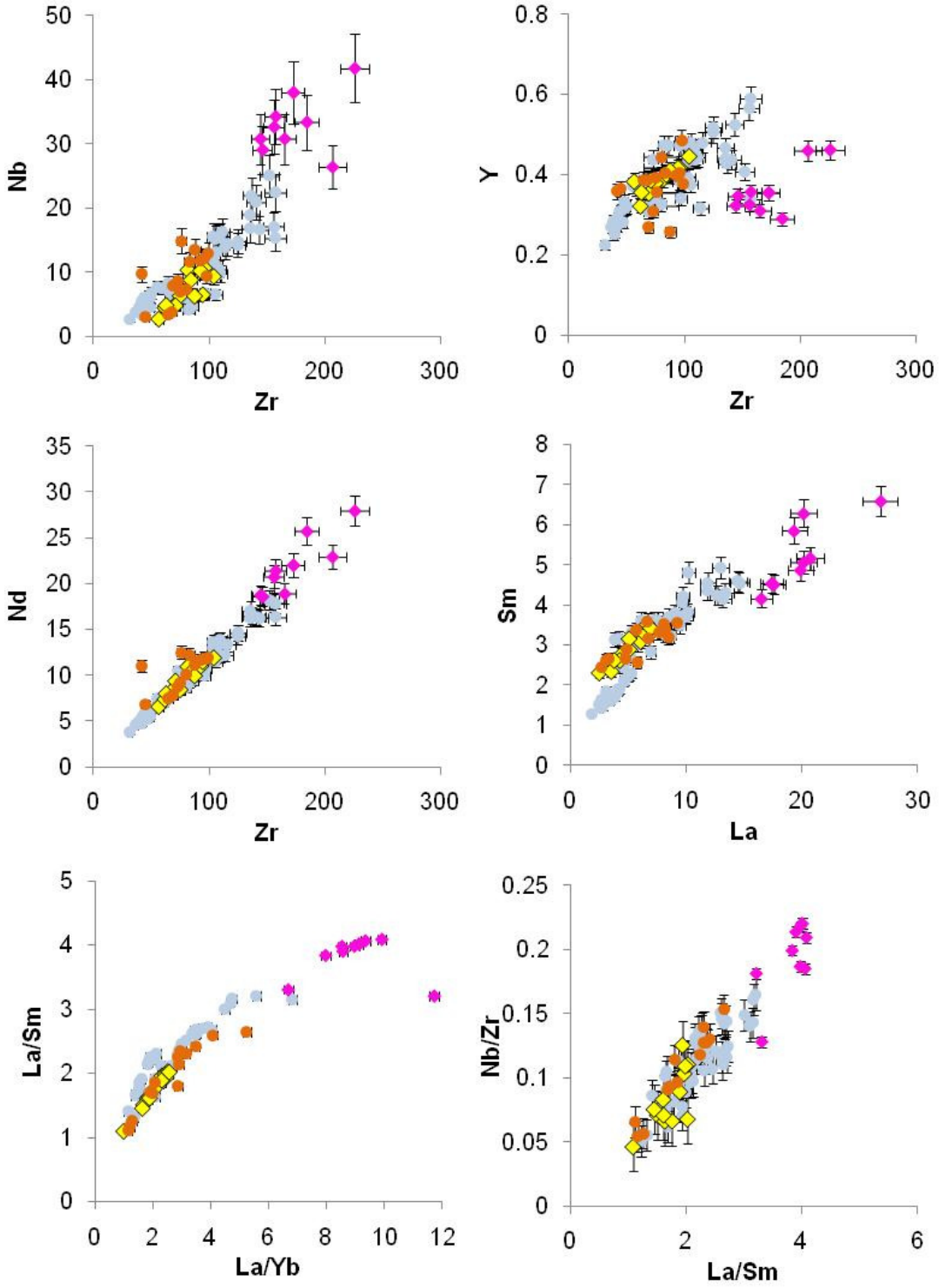

Figure 60: Trace element ratio data illustrating the geochemical variations across the dome of the 13°19'N core complex. M1 (yellow) and M2 (pink) basalts are bimodal, bracketing the composition of basaltic talus (orange) and on-axis basalts from 12°60'-14°N (blue).

Data Summary

Basalts from on-axis sites between 12°60'N-14°N are N-MORB-like to E-MORB in character, with E-MORB compositions focused on 14°N as predicted by previous studies. Most rocks fall into the E-MORB compositional range, with a substantial proportion of samples having trace element compositions (e.g. high Zr, Nb) extending into the OIB range. Compositions become more N-MORB-like to the south at the Marathon Fracture Zone. Basalts are lower in Na[8] than average for the central MAR, but extend to higher concentrations of K, Ti and P. Dolerite dykes sampled from the toe of the OCC at 13°19'N have similar major element compositions to on-axis basalts.

Many of the samples are enriched in incompatible trace elements, such as Sr, Nb, Nd, Ce, Zr, U, Pb, Ta and La. Their compositions extend to lower concentrations of Y and Yb than other areas of the central MAR. Nd, Sr and Pb isotope ratios fall within the MAR basalt array. However, $^{87}Sr/^{86}Sr$ ratios are higher than those found in most areas of the surrounding MAR, and $^{143}Nd/^{144}Nd$ typically lower. $^{206}Pb/^{204}Pb$ is high, though not the highest in the central MAR.

The chemistry of off-axis sites at 13°19'N is different to that of the on-axis sites. These rocks, which are thought to represent ridge chemistry prior to OCC initiation, are strongly bimodal in composition. Group M1 basalts have extremely enriched E-MORB compositions. They are rich in Ti, K, P, and incompatible trace elements Sr, Nb, Nd, Ce, Zr, U, Pb, Ta and La, and have REE profiles that are substantially steeper than typical Mid-Atlantic E-MORB. These profiles show extreme LREE enrichment and also depletion in the HREE, which may suggest melting in the garnet stability field. They have lower Y and Yb values than predicted by the local on-axis trend, having high La/Yb and, and low Dy/Yb and Y/Zr ratios, which also suggest the presence of garnet in the source. These basalts have high $^{206}Pb/^{204}Pb$ and $^{87}Sr/^{86}Sr$, but low $^{143}Nd/^{144}$ Nd. Pb isotope systematics show that M1 basalts fall outside the Atlantic Array, and have exceptionally low Δ8/4 values, extending to <-40. M2 basalts are N-MORB-like, with flat REE profiles. These basalts are the most LREE depleted in the study. Their isotope ratios fall within the Atlantic array.

CHAPTER SEVEN - DATA INTERPRETATION

The area around the Fifteen-Twenty Fracture Zone is a geological paradox. As this, and other studies have shown, basalts here are geochemically enriched (E-MORB) for ~290km along axis, between 12°60'-15°20'N.

Whilst isolated E-MORB compositions are frequently produced on N-MORB segments (e.g. Langmuir *et al.*, 1986 and references therein) by melting at low melt fraction or by fractionation, the consistent generation of E-MORB basalts over wide geographic areas usually indicates extensive melting of an enriched mantle source. Examples of this are seen in E-MORB/OIB generating, bathymetrically elevated sites in the Atlantic (Azores, Iceland), which have pronounced gravity anomalies implying the presence of thickened crust. However, unlike these 'hotspot' sites, 12°60'-15°20'N produces very thin crust, and is not associated with a pronounced bathymetric high. Rather, it has an axial valley, typical for a slow-spreading mid-ocean ridge segment. Magmatism in the axis is sporadic, and ridge spreading in several areas is taken up on OCCs. Though the causes of OCC formation are not understood, it has been postulated that spreading on detachment faults occurs in response to low melt supply (e.g. MacLeod *et al.*, 2009).

To date, it remains unclear how contradictory geochemical and tectonic observations in this region can be reconciled. This thesis presents a number of original hypotheses to explain why magmatism between 12°60'-15°20'N is sporadic. These relate to changes in either the provision of melt to the ridge axis, or to the production of melt in the mantle beneath it, and are summarised as follows:

1) Mantle focusing dictates that mantle upwells beneath magmatic areas, but not beneath OCCs. Therefore, very little melt is available to erupt in the axis at OCCs. This implies that '3D' mantle upwelling beneath 12°6'-15°20'N varies on a geographic scale of 15-30km.

2) Crustal plumbing prevents melt from reaching the surface beneath OCCs, but not at magmatic sites. This implies that, due to structural characteristics of the

crust underlying OCC sites, melt is unable to reach the surface. Melt produced beneath the axis must either be diverted into dykes and carried away from the OCC, or frozen into the crust beneath the surface, forming gabbro bodies.

3) Variations in mantle source composition or temperature lead to low degrees of melting at OCC sites, but not at magmatic sites. This implies that geochemical characteristics (including hydration) or temperature of the mantle source beneath OCC sites is such that the mantle produces insufficient melt to sustain volcanism at the ridge axis.

It is the aim of this chapter to discuss geochemical data and structural observations from 12°60'-15°20'N in a local and regional context. The hypotheses above will be addressed to determine their validity, and the generation of OCCs and the origins of E-MORB in the 12°6'-15°20'N region will be explained in light of this evidence.

7.1 - INTERPRETATION OF ANALYTICAL DATA

7.1.1 - Basalt Textures and Eruptive History, 12°60'-14°N

Textural differences between on-axis (12°60'-14°N) and off-axis (13°19'N) rocks were discussed in chapter 6. Many on-axis samples contain large (~2-8mm), rounded plagioclase crystals. The size of these crystals is inconsistent with rapid cooling suggested by the small olivine and plagioclase crystals in the groundmass. The rounded appearance of the large plagioclase crystals and the signs of chemical disequilibrium that they exhibit suggest that they are in disequilibrium with the surrounding melt.

Plagioclase separates slowly in comparison to co-crystallising olivine or pyroxene (Ethlon, 1984). It is neutrally buoyant in basaltic magmas (Grove *et al*, 1984). When high-temperature, primitive basaltic liquids are added to a magma chamber, a proportion of solid plagioclase can remain suspended in the liquid

(Ethlon, 1984). This accumulated plagioclase is partially to completely melted, resulting in changes in bulk geochemistry known as plagioclase accumulation effects.

Large plagioclase crystals in on-axis rocks from this study are interpreted to have erupted as an accumulated phase along with the on-axis melts. Rounding of crystal edges, dissolution blebs and alteration result from partial disequilibrium and remelting of the crystals as they were carried in the melt. Geochemical evidence such as positive Eu anomalies, high Al and Ca, and low Fe in these rocks support this conclusion.

Plagioclase accumulation appears to be a common in basalts between 12°60'-14°N. Accumulation of calcic plagioclase (An70-90) is also reported to be widespread at other sites along the MAR (Flower, 1980). This indicates that the prevailing PT conditions and residence times in shallow magma chambers along these parts of the ridge favour the formation of large, euhedral plagioclase phenocrysts.

The bimodal size distribution of plagioclase in 12°60'-14°N rocks suggests that the smaller, more euhedral generation of plagioclase formed separately to the large ones. As the small, euhedral crystals appear fresh and in equilibrium with the melt surrounding them, this suggests that they crystallised post-eruption, see Figure 61.

Off-axis rocks have similar textures, apart from the fact that large, accumulated plagioclase phenocrysts are (generally) absent, indicating that plagioclase accumulation was not a significant process in magma chambers beneath the ridge at 13°19'N. This is supported by a lack of positive Eu anomalies in the vast majority of off-axis basalts (refer to Figure 48).

In many samples, olivine and plagioclase crystals occur in radial clusters, each individual crystal having skeletal or dendritic morphology. Examples of these crystal shapes and associations are shown in chapter 6, and Figure 62.

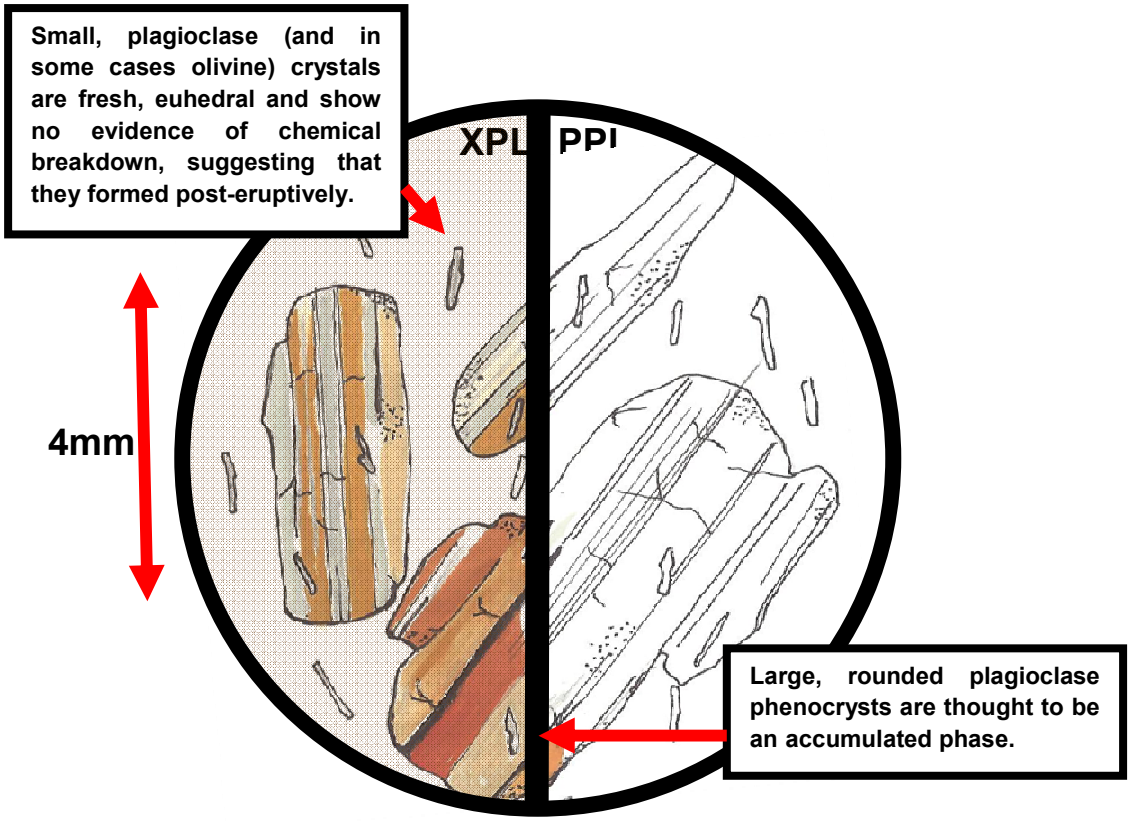

Figure 61: Thin-section sketch (10x magnification) to illustrate key textural features of large (~2-8mm), rounded plagioclase phenocrysts in on-axis basalt samples from 12°6'-14°N. The brownish cast (when viewed with crossed polars) results from the thickness of the section.

The radial groupings of crystals and their small average size suggest that they formed during rapid post-eruptive cooling. Radial clustering indicates that crystallisation began via nucleation around a single point. The variable size of the post-eruptive olivine and plagioclase crystals between samples suggest that cooling times are variable.

The morphology of the olivine and plagioclase crystals also suggests rapid cooling. Experiments show that the shape of plagioclase crystals changes progressively from tabular to elongate skeletal to dendritic and spherulitic with increasing degree of supercooling below the liquidus (Iyer and Banerjee, 1998). Plagioclase crystals from radial crystal clusters at 13°19'N are skeletal to dendritic in shape, suggesting a substantial degree of supercooling.

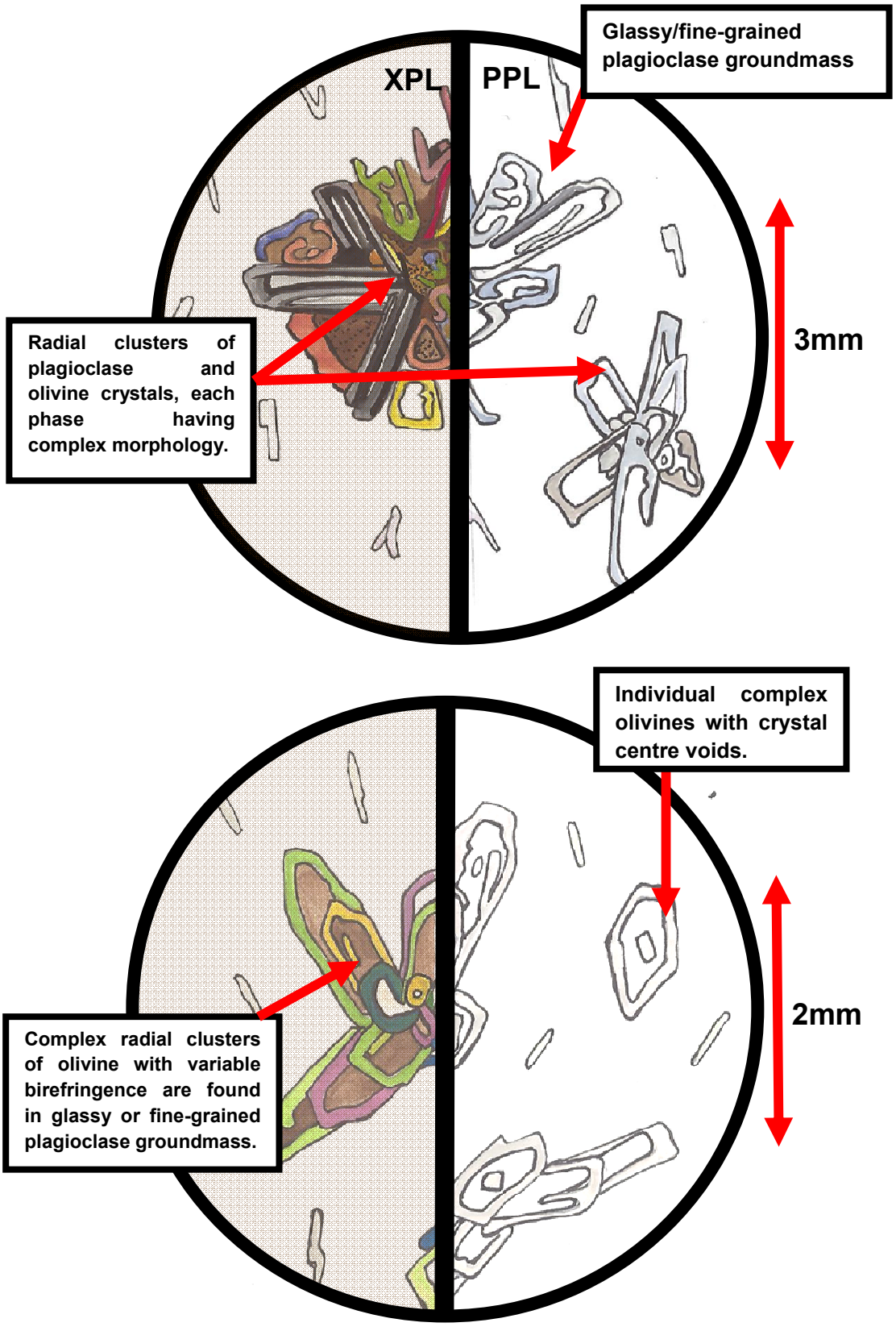

Figure 62: Thin section sketches (20x magnification) to illustrate the textural features and associations of radial plagioclase and olivine crystal clusters in rock samples from the 13°19'N OCC.

The morphology of olivine crystals also provides information on cooling histories. Olivine crystals evolve in a complex sequence of 10 morphological types with increased cooling rate and degree of supercooling, as described by Donaldson (1976). These morphologies have been simplified into three 'bins' (tabular, hopper (skeletal) and dendrite) by later studies (Faure *et al.*, 2003, Faure and Schiano, 2004).

Complex olivine crystals from 13°19'N off-axis rocks display a range of morphologies, from dendritic 'chain lattice and swallowtail' crystals, to skeletal hopper crystals (glass pockets in the crystal are open to the surrounding glass) and 'closed hoppers' (glass pockets in the crystal are sealed and do not contact the glassy groundmass).

Dendritic olivine crystals are interpreted to form by rapid crystallisation of olivine in contact with seawater. Open and closed hoppers result from several cycles of cooling-heating (corresponding to a maximum degree of undercooling of 20-25°C) during crystal growth. These thermal variations occur before eruption and are interpreted to result from turbulent convection in a small magmatic body beneath the ridge (Faure and Schiano, 2004).

In summary, olivine and plagioclase morphology at 13°19'N (off-axis) suggests that melts were held in a small, turbulently convecting magma body beneath the ridge for a very short time, allowing small hopper olivine crystals to form, before being erupted to the seafloor and rapidly cooled, resulting in the growth of skeletal plagioclase laths and olivine dendrites. Hopper crystals in these rocks do not exhibit significant dendritic overgrowths. This suggests that they were cooled very quickly post-eruption (Faure and Schiano, 2004).

Studies of a suite of rare gas rich 'popping rocks' near 14°N (MAR) suggest that these rocks retain their gas content because vesicles forming in the melts are not removed by physical sorting during magma chamber processes (Sarda and Graham, 1989). This adds weight to the argument that melts beneath this region are stored in small conduits or lenses prior to eruption directly to the surface, and not processed in large magma chambers.

In stark contrast to the surrounding olivine and plagioclase, clinopyroxene (augite) crystals are large (3mm) and euhedral (Figure 63).

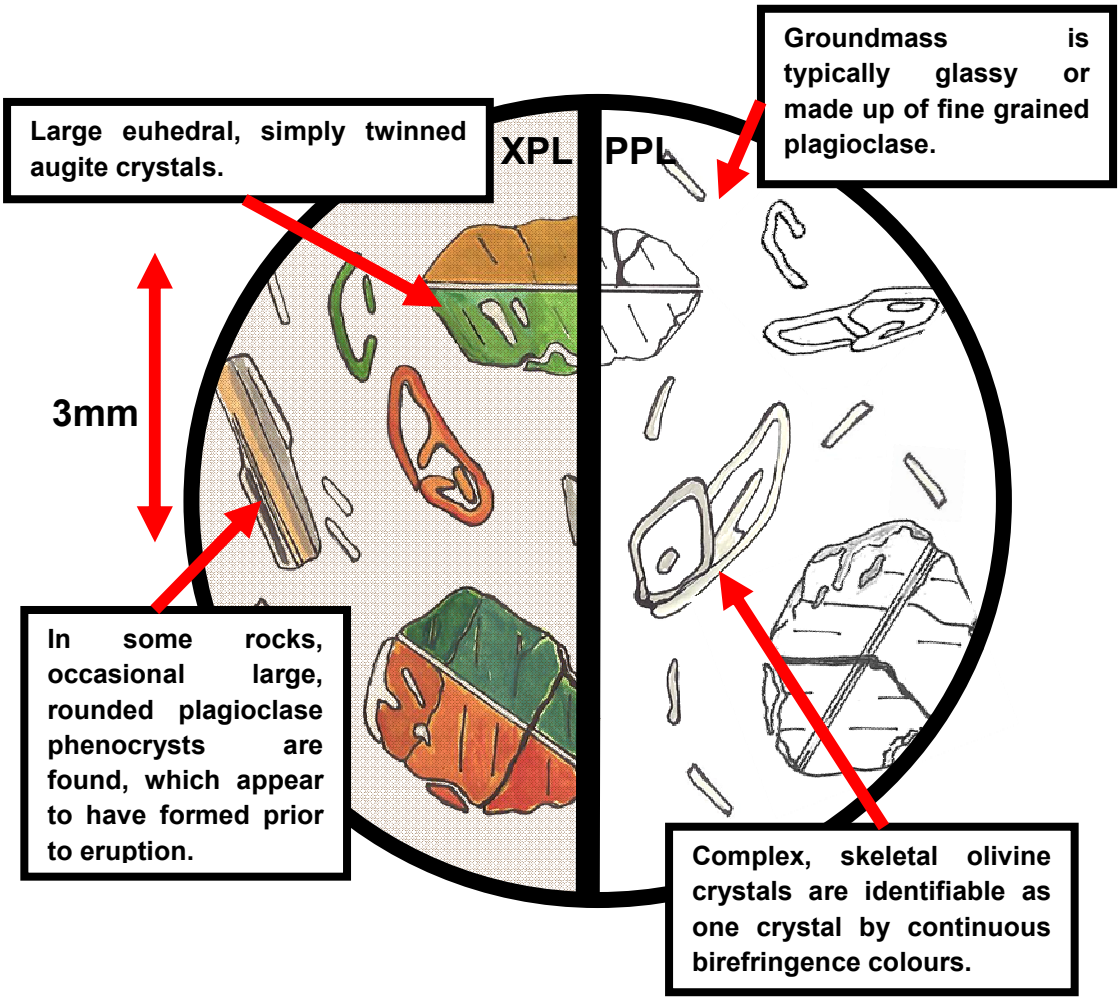

Figure 63: Thin section sketch (10x magnification) illustrating the key textural features and associations of rounded, simply twinned clinopyroxene crystals found in basalts from dredges D05 and D10, 13°19'N.

The large size and euhedral (occasionally subhedral) shape of these crystals suggests initial slow growth during residence in a magma chamber, rather than the rapid post-eruptive growth that formed the olivine and plagioclase.

This textural association suggests that the augites are an accumulated phase, and were carried to the surface as solid crystals formed in the melt. Corroded

crystal rims and subhedral morphology of some crystals suggest that they were, for some time, in disequilibrium with the surrounding melt. The morphology of olivine and plagioclase shows that post-eruptive cooling was rapid, and this precluded any significant post-eruptive recrystallisation of the augite.

Analysis of rock textures from 12°60'-14°N shows that there are significant differences between off-axis and on-axis rocks. On-axis, rocks range from aphyric to plagioclase and olivine phyric, and plagioclase accumulation is a feature of many samples. Off-axis at 13°19'N, plagioclase accumulation is not significant. However, augite crystals are an accumulated phase here. Complex olivine and plagioclase morphology (dendritic/hopper crystals) indicates very rapid eruption of melts. This suggests that magma chamber conditions (within which the melts and accumulated crystals form beneath the OCC) are different to those in the surrounding axis.

Many studies have been carried out into the crystallisation conditions of MORB melts beneath MORs. These processes are studied by mathematical modelling, using real (e.g. Danyushevsky *et al*., 1996, 2001; Almeev *et al*., 2008) and modelled melt compositions (e.g. Presnall *et al*., 1978, Guohao *et al*., 1991), and also by high pressure and temperature 'sandwich' capsule experiments (e.g. Stolper, 1980). The common low-pressure MORB crystallization sequence is: olivine, olivine + plagioclase, olivine + plagioclase + clinopyroxene. However, data from crystallisation studies shows that increasing pressure increases the temperature of crystallisation of clinopyroxene compared to the crystallisation temperatures of olivine and plagioclase, forcing clinopyroxene to appear earlier on the liquidus. Modelling in the system CaO-MgO-Al_2O_3-SiO_2 shows that as model pressure increases, the forsterite and anorthite fields contract, whilst the diopside field expands (Presnall *et al.*, 1978).

Melt-crystallisation experiments on real alkali basalt samples (similar in composition to M1) from Minqing, Fujian Province, China, in both dry and water-bearing systems at high pressures, indicate that clinopyroxene crystallizes from basaltic melt at 13.5–23.7 kbar. With increasing pressure, the $CaSiO_3$ content of clinopyroxene increases, and $FeSiO_3$ decreases. The study also finds that

crystals are larger and more euhedral in the water-bearing system (Guohao *et al.*, 1991).

Almeev *et al.* (2008) showed that MORB magmas beneath different segments of the MAR crystallise over a wide pressure range (100-900MPa), with each segment possessing a specific crystallisation history. Nearly isobaric, wet (0.4-1wt%) crystallisation conditions (100-300MPa) are reported for geochemically enriched segments, with N-MORBs from other segments crystallising from near anhydrous melts over a range of pressures (200-900MPa).

A study of primitive basalts from the FAMOUS area (MAR) shows that for these basalts olivine is the liquidus phase at 1 atm, with olivine crystallisation followed by plagioclase and then clinopyroxene. Above 10.5kbar clinopyroxene is the liquidus phase, and most clinopyroxene in the FAMOUS rocks crystallised at pressures ~10kbar (Bender *et al*., 1978).

The presence of clinopyroxene in the basalts from 13°19'N shows that magma chambers beneath the ridge here exist at depths conducive to the crystallisation of clinopyroxene crystals from basaltic melt (10.5-24kbar according to the studies described above).

Mineral phases that are stable on/near the liquidus do not react with the surrounding melt, whereas those that are relatively unstable in the melt show strong evidence of dissolution such as complex reaction textures and recrystallisation (Brearley and Scarfe., 1986). The shape of the subhedral clinopyroxenes from the 13°19'N OCC suggests that they remained in equilibrium with the melt (i.e. at clinopyroxene crystallisation depth) until shortly before they were rapidly extracted to the surface. The absence of clinopyroxene and presence instead of accumulated plagioclase along the rest of the segment suggests that magma chamber depths here are shallower.

7.1.2 - Source Geochemistry and Melting Conditions 12°60'-14°N

Geochemical data from on-axis sites between 12°60'-14°N shows that there is no systematic difference between the major element, trace element and isotope geochemistry of basalt at OCC and magmatic localities. Therefore, there is no evidence to indicate lower melt production at OCC on-axis sites versus volcanic sites. On-axis OCC sites are isotopically indistinguishable from their magmatic counterparts, indicating that there is no mantle source variation between them in terms of end-member composition. Trace element ratio vs. isotope ratio plots (Figure 64) illustrate this.

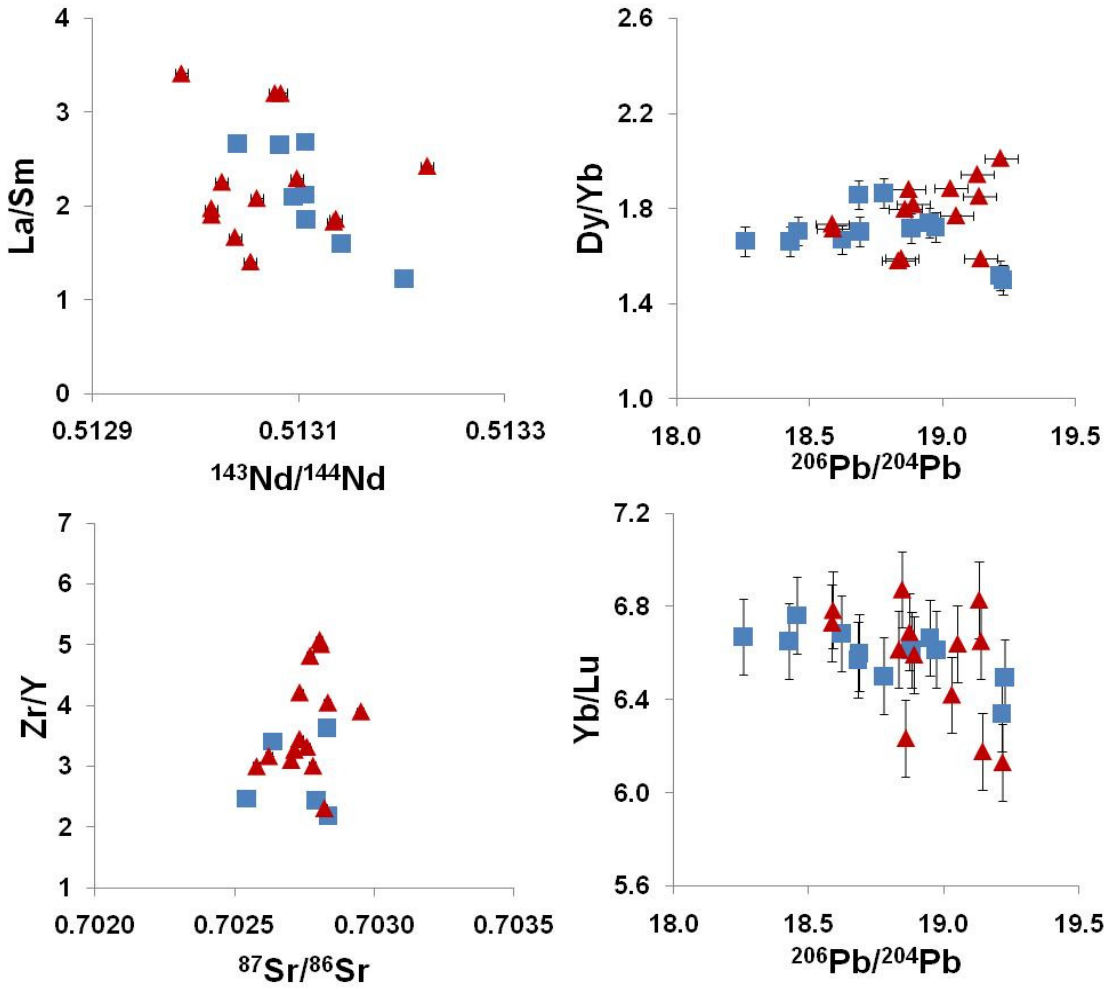

Figure 64: Trace element ratio vs. isotope data for basalts from 12°6'-14°N. On-axis OCC spreading sites (blue) and magmatic spreading (red) sites are shown.

7.1.3 - Insights from Off-Axis Geochemistry at 13°19'N

Off-axis basalt geochemistry at the 13°19'N OCC is shown to differ from the chemistry of on-axis basalts in major, trace element and isotope ratio space. Off-axis basalts are known to have formed at some time prior to (or during) the OCC initiation process. Their geochemical characteristics may therefore be representative of conditions favourable for OCC formation.

Incompatible major element enrichments (Na, K, P, Ti) in off-axis rocks are not likely to be related to fractionation. Some of the most enriched samples in the area (M1) are also the most primitive (highest Mg#). Therefore, enrichments at 13°19'N must reflect the geochemistry of the source and/or the extent of mantle melting.

Enrichment in basalt is strongly dependent on melt fraction. Low melt fractions contain much higher concentrations of highly incompatible elements than higher melt fractions, where the concentrations of incompatible elements are 'diluted' by the presence of moderately incompatible and compatible elements. Variations between low melt fraction (M1) and higher melt fraction (M2) may explain the bimodality of compositions at 13°19'N.

Ratios of highly incompatible to moderately incompatible elements reflect variations in source conditions, and also enrichment effects arising from variable melt fraction. They are affected very little by fractionation processes. M1 basalts have high ratios for many elements, e.g. La/Sm, Nb/Zr, (see chapter 6) whereas corresponding values are substantially lower for M2. This suggests variable levels of enrichment which may be a function of source or melt fraction, or both, but are fractionation independent.

Incompatible elements at 13°19'N span a broad compositional range. M1 rocks have highly E-MORB compositions with very steep REE profiles (Figure 55). M2 have more N-MORB-like compositions. REE profiles range from slightly LREE enriched, to slightly LREE depleted. FTIR data shows that M1 basalts are H_2O rich compared to M2, which have low H_2O concentrations typical for the depleted end of the regional (12°60'-14°N) geochemical array.

Broad compositional ranges in MORB are easily produced in cases where small amounts of melt are infrequently tapped and infrequently mixed, when compared to steady rates of extraction and eruption. Infrequent sampling of low melt fraction melts beneath 13°19'N may produce the wide compositional range found here. This suggests that small melt lenses, rather than large magma chambers provide melt to this site, as large magma chambers lead to well-mixed melt compositions.

At off-axis sites, basalts are geochemically bimodal, comprising both N-MORB (M2) and extremely enriched E-MORB (M1). Compositional bimodality suggests that individual melt batches do not encounter each other as they rise through the crust. This lends support to the argument for infrequently tapped, small-scale melt lenses, rather than established magma chambers which allow melts to mix.

M1 basalts have extremely depleted HREE relative to LREE. This may indicate the presence of residual garnet in the source, as garnet preferentially holds HREE during melting. Garnet is a stable mantle phase at depths exceeding ~60km, and the presence of a 'garnet signature' in M1 rocks suggests that they segregated from the mantle at these depths. This is supported by their Yb/Lu and Dy/Yb ratios, which are strongly fractionated by the presence of garnet in the mantle source, producing lower Yb/Lu and higher Dy/Yb ratios than other phases. These ratios are significantly changed from the ridge trend in the M1 rocks (see chapter 6).

M2 basalts do not show the same displacement in Yb/Lu and Dy/Yb. This indicates that the melting which formed M2 basalts did not take place in the garnet field, or that the melting took place in the garnet field but persisted for some time in the spinel field, where melt compositions were swamped by more chondritic Yb/Lu and Dy/Yb.

Major and trace element data for off-axis at 13°19'N suggests that M1 and M2 basalts experienced different melting histories in terms of extent of melting, depth of melting, and length of the melting path. Signatures arising from melting processes must be distinguished from those arising from source geochemistry, in order to further constrain the geological history of these basalts.

7.1.4 – Isotopic Trends, Mantle Components and the Origins of Mantle Heterogeneity

Radiogenic isotope ratios are not affected by degree of melting, or by crystal fractionation. Hence they are ideal parameters for determining differences in composition between the mantle sources of basaltic melts. Enriched M1 and more depleted M2 rocks from the 13°19'N OCC lie on distinct isotopic trends from on-axis sites. These trends can be used to identify mantle source characteristics which contribute to basalt formation.

Geochemical and geophysical models of the mantle today require a heterogeneous, multi-component source in order to generate all of the known compositions of MORB (Davies, 2009). Evidence for numerous isotopic end-members in the mantle is widespread, but constraints on the geometry of these reservoirs are very poor (Becker *et al*., 1999, Kogiso *et al*., 2003). Therefore, the nature, extent and longevity of mantle compositional heterogeneities are a source of much debate.

Mantle material upwells and erupts at MORs, whilst cold crustal material is subducted and sinks. Stirring times in the mantle are thought to be too slow for subducted material to completely re-homogenise, given the low chemical diffusivity of solid mantle. Hence the mantle is likely to be a mixture of non-homogenised crustal and harzburgitic material (Ritsema *et al*., 2009). It is thought that gravitational settling of subducted crustal material at the base of the mantle aids the preservation of crustally-derived isotopic reservoirs on long geological timescales, provided that convection is not more vigorous than previously thought (Brandenburg and Van Keken, 2007).

Recent work by Hellfrich (2002) suggests that the lower mantle contains abundant, small scale (~8km) elastic heterogeneities that likely represent recycled oceanic crust, a component which makes up ~10% of the Earth's mantle material. Diffusivity studies show that chemically heterogeneous domains of a threshold size of a few metres remain separate from the surrounding mantle on geological timescales long enough to generate and expel isotopically distinct

partial melts (Kogiso *et al*., 2003). Models such as those developed by Manga *et al*. (1996) and Becker *et al*. (1999), suggest that small heterogeneous high-viscosity blobs could persist in the mantle on geologically significant timescales without being substantially chemically or mechanically mixed into the material that surrounds them. Walter *et al*., (2008) suggest that 'small-degree melts of subducted crust can be viewed as agents of chemical mass-transfer in the upper mantle and transition zone,' and argue that this chemical imprint could persist for billions of years.

Mantle plumes or 'hot-spots' are one well-described form of mantle heterogeneity, generating highly enriched, isotopically distinct basaltic compositions (OIB) (Boschi *et al*., 2007).

Identification of the surface expression of mantle plumes is aided by the fact that they frequently exhibit specific characteristics. These include velocity anomalies in global seismic tomography studies (e.g. Ritsema *et al*., 1999, Zhao 2009), elevated topography, anomalously high buoyancy flux, and in some cases, such as the Emperor-Hawaii Chain, time-progressive linear island chains (Boschi *et al*., 2007).

All plumes were originally thought to be from the base of the mantle (Morgan, 1971), though later analysis of global seismic tomography suggests that not all plumes have a deep mantle origin (Boschi *et al*., 2007). Whilst many plumes exhibit the low shear velocity anomalies we would expect (i.e. Hawaii, Easter, Iceland), others do not, and the formation and origin of mantle plumes still remain contentious (Ritsema and Allen, 2002).

Although many plumes occur in intraplate settings (Hawaii), others interact directly with the ridges (Iceland, La Reunion, and Azores), having some clear tectonic, topographic or geophysical association with the adjacent ridge system. Plume-ridge interaction has been well studied, as these localities are ideal for examining a cross section through the mantle flow associated with the plume (Bourdon *et al*., 1996). This provides an opportunity to deconvolute plume activity from magmatism and chemistry associated with decompression melting beneath a MOR. Bourdon *et al*. (1996) demonstrated that whilst excess ^{230}Th on the MAR at 37°30'-40°30'N is likely to result from the influence of the nearby Azores

plume, the $^{230}Th/^{238}U$ ratio cannot be explained by source composition, and is rather related to axial depth of the ridge. A study by Niu *et al.* (1999) at 11°20'N on the EPR identifies a 'distal ridge-plume interaction' origin for E-MORB material, which is identified as Hawaiian on the basis of isotopic and trace element data, coupled with seismic tomography. Gee *et al.* (1998) show that isotopic variations on the Reykjanes Peninsula result from crustal processes such as magma mixing, and to a lesser extent assimilation, rather than source heterogeneity.

Plumes have commonly been invoked at ridge settings as an explanation for localised E-MORB signatures, even where there is no tectonic or geophysical evidence for plume interaction. The widespread occurrence of E-MORB on localised areas of the MORs suggest that enriched areas in the mantle that are unconnected to plume behaviour are common beneath both slow- and fast-spreading ridge systems (Donnelly *et al*., 2004). There are a number of possible sources of mantle compositional heterogeneity, apart from hotspots.

Pilet *et al*. (2005) present petrological data that suggest that the isotopic and trace element geochemistry of OIB can be best reproduced by the partial melting of peridotite in the presence of CO_2 or Si-deficient pyroxenite. Over time, subduction and isolation of this metasomatized lithosphere generates isotopic variations which are equivalent to those found in OIB, and which correlate with trace element ratios. This model does not require separately generated end-member mantle components in order to generate OIB. However, examination of large OIB datasets suggests that melting of peridotitic mantle cannot generate the TiO_2 concentrations seen in OIB. The only enriched component capable of generating this TiO_2 content is recycled oceanic crust. Despite this, recycled oceanic crust is itself insufficiently isotopically variable to produce OIB, and so the source must include some metasomatic veins or sedimentary contaminant (Prytulak and Elliot, 2007).

Many areas of the mantle are thought to have experienced multiple episodes of melting leading to localised depletion, whilst others have interacted with melts of mantle or subducted crustal origin, causing localised enrichment. For example, the MARK area, (MAR), an N-MORB producing ridge region with no apparent

hotspot influence has small scale, localised E-MORB production arising from mantle that has been metasomatized by low-degree melts prior to later, extensive melting. The first melting episode occurred beneath the subduction zone, where the mantle is exposed to low-degree melts of subducted crustal material. Later melting of the enriched mantle took place beneath the MAR (Donnelly *et al*., 2004). Niu and Batiza's (1997) study of seamounts near to the EPR shows trace element fractionation characteristic of subducted oceanic crust, suggesting that the enriched component contributing to these seamount basalts was originally crustal in origin.

Bideau *et al.* (1995) suggest that small scale heterogeneities in the composition of EPR basalts (13°N) over time are the result of multiple melting events followed by periods of quiescence. Exact compositions derived on the surface are then fine-tuned as a result of the amount of mixing and fractionation experienced by the original source material.

These studies show that mantle heterogeneities originate from a number of sources, such as long-lived plumes from the CMB, melt refertilisation, metasomatism and contamination with melts derived from subducted ocean crust and sedimentary material. Many recent studies (e.g. Armienti and Gasperini, 2007) endorse the 'marble-cake' mantle first proposed by Sleep (1984), with geochemical heterogeneities preserved as small scale blobs and veins throughout the depleted host mantle. The mantle convects, mixing these heterogeneities together. Some authors invoke whole mantle convection models, whereas others suggest that convection is impeded by the 660km thermal boundary layer, and/or other boundaries corresponding to major mantle phase transitions. A summary of the existing models is provided by Albarède and van der Hilst (1999), see Figure 65.

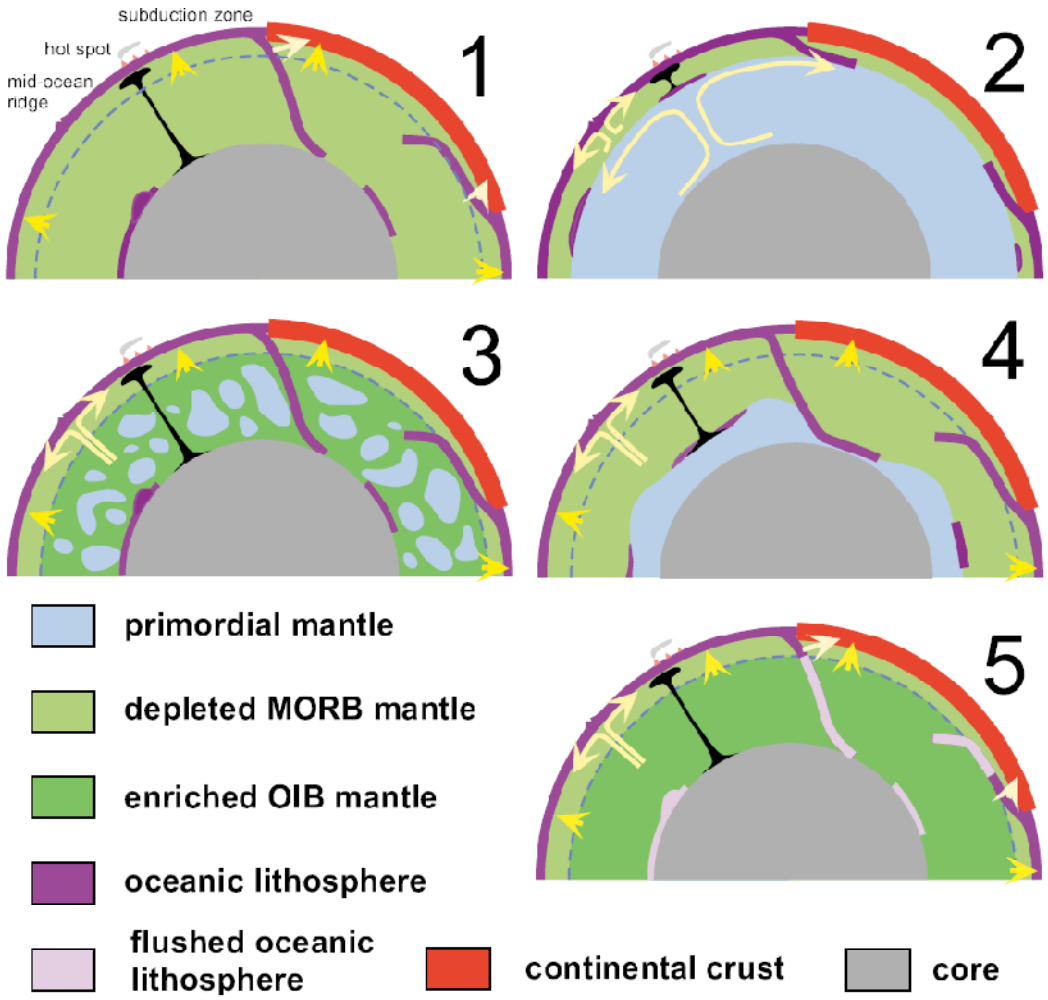

Figure 65. Summary of mantle convection models. 1) Whole mantle convection: plates break through the transition zone. 2) Layered mantle convection: plates are confined to the upper mantle. 3) Whole mantle convection with deep blobs of primordial mantle. 4) Layered mantle convection with a deep layer of primordial mantle. 5) Whole mantle convection with plate depletion at subduction zone. From Albarède and van der Hilst (1999).

The isotopic variability in oceanic basalts suggests that most mantle sources consist of two or more components with isolated long-term chemical evolution (Stracke and Bourdon, 2009). Basalt compositions are commonly described in isotopic space in terms mantle end-member components (White, 1985). Specifically, four end-member compositions are used, DMM, EMI, EMII and HIMU (Zindler and Hart, 1986; Hart *et al.*, 1992). These end-member components are geochemical devices to explain the variability in the compositions of MORB (formed from degassed, depleted upper mantle) and OIB

(from incompatible element enriched lower mantle material), and are not intended to be considered as distinct, accessible portions of the mantle (Armienti and Gasperini, 2007).

The existence in reality of long lived, distinct, internally homogeneous mantle reservoirs is unlikely, given geophysical evidence for whole mantle convection (Hart *et al*., 1992) and geochemical evidence for a growing number of varied source combinations contributing to the formation of MORB and OIB. It is more likely that mantle composition varies on a local scale as a result of mantle processes (e.g. Kellogg *et al*., 2002), resembling a streaky or marble cake model of compositional variation (Armienti and Gasperini, 2007).

DMM (depleted MORB mantle) is the source reservoir for generation of MORB, and is thought to represent >30% of the mass of the silicate Earth, and to be depleted by 2-3% melting (Workman and Hart, 2004). Workman and Hart (2004) provide an estimate of the geochemistry of DMM based upon a abyssal peridotite compositions. They demonstrate that DMM is 'roughly balanced by the continental crust and better balanced upon inclusion of ocean island basalt source and oceanic crust components'.

The high-μ or HIMU (high ^{238}U to ^{204}Pb, low ^{87}Sr /^{86}Sr) was originally a definition applied to a group of high $^{238}U/^{204}Pb$ basalts found at St Helena and the Cook-Austral islands, although 'HIMU' has since been used as a term to describe basalts from other regions with similar Pb isotope ratios (Stracke *et al*., 2005). The origin of HIMU mantle is a matter for debate. Many mechanisms have been suggested to explain the characteristic trace element geochemistry it possesses. These include Pb and Rb pumping in the core (Vidal and Dosso, 1978), U/Pb mineral fractionation in the upper mantle (Halliday *et al*., 1990), and recycling of hydrothermally altered crust (e.g. Zindler *et al*., 1982; Hart and Staudigel, 1982). Many variations on subduction models have been offered, notably subduction of partially melted crust into the deep mantle (Dupuy *et al*., 1987), subduction of hydrothermally altered crust suffering subduction-related lead loss (Chauvel *et al*., 1992), subducted crust and sediment combinations (Hanyu *et al*., 1997; Hanyu and Nakamura, 2000) and selective extraction of Pb into the core from subducted ancient oceanic crust (Tatsumi and Kogiso, 1995). Others warn that

its composition can only be created by recycling oceanic crust if the material has undergone significant modification during the subduction process (Stracke *et al*., 2003) It must therefore be generated by a rare combination of age and composition of subduction modified crust (Stracke *et al*., 2005).

Collerson *et al*. (2010) present an alternative HIMU formation model whereby HIMU and EM reservoirs are generated near the base of the lower mantle by partial melting of 'pristine' mantle domains, whereby carbon rich partial melts form EM, with the residues of melting evolving over a substantial period of time to form HIMU. It has also been suggested that the HIMU component is likely to arise from intra-mantle metasomatism (Hart, 1988). The generation of HIMU implies a source that is strongly depleted in Pb (or enriched in U). A slab containing only 56% of its original Pb concentration is required in order to generate a HIMU source within 2Ga (Chauvel *et al*., 1992). Muhe *et al*., (1997) calculate that during hydrothermal alteration, large amounts of Pb are concentrated in greenstones, depleting the surrounding material by ~58%, and therefore providing a plausible mechanism for the generation of Pb depletion signatures prior to subduction that are required to generate the HIMU source. OIBs with a HIMU signature typically exhibit high CaO/Al_2O_3, FeOT, and TiO_2 and low SiO_2 and Al_2O_3 (Jackson and Dasgupta, 2008).

The HIMU-type FOZO component (Hart *et al*., 1992) is slightly less radiogenic in Pb and more radiogenic in Sr and lies on the Atlantic-Pacific MORB array. The MORB-FOZO array is thought to be generated by the processes of mantle melting and subduction (Stracke *et al*., 2005). It is unclear whether HIMU and FOZO are generated by the same process, as they have similar trace element compositions, favouring a similar source. However, this is not the case for lavas at Rurutu, where trace element and isotopic variations are seen between FOZO and HIMU lavas (Chauvel *et al*., 1997). It is unclear whether these variations are a specific feature of this volcano alone, or whether they indicate separate source histories for HIMU and FOZO melts (Stracke *et al*., 2005). It has been suggested that FOZO is representative of deep mantle plume material (Wilson and Spencer, 2003)

Mantle components with enrichments in certain elements are known as EM-1 (intermediate $^{87}Sr/^{86}Sr$, low $^{206}Pb/^{204}Pb$) and EM-2 (high $^{87}Sr/^{86}Sr$, intermediate $^{206}Pb/^{204}Pb$). These rocks have higher K_2O and K_2O/TiO_2 than HIMU. EM basalts have some trace element characteristics (e.g., high Rb/La, Ba/La, Th/U, and Rb/Sr and low Nb/La and U/Pb) that distinguish them from HIMU basalts, which have much more uniform trace element ratios, and are depleted in Rb, U, Th, Ba and Pb, and enriched in Nb and Ta relative to EM (Willbold and Stracke, 2006). EM1 and EM2 can be differentiated by the exceptionally low CaO/Al_2O_3 compositions found in EM1 (Jackson and Dasgupta, 2008), but cannot be clearly distinguished from each other on the basis of trace element ratios (Willbold and Stracke, 2006). The origins of the EM-1 source are complex to understand. Some argue that it is best described as a modified bulk-earth component (Hart, 1988).

The mantle source end-members described here provide a comparative framework of mantle origin within which the origins of basalts, the products of mantle melting, can be interpreted. To summarise the proposed origins of these components, EMI and EMII sources are thought to originate from subducted sediment, of pelagic and terrigeneous origins respectively. The DMM end-member represents the strongly depleted convecting upper mantle. The HIMU source is thought to represent subducted oceanic crust, whilst the FOZO component is postulated to originate from a lower mantle or plume source. Combining these distinctive heterogeneities into end-member ‘bins’ allows broad mantle origins to be defined for a given group of basalt samples, but is doubtless an oversimplification of the complexity of chemical heterogeneity in the mantle.

7.1.5 - Application of Mantle Component Analysis to Isotopic Signatures 12°60-14°N

The fields of DMM, HIMU, FOZO, EM1 and EM2 in the following section are from data from Hamelin and Allègre (1985); Zindler and Hart (1986); Hart (1984); Hart (1988); Hart and Staudigel (1989); Hart *et al.* (1992); Rollinson (1993); Hauri *et*

al. (1994) and Stracke *et al.* (2005). Isotopic characteristics of the mantle end-members are summarised in Table 14.

Source	$^{87}Sr/^{86}Sr$	$^{143}Nd/^{144}Nd$	$^{206}Pb/^{204}Pb$	$^{207}Pb/^{204}Pb$
DMM	0.7026	0.5131	15.511	15.36
HIMU	0.7025-0.7035	0.5110-0.5121	21.2-21.7	15.80-15.90
EMI	~0.7050	<0.5112	17.6-17.7	15.46-15.49
EMII	>0.7220	0.5110-0.5120	~18.6	~15.70
FOZO	0.7028-0.7034	0.51287-0.51301	19.5-20.5	15.55-15.71

Table 14: DMM isotope values from Su and Langmuir (2003), HIMU, EMI and EMII isotope values, from Rollinson (1993) p233-236, FOZO data from Hauri *et al*. (1994) and Stracke *et al*. (2005).

Isotopic data from 12°60'-14°N is shown in plots presented within the framework of the mantle end-members (DMM-EMI-EMII-HIMU-FOZO). The Atlantic data array (5°S-89°N) shows that basalts from the central Atlantic region have variable source contributions lying between DMM and various enriched components.

$^{208}Pb/^{204}Pb$ vs. $^{206}Pb/^{204}Pb$ data (Figure 66) show that the 12°60'N-14°N on-axis array lies parallel to the NHRL (Northern Hemisphere Reference Line) and appears to primarily represent mixing between DMM and FOZO. Displacement off the trend to higher $^{206}Pb/^{204}Pb$ values is seen for group M1 and group M2. In the case of group M2, this displacement appears to represent three-component mixing between DMM-HIMU-FOZO.

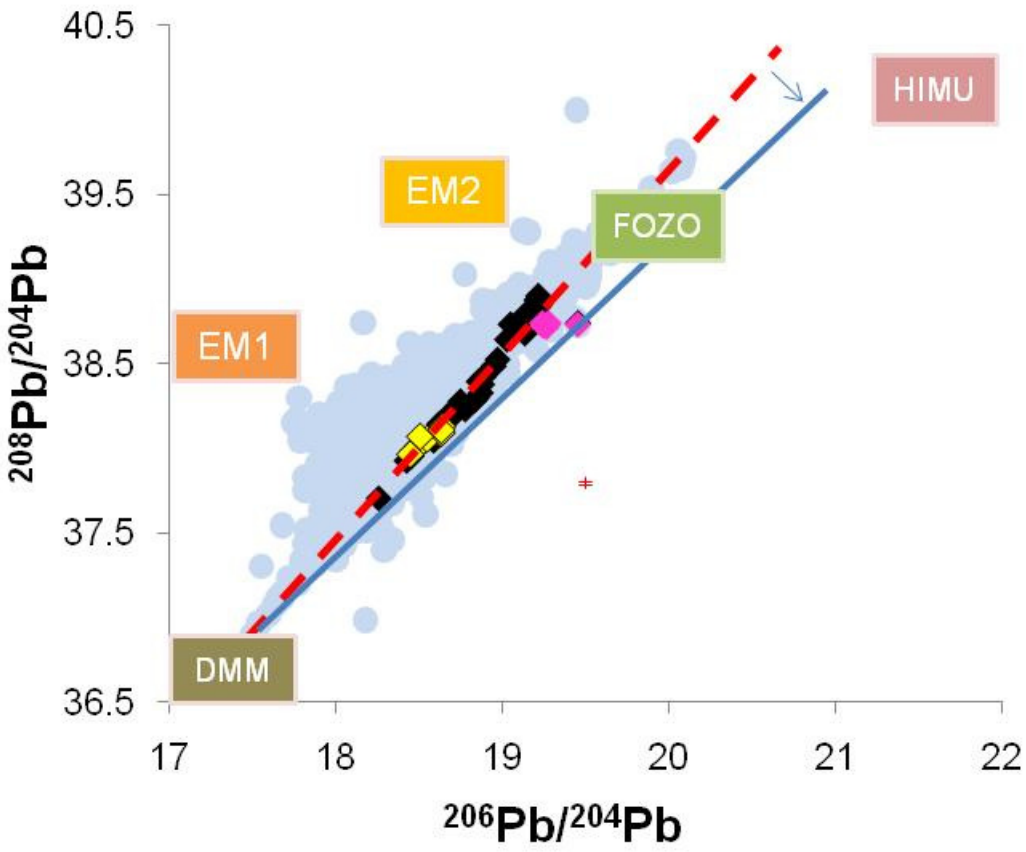

Figure 66: In the $^{208}Pb/^{204}Pb$ vs. $^{206}Pb/^{204}Pb$ plot, the 12°60'N-14°N on-axis array (black) lies parallel to the NHRL (Northern Hemisphere Reference Line, red broken line). The triangular array formed by Atlantic PetDB MORB data is shown in blue. The on-axis array appears to primarily represent mixing between DMM and FOZO. Displacement off the trend to higher $^{206}Pb/^{204}Pb$ values is seen for off-axis M1 (pink) and to a lesser extent for M2 (yellow) basalts, and appears to represent three-component mixing between DMM-HIMU-FOZO. Note that for M1, n=6, sample markers overlap. Mixing between DMM and a higher proportion of HIMU-FOZO is shown by the solid blue line. Errors for the data from this study (M1, M2, on-axis) are shown by red marker.

In $^{206}Pb/^{204}Pb$ vs. $^{143}Nd/^{144}Nd$, $^{87}Sr/^{86}Sr$, and $^{207}Pb/^{204}Pb$ isotope plots (Figures 66, 67, 68, 69, 70), a similar compositional range seen, defining mixing between primarily DMM-HIMU-FOZO, with M1 and M2 group basalts trending toward mixing with a greater proportion of HIMU. Plotting $^{143}Nd/^{144}Nd$ vs. $^{87}Sr/^{86}Sr$ (Figure 69) separates the HIMU and FOZO end-members spatially from EMI and EMII, showing that FOZO and HIMU are the enriched end-member components.

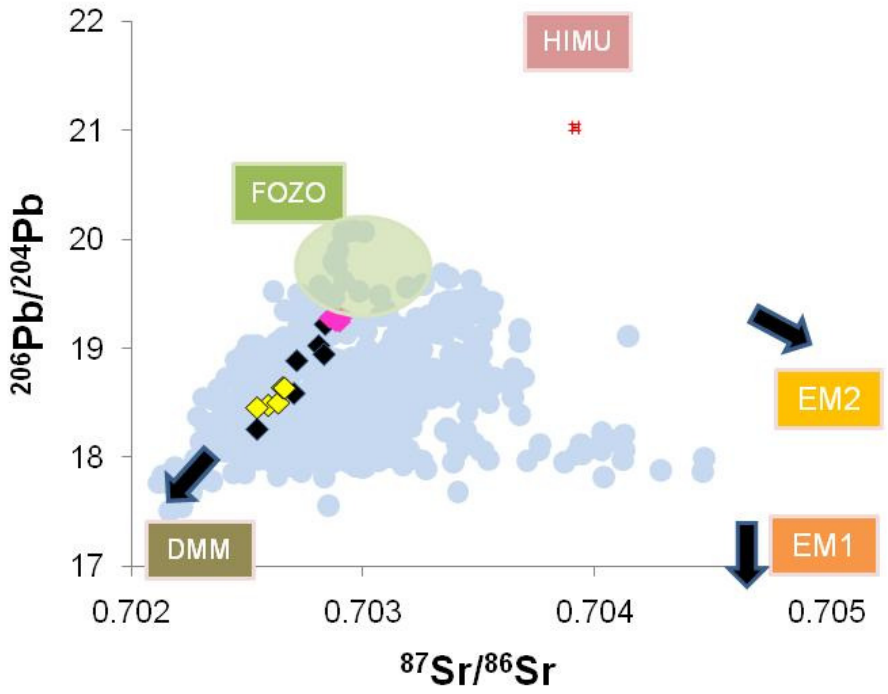

Figure 67: $^{206}Pb/^{204}Pb$ vs. $^{87}Sr/^{86}Sr$ isotope data for the Atlantic (blue, PetDB MORB data), on-axis rocks from 12°60'-14°N (black) and off-axis M1 (pink) and M2 (yellow) basalts. M1, M2 and on-axis rocks define mixing between primarily DMM-HIMU-FOZO, with M1 and M2 group basalts trending toward mixing with a greater proportion of HIMU. The translucent green oval shows the position of the FOZO array with greater precision than the label.

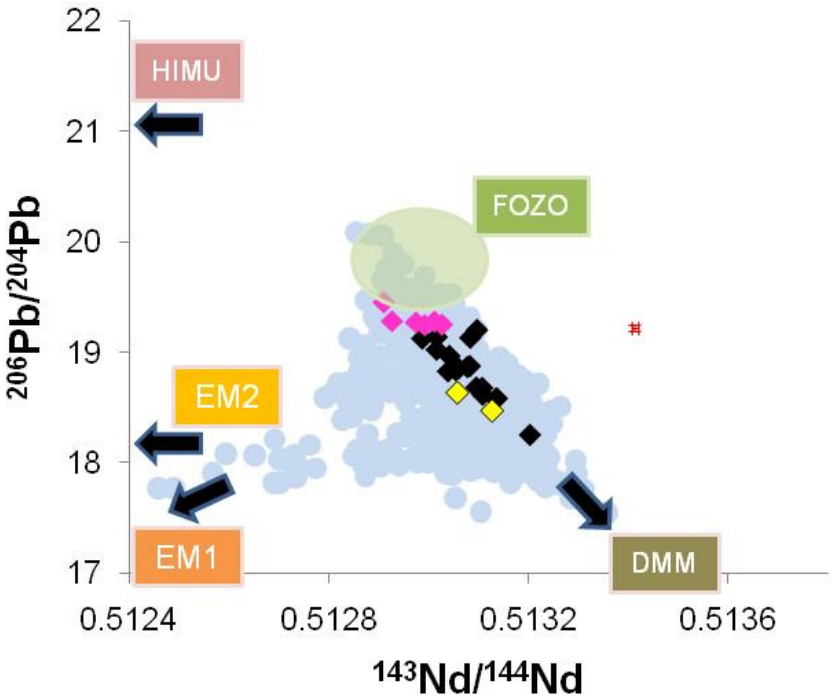

Figure 68: ^{143}Nd /^{144}Nd vs. $^{206}Pb/^{204}Pb$ isotope data for the Atlantic (PetDB, MORB blue), on-axis samples from 12°60'-14°N (black), and off-axis M1 (pink) and M2 (yellow) basalts define mixing between primarily DMM-HIMU-FOZO. The translucent green oval shows the position of the FOZO array with greater precision than the label.

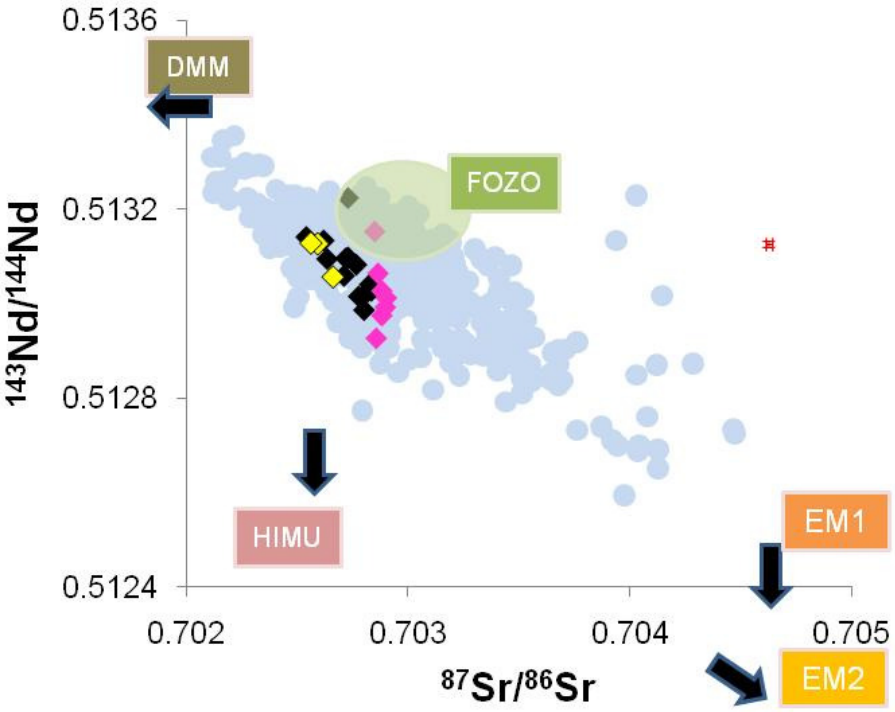

Figure 69: ^{143}Nd /^{144}Nd vs. $^{87}Sr/^{86}Sr$ data (Atlantic PetDB MORB data –blue, on-axis 12°60'N-14°N - black, off-axis M2 - yellow, M1 - pink) separates the HIMU and FOZO end-members spatially from EMI and EMII, showing that FOZO and HIMU are the enriched end-member components contributing to the 12°60'N-14°N array, and that M1 forms primarily from mixing between HIMU and FOZO.The translucent green oval shows the position of the FOZO end-member with greater precision than the label.

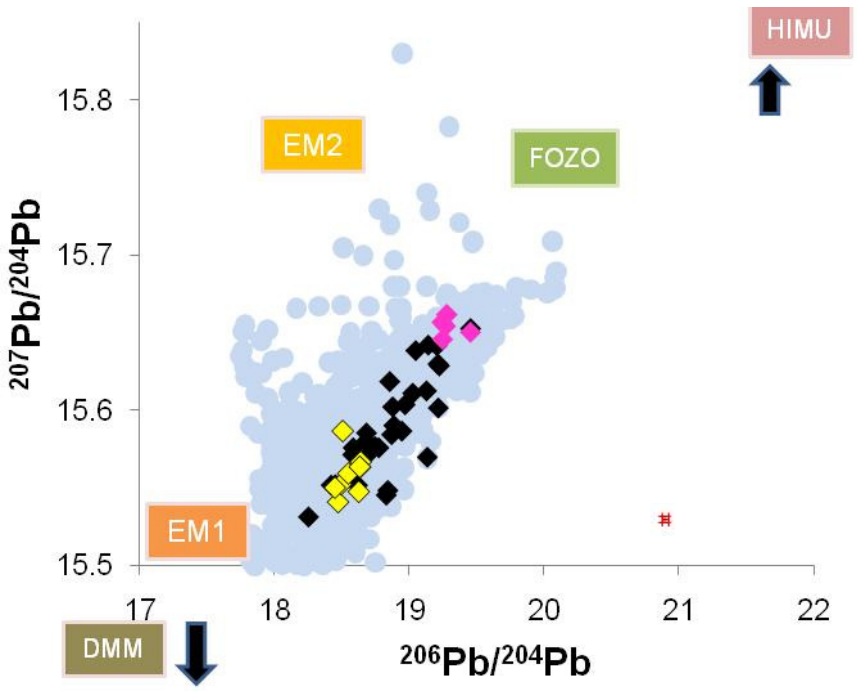

Figure 70: $^{207}Pb/^{204}Pb$ vs. $^{206}Pb/^{204}Pb$ isotope data for the Atlantic (PetDB MORB, blue), on-axis samples from 12°6'-14°N (black), and off-axis M1 (pink) and M2 (yellow) basalts define mixing between primarily DMM-HIMU-FOZO. The translucent green oval shows the position of the FOZO array with greater precision than the label.

The Δ7/4 and Δ8/4 parameters represent the distance of a sample from a point on the NHRL with the same $^{206}Pb/^{204}Pb$, the distance being in units of $^{207}Pb/^{204}Pb$ and $^{208}Pb/^{204}Pb$ respectively (see Hart, 1984). The Δ7/4 and Δ8/4 plots (Figure 71) show a trend toward HIMU for M1 and M2 basalts. This trend is most clearly illustrated by the Δ8/4 vs. $^{206}Pb/^{204}Pb$, where M1 basalts extend to very low values of Δ8/4 (~-40).

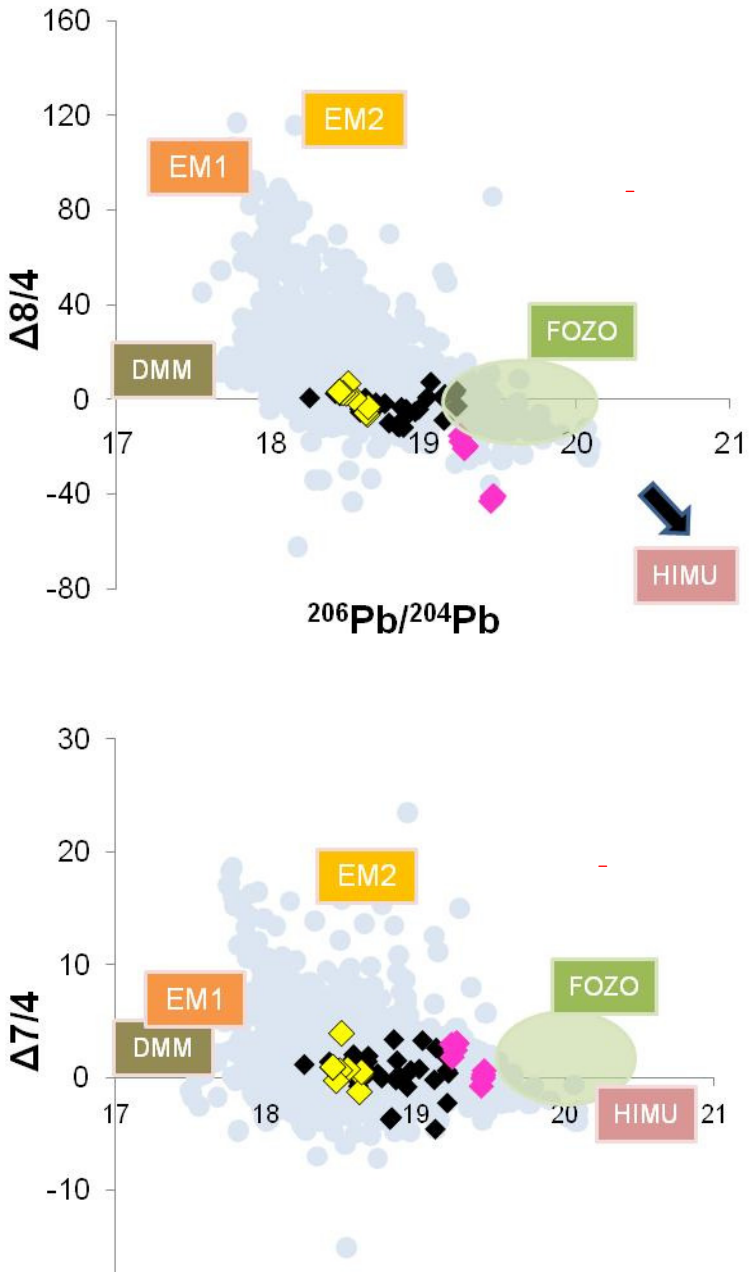

Figure 71: Δ7/4 and Δ8/4 plots for Atlantic (PetDB MORB, blue), on-axis 12°6'N-14°N (black), and off-axis basalts M2 (yellow) and M1 (pink) show a trend toward HIMU for M1 and M2 basalts. This trend is most clearly illustrated by the Δ8/4 vs. $^{206}Pb/^{204}Pb$, where M1 basalts extend to very low values of Δ8/4 (~-40). The translucent green oval shows the position of the FOZO array with greater precision than the label.

The isotope data presented above suggests that basalts in the 12°60'-14°N region are formed by combination of DMM with HIMU-FOZO sources. Whilst on-axis and M2 data appears to form triangular arrays vectoring between all three components, M1 appear to lie on a single vector perpendicular to the general DMM – HIMU trend, suggesting mixing dominated by the enriched end-member components FOZO and HIMU. This HIMU-FOZO mixing is very clear in the diagram of $^{87}Sr/^{86}Sr$ vs. $^{143}Nd/^{144}Nd$, where M1 samples form a vertical trend between the two end-members. Similar clear tends are evident in Δ8/4 and Δ7/4 vs. $^{206}Pb/^{204}Pb$ plots.

The HIMU end-member also appears to contribute more to the formation of M2 data than to the on-axis array. The Δ8/4 vs. $^{206}Pb/^{204}Pb$ data (Figure 70) illustrates these trends clearly. At the point along the ridge where the M1 melts are generated, the enriched end-member components become suddenly more significant, especially in the case of HIMU. Since M2 melts, which clearly form from mixing between DMM-HIMU-FOZO are produced at the same site as M1 melts, the mantle source lying beneath the 13°19'N OCC must contain all three components.

Very low melt-fraction melting of this three component source could generate HIMU-FOZO M1 melts with negligible contributions from DMM. This is because at very low melt fraction, incompatible elements abundant in HIMU and FOZO source material will be preferentially taken up in the melt, whilst less fusible components in DMM will not be extracted until higher melt fractions are reached.

However, this limits production of M1 melts to a short timeframe, where initial melting of the source rapidly strips out the volatile and LREE-rich material provided by HIMU and FOZO. Less enriched source material would be available for subsequent melts produced at this site, leading to the production of compositions more dominated by DMM, such as M2.

The production M1-like, HIMU-FOZO dominated melts may occur at other sites (other OCCs?) along the segment and further afield, if very low melt fractions are produced from the same bulk source.

Trace element data and trace element ratio data can be used to further elucidate the nature of mantle sources and distinguish between source reservoirs. The ratio of a pair of highly incompatible elements will vary little during fractional crystallisation or partial melting, and therefore could potentially be used to identify source characteristics.

Plots of highly incompatible element ratios are therefore used to investigate patterns of source enrichment independent of fractional crystallisation and degree of partial melting. These plots show that M1 basalts formed from a highly incompatible element enriched source, whilst the source of on-axis and M2 basalts is substantially less enriched.

Table 15 summarises trace element ratio concentration data for a range of incompatible trace element pairs in this study, and also shows average values for basalts with various source characteristics. Note the similarity between HIMU OIB and M1 basalts.

General	**Zr/Nb**	**La/Nb**	**Ba/Nb**	**Rb/Nb**	**Ba/La**	**Ce/Pb**
N MORB	30.0	1.07	1.7-8.0	0.36	4	25.0
E MORB			4.9-8.5			
HIMU OIB	**3.2-5.0**	**0.66-0.77**	**4.9-6.9**	**0.35-0.38**	**6.8-8.7**	**31.5**
EMI OIB	4.2-11.5	0.86-1.19	11.4-17.8	0.88-1.17	13.2-16.9	21.4
EMII OIB	4.5-7.3	0.89-1.09	7.3-13.3	0.59-0.85	8.3-11.3	21.2
12°6'-14°N	Data from this study:					
On- Axis	8.9	0.68	6.9	0.53	9.8	24.0
M1	**4.9**	**0.60**	**6.1**	**0.42**	**10.2**	**29.6**
M2	12.1	0.79	6.3	0.57	8.2	21.7

Table 15: Trace element ratio concentration data for a range of incompatible trace element pairs, showing average values for basalts with a variety of source characteristics. Data from Hart *et al*. (1992), Armienti and Gasperini (2007), this study.

These data show that the M1 basalt enrichment is geochemically similar in trace element space to that found in average HIMU OIB, and that the enrichment does

not resemble enrichment patterns arising from EMI or EMII sources. Plotting two of these ratios against each other shows the trend of 12°60'N-14°N data from DMM toward HIMU type compositions, with M1 compositions characteristic of HIMU OIB (Figure 72).

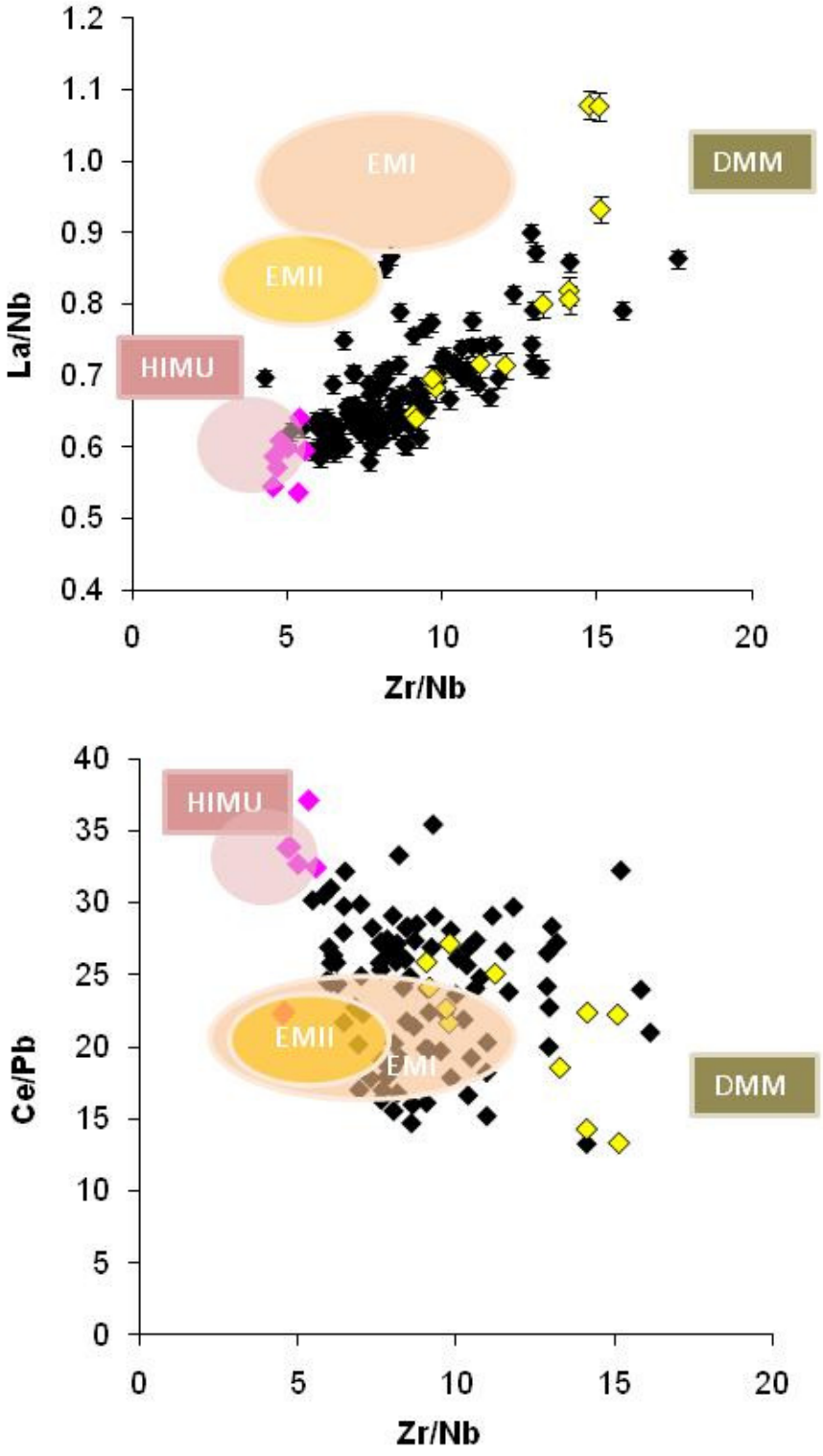

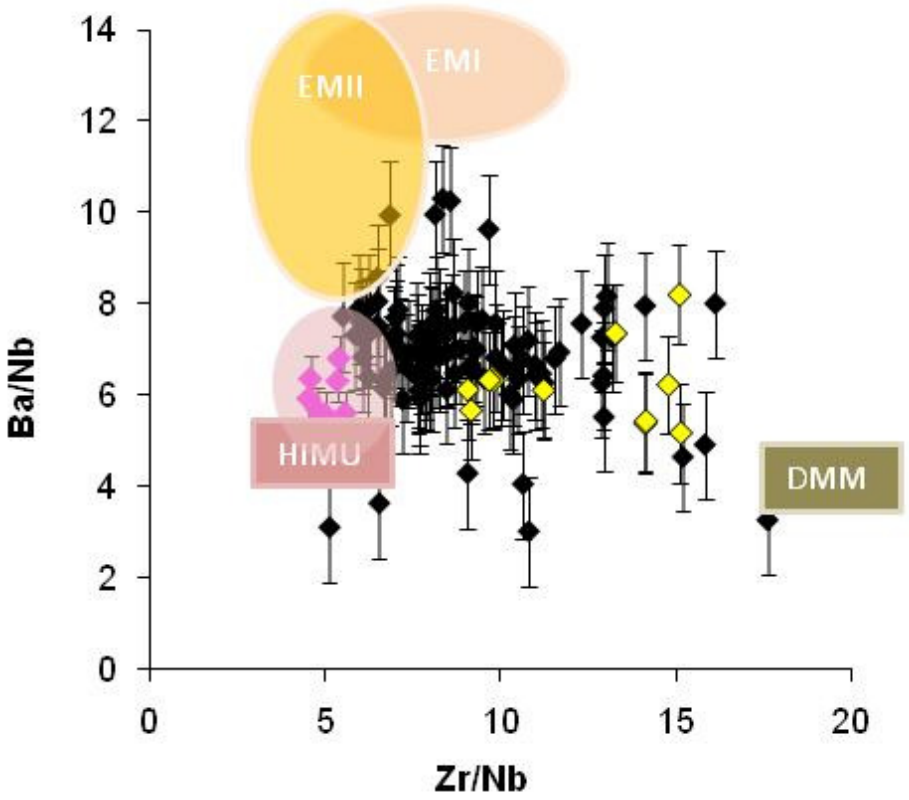

Figure 72: Trace element ratio data for on-axis (black), and off-axis M2 (yellow) and M1 (pink) basalts. This trace element ratio data is fractionation and melt fraction independent, and shows that M1 rocks form from an enriched HIMU source, whilst on-axis and M2 rocks form from more depleted bulk sources. For the sources component field positions, refer to Table 13.

HIMU (high μ) sources are enriched in U and Th relative to Pb, without an accompanying increase in Rb/Sr. Figure 73 shows that M1 basalts trend toward high U/Pb and Th/Pb values, but have Rb/Sr values which lie within the on-axis array, suggesting a HIMU-like origin.

Radiogenic isotope ratios are primarily a function of time integrated daughter ingrowth reflecting source composition. As such they can be used in conjunction with trace element ratios (a function of both source and melt fraction with minimal crystallisation effects) to distinguish trends arising from variable degrees of melting with those arising from source characteristics. Figure 74 combines isotope and trace element ratio parameters, and shows that M1 basalts are the most enriched in terms of source, and M2 basalts are some of the most depleted (enriched here referring to radiogenic Sr and Pb, and unradiogenic Nd isotopes).

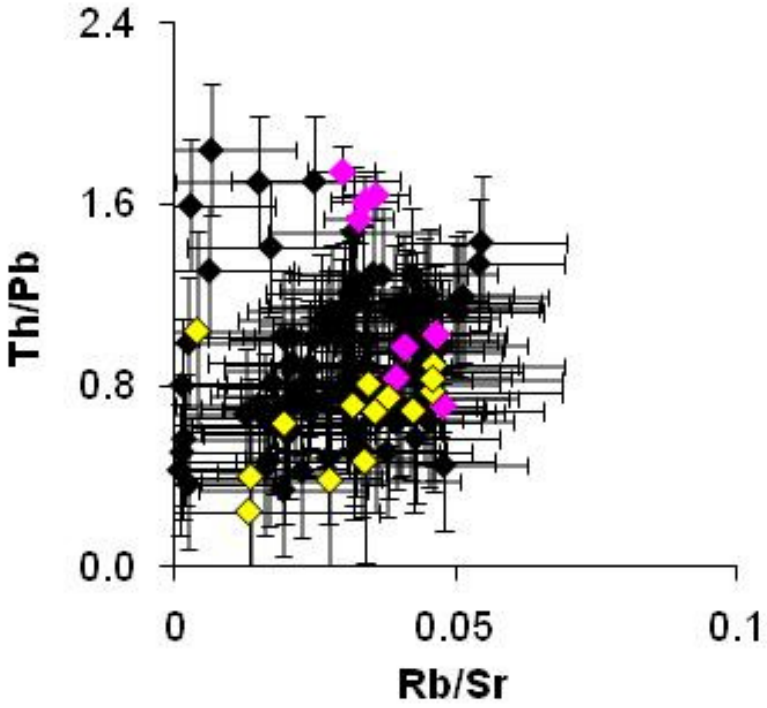

Figure 73: Trace element ratio data for on-axis (black) and off-axis M2 (yellow) and M1 (pink) basalts. HIMU sources are enriched in Th relative to Pb, without an accompanying increase in Rb/Sr. M1 basalts trend toward high Th/Pb values, but have Rb/Sr values which lie within the on-axis array.

The data also suggest that melt fraction is very variable in on-axis rocks, but appears substantially less so in OCC samples from M1 and M2, where data are tightly clustered on the correlation line. For example, the on-axis symbols show variable La/Sm for a given isotope ratio, indicating more variable melt fractions than M1 and M2. Several samples have higher melt fraction than the main trend (i.e. they lie at lower La/Sm for given $^{206}Pb/^{204}Pb$).

A line joining M1 and M2 appears to define the upper envelope of high La/Sm, Zr/Y and Dy/Yb for a given isotope ratio, and hence defines the trend with the lowest melt fraction. The on-axis samples all lie either on or beneath this M1-M2 line and hence have variably higher melt fraction. This observation shows that the lowest melt fractions produced on the ridge from before OCC initiation to the present were formed prior to the development of the OCC, and reinforces the connection between decreased melt fraction and OCC development.

The very good correlations between isotopes and trace element ratios indicate that the data array here results mostly from variations in bulk source enrichment, whilst melt fraction exerts a secondary control.

M1 basalts have discordant correlations to the on-axis and M2 data, which suggests contributions from different end-member sources, forming an enriched bulk source, with little contribution from the depleted end-member DMM. These trends support the findings of the isotope data earlier in this chapter, where formation of M1 is attributed to mixing between primarily HIMU and FOZO end-member sources. In chapter 6, the trace element composition of talus from the 13°19'N core complex was shown to be indistinguishable from that of M2 basalts, but clearly substantially different from M1. This talus must have originated from the ridge axis (i.e. forming the hanging wall of the OCC), before being dragged over the OCC surface to its present day position. As the talus is very similar in composition to M2, but different from M1, this supports the hypothesis that M1 melts were produced for only a very short period in time, prior to the initiation of the core complex.

The duration of generation of M1 melts must have been short, and ceased rapidly after OCC onset. If M1 melting had proceeded for long, we would expect to find M1 material in the OCC talus, dragged from the axis as OCC formation continued. Eruption of M2 must have begun shortly before OCC onset, as M2 melts are found on the breakaway ridge of the OCC, as well as on the younger parts of the surface. M2 melts are sampled by the OCC throughout its lifetime, and this suggests that a more substantial amount of M2 than M1 melt is produced. This may also indicate that production of M2 lasts for some time following core complex formation.

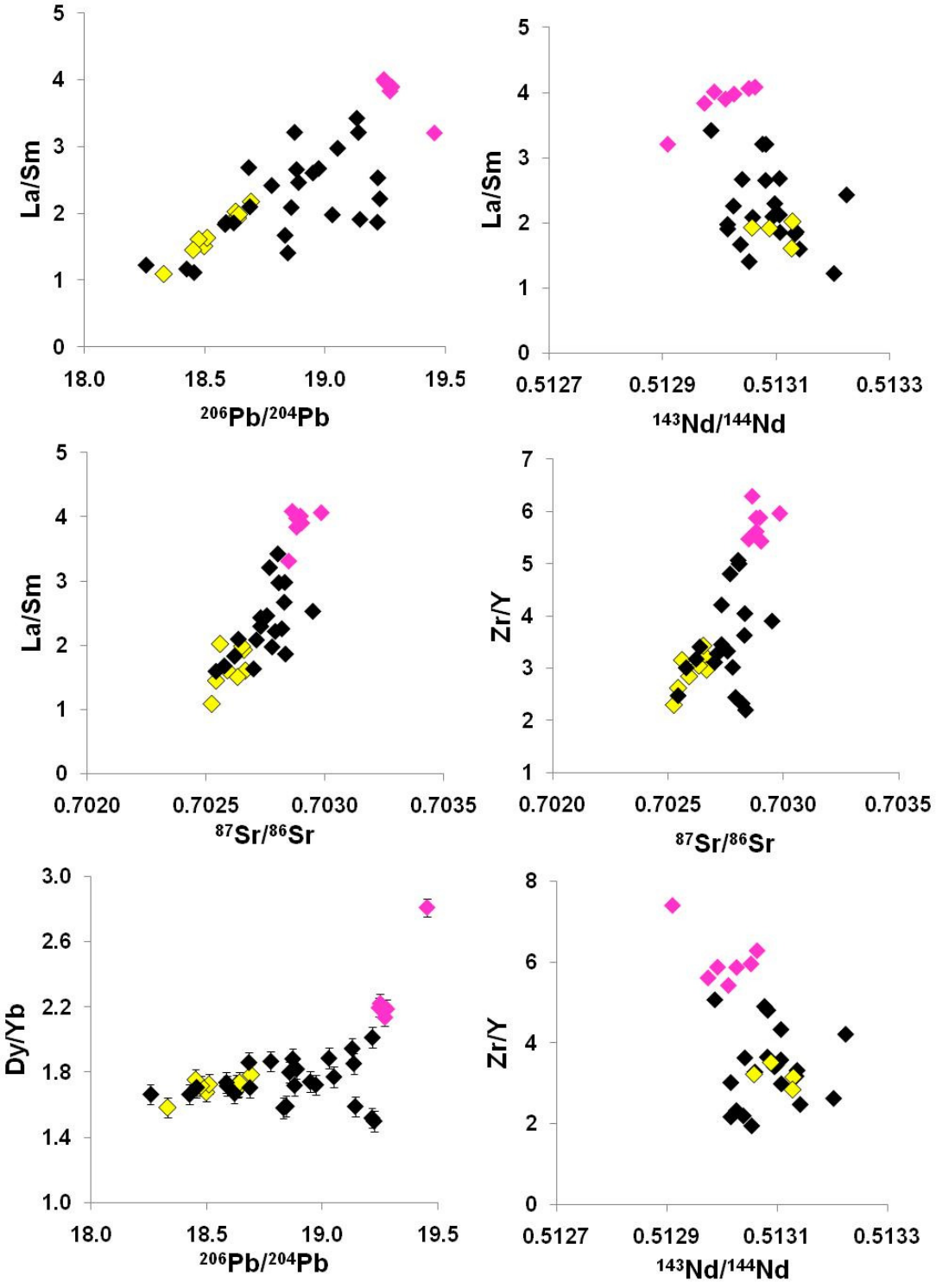

Figure 74: Isotope ratio vs. trace element ratio plots show that off-axis M1 (pink) basalts are the most enriched in terms of source, whilst M2 (yellow) basalts are some of the most depleted (enriched here referring to radiogenic Sr and Pb, and unradiogenic Nd isotopes). The on-axis array from 12°6'-14°N (black) occupies the centre of the compositional array.

7.1.6 – Summary

Data indicate that M1 (E-MORB) and M2 (E-MORB to N-MORB), as well as their on-axis counterparts, were generated by a combination of the depleted MORB mantle source (DMM) with enriched components HIMU and FOZO. The identification of mixing in the region between DMM-HIMU and at least one other component confirms the findings of Dosso *et al.* (1991), and echoes the findings of Hannigan *et al*. (2001) for segments further south on the central MAR, raising the possibility that these geographically close segments share mantle source origins.

On-axis basalts appear to have a wide range of compositions inherited from the source, from N-MORB to E-MORB. Most rocks fall within the E-MORB field, and are more enriched in trace elements such as Nb and Zr (see TE data, chapter 6) than expected for typical MORB, reflecting input from FOZO and HIMU source material. They contain accumulated plagioclase as evidenced by high Al_2O_3, CaO and low Fe_2O_3, as well as positive Eu anomalies. Trace element ratio vs. isotope ratio plots show that on-axis basalts represent variable melt fractions. There are no geochemical differences between on-axis basalts from OCC and magmatic sites.

M1 and M2 basalts, formed off-axis at the time of initiation of the 13°19'N OCC, have strongly bimodal compositions. The range of compositions in these rocks is shown to be independent of fractionation and arises as a function of both source composition and melt fraction.

The HREE depletion and low Yb/Lu and Dy/Yb ratio values for M1 basalts suggests that the melting episode that formed these rocks started at depths >60km, in the stability field of garnet. This finding is supported by textural and mineralogical evidence, which suggests that the melts segregated at pressures greater than ~10Kbar, forming clinopyroxene crystals. These were then carried as an accumulated phase in melts rapidly erupted from their formation depth and quenched on the seafloor, forming dendritic olivines. Mineral textures indicate short residence times in small melt lenses, rather than large magma chambers.

The M1 and M2 basalts form isotope ratio trends which point more strongly toward HIMU than the on-axis basalts. The extreme incompatible element enrichments and isotope ratio vectors of M1 magmas suggest that they form as small melt fractions of a fertile HIMU-FOZO source, with negligible contribution from DMM. Since DMM is present in the source of M1, the melting episode that formed these lavas must have generated very low melt fractions, but ceased before significant amounts of more compatible elements (e.g. HREE) entered the melt. M2 rocks may form from higher melt fractions than M1, where the HIMU-FOZO input is diluted by DMM to produce compositions approaching N-MORB.

Isotopic evidence and data on the composition of basaltic talus on the core complex dome at 13°19'N both suggest that M1 basalts were produced over a very short time. Once HIMU-FOZO material was stripped out of the source, more DMM-dominated melts were produced, probably forming M2 melts as well as erupting material which ultimately broke up on the detachment surface and was dragged over the OCC dome as talus. If M1 melts coexisted with M2 melts, we would expect melt mixing to dilute the low melt fractions with DMM, and so it is clear that M1 melting occurred as a short-lived and separate magmatic phase, prior to core complex development.

7.2. – MELT FRACTION AND SOURCE MODELLING AT THE 13°19'N OCC

Geochemical data suggest that M1 and M2 off-axis (13°19'N) basalts and on-axis rocks from 12°60'-14°N, vary in terms of melt fraction, source composition and melting conditions such as depth of melting and length of the melting path.

To test the conditions of melting for M1, M2 and on-axis rock samples, and the geochemistry of the source material that formed them, a simple fractional melting model was employed, using REE compositions, and the equations of Shaw (1970) which describe trace element distribution during melting.

Melts are generated by iteratively removing 0.1% melt fractions from the bulk residuum. These instantaneous melts are combined with each iteration to form an extracted bulk melt.

In fractional melting models, melt leaves the system as soon as it is formed, and the bulk composition of the solid residuum changes continuously. This is thought to be more likely to occur at mid-ocean ridges than batch melting, whereby melt remains in contact with the residual solid throughout melting (Johnson *et al.,* 1990). This model does not take into account the effects of fractional crystallisation on the elemental species which occupy the melt at any particular time. Rather, the model creates a homogeneous melt which does not crystallise. Whilst this is a limitation, the model produces valid estimates of bulk chemistry.

Modelling melting in the mantle is complex, and requires many assumptions, which simplify the processes involved. In reality, melting is likely to lie somewhere between the batch and fractional melting end-members. Further to this, geochemistry is complicated by interaction of rising melt with wall rock, so that the composition of a melt does not simply evolve from the composition of the isolated mantle source. Further to this, in reality, rising melts mix with each other as they pass through the mantle, altering the compositions of the basalts that result.

In real systems, the presence of H_2O in the source greatly alters melting conditions. The addition of a small amount of water can significantly lower the melting temperature of the mantle. In addition, the presence of water broadens the temperature range of melting (e.g. Inoue, 1994).

The melting model applied here assumes completely fractional melting, and cannot account for the effects of varying H_2O content in the source on the temperature and pressure of melting. This is a major assumption, as H_2O content substantially modifies melting behaviour. However, melting is the presence of H_2O is highly complex, and beyond the scope of this study.

The model assumes a bulk source with compositions formed by various combinations of HIMU and DMM end-members, as modelled by others (see Tables 15 and 16. It should be noted that the model only uses a single set of

mineral modes for all combinations of DMM-HIMU. In reality, a HIMU mantle may have a higher garnet mode than DMM.

7.2.1 - Model Setup

The melting model developed applies the equations of Shaw (1970) which describe trace element distribution during melting. The model generates REE compositions (La to Lu) for melts of a source which is input into the model. This source is melted iteratively (each iteration removing a melt fraction of 0.1%) to produce a series of cumulative melt fractions. Trace element partition coefficients used in these calculations are from McKenzie and O'Nions (1991), and can be found in Appendix 4.

Data output from the model are analysed to determine which mantle mineral assemblage and melt fraction best reproduces end-member compositions for M1, M2 and on-axis basalts.

Geochemical data has shown that the mantle source beneath the region surrounding the Fifteen-Twenty Fracture Zone (Dosso *et al.*, 1991; this study) and other segments on the central MAR (Schilling *et al.*, 1994, Hannigan *et al*., 2001) is best described as a combination of DMM and HIMU with another less well defined source or sources. This source is FOZO-like in the case of the region underlying the Fifteen-Twenty Fracture Zone (Hannigan *et al*., 2001).

To attempt to reproduce the main variability of the 12º60'-14°N basalt compositions, the mantle source input for this model (ppm concentrations of La to Lu) is based primarily upon mixing of source end-member compositions of DMM and HIMU in a range of proportions to form different bulk sources.

Various DMM and HIMU compositions and combinations are used in the model (summarised in Table 16).

Source: (ppm)	HIMU	Av. DMM	Enr. DMM	Dep. DMM
Composition:				
La	2.442	0.192	0.253	0.134
Ce	4.415	0.55	0.726	0.421
Pr	0.465	0.107	0.132	0.087
Nd	1.801	0.581	0.703	0.483
Sm	0.398	0.239	0.273	0.210
Eu	0.131	0.096	0.108	0.086
Gd	0.422	0.358	0.397	0.324
Tb	0.081	0.070	0.076	0.064
Dy	0.487	0.505	0.543	0.471
Ho	0.102	0.115	0.123	0.108
Er	0.299	0.348	0.369	0.329
Tm	0.041	*0.0510*	*0.0538*	*0.0484*
Yb	0.278	0.365	0.382	0.348
Lu	0.043	0.058	0.06	0.056

Table 16: Raw compositions of input sources. Modelled HIMU composition from Hannigan *et al*. (2001). Enriched, depleted and average DMM are from Workman and Hart, (2004). Tm data for DMM are unavailable, and so data (red, italicised) are interpolated and included to allow plotting of data on logarithmic REE plots.

The compositions of these mantle end-members are shown on the REE plot (Figure 75):

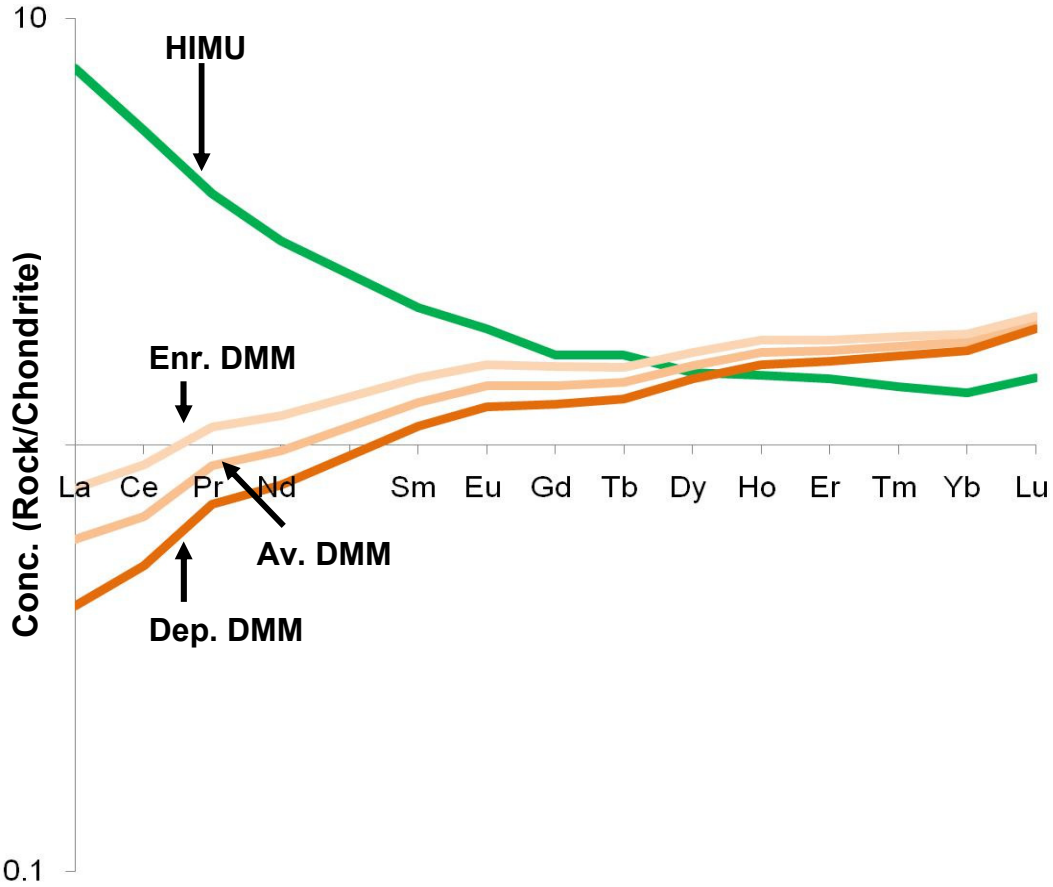

Figure 75: REE plot showing mantle end-member inputs for modelling. HIMU (green) composition is that of Hannigan *et al*., (2001). Enriched (pale brown), depleted (dark brown) and average DMM (medium brown) compositions are from Workman and Hart (2004).

The HIMU and DMM compositions have been mixed together in the following combinations and proportions (Tables 17-19) to form a series of bulk model sources. The REE chemistry of the bulk input sources is illustrated in the REE plots (76-78), where figures indicate the proportion of HIMU in the source.

MODEL 1: Bulk Sources Calculated from HIMU and Av. DMM Combinations:

Bulk Source (HIMU-Av. DMM) Composition (ppm)

% DMM	50	55	60	65	70	75	80	85	90	59	100
% HIMU	50	45	40	35	30	25	20	15	10	5	0
La	1.317	1.205	1.092	0.980	0.867	0.755	0.642	0.530	0.417	0.305	0.192
Ce	2.483	2.289	2.096	1.903	1.710	1.516	1.323	1.130	0.937	0.743	0.550

Pr	0.286	0.268	0.250	0.232	0.214	0.197	0.179	0.161	0.143	0.125	0.107
Nd	1.191	1.130	1.069	1.008	0.947	0.886	0.825	0.764	0.703	0.642	0.581
Sm	0.319	0.311	0.303	0.295	0.287	0.279	0.271	0.263	0.255	0.247	0.239
Eu	0.114	0.112	0.110	0.108	0.107	0.105	0.103	0.101	0.100	0.098	0.096
Gd	0.390	0.387	0.384	0.380	0.377	0.374	0.371	0.368	0.364	0.361	0.358
Tb	0.076	0.075	0.074	0.074	0.073	0.073	0.072	0.072	0.071	0.071	0.070
Dy	0.496	0.497	0.498	0.499	0.500	0.501	0.501	0.502	0.503	0.504	0.505
Ho	0.109	0.109	0.110	0.110	0.111	0.112	0.112	0.113	0.114	0.114	0.115
Er	0.324	0.326	0.328	0.331	0.333	0.336	0.338	0.341	0.343	0.346	0.348
Tm	0.046	0.047	0.047	0.048	0.048	0.049	0.049	0.050	0.050	0.051	0.051
Yb	0.322	0.326	0.330	0.335	0.339	0.343	0.348	0.352	0.356	0.361	0.365
Lu	0.051	0.051	0.052	0.053	0.054	0.054	0.055	0.056	0.057	0.057	0.058

Table 17: Bulk compositions calculated from mixing between Av. DMM (Workman and Hart (2004), and HIMU (Hannigan *et al*., (2001) end-members.

The compositions are shown on the REE plot (Figure 76) below:

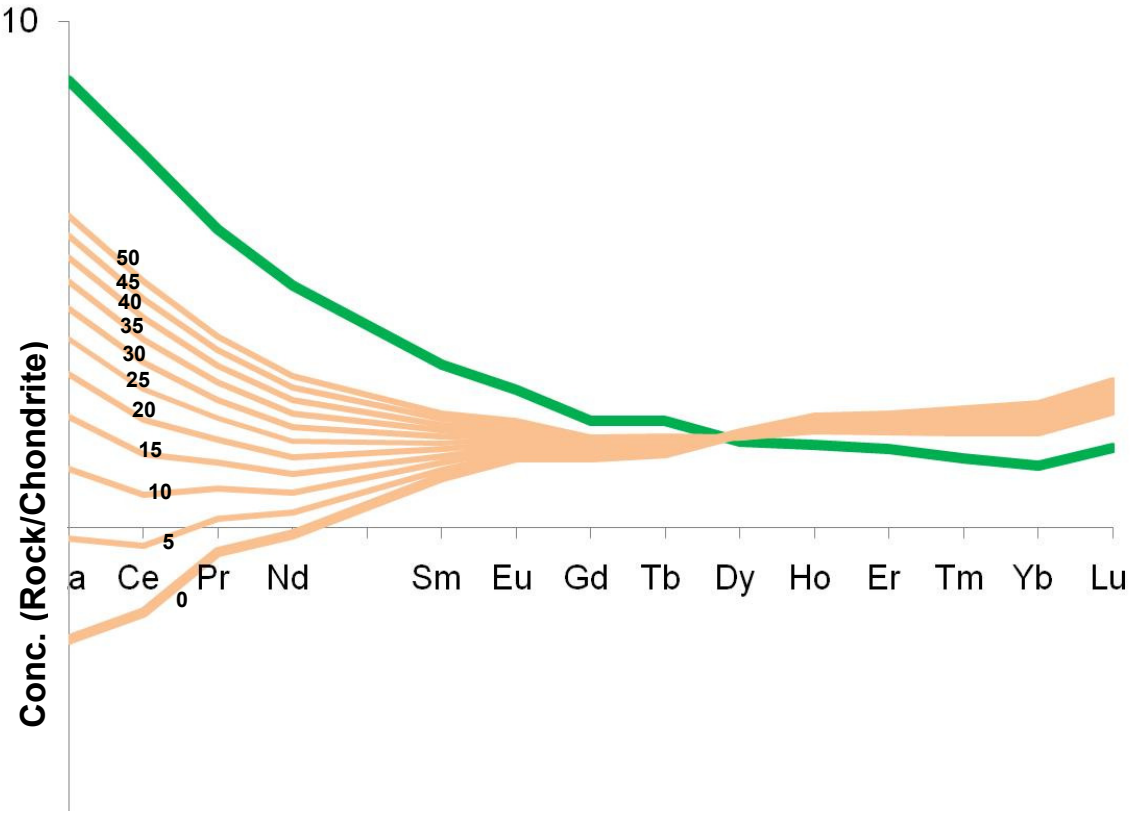

Figure 76: REE plot to illustrate bulk compositions calculated from mixing between Av. DMM (Workman and Hart (2004), and HIMU (Hannigan *et al,*. (2001) end-members.

MODEL 2: Bulk Sources Calculated from HIMU and Enr. DMM Combinations

Bulk Source (HIMU- Enr. DMM) Composition (ppm)											
% DMM	50	55	60	65	70	75	80	85	90	59	100
% HIMU	50	45	40	35	30	25	20	15	10	5	0
La	1.348	1.238	1.129	1.019	0.910	0.800	0.691	0.581	0.472	0.362	0.253
Ce	2.571	2.386	2.202	2.017	1.833	1.648	1.464	1.279	1.095	0.910	0.726
Pr	0.299	0.282	0.265	0.249	0.232	0.215	0.199	0.182	0.165	0.149	0.132
Nd	1.252	1.197	1.142	1.087	1.032	0.978	0.923	0.868	0.813	0.758	0.703
Sm	0.336	0.329	0.323	0.317	0.311	0.304	0.298	0.292	0.286	0.279	0.273
Eu	0.120	0.118	0.117	0.116	0.115	0.114	0.113	0.111	0.110	0.109	0.108
Gd	0.410	0.408	0.407	0.406	0.405	0.403	0.402	0.401	0.400	0.398	0.397
Tb	0.079	0.078	0.078	0.078	0.078	0.077	0.077	0.077	0.077	0.076	0.076
Dy	0.515	0.518	0.521	0.523	0.526	0.529	0.532	0.535	0.537	0.540	0.543
Ho	0.113	0.114	0.115	0.116	0.117	0.118	0.119	0.120	0.121	0.122	0.123
Er	0.334	0.338	0.341	0.345	0.348	0.352	0.355	0.359	0.362	0.366	0.369
Tm	0.047	0.048	0.049	0.049	0.050	0.051	0.051	0.052	0.053	0.053	0.054
Yb	0.330	0.335	0.340	0.346	0.351	0.356	0.361	0.366	0.372	0.377	0.382
Lu	0.052	0.052	0.053	0.054	0.055	0.056	0.057	0.057	0.058	0.059	0.060

Table 18: Bulk compositions calculated from mixing between Enr. DMM (Workman and Hart (2004), and HIMU (Hannigan *et al*., (2001) end-members.

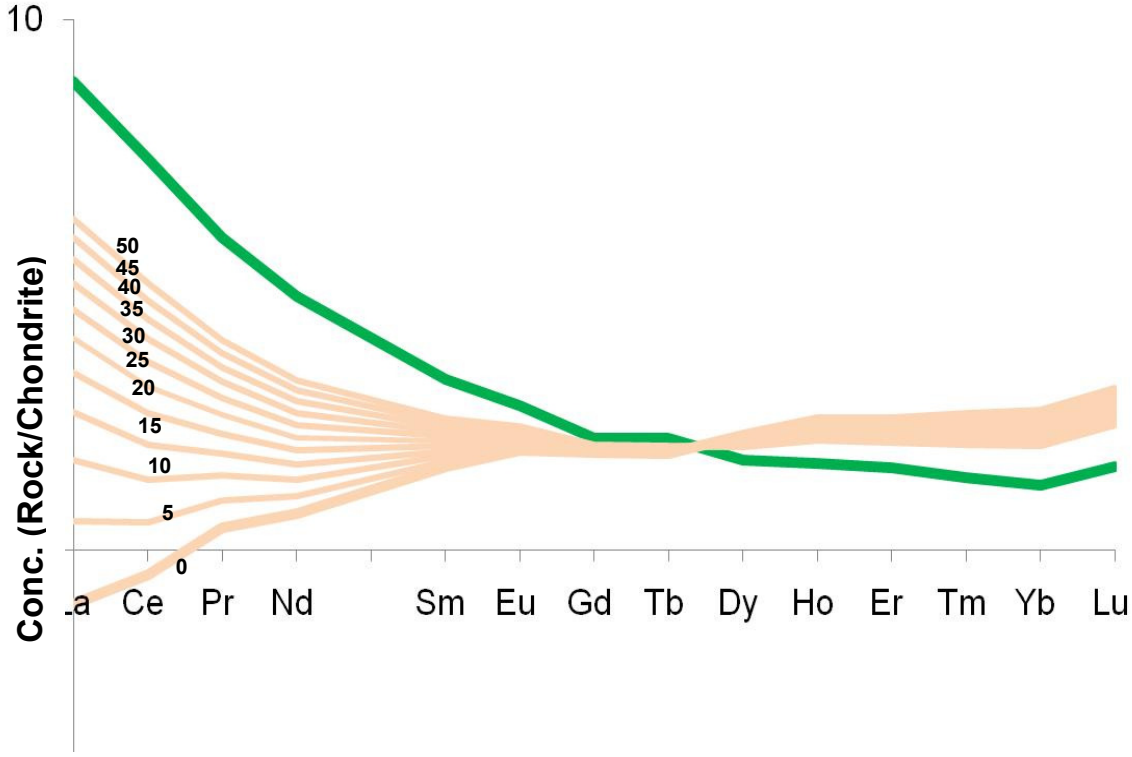

Figure 77: REE plot to illustrate bulk compositions calculated from mixing between Enr. DMM (Workman and Hart (2004), and HIMU (Hannigan *et al*., (2001) end-members.

MODEL 3: Bulk Sources Calculated from HIMU and Dep. DMM Combinations

Bulk Source (HIMU Dep. DMM) Composition (ppm)											
% DMM	50	55	60	65	70	75	80	85	90	59	100
% HIMU	50	45	40	35	30	25	20	15	10	5	0
La	1.288	1.173	1.057	0.942	0.826	0.711	0.596	0.480	0.365	0.249	0.134
Ce	2.418	2.218	2.019	1.819	1.619	1.420	1.220	1.020	0.820	0.621	0.421
Pr	0.276	0.257	0.238	0.219	0.200	0.182	0.163	0.144	0.125	0.106	0.087
Nd	1.142	1.076	1.010	0.944	0.878	0.813	0.747	0.681	0.615	0.549	0.483
Sm	0.304	0.295	0.285	0.276	0.266	0.257	0.248	0.238	0.229	0.219	0.210
Eu	0.109	0.106	0.104	0.102	0.100	0.097	0.095	0.093	0.091	0.088	0.086
Gd	0.373	0.368	0.363	0.358	0.353	0.349	0.344	0.339	0.334	0.329	0.324
Tb	0.073	0.072	0.071	0.070	0.069	0.068	0.067	0.067	0.066	0.065	0.064
Dy	0.479	0.478	0.477	0.477	0.476	0.475	0.474	0.473	0.473	0.472	0.471
Ho	0.105	0.105	0.106	0.106	0.106	0.107	0.107	0.107	0.107	0.108	0.108
Er	0.314	0.316	0.317	0.319	0.320	0.322	0.323	0.325	0.326	0.328	0.329
Tm	0.045	0.045	0.045	0.046	0.046	0.047	0.047	0.047	0.048	0.048	0.048
Yb	0.313	0.317	0.320	0.324	0.327	0.331	0.334	0.338	0.341	0.345	0.348
Lu	0.050	0.050	0.051	0.051	0.052	0.053	0.053	0.054	0.055	0.055	0.056

Table 19: Bulk compositions calculated from mixing between Dep. DMM (Workman and Hart (2004), and HIMU (Hannigan *et al*., (2001) end-members.

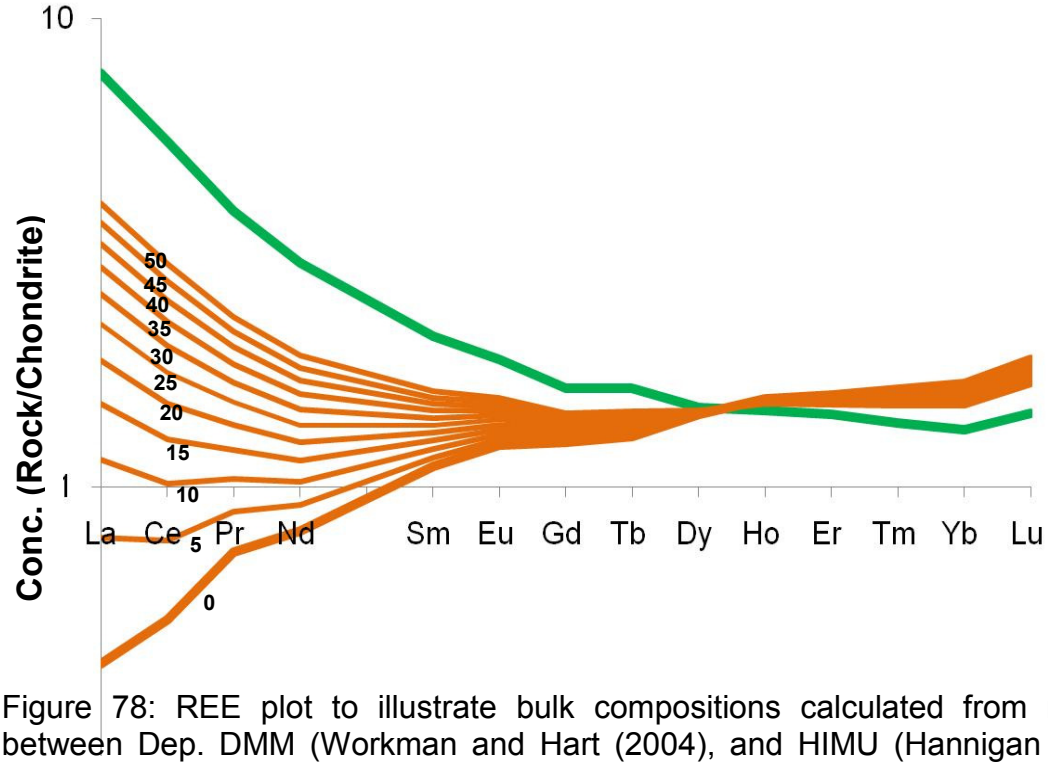

Figure 78: REE plot to illustrate bulk compositions calculated from mixing between Dep. DMM (Workman and Hart (2004), and HIMU (Hannigan *et al*., (2001) end-members.

The model incorporates two separate mantle assemblages. Above ~410km, the mantle is thought to consist of peridotites; ultramafic rocks of variable

composition consisting mostly of olivine and ortho-/clinopyroxene, accompanied by garnet (typically pyrope), spinel (typically chromite) or plagioclase, depending on PT conditions (Mysen and Boettcher, 1974).

Plagioclase is stable at very shallow levels in the mantle, above ~25km, and is unlikely to represent a significant length of the melting path; spinel is stable to ~60km, and garnet at greater depths. On the basis of this mantle mineralogy, the model uses the simplified assemblages and mineral proportions of McKenzie and O'Nions (1991) as shown in Table 20.

MINERAL PROPORTIONS						
	OLIVINE	**OPX**	**CPX**	**PLAG**	**SPINEL**	**GARNET**
SPINEL PERIDOTITE	0.578	0.27	0.119	0	0.033	0
GARNET PERIDOTITE	0.598	0.211	0.076	0	0	0.115

Table 20: Simplified garnet-phase and spinel-phase assemblages and mineral proportions for the mantle source. From McKenzie and O'Nions (1991).

Yb/Lu ratio data from M1 basalts (OCC at 13°19'N) indicates that the melting that formed these rocks began within the garnet stability field, suggesting that depths >60km are appropriate for the onset of melting, at least beneath the 13°19'N Oceanic Core Complex. Models are run for different proportions of melting in garnet and spinel peridotite as follows (Table 21):

GARNET-SPINEL FIELD MODEL		
	Melting (%) Proportion	
	Garnet Field	**Spinel Field**
Scenario		
1	0	100
2	5	95
3	10	90
4	15	85
5	20	80

6	25	75
7	30	70
8	35	65
9	40	60
10	45	55
11	50	50

Table 21: The proportions of melting in the spinel- and garnet phase melting fields applied in the model.

The proportions of the assemblages are varied in successive model scenarios, as denoted by the numbers 1-11 in the table above. Each set of scenarios is calculated for each of the bulk sources described above, in order to find the best fit for the concentrations of real end-member rocks from the on-axis, M1 and M2 basalt groups. Figure 79 below shows the end-member DMM and HIMU sources, and the compositions of real rocks to be modelled from them.

M1E, M1D and AXE have especially LREE enriched compositions. The compositional range between M1E and M1D is narrow, suggesting that these rocks were formed by similar sources, and similar extents of melting. AXE and AXD, at the opposite end of the scale, show a wide range of compositions. These rocks are probably formed by a range of different melt fractions and source compositions. AXD and AXE represent rocks from a wide geographical area, and therefore they might be expected to show greater compositional variability than the M1 and M2 rocks, which originate from a single site at 13°19'N.

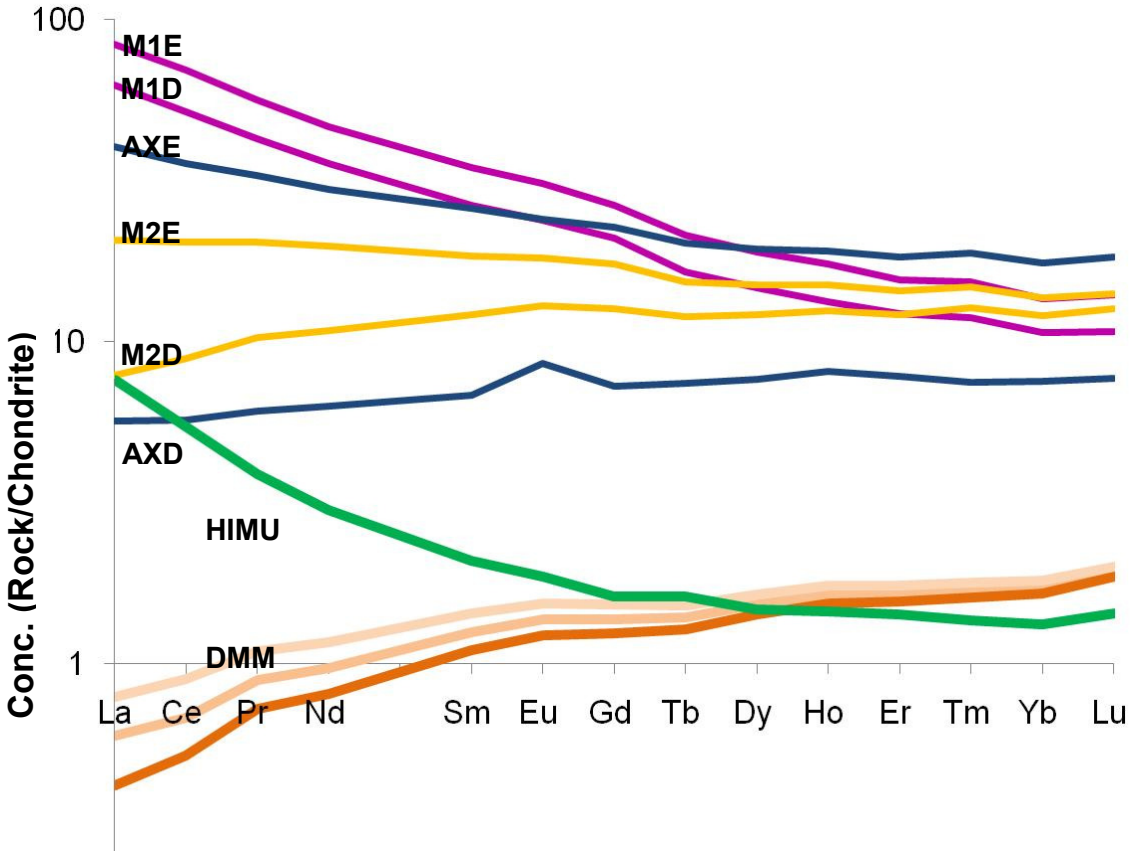

Figure 79: Compositions of real rocks from on-axis (12°60'-14°N – AXD and AXE), and off-axis (13°19'N, M1D, M1E, M2D and M2E). These samples represent the compositional end-members of the three basalt groups. These compositions are colour coded, blue for on-axis rocks, yellow for M2, and pink for M1. The two compositions in each colour represent the enriched (E) and depleted (D) ends of the compositional spectrum for each basalt type in the ~15°N region.Their compositions will be reproduced by the model in order to calculate melting conditions at 12°60'-14°N. Compositions of DMM (brown colours, Workman and Hart, 2004), and HIMU (Green; Hannigan *et al*., 2001) are shown for comparison.

The compositions of the natural end-member samples are reproduced numerically in Table 22.

REE COMPOSITIONS - REAL SAMPLES (ppm):

	M2D	M2E	M1D	M1E	AXD	AXE
La	2.527	6.645	20.140	26.790	1.821	12.960
Ce	7.184	16.540	42.000	56.600	4.645	28.980
Pr	1.235	2.446	5.135	6.775	0.734	3.953
Nd	6.520	11.870	21.420	27.960	3.783	17.880
Sm	2.314	3.515	5.060	6.593	1.294	4.925
Eu	0.906	1.277	1.672	2.180	0.599	1.682
Gd	3.292	4.540	5.477	6.917	1.898	5.883
Tb	0.599	0.766	0.827	1.070	0.372	1.013
Dy	4.004	4.968	4.861	6.277	2.525	6.426
Ho	0.872	1.050	0.930	1.219	0.569	1.342
Er	2.544	3.025	2.567	3.277	1.638	3.842
Tm	0.383	0.445	0.356	0.461	0.225	0.565
Yb	2.527	2.870	2.246	2.865	1.588	3.682
Lu	0.380	0.424	0.323	0.420	0.231	0.549

Table 22: Compositions of real rocks from on-axis (12°60'-14°N), and off-axis (13°19'N, M1 and M2). These samples represent the compositional end-members of the three basalt group. Their compositions will be reproduced by the model in order to calculate melting conditions at 12°60'-14°N.

The model is run for melt fractions between 0 and 20%, for each of the melting assemblage scenarios 1-11 (refer to Table 19). The model obtains best fits to the natural compositions above. This is achieved by calculating the deviation (positive or negative) for each element of each modelled composition from the real composition.

7.2.2. - Example Data

The model fit results (deviation values for La-Lu) are combined to generate an overall deviation from the desired composition, the RMS misfit. A lower RMS misfit value denotes a better fit. An example of output data is shown in Table 21 below for illustrative purposes. In the yellow column is a real composition (M2D) which the model is attempting to match. Table 23 shows a subset of three modelled compositions (melt fractions 9.8-10%), and the accompanying misfit functions, expressed as a percentage deviation from the original composition. Also shown is the RMS misfit (applied to account for the presence of positive and negative deviations from the actual composition). The RMS misfit function is closest to 0% in the case of a 10% melt fraction, and therefore this composition is most akin to the real composition in terms of overall deviation from the real chemistry.

	REAL COMPOSITION	**MODELLED COMPOSITIONS**			**MISFIT FUNCTION - % Deviation**		
	MELT FRACTION (%)	**9.8%**	**9.9%**	**10.0%**	**9.8%**	**9.9%**	**10.0%**
REE							
La	2.527	2.524	2.498	2.473	0.1	1.1	2.1
Ce	7.184	7.141	7.069	6.998	0.6	1.6	2.6
Pr	1.235	1.275	1.262	1.250	3.2	2.1	1.2
Nd	6.520	6.658	6.591	6.525	2.1	1.1	0.1
Sm	2.314	2.529	2.503	2.478	9.3	7.5	6.6
Eu	0.906	0.957	0.951	0.945	5.6	4.7	4.1
Gd	3.292	3.414	3.396	3.378	3.7	3.0	2.5
Tb	0.599	0.624	0.621	0.619	4.2	3.6	3.2
Dy	4.004	4.227	4.215	4.202	5.6	5.0	4.7
Ho	0.872	0.941	0.939	0.937	7.9	7.1	6.9
Er	2.544	2.778	2.773	2.768	9.2	8.2	8.1
Tm	0.383	0.390	0.390	0.390	1.9	1.8	1.7
Yb	2.527	2.699	2.699	2.698	6.8	6.4	6.4
Lu	0.380	0.406	0.407	0.407	7.0	6.6	6.6
	RMS MISFIT VALUE:				0.127	0.120	0.119

Table 23: Example data to illustrate the working model. A real composition (M2D) is shown alongside three modelled iterations (melt fractions 9.8-10%), as well as the misfit function data for these three iterations. A lower RMS misfit indicates less deviation from the natural data.

7.2.3. - Model Outcomes, Source Modelling – 12°60'-14°N

The best outcomes of the three source-combination models are summarised in Table 24 below. The red blocks highlight the best outcomes for each real composition. The best performing model is HIMU/Enriched.DMM, which produces the best outcomes for M2D, M1D, M1E and AXE. The HIMU/Average DMM model produces the best outcomes for M2E AXD is best reproduced by the HIMU/Depleted DMM model.

HIMU AND AV. DMM				
MATCH	**% HIMU**	**% GRT**	**MELT FRACTION**	**RMS MISFIT**
M2D	0	50	7.8	0.18
M2E	5	35	4.0	0.13
M1D	20	20	2.9	0.97
M1E	50	10	4.2	1.98
AXD	0	50	10.0	0.81
AXE	0	5	1.0	0.40
HIMU AND ENR. DMM				
M2D	0	50	10.0	0.12
M2E	5	35	5.4	0.15
M1D	20	25	3.2	0.60
M1E	40	15	3.7	1.72
AXD	0	50	10.0	1.28
AXE	5	15	2.8	0.25
HIMU AND DEP. DMM				
M2D	5	45	8.0	0.16
M2E	5	20	4.0	0.22
M1D	35	25	4.2	1.23
M1E	50	10	4.1	2.14
AXD	0	50	10.0	0.60
AXD EXTENDED	0	50	12.8	0.29
AXE	5	5	2.0	0.92

Table 24: Table outcome data, showing the best model outcomes for each of the three source models. The table also shows the percentage of HIMU contributing to the melt composition, the percentage of garnet melting contributing to the composition, the melt fraction of the melt, and the goodness of fit value for each outcome. Outcomes from Depleted DMM and Average DMM produce better goodness of fit data than Enriched DMM combinations.

Since reproducibility of AXD was poor in models running to 10% melting, and since the REE profile is suggestive of extensive melting, the HIMU/Depleted DMM model was extended to 20% melting to improve the outcome. The HIMU/Depleted DMM model was selected for this operation, as it provided the best outcome for AXD at the 10% melting threshold.

The best of the model outcomes in terms of misfit and gradient are shown on the REE plots below (Figures 80-82).

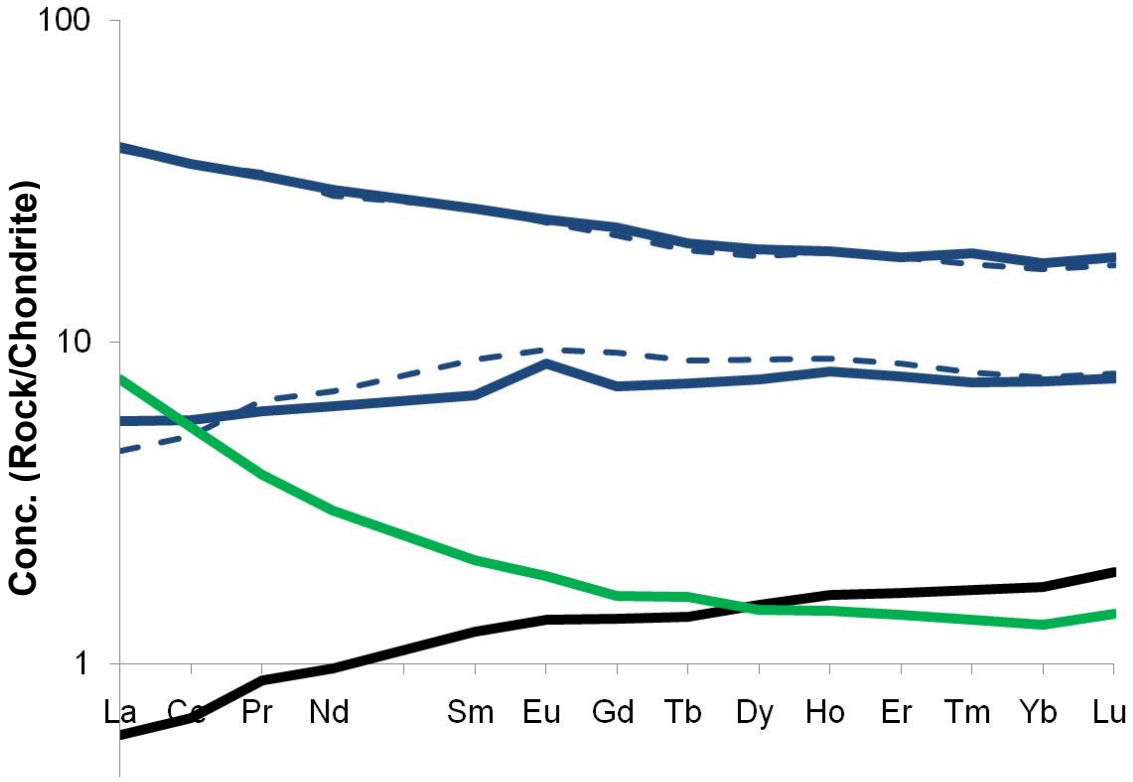

Figure 80: Modelled compositions (dotted lines) matching on-axis real rock samples AXD and AXE (solid blue lines). Also shown are HIMU in green (Hannigan et al., 2001) and Average DMM in black (Workman and Hart, 2004). The dotted lines illustrate the model compositions most closely matching those of the natural rocks. The models match the compositions closely, though the LREE end of the modelled AXD equivalent is too depleted to match the natural rock.

For the on-axis samples AXE and AXD, model data closely matches the natural compositions, as shown in Figure 80. The model data suggests that between 15-50% of melting takes place in the garnet field, and that melt fractions cover a broad range from 2.8-12.8%. The depleted end-member composition (AXD) is

best reproduced by melting of only depleted DMM, whereas LREE enriched AXE is best reproduced when including 5% material from a HIMU source.

The AXD modelled composition is overly enriched in MREE, suggesting that accurate reproduction of AXD requires reduced MREE in the bulk source.

In off-axis rocks (Figure 81), the depleted end-member M2D is well reproduced by the model, and is best matched by 35% garnet field melting of HIMU/Enriched DMM, at melt fractions of ~10%, with no contribution from a HIMU source.

The enriched composition M2E is well reproduced by the HIMU/Average DMM model. The model suggests that 50% of melting (melt fraction = 4%) took place in the garnet field, and that there was a 5% contribution of HIMU to the source.

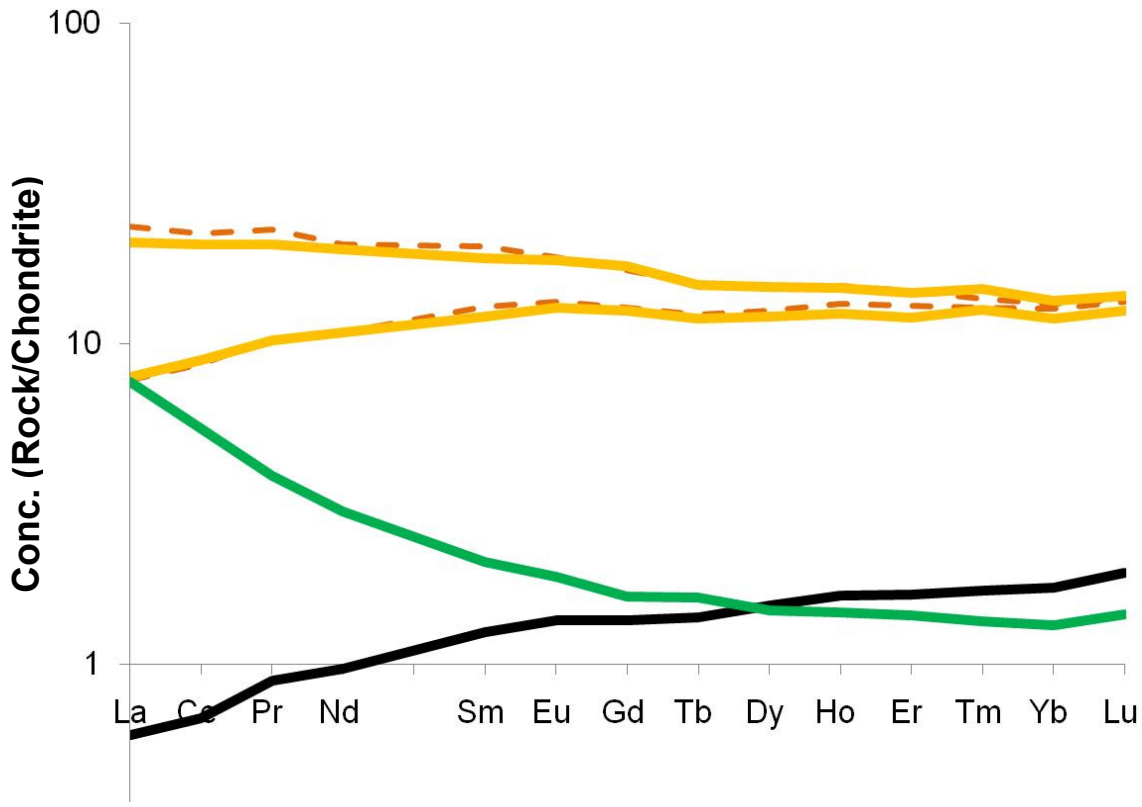

Figure 81: Modelled compositions (dotted lines) matching off-axis real rock samples M2D and M2E (solid yellow lines). Also shown are HIMU (Hannigan et al., 2001) and Average DMM (Workman and Hart, 2004). The dotted lines illustrate the model compositions most closely matching those of the natural rocks. The models reproduce the compositions well.

M1 rocks (Figure 82) are less well reproduced than M2 and on-axis samples. Whilst the reproduction of M1D is good, the modelled composition for M1E is substantially depleted in the MREE and enriched in the HREE relative to the natural composition. The M1D composition is best reproduced at 25% garnet field melting, where the HIMU component is 25% and the melt fraction is comparatively low (~3.2%). M1E is best reproduced by 15% melting in the garnet field, with a 40% contribution from HIMU, and at a melt fraction of 3.7%. The HIMU/Enriched DMM model performs best for matching the natural compositions of these samples.

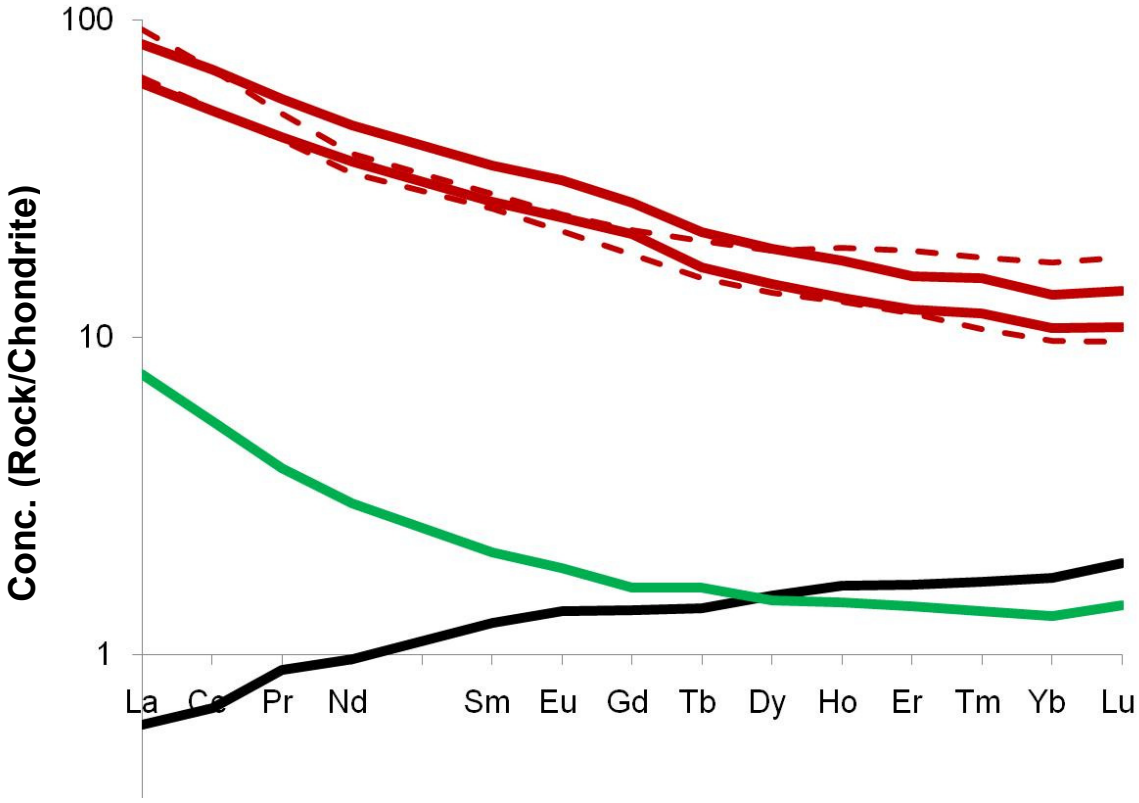

Figure 82: Modelled compositions (dotted lines) matching off-axis real rock samples M1D and M1E (solid red lines). Also shown are HIMU (Hannigan et al., 2001) and Average DMM (Workman and Hart, 2004). The dotted lines illustrate the model compositions most closely matching those of the natural rocks. The models do not reproduce the compositions well, especially at the M- and HREE end of the compositional spectrum.

At spinel and garnet melting field inputs of 0-50%, and melt fractions of 0-20%, with HIMU contents extending from 0-50%, the conditions applied in this model are very wide ranging, covering all conditions we would expect for MOR melting at 12°60'-14°N. The poor reproduction of M1E despite this wide range of model

conditions indicates that these conditions are not sufficient to generate the composition of M1E.

There are a number of limitations which could contribute to the poor fit obtained for M1E. For instance, during the real melting episode, the melt may have interacted with other melts or wall rock. The presence of water may have affected melting behavior during the production of this melt. Alternatively, the poor fit may result from the limitations of using a purely fractional melting model. It is also possible that the HIMU-DMM source composition used in the model is unsuitable, and this prevents the model from reproducing M1 rocks.

Geochemical data presented in this thesis suggests that M1 rocks form from a combination of HIMU-FOZO and DMM sources. Isotope data shows that M1 compositions form from a significant amount of HIMU-FOZO mixing, with a reduced contribution from DMM. The model does not account for the presence of an additional enriched component such as FOZO, and therefore may lack the appropriate input chemistry to form the M1 compositions.

In order to investigate the nature of the additional mantle component (or components) involved in the formation of M1E, a model inversion was performed. This was achieved by manually adjusting the bulk source composition (La-Lu) input of the model, to force the generation of a melt identical to M1D.

The starting point for this operation was chosen as HIMU/Enr.DMM, 40% HIMU, at a melt fraction of 3.7%. This is best fit to M1E obtained from the DMM-HIMU combinations used in the model. The melt obtained is shown on Figure 83, along with the composition of the new bulk source.

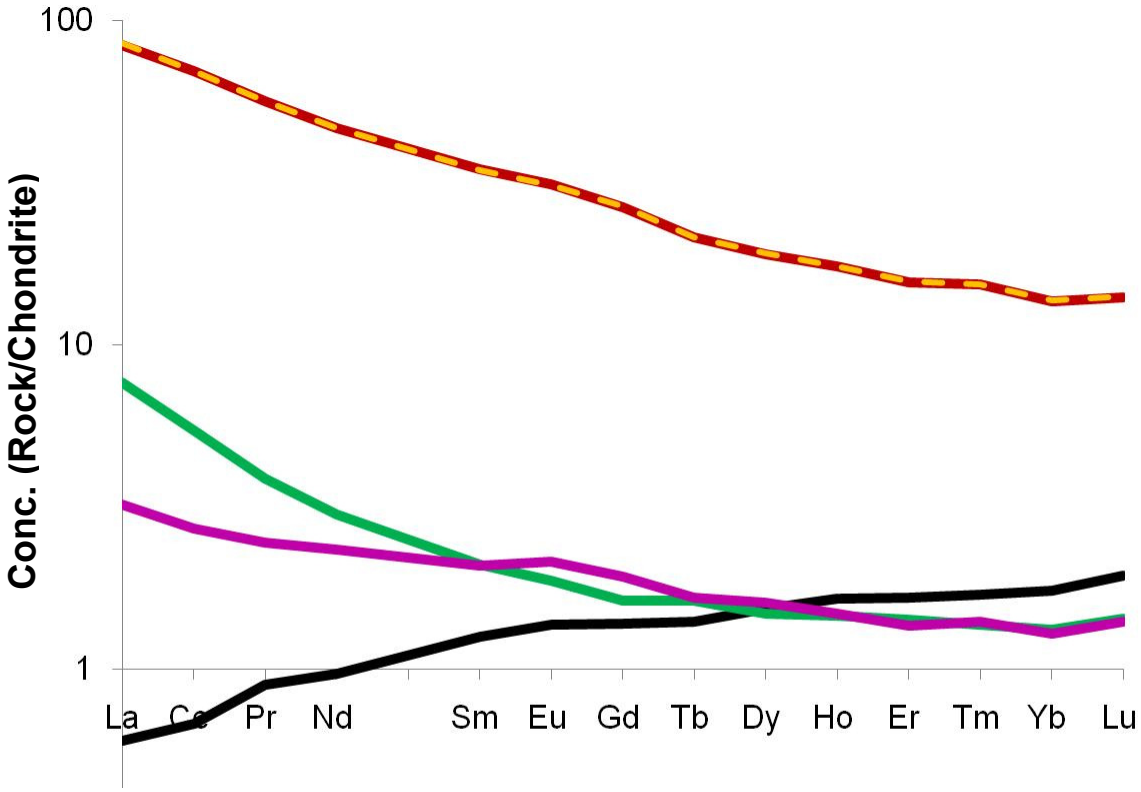

Figure 83: Diagram to show the natural composition of M1E (red), and the modelled composition (yellow dashed), resulting from the model inversion. The new bulk composition (purple) obtained is shown. Also shown are HIMU (Hannigan et al., 2001) and Average DMM (Workman and Hart, 2004).

The composition of the modified bulk source is shown in Table 25 below.

La	Ce	Pr	Nd	Sm	Eu	Gd	Tb	Dy	Ho	Er	Tm	Yb	Lu
1.03	2.2016	0.295	1.4	0.395	0.15	0.5	0.083	0.53	0.104	0.285	0.042	0.27	0.042

Table 25: The composition of the modelled modified bulk source, calculated by force-fitting the model to reproduce the composition of the real rock ‘M1E’.

This data shows that the ‘missing’ source required to generate M1E has a higher MREE content than the HIMU-DMM bulk source originally used.

Although these data cannot be used to determine the absolute composition of the third mantle component because the proportion of this component present in the mantle is not known, the bulk compositional data can be reinserted into another

forward model to attempt to improve the fit of modelled compositions to other natural data.

This operation is attempted to reproduce M1D at 20% HIMU, 25% garnet, (HIMU/Enr. DMM). M1E is very similar in REE space to M1D, and should have formed under very similar conditions. These melts were formed spatially very close together (at the breakaway ridge 13°19'N), and so are likely to have shared the same bulk mantle source. If this is true, then the new bulk source generated for M1E should also reproduce M1D well.

The resulting composition (Figure 84) closely mirrors the natural composition of M1E at a melt fraction of 5%, (slightly higher than the melt fraction from the original model). The RMS misfit value is 0.56, which is an improvement on the figure of 0.60 obtained using purely DMM-HIMU.

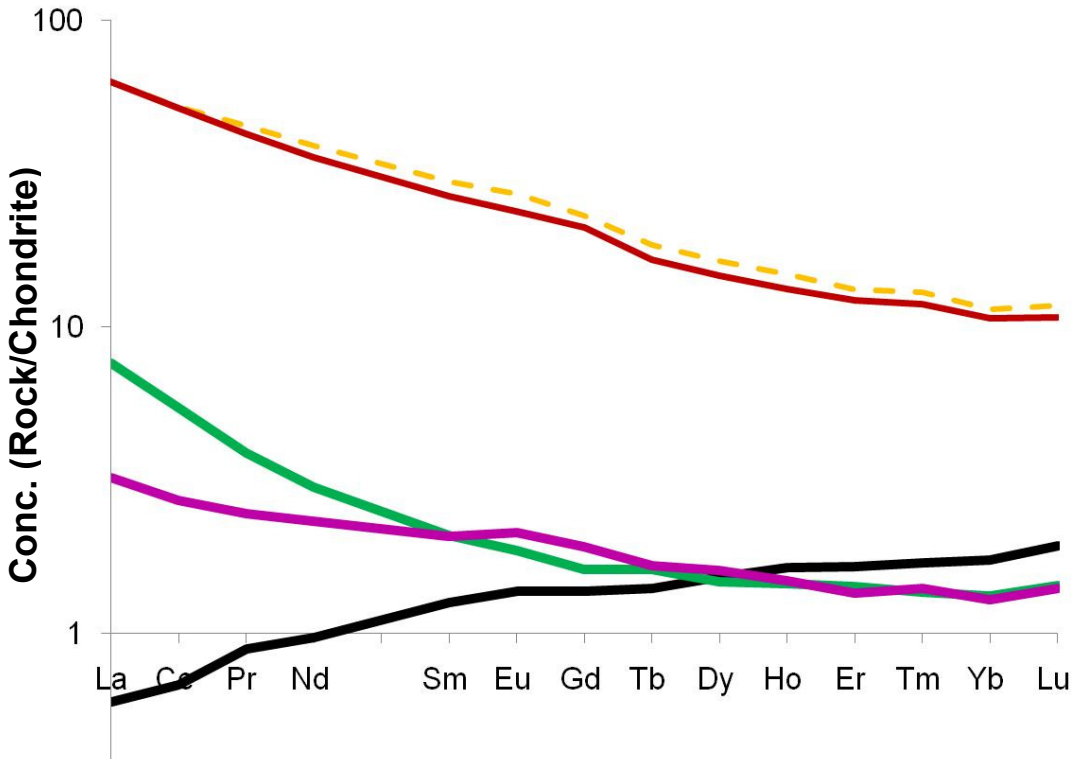

Figure 84: Diagram to show the natural composition of M1E (red), and the modelled composition (yellow dashed), resulting from the input of the new bulk composition (purple). Also shown are HIMU (Hannigan et al., 2001) and Average DMM (Workman and Hart, 2004). The diagram shows that the model composition now closely resembles the natural composition, representing a substantial improvement over the initial model output.

7.2.4. - Discussion of Model Outcomes

REE modelling results are summarised below. The outcomes broadly confirm the geochemical findings presented earlier in this chapter.

Summary of Results			
Melt ID	Melt Fraction	HIMU %	Length of Melt Path
M1 Lavas	3-4%	20-50	~100-45km
M2 Lavas	4-10%	0-5	~100-55km
On-Axis	2-12%	0-5	~100-30km

The enriched DMM composition of Workman and Hart (2004) performs better in four of the six modelling cases than the average and depleted DMM variants. The depleted DMM performs well in reproducing AXD, which is unsurprising; as this composition has a flat to LREE depleted composition. It is interesting to note that AXE is reproduced more successfully by Average DMM than Enriched DMM, whereas the opposite is true for AXD.

The model predicts a low HIMU component (0-5%) in M2 melts, but a much higher HIMU component (20-40%) for M1 melts. These rocks are found at the same sites at 13°19'N, and this close spatial association suggests that they are likely to have shared a mantle source. It is possible, therefore, that M2 compositions may result from melting after enriched material has been previously removed from the source to form M1 melts, as predicted earlier in this chapter.

Reverse modelling of the three (or more) component bulk source for 13°19'N shows that the addition of a third (enriched) component which increases the MREE content of the bulk source improves the ability of the model to reproduce natural M1 compositions, in which the percentage contribution of the third component is likely to be significant, and therefore the reproducibility of the compositions by the DMM-HIMU binary source is poor.

The addition of a further component or components is consistent with the modelling of Hannigan *et al*. (2001), who predicted the presence of mantle components with lower LREE and higher M-HREE compositions than HIMU beneath the central MAR.

The models predict that the component HIMU contributes significantly to the generation of M1 basalts (20-50%). This is consistent with isotopic evidence which suggests that these melts are formed from an enriched source with a substantially lower contribution from the DMM than M2 or on-axis rocks.

M2 melts (melt fraction 4-10%) contain 0-5% HIMU source material, a value substantially lower than that for M1. This difference may be partially due to higher melt fraction melting of M2, as at higher melt fractions DMM becomes a more significant component, diluting the HIMU contribution. However, the low HIMU component in these melts may also reflect enriched material having been previously removed from the source to form M1 melts, as predicted earlier in this chapter. Attempts to model this process proved fruitless, as the modelling process is iterative, and the residue from an episode of melting cannot be easily back-calculated to form a bulk source suitable for re-insertion into the model.

On-axis rocks are shown by the model to form from a wide range of melt fractions (2-12% melting). The model predicts that 5-50% of this melting which produces on-axis rocks takes place in the garnet field (depths >60km), but garnet signatures (Yb/Lu) in these samples are not pronounced. The model predicts a 0-5% HIMU component contribution to the melt.

At the 13°19'N OCC, the melting models predict a variable garnet component in the melt (M1: 10-25%, M2: 20-50%), though this is partially linked to the extent of melting the model reaches for each composition. Prominent Yb/Lu anomalies are seen in the M1 rocks (see Figure 55), and textural evidence (hopper olivines, indicative of rapid eruption and large, euhedral accumulated pyroxene) suggests increased depth of melting at the OCC site.

Plentiful garnet in the source, combined with low melt fraction in comparison to typical MORB suggests deep initial melting for M2, and a very short, deep melting path. Melt fraction and garnet content are much more variable in on-axis

rocks, suggesting a range of melt path lengths and melt interactions beneath the ridge along axis.

The models show that off-axis M1 melts are from smaller melt fraction and relatively less garnet field melting, indicating that they are *shallower* low melt fractions than average on-axis and M2 rocks.

The marked decrease in average melt fraction at M1 (3-4.0%) is also consistent with predictions of a short melting path for these melts, and may support a theory of rapid eruption. The melts do not appear to have remained beneath the ridge for sufficient time to homogenise with melts of higher melt fraction or different composition. This, however, may simply be indicative of the fact that no other melts of higher or more depleted melt fraction were present alongside M1. The lack of M1-like compositions in the talus on the OCC surface suggest that M1 and M2 compositions did not coexist beneath the ridge for any significant length of time.

The short but relatively shallow melt path for M1 rocks has implications for the thermal structure beneath the axis, suggesting that M1 may have formed from a cooler mantle than that which produces the average on-axis rocks.

The variations in melt column length predicted by the model suggest that under the axis, melt paths are variable, but substantial garnet components indicate that the onset of melting is deep. Although melt fractions extend to 12%, which is higher than off-axis rocks, the melt fraction is low in comparison to average melting expected for the formation of MORB (see Langmuir et al., 1992; Kinzler and Grove, 1992). This may indicate that a thick lithosphere underlies the 12°60'-14°N region.

.

7.3 - THE NATURE AND ORIGIN OF ENRICHED COMPOSITIONS ON THE MAR

There has been much speculation about the origins of the pronounced LREE enrichment anomaly in the 14°N region, as it is unusual to find such a geographically widespread and consistent E-MORB signature at a MOR which is apparently outside the influence of mantle plume activity.

The discussions in this thesis have shown that the extent to which the mantle melts beneath the ridge has dramatic implications for the formation of OCCs in the 12°6-14°N region. Since the extent of melting is at least partially dependent on composition of the mantle, the development of segment centre OCCs in this region may be directly linked to an unusual interaction of mantle source material beneath the ridge.

This section will explore the possible origins of the mantle underlying the 12°6-14°N region, and its implications for the development of pronounced E-MORB signatures and segment-centre core complexes on this area of the MAR.

Basalts from both axial and off-axis sites between 12°60'Nand 14°N are E-MORBs, with a general increase in E-MORB character toward 14°N as described by previous studies (e.g. Hémond et al., 2006). These compositions become more N-MORB-like to the south near the Marathon Fracture Zone, though LREE enrichment is a feature of most samples.

It is the aim of this section to identify the origins of E-MORB signatures produced in the ~15°N region, by comparing data from this study with existing data for the MAR, and by addressing previous hypotheses suggesting the presence of plumes (e.g. Dosso et al, 1991), or necessity of plume-ridge interaction to explain the presence of HIMU-derived E-MORB compositions in the area.

As Wilson (1989) states, historically, global MORB compositions were thought to be exceptionally uniform N-MORBs.

However, since the 1970s, E-MORB compositions have been identified as widespread (e.g. Le Roex et al., 1983) on MORs. There are a number of

mechanisms by which E-MORB can be generated in the MOR environment, related to both source compositional heterogeneity (e.g., Donnelly et al., 2004, Kent, 2004, Janney, 2005) and magmatic processes such as fractionation. E-MORB generation is especially likely in slow-spreading environments, where melting is suppressed by a thick lithospheric lid (i.e. Humphreys and Niu, 2009). This leads to shorter melting paths and a lack of large homogenising magma chambers, and therefore melt fractions are variable, fractionation is significant, and wide compositional ranges result.

OIB at hotspots is considered to originate from high temperature, high-degree melting of less depleted or even somewhat enriched mantle sources (sources, see Zindler and Hart, 1986) transported in mantle plumes which, in many cases, differ in depth of origin to the depleted MORB source (White, 2010). However, it has been demonstrated that OIB can also be generated by preferential melting of enriched components in the upper mantle (i.e. Morris and Hart, 1983, Zindler et al., 1984).

Fitton (2007) argues, on the basis of the ΔNb parameter (see Fitton *et al.*, 1997), that OIB source components are present at all scales in the mantle, from small heterogeneities forming E-MORB on ridges and OIB on seamounts, to large 'plume' upwellings. This suggests that OIB compositions are not a diagnostic feature of mantle plumes, and are likely generated by a combination of plumes and enriched blobs/streaks in the upper mantle (Fitton, 2007).

Despite the abundance of E-MORB on MORs, and the demonstrable existence of mechanisms for generation of enriched compositions from the upper mantle, interaction of the DMM with plumes is commonly offered as an explanation for geographically widespread E-MORB signatures (e.g., Rhodes et al., 1990, Douglass et al., 1999), so much so that E-MORB were originally labelled plume-type (P-type) MORB (e.g. Schilling et al., 1983).

Prominent sites of plume-ridge interaction such as the Azores and Iceland (MAR) are identified by the presence of enriched basalt compositions (which are by definition both OIB and E-MORB) associated with pronounced bathymetric rises, gravity anomalies, thick crust (implying extensive melting) and hot underlying mantle.

A number of previous studies of central MAR segments have found that the mantle beneath the region has HIMU (high U/Pb) character (Dosso et al, 1991; Schilling et al, 1994; Hannigan et al, 2001), a source end-member which is normally associated with ocean islands such as St Helena (see Chaffey et al., 1989) and not identified in other MORBs (Dosso et al, 1991). This suggests a more complex mantle origin than that usually envisioned for MORB, (Dosso et al, 1991). Dosso et al (1991) invoke the presence of an 'incipient, ridge-centred plume' to explain geochemical and topographic anomalies at 14°N.

It is clear that the MAR at ~15°N exhibits a number of unusual geochemical characteristics, which have been attributed by many to plume sources. However, geophysical evidence for a current plume in the region is lacking, and although Dosso et al (1991) report a bathymetric anomaly at 14°N which they attribute to a plume, the magnitude of this feature is very limited in comparison to the plateaux, elevated ridges and islands produced at many other recognised hotspots.

Furthermore, the 2-12**%** melting in the 12°6'-14°N region is consistently low by comparison with the 6-20% thought to generate typical N-MORB (Langmuir et al., 1992, Kinzler and Grove, 1992). The segment has a deep axial valley, and the crust is thin, exposing ultramafic rocks on detachment faults. These characteristics are at odds with those we would expect for a major E-MORB generating region. The tectonic features described here are atypical for areas of plume-ridge interaction, where the plume typically exerts substantial morphological control on the ridge, generating areas of thick crust and clear geophysical anomalies (i.e. Keller *et al.,* 2000; Gaherty, 2001; Murton *et al.*, 2002).

The Azores hotspot (~38-40°N) lies geographically close to the equatorial MAR region. Thibaud et al (1998) conducted a systematic study of seafloor depth, ridge segment morphology, and mantle Bouguer anomalies along the central MAR between 15°N and the Azores. This study showed that the bathymetric and geophysical influence of the Azores hotspot is detectable on the ridge to latitudes only as far south as 26°N. Between ~17°10'N and 20°N, the MAR produces extremely uniform N-MORB compositions (Dosso et al., 1993). This evidence

suggests that the ~15°N region is outside the zone of physical and geochemical influence of the Azores hotspot.

In the central MAR (5°S- 65°N) a number of E-MORB producing areas like the ~15°N region exist which are not associated with bathymetric or geophysical anomalies, or with previously recognised hotspots.

Bougault et al (1988) produced a series of plots to show E-MORB-producing regions the central MAR, and their association with variations in seafloor depth. These plots are reproduced here (Figure 85), along with new data (this study) from the 12°60'-14°N region. The plots of Nb/Zr and La/Sm against latitude and ridge axis depth clearly identify pronounced enrichment zones associated with Iceland and the Azores. The accompanying elevations in the ridge axis depth are also clear. The plots show the pronounced enrichment between the FTFZ and Marathon Fracture Zone. The striking feature of these data is that the enrichment zone is almost equivalent in magnitude to that associated with the Azores hotspot, but is not accompanied by any major change in axial seafloor depth.

Less prominent zones of enrichment are found at 23°N (Kane FZ), and at 45°N. A significant E-MORB-producing zone has also been identified on the equatorial MAR (7°S-5°N - Schiiling et al, 1994; 2°N-1°S - Suschevskeya et al., 2002; 5°N-5°S - Hannigan et al, 2001) though these data were not available in the Bougault (1988) study. None of these areas correlate with elevated seafloor.

Between E-MORB sites, there are ridge segments where uniform N-MORB compositions are produced. The geochemical gradient extending from 10°N northward (Dosso et al., 1993) has a limit that occurs at ~17°10'N. This geochemical limit is not obviously related to any structural feature, but basalts north of the limit have very homogeneous N-MORB. South of the limit, basalt compositions are highly variable, ranging from depleted to enriched. This information is summarised in Figure 86. The position of the 17°10'N geochemical limit is identified on the plot. Concentrations of incompatible major and trace elements between 12°60'N-14°N are typically higher than those seen north of 17°10°N. Average Sr isotope ratios from 12°60'N-14°N are higher (0.70275 ± 0.00025), and substantially more variable than those to the north of the 17°10'N geochemical limit. Nb/Zr ratios are higher than those the north of the limit,

typically 0.122 ± 0.08. K/Nb ratios are lower than those found north of the limit (306 ± 313), and are not constant as described by Dosso et al (1993).

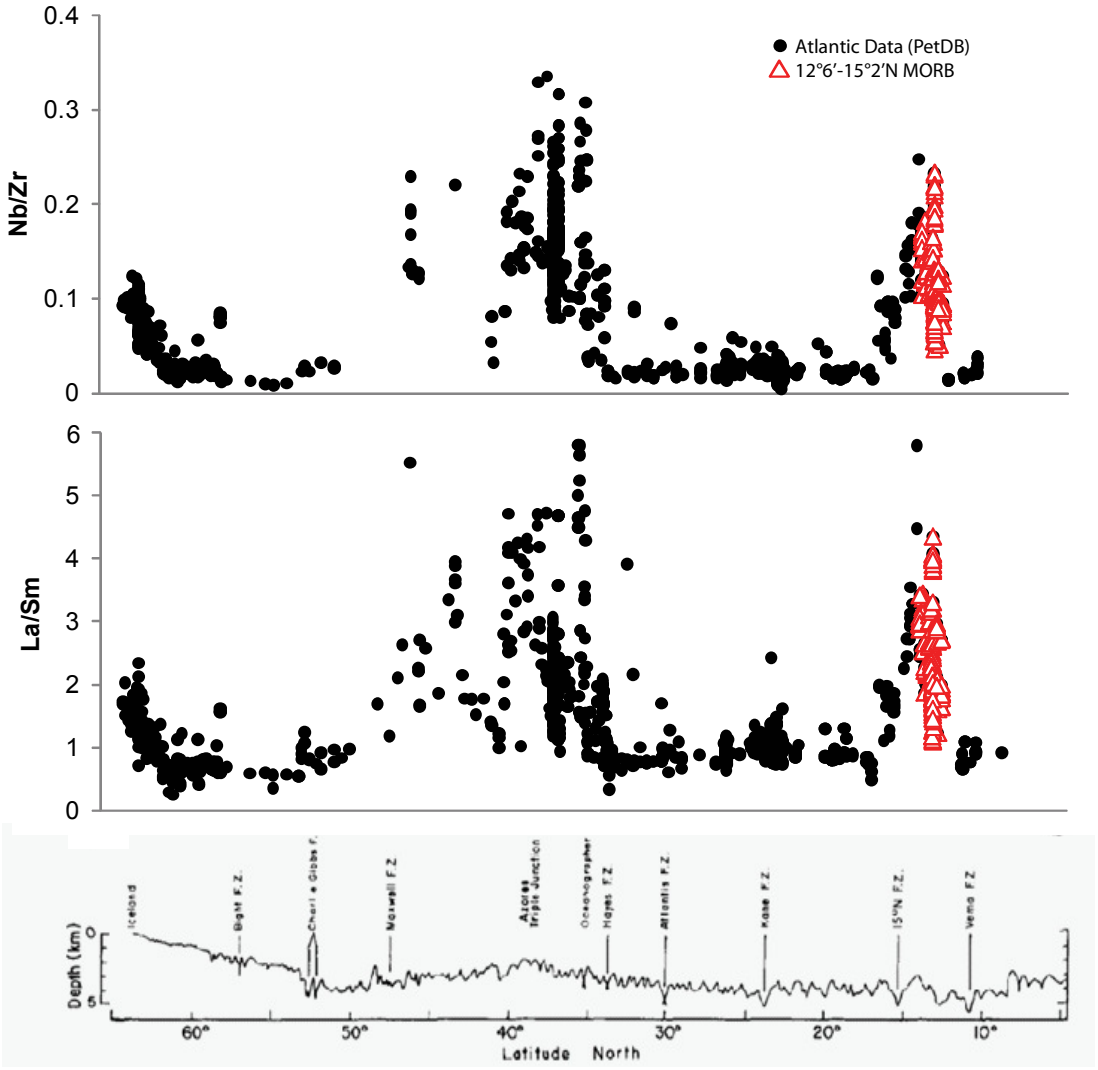

Figure 85: Enrichment zones and their correlation with bathymetric highs at sites such as the Iceland and Azores hotspots. An enrichment zone is also seen at the FTFZ, despite the lack of gravimetric or bathymetric evidence to suggest the influence of a mantle hotspot here. After Bougault *et al*. (1988), data from PetDB (black) and this study (red).

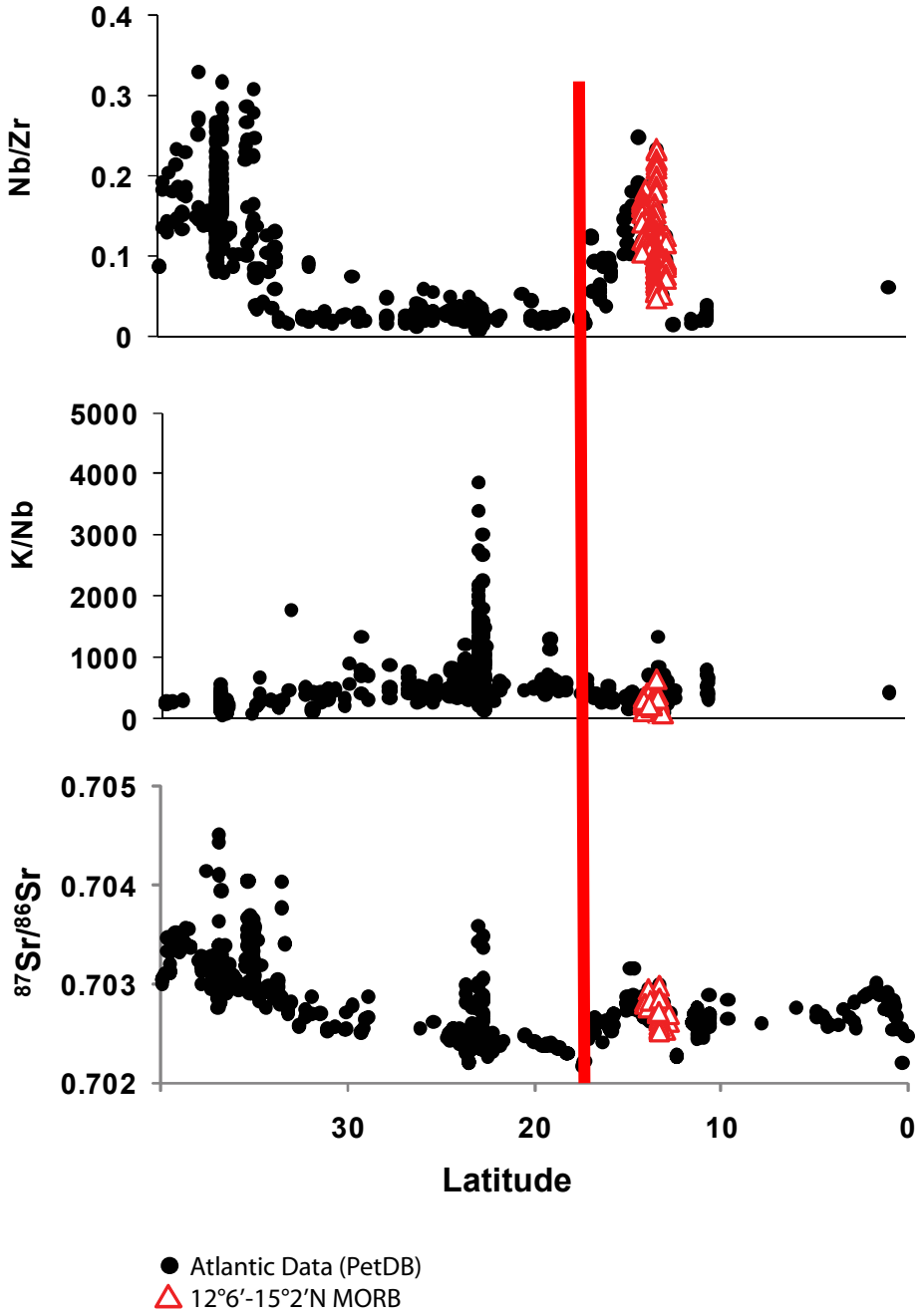

Figure 86: Geochemical characteristics of MAR basalts (0-50°N). A red line denotes the position of the geochemical limit at 17°1'N. After Dosso (1993). Data from PetDB (black) and this study (red).

E-MORB areas identified along the MAR have variable geochemical characteristics, which are illustrated by plots of isotope ratios against latitude (Figure 87).

Many E-MORB areas in the central MAR (5°S-65°N) have similar average Yb/Lu ratios, though the range of values varies substantially at Iceland, the Azores and Kane FZ (23°N), whilst remaining very close to the average value at 12°60'N-14°N and 2°N-1°S. Kane FZ and 2°N-1°S typically have Zr/Y values which are average for the region, whereas elevated Zr/Y ratios are found at the other sites.

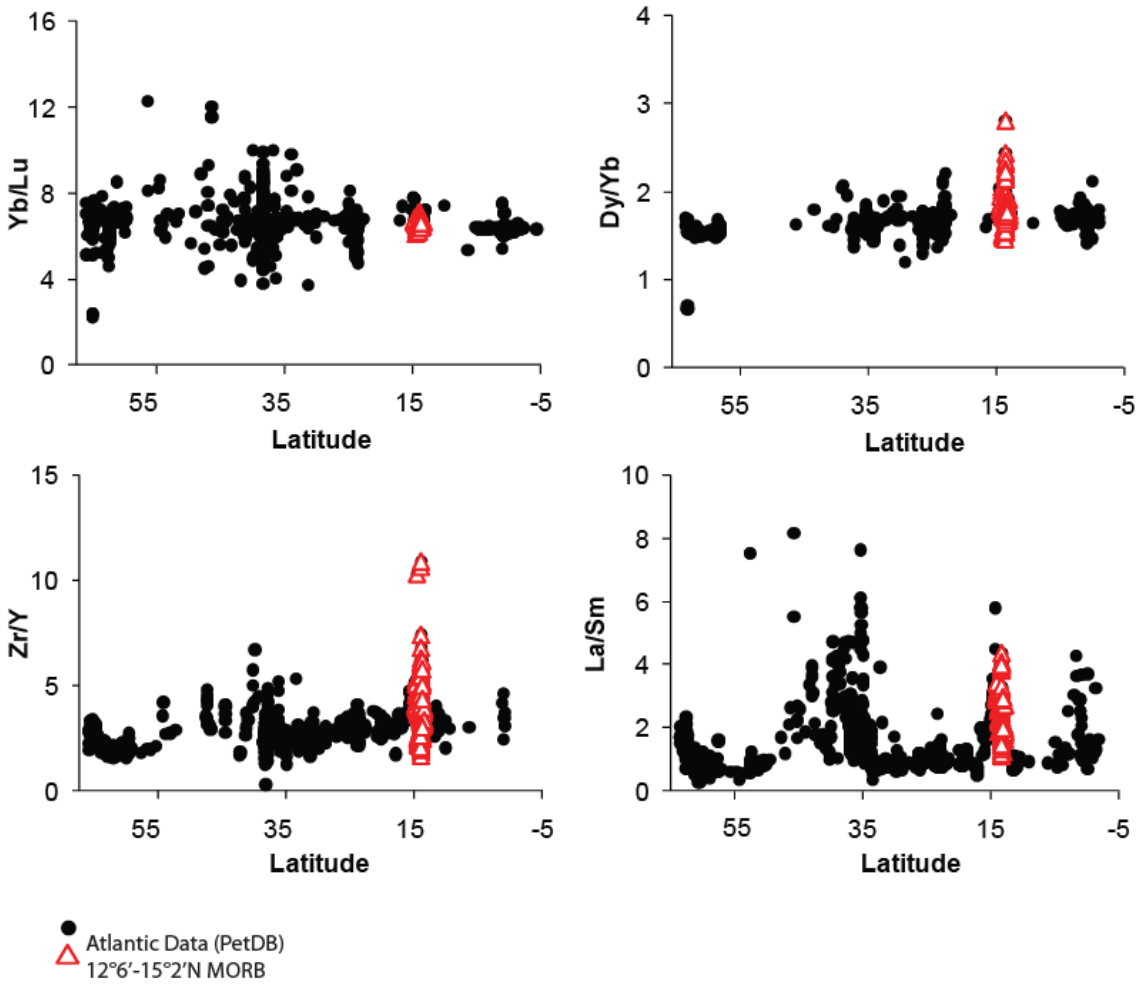

Figure 87: Variations in trace element ratios with latitude on the MAR (5°S-60°N). Data from PetDB (black) and this study (red).

There are substantial variations in Nd, Sr and Pb isotope ratios with latitude throughout the central MAR region (Figure 88). Most areas of the ridge have low $^{143}Nd/^{144}Nd$ ratios, though Kane FZ (23°N) is an exception. The 0-5°N and 30-35°N regions are characterised by high $^{87}Sr/^{86}Sr$ and $^{206}Pb/^{204}Pb$ ratios.

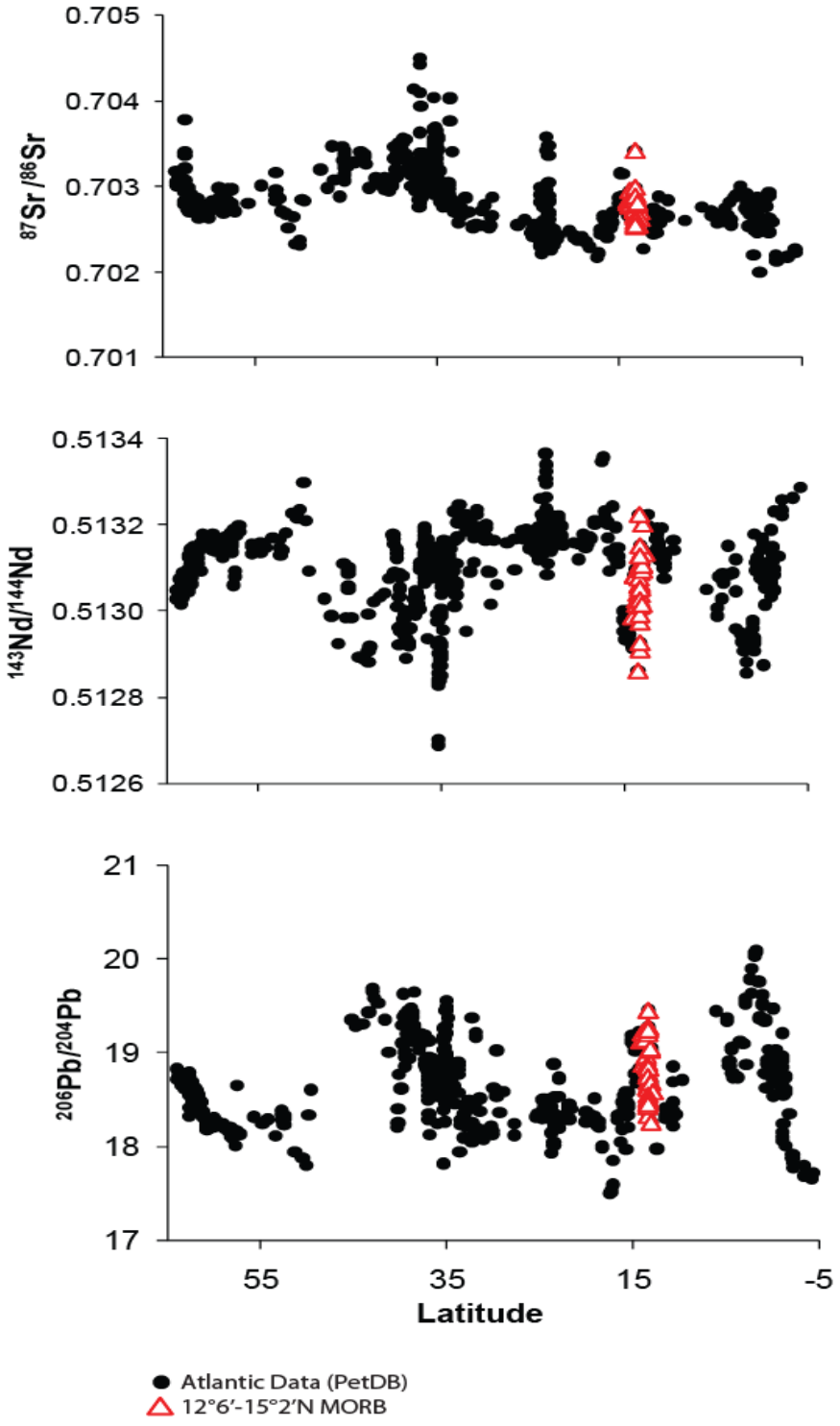

Figure 88: Variations in $^{206}Pb/^{204}Pb$, $87^{Sr}/^{86}Sr$ and $^{143}Nd/^{144}Nd$ data with latitude on the MAR (5°S-60°N). Data from PetDB (black) and this study (red).

In order to compare the E-MORB zones of the central MAR to determine which characteristics they share, compositional data are summarised in Table 25, which was produced using PetDB MORB compositions (5°S-65°N). The table uses a key to describe the qualitative properties of each site in terms of deviation from the regional average value. The table also shows scores which are assigned for specific characteristics. These numbers are arbitrary numbers, and are used to generate data rose diagrams (Figures 89-90). The numbers allow the data to be plotted visually, so clearer comparisons between the sites can be made.

Site: Geochemistry:	Iceland	45°N	Azores	Kane FZ	12.6-15.2°N	2°N-1°S
Ba/Sr						
Ba/Nb						
Ba/Zr						
Dy/Yb						
La/Sm						
La/Yb						
Nb/Zr						
Rb/Sr						
Ta/Zr						
Th/Zr						
Yb/Lu						
Zr/Y						
K/Nb						
$^{87}Sr/^{86}Sr$						
$^{143}Nd/^{144}Nd$						
$^{206}Pb/^{204}Pb$						
Pb Δ7/4						
Pb Δ8/4						
$^{208}Pb/^{206}Pb^*$						
SiO_2 wt%						
Na_2O wt%						
$Na_2O + K_2O$ wt%						
MgO Wt%						
TiO_2 wt%						
Ce ppm						

Table Key		
	Higher than average	20
	Average	10
	Lower than average	-10
	Higher and lower than average	0
	No data	N/A

Table 26: Qualitative illustration of the variation in a range of geochemical characteristics between different enrichment zones on the MAR. Cell colours are used to denote variations from the average value. Data used to obtain averages is PetDB data for basalt 5°S-60°N on the MAR. See colour key for details.

The N-MORB region between 17°10'N and 23°N is characterised by low $^{87}Sr/^{86}Sr$ and $^{206}Pb/^{204}Pb$ ratios, and high $^{143}Nd/^{144}Nd$. Samples from 12°60'–14°N extend to very high $^{87}Sr/^{86}Sr$ and low $^{143}Nd/^{144}Nd$ values, with $^{206}Pb/^{204}Pb$ values higher than those found 17°10'N-23°N, but lower than those at 0-5°N.

It has been suggested on the basis of isotope geochemistry that the basalt enrichment in the ~15°N region is similar to that of the 2°N-1°S region (Suschevskeya et al., 2002). Enriched melts from 2°N-1°S are noted for $^{206}Pb/^{204}Pb = 20.0$, $^{207}Pb/^{204}Pb = 15.6$, $^{208}Pb/^{204}Pb = 39.5$, and $^{87}Sr/^{86}Sr = 0.7030$ at a $^{143}Nd/^{144}Nd$ ratio as low as 0.5128, as well as high Si and Na. Data from 12°60'N-14°N gives lower average Pb ratios of $^{206}Pb/^{204}Pb = 18.9$, $^{207}Pb/^{204}Pb = 15.5$, $^{208}Pb/^{204}Pb = 38.4$, at $^{87}Sr/^{86}Sr = 0.7028$, and $^{143}Nd/^{144}Nd = 0.5131$. Also, Na concentrations extend to lower average values here. Off-axis low melt fraction melts at the OCC at 13°19'N give average $^{206}Pb/^{204}Pb = 19.3$, $^{207}Pb/^{204}Pb = 15.6$, $^{208}Pb/^{204}Pb = 38.7$, at $^{87}Sr/^{86}Sr = 0.7029$ and $^{143}Nd/^{144}Nd = 0.5130$, with higher Na values, which are more similar in character to the 2°N-1°S melts.

Figures 89 and 90 use the numerical scores attached to the geochemical characteristics in Table 25 to generate a shape for each locality. These shapes are then compared to determine which localities are most alike. The more similar the shapes, the more similar the geochemical characteristics of a site. The raw shapes for each locality are shown (Figure 89). The diagram shows that the 15°2'-12°60'N pattern is similar to that of the Azores, but shares somewhat fewer characteristics with the other areas. This information is seen more clearly when the shapes are overlaid onto each other.

In Figure 90, the 12°60'N-15°20'N data are overlaid in each case with the data from a different locality (labelled). Using this method, it can be seen that the Azores data almost completely overlaps the 12°60'-15°20'N data, and therefore, they are very similar.

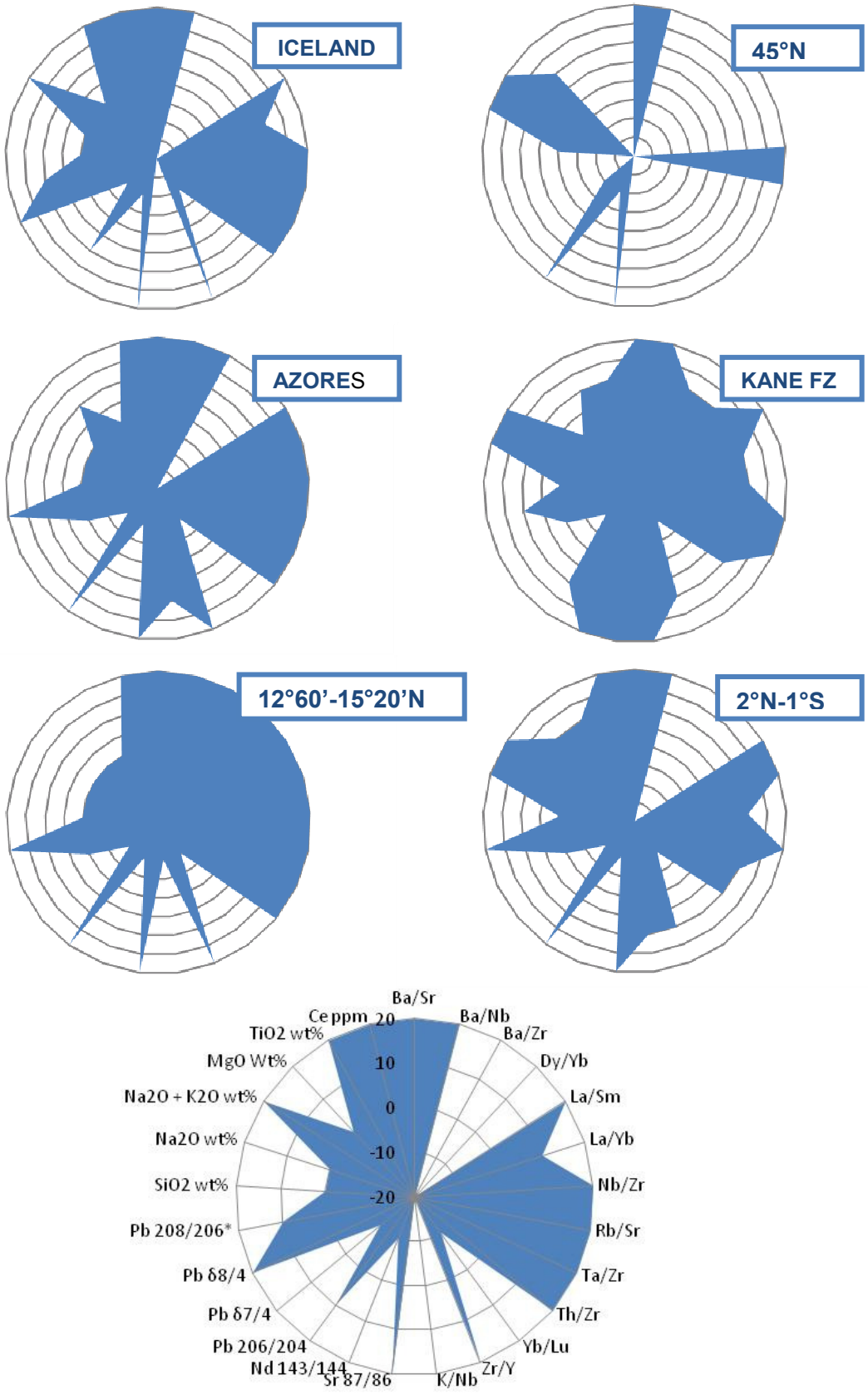

Figure 89: Rose diagrams generated by the qualitative data from Table 24. The diagram shows that the 15°20'-12°60'N shape is similar to that of the Azores, but shares somewhat fewer characteristics with the other shapes. The bottom circle acts as a key, showing the positions of different scores and geochemical attributes.

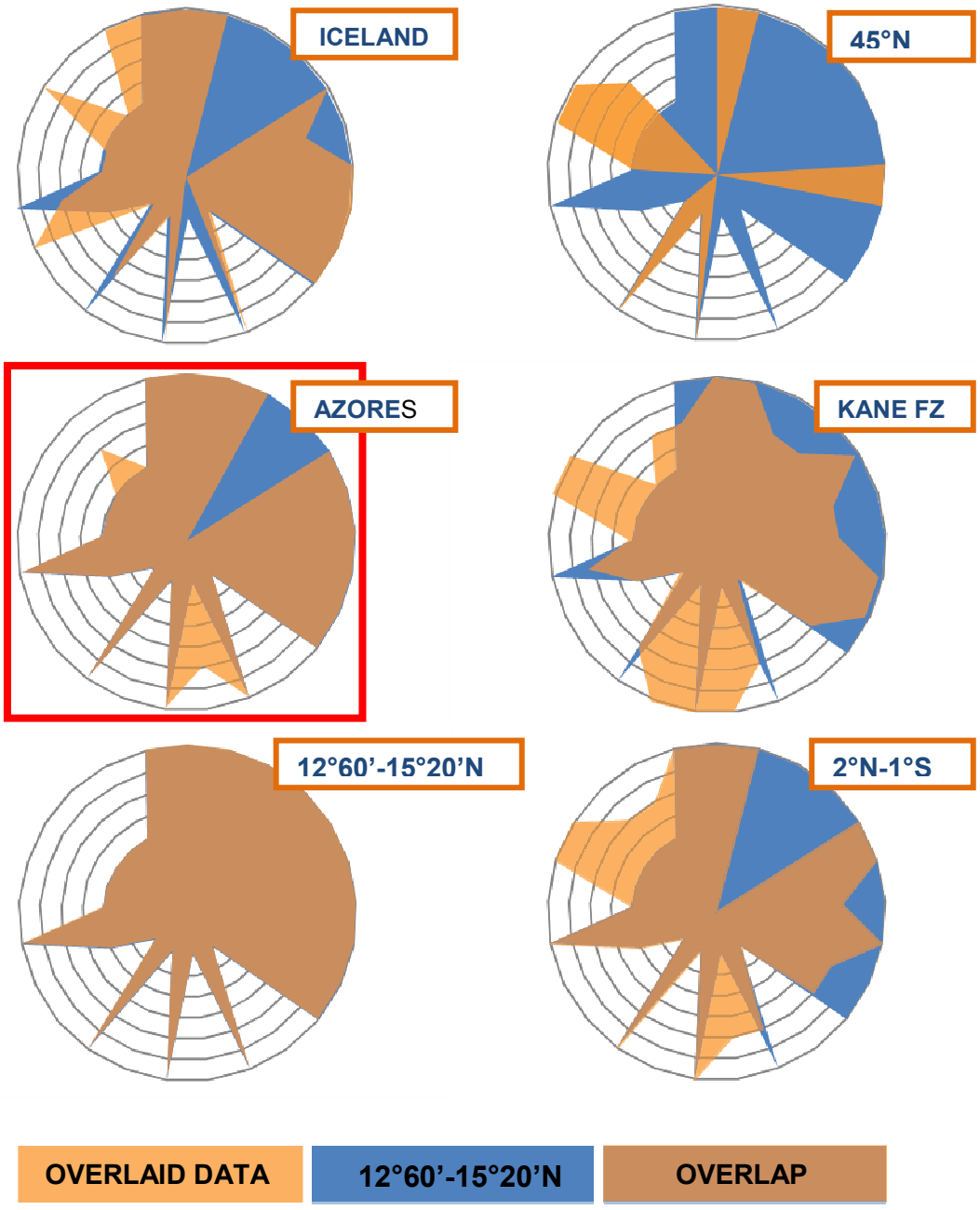

Figure 90: Overlaid rose diagrams are used to compare the sites directly. In each case, 12°60'N-15°20'N data are overlaid with the data from another site. In this way, 12°60'N -15°20'N data which are not matched shows through as blue, data from the overlapping locality which is not matched is orange, but overlap (where the data is the same) is brown. Hence, when 12°60'N-15°20'N is overlaid with 12°60'N -15°20'N data, the whole shape is brown. The best match to the 12°60'N -15°20'N data is the Azores data.

This qualitative assessment suggests that the 12°60'N -15°20'N E-MORB signal is most closely matched by the geochemistry of the Azores Hotspot E-MORB/OIB. Major and trace element data are limited for 1°S -2°N and 45°N, but the 12°60'-15°20'N and Azores fields can be clearly differentiated from those of Kane FZ and Iceland. Bivariate plots of selected geochemical characteristics from the table above show this relationship quantitatively (Figure 91).

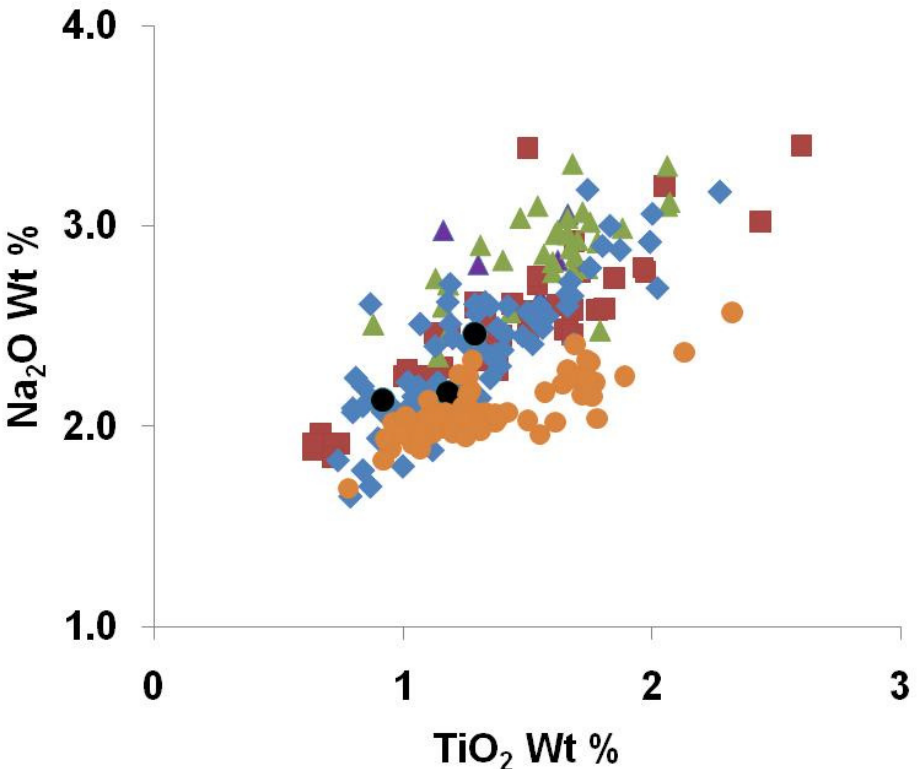

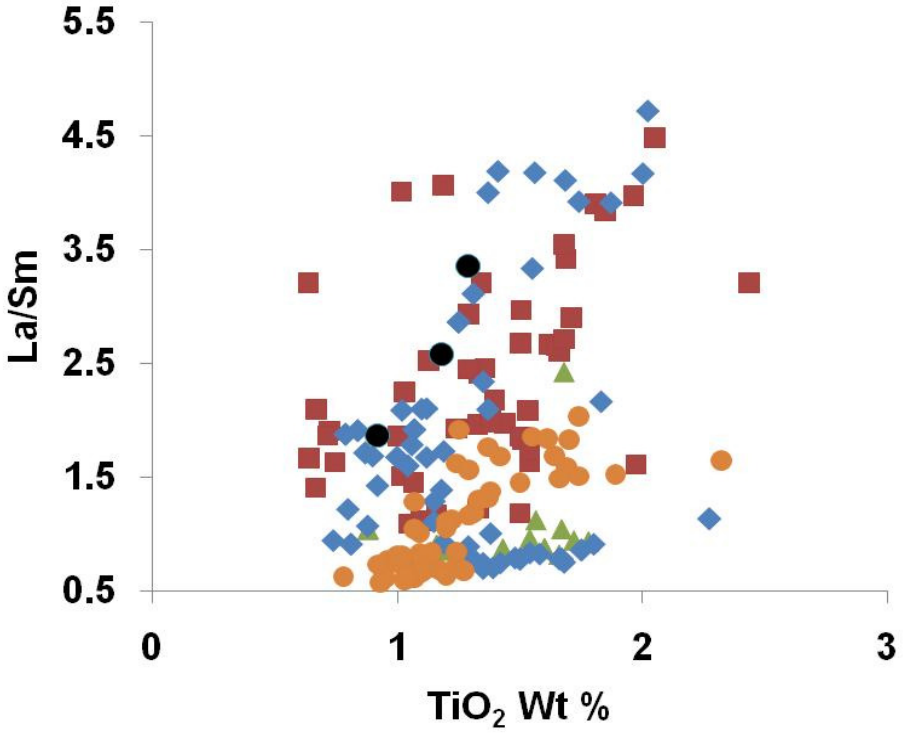

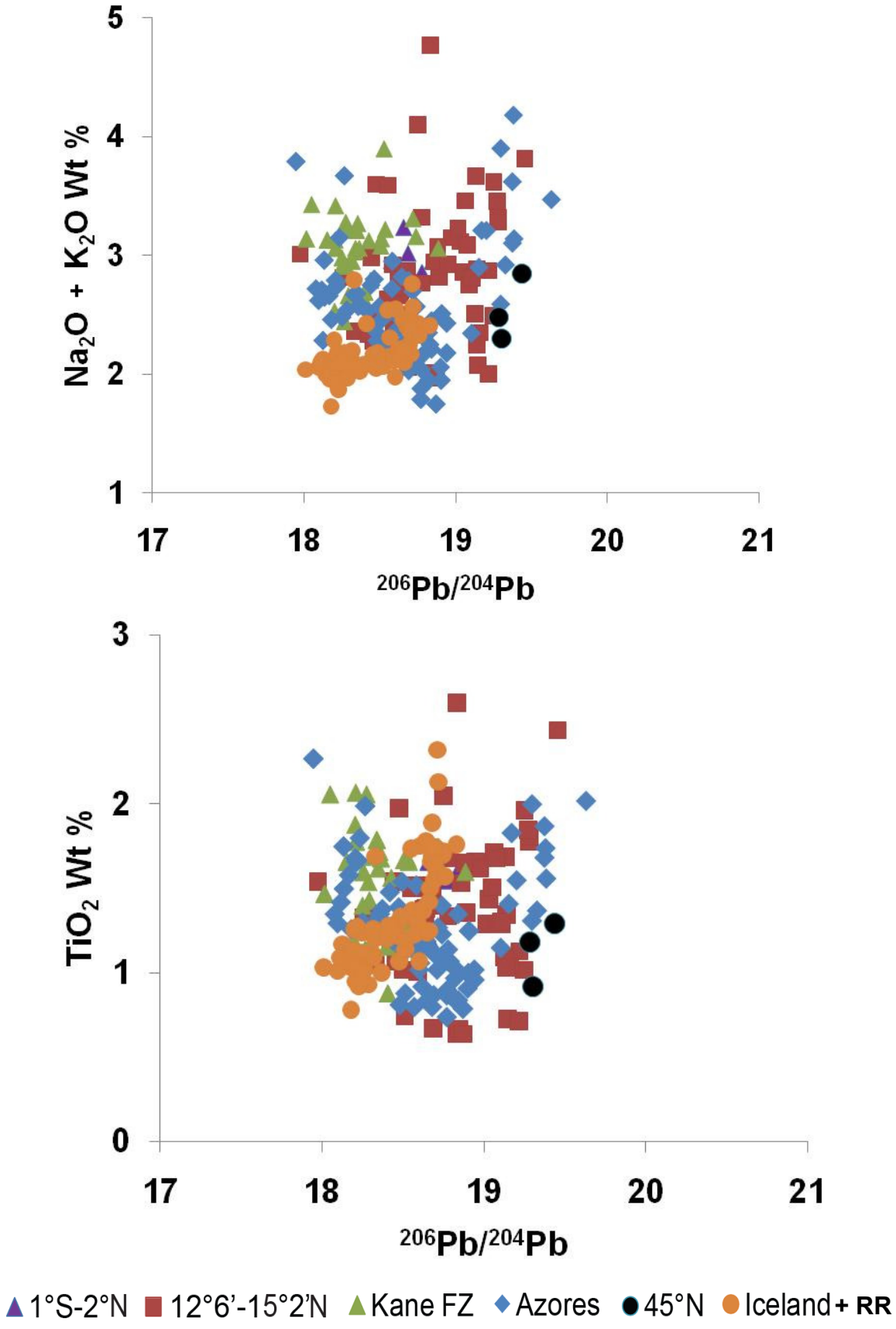

Figure 91: Major element, trace element and isotopic data for basalt enrichment zones on the MAR. 12°60'-15°20' data from this study and PetDB. All other data from PetDB. RR= Reykjanes Ridge. The data show that the 12º60'-15º20'N area is geochemically most similar to the Azores.

Basalts from 12°60'N-15°20'N are also similar to the 45°N data, though the 45°N dataset is not large enough to thoroughly explore this relationship.

12°60'N-15°20'N rocks are lower in Na[8] than average for the central MAR, but extend to higher concentrations of K, Ti and P. The E-MORBs extend to extremely high concentrations of trace elements, such as Sr, Nb, Nd, Ce, Zr, U, Pb, Ta and La, and to lower concentrations of Yb than other areas of the central MAR. Enrichment commonly appears to mirror that of the Azores hotspot. Like typical OIBs, M1 (13°19'N OCC) basalts have enriched K, Rb, Cs, Ba, Pb, Sr, Th, U, Ce, Zr, Hf, Nb, Ta, and Ti relative to MORB. M1 basalts have enriched LREE and progressive depletion relative to chondrite through the HREE, giving much steeper REE plots than N- and E-MORB, but resembling many OIBs.

Trace element ratio plots (Figure 92) also show the similarity between the 12°60'-15°20'N, Azores and 45°N regions. Both sites clearly differ from the Iceland and Kane FZ datasets, extending to substantially higher trace element ratios.

At 12°60'-15°20'N, Zr/Nb values (commonly used to distinguish between sources) are in the OIB range of <10 (On-axis = 9, M2=12, M1=5) and substantially lower than the N-MORB value (>30). However, K/Ba ratios (Figure 93) are more typical of N-MORB (>100) to E-MORB (~35) compositions (Axial=46, M2=60, M1=42), rather than OIB (20-40).

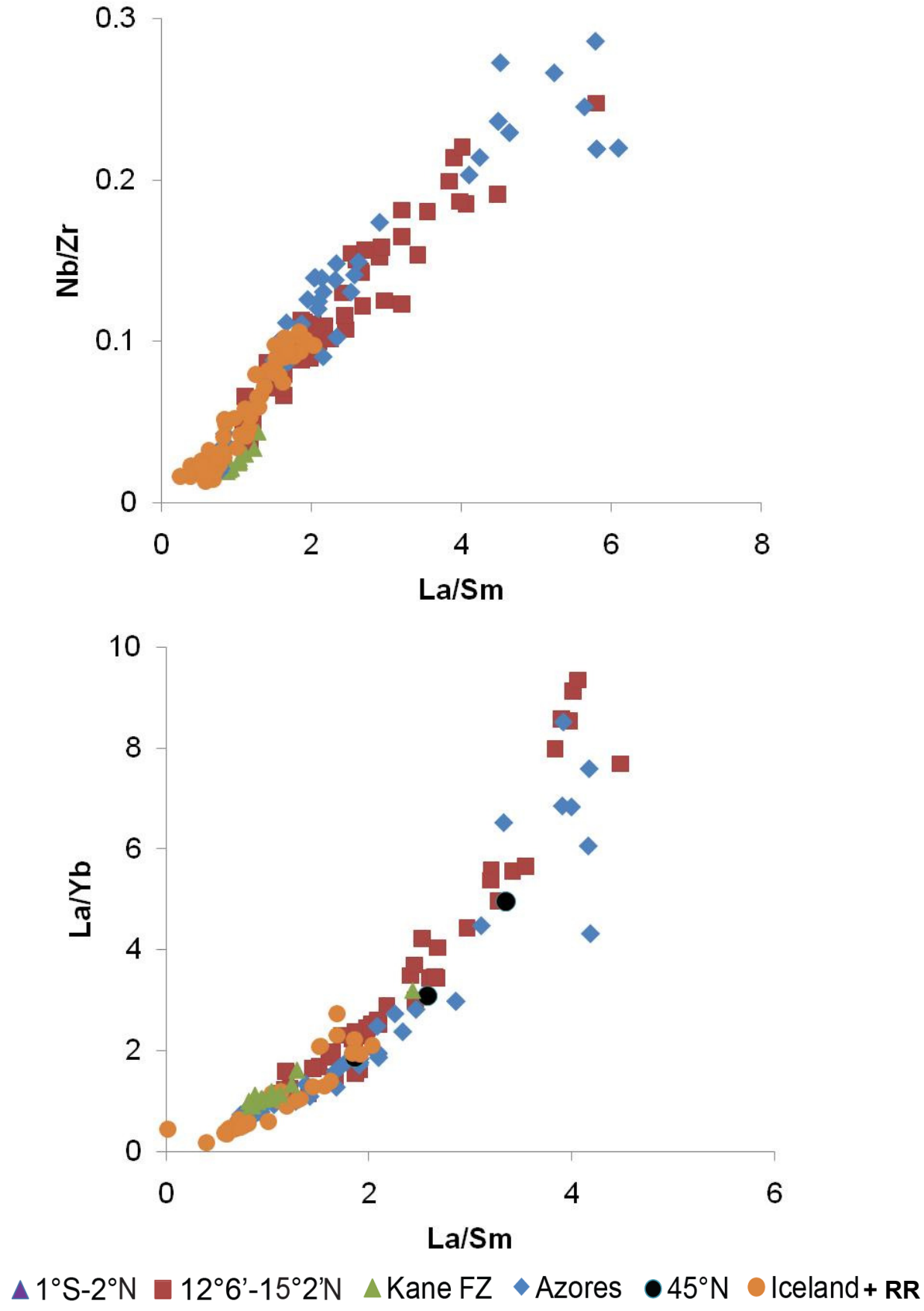

Figure 92: Trace element ratio data for enrichment zones on the MAR. 12°60'-15°20' data from this study and PetDB. All other data from PetDB. Data for each region is shown where available. Once again, the 12º60'-15º20'N area is geochemically most similar to the Azores.

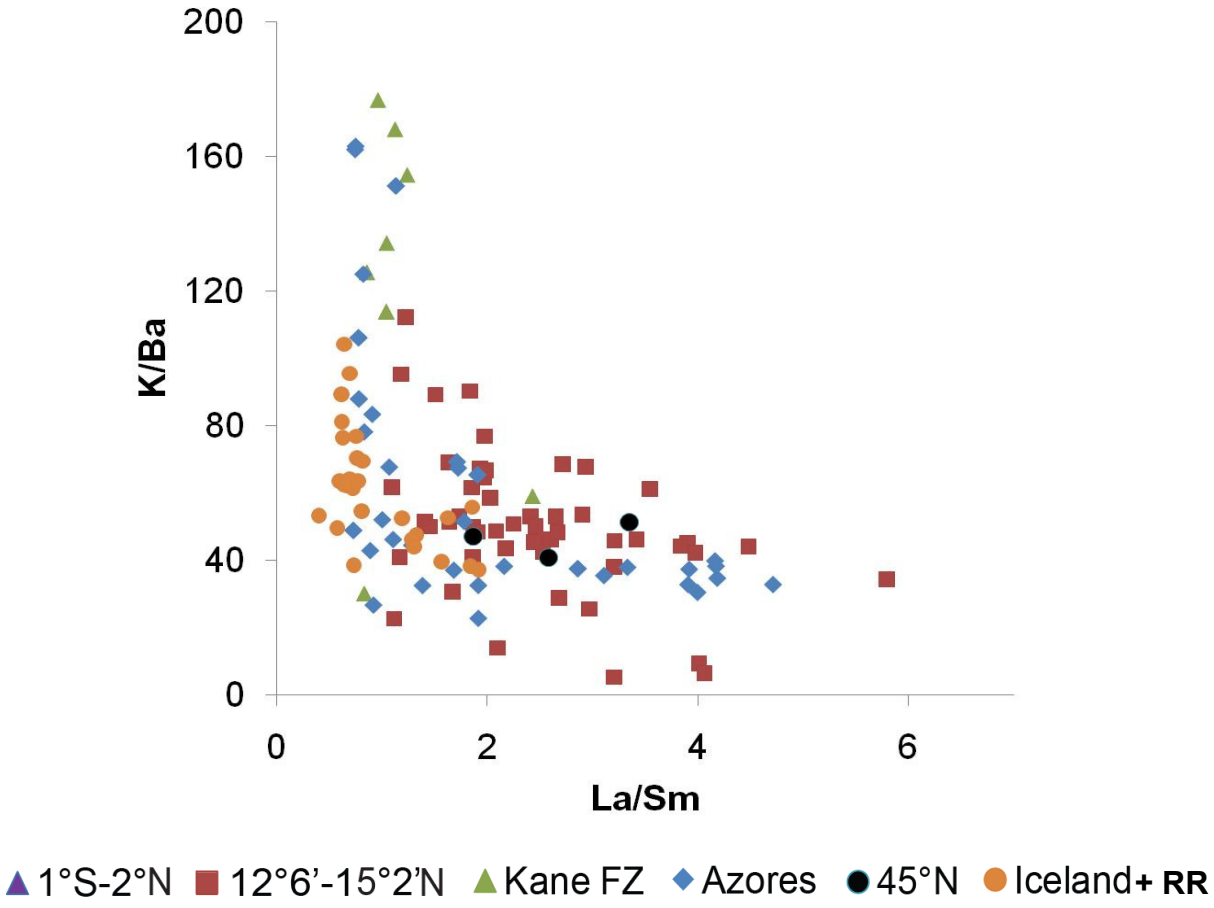

Figure 93: K/Ba vs. La/Sm data for enrichment zones on the MAR. 12°6'-15°2' data from this study and PetDB. All other data from PetDB. Data for each region is shown where available. Once again, the 12º60'-15º20'N area is geochemically most similar to the Azores.

The logarithmic Nb/Y vs. Zr/Y (ΔNb) discrimination diagram of Fitton *et al.* (1997) is used to distinguish between basalts of MORB and OIB origin. Virtually all N-MORBS, having negative ΔNb, plot below the 'ΔNb=0' line. The Icelandic OIB array has ΔNb > 0, and plots above the 'ΔNb=0' line. E-MORB with ΔNb > 0 is abundant on MORs, notably in the south Atlantic and south Indian oceans (Fitton, 2007). Movement parallel to the ΔNb=0 line on this diagram denotes compositional changes related to magmatic processes, whereas vertical movement denotes source composition. The discrimination diagram (Figure 94) illustrates the OIB-like nature of 12°60'-15°20'N E-MORB basalts. As shown, M1, M2 and on-axis basalts from this segment all plot within the OIB array. The left-right evolution from M1 to M2 basalts results from variable melt fraction.

HIMU OIB are particularly noted for their high ΔNb values (Fitton, 2007). The presence of HIMU in the 12°60'-15°20'N source provides an explanation for the OIB-like position of the array.

Figure 95 shows the arrays for the source regions discussed previously in this section, along with an additional array to represent the N-MORBS of the 17°10'-20°N region sampled by Dosso, for comparison to the OIB suites.

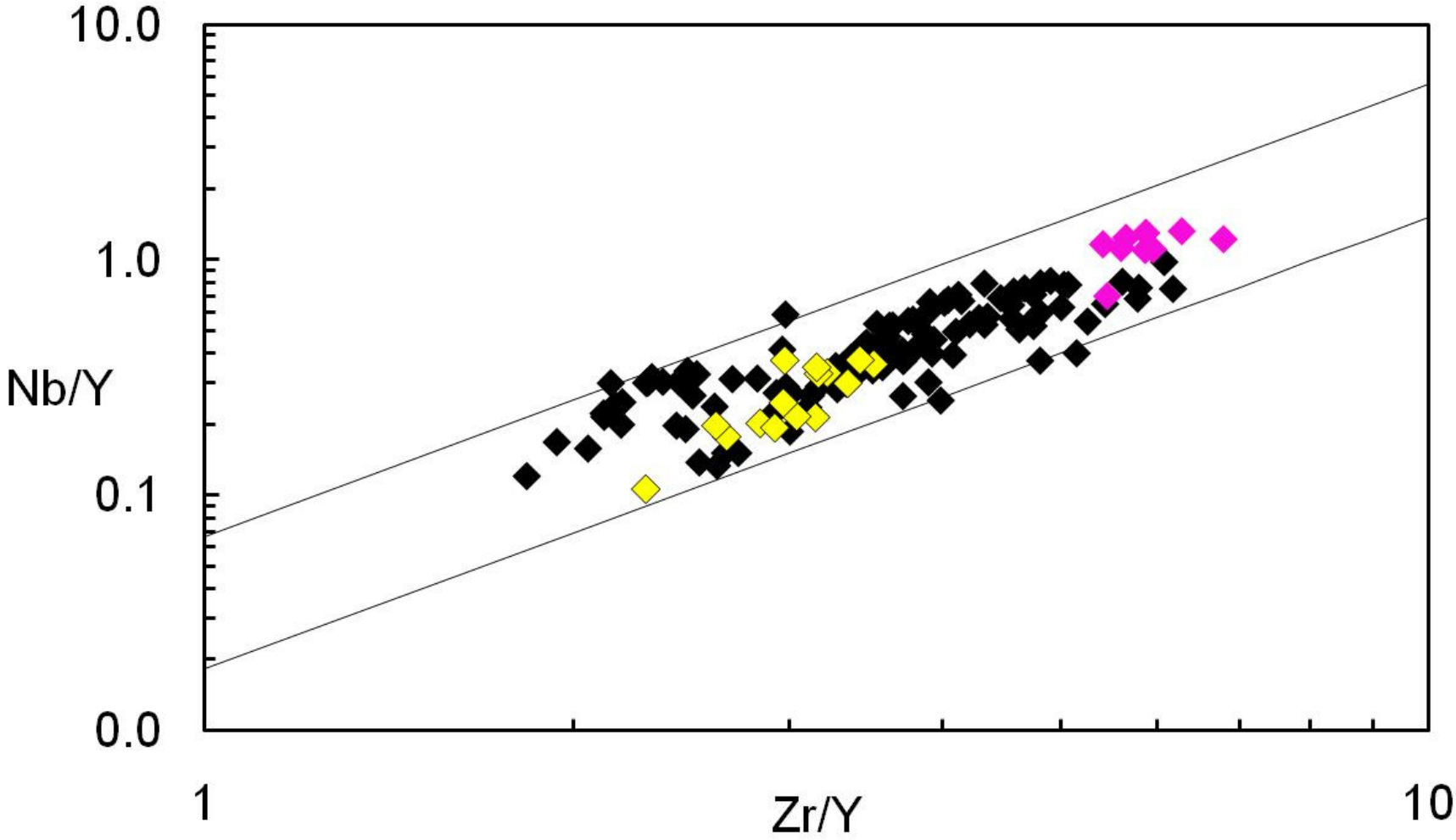

Figure 94: ΔNb plot for the discrimination of MORB and OIB, as described by Fitton (2007). The plot shows 12°6'N-14°N on-axis (black), M1 (pink) and M2 (yellow) data. All data lie above the 'ΔNb=0' line (the lower line on the diagram), and are therefore in the OIB range.

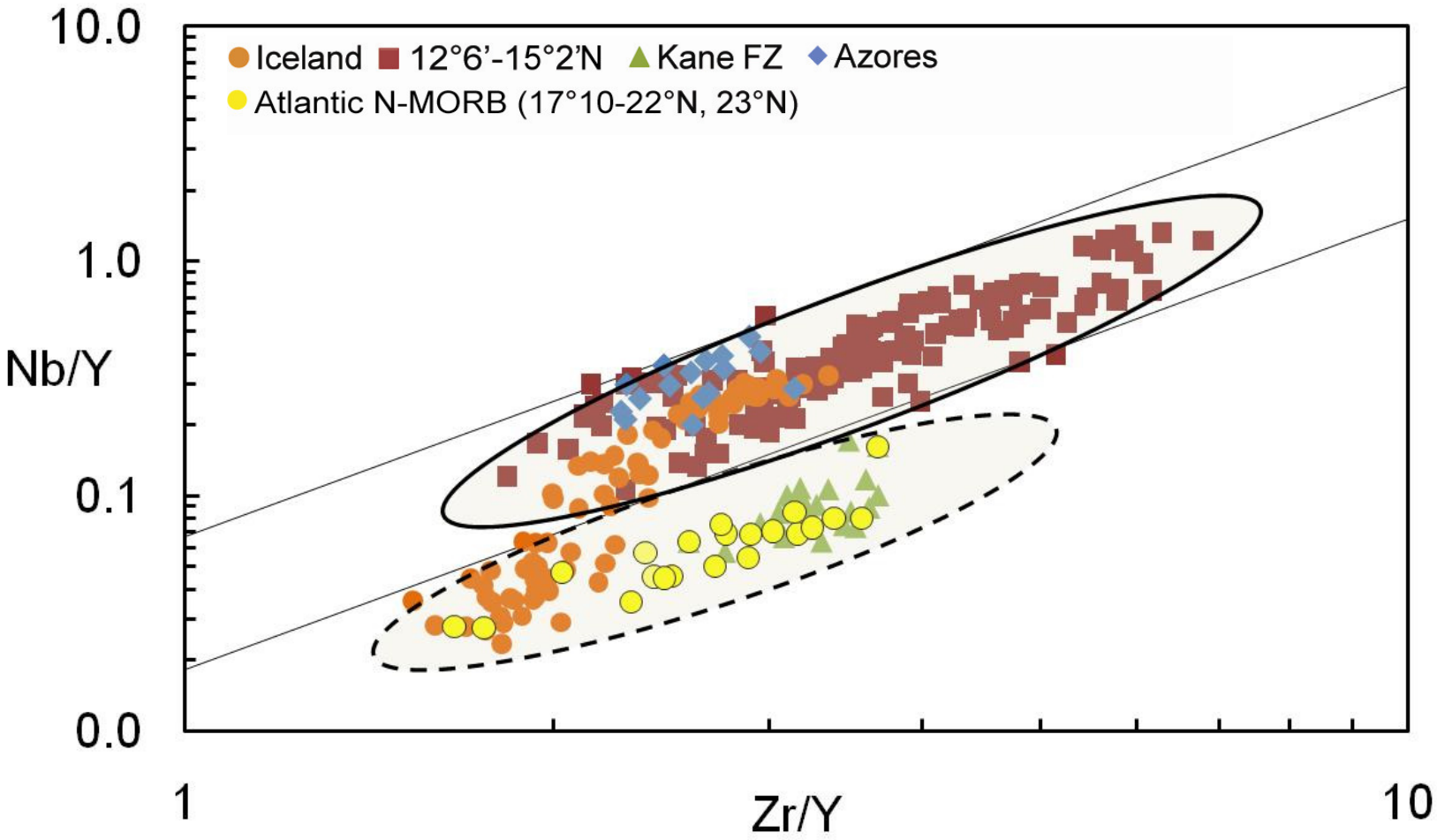

Figure 95: ΔNb plot for the discrimination of MORB and OIB, as described by Fitton *et al*., (1997) and Fitton (2007). 12°60'-15°20' data and Azores data lie within the OIB range. 17°1'-22°N data and 23°N data (yellow group) fall below the ΔNb=0 line (the lower line on the diagram) in the N-MORB range. The Iceland data array includes data for the Reykjanes Ridge, and crosses the ΔNb=0 line from OIB into N-MORB south of Iceland on the Reykjanes Ridge, where the hotspot ceases to interact with the ridge. 12°60'-15°20' data from this study and PetDB. All other data from PetDB. There is no data available for 45°N or 1°S-2°N.

This plot clearly shows the divide between N-MORB suites (17°10'-20°N, Kane FZ) and the OIB/E-MORB suites 12°60'-15°20'N and the Azores.

Kane FZ region (~23°N) sits geographically between 12°60'-15°20'N and the Azores, and is N-MORB-like in character according to the ΔNb diagram. This shows conclusively that the 12°60'-15°20'N region does not inherit its enriched LREE trace element geochemistry from the Azores plume, otherwise such material would have to pass through the Kane region, and enrichment would be present here also. The Icelandic data shown here includes a portion of the MAR south of the hotspot (Reykjanes Ridge), and this allows us to clearly see in the data a transition between OIB and N-MORB as the hotspot ceases to interact with the ridge in terms of trace element geochemistry. It should be noted, however, that this trace element behaviour does not necessarily coincide with the cessation of the isotopic influence of the ridge, as shown by Taylor et al. (1997).

N-MORB have negative Delta-Nb values, whereas Iceland and other OIBs have positive values. When ΔNb is plotted against latitude for 0-45°N (Figure 96), the resulting plot clearly shows a positive ΔNb 'spike' around 12°60'-15°20'N, rapidly returning to negative ΔNb values beyond ~17°N. This suggests that the mantle lying beneath ~15°N contains enriched material, which may originate from a random heterogeneity in the mantle, but could also be evidence for a blob of detached plume material, possibly originating from the nearby Azores plume, which shares many geochemical characteristics with ~15°N.

Isotope geochemistry is a useful discriminator of mantle source reservoirs. In Pb isotopic space, the 12°60'-15°20'N region resembles both 1°S-2°N and Azores sites, to different degrees. 15°20'N Sr and Nd isotopic values are lower than those in the Azores basalts, separating the arrays clearly (Figure 107).

This evidence suggests that whilst the geochemistry of the Azores and 12°60'-15°20'N are similar, and may therefore have similar origins, the 12°60'-15°20'N rocks do not share a source with the Azores plume. On the basis of isotope geochemistry, 12°60'-15°20'N may share source material with 1°S-2°N.

It has been suggested that rocks from ~12°-18°N form from geochemically distinct mantle sources to the surrounding MAR, perhaps originating from a geochemically heterogeneous plume (Silantyev et al., 2008).

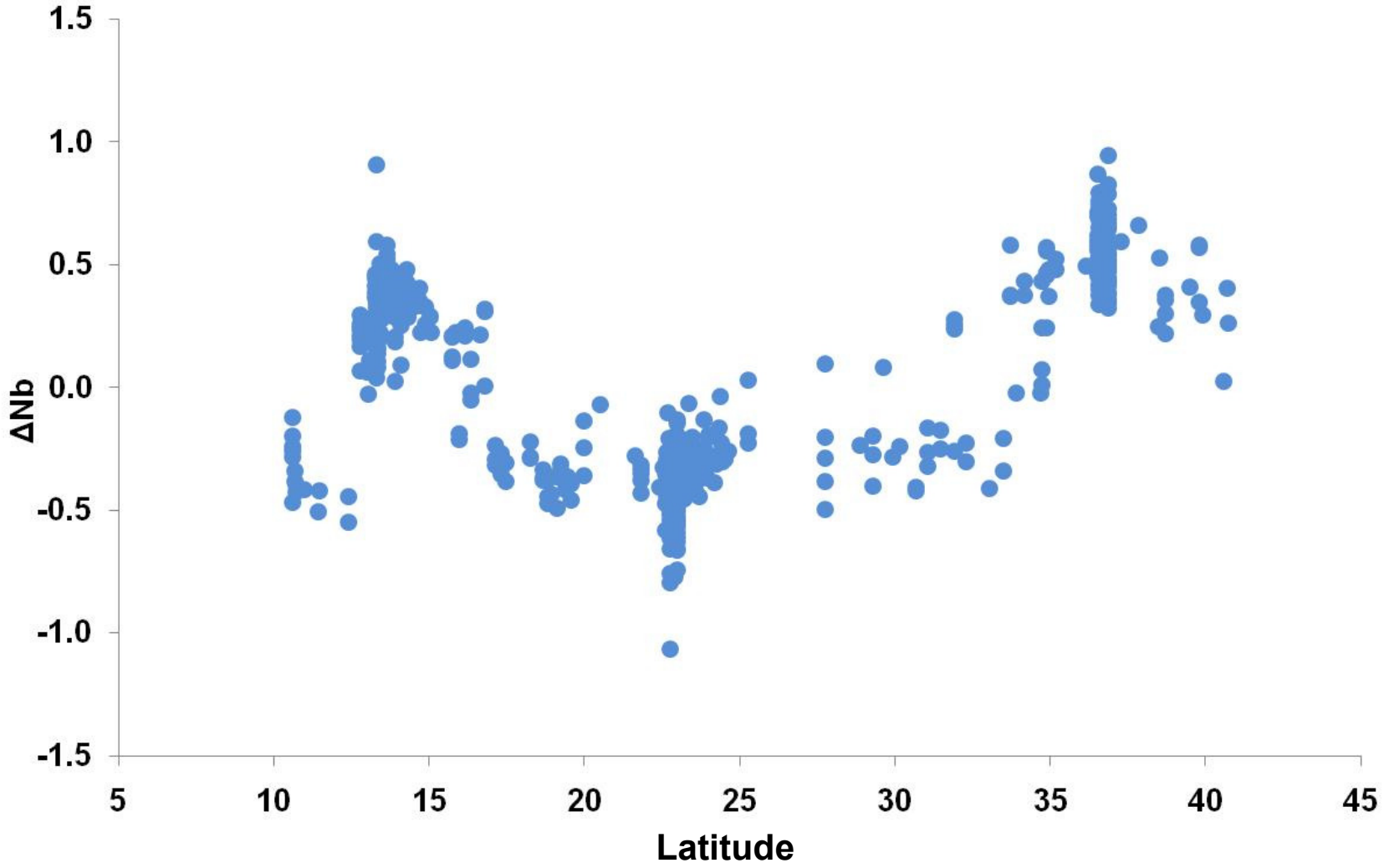

Figure 96: ΔNb vs. latitude plot for the discrimination of MORB and OIB. The plot shows data fom PetDB and this study.

Mantle source variations at the segment scale or smaller are favoured as an explanation for geochemical signatures in the region according to Dosso et al (1993). Geochemical enrichment has been attributed to mantle thermal plume or metasomatized H_2O rich mantle domains, which would cause enhanced melting and provide a source for basalt enrichment, and which may be relics of an originally subcontinental mantle (Bonatti, 1992).

Skolotnev et al (1999) report a correlation on the MAR 12°1'N-15°20'N between enriched basalts and segment centre areas with elevated lithospheric permeability. They suggest that these basalts are formed by fractionation in large intermediate magma chambers, and attribute their unusual nature to association with a mantle plume.

Like the OIBs of the Azores, the basalts of 12°60'-14°N originate from a source with HIMU (high U/Pb, and commonly low $^{87}Sr/^{86}$ Sr) flavour (Dosso et al, (1991) and this study), though 12°60'-14°N rocks also exhibit characteristics of the mantle end-member FOZO.

M1 basalts from 13°19'N have average Ce/Pb values (29.6) higher than those expected for MORB (~25, see Table 14). M1 data tend toward the higher values expected for the HIMU source (31.5). M2 (21.7) and on-axis basalts (24.0) are more MORB like, though M2 Ce/Pb values are much lower than N-MORB, suggesting a decreased contribution from a HIMU component. This is consistent with formation from a highly depleted source where the HIMU component is not extensively sampled.

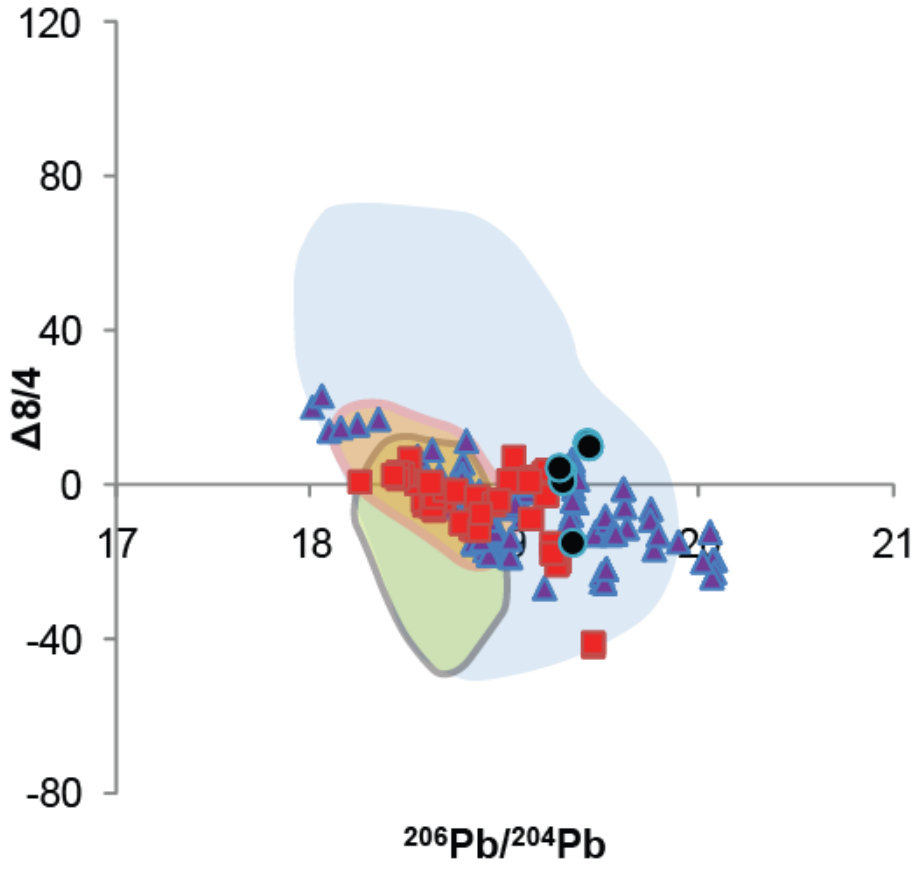
120
80
40
0
-40
-80
Δ8/4
17
18
21
206Pb/204Pb

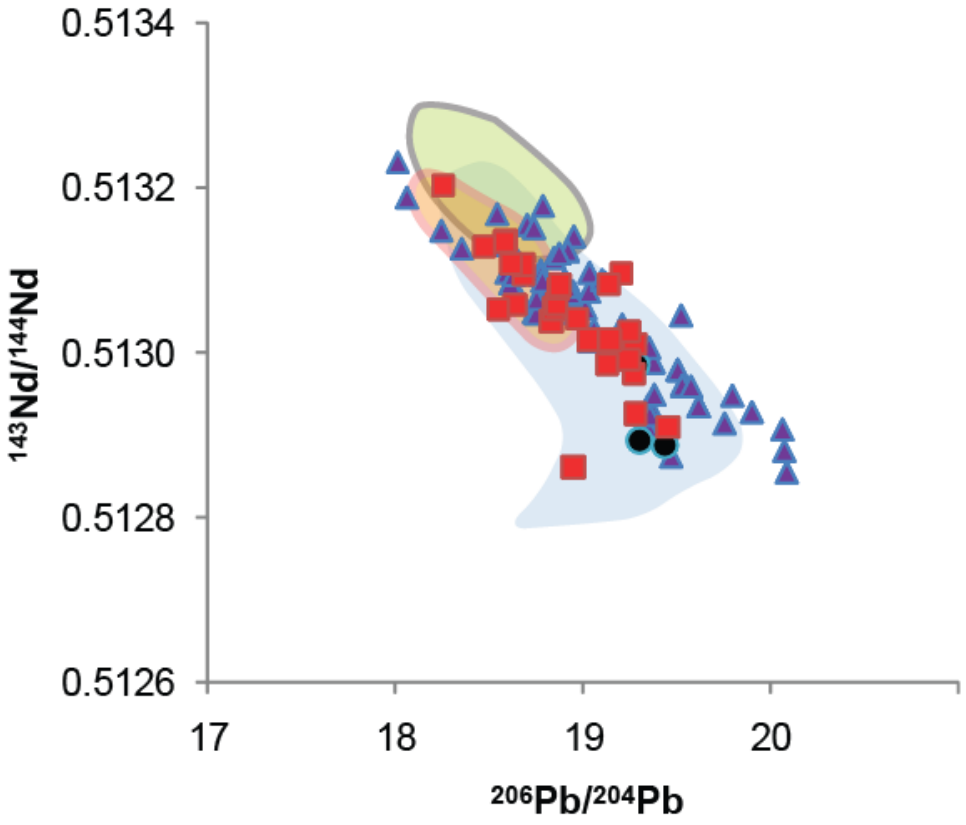
0.5134
0.5132
0.5130
0.5128
0.5126
143Nd/144Nd
17
18
19
20
206Pb/204Pb

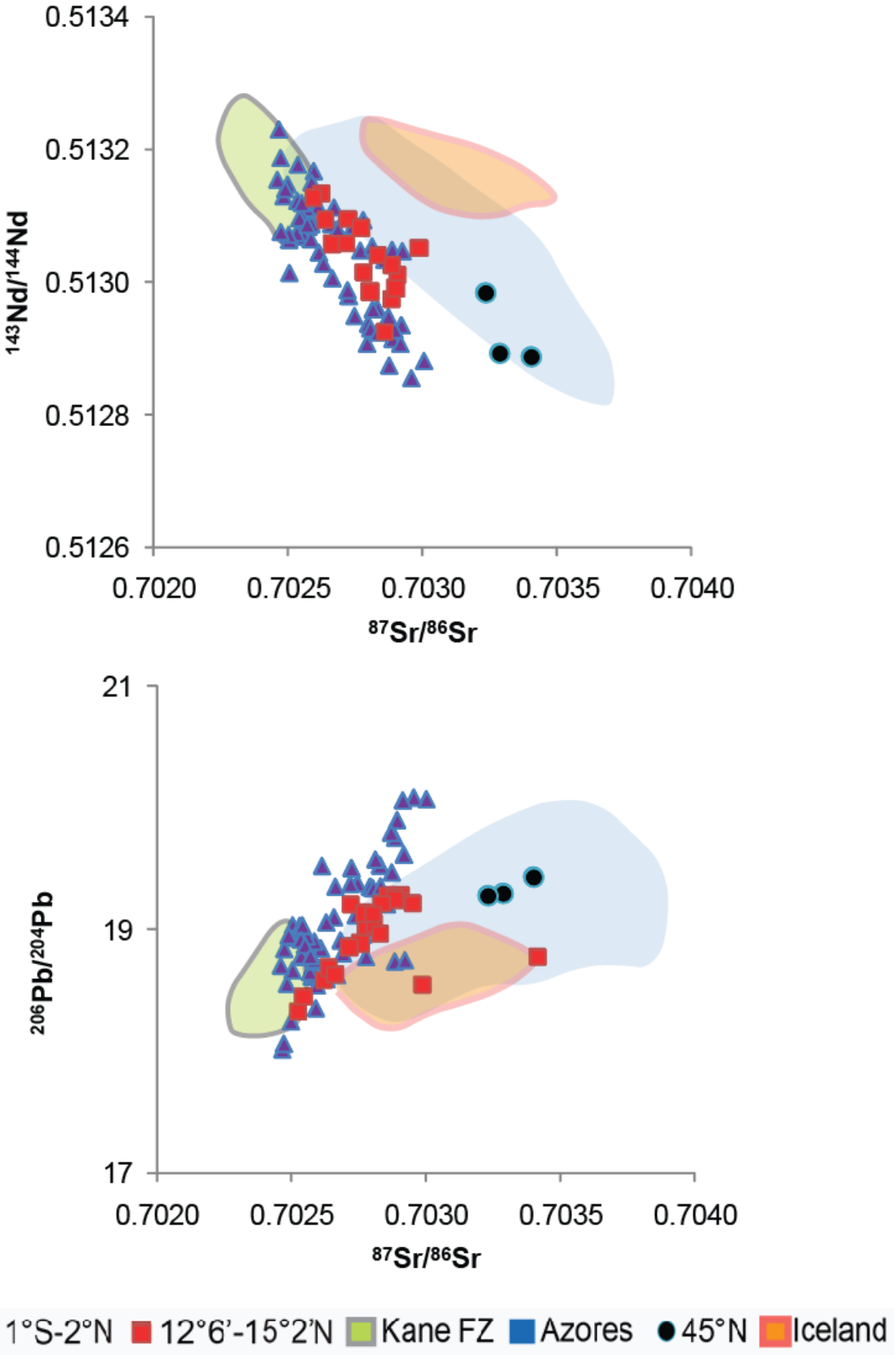

Figure 97: $^{206}Pb/^{204}Pb$, $^{87}Sr/^{86}Sr$, $^{143}Nd/^{144}Nd$ and Pb Δ8/4 data for enrichment zones on the MAR. 12°60'-15°20' data from this study and PetDB. All other data from PetDB. Kane FZ, Azores and Iceland data fields are shown as clouds to improve clarity of the plots.

HIMU sources have been identified in basalts from a number of continental and ocean island sites globally. The term 'HIMU' is sometimes used to describe compositions from specific islands such as St Helena (Chaffey et al., 1989), but is also used in a more general sense as a descriptor for a (high U/Pb) high $^{206}Pb/^{204}Pb$ mantle component.

HIMU-like signals are identified in the Antipodes and Chapham Islands (New Zealand, see Panter et al, 2006); on the East Tasman Plateau (Crawford et al., 1997); in the Pacific Ocean, at Ua Pou (Marquesas), Mururoa and Fangataufa (Gambiers) (Grall et al., 1986; Rocaboy, 1987) and Guadalupe (Sun, 1980); in the Atlantic at the Azores (Beier et al., 2007) and Cape Verde Islands (Davies et al., 1989; Dupre et al., 1982), Canaria (Hoernle et al., 1991); in the Cook-Austral Islands (Polynesia) e.g. Tubuai, (see Vidal et al, 1984; Parai et al, 2009), Mangaia, (see Woodhead 1995; Kogiso et al., 1997) and Rurutu; in the Balleny Islands (Hart. 1988; Lanyon. 1994) and in the alkali rocks of the Cameroon line (Halliday et al, 1990; Ballentine et al, 1997). The above mentioned sites are either ocean islands, forming OIB, or sites of continental volcanism. Compositions close to end-member HIMU are very unusual for the MOR system.

However, studies of 5°N-5°S on the central MAR region show that basalts here also have a DMM-HIMU flavour (Hannigan et al, 2001), which has previously been attributed to the influence of the Sierra Leone mantle plume (Schilling et al, 1994).

The origin of HIMU is a matter of much debate, and is discussed in detail earlier in this chapter. Regardless of the geochemical origin of the source, many studies agree that HIMU melts form when subducted material which has been stored in the deep mantle is returned to the surface by mantle plumes (i.e. Hofmann, 1997; Moreira & Kurz, 1999).

The HIMU component is thought by others, however, to arise from intra-mantle metasomatism and melt infiltration, without deep mantle involvement (Hart, 1988; Stein et al., 1997; Blusztajn & Hegner, 2002; Pilet et al., 2005).
On the basis of isotope compositions, Vidal (1992) draws a distinction between groups of regions producing HIMU melts. Group 1 (St Helena, Tubuaii, Mangaia) are identified as having long lived U/Pb ratios, whereas Pacific and Atlantic HIMU

(e.g. Azores) ‘exhibit a much less pronounced enrichment in radiogenic lead due to only a recent increase in the μ ratio, whereas HFSE enrichment and lead depletion are more pronounced than in Group I’. The origin of OIB compositions from young HIMU mantle is discussed in detail by Thirlwall (1995, 1997). The 12°60’-15°20’N region falls into group 1 on the basis of isotope and trace element compositions, being more comparable to other Atlantic HIMU islands than to the St Helena type locality.

The other mantle component contributing to chemistry of the 12°60’-15°20’N region is the HIMU-type FOZO component (Hart et al., 1992). It is slightly less radiogenic in Pb and more radiogenic in Sr than HIMU and lies on the Atlantic-Pacific MORB array. The MORB-FOZO array is thought to be generated by the processes of mantle melting and subduction (Stracke et al., 2005).

Wilson and Spencer, (2003) suggest that FOZO is representative of deep mantle plume material. HIMU and FOZO may be generated by the same process, as they have analogous trace element compositions, favouring a similar source. However, this is not the case for lavas at Rurutu, where trace element and isotopic variations are seen between FOZO and HIMU lavas (Chauvel et al., 1997). It is unclear whether these variations are a specific feature of this volcano alone, or whether they indicate separate source histories for HIMU and FOZO melts (Stracke et al., 2005).

This study has shown that the melts of the 12°60’N-14°N regions are strikingly similar to those of the previously documented equatorial MAR enrichment (e.g. Schilling et al, 1994, Hannigan et al, 2001), and also to those of the Azores OIB in terms of trace element and Pb isotopic compositions. PetDB data show that the magnitude of the major and trace element enrichment of the 12°60’-14°N E-MORB zone is similar to that generated by the Azores plume. There is, however, no clear bathymetric or geophysical evidence for the presence of a mantle plume beneath 12°60’N-14°N.

Clearly, the central MAR region hosts a number of ‘hotspot like’ E-MORB enrichment zones that are not related directly to hotspot volcanism, or plume-ridge interaction. This fact was recognised previously by White (2010) for the case of the 45°N area. The magnitude and geographic scale of these zones indicates that they exemplify a significant mechanism for the generation of E-MORB at the slow-spreading MAR.

Zones of anomalous E-MORB production that are not fed by hotspots must acquire their enriched signatures via normal MOR processes. The presence of a sharp boundary of geochemical change at 17°10'N, which is unrelated to structural or geophysical features, shows that the parameters that control the transition between N-MORB and E-MORB production are capable of sharp, as well as gradational change.

On slow-spreading ridges, a cold, thick lithospheric lid can lower the degree of melting, leading incompatible-element rich, small melt fractions to be extracted, which have E-MORB signatures. Alternatively, variations in source composition can arise due to re-fertilisation of the DM mantle with sources of different compositions, acquired during subduction, or previous melting episodes.

A number of studies have been carried out into the nature and chemistry of the residual mantle peridotite in the region surrounding the FTFZ. They find that peridotites from the region have experienced high levels of melt extraction (Seyler et al., 2007; Godard et al., 2008; Suhr et al., 2008). The peridotites represent the most refractory compositions yet to be sampled at a slow spreading ridge (Godard et al., 2005), as they lack residual clinopyroxene, but have olivine Mg# up to 0.92 and spinel Cr# (~0.5). These features are indicative of high degrees of partial melting (Seyler et al., 2007). Other studies have found that in general, peridotites from the region south of the FTFZ are the most refractory on the MAR (Dosso et al., 1993).

Seyler et al. (2007) suggest that the ultra-refractory compositions at ODP Site 1274A formed as a result of previous partial melting of the mantle, followed by melt-rock reaction and refertilisation, before upwelling and remelting at the ridge today. The ultra-depleted compositions resulted from melt re-equilibration with residual harzburgites. Textural and geochemical analyses of Sites1272A and 1274A peridotites suggest reaction of the peridotites with a mafic silicate melt prior to serpentinisation (Vils et al., 2008). Recent work by Collier and Kelemen (2010) suggests that reaction of peridotite with MORB melts during early cooling and crystallisation is a significant process contributing to the composition of fractionation corrected MORB, as well as that of the peridotite residue.

Variable refertilisation of the ultra-depleted mantle by enriched HIMU-FOZO-like melt material in veins provides a logical explanation for E-MORB generation on this region of the MAR.

Geochemical data show that the 12°60'-15°20'N basalts form a HIMU-FOZO-DMM source. In order for the HIMU/FOZO material to be present, the mantle must have experienced an earlier episode of refertilisation/metasomatism. Given the extensive melting and melt-rock reaction evidenced by harzburgite sampled in the region, this refertilisation is likely to have occurred as small volumes of melt were frozen into the source following an episode of extensive melting of an enriched mantle source with HIMU-FOZO flavour. The HIMU-FOZO material is therefore likely to exist as volatile-rich veins within the harzburgitic source, rather than as a distinct or cohesive plume.

At the slow-spreading MAR, the lithosphere is thick, and this restricts upwelling, so that the mantle melts less by decompression than in a fast-spreading environment, producing lower melt fractions at higher pressures (Humphreys and Niu, 2009).

This study concludes that the unusually depleted nature of the host (DMM) mantle beneath 12°60'-15°20'N means that even at the normal PT conditions of melting for the MAR, comparatively little melt is likely to be produced. When fusible HIMU-FOZO veins are preferentially melted out at low melt fraction, a pronounced E-MORB signature is generated. This signal is of a similar magnitude to that which would be produced by extensive melting of an enriched, plume-like source. By this mechanism, small-scale 'marble-cake' mantle heterogeneities, whatever their origin, are capable of generating enriched, and even plume-like signatures at mid-ocean ridges, without the need for plume-ridge interaction or any other complex mantle process.

Finite mantle heterogeneities such as these can generate sharp geochemical transitions between E- and N-MORB. Local, small-scale variability in DMM depletion and HIMU-FOZO re-enrichment beneath the ridge can produce a wide range of basalt compositions along the segment.

Given the extreme extent of melting experienced by the harzburgitic residual mantle beneath 12°6'-15°2'N, and the (arguably) deep-mantle origin of the refertilising HIMU-FOZO material, it is possible the packet of mantle now lying beneath the 12°60'-15°20'N experienced the passage of a mantle plume earlier in its history. This plume would have stripped the mantle of fusible components, leaving harzburgite veined with a small proportion of enriched plume residues, of a HIMU-FOZO flavour. Upon later, low melt fraction re-melting beneath the thick lithospheric lid of the slow-spreading MAR, a geochemical 'ghost plume' emerges. If this is the case, any plume activity associated with this area of the ridge affected the mantle historically, and there is no compelling evidence for the presence of a plume here today.

7.4 - CAUSES OF MID-SEGMENT OCC DEVELOPMENT - 12°60'-14°N

The region around the FTFZ hosts a number of OCCs. These structures expose mantle peridotite on the seafloor, and normally develop at the end of slow-spreading ridge segments, where mantle focusing away toward the segment centre is thought to locally starve the ridge of melt.

Contrary to this pattern, OCCs between 12°60'-14°N are distributed throughout the centre of the magmatic segment, and fresh lava flows are absent in much of the axis, leading to the suggestion that their development here must be a consequence of low melt supply across the whole segment. A number of hypotheses were posed by this thesis to explain this dramatic reduction in melt supply.

Melt may be produced in the mantle, but not provided to the ridge if mantle focusing away from the region dictates that no melt is physically available at OCC sites. This implies that mantle upwelling in the region operates on a geographic scale of 15-30km, so that melt is delivered to magmatic areas, but not to the OCCs between them. This is a much finer scale than that usually invoked for mantle focusing on slow-spreading ridge segments.

Basalt geochemistry from the length of the ridge segment 12°60'-14°N indicates that all areas on the axis are currently receiving a good supply of melt, with melt fraction remaining relatively constant, in magmatic and OCC areas. This suggests that mantle focusing away from the OCC region historically would need to have been transient on geological timescales as short as the lifetime of the OCC (~1Ma).

Data from 13°19'N shows that poor melt supply prior to OCC formation results from low melt production in the mantle, which formed the low melt fraction M1 and M2 basalts. Evidence from the composition of basaltic talus on the OCC surface showed that a low but consistent supply of M2 melt was sustained throughout almost all of the OCC evolutionary stages. It is therefore unlikely that fine-scale mantle focusing effects are a major factor in the development of the unusual morphology of the 12°60'-14°N region.

'Crustal plumbing' variations have also been hypothesised as a potential mechanism whereby mantle melt is prevented from reaching the surface. This implies that melt produced in a normal quantity beneath the ridge is unable to reach the surface due to the structural characteristics of the ridge at OCC sites. Melt that is produced beneath the axis must, according to this theory, be either transported in dykes away from the axis or frozen into the crust beneath the surface, forming gabbro bodies.

The composition of basalts at the 13°19'N OCC suggests that melt production in the mantle was substantially reduced prior to OCC formation. Crustal plumbing therefore is unlikely to be the main process contributing to the lack of volcanism at the OCC site historically. If crustal plumbing was the main control on melt provision at the time of OCC initiation, we should expect to find melts of a higher melt fraction (normal for the ridge axis). However, there is substantial evidence to suggest that crustal plumbing affects melt provision at the 13°19'N OCC today. Geochemical analyses show that melt fraction at the axis near the 13°19'N OCC is the same as elsewhere on the axis. However, there is much less evidence of volcanism at the surface here than in areas of the axis not associated with OCCs.

The presence of dykes on the OCC dome with compositions indistinguishable from those of the axis suggests that melt from the axis is partially diverted into

the fault plane of the OCC, rather than erupted. This suggests that the crustal architecture at OCC sites, specifically the presence close to the axis of an active detachment fault (or faults), has a significant effect on the pathways used by melt to reach the surface (see Figure 98). Some melts may also be frozen into the OCC as gabbro bodies, though the lack of gabbro sampled from the OCC site at 13°19'N (~2% dredge recovery by weight) suggests that this mechanism does not account for significant amounts of melt at this site, perhaps because the typical melt production at the axis in the FTFZ region is relatively low, and therefore intermediate magma chambers are unlikely to form.

Figure 107 below illustrates the possible mechanisms by which melt is diverted into the fault plane, resulting in little melt being erupted at the surface.

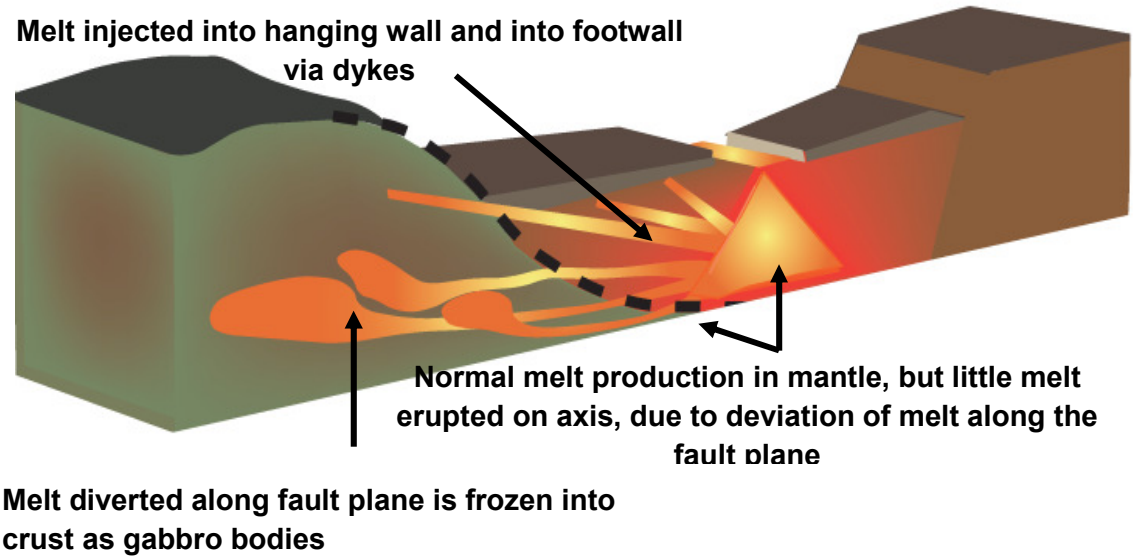

Figure 98: Block diagram to illustrate the mechanisms by which melt is diverted along the fault plane of a detachment fault, and away from the magmatic axis. The diagram shows melt frozen into the crust beneath the core complex as gabbro bodies, and also melt in dykes which cut across the footwall, as found at 13°19'N.

Geochemical data from prior to the time of OCC initiation at 13°19'N show a substantial reduction in the melt fraction produced by the mantle source, forming M1 and M2 type melts. During OCC formation, a low but consistent supply of M2 type melt was generated, as evidenced by the composition of basaltic talus

dragged from the axis onto the OCC dome. Low melt production in the mantle may result from a decrease in mantle source temperature, producing a mantle 'cold spot'. This implies that variations in local temperature (on a 15-30km scale) of the mantle beneath the ridge prevent the generation of sufficient melt to sustain volcanism. Such mantle cold spots could perhaps be generated by previous localised extraction of melt (and with it heat). Whilst cold spots would only have a finite lifespan in the mantle, 15-30km scale cold spots may be able to persist for a sufficient length of time to affect ridge activity sufficiently for OCC formation to take place.

In a cooler mantle, melting does not begin as deep, and melting paths are therefore shorter. Hotter mantle melts deeper, and a hot mantle of a given composition produces more melt than a cooler mantle (Figure 99).

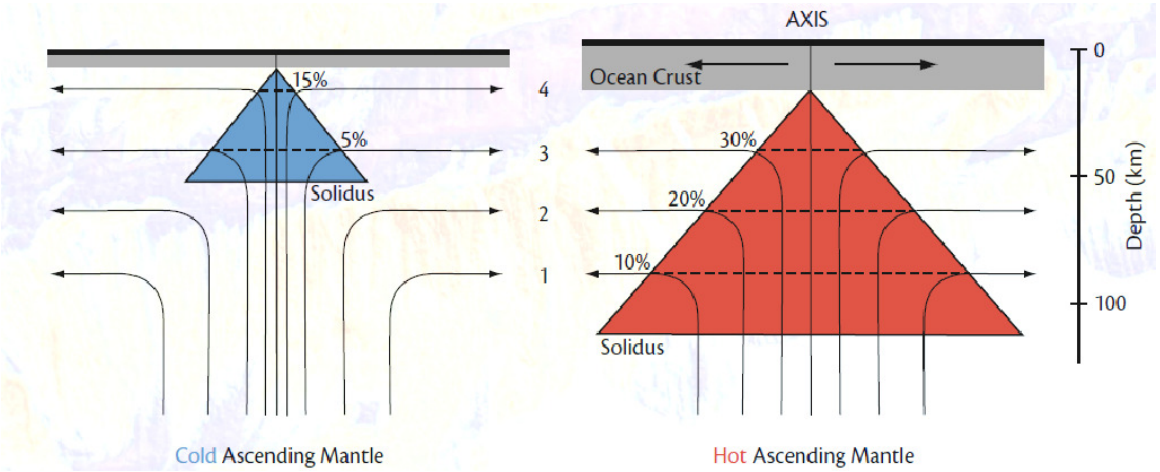

Figure 99: Diagram to illustrate the variations in melt path between hot and cold mantle sources. In cold mantle, the melting triangle is smaller, so melting begins later, at shallow depths, and melting paths are shorter. In hot ascending mantle, melting begins at greater depths, the melting triangle is larger, and melting paths are longer. From Langmuir and Forsyth, (2007).

We expect to see a decreased garnet component in melt associated with cold spots in the mantle, as melting occurs at shallower levels than with hot upwelling mantle. Yb/Lu data from the OCC at 13°19'N shows that there is a substantial garnet component in the melts produced there. However, evidence from modelling suggests that M1 melts have short melting paths, which are shallower

than those for M2 melts. These data suggest that a cold spot in the mantle may have contributed to low melt production at the 13°19'N region, and hence formation of the OCC. Modelling of M2 compositions suggests that the ridge may have begun to sample a warmer source (i.e. reached the end of a 'cold spot') after the formation of M1 melts, leading to deepening of the melt path.

Melt production may also be limited by differences in the chemical composition of the mantle. This implies that, in the 12°60'-14°N region, geochemical characteristics (including hydration) of the mantle source are such that, for a given temperature, the mantle at OCC sites produces insufficient melt to sustain volcanism at the ridge axis.

It is hypothesised that mantle hydration variations along the ridge could cause the differences in melt provision between OCCs and highly magmatic areas. These highly magmatic areas, with high melt productivity, would therefore correspond with wet spots in the mantle, which are rich in incompatible elements and volatiles. The effect of their high water content would be to lower the mantle solidus and allow melts to emerge at a lower temperature than in OCC areas. However, the 13°19'N OCC appears to host the most volatile rich basalts in the study area (low-degree melts). Rocks from the magmatic axis at the 14°N 'enrichment anomaly' are almost as volatile rich (relatively high degree melts), and there is no correlation between volatile content and spreading style.

Since OCCs demonstrably do not correspond with mantle dry spots, it seems that variations in volatile content along the ridge axis are observed due to variations in source chemistry, but are not significant in terms of controlling melt production at core complex sites. Other geochemical variations, however, appear to have a significant effect. Melts in the axis at the 12°6'-14°N study area are predominantly E-MORB in character with variable melt fraction, and are produced by the melting of DMM-HIMU-FOZO mantle components.

Off-axis melts corresponding to the development of the OCC at 13°19'N are bimodal, with some melts being extremely LREE enriched E-MORB, others being N-MORB like. These rocks are all formed by low degrees of melting in comparison to rocks in the rest of the segment.

The levels of enrichment and depletion in these rocks are demonstrated to be a function of source composition as well as of melt fraction, with M1 basalts forming a trend between HIMU and FOZO end-member compositions, with reduced DMM involvement in comparison to the formation of on-axis melts. This shows that it is a change in the geochemistry of the source beneath the ridge which drives the change to low melt fraction, reducing the magmatism at the ridge axis prior to OCC initiation, and creating conditions at the axis that are conducive to OCC development.

As discussed previously, numerous studies have shown that the harzburgitic mantle peridotite in the FTFZ is ultra depleted, with abundant evidence of melt-rock interaction found at a number of sites. This suggests that at some time in its history, the 'packet' of mantle now sitting beneath the FTFZ region experienced extremely high degrees of melting. Geochemical data from this study shows that the source material in the 12°6'-14°N segment is best described by a combination of the mantle end-member components DMM-HIMU-FOZO, so the refertilising material that infiltrates the harzburgite here is HIMU-FOZO-like in composition. HIMU signals are thought to originate from subducted oceanic crust, and FOZO is thought to have a possible lower mantle or plume origin. Therefore, the mantle beneath the 12°6'-14°N region is best envisioned as an ultra-depleted harzburgitic mantle variably veined by a highly volatile-rich, LREE enriched HIMU-FOZO veins. During the previous melting event, some areas of mantle will have been almost completely melted out, whilst others may have experienced a little less melting, and therefore retained a little lherzolitic character. Additionally, some areas will have been substantially refertilised, whereas some will have experienced very efficient melt extraction, and therefore will host very few enriched veins. It is the variable depletion and re-enrichment of the mantle beneath the FTFZ region which produces the range of LREE enriched E-MORBs seen, and which is also the potential trigger for the development of segment centre OCCs.

Figure 100 (key- see p) shows the process of depleted mantle source sampling leading to OCC development. The block diagrams show three sections of a slow-spreading ridge segment. The first and third sections sample a mantle source consisting of DMM (green) and enriched HIMU-FOZO veins (purple). The mantle

source here allows for the production of sufficient melt for normal ridge spreading.

The central section of the diagram, however, represents an area of the ridge where the mantle source is ultra- depleted, consisting of DMM with very few enriched veins. Melt production is low due to the unavailability of fusible components and magmatism is therefore reduced at the axis. The top-down view and 3D block diagrams allow the changes in the melt production, melt provision and morphology of the axis to be seen in greater detail.

a) In an exceptionally depleted packet of mantle, where the abundance of refertilising veins is very low, there is very little material available to melt out. The centre section of the diagram represents a mantle source consisting of ultra-depleted material with very little enriched vein material. Due to the paucity of fusible material, melt production is dramatically reduced.

b) The first melts from the depleted mantle source are produced (pink). These M1-type melts are very low melt fractions which are formed as the fusible veins are stripped rapidly out of the mantle source, along with a little DMM. The melts are extremely incompatible element enriched, reflecting the enriched compositions of their source, and also preserve the distinct isotopic signatures of the vein source material. The rapid stripping of fusible components out of the mantle causes localised cooling and dehydration in the source, and melting ceases. The lack of M1 compositions in the talus on the OCC dome supports the theory that the M1 melt producing stage is very rapid, and produces very little melt at the axis. Evidence from modelling suggests that the mantle beneath the OCC is locally cold at this time, contributing to short melt paths and low melt production.

c) As the source mantle re-enters melting conditions, low-degree melting resumes. Modelling results show that the onset of melting deepens here, suggesting that the underlying mantle is warmer than when M1 was produced. Very little enriched material remains, and so M2 (N-MORB like) melts (yellow) are produced from melting of predominantly DMM. The fact that OCC dome talus has M2 compositions indicates that a more substantial amount of M2 melt is erupted

at the axis (than M1), and may indicate that this phase proceeds for some time prior to/during OCC development.

d) Low melt production of M2-like melts continues for an unknown period of time. Melt production is insufficient to sustain normal ridge spreading, and so eventually, spreading shifts to a nearby normal fault (represented by a broken line). This fault then rotates to a shallow angle as spreading continues.

e) Spreading on the detachment fault results in the formation of an OCC by unroofing of ultramafic material. At some time during the lifetime of the fault, the ridge begins to sample mantle containing more enriched material. Melt production increases, and magmatism at the axis becomes more evident. Volcanism forms triangular neovolcanic zones which cut into the axis toward the fault line. This volcanism will eventually cut the OCC fault completely, and normal magmatic spreading will resume.

At this stage, therefore, the ridge is once again sampling a ‘normal’ mantle source for the region. This suggests that ultra-depletions in the mantle source are short-lived, as they do not persist beneath the ridge throughout the lifetime of the core complex. The four OCC structures identified in the 12°60’-14°N region are each of a size thought to be representative of ~1Myr of spreading. Thus we can suggest that the time taken for the ridge to process ultra depleted mantle ‘packets’ is ≥~1Ma. However, it is unclear what length of time passes in phase C (production of M2 melts at low F) before spreading switches to a fault in stage D.

7.4.1 – OCC Formation Summary

The segment centre OCCs which exist in the 12°60’-14°N region form as a result of the unusually depleted and cold nature of the underlying mantle source, which geochemically limits melt production in the region, starving the ridge of melt. These OCCs form by the rotation of a normal fault and exhumation of peridotite, the same physical mechanism as their segment-end situated analogues. However, the trigger for their formation is different.

At segment ends, OCCs are thought to form because the upwelling mantle is focused away to the segment centre, and therefore the segment ends are cold and starved of melt. In the 12°60'-14°N segment, this study shows that the unavailability of melt that drives OCC formation is a result of extreme depletion in the source, rather than mantle focusing effects.

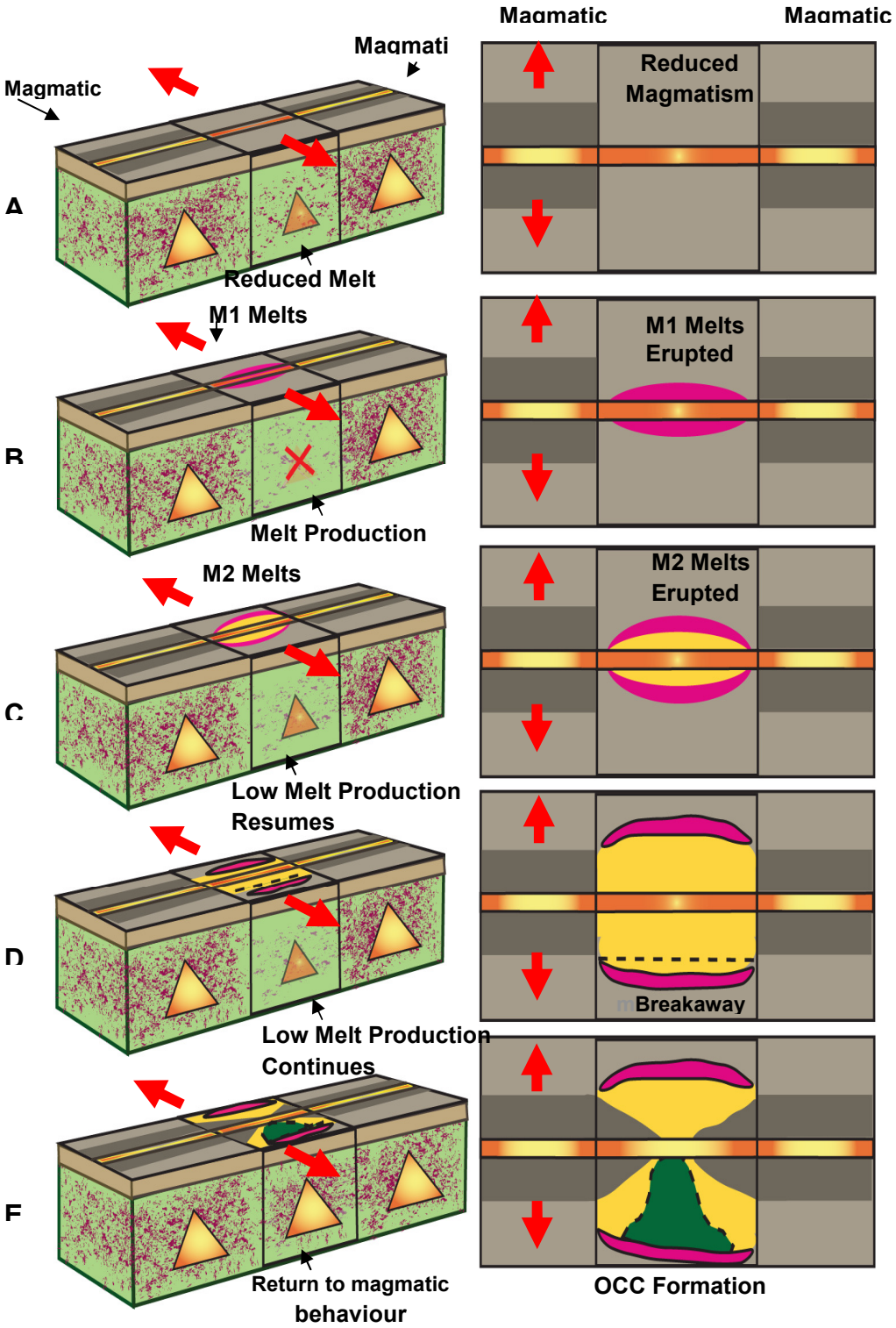

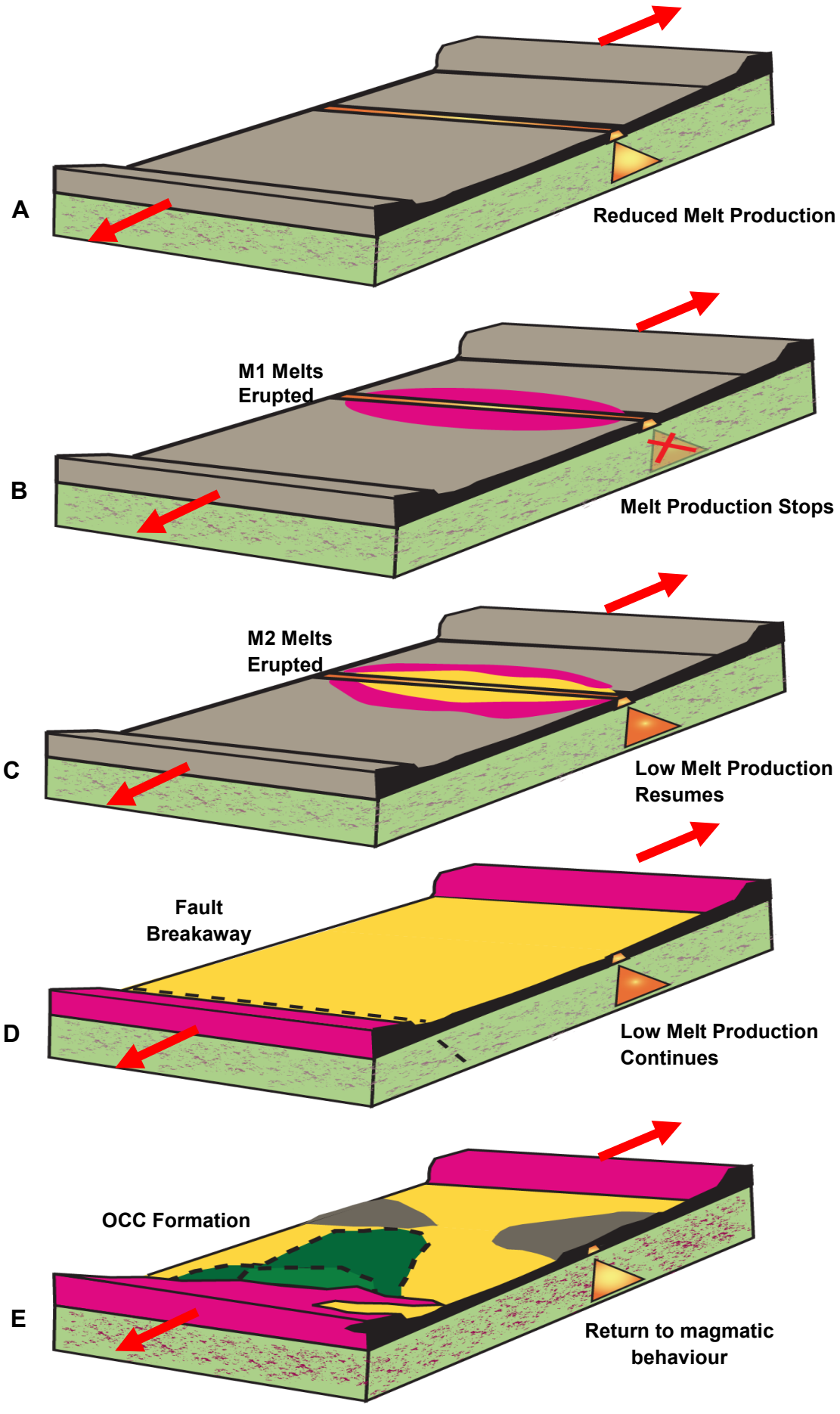
A
Reduced Melt Production
M1 Melts
Erupted
B
Melt Production Stops
M2 Melts
Erupted
C
Low Melt Production
Resumes
Fault
Breakaway
D
Low Melt Production
Continues
OCC Formation
E
Return to magmatic
behaviour

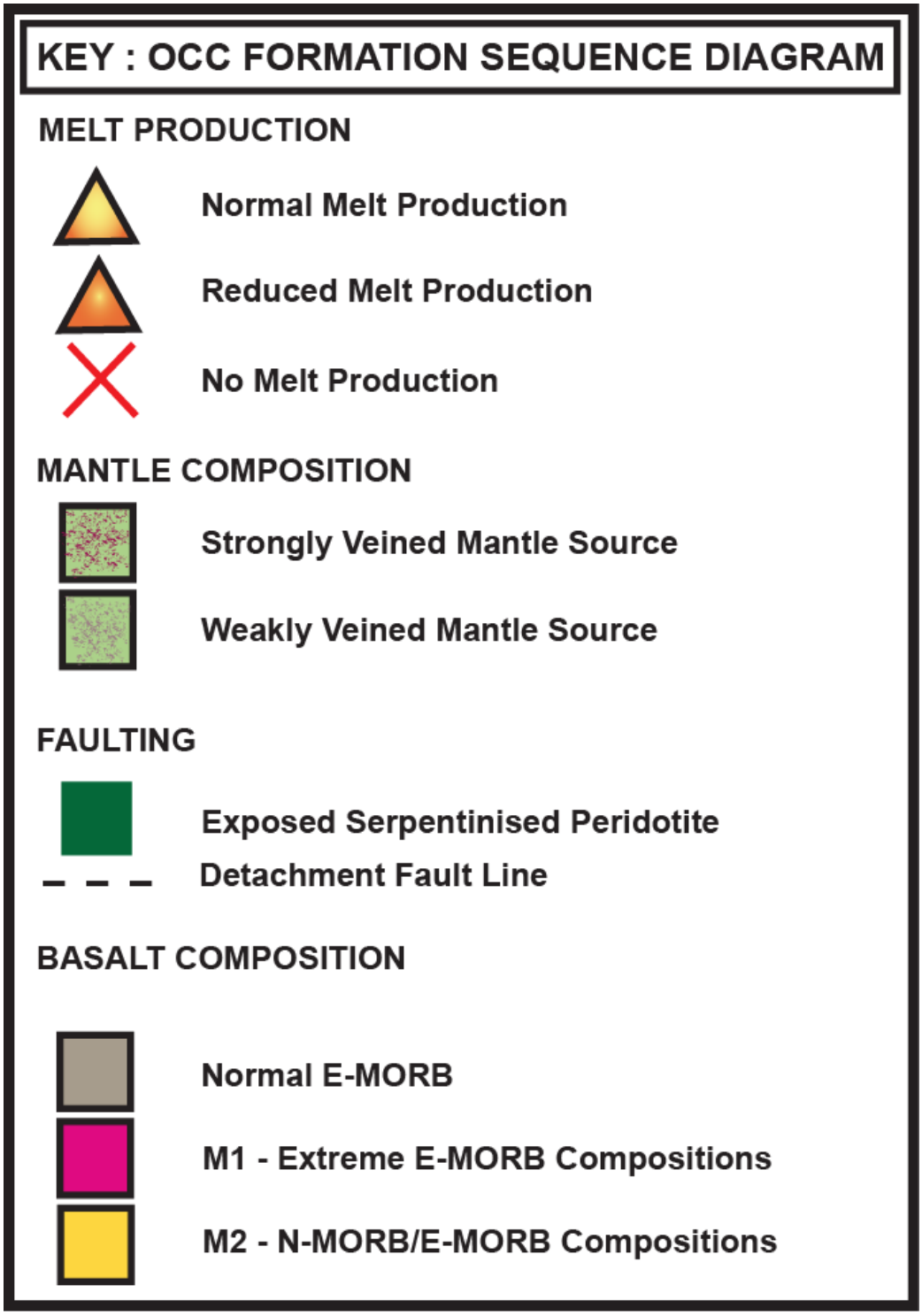

Figure 100: Sequential diagram to illustrate the stages of core complex development, and their relation to underlying mantle composition. The diagram shows the variations in basalt compositions erupted at different stages during the development and evolution of the core complex. Block diagrams, plan views and close-up block diagrams are shown for each developmental stage A-E.

CHAPTER EIGHT – CONCLUSIONS

The 12°60'-15°20'N region of the MAR is morphologically and geochemically unusual, and this has led to many questions about the nature of source composition, mantle melting and ridge tectonics in the area. The region produces extremely enriched E-MORB compositions, which are usually found in melt-rich, volcanically active regions with thick crust, such as those influenced by mantle plumes. However, the crust at 12°60'-15°20'N is thought to be extremely thin. TOBI imagery suggests that there is very little recent volcanism in some parts of the ridge axis. Several long lived, shallow detachment faults are found here, akin to those found at cold, magma-starved segment ends.

This study shows that the OIB-like E-MORB compositions and fault-dominated morphology of the 12°60'-15°20'N region are both consequences of the unusual geochemical characteristics of the mantle underlying the ridge.

Trace element ratios and isotopic data show that the mantle source beneath this region is best described by mixing between the mantle component end-members DMM-HIMU-FOZO. This is consistent with the presence of HIMU signals reported by earlier studies of the mantle source beneath the ridge in this (and adjacent) segments (see Dosso *et al*., 1991, Hannigan *et al*., 2001).

Harzburgitic residual peridotite with evidence of melt-rock interaction suggests that the mantle beneath the ~15°N region previously experienced a major melting event. This event would have stripped fusible components from the source, leaving harzburgite re-enriched with a small volume of (HIMU-FOZO) melt in the form of metasomatized veins.

The mantle underlying the ~15°N area appears to share characteristics with the 1°S-2°N and Azores regions of the MAR, and the resultant melts are OIB-like in their incompatible trace elements, occupying the $\Delta Nb>0$ region of the discrimination diagram of Fitton *et al*. (1997). This shows that the large-scale melting and refertilisation event described above involved a (HIMU-FOZO) OIB-like mantle source. It is possible that this material may originate from the passage

of a plume through the mantle earlier in its history. However, activity of a plume is not required by the model at any time.

This study has shown that local, small-scale variability in DMM depletion and HIMU-FOZO re-enrichment beneath the 12°60'-14°N segment controls the extent of melting here. This variability can produce the range of E-MORB compositions found between 12°60'-14°N. HIMU-FOZO material present in veins and melted out preferentially at low melt fraction allows the development of a strong zone of E-MORB geochemical enrichment at normal slow-spreading (or lower) melt fractions. The geochemical enrichment zone appears as significant as that generated by the Azores plume in incompatible trace elements, but is not accompanied by the extensive melting associated with plumes.

This study concludes that this signal arises from melting out of HIMU-FOZO material left behind by either the earlier passage of a plume or a HIMU-FOZO 'blob' through the mantle that now underlies the ridge. By this mechanism, small-scale mantle heterogeneities, whatever their origin, are capable of generating enriched, and even plume-like signatures at mid-ocean ridges, without the need for a current, ridge-centred geochemical plume, or any other complex mantle process.

Small-scale mantle compositional heterogeneity may also promote the formation of OCCs in the ~15°N region. This study presents a model for segment centre OCC development whereby a spot of localised (~15km along axis) mantle depletion (ultra-harzburgitic DMM with few HIMU-FOZO veins) triggers a dramatic localised reduction in melt production, and promotes a switch to tectonic spreading.

Immediately prior to OCC formation, the onset of melting of the localised 'depleted/cold spot' leads to the rapid and efficient removal from the source of enriched HIMU-FOZO bearing veins (forming M1 basalts). This leads to almost complete exhaustion of fusible components and volatiles in the source, and triggers a period of reduced melt production (M2), where melt generation is limited by the extreme depletion of the source.

During this period, modeling suggests that melt production is insufficient to maintain magmatic spreading, and therefore the locus of spreading shifts to a valley wall fault, triggering the formation of an OCC.

Compositional data from dolerite dykes confirms that after OCC initiation, when melt production at OCC sites increases but the fault is still active, melt is diverted from the axis along the detachment. It may also freeze into the crust as small gabbro bodies, though the low recovery of gabbro (~2%) suggests that this is not a significant mechanism at 13°19'N. The diversion of melt into the fault leads to the impression of a magma starved ridge axis, but on-axis basalt compositions from this study show that after OCC initiation (but before OCC termination) melt production returns to normal values for the segment.

REFERENCES

Akishin, P.A., Nikitin, O.T., Panchenkov, G.M., (1957), A new effective ion emitter for the isotopic lead analysis, *Geokhimiya,* 5; 429–434

Allerton, S., Escartín, J., and Searle, R.C., (2000), Extremely asymmetric magmatic accretion of oceanic crust at the ends of slow-spreading ridge segments, *Geology, 28, (2.);* 179-182

Allerton, S., Murton, B.J., Searle, R.C., and Jones, M., (1993), Extensional Faulting and Segmentation of the Mid-Atlantic Ridge North of the Kane Fracture Zone (24°00'N to 24°40'N), *Marine Geophysical Researches, 17;* 37-61

Allerton, S., and Tivey, M.A., (2001), Magnetic polarity structure of the oceanic crust, *Geophysical Research Letters, 28;* 423-426

Almeev, R., Holtz, F., Koepke, J., Haase, K., and Devey, C., (2008), Depths of Partial Crystallization of H2O-bearing MORB: Phase Equilibria Simulations of Basalts at the MAR near Ascension Island (7-11°S), *Journal of Petrology*, 49, (1); 25-45

Alt, J.C., Shanks III, W.C., Bach, W., Paulick, H., Garrido, C.J., Beaudoin, G., (2007), Hydrothermal alteration and microbial sulphate reduction in peridotite and gabbro exposed by detachment faulting at the Mid-Atlantic Ridge, 15°20'N (ODP Leg 209): A sulphur and oxygen isotope study, *Geochemistry, Geophysics, Geosystems, 8, (8);* doi:10.1029/2007GC001617

Anderson, E.M., (1951), The Dynamics of Faulting. (2nd Edition) Oliver and Boyd, Edinburgh

Anonymous, (1972), Penrose field conference on ophiolites, *Geotimes*, 17; 24-25.

Armienti, P., and Gasperini, D., (2007), Do We Really Need Mantle Components to Define Mantle Composition?, *Journal of Petrology, 48, (4);* 693-709

Asimow, P.D., and Langmuir, C.H., (2003) The importance of water to oceanic mantle melting regimes, *Nature, 421*; 815-820.

Augustin, N., Lackschewitz, K.S., Kuhn, T., Devey, C.W., (2008), Mineralogical and chemical mass changes in mafic and ultramafic rocks from the Logatchev hydrothermal field (MAR 15°N), *Marine Geology, 256;* 18–29

Auzende, J.M., Bideau, D., Bonatti, E., Cannat, M., Honnorez, J., Lagabrielle, Y., Malavieille, J., Mamaloukas-Frangoulis, V., and Mével, C., (1989), Direct observations of a section through slow-spreading oceanic crust, *Nature, 337;* 726-729

Auzende, J.M., Cannat, M., Gente, P., Henriet, J.P., Juteau, T., Karson, J., Lagabrielle, Y., Mével, C., Tivey M., (1994), Observation of sections of oceanic crust and mantle cropping out on the southern wall of Kane FZ (N-Atlantic),*Terra Nova, 6, (2)*; 143-148

Bach, W., Garrido, C.J., Paulick, H., Harvey, J., Rosner, M., (2004), Seawater-peridotite interactions: First insights from ODP Leg 209, MAR 15°N, *Geochemistry, Geophysics, Geosystems, 5, (9);* Q09F26, doi:10.1029/2004GC000744

Baines, A.G., Cheadle, M.J., Dick, H.J.B., Scheirer, A.H., John, B.E., Kusznir, N.J., Matsumoto, T., (2003), Atlantis Bank, southwest Indian Ridge Mechanism for generating the anomalous uplift of oceanic core complexes*: Geology, 31*; 1105-1108

Ballentine, C.J., Lee, D.C. and Halliday, A.N., (1997), Hafnium isotopic studies of the Cameroon line and new HIMU paradoxes, *Chemical Geology*, 139; 111-124

Barling, J., and Weis, D., (2008), Influence of non-spectral matrix effects on the accuracy of Pb isotope ratio measurement by MC-ICP-MS: implications for the external normalization method of instrumental mass bias correction, *Journal of Analytical Atomic Spectrometry, 23;* 1017–1025

Batiza, R., (1996), Magmatic segmentation of mid-ocean ridges: a review, *Geological Society, London, Special Publications*; 118; 103-13

Becker, T.W., Kellogg, J.B., O'Connell, R.J., (1999), Thermal constraints on the survival of primitive blobs in the lower mantle, *Earth and Planetary Science Letters*, 171; 351–365

Beier, C., Stracke, A. And Haase, K.M., (2007), The peculiar geochemical signatures of São Miguel (Azores) lavas: Metasomatised or recycled mantle sources?, Earth and Planetary Science Letters, 259, (1-2); 186-199

Beltenev, V., Ivanov, V., Rozhdestvenskaya, I., Cherkashov, G., Stepanova, T., Shilov, V., Pertsev, A., Davydov, M., Egorov, I., Melekestseva, I., Narkevsky, E., and Ignatov, V., (2007), A New Hydrothermal Field at 13º30'N on the Mid-Atlantic Ridge, *International Research (InterRidge) 16;* 9

Bender, J.F., Hodges, F.N., and Bence, A.E., (1978), Petrogenesis of basalts from the project FAMOUS area: Experimental study from 0 to 15 kbar*, Earth and Planetary Science Letters,* 41; 277-302

Bideau, D., and Hékinian, R., (1995), A dynamic model for generating small-scale heterogeneities in ocean floor basalts, *Journal of Geophysical Research, 100, (B7);* 10141-10162

Bird, D.E., Hall, S.A., Burke, K., Casey, J.F., Sawyer, D.S., (2007), Early Central Atlantic Ocean seafloor spreading history, *Geosphere, 3,* (5); 282–298

Blackman, D.K., Canales, J.P., Harding, A., (2009), Geophysical signatures of oceanic core complexes, *Geophysical Journal International,* 178; 593–613

Blackman, D.K., Cann, J.R., Smith, D.K., (1998), Origin of extensional core complexes: Evidence from the Mid-Atlantic Ridge at Atlantis Fracture Zone, Journal of Geophysical Research, 103, (B9); 21315-21333

Blackman, D.K., Ildefonse, B., John, B.E., Ohara, Y., Miller, D.J., MacLeod, C.J. and the Expedition 304/305 Scientists,(2006), Oceanic core complex formation, Atlantis Massif, *Proceedings of the Integrated Ocean Drilling Program, 304/305*; doi:10.2204/iodp.sp.304305.2004

Blackman, D.K., Karson, J.A., Kelley, D.S., Cann, J.R., Früh-Green, G.L., Gee, J.S., Hurst, S.D., John, B.E., Morgan, J., Nooner, S.L., Ross, D.K., Schroeder, T.J., and Williams, E.A., (2002),Geology of the Atlantis Massif (Mid-Atlantic Ridge, 30◦ N): Implications for the evolution of an ultramafic oceanic core complex, *Marine Geophysical Researches, 23;* 443–469

Blondel, P., and Murton, B.J., (1997), Handbook of Seafloor Sonar Imagery, *Wiley, West Sussex, England*

Blusztajn, J. and Hegner, E., (2002), Osmium isotopic systematics of melilitites from the Tertiary Central European Volcanic Province in SW Germany, *Chemical Geology,* 189; 91–103

Bohnenstiehl, D.R., Tolstoy, M., Smith, D.K., Fox, C.G., Dziak, R.P., (2003), Time-clustering behavior of spreading-center seismicity between 15 and 35°N on the Mid-Atlantic Ridge: observations from hydroacoustic monitoring, *Physics of the Earth and Planetary Interiors, 138*; 147–161

Bonatti, E., Honnorez, J., Ferrara, G., (1971), Peridotite-gabbro-basalt complex from the equatorial Mid-Atlantic Ridge, *Philosophical Transactions of the Royal Society of London, A, 268;* 385-402

Bonatti, E., Peyve, A., Kepezhinskas, P., Kurentsova, N., Seyler, M., Skolotnev, S., Udintsev, G., (1992), Upper Mantle Heterogeneity Below The Mid-Atlantic Ridge, 0-Degrees-15-Degrees-N, *Journal of Geophysical Research-Solid Earth*, 97 (B4); 4461-4476

Boschi, L., Becker, T.W., Steinberger, B., (2007), Mantle plumes: Dynamic models and seismic images, *Geochemistry, Geophysics, Geosystems*, 8, (10); Q10006, doi 10.1029/2007GC001733

Boschi, C., Dini, A., Früh-Green, G.L., Kelley, D.S., (2008), Isotopic and element exchange during serpentinization at the Atlantis Massif (MAR 30°N): Insights from B and Sr isotope data, *Geochimica et Cosmochimica Acta*, 72; 1804-1823

Boschi, C., Früh-Green, G.L., Delacour, A., Karson, J.A., and Kelley, D.S., (2006), Mass transfer and fluid flow during detachment faulting and development of an oceanic core complex, Atlantis Massif (MAR 30°N), *Geochemistry, Geophysics, Geosystems*, 7; Q01004, doi:10.1029/2005GC001074.

Boschi, C., Früh-Green, G.L., Escartín, J., (2006), Occurrence and significance of serpentinite-hosted, talc- and AMPHIBOLE-RICH fault rocks in modern oceanic settings and ophiolite complexes: An overview, *Ofioliti*, 31 (2); 129-140

Bougault, H., Dmitriev, L., Schilling, J.G., Sobolev, A., Joron J.L., Needham, H.D., (1988), Mantle heterogeneity from trace elements: MAR triple junction near 14°N, *Earth and Planetary Science Letters,* 88; 27-36

Bourdon, B., Langmuir, C.H., Zindler, I. A., (1996), Ridge-hotspot interaction along the Mid-Atlantic Ridge between 37°30' and 40°30'N: the U-Th disequilibrium evidence, *Earth and Planetary Science Letters*, 142; 175-189

Bowen, N. L., (1928), The evolution of the igneous rocks: Princeton, New Jersey, Princeton University Press, 334; (second edition, 1956), New York, Dover

Bowin, C., (1976), Caribbean gravity field and plate tectonics. *Special paper of the Geological Society of America;* 169

Boyet, M., and Carlson, R.W., (2005), ^{142}Nd Evidence for Early (>4.53 Ga) Global Differentiation of the Silicate Earth, *Science*, 309, 5734; 576-581

Boyet, M., and Carlson, R.W., (2006), A new geochemical model for the Earth's mantle inferred from 146Sm–142Nd systematics, *Earth and Planetary Science Letters*, 250; 254–268

Brandenburg, J.P., and van Keken, P.E., (2007), Deep storage of oceanic crust in a vigorously convecting mantle, Journal of Geophysical Research, 112, B06403; doi:10.1029/2006JB004813

Brearley, M. and Scarfe, C.M., (1986), Dissolution Rates of Upper Mantle Minerals in an Alkali Basalt Melt at High Pressure: An Experimental Study and Implications for Ultramafic Xenolith Survival, *Journal of Petrology,* 27, (5); 1137-1182

Brun, J., Sokoutis, D., Van Den Driessche, J., (1994), Analogue modelling of detachment fault systems and core complexes, *Geology*, 22; 319-322

Bu, W., Shi, X., Peng, J., Liu J., Zhang M., Ql L., (2008), Low-temperature alteration of oceanic island basalts and their contribution to transition metal circulation of the ocean, *Acta Oceanologica Sinica*, 27; 35-54

Buck, W.R., (1988), Flexural Rotation of Normal Faults, *Tectonics*, 7, (5); 959-973

Buck, W.R., Lavier, L.L., Poliakov, A.N.B., (2005), Modes of faulting at mid-ocean ridges, *Nature*, 434; 719-723

Cameron, A.E., Smith, D.H., and Walker, R.L, (1969), Mass Spectrometry of Nanogram-Size Samples of Lead, *Analytical Chemistry*, 41, (3); 525-526

Canales, J.P., Collins, J.A., Escartín, J., Detrick, R.S., (2000),Seismic structure across the rift valley of the Mid-Atlantic Ridge at 23°20′ (MARK area): Implications for crustal accretion processes at slow spreading ridges, *Journal of Geophysical, Research*., *105, (B12); 28411–28425*

Canales, J.P., Sohn, R.A., deMartin, B.J., (2007), Crustal structure of the Trans-Atlantic Geotraverse (TAG) segment (Mid-Atlantic Ridge, 26°10'N): Implications for the nature of hydrothermal circulation and detachment faulting at slow spreading ridges, *Geochemistry, Geophysics, Geosystems*, 8, (8), Q08004; doi:10.1029/2007GC001629

Canales, J.P., Tucholke, B.E., Collins, J.A., (2004), Seismic reflection imaging of an oceanic detachment fault: Atlantis megamullion (Mid-Atlantic Ridge, 30°10'N), *Earth and Planetary Science Letters*, 222; 543– 560

Canales, J.P., Tucholke, B.E., Xu, M., Collins, J.A., DuBois, D.L., (2008), Seismic evidence for large-scale compositional heterogeneity of oceanic core complexes, *Geochemistry, Geophysics, Geosystems,* 9, (8); Q08002, doi:10.1029/2008GC002009

Cann, J.R., Pritchard, H.M., Malpas, J.G and Xenophontos, C., (2001), Oceanic inside corner detachments of the Limassol Forest area, Troodos ophiolite, Cyprus, *Journal of the Geological Society*, 158; 757-767

Cann, J.R., Blackman, D.K., Smith, D.K, McAllister, E., Janssen, B., Mello, S., Avgerinos, E., Pascose, A.R., Escartín, J., (1997), Corrugated slip surfaces formed at ridge-transform intersections on the Mid-Atlantic Ridge, *Nature*, 385; 329-332

Cannat, M., (1993), Emplacement of Mantle Rocks in the Seafloor at Mid-Ocean Ridges, *Journal of Geophysical Research*, 98, (B3); 4163-4172

Cannat, M., (1996), How thick is the magmatic crust at slow spreading oceanic ridges?, *Journal of Geophysical Research*, 101, (B2); 2847-2857

Cannat, M., Lagabrielle, Y., Bougault, H., Casey, J., de Coutures, N., Dmitriev, L., Fouquet, Y., (1997), Ultramafic and gabbroic exposures at the Mid-Atlantic Ridge: geological mapping in the 15°N region, *Tectonophysics,* 279; 193-213

Cannat, M., Mével, C., Maia, M., Deplus, C., Pascal, C.D., Agrinier, P., Belarouchi, A., Dubuisson, G., Humler, E., Reynolds, J., (1995), Thin crust, ultramafic exposures, and rugged faulting patterns at the Mid-Atlantic Ridge (22°–24°N), *Geology*; 23; 49–52

Cannat, M., Sauter, D., Bezos, A., Meyzen, C., Humler, E., Le Rigoleur, M., (2008), Spreading rate, spreading obliquity, and melt supply at the ultraslow spreading Southwest Indian Ridge, *Geochemistry, Geophysics, Geosystems*, 9, (4); Q04002, doi:10.1029/2007GC001676

Cannat, M., and Seyler, M., (1995), Transform tectonics, metamorphic plagioclase and amphibolitization in ultramafic rocks of the Vema transform fault, (Atlantic Ocean), *Earth and Planetary Science Letters*, 133; 283-298

Carbotte, S.M., and Macdonald, K.C., (1990), Causes of variation in fault facing direction on the ocean floor, *Geology, 18*; 749-752

Casey, J.F., Searle, R.C., MacLeod, C.J., Murton, B.J., (2008)., Extensive Core Complex Formation in a Magma Starved Segment of the Mid-Atlantic Ridge Between 12°-16°N: Strain Softening and a Coupled Crust-Mantle Rheology, *Geological Society of America*, *Abstracts with Programs*, 40, (6); 107

Chaffey, D. J., Cliff R.A. and Wilson B.M., (1989), Characterization of the St Helena magma source, *Geological Society, London, Special Publications*, 42; 257-276

Charlou, J.L., Fouquet, Y., Bougault, H., Donval, J.P., Etoubleau, J., Phillipe, J., Dapoigny, A., Appriou, P., Rona, P., (1998), Intense CH4 plumes generated by serpentinization of ultramafic rocks at the intersection of the 15°20*N fracture zone and the Mid-Atlantic Ridge, *Geochimica et Cosmochimica Acta*, 62, (13); 2323–2333

Chauvel, C., Hofmann, A.W., Vidal, P., (1992), HIMU-EM: The French Polynesian connection, *Earth and Planetary Science Letters,* 110; 99-119

Chauvel, C., McDonough, W., Guille, G., Maury, R and Duncan, R., (1997), Contrasting old and young volcanism in Rurutu Island, Austral chain, *Chemical Geology*, 139; 125-143

Chen, Y., and Morgan, W.J., (1990a), Rift valley/No rift valley transition at Mid-Ocean Ridges, *Journal of Geophysical Research,* 95; 17571–17581

Chen, Y., and Morgan, W.J., (1990b), A nonlinear rheology model for Mid-Ocean Ridge axis topography, *Journal of Geophysical Research,* 95; 17583–17604

Chen, Y.,(1989), A Mechanical Model for the Inside Corner Uplift at a Ridge-Transform Intersection, *J.Geophys. Res*. 94, (B7), 9275-9282,

Choblet, G., and Parmentier, E.M., (2000), Mantle upwelling and melting beneath slow spreading centers: effects of variable rheology and melt productivity, *Earth and Planetary Science Letters*, 184; 589-604

Christie D. M., West B. P., Pyle D. G., Hanan B. B., (1998), Chaotic topography, mantle flow and mantle migration in the Australian–Antarctic discordance, *Nature*, 394; 637–644

Cipriani, A., Bonatti, E., Seyler, M., Brueckner, H.K., Brunelli, D., Dallai, L., Hemming, S.R., Ligi, M., Ottolini, L., Turrin, B.D., (2009), A 19 to 17 Ma amagmatic extension event at the Mid-Atlantic Ridge: Ultramafic mylonites from the Vema Lithospheric Section, *Geochemistry, Geophysics, Geosystems*, 10, (10); Q10011, doi:10.1029/2009GC002534

Colletta, B., and Angelier, J., (1983), Fault tectonics in northwestern Mexico and opening of the Gulf of California: *Bull. Centres Rech. Explor.-Prod, Elf-Aquitaine, 7, (1)*; 433-446

Collette, B.J., and Roest, W.R., (1992), Further investigations of the North-Atlantic between 10-degrees-N and 40-degrees-N and an analysis of spreading from 118-Ma ago to present, *Proceedings of the Koninklijke Nederlandse Akademie van Wetenschappen,* 95, (2); 159

Collettini, C., and Holdsworth, R.E., (2004), Fault zone weakening and character of slip along low-angle normal faults: insights from the Zuccale fault, Elba, Italy, *Journal of the Geological Society,* 161; 1039–1051.

Collier, M.L., and Kelemen, P.B., (2010), The Case for Reactive Crystallization at Mid-Ocean Ridges, *Journal of Petrology*, 51; 1913-1940

Compston, W., and Oversby, V.M., (1969), Lead isotopic analysis using a double spike, *Journal of Geophysical Research*, 74; 4338–4348

Collerson, K.D., Williams, Q., Ewart, A.E., and Murphy, D., (2010), Origin of HIMU and EM-1 domains sampled by ocean island basalts, kimberlites and carbonatites: The role of CO2-fluxed lower mantle melting in thermochemical upwellings, *Physics of the Earth and Planetary Interiors,* 181; 112–131

Connolly J.A.D., Schmidt, M.W., Solferino, G., Bagdassarov, N., (2009), Permeability of asthenospheric mantle and melt extraction rates at mid-ocean ridges, *Nature*, 462, 209-213

Coogan, L.A., MacLeod, C.J., Dick, H.J.B., Edwards, S.J., Kvassnes, A., Natland, J.H., Robinson, P.T., Thompson, G., O'Hara, M.J., (2000), Whole-rock geochemistry of gabbros from the Southwest Indian Ridge: constraints on geochemical fractionations between the upper and lower oceanic crust and magma chamber processes at very slow-spreading ridges, *Chemical Geology*, 178; 1–22

Cooper, K.M., Eiler, J.M., Asimow, P.D., Langmuir, C.H., (2004), Oxygen isotope evidence for the origin of enriched mantle beneath the mid-Atlantic ridge, *Earth and Planetary Science Letters*, 220; 297-316

Cordery, M.J., and Morgan, J.P., (1992), Melting and mantle flow beneath a mid-ocean spreading center, *Earth and Planetary Science Letters*, 111, (2-4); 493-516

Cox, K.G., Bell, J.D., nand Pankhurst, R.J., (1979) The Interpretation of Igneous Rocks, *George Allen and Unwin*, ISBN-10: 004552016X

Crawford, J., Lanyon, R., Elmes, M. and Eggins, S., (1997), Geochemistry and significance of basaltic rocks dredged from the South Tasman Rise and adjacent seamounts, *Australian Journal of Earth Sciences,* 44; 621-632

Dannowski, A., Grevemeyer, I., Ranero, C.R., Maia, M., (2008), Oceanic Core Complex Structure from Seismic Evidence, *American Geophysical Union, Fall Meeting 2008, abstract*, T43B-2015

Danyushevsky, L.V., Sobolev, A.V., and Dmitriev, L.V., (1996), Estimation of the pressure of crystallization and H_2O content of MORB and BABB glasses: Calibration of an empirical technique, *Mineralogy and Petrology*, 57, (3-4); 185-204

Danyushevsky, L.V., (2001), The effect of small amounts of H_2O on crystallisation of mid-ocean ridge and backarc basin magmas, *Journal of Volcanology and Geothermal Research*, 110; 265-280

Davaille, A., Girard, F., Le Bars, M., (2002), How to anchor hotspots in a convecting mantle?, *Earth and Planetary Science Letters*, 203; 621-634

Davies, G.F. (2009), Reconciling the geophysical and geochemical mantles: Plume flows, heterogeneities, and disequilibrium, *Geochemistry, Geophysics, Geosystems*; 10, Q10008, doi: 10.1029/2009GC002634.

Davies, G.R., Norry, M.J., Gerlach, D.C. and Cliff, R.A., (1989), A combined chemical and Pb-Sr-Nd isotope study of the Azores and Cape Verde hot-spots: The geodynamic implications, In *Magrnatism in the Ocean Basins* (ed. A. D. Saunders and M. J. Norry), *GSA Special Publications, 42; 23 l-255*

Davis, G.H., (1983), Shear-zone model for the origin of metamorphic core complexes, *Geology,* 11; 342–347

Davis, G.H., and Lister, G.S., (1988), Detachment faulting in continental extension: perspectives from the southwestern U.S. Cordillera, *Processes in Continental Lithospheric Deformation*, *Geological Society of America, Special Papers*, 218; 133–159

De Carlo, E.H., McMurty, G.M., Hyun Kim, K., (1987), Geochemistry of ferromanganese crusts (from the Hawaiian Archipelago I. Northern survey areas, *Deep-Sea Research,* 34, (3); 441-467

DeMartin, B.J., Sohn, R.A., Canales, J.P., Humphris, S.E., (2007), Kinematics and geometry of active detachment faulting beneath the Trans-Atlantic Geotraverse (TAG) hydrothermal field on the Mid-Atlantic Ridge, *Geology*, 35, (8); 711–714

DeMets, C., Gordon, R.G., Argus, D.F., Stein, S., (1994), Effect of recent revisions to the geomagnetic reversal time scale on estimates of current plate motions, *Geophysical Research Letters*, 21, (20); 2191-2194

De Muynck, D., Cloquet, C., Vanhaecke, F., (2007), Development of a new method for Pb isotopic analysis of archaeological artefacts using single-collector ICP-dynamic reaction cell-MS, *Journal of Analytical Atomic Spectrometry,* 23; 62 – 71

DePaolo, D. J., and Wasserburg, G.J., (1976), Nd isotopic variations and petrogenetic models, *Geophysical Research Letters*, 3, (5); 249-252

Dick, H.J.B., (1989), Drilling the Oceanic Lower Crust and Mantle, JOI/*USSAC Workshop Report*, Woods Hole Oceanographic Institution, Woods Hole, MA; 115

Dick, H.J.B., Bryan, W.B., and Thompson, G., (1981), Low-angle detachment faulting and steady-state emplacement of plutonic rocks at ridge-transform intersections, *Eos, Transactions, American Geophysical Union*, 62; 406.

Dick, H.J.B., Lin, J., Schouten, H., (2003), An ultraslow-spreading class of ocean ridge, *Nature*, 426; 405-412

Dick, H.J.B., Meyer, P.S., Bloomer, S., Kirby, S., Stakes, D., and Mawer, C., (1991), Lithostratigraphic evolution of an in-situ section of oceanic Layer 3. *In* Von Herzen, R.P., Robinson, P.T., *et al*., *Proceedings of the Ocean Drilling Program, Scientific Results,* 118, College Station, TX (Ocean Drilling Program); 439-538

Dick, H.J.B., Natland, J.H., Alt, J.C., Bach, W., Bideau, D., Gee, J.S., Haggas, S., Hertogen, J.G.H., Hirth, G., Holm, P.M., Ildefonse, B., Iturrino, G.J., Jogn, B.E., Kelley, D.S., Kikawa, E., Kingdon, A., LeRoux, P.J., Maeda, J., Meyer, P.S., Miller, D.J., Naslund, H.R., Niu, Y., Robinson, P.T., Snow, J., Stephen, R.A., Trimby, P.W., Worm, H., Yoshinobu, A., (2000), A long in situ section of the lower ocean crust: results of ODP Leg 176 drilling at the Southwest Indian Ridge, *Earth and Planetary Science Letters*, 179; 31-51

Dick, H.J.B., Natland, J.H., Ildefonse, B., (2006), Past and Future Impact of Deep Drilling in the Oceanic Crust and Mantle, *Oceanography*, 19, (4); 72-80

Dick, H.J.B., Natland, J.H., Miller, D.J., Alt, J.C., Bach, W., Bideau, D., Gee, J.S., Haggas, S., Hertogen, J.G.H., Hirth, G., Holm, P.M., Ildefonse, B., Iturrino, G.J., John, B.E., Kelley, D.S., Kikawa, E., Kingdon, A., Le, R.P.J., Maeda, J., Meyer, P.S., Naslund, H.R., Niu, Y., Robinson, P.T., Snow, J.E., Stephen, R.A., Trimby, P.W., Worm, H.U., Yoshinobu, A., (1999), Leg 176 summary. *In*: Marin, J.A., *et al*., (eds.) *Proceedings of the Ocean Drilling Program, Initial Reports*, Leg 176. Ocean Drilling Program, College Station, TX

Dick, H.J.B., Thompson, G., and Bryan, W.B., (1981), Low-angle faulting and steady-state emplacement of plutonic rocks at ridge-transform intersections, *Eos, Transactions, American Geophysical Union,* 62; 406.

Dick, H.J.B., Tivey, M.A., Tucholke, B.E., (2008), Plutonic foundation of a slow-spreading ridge segment: Oceanic core complex at Kane Megamullion, 23°30'N-45°20'W, *Geochemistry, Geophysics, Geosystems*, 9, (5); Q05014, doi:10.1029/2007GC001645

Dijkstra, A.H., Barth, M.G., Drury, M.R., Mason, P.R.D., Vissers, R.L.M., (2003), Diffuse porous melt flow and melt-rock reaction in the mantle lithosphere at a slow-spreading ridge: A structural petrology and LA-ICP-MS study of the Othris Peridotite Massif (Greece), *Geochemistry, Geophysics, Geosystems*, 4, (8); 8613, doi:10.1029/2001GC000278

Dilek, Y., and Newcomb, S., (2003), Ophiolite concept and the evolution of geological thought, *Geological Society of America, inc. Special paper 373*; 3300 Penrose Place, P.O box 9140, Boulder, Colorado, 80301, USA

Donnelly, K.E., (2002), The genesis of E-MORB: extensions and limitations of the hot spot model, *PhD. thesis, Columbia University*; 220

Donnelly, K.E., Goldstein, S.L., Langmuir, C.H., Spiegelman, M., (2004), Origin of enriched ocean ridge basalts and implications for mantle dynamics, *Earth and Planetary Science Letters*, 226; 347– 366

Dosso, L., Bougault, H., Joron, J.L., (1993), Geochemical morphology of the north Mid-Atlantic Ridge, 10-degrees-24-degrees-N – Trace element-isotope complementarity, *Earth and Planetary Science Letters,* 120, (3-4); 443-462

Dosso, L., Hanan, B.B., Bougault, H., Schilling, J.G. and Joron, J.-L., (1991), Sr-Nd-Pb geochemical morphology between 10° and 17°N on the Mid-Atlantic Ridge: A new MORB isotope signature, Earth and Planetary Science Letters, 106; 29-43

Doucelance, R., and Manhés, G., (2001), Re-evaluation of precise lead isotope measurements by thermal ionization mass spectrometry: comparison with determinations by plasma source mass spectrometry, *Chemical Geology*, 176; 361–377

Douglass, J., Schilling, J.G. and Fontignie, D., (1999), Plume-ridge interactions of the Discovery and Shona mantle plumes with the southern mid-Atlantic Ridge (40°–55°S). *Journal of Geophysical Research*, 104; 2941–2962

Dresser, M.J., (1968), The Saha-Langmuir Equation and its Application, *Journal of Applied Physics*, 39, (1); 338+

Drolia, R.K., and DeMets, C., (2005), Deformation in the diffuse India- Capricorn-Somalia triple junction from a multibeam and magnetic survey of the northern Central Indian Ridge, 3◦S–10◦S, *Geochemistry, Geophysics, Geosystems,* 6; Q09009, doi:10.1029/2005GC000950.

Dupre, B., Lambret, B. and Allzgrec, J., (1982), Isotopic variations within a single oceanic island: The Terceira case, *Nature, 299; 620-622*

Dupuy, C., Vidal, P.H., Barczus, H.G. and Chauvel, C., (1987), Origin of basalts from the Marquesas Archipelago (south central Pacific Ocean): Isotope and trace element constraints*, Earth and Planetary Science Letters,* 82; 145-152

Eberhardt, R. Delwiche and J. Geiss, (1964), Isotopic effects in single filament thermal ion sources, *Z, Naturforsch,* 19A; 736–740.

Eickmann, B., and Peckmann, J., (2007), Petrography, geochemistry and isotope characteristics of authigenic carbonates from the Mid-Atlantic Ridge, *Goldschmidt Conference Abstracts*; A251

Eiler, J.M., Schiano, P., Kitchen, N., Stolper, E.M., (2000), Oxygen-isotope evidence for recycled crust in the sources of mid-ocean-ridge basalts, *Nature*, 403; 530-534

Elliott, T., (2002), Caught Offside, *Science*, 295; 55-57

Escartín, J., and Cannat, M., (1999), Ultramafic exposures and the gravity signature of the lithosphere near the Fifteen–Twenty Fracture Zone (Mid-Atlantic Ridge, 14º–16.5ºN), *Earth and Planetary Science Letters*, 171; 411–424

Escartín, J., Cowie, P.A., Searle, R.C., Allerton, S., Mitchell, N.C., MacLeod, C.J., Slootweg, A.P., (1999), Quantifying tectonic strain and magmatic accretion at a slow spreading ridge segment, Mid-Atlantic Ridge, 29°N, Journal *of Geophysical Research*, 104, (B5); 10421-10437

Escartín, J., Hirth, G., Evans, B., (1997), Effects of serpentinization on the lithospheric strength and the style of normal faulting at slow-spreading ridges, *Earth and Planetary Science Letters*, 151; 181-189

Escartín, J., Mével, C., MacLeod, C.J., (2004), Oceanic detachments: Formation and associated deformation, *Goldschmidt Abstracts, 5.6 Dynamics of slow and ultra-slow spreading ridges*; A693

Escartín, J, Mével, C., MacLeod, C.J., McCaig, A.M., (2003), Constraints on deformation conditions and the origin of oceanic detachments: The Mid-Atlantic Ridge core complex at 15°45'N, *Geochemistry, Geophysics, Geosystems*, 4, (8),1067; doi:10.1029/2002GC000472

Escartín, J., Smith, D.K., Cann, J., Schouten, H., Langmuir, C.H., and Escrig, S., (2008), Central role of detachment faults in accretion of slow-spreading oceanic lithosphere, *Nature*, 455; 790-795

Ethlon, D., (1984), Plagioclase buoyancy in oceanic basalts: Chemical effects, *Geochimica et Cosmochimica Acta*, 48; 753-768

Falkner, K.K., Klinkhammer, G.P., Ungerer, C.A., Christie, D.M., (1995), Inductively coupled plasma mass spectrometry in geochemistry, Annual Reviews, *Earth and Planetary Science Letters*, 23; 409-449

Farnetani, D.G., and Richards, M.A., (1995), Thermal entrainment and melting in mantle plumes, *Earth and Planetary Science Letters*, 136; 251-267

Faure, F., Trolliard, G., Nicollet, C., Montel, J., (2003), A developmental model of olivine morphology as a function of the cooling rate and the degree of undercooling, *Contributions to Mineralogy and Petrology*, 145; 251–263

Faure, F., Schiano, P., (2004), Crystal morphologies in pillow basalts: implications for mid-ocean ridge processes, *Earth and Planetary Science Letters*; 331-344

Ferreira, P.L., (2006), Melt supply and magmatic evolution at a large central MOR volcano located in the Lucky Strike segment, 37º N on the Mid-Atlantic Ridge, Azores region, *PhD Thesis, University of Southampton*

Fitton, J.G., (1997), The OIB Paradox, *in* Foulger, G.R., and Jurdy, D.M., eds., *Plates, Plumes, and Planetary Processes*: *Geological Society of America Special Paper*; 430

Fitton, J.G., Saunders, A.D., Norry, M.J., Hardarson, B.S., and Taylor, R.N., (1997). Thermal and chemical structure of the Iceland plume, *Earth and Planetary Science Letters*, 153; 197–208

Fletcher, I.R., (2007), Using the common-Pb standards SRM-981 and SRM-982 as double spikes, *International Journal of Mass Spectrometry*, 261; 234–238

Flower, M.F.J., (1980), Accumulation of calcic plagioclase in ocean-ridge tholeiite: an indication of spreading rate?, *Nature*, 287; 530-532

Fontaine, F.J, Cannat M., Escartin, J. (2008) Hydrothermal circulation at slow-spreading mid-ocean ridges: the role of along-axis variations in axial lithospheric thickness, *Geology*, 36, 759–62

Forsyth, D.W., (1977), The evolution of the upper mantle beneath mid-ocean ridges, In: J. Bonnin and R.S. Dietz (editors), Present State of Plate Tectonics, *Tectonophysics*, 38, (1-2); 89-118

Forsyth, D.W., Webb, S., and Shen, Y., (2000), Three-dimensional mantle structure beneath the East Pacific Rise in the MELT area from Rayleigh wave dispersion, paper presented at: *RIDGE Workshop on Mantle Flow and Melt Generation Beneath Mid-Ocean Ridges*, Providence, RI

Fox, P.J., Detrick, R.S. Purdy, G.M., (1980), Evidence for crustal thinning near fracture zones: implications for ophiolites. In: A. Panayiotou, Editor, *Proceedings of the International Ophiolite Symposium, Ministry of Agriculture and Natural Resources, Cyprus Geological Survey Dept;* 161–168

Fox, P.J., and Gallo, D.G., (1984), A tectonic model for ridge–transform–ridge plate boundaries: implications for the structure of oceanic lithosphere, *Tectonophysics*, 104; 205–242

Francheteau, J., Choukroune, P., Hekinian, R., Le Pichon, X., Needham, H.D., (1976), Oceanic fracture zones do not provide deep sections in the crust, *Canadian Journal of Earth Sciences*, 13; 1223-1235

Fujiwara, T., Lin, J., Matsumoto, T., Kelemen, P., Tucholke, B.E., Casey, J.F., (2003), Crustal Evolution of the Mid-Atlantic Ridge near the Fifteen-Twenty Fracture Zone in the last 5 Ma, *Geochemistry, Geophysics, Geosystems,* 4, (3), 1024; doi:10.1029/2002GC000364

Gac, S., Dyment, J., Tisseau, C., and Goslin, J., (2003), Axial magnetic anomalies over slow-spreading ridge segments: Insights from numerical 3-D thermal and physical modelling, *Geophysical Journal International*, 154; 618-632

Gaherty, J.B., (2001), Seismic Evidence for Hotspot-Induced Buoyant Flow Beneath the Reykjanes Ridge, *Science,* 293, (5535); 1645 - 1647

Galer, S.J.G., (1999), Optimal double and triple spiking for high precision lead isotopic measurement, *Chemical Geology*, 157; 255–274

Gao, D. (1997), Sea-floor geology at the eastern intersection of the Mid-Atlantic Ridge and the Kane Transform Fault (23°40'N): a new perspective from side-scan sonar image analysis. *PhD thesis, Duke University*; Durham, NC, USA
Gao, D., Hurst, S. D., Karson, J. A., Delaney, J. R. and Spiess, F. N., (1998), Computer-aided interpretation of side-looking sonar images from the eastern intersection of the Mid-Atlantic Ridge with the Kane transform, *Journal of Geophysical Research*, 103; 20997-21014

Garcés, M., and Gee, J.S., (2007), Palaeomagnetic evidence of large footwall rotations associated with low-angle faults at the Mid-Atlantic Ridge, *Geology*, 35, (3); 279–282

Gartrell, A.P., (1997), Evolution of rift basins and low-angle detachments in multilayer analog models, *Geology;* 25, (7); 615–618

Gass, I.G., (1968), Is the Troodos massif of Cyprus a fragment of Mesozoic ocean floor?, *Nature*, 220; 39-42

Gazulla, M.F., Barba, A., Orduña, M., and Rodrigo, M., (2008), Bead-releasing agents used in the preparation of solid samples as beads for WD-XRF measurement, *X-Ray Spectrometry,* 37; 603–607

Gee, M.A.M., Thirlwall, M.F., Taylor, R.N., Lowry, D., Murton, B.J., (1998), Crustal Processes: Major Controls on Reykjanes Peninsula Lava Chemistry, SW Iceland, *Journal of Petrology*, 39, (5); 819–839

Gillis, K.M., and Thompson, G., (1993), Metabasalts from the Mid-Atlantic Ridge: new insights into hydrothermal systems in slow-spreading crust, *Contributions to Mineralogy and Petrology,* 113; 502–523

Gillson, G.R., Douglas, D.J., Fulford, J.E., Halligan, K.W., Tanner, S.D., (1988), Nonspectroscopic Interelement Interferences in Inductively Coupled Plasma Mass Spectrometry, *Analytical Chemistry*, 60; 1472-1474

Godard, M., Awaji, S., Hansen, H., Hellebrand, E., Brunelli, D., Johnson, K., Yamasaki, T., Maeda, J., Abratis, M., Christie, D., Kato, Y., Mariet, C., Rosner, M., (2009), Geochemistry of a long in-situ section of intrusive slow-spread oceanic lithosphere: Results from IODP Site U1309 (Atlantis Massif, 30°N Mid-Atlantic-Ridge, *Earth and Planetary Science Letters*, 279; 110–122

Godard, M., Lagabrielle, Y., Alard, O., Harvey, J., (2008), Geochemistry of the highly depleted peridotites drilled at ODP Sites 1272 and 1274 (Fifteen-Twenty Fracture Zone, Mid-Atlantic Ridge): Implications for mantle dynamics beneath a slow spreading ridge, *Earth and Planetary Science Letters*, 267; 410–425

Godard, M., Seyler, M., Harvey, J. and Alard, O., (2005), Geochemical Study of Mid Atlantic Ridge Peridotites at 15°N (ODP Site 1272 and ODP Site 1274), *Geophysical Research Abstracts*, 7, 04548, ID: 1607-7962/gra/EGU05-A-04548

Gràcia, E., and Escartín, J., (1999), Crustal accretion at mid-ocean ridges and backarc spreading centers: Insights from the Mid-Atlantic Ridge, the Bransfield Basin and the North Fiji Basin, Contributions to Science, 1, (2); 175-192

Grall, H., Fontignie, D., Hanan, B, and Shilling, J.G., (1986), Pb and Sr isotopes in basalts from Mururoa and Fangataufa Atolls, Tuamotu Archipelago, *Eos*, 67, (4); 14

Gray, A.L., (1975), Mass-spectrometric analysis of solutions using an atmospheric pressure ion source, *Analyst*, (London), 100; 289-299

Gray, A.L. and Date, A.R., (1983), Inductively coupled plasma source mass spectrometry using continuum flow ion extraction, *Analyst* (London), 108; 1033-1050

Green, T.H., and Ringwood, A.E., (1967), Crystallisation of basalt and andesite under high pressure hydrous conditions, *Earth and Planetary Science Letters*, 3; 481-489

Grindlay, N.R., and Fox, P.J., MacDonald, K.C., (1990), Second-Order Ridge Axis Discontinuities in the Atlantic: Morphology, Structure, and Evolution South Atlantic: Morphology, Structure, and Evolution, *Marine Geophysical Researches,* 13; 21-49

Guohao, R., Hongsen, X., and Xiande, X., (1991), An experimental melting-crystallization study on basalt at high pressures, *Chinese Journal of Geochemistry*, 10, (2); 174-179

Guseva, L.I., (2005), A Study of Ion-Exchange Behavior of Pb in Dilute HBr Solutions, Aimed to Evaluate the Possibility of on-Line Isolation of Element 114. 228Ra - 212Pb Generator, *Radiochemistry, 49, (1); 92-96*

Hajash, A. and Archer, P., (1980), Experimental seawater/basalt interactions: effects of cooling, *Contributions to Mineralogy and Petrology,* 75; 1–13.

Halliday, A.N., Davidson, J.P., Holden, P., DeWolf, C., Lee D.C. and Fitton, J.G., (1990), Trace-element fractionation in plumes and the origin of HIMU mantle beneath the Cameroon line, *Nature*, 347; 523-528

Hamelin, B., Manhes, G., Albarede, F. and Allègre, C.J., (1985), Precise lead isotope measurements by the double spike technique: a reconsideration, *Geochimica et Cosmochimica Acta*, 49; 173-182

Hanan, B.B., (2000), Mantle recycled in Sardinia, *Nature*, 408; 657-659

Hannigan, R.E., Basu, A.R., Teichmann, F., (2001), Mantle reservoir geochemistry from statistical analysis of ICP-MS trace element data of equatorial mid-Atlantic MORB glasses, *Chemical Geology*, 175; 397–428

Hanyu, T. and Kaneoka, I., (1997), The uniform and low $^{3}He/^{4}He$ ratios of HIMU basalts as evidence for their origin as recycled materials, *Nature*, 390

Hanyu, T. and Nakamura, E., (2000), Constraints on HIMU and EM by Sr and Nd isotopes re-examined, *Earth Planets and Space,* 52, 61–70

Harigane, Y., Michibayashi, K., Ohara, Y., (2008), Shearing within lower crust during progressive retrogression: Structural analysis of gabbroic rocks from the Godzilla Mullion, an oceanic core complex in the Parece Vela backarc basin, *Tectonophysics*, 457; 183–196

Harrison, C.G.A., (1974), Tectonics of mid-ocean ridges, *Tectonophysics*; 301-310

Harrison, C.G.A., and Ball, M., (1973), The Role of Fracture Zones in Sea Floor Spreading, *Journal of Geophysical Research*, 78, (32); 7776-7785

Harrison, C.G.A., and Stieltjes, L., (1977), Faulting within the median valley, *Tectonophysics,* 38; 137–144

Hart, S.R., (1984), A large-scale isotope anomaly in the Southern Hemisphere mantle, *Nature*, 309; 753-757

Hart, S.R, (1988), Heterogeneous mantle domains: signatures, genesis and mixing chronologies, *Earth and Planetary Science Letters,* 90; 273-296 273

Hart, S. R., and Dunn, T., (1993), Experimental CPX/melt partitioning for 24 trace elements, *Contributions to Mineralogy and Petrology*, 113; 1-8

Hart, S.R., Hauri, E.H., Oschmann L.A., and Whitehead J.A., (1992), Mantle plumes and entrainment: The isotopic evidence, *Science*, 256; 517-520

Hart, S.R. and Staudigel, H., (1982) The control of alkalis and uranium in seawater by ocean crust alteration, *Earth and Planetary Science Letters*, 58; 202-212

Hart, S.R., (1984), A large-scale isotope anomaly in the Southern Hemisphere mantle, *Nature*, 309; 753-757

Hart, S.R., and Staudigel, H., (1989), Isotopic characterization and identification of recycled components, 15-28. *In: Crust/Mantle Recycling at Convergence Zones, S. R. Hart and L. Gulen, eds.,* NATO ASI Series, 258, Series C

Hart, S.R., and Zindler, A, (1986), In search of a bulk earth composition, *Chemical Geology*, 57; 247-267

Hart, S.R., and Zindler, A, (1989), Constraints on the nature and development of chemical heterogeneities in the mantle, *In*: Mantle Convection, W. R. Peltier, ed., Gordon Breach Publishers; 261-387

Harvey, J., and Baxter, E., (2009), An improved method for TIMS high precision neodymium isotope analysis of very small aliquots (1–10ng), *Chemical Geology*, 258; 251–257

Harvey, P.K., Taylor, D.M., Hendry, R.D., and Bancroft, F., (1973), An accurate fusion method for the analysis of rocks and chemically related materials by x-ray fluorescence spectrometry, *X-ray spectrometry*, 2; 33-44

Hauri, E.H., Whitehead, J.A., Hart, S.R., (1994), Fluid dynamic and geochemical aspects of entrainment in mantle plumes *Journal of Geophysical Research,* 99; 24275–24300

Hekinian R. and Hoffert, M., (1975), Rate of palagonitisation and manganese coating on basaltic rocks from the rift valley in the Atlantic Ocean for 36°50′N, *Mar. Geol.* 19**,** 91–109

Hellfrich, G., (2002), Chemical and seismological constraints on mantle heterogeneity, *Philosophical. Transactions of the Royal Society of London,* A, 360; 2493–2505

Hémond, C., Hofmann, A.W., Vlastélic, I., Nauret, F., (2006), Origin of MORB enrichment and relative trace element compatibilities along the Mid-Atlantic Ridge between 10° and 24°N, *Geochemistry, Geophysics, Geosystems*, 7, (12); Q12010, doi:10.1029/2006GC001317

Herzberg, C., (2004), Partial Crystallization of Mid-Ocean Ridge Basalts in the Crust and Mantle, *Journal of Petrology*, 45, (12); 2389–2405

Hess, H.H., (1962), History of ocean basins, *Geological Society of America Bulletin*, Buddington; 599–620

Heymon, R.M., and White, S.M., (2004), Fine-scale segmentation of volcanic/hydrothermal systems along fast-spreading ridge crests, *Earth and Planetary Science Letters*, 226; 367– 382

Hickey-Vargas, R., (1992), A refractory HIMU component in the sources of island-arc magma, *Nature*; 360

Hilton, D. R., Thirlwall, M. F., Taylor, R. N., Murton, B. J.; Nichols, A., (2000), Controls on magmatic degassing along the Reykjanes Ridge with implications for the helium paradox, *Earth and Planetary Science Letters*, Volume 183, 1-2; 43-50

Hirchmann, M., (1995), Melt pathways in the mantle, *Nature,* 375; 737-738: doi: 10.1038/375737a0.

Hobbs, S.E., and Olesik, J., (1992), Inductively Coupled Plasma Mass Spectrometry Signal Fluctuations Due to Individual Aerosol Droplets and Vaporizing Particles, *Analytical Chemistry, 64;* 274-2133

Hoernle, K., Tilton, G. and Schmincke, H.U., (1991), Sr-Nd-Pb isotopic evolution of Gran Canaria: Evidence for shallow enriched mantle beneath the Canary Islands, *Earth and Planetary Science Letters, 106; 44-63*

Hofmann, A.W., (1988), Chemical differentiation of the Earth: the relationship between mantle, continental crust, and oceanic crust, *Earth and Planetary Science Letters,* 90; 297-314
Hofmann, A.W., (1997). Mantle geochemistry: a message from oceanic volcanism, *Nature*, 385; 219–229

Hofmann, A.W. (2003), Sampling mantle heterogeneity through oceanic basalts: isotopes and trace elements*, Treatise on Geochemistry*, Volume 2, pages 61–101

Hofmann, A.W., and Hémond, C., (2006), The origin of E-MORB, *Goldschmidt Conference Abstracts*, A257; doi:10.1016/j.gca.2006.06.517

Hubbert, M.K., (1951), Mechanical basis for certain familiar geologic structures, *Bulletin of the Geological Society of America,* 62; 355–372

Humphris, S.E., (1976), The hydrothermal alteration of oceanic basalts by seawater, *PhD Thesis, doi:10.1575/1912/1351*

Humphris, S.E., and Thompson, G., (1977), Hydrothermal alteration of oceanic basalts by seawater, *Geochimica et Cosmochimica Acta,* 41; 107–125

Humphreys, E.R. and Niu, Y., (2009), On the composition of ocean island basalts (OIB): The effects of lithospheric thickness variation and mantle metasomatism, *Lithos*, 112; 118–136

Hyndman, D.W., (1985), Petrology of Igneous and Metamorphic Rocks (2nd. Edition) McGraw

Ihinger, P.D., Hervig, R.L., and McMillan, P.F., (1994), Analytical methods for volatiles in glasses. *Reviews in Mineralogy,* 30; 67–121

Ildefonse, B., Blackman, D.K., John, B.E., Ohara, Y., Miller, D.J., MacLeod, C.J., Integrated Ocean Drilling Program Expeditions 304/305 Science Party, *Geology,* 35, (7)., 623–626

Ingram, M.G. and Chupka, W.A., (1953), Surface ionisation source using multiple filaments, *Review of Scientific Instruments*, 24, 518-520

Inoue, T., (1994), Effect of water on melting phase relations and melt composition in the system Mg_2SiO_4-$MgSiO_3$-H_2O) up to 15GPa, *Physics of the Earth and Planetary Interiors*, 85; 237-263

Ito, E., White, W.M., and Gopel, C., (1987), The O, Sr, Nd and Pb isotope geochemistry of MORB, *Chemical Geology*, 62; 157-176

Ito, G., (2001), Reykjanes "V"-shaped ridges originating from a pulsing and dehydrating mantle plume, *Nature,* 411; 681-684

Ito, G., and Behn, M.D., (2008), Magmatic and tectonic extension at mid-ocean ridges: 2. Origin of axial morphology, *Geochemistry, Geophysics, Geosystems,* 9; Q09O12; doi: 10.1029/2008GC001970.

Ito, G., and Mahoney, J.J., (2005), Flow and melting of a heterogeneous mantle: Method and importance to the geochemistry of ocean island and mid-ocean ridge basalts, *Earth and Planetary Science Letters*, 230; 29– 46

Iyer, S.D., and Banerjee, R., (1998), Importance of plagioclase morphology and composition in magmagenesis of the Carlsberg Ridge basalts, *Journal of the Indian Geophysical Union*, 1, (2); 63-72

Jackson, J.A., (1987), Active normal faulting and crustal extension: in Coward, M., *et al*., eds., Continental extensional tectonics: *Geological Society,* [London] Special Publication 28; 3-17

Jackson, J.A., and White, N.J., (1989), Normal faulting in the upper continental crust: observation from regions of active extension, *Journal of Structural Geology*, 11; 15–36

Jackson, M.G., and Dasgupta, R., (2008), Compositions of HIMU, EM1, and EM2 from global trends between radiogenic isotopes and major elements in ocean island basalts, *Earth and Planetary Science Letters*, 276; 175–186

Janney, P.E., Roex, A.P.L. and Carlson, R.W., (2005), Hafnium isotope and trace element constraints on the nature of mantle heterogeneity beneath the Central Southwest Indian Ridge (13°E to 47°E), *Journal of Petrology*, 46; 2427-2464

Jarvis, K.E., Gray, A.L., and Houk. R.S., (1992), Handbook of Inductively Coupled Plasma Mass Spectrometry, Chapman and Hall: New York

Jarvis, K.E., and Williams, J.G., (1993), Laser ablation inductively coupled plasma mass spectrometry (LA-ICP-MS): a rapid technique for the direct, quantitative determination of major, trace and rare-earth elements in geological samples, *Chemical Geology,* 106; 251 -262

Jochum, K.P., Seufert, H.M., Thirlwall, M.F., (1990), High-sensitivity Nb analysis by spark-source mass spectrometry (SSMS) and calibration of XRF Nb and Zr, *Chemical Geology,* 81,(1-16); 1

Jochum, K.P., and Verma, S.P., (1996), Extreme enrichment of Sb, Tl and other trace elements in altered MORB, *Chemical Geology*, 130 (3-4)., 289-299

John, B.E., and Foster, D.A., (1993), Structural and thermal constraints on the initiation angle of detachment faulting in the southern Basin and Range: The Chemehuevi Mountains case study, *GSA Bulletin*, 105, (8); 1091-1108

Johnson, K.T.M., Dick, H.J.B. and Shimizu, N., (1990), Melting in the oceanic upper mantle: an ion microprobe study of diopsides in abyssal peridotites. *Journal of Geophysical Research*, 95, B3; 2661-2678

Jöns, N., Bach, W., Schroeder, T., (2009) Formation and alteration of plagiogranites in an ultramafic-hosted detachment fault at the Mid-Atlantic Ridge (ODP Leg 209), *Contributions to Mineralogy and Petrology*, 157; 625–639

Juteau, T., Cannat, M., Lagabrielle, Y., (1990), Serpentinised peridotites in the upper oceanic crust away from transform zones: A comparison of the results of previous DSDP and ODP Legs, in Detrick, R., Honnorez, J., Bryan, W. B., Juteau, T., *et al*., *Proceedings of the Ocean Drilling Program, Scientific Results,* Vol. 106/109

Kandilarov, A., Mjelde, R., Okino, K., Murai, Y., (2008), Crustal structure of the ultra-slow spreading Knipovich Ridge, North Atlantic, along a presumed amagmatic portion of oceanic crustal formation, *Marine Geophysical Researches*, 29; 109–134

Karson, J.A., (1990), Seafloor spreading on the Mid-Atlantic Ridge: implications for the structure of ophiolites and oceanic lithosphere produced in slow-spreading environments, *In* Malpas, J., Moores, E.M., Panayiotou, A., and Xenophontos, C. (Eds.), *Ophiolites: Oceanic Crustal Analogues*: Proc. Symp. “Troodos 1987”, Geological Survey Dept., Nicosia, Cyprus; 547–55

Karson, J.A., (1999), Geological investigation of a lineated massif at the Kane Transform Fault: implications for oceanic core complexes, *Philosophical Transactions of the Royal Society of London*, A, 357; 713-740

Karson, J.A., and Brown, J.R., (1988), Geologic Setting of the Snake Pit Hydrothermal Site: An Active Vent Field on the Mid-Atlantic Ridge, *Marine Geophysical Researches,* 10; 91-107

Karson, J.A., and Dick, H.G.B., (1983), Tectonics of ridge-transform at the Kane Fracture Zone, *Marine Geophysical Researches, 6,* 51-98

Karson, J.A., Früh-Green, G.L., Kelley, D.S., Williams, E.A., Yoerger, D.R., Jakuba, M., (2006), Detachment shear zone of the Atlantis Massif core complex, Mid-Atlantic Ridge, 30°N, 7, (6); Q06016, doi:10.1029/2005GC001109

Karson, J.A., and Lawrence, R.M., (1997), Tectonic setting of serpentinite exposures on the western median valley wall of the MARK area in the vicinity of Site 920, in *Proceedings of the ODP, Scientific Results,* 5–21

Kelemen, P.B., Braun, M., Hirth, G., (2000), Spatial distribution of melt conduits in the mantle beneath oceanic spreading ridges: Observations from the Ingalls and Oman ophiolites, *Geochemistry, Geophysics, Geosystems*, 1, Paper number; 1999GC000012

Kelemen, P.B., Kikawa, E., Miller, D.J., and Shipboard Scientific Party, (2004), Proceedings of the Ocean Drilling Program, Initial Reports, Volume 209: College Station, Texas, Ocean Drilling Program, doi; 10.2973/ odp.proc.ir.209.2004

Kelemen, P.B., Kikawa, E., and Miller, D.J and Shipboard Scientific Party, (2007), Leg 209 summary: Processes in a 20km thick conductive boundary layer beneath the Mid-Atlantic Ridge 14°–16°N, *Proceedings of the Ocean Drilling Program, Scientific Results;* 209

Kelemen, P.B., Shimizu, N., Salters, V.J.M., (1995a) Extraction of mid-ocean-ridge basalt from the upwelling mantle by focused flow of melt in dunite channels, *Nature,* 375., 747 – 753

Kelemen, P.B., Whitehead, J.A., Aharonov, E, Jordahl, K.A., (1995b), Experiments on flow focusing in soluble porous media, with applications to melt extraction from the mantle, Journal of Geophysical Research, 100, (B1)., 475-496

Keller, R.A., Fisk, M.R., White, W.M., (2000), Isotopic evidence for Late Cretaceous plume–ridge interaction at the Hawaiian hotspot, *Nature,* 405; 673-676

Kellogg, J.B., Jacobsen, S.B., O'Connell, R.J., (2002), Modelling the distribution of isotopic ratios in geochemical reservoirs, *Earth and Planetary Science Letters*, 204; 183-202

Kennish, M.J., and Lutz, R.A., (1992), Geology of deep-sea hydrothermal vents and seafloor spreading centers, *Reviews in Aquatic Sciences*, 6, (2); 97-120

Kent, A.J.R., Stolper, E.M., Francis, D., Woodhead, J., Frei, R. And Eiler, J., (2004), Mantle heterogeneity during the formation of the North Atlantic Igneous Province: Constraints from trace element and Sr-Nd-Os-O isotope systematics of Baffin Island picrites, *Geochemistry Geophysics Geosystems*, 5; doi: 10.1029/2004GC000743

Kincaid, C., Sparks, D.W., Detrick, R., (1996), The relative importance of plate-driven and buoyancy driven flow at mid-ocean ridges, *Journal of Geophysical Research*, 101, (B7); 16,177-16,193

Kinzler, R.J. and Grove, T.L., (1992), Primary magmas of Mid-Ocean Ridge Basalts 2 - Applications, *Journal of Geophysical Research*, 97; 6907-6926.

Klein, E.M., and Langmuir, C.H., (1987), Global Correlations of Ocean Ridge Basalt Chemistry with Axial Depth and Crustal Thickness, *Journal of Geophysical Research*, 92, (B8); 8089-8115

Klein, E.M., and Langmuir, C.H., (1989), Local versus global variations in ocean ridge basalt compositions: A reply, *Journal of Geophysical Res*earch, 94; 4241-4252

Koepke, J., Feig, S.T., and Snow, J., (2005), Late stage magmatic evolution of oceanic gabbros as a result of hydrous partial melting: Evidence from the Ocean Drilling Program (ODP) Leg 153 drilling at the Mid-Atlantic Ridge, *Geochemistry, Geophysics, Geosystems*, 6, (2); Q02001, doi:10.1029/2004GC000805

Koepke, J., Feig, S.T., Snow, J., Freise, M., (2004), Petrogenesis of oceanic plagiogranites by partial melting of gabbros: an experimental study, *Contributions to Mineralogy and Petrology*, 146; 414–432

Kogiso, T., Hirchmann, M.M., Reiners, P.W., (2003), Length scales of mantle heterogeneities and their relationship to ocean island basalt geochemistry, *Geochimica et Cosmochimica Acta*, 68, (2); 345–360

Kogiso, T., Tatsumi, Y., Shimoda, G., Barsczus, H.G,. (1997), High mu (HIMU) ocean island basalts in southern Polynesia: New evidence for whole mantle scale recycling of subducted oceanic crust, *Journal of Geophysical Research- Solid Earth*, 102, (B4); 8085-8103

Krolikowska-Ciaglo, S., Deyhle, A., Hauff, F., Hoernle, K., (2007), Boron isotope geochemistry and U–Pb systematics of altered MORB from the Australian Antarctic Discordance (ODP Leg 187), *Chemical Geology*, 242; 455–469

Kuritani, T., and Nakamura, E., (2002), Precise isotope analysis of nanogram-level Pb for natural rock samples without use of double spikes, *Chemical Geology,* 186; 31– 43

Kuritani, T., Usui, T., Yokoyama, T., Nakamura, E., (2006), Accurate Isotopic and Concentration Analyses of Small Amounts of Pb Using Isotope Dilution Coupled with the Double Spike Technique, *Geostandards and Geoanalytical Research*, 30, (3); 209-220

Lagabrielle, Y., and Cannat, M., (1990), Alpine Jurassic ophiolites resemble the modern central Atlantic basement, *Geology*, 18, (4); 319-322

Langmuir, C.H., Klein, E.M., and Plank, T., (1992), Petrological systematics of mid-ocean ridge basalts: Constraints on melt generation beneath ocean ridges, In: Phipps Morgan, J., Blackman, D. K. and Sinton, J. M. (eds.), Mantle Flow and Melt Generation at Mid-Ocean Ridges, *Geophysical Monograph Series, 71, American Geophysical Union*; 183-280

Langmuir, C.H., Bender, J.F. and Batiza, R., (1986), Petrological and tectonic segmentation on the East Pacific Rise, 5°30'-14°30'N, *Nature*, 322, 6078, 422-429

Lanyon, R., (1994), Mantle reservoirs and mafic magmatism associated with the break-up of Gondwana-the Balleny Plume and the Australian-Antarctic Discordance. U-Pb zircon dating of a Proterozoic mafic dyke swarm in the Vestfold Hills. East Antarctica. Ph.D. Thesis. University of Tasmania

Lavier, L., and Buck, W.R., (1999), Self-consistent rolling-hinge model for the evolution of large-offset low-angle normal faults, *Geology,* 27, (12); 1127–1130

Lavier, L., Buck, R., Poliakov, A.N.B., (2000), Factors controlling normal fault offset in an ideal brittle layer, *Journal of Geophysical Research*, 105, (B10); 23,431-23,442

Le Douaran, S., and Francheteau, J., (1981), Axial depth anomalies from 10 to 50° north along the Mid-Atlantic Ridge: correlation with other mantle properties, *Earth and Planetary Science Letters*, 54, (1); 29-47

Lechler, P.J., and Desilets, M.O., (1987), A review of the use of loss on ignition as a measurement of total volatiles in whole-rock analysis, *Chemical Geology*, 63; 341-344

Le Maitre, R.W., (1976), A new approach to the classification of igneous rocks using the basalt-andesite-dacite-rhyolite suite as an example, *Contributions to Mineralogy and Petrology*, 56, (2); 10.1007/BF00399604

Lenz, H., and Wendt, I., (1976), Use of a double collector for high-precision isotope ratio measurements in geochronology. In: *Proc. 7th Int. Conf. on Mass Spectrometry,* Florence, Aug. 30–Sept. 3, 1976, *Advances in Mass Spectrometry;* 7A, 565–568

Le Roex, A.P., Dick, H.J.B., Erlank, A.L., Reid A.M., Frey, F.A., and Hart, S.R., (1983), Geochemistry, mineralogy and petrogenesis of lavas erupted along the southwest Indian Ridge between the Bouvet Triple Junction and 11 degrees east, *Journal of Petrology*, 24; 267– 318

Lin, J., and Phipps-Morgan, J., (1992), The spreading rate dependence of three dimensional mid-ocean ridge gravity structure, *Geophysical Research Letters*, 19, (1); 13-16

Lin, J., Purdy, G.M., Schouten, H., Sempéré, J.-C., and Zervas, C., (1990), Evidence from gravity data for focused magmatic accretion along the Mid-Atlantic Ridge, *Nature,* 344; 627–632

Lister, C.R.B., (1972), On the thermal balance of a mid-ocean ridge, *Geophysical Journal of the Royal Astronomical Society*, 26; 515-535

Lister, C.R.B., (1974), On the penetration of water into hot rock, *Geophysical Journal of the Royal Astronomical Society*, 39; 465-509

Lister, G.S., and Davis, G.A., (1989), The origin of metamorphic core complexes and detachment faults formed during Tertiary continental extension in the northern Colorado River region, U.S.A., *Journal of Structural Geology,* 11, (1-2); 65-94

Lister G., and Forster, M.A., (2004), The nature and origin of detachment faults, Paper No. 237-1, *Denver Annual Meeting*

Lizarralde, D., Gaherty, J.B., Collins, J.A., Hirth, G., and Kim, S., (2004), Spreading-rate dependence of melt extraction at mid-ocean ridges from mantle seismic refraction data, *Nature*, 432; 744-747

Long, S.E., and Browner, R.F., (1988), Influence of water on conditions in the inductively coupled argon plasma, *Spectrochimica Acta*, 43B; 1461-1471

Lozano, R., and Bernal, J.P., (2005), Characterization of a new set of eight geochemical reference materials for XRF major and trace element analysis, *Revista Mexicana de Ciencias Geológicas, 22, (3); 329-344*

Ludwig, K.R., (1997), Optimization of multicollector isotope-ratio strontium and neodymium, *Chemical Geology*, 135; 325-334

MacDonald, K.C., (1977), Near-bottom magnetic anomalies, asymmetric spreading, oblique spreading, and tectonics of the Mid-Atlantic Ridge near lat. 37°N, *Geological Society of America Bulletin*, 88; 541-555

MacDonald, K.C., Fox, P.J., Perram, L.J., Eisen, M.F., Haymon, R.M., Miller, S.P., Carbotte, S.M., Cormier M.H., and Shor, A.N., (1988), A new view of the Mid-Ocean Ridge from the behavior of ridge-axis discontinuities, *Nature,* 335., 217–225

MacDonald, K.C., Scheirer, D.S., Carbotte, S.M., (1991), Mid-Ocean Ridges: Discontinuities, Segments and Giant Cracks, *Science,* 253, (5023); 986 – 994

Machida, S., Hirano, N., Kimura, J., (2009), Evidence for recycled plate material in Pacific upper mantle unrelated to plumes, *Geochimica et Cosmochimica Acta,* 73; 3028–3037

MacLeod, C.J., (1990), Role of the Southern Troodos Transform Fault in the rotation of the Cyprus microplate: evidence from the Eastern Limassol Forest Complex. In: Malpas, J., Moores, E.M., Panayiotou, A., Xenophontos, C. (Eds.), Ophiolites: Ocean Crustal Analogues. In: Proc. Symp. 'TROODOS 1987'. Geological Survey Dept., Nicosia, Cyprus, pp. 75–85

MacLeod, C.J., Dick, H.J.B., Allerton, S., and Robinson, P.T., and the JR31 Scientific Party (1999), Structure of Atlantis Bank, SW Indian Ridge: An eroded megamullion surface?, *Geophysical Research Abstracts*, 1; 186

MacLeod, C.J., Escartín, J., Banerji, D., Banks, G.J., Gleeson, M., Irving, D.H.B., Lilly, R.M., McCaig, A.M., Niu, Y., Allerton, S., and Smith, D.K., (2002), Direct geological evidence for oceanic detachment faulting: The Mid-Atlantic Ridge, 15°45'N, *Geology,* 30, (10); 879–882

MacLeod, C.J., Searle, R.C., Murton, B.J., Casey, J.F., Mallows, C., Unsworth, S.C., Achenbach, K.L., Harris, M., (2009), Life cycle of oceanic core complexes, *Earth and Planetary Science Letters,* 287; 333–344

Magde, L.S., and Sparks, D.W., (1997), Three-dimensional mantle upwelling, melt generation, and melt migration beneath segment slow spreading ridges, *Journal of Geophysical Research*, 102, (B9); 20571-20583

Magde, L.S., Sparks, D.W., and Detrick, R.S., (1997) The relationship between buoyant mantle flow, melt migration, and gravity bull's eyes at the Mid-Atlantic Ridge between 33°N and 35°N, *Earth and Planetary Science Letters*, 148; 59-67

Maia, M., Goslin, J., Gente, P., (2007), Evolution of the accretion processes along the Mid-Atlantic Ridge north of the Azores since 5.5 Ma: An insight into the interactions between the ridge and the plume, *Geochemistry, Geophysics, Geosystems*, 8, (3); Q03013, doi: 10.1029/2006GC001318

Malpas, J.G., and Robinson, P.T., (1997), The origin and evolution of oceanic lithosphere, *Geoscience Canada*, 24, (2); 99

Manga, M., (1996), Mixing of heterogeneities in the mantle: effect of viscosity differences, *Geophysical Research Letters*, 23, (4); 403-406

Markey, R., Hannah, J.L., Morgan, J.W., Stein, H.J., (2003), A double spike for osmium analysis of highly radiogenic samples, *Chemical Geology*, 200, (3-4); 395-406

Martinez, F., Karsten, J. and Klein, E.M., (1998), Recent kinematics and tetonics of the Chile Ridge, *Eos Trans. Am. Geophys*. 79(45) Fall Mtg. Suppl., F836

McCaig, A.M., Cliff, R.A., Escartín, J., Fallick, A.E., MacLeod, C.J., (2007), Oceanic detachment faults focus very large volumes of black smoker fluids, *Geology*, 35, (10); 935–938

McKenzie, D., and Bickle, M.J., (1988), The Volume and Composition of Melt Generated by Extension of the Lithosphere, *Journal of Petrology,* 29, (3); 623-679

McKenzie, D. and O'Nions, R.K., (1991), Partial Melt Distributions from Inversion of Rare Earth Element Concentrations, *Journal of Petrology*, 32, (5); 1021-1091

Melson, W.G., and Thompson, G., (1971), Petrology of a Transform fault zone and adjacent ridge segments, *Philosophical Transactions of the Royal Society of London. A*, 268; 423-441

Menard, H.W. (1967), Sea-floor spreading, topography and the second layer, *Science,* 157; 923–924

Menzies, M., Blanchard, D., and Xenophontos, C., (1980), Genesis of the Smartville arc-ophiolite, Sierra Nevada foothills, California, *American Journal of Science,* 280A; 329–344

Meschede, M., (1986), A method of discriminating between different types of mid-ocean ridge basalts and continental tholeiites with the Nb-Zr-Y diagram, *Chemical Geology*, 56; 207-218

Mével, C., Cannat, M., Gente, P., Marion, E., Auzende, J.M., Karson, J.A., (1991), Emplacement of deep crustal and mantle rocks on the west wall of the MARK area (Mid-Atlantic Ridge, 23°N), *Tectonophysics*, 190; 31–53

Michael, P.J., and Bonatti, E., (1985), Petrology of ultramafic rocks from Sites 556, 558, and 560 in the North Atlantic, In: Bougault, H. and Cande, S. (eds.) *Initial Reports of the Deep Sea Drilling Project*, Washington, D.C.: US Government Printing Office; 523-528

Michael, P.J., (1995), Regionally distinctive sources of depleted MORB: evidence from trace elements and H_2O, *Earth and Planetary Science Letters* 131; 301–320

Miller, D.J., and Christensen, N.I., (1997), Seismic velocities of lower crustal and upper mantle rocks from the slow-spreading Mid-Atlantic Ridge, South of the Kane transform zone (MARK), *Proceedings of the Ocean Drilling Program, Scientific Results,* 153; 437–454

Miller, J., Kelemen, P.B., Kikawa, E., ODP Leg Shipboard Scientific Party, (2004), Petrogenesis, alteration, and deformation in mantle peridotite from 14° to 16°N on the Mid-Atlantic Ridge: ODP Leg 209, *Goldschmidt Abstracts, In session 5.6: Dynamics of slow and ultra-slow spreading ridges*; 5.6.11

Minster, B.J., and Jordan, T.H., (1978), Present day plate motions, *Journal of Geophysical Research,* 83, (B11); 5331–5354

Miranda, J.M., Silva, P.F., Lourenco, N., Henry, B., Costa, R. & Shipboard Team, (2002), Study of the Saldanha Massif (MAR, 36◦ 34'N): constraints from rock magnetic and geophysical data, *Mar. Geophys. Res*., 23, 299–318

Mitchell, N.C., Allerton, S., Escartín, J., (1998), Sedimentation on young ocean floor at the Mid-Atlantic Ridge, 29"N, *Marine Geology*, 148; l-8

Miyazaki, T., Shibata, T. and Yoshikawa, M., (2003), New synthesis method of silica-gel for lead isotope analysis, Proceedings of the Japan Academy 79, B, (2); 58-62

Moore, D.E., and Lockner, D.A., (2008), Talc friction in the temperature range 25°–400 °C: Relevance for Fault-Zone Weakening, *Tectonophysics*, 449; 120–132

Moores, E.M., Kellogg, L.H., Dilek, Y., (2000), Tethyan ophiolites, mantle convection, and tectonic "historical contingency": a resolution of the "ophiolite conundrum", *In*: Dilek, Y., Moores, E.M., Elthon, D., Nicolas, A. (Eds.), Ophiolites and oceanic crust: new insights from field studies and the Ocean Drilling Program, *Geological Society of America Special Paper*, 349, Boulder, CO, USA; 3–12

Moreira, M. and Kurz, M.D., (1999), Subducted oceanic lithosphere and the origin of the 'high m' basalt helium isotopic signature, *Earth and Planetary Science Letters,* 189; 49–57

Morgan, W.J., (1971), Convection plumes in the lower mantle, *Nature*, 230; 42-43

Morris, A., Gee, J.S., Pressling, N., John, B.E., MacLeod, C.J., Grimes, C.B., Searle, R.C., (2009), Footwall rotation in an oceanic core complex quantified using reoriented Integrated Ocean Drilling Program core samples, *Earth and Planetary Science Letters*, 287; 217–228

Morris, J.D, and Hart, S.R. (1983), Isotopic and incompatible element constraints on the genesis of island arc volcanics from Cold Bay and Amak Island, Aleutians, and implications for mantle structure, *Geochimica et Cosmochimica Acta,* 47; 2015–2030

Mozgova, N.N., Trubkin N.V., Borodaev, Y.S., Cherkashev, G.A., Stepanova, T.V., Semkova, T.A., Uspenskaya, T.Y., (2008), Mineralogy of massive sulfides from the Ashadze hydrothermal field, 13 degrees N, Mid-Atlantic Ridge, *Canadian Mineralogist*, 46; 545-567

Mottl, M.J., (1983), Metabasalts, axial hot springs, and the structure of hydrothermal systems at mid-ocean ridges, *Geological Society of America Bulletin*, 94; 161-180

Mottl, M.J., and Holland, H.D., (1978), Chemical exchange during hydrothermal alteration of basalt by seawater- I. Experimental results for major and minor components of seawater, *Geochimica et Cosmochimica Acta,* 42; 1103–1115

Miihe, R., Peucker-Ehrenbrink, B., Devey, C.W., Garbe-Schönberg, D., (1997), On the redistribution of Pb in the oceanic crust during hydrothermal alteration, *Chemical Geology*, 137; 67-77

Muller, M.R., Minshull, T.A. White, R.S., (2000), Crustal structure of the Southwest Indian Ridge at the Atlantis II Fracture Zone, *Journal of Geophysical Research*, 105, (25); 25809–25828

Muller, M.R., Robinson, C.J., Minshull, T.A., White R.S., and Bickle, M.J., (1997), Thin crust beneath ocean drilling program borehole 735B at the Southwest Indian Ridge?, *Earth and Planetary Science Letters,* 148; 93–107

Muller, R.D., and Smith, W.H.F., (1993), Deformation of the Oceanic Crust Between the North American and South American Plates, *Journal of Geophysical Research*, 98, (B5); 8275-8291

Müntener, O., and Piccardo, G.B., (2003), Melt migration in ophiolites: The message from Alpine– Apennine peridotites and implications for embryonic ocean basins, *in* Dilek, Y., and Robinson, P.T., eds., Ophiolites in Earth history, *Geological Society, London, Special Publications*, 218; 69–89

Murton, B.J., Taylor, R.N., and Thirlwall, M.F., (2002), Plume-ridge interaction: a geochemical perspective from the Reykjanes Ridge, *Journal of Petrology*, 43, (11); 1987-2012

Murton, B.J., Tindle, A.G., Milton, J.A., Sauter, D., (2005), Heterogeneity in southern Central Indian Ridge MORB: Implications for ridge–hot spot interaction, *Geochemistry, Geophysics, Geosystems*, 6, (3); Q03E20, doi: 10.1029/2004GC000798

Mutter, J.C., and Karson, J.A., (1992), Structural Processes at Slow-Spreading Ridges, *Science,* 257, (5070); 627 – 634

Mysen, B.O., and Boettcher, A.L., (1974), Melting of a Hydrous Mantle: I. Phase Relations of Natural Peridotite at High Pressures and Temperatures with Controlled Activities of Water, Carbon Dioxide, and Hydrogen, Journal *of Petrology*, 16, (3); 520-548

Nakamoto, K., (1997), Infrared and Raman Spectra of Inorganic and Coordination Compounds, (5th ed.), Wiley: New York

Nakayama, K., and Nakamura, T., (2008), Calibrating standards using chemical reagents for glass bead x-ray fluorescence analyses of geochemical samples, *X-Ray Spectrometry,* 37; 204–209

Nam, S., Chung, H., Kim, J., and Lee, Y., (2008), Mass Background Spectra of ICP-MS with Various Acids, *Bulletin of the Korean Chemical Society*, 29, (11); 2237-2240

Nash, W.P., and Crecraft, H.R., (1985), Partition coefficients for trace elements in silicic magmas, *Geochimica et Cosmochimica Acta,* 49; 2309-2322

Natland, J.H., and Dick, H.J.B., (2002), Stratigraphy and composition of gabbros drilled in Ocean Drilling Program Hole 735B, Southwest Indian Ridge: a synthesis

of geochemical data, *Proceedings of the Ocean Drilling Program Scientific Results,* 179; 69

Nauret, F., Abouchami W., Galer S.J.G., Hofmann A.W., Hemond C., Chauvel C., Dyment, J., (2006), Correlated Trace Element-Pb isotope enrichments in Indian MORB along 18-20S, Central Indian Ridge, *Earth and Planetary Science Letters,* 245, 137-152

Newman, K., Freedman, P.A., Williams, J., Belshaw, N.S., Halliday, A.N., (2009), High sensitivity skimmers and non-linear mass dependent fractionation in ICP-MS, *Journal of Analytical Atomic Spectrometry*, 24; 742–751

Niu, Y., (1997), Mantle Melting and Melt Extraction Processes beneath Ocean Ridges: Evidence from Abyssal Peridotites, *Journal of Petrology*, 38, (8); 1047-1074

Niu, Y., and Batiza, R., (1997), Trace element evidence from seamounts for recycled oceanic crust in the Eastern Pacific mantle, *Earth and Planetary Science Letters*, 148; 47 l-483

Niu, Y., Bideau, D., Hékinian, R., Batiza, R., (2001), Mantle compositional control on the extent of mantle melting, crust production, gravity anomaly, ridge morphology, and ridge segmentation: a case study at the Mid-Atlantic Ridge 33°35³N, *Earth and Planetary Science Letters*, 186; 383-399

Niu, Y., Collerson, K.D., Batiza, R., Wendt, J.I., Regelous, M., (1999), Origin of enriched-type mid-ocean ridge basalt at ridges far from mantle plumes: The East Pacific Rise at 11°20'N, *Journal of Geophysical Research*, 104, (B4); 7067-7087

Niu, Y., and Hékinian, R., (1997), Spreading-rate dependence of the extent of mantle melting beneath ocean ridges, *Nature*, 385; 326-329

Niu, Y., and O'Hara, M.J., (2008), Global Correlations of Ocean Ridge Basalt Chemistry with Axial Depth: a New Perspective, *Journal of Petrology*, 49, (4); 633-664

Noble, S.R., Lightfoot, P.C., Scharer, U., (1989), A new method for single-filament isotopic analysis of Nd using in situ reduction, *Chemical Geology (Isotope Geoscience Section)*, 79; 15-19

Norrish, K., and Hutton, J.T., (1969), An accurate X-ray spectrographic method for the analysis of a wide range of geological samples, *Geochimica et Cosmochimica Acta,* 33; 431–453

Ohara, Y., Yoshida, T., Kato, Y., Kasuga, S., (2001), Giant Megamullion in the Parece Vela Backarc Basin, *Marine Geophysical Researches,* 22; 47–61

Ohara, Y., Fujioka, K., Ishii, T., Yurimoto, H., (2003), Peridotites and gabbros from the Parece Vela backarc basin: Unique tectonic window in an extinct

backarc spreading ridge, *Geochemistry, Geophysics, Geosystems*, 4, (7); 8611, doi:10.1029/2002GC000469

Ohara, Y., Okino, K., Kasahara, J., (2007), Seismic study on oceanic core complexes in the Parece Vela back-arc basin, *Island Arc,* 16; 348–360

Okino, K., Kasuga, S., and Ohara, Y., (1998), A new scenario of the Parece Vela Basin genesis, *Marine Geophysical Researches*, 20; 21-40.

Okino, K., Matsuda, K., Christie, D.M., Nogi, Y., Koizumi, K., (2004), Development of oceanic detachment and asymmetric spreading at the Australian-Antarctic Discordance, *Geochemistry, Geophysics, Geosystems*, 5, (12); Q12012, doi:10.1029/2004GC000793

Ondreas, H., Cannat, M., Cherkashov, G., Fouquet, Y., Normand, A., Serpentine Scientific Party, A., (2007), High Resolution Mapping of the Ashadze and Logachev Hydrothermal Fields, Mid Atlantic Ridge 13-15°N, *American Geophysical Union, Fall Meeting 2007*; abstract #T53B-1310

O'Nions, R.K., Carter, S.R., Evensen, N.M., and Hamilton, P.J., (1979), Geochemical and cosmochemical applications of Nd isotope analysis, *Annual Reviews in Earth and Planetary Science*, 7; 11-38

Osborn, E.F., and Tait, D.B., (1952), The system diopside-forsterite-anorthite, *American Journal of Science, Bowen Volume*; 413-433.

Parai, R., Mukhopadhyay, S and Lassiter, J., (2009), New constraints on the HIMU mantle from neon and helium isotopic compositions of basalts from the Cook–Austral Islands, *Earth and Planetary Science Letters*, 277; 253–261

Parsons, T., and Thompson, G.A., (1993), Does magmatism influence low-angle normal faulting?, *Geology, 21;* 247-250

Pearce, J.A., (1991), Ocean floor comes ashore, *Nature,* 354; 110–111

Pearce, J.A., and Cann, J.R., (1973), Tectonic setting of basic volcanic rocks determined using trace element analyses, *Earth and Planetary Science Letters,* 19; 290–300

Perfilev, A.S., Raznitsin, Y.N., Peive, A.A., Pertsev, A.N., Kolobov, V.Y., (1996), MAR rift valley and fifteen twenty fracture zone intersection: Magmatism and structure, *Petrology*, 4, (2); 168-183

Pertsev, A.N., Bortnikov, N.S., Aranovich, Ya., L., Vlasov, E.A., Beltenev, V.E., Ivanov, V.N., and Simakin, S.G., (2009), Peridotite–Melt Interaction under Transitional Conditions between the Spinel and Plagioclase Facies beneath the Mid-Atlantic Ridge: Insight from Peridotites at 13°N, *Petrology,* 17, (2); 124–137

Petersen, S., Kuhn, K., Kuhn, T., Augustin, N., Hékinian, R., Franz, L., Borowski, C., (2009), The geological setting of the ultramafic-hosted Logatchev hydrothermal field (14°45′N, Mid-Atlantic Ridge) and its influence on massive sulfide formation, *Lithos*, 112; 40–56

Phipps-Morgan, J., and Parmentier, E.M., (1987), Mechanisms for the Origin of Mid-Ocean Ridge Axial Topography: Implications for the Thermal and Mechanical Structure of Accreting Plate Boundaries, *Journal of Geophysical Research*, 92, (B12); 12823-12836

Pilet, S., Hernandez, J., Sylvester, P., Poujol, M., (2005), The metasomatic alternative for ocean island basalt chemical heterogeneity, *Earth and Planetary Science Letters*, 236; 148– 166

Pockalny, R.A., Detrick, R.S. and Fox, P.J., (1988), Morphology and tectonics of the Kane Transform from Sea Beam bathymetry data, *Journal of Geophysical Research,* 93, (B4); 3179–3193

Potts, P.J., (1992), A handbook of silicate rock analysis, Glasgow: Blackie; New York: Chapman and Hall, 1987

Powell, R., Woodhead, J., Hergt, J., (1998), Uncertainties on lead isotope analyses: deconvolution in the double-spike method, *Chemical Geology*, 148; 95–104

Presnall, D.C., Dixon, S.A., Dixon, J.R., O'Donnell, T.H., Brenner, N.L., Schrock, R.L., and Dycus, D.W., (1978), Liquidus phase relations on the join diopside-forsterite-anorthite from 1 atm to 20 kbar: Their bearing on the generation and crystallization of basaltic magma, *Contributions to Mineralogy and Petrology*, 66, (2); 203-220

Presnall, D.C., Gudfinnsson, G.H., Walter, M.J., (2002), Generation of mid-ocean ridge basalts at pressures from 1 to 7 GPa, *Geochimica et Cosmochimica Acta*, 66, (12); 2073–2090

Prytulak, J., and Elliott, T., (2007), TiO2 enrichment in ocean island basalts, *Earth and Planetary Science Letters*, 263; 388–403

Qin, R., and Buck, W.R., (2005), Effect of lithospheric geometry on rift valley relief, *Journal of Geophysical Research*, 110, B03404; doi:10.1029/2004JB003411

Quick, J.E., and Denlinger, R.P., (1993), Ductile Deformation and the Origin of Layered Gabbro in Ophiolites

Ramebäck, H., Berglund, M., Kessel, R., Wellum, R., (2002), Modelling isotope fractionation in thermal ionisation mass spectrometry filaments having diffusion controlled emission, *International Journal of Mass Spectrometry*, 216; 203–208

Rampone, E., Piccardo, G.B., Vannuci, R., Bottazzi, P., (1997), Chemistry and origin of trapped melts in ophiolitic peridotites, *Ceochimica et Cosmochimica Acta*, 61, (21); 4557-4569

Ranero, C.R., and Reston, T.J., (1999), Detachment faulting at ocean core complexes, *Geology,* 27, (11); 983–986

Reston, T.J., Ranero, C.R., Ruoff, O., Perez-Gussinye, M., Dañobeitia, J.J., (2004), Geometry of extensional faults developed at slow-spreading centres from

pre-stack depth migration of seismic reflection data in the Central Atlantic (Canary Basin), *Geophysical Journal International,* 159; 591–606

Reston, T.J., Weinrebe, W., Grevemeyer, I., Flueh, E.R., Mitchell, N.C., Kirstein, L., Kopp, C., Kopp, H., participants of Meteor 47/2, (2002), A rifted inside corner massif on the Mid-Atlantic Ridge at 5°S, *Earth and Planetary Science Letters*, 200; 255-269

Reynolds, S.J., and Lister, G.S., (1987), Structural aspects of fluid-rock interactions in detachment zones, *Geology*, 15; 362-366

Reynolds, S.J., and Lister, G.S., (1990), Folding of mylonitic zones in Cordilleran metamorphic core complex: Evidence from near the mylonitic front, *Geology*, 18; 216-219

Rhodes, J.M., Morgan, C. and Liias, R.A., (1990), Geochemistry of axial seamount lavas: Magmatic relationship between the Cobb hotspot and the Juan de Fuca ridge. *Journal of Geophysical Research*, 95; 12713–12733

Richardson, C., and McKenzie, D., (1994), Radioactive disequilibria from 2D models of melt generation by plumes and ridges, *Earth and Planetary Science Letters,* 128; 425–437

Ridley, W.I., Perfit, M.R., Jonasson, I.R., Smith, M.F., (1994), Hydrothermal alteration in oceanic ridge volcanics – A detailed study at the Galapagos fossil hydrothermal field, *Geochimica et Cosmochimica Acta*, 58, (11); 2477-2494

Ritsema, J., and Allen, R.M, (2002), The elusive mantle plume, *Earth and Planetary Science Letters*, 207; 1-12

Ritsema, J., van Heijst, H.J., Woodhouse, J.H., (1999), Complex shear wave velocity structure imaged beneath Africa and Iceland, *Science*, 286; 1925–1928

Ritsema, J., Xu, W., Stixrude, L., Lithgow-Bertelloni, C., (2009), Estimates of the transition zone temperature in a mechanically mixed upper mantle, *Earth and Planetary Science Letters*, 277; 244–252

Robinson, C.J., Bickle, M.J., Minshull, T.A., White, R.S., Nichols, A.R.L., (2001), Low degree melting under the Southwest Indian Ridge: the roles of mantle temperature, conductive cooling and wet melting, *Earth and Planetary Science Letters*, 188; 383-398

Rocaboy, A., (1987), Petrogenese des basaltes en contexte intraplaque oceanique. Exemple de Mururoa, Fangataufa, Gambier (Polynesie Francaise). *DEA Universitie Blake Pascul.* Clermont-Ferrand

Roeder, P.L., and Emslie, R.F., (1970), Olivine–liquid equilibrium, *Contributions to Mineralogy and Petrology*, 29; 275–289

Roest, W.R., and Collette, B.J., (1986), The Fifteen Twenty Fracture Zone and the North American-South American plate boundary, *Journal of the Geological Society, London,* 143; 833-843

Rollinson, H.R., (1993), Using Geochemical Data: Evaluation, Presentation, Interpretation, Longman, UK. [Co-published by J. Wiley and Sons. Inc. in the USA]

Rona, P.A., (1976), Asymmetric fracture zones and seafloor spreading, *Earth and planetary Science Letters*, 30; 109-116

Rona, P.A., Bougault, H., Appriou, P., Nelsen, T.A., Trefry, J.H., Eberhart, G.L., Barone, A., Needham, H.D., (1992), Hydrothermal circulation, serpentinisation, and degassing at a rift valley-fracture zone intersection: Mid-Atlantic Ridge near 15°N, 45°W, *Geology*, 20; 783-786

Rubin, K.H., Sinton, J.M., Maclennan, J., Hellebrand, E., (2009), Magmatic filtering of mantle compositions at mid-ocean-ridge volcanoes, *Nature Geoscience*; doi:10.1038/ngeo504

Rusakov, V. Yu., (2007), Comparative Analysis of the Mineral and Chemical Compositions of Black Smoker Smoke at the TAG and Broken Spur Hydrothermal Fields, Mid-Atlantic Ridge, *Geochemistry International,* 45, (7); 698–716

Russell, W.A., Papanastassiou, D.A., and Tombrello, T.A., (1979), Ca isotope fractionation on the Earth and other solar system materials, *Geochimica et Cosmochimica Acta*, 42; 1075-1090

Salters, V.J.M, (1996), The generation of mid-ocean ridge basalts from the Hf and Nd isotope perspective, *Earth and Planetary Science Letters*, 141; 109-123

Sarda, P. And Graham, D., (1990), Mid-ocean ridge popping rocks: implications for degassing at ridge crests, *Earth and Planetary Science Letters,* 97; 268-289

Sauter, D., Cannat, N. and Mendel, V. (2008), Magnetization of 0 – 26.5 Ma seafloor at the ultraslow spreading Southwest Indian Ridge, 61° – 67°E, *Geochem. Geophys. Geosyst.,* 9, Q04023, doi:10.1029/2007GC001764.

Sauter, D., Mendel, V., Rommevaux-Jestin, C., Parson, L.M., Fujimoto, H., Mével, C., Cannat, M., Tamaki, K., (2004), Focused magmatism versus amagmatic spreading along the ultra-slow spreading Southwest Indian Ridge: Evidence from TOBI side scan sonar imagery, *Geochemistry, Geophysics, Geosystems,* 5, (10); Q10K09, doi:10.1029/2004GC000738

Schiano, P., Birck, J., Allègre, C.J., (1997), Osmium-strontium-neodymium-lead isotopic covariations in mid-ocean ridge basalt glasses and the heterogeneity of the upper mantle, *Earth and Planetary Science Letters*, 150; 363-379

Schilling, J.G., (1973), Iceland Mantle Plume: Geochemical Study of Reykjanes Ridge, *Nature*, 242; 565-571

Schilling, J.G., Hanan, B.B., McCully, B., Kingsley, R.H., (1994), Influence of the Sierra Leone mantle plume on the equatorial MAR: a Nd–Sr–Pb isotopic study, *Journal of Geophysical Research*, 99; 12005–12028

Schilling, J.G., Thompson, M., Zajec, M. *et al*., (1983), Petrologic and geochemical variations along the Mid-Atlantic Ridge from 27°N to 73°N, *American Journal of Science*, 283; 510–586

Schmidt, K., Koschinsky, A., Garbe-Schönberg, D., de Carvalho, L.M., Seifert, R., (2007), Geochemistry of hydrothermal fluids from the ultramafic-hosted Logatchev hydrothermal field, 15°N on the Mid-Atlantic Ridge: Temporal and spatial investigation, *Chemical Geology*, 242; 1–21

Schouten, H., Klitgord, K.D., and Whitehead, J.A., (1985), Segmentation of Mid-Ocean Ridges, *Nature,* 317; 225–229

Schouten, H., Smith, D.K., Cann, J.R. and Escartín, J., (2010), Tectonic versus magmatic extension in the presence of core complexes at slow-spreading ridges from a visualization of faulted seafloor topography, *Geology,* 38; 615-618

Schroeder, T., Cheadle, M.J., Dick, H.J.B., Faul, U., Casey, J.F., Kelemen, P.B., (2007), Nonvolcanic seafloor spreading and corner-flow rotation accommodated by extensional faulting at 15°N on the Mid-Atlantic Ridge: A structural synthesis of ODP Leg 209, *Geochemistry, Geophysics, Geosystems,* 8, (6); Q06015, doi:10.1029/2006GC001567

Schroeder, T., and John, B.E., (2004), Strain localization on an oceanic detachment fault system, Atlantis Massif, 30°N, Mid-Atlantic Ridge, *Geochemistry, Geophysics, Geosystems*, 5, (11); Q11007, doi:10.1029/2004GC000728

Schulz, N.J., Detrick, R.S,. Miller, S.P., (1988), Two- and three-dimensional inversions of magnetic anomalies in the MARK Area (Mid-Atlantic Ridge 23°N), *Marine Geophysical Researches*, 10; 41-57

Scott, R.J., and Lister, G.S, (1992), Detachment faults: Evidence for a low-angle origin, *Geology*, 20; 833-836

Scott, R.J., and Lister, G.S, (1995), Analogue modelling of detachment fault systems and core complexes: Comment and Reply, *Geology*, 23; 287-288

Scott, R.J., Lister, G.S., Brun, J., Sokoutis, D., Van Den Driessche, J., (1995), Analogue modeling of detachment fault systems and core complexes: Comment and Reply, *Geology*, 23, (3); 287-288

Searle, R.C., Cannat, M., Fujioka, K., Mével, C., Fujimoto, H., Bralee, A., Parson, L., (2003), FUJI Dome: A large detachment fault near 64°E on the very slow-spreading southwest Indian Ridge, Geochemistry, Geophysics, Geosystems, 4, (8); 9105, doi:10.1029/2003GC000519

Searle, R.C., and Laughton, A.S., (1981), Fine-scale sonar study of tectonics and volcanism on the Reykjanes Ridge, *Oceanologica Acta*, 4 (suppl.); 5-13

Sempéré, J.C., Cochran, J.R., Christie, D., Eberle, M., Geli, L., Goff, J., Kimura, H., Ma, Y., Shah, A., Small, C., Sylvander, B., West, B. and Zhang, W., (1997), The Southeast Indian Ridge between 88°E and 118°E: variations in crustal

accretion at constant spreading rate, *Journal of Geophysical Research,* 102; 14489–15505

Sempéré, J.C., Lin, J, Brown, H.S., Schouten, H, and Purdy, G.M., (1993), Segmentation and morphotectonic variations along a slow spreading center: the Mid-Atlantic Ridge, *Marine Geophysical Research*, 15; 153-200

Severinghaus, J.P. and Macdonald, K.C., (1988), High inside corners at ridge–transform intersections, *Marine Geophysical Researches*, 9, 353–367

Seyfried Jr, W.E., and Bischoff, J.L., (1979), Low temperature basalt alteration by seawater: an experimental study at 70°C and 150°C, *Geochimica et Cosmochimica Acta*, 43; 1937-1947

Seyfried Jr., W.E., and Mottl, M.J, (1982), Hydrothermal alteration of basalt by seawater under seawater-dominated conditions, *Geochimica et Cosmochimica Acta*, 46; 985-1002

Seyler, M., Lorand, J.P., Dick, H.G.B., Drouin, M., (2007), Pervasive melt percolation reactions in ultra-depleted refractory harzburgites at the Mid-Atlantic Ridge, 15°20'N: ODP Hole 1274A, *Contributions to Mineralogy and Petrology*, 153; 303–319

Seyler, M., Toplis, M.J., Lorand, J., Luguet, A., Cannat, M., (2001), Clinopyroxene microtextures reveal incompletely extracted melts in abyssal peridotites, *Geology*; 29, (2); 155-158

Shau, Y.H., and Peacor, D.R., (1992) Phyllosilicates in hydrothermally altered basalts from DSDP hole 504 B, Leg 83, a TEM and AEM study, *Contributions to Mineralogy and Petrology*, 112; 119-133

Shaw, D.M., (1970), Trace element fractionation during anatexis, *Geochemica et Cosmochemica Acta*, 34; 237-243

Shaw, P., and Lin, J., (1993), Causes and Consequence of Variations in Faulting Style, *Journal of Geophysical Research*, 98, (B12); 21839-21851

Shaw, P., and Lin, J., (1996), Models of ocean ridge lithospheric deformation: Dependence on crustal thickness, spreading rate, and segmentation, *Journal of Geophysical Research*, 101, B8: 17,977-17,993

Shen, Y., and Forsyth, D., (1995), Geochemical constraints on initial and final depths of melting beneath mid-ocean ridges, *Journal of Geophysical Research*, 100, (B2); 2211-2237

Shervais, J.W., and Kimbrough, D.L., (1985), Geochemical evidence for the tectonic setting of the Coast Range Ophiolite: A composite island arc-oceanic crust terrane in Western California, *Geology*, 13; 35-38

Shipboard Scientific Party, (1988), Site 669. *In* Bryan, W. B., Juteau, T, *et al*., *Proceedings of the Ocean Drilling Program, Initial Reports, (Pt. A),* 109; College Station, TX (Ocean Drilling Program)

Silantyev, S.A., (1998), Origin conditions of the Mid-Atlantic Ridge plutonic complex at 13 degrees-17 degrees N, *Petrology*, 6, (4); 351-387

Silantyev, S.A., Danyushevsky, L.V., Plechova, A.A., Dosso, L., Bazylev, B.A., Beltenev, V.E., (2008), Geochemical and isotopic signatures of magmatic products in the MAR rift valley at 12 degrees 49'-17 degrees 23'N and 29 degrees 59'-33 degrees 41'N: Evidence of Two contrasting sources of the parental melts, *Petrology*, 16, (1); 36-62

Simonov, V.A., and Milosnov, A.A., (1996), Physicochemical conditions of hydrothermal processes in the Mid-Atlantic ridge, Fifteen Twenty Fracture Zone, *Geokhimiya*, 8; 760-766

Sinton, J.M., and Detrick, R.S., (1992), Mid ocean ridge magma chambers, *Journal of Geophysical Research*, 97, (B1); 197-216

Skolotnev, S.G., Peive, A.A., and Lyapunov, S.M., (1999), Tectono-Volcanic Activity at the Axial Zone of the Mid-Atlantic Ridge between the Fifteen Twenty and Mercurius Zones, Central Atlantic, *Petrologiya,* 7 (6); 591–610

Sleep, N. H., (1984), Tapping of magmas from ubiquitous mantle heterogeneities: An alternative to mantle plumes?, *J. Geophys. Res*., 89, 10029 – 10041

Sleep, N.H, and Rosendahl, B.R., (1976), Topography and Tectonics of Mid-Ocean Ridge axes, *Journal of Geophysical Research*, 84, (B12); 8B1305/.0148-0227/79/008B-1305$01.00

Smith, P. M., and Asimow P. D. (2005), Adiabat_1ph: A new public front-end to the MELTS, pMELTS, and pHMELTS models, *Geochem. Geophys. Geosyst*., 6, Q02004, doi:10.1029/2004GC000816

Smith, D.K., Cann, J.R., Escartín, J., (2006), Widespread active detachment faulting and core complex formation near 138N on the Mid-Atlantic Ridge, *Nature*, 442; 440-443

Smith, D.K., Escartín, J., Cannat, M., Tolstoy, M., Fox, C.G., Bohnenstiehl, D.R., Bazin, S., (2003), Spatial and temporal distribution of seismicity along the northern Mid-Atlantic Ridge (15°–35°N), *Geophysical Research Letters*, 108, (B3); 2167, doi:10.1029/2002JB001964

Smith, D.K., Escartín, J., Schouten, H., Cann, J.R., (2008), Fault rotation and core complex formation: Significant processes in seafloor formation at slow-spreading mid-ocean ridges (Mid-Atlantic Ridge, 13°–15°N), *Geochemistry, Geophysics, Geosystems*, 9, (3); Q03003, doi:10.1029/2007GC001699

Smith, D.K., Tolstoy, M., Fox, C.G., Bohnensteihl, D.R., Matsumoto, H., Fowler, M.J., (2002), Hydroacoustic monitoring of seismicity at the slow-spreading Mid-Atlantic Ridge, *Geophysical Research Letters*, 29., (11); 1518, 10.1029/2001GL013912

Snow, J.E., (1993), The Isotope Geochemistry of Abyssal Peridotites and Related Rocks, *PhD Thesis, Woods Hole Oceanographic Institution and Massachusetts Institute of Technology*, WHOI-93-36, AD-A279-435

Spencer, J.E., (1982), Origin of folds of Territory low-angle fault surfaces, southeastern California and western Arizona, *in* Frost, E.G., and Martin, D.L., eds., Mesozoic-Cenozoic tectonic evolution of the Colorado River region, California, Arizona, and Nevada: San Diego, California, Cordilleran Publishers; 123–134

Spencer, J.E., (2000), Possible origin and significance of extension-parallel drainages in Arizona's metamorphic core complexes, *GSA Bulletin,* 112, (5); 727–735

Spooner, E.T.C., (1976), The strontium isotopic composition of seawater, and seawater-oceanic crust interaction, *Earth and Planetary Science Letters,* 31; 167–174

Stakes, D.S., Taylor, H.P., and Fisher, R.L., (1984), Oxygen isotope and geochemical characterization of hydrothermal alteration in ophiolite complexes and modern oceanic crust, *In:* I.G. Gass, S.J. Lippard and A.W. Shelton, Editors, *Geological Society of London Special Publications,* 13; 199–214

Stein, M., Navon, O. and Kessel, R., (1997), Chromatographic metasomatism of the Arabian–Nubian lithosphere, *Earth and Planetary Science Letters*, 152, 75–91

Stolper, E., (1980), A phase diagram for mid-ocean ridge basalts: Preliminary results and implications for petrogenesis**,** 74, (1); 13-27

Stracke, A., Bizimis, M., Salters, V.J.M., (2003), Recycling oceanic crust: Quantitative constraints, *Geochemistry, Geophysics, Geosystems*, 4, (3); 8003, doi:10.1029/2001GC000223

Stracke, A., and Bourdon, B., (2009), The importance of melt extraction for tracing mantle heterogeneity, *Geochimica et Cosmochimica Acta*, 73; 218–238

Stracke, A., Bourdon, B., McKenzie, D., (2006), Melt extraction in the Earth's mantle: Constraints from U–Th–Pa–Ra studies in oceanic basalts, *Earth and Planetary Science Letters*, 244; 97–112

Stracke, A., Hofmann, A.W., Hart, S.R., (2005), FOZO, HIMU, and the rest of the mantle zoo, *Geochemistry, Geophysics, Geosystems*, 6, (5); Q05007, doi:10.1029/2004GC000824

Stroncik N. A. and Schmincke H. U. (2002) Palagonite; a review. *International Journal of Earth Sciences,* 91, (4), 680-697

Stroncik, N.A., Niedermann, S., Haase, K.M., (2007), Neon and helium isotopes as tracers of mantle reservoirs and mantle dynamics, *Earth and Planetary Science Letters*, 258, (1-2); 334-344

Su, Y. and Langmuir, C.H., (2003), Global MORB chemistry compilation at the segment scale, Ph.D. Thesis, Department of Earth and Environmental Sciences, Columbia University, Available at: http://petdb.ldeo.columbia.edu/documentation/morbcompilation/.

Suhr, G., Kelemen, P., Paulick, H., (2008), Microstructures in Hole 1274A peridotites, ODP Leg 209, Mid-Atlantic Ridge: Tracking the fate of melts percolating in peridotite as the lithosphere is intercepted, *Geochemistry, Geophysics, Geosystems*, 9, (3); Q03012, doi: 101029/2007GC001726

Sun, S.S., (1980), Lead isotopic study of young volcanic rocks from mid-ocean ridges, ocean islands and island arcs, *Philosophical Transactions of the Royal Society of London,* A297; 409-445

Sun, S.S., and Hanson, G.N., (1975) Evolution of the mantle: geochemical evidence from alkali basalt, *Geology,* 3; 297-302

Sun, S.S., and McDonough, W.F., (1989), Chemical and isotopic systematics of oceanic basalts: implications for mantle composition and processes, *In*: A.D. Saunders and M.J. Norry, Editors, *Magmatism in the Ocean Basins, Geological Society Special Publications,* 42; 313–345

Sundberg, M., Hirth, G., Kelemen, P.B., (2010), Trapped Melt in the Josephine Peridotite: Implications for Permeability and Melt Extraction in the Upper Mantle, *Journal of Petrology Advance Access,* 0, (1-2); doi:10.1093/petrology/egp089

Sushchevskaya, N.M., Bonatti, E., Peive, A.A., Kamenetskii, V.S., Belyatskii, B.V., Tsekhonya, T.I., Kononkova, N.N. (2002), Heterogeneity of rift magmatism in the Equatorial province of the Mid-Atlantic Ridge (15 degrees N to 3 degrees S), *Geochemistry International*, 40, (1); 26-50

Tatsumi, Y. and Kogiso, T., (1995), Polynesian Super Plume: A Window down to the Core/Mantle Boundary, The Earth's Central Part: Its Structure and Dynamics, Terrapub, Tokyo

Taylor, R.N., Thirlwall, M.F., Murton, B.J., Hilton, D.R. and Gee, M.A.M., (1997), Isotopic constraints on the influence of the Icelandic plume, *Earth and Planetary Science Letters*, 148; E1-E8

Thibaud, R.., Gente, P., and Maia, M., (1998), A systematic analysis of the Mid-Atlantic Ridge morphology and gravity between 15°N and 40°N: Constraints of the thermal structure, *Journal of Geophysical Research*, 103; 223–243

Thirlwall, M.F., (1991), High-precision multicollector isotopic analysis of low levels of Nd as oxide, *Chemical Geology*, 94, (1); 13-22

Thirlwall, M.F., (1995), Generation of the Pb isotopic characteristics of the Iceland plume, *Journal of the Geological Society of London*, 152; 991-996

Thirlwall, M.F., (1997), Pb isotopic and elemental evidence for OIB derivation from young HIMU mantle, *Chemical Geology*, 139, 1; 51-74

Thirlwall, M.F, (2000), Inter-laboratory and other errors in Pb isotope analyses investigated using a 207Pb–204Pb double spike, *Chemical Geology*, 163; 299–322

Thirlwall, M.F., (2002), Multicollector ICP-MS analysis of Pb isotopes using a ^{207}Pb–^{204}Pb double spike demonstrates up to 400 ppm/amu systematic errors in Tl-normalization, *Chemical Geology,* 184; 255–279

Tilmann, F., Flueh, E., Planert, L., Reston, T., Weinrebe, W., (2004), Microearthquake seismicity of the Mid-Atlantic Ridge at 5°S: A view of tectonic extension, *Journal of Geophysical Research*, 109; B06102, doi:10.1029/2003JB002827

Tivey, M.A., Schouten, H., and Kleinrock, M.C., (2003), A near-bottom magnetic survey of the Mid-Atlantic Ridge axis at 26°N, Implications for the tectonic evolution of the TAG segment, *Journal of Geophysical Research*, 108, 2277; doi: 10.1029/2002JB001967

Tivey, M., Takeuchi, A., Scientific Party, (1998), A submersible study of the western intersection of the Mid-Atlantic ridge and Kane fracture zone (WMARK), *Marine Geophysical Researches*, 20, (3); 195-218

Tomasson, J., and Kristmannsdottir, H., (1972), High temperature alteration minerals and thermal brines, Reykjanes, Iceland, *Contributions to Mineralogy and Petrology,* 36; 123-134

Tremblay, A., Meshi, A., Bédard, J.H., (2009), Oceanic core complexes and ancient oceanic lithosphere: Insights from Iapetan and Tethyan ophiolites (Canada and Albania), *Tectonophysics*, 473; 36–52

Tucholke, B.E, Behn, M.D., Buck, W.R., Lin, J., (2008), Role of melt supply in oceanic detachment faulting and formation of megamullions, *Geology,* 36; 455-458

Tucholke, B.E., Fujioka, K., Ishihara, T., Hirth, G., Kinoshita, M., (2001), Submersible study of an oceanic megamullion in the central North Atlantic, *Journal of Geophysical Research,* 106, (B8); 16145-16161

Tucholke, B.E., and Lin, J., (1994), A geological model for the structure of ridge segments in slow spreading ocean crust, *Journal of Geophysical Research*, 99, (B6); 11937-11958

Tucholke, B.E., Lin, J., Kleinrock, M.C., (1998), Megamullions and mullion structure defining oceanic metamorphic core complexes on the mid-Atlantic ridge, *Journal of Geophysical Research*, 103, (B5); 9857-9866

Tucholke, B.E., Lin, J., Kleinrock, M., Tivey, M.A., Reed, T.B., Goff, J., Jaroslow, G.E., (1997), Segmentation and crustal structure of the western Mid-Atlantic

Ridge flank, 25°25'-27°10'N and 0-29 m.y., *Journal of Geophysical Research*, 102, (B5); 10203-10223

Urey, H.C., (1947), The thermodynamics of isotopic substances, *Journal of the Chemical Society of London;* 562–81

Van de Flierdt, T., Frank M., Halliday A.N., Hein J.R., Hattendorf B., Gunther D. and Kubik P.W., (2003), Lead isotopes in North Pacific deep water – implications for past changes in input sources and circulation patterns, *Earth and Planetary Science Letters*, 209; 149-164

Van Wijk, J.W., and Blackman, D.K., (2005), Deformation of oceanic lithosphere near slow-spreading ridge discontinuities, *Tectonophysics*, 407; 211 –225

Vaughan, M.A., Horlick, G., Tan, S.H., (1987), Effect of Operating Parameters on Analyte Signals in Inductively Coupled Plasma Mass Spectrometry, *Journal of Analytical Atomic Spectroscopy*, 2; 765-772

Verma, S.P., (1992), Seawater alteration effects on REE, K, Rb, Cs, Sr, U, Th, Pb and Sr-Nd-Pb isotope systematics in Mid-Ocean Ridge Basalt, *Geochemical Journal*, 26; 159-177

Vidal, P.H., (1992), Mantle: More HIMU in the future?, *Geochimica et Cosmochimica Acta*, Vol. 56; 4295-4299

Vidal, P.H. and Dosso, L., (1978) Core formation: Catastrophic or continuous? Sr and Pb isotope geochemistry constraints, *Geophysical Research Letters, 5;* 169-172

Vidal, P.H., Chauvel, C., and Brousse, R., (1984), Large mantle heterogeneity beneath French Polynesia, *Nature,* 307; 536-538

Vils, F., Pelletier, L., Kalt, A., Müntener, O., Ludwig, T., (2008), The Lithium, Boron and Beryllium content of serpentinised peridotites from ODP Leg 209 (Sites 1272A and 1274A): Implications for lithium and boron budgets of oceanic lithosphere, *Geochimica et Cosmochimica Acta*, 72; 5475–5504

Vils, F., Tonarini, S., Kalt, A., Seitz, H., (2009), Boron, lithium and strontium isotopes as tracers of seawater–serpentinite interaction at Mid-Atlantic ridge, ODP Leg 209, *Earth and Planetary Science Letters*, 286; 414–425

Vine, F.J. and Matthews. D.H., (1964). Magnetic anomalies over oceanic ridges. *Nature*, 201, 591-592

Vogt, P.R., and Perry, R.K., (1981), North Atlantic Ocean: Bathymetry and Plate Tectonic Evolution. Geological Society of America, Map and Chart Series, MC–35

Von Damm, K.L., (1990), Seafloor hydrothermal activity: Black smoker chemistry and chimneys, *Annual Review of Earth and Planetary Science*, 18; 173-204

Vroon, P.Z., van der Wagt, B., Koornneef, J.M., and Davies, G.R., (2008), Problems in obtaining precise and accurate Sr isotope analysis from geological

materials using laser ablation MC-ICPMS, *Analytical and Bioanalytical Chemistry*, 390; 465–476

Waight, T., Baker, J., Peate, D., (2002), Sr isotope ratio measurements by double-focusing MC-ICPMS: techniques, observations and pitfalls, *International Journal of Mass Spectrometry*, 221; 229–244

Walter, M.J., Bulanova, G.P., Armstrong, L.S., Keshav, S., Blundy, J.D Gudfinnsson, G., Lord, O.T., Lennie, A.R., Clark, S.M. Smith, C.B. & Gobbo, L., (2008), Primary carbonatite melt from deeply subducted oceanic crust, *Nature,* 454, 622-625

Warren, J.M., Shimizu, N., Dick, H., (2002), High pressure melt impregnation in a mantle peridotite, *Goldschmidt Conference Abstracts*, A822

Weiss, D., Kieffer, B., Maerschalk, C., Barling, J., de Jong, J., Williams, G., Hanaho, D., Pretorius, W., Mattielli, N., Scoates, J.S., Goolaerts, A., Friedman, R.M., Mahoney, J.B., (2006), High-precision isotopic characterization of USGS reference materials by TIMS and MC-ICP-MS, *Geochemistry, Geophysics, Geosystems*, 7, (8); Q08006, doi:10.1029/2006GC001283

Wemicke, B.P., (1985), Uniform-sense normal simple shear of the continental lithosphere, *Canadian Journal of Earth Science,* 22; 108–125

Wernicke, B., (1995), Low-angle normal faults and seismicity: A review, *Journal of Geophysical Research*, 100, (B10); 20159-20174

Wernicke, B., and Axen, G.J., (1988), On the role of isostasy in the evolution of normal fault systems, *Geology*, 16; 848-851

Westaway, R., (1999), The mechanical feasibility of low-angle normal faulting, *Tectonophysics*, 308; 407–443

White, W.M., (1985), Sources of oceanic basalts: radiogenic isotope evidence., *Geology,* 13; 115–118

White, W.M., (2010), Oceanic Island Basalts and Mantle Plumes: The Geochemical Perspective, *Annual Reviews in Earth and Planetary Science*, 38; 133–60

White, W.M., Albarède, F., Télouk, P., (2000), High-precision analysis of Pb isotope ratios by multi-collector ICP-MS, *Chemical Geology,* 167; 257–270

White, R.S., Brown, J.W. and Smallwood, J. R., (1995), The temperature of the Iceland plume and origin of outward propagating V-shaped ridges, *Journal of the Geological Society of London*, 152; 1039-1045

White, R.S., McKenzie, D., and O'Nions, R.K., (1992), Oceanic crustal thickness from seismic measurements and rare earth element inversions, *Journal of Geophysical Research*, 97; 19683-19716

White, R.S., Minshull, T.A., Bickle, M.J., Robinson, C.J., (2001), Melt Generation at Very Slow-Spreading Oceanic Ridges: Constraints from Geochemical and Geophysical Data, *Journal of Petrology*, 42, (6); 1171-1196

White, W.M., and Schilling, J.G., (1978), The nature and origin of geochemical variation in mid-Atlantic ridge basalts from the central North Atlantic, *Geochimica et Cosmochimica Acta,* 42; 1501–1516

Whitehead Jr., J.A., Dick, H.G.B., Schouten, H., (1984), A mechanism for magmatic accretion under spreading centres, *Nature*, 312; 146-148

Willbold, M., and Stracke, A., (2006), Trace element composition of mantle end-members: Implications for recycling of oceanic and upper and lower continental crust, *Geochemistry, Geophysics, Geosystems*, 7, (4); Q04004, doi:10.1029/2005GC001005

Williams, C.M., Tivey, M.A., Behn, M.D., (2006), The magnetic structure of Kane Megamullion: Results from marine magnetic anomalies, paleomagnetic data and thermal modelling, *EOS Transactions, American Geophysical Union, Fall Meeting Supplement*, 87; Abstract T24A-03

Wills, S., and Buck, W.R., (1997), Stress-field rotation and rooted detachment faults: A Coulomb failure analysis, *Journal of Geophysical Research*, 102, (B9); 20503-20514

Wilson, B.M., (1989), Igneous Petrogenesis: A Global Tectonic Approach, Springer' New edition, ISBN-10: 0412533103

Wilson, M. and Spencer, E.A., (2003), The origin and evolution of the FOZO/PREMA and HIMU mantle components - the carbonatite perspective, Warsaw (3) 6-9th October 2003

Wood, D.A., (1979), A variably veined suboceanic upper mantle-˜Genetic significance for mid-ocean ridge basalts from geochemical evidence, *Geology*, 7.; 499-503

Woodhead, J.D., (2003), Isotope Ratio Determination in the Earth and Environmental Sciences: Developments and Applications in 2003, Geostandards and Geoanalytical Research; 26-36

Woodhead, J.D., (2008), Isotope Ratio Determination in the Earth and Environmental Sciences: Developments and Applications in 2006-2007, Geostandards and Geoanalytical Research, 32, (4); 495-507

Woodhead, J.D., and Hergt, J.M., (2000), Pb-isotope analyses of USGS reference materials, *Geostandards Newsletter: The Journal of Geostandards and Geoanalysis*, 24; 33–38

Woodhead, J.D., Volker, F., McCulloch, M.T., (1995), Routine lead isotope determinations using a ^{207}Pb-^{204}Pb double spike: A long-term assessment of analytical precision and accuracy. *The Analyst*, 120; 35–39

Workman, R.K., and Hart, S.R., (2004), Major and trace element composition of the depleted MORB mantle (DMM), *Earth and Planetary Science Letters*, 231; 53– 72

Xu, M., Canales, J.P., Tucholke, B.E., DuBois, D.L., (2009), Heterogeneous seismic velocity structure of the upper lithosphere at Kane oceanic core complex, Mid-Atlantic Ridge, *Geochemistry, Geophysics, Geosystems*, 10, (10); Q10001, doi:10.1029/2009GC002586

Yang, T., Shen, Y., van der Lee, S., Solomon, S.C., Hung, S., (2006), Upper mantle structure beneath the Azores hotspot from finite-frequency seismic tomography, *Earth and Planetary Science Letters*, 250; 11–26

Yin, A., (1989), Origin of regional, rooted low-angle normal faults: a mechanical model and its tectonic implications, *Tectonics*, 8; 469–482

Yin, A., (1991), Mechanisms for the formation of domal and basinal detachment faults: a three-dimensional analysis, *Journal of Geophysical Research,* 96; 14577–14594

Yip, Y., Lam, J.C., Tong, W., (2008), Applications of lead isotope ratio measurements, *Trends in Analytical Chemistry*, 27, (5); 460-480

Yoder, H.S., Jr., and Tilley, C.E., (1962), Origin of basalt magmas: an experimental study of natural and synthetic rock, *Journal of Petrology*, 3 (3); 342-532

Zhao, D., (2009), Multiscale seismic tomography and mantle dynamics, *Gondwana Research*, 15; 297–323

Zhao, X., and Tominaga, M., (2009), Paleomagnetic and rock magnetic results from lower crustal rocks of IODP Site U1309: Implication for thermal and accretion history of the Atlantis Massif, *Tectonophysics,* 474; 435–448

Zheng, Y., (1992), A quantitative analysis of the angle between conjugate sets of extensional crenulation cleavages: an explanation of the low angle-normal-fault development, *29th International Geological Congress*, Abstracts, (3-1), 131; Kyoto, Japan

Zheng, Y., Wang, T., Ma, M., Davis, G.A., (2002), Maximum effective moment criterion and the origin of low-angle normal faults, *Journal of Structural Geology*, 26; 271–285

Zhong, S., (2006), Constraints on thermochemical convection of the mantle from plume heat flux, plume excess temperature and upper mantle temperature, *Journal of Geophysical Research*, 111; B04409, doi:10.1029/2005JB003972

Zindler, A.W, and Hart, S.R., (1986), Chemical geodynamics, *Annual Review of Earth and Planetary Sciences,* 14; 493–571

Zindler, A., Jagoutz, E. and Goldstein, S., (1982), Nd, Sr, and Pb isotopic systematics in a three-component mantle: A new perspective, *Nature* 298, (5); 19-523.

Zindler, A., Staudigel, H. and Batiza, R. (1984), Isotope and trace element geochemistry of young Pacific seamounts: Implications for the scale of upper mantle heterogeneity, *Earth and Planetary Science Letters*, 70, 175-195

APPENDIX 1

SRM	ROCK TYPE	DATA SOURCE	WEB DATA AT
BHVO-2	BASALT, HAWAII	USGS	http://minerals.cr.usgs.gov/geo_chem_stand/basaltbhvo2.html
BIR-1	BASALT, ICELANDIC	USGS	http://minerals.cr.usgs.gov/geo_chem_stand/icelandic.html
JB1-A	BASALT, JAPANESE	AIST, JAPAN	http://riodb02.ibase.aist.go.jp/geostand/igneous.html
JB-3	BASALT, JAPANESE	AIST, JAPAN	http://riodb02.ibase.aist.go.jp/geostand/igneous.html
JGB-1	BASALT, JAPANESE	AIST, JAPAN	http://riodb02.ibase.aist.go.jp/geostand/igneous.html

SRM	Oxide Wt%	Al_2O_3	CaO	Fe_2O_3T	Fe_2O_3	FeO	K_2O	MgO	MnO	Na_2O	P_2O_5	SiO_2	TiO_2
BHVO-2	WT%	13.50	11.40	12.30			0.52	7.23		2.22	0.27	49.90	2.73
	±	0.20	0.20	0.20			0.01	0.12		0.08	0.02	0.60	0.04
BIR-1	WT%	15.50	13.30	11.30	2.06	8.34	0.03	9.70	0.18	1.82	0.02	47.96	0.96
	±	0.15	0.12	0.12	0.10	0.10	0.00	0.08	0.00	0.05	0.00	0.19	0.01
JB1-A	WT%	14.45	9.31	9.05	2.55	5.78	1.40	7.83	0.12	2.73	0.26	52.41	1.28
	±	0.39	0.40		0.21	0.24	0.12	0.12	0.01	0.13	0.02	0.70	0.04
JB-3	WT%	17.20	9.79	11.82	3.20	7.85	0.78	5.19	0.18	2.73	0.29	50.96	1.44
	±	0.36	0.12	0.28	0.40	0.24	0.04	0.10	0.01	0.11	0.03	0.30	0.06
JGB-1	WT%	17.49	11.90	15.06	4.79	9.43	0.24	7.85	0.19	1.20	0.06	43.66	1.60
	±	0.42	0.20	0.37	0.46	0.47	0.03	0.18	0.02	0.08	0.01	0.32	0.08

SRM	Conc. ppm	Nd	Ni	Rb	Sc	Sr	V	Y	Zn	Zr	Ba	Ce	Co
BHVO-2	ppm	25.00	119.00	9.80	32.00	389.00	317.00	26.00	103.00	172.00	130.00	38.00	45.00
	±	1.80	7.00	1.00	1.00	23.00	11.00	2.00	6.00	11.00	13.00	2.00	3.00
BIR-1	ppm	2.50	170.00		44.00	110.00	310.00	16.00	70.00	18.00	7.00	1.90	52.00
	±	0.70	6.00		1.00	2.00	11.00	1.00	9.00	1.00		0.40	2.00
JB1-A	ppm	26.00	139.00	39.20	27.90	442.00	205.00	24.00	82.10	144.00	504.00	65.90	38.60
	±	3.10	15.00	4.20	3.70	19.00	16.00	2.50	5.10	9.50	26.00	5.00	4.20
JB-3	ppm	15.60	36.20	15.10	33.80	403.00	372.00	26.90	100.00	97.80	245.00	21.50	34.30
	±	2.10	6.10	2.30	2.70	36.00	34.00	3.00	8.10	7.40	26.00	1.70	5.50
JGB-1	ppm	5.47	25.40	6.87	35.80	327.00	635.00	10.40	109.00	32.80	64.30	8.17	60.10
	±	0.83	5.70	3.00	2.10	39.00	58.00	2.40	8.00	6.80	17.10	1.00	5.80

SRM	Conc. ppm	Cr	Cs	Cu	Ga	Hf	La	Mn	Dy	Eu	Pb	Cl	F
BHVO-2	ppm	280.00		127.00	21.70	4.10	15.00	1290.00					370.00
	±	19.00		7.00	0.90	0.30	1.00	40.00					
BIR-1	ppm	370.00		125.00	16.00	0.60	0.63		4.00	0.55	3.00	26.00	44.00
	±	8.00		4.00		0.08	0.07		1.00	0.05			
JB1-A	ppm	392.00	1.31	56.70	17.90	3.41	37.60		3.99	1.46	6.76		357.00
	±	40.00	0.24	3.60	1.80	0.36	2.50		0.68	0.08	1.43		19.00
JB-3	ppm	58.10	0.94	194.00	19.80	2.67	8.81		4.54	1.32	5.58		253.00
	±	5.60	0.21	16.00	2.30	0.12	0.77		0.37	0.12	1.87		50.00
JGB-1	ppm	57.80	0.26	85.70	17.90	0.88	3.60		1.56	0.62	1.92	74, 87	133.00
	±	13.50	0.08	5.60	3.30	0.19	0.56		0.37	0.05	0.74		38.00

SRM	Conc. ppm	Gd	Ge	Ho	Li	Lu	Mo	Nb	Sm	Sn	Ta	Tb	Th	Yb
BHVO-2	ppm	6.30		1.04	5.00	0.28		18.00	6.20	1.90	1.40	0.90	1.20	2.00
	±	0.20		0.04		0.01		2.00	0.40				0.30	0.20
BIR-1	ppm	1.80			3.60	0.26		0.60	1.10					1.70
	±	0.40			0.20									0.10
JB1-A	ppm	4.67	1.0 - 3.89	0.71	10.90	0.33	1.57	26.90	5.07	2.24	1.93	0.69	9.03	2.10
	±	0.53		0.14	2.00	0.05	0.30	1.90	0.38	0.39	0.49	0.07	0.94	0.21
JB-3	ppm	4.67	1.12	0.80	7.21	0.39	1.09	2.47	4.27	0.94	0.15	0.73	1.27	2.55
	±	0.64	0.28	0.15	1.13	0.06	0.20	0.85	0.24	0.14	0.05	0.09	0.29	0.47
JGB-1	ppm	1.61	1.01	0.33	4.59	0.15	0.59	3.34	1.49	0.48	0.18	0.29	0.48	1.06
	±	0.14	0.39	0.05	0.90	0.03	0.23	1.33	0.19	0.13	0.08	0.07	0.10	0.30

APPENDIX 2

Procedure for Column Separation of Nd using cation and reverse phase columns

Cation columns

(Columns contain 6.5ml Dowex AG50W-X8 (200-400mesh, the procedure uses 2.2M HCl which is titrated and accurate. Columns are stored in ELGA water.)

1. Subsample the mother solution for 1µg Nd and dry down in a Teflon vial.
2. Dissolve the residue in 2ml 2.2M HCl
3. Run columns as described in the table below:
4. The collect fraction should be collected in Teflon vials
5. Dry the collect fraction down ready for running on reverse phase columns

Step	Volume	Reagent
Condition	20ml	2.2M HCl
Load	2ml	2.2M HCl
Wash in	2ml	2.2M HCl
Elute	22ml	2.2M HCl
Collect	16ml	6M HNO_3
Clean	10ml	6M HNO_3
Clean	10ml	6M HCl
Clean	10ml	ELGA H_2O

Reverse Phase Columns

(Columns must always be stored in water and must not be allowed to dry out. 0.15M and 0.2M HCl in this procedure is titrated and accurate)

1. Dissolve the sample from the cation columns in 100µ1 0.15M HCl (3 drops)
2. Run columns as below. Collect the Nd fraction in Teflon vials and dry down ready for loading.

Step	Volume	Reagent
Condition	10ml	0.15M HCl
Load	100µl	0.15M HCl
Wash in	100µl	0.15M HCl
Wash in	100µl	0.15M HCl
Elute Ba	20ml	0.15M HCl
Elute	7ml	0.2M HCl
Collect Nd	12ml	0.2M HCl
Wash	15ml	6M HCl
Wash	15ml	H_2O

Procedure for Column Separation of Sr using Sr-spec resin

1. Subsample mother solution to give approx. 1µg of Sr and transfer to Savillex vial.
2. Dry subsample down
3. Remove columns from 10% HNO_3 acid bath and rinse well with ELGA water. Place in rack with small Teflon pots beneath.
4. Fill the columns with water and squeeze gently to start flow
5. Shake the resin bottle. Using a clean pipette, add resin to the column until it reaches the neck of the column.
6. Run the columns as shown in table below, taking care to avoid disturbing the resin unnecessarily.
7. For load step – dissolve sample in 200µl and load carefully onto resin.
8. After elute, place Teflon vials under the columns to collect sample.
9. Once collected, dry sample down on hotplate.
10. Wash resin out of columns and return to acid bath ensuring acid is washed through columns fully, including the frit.

Step	Volume	Reagent
Clean	1.5 ml	H_2O
Clean	1.5 ml	SB 3M HNO_3
Clean	1.5 ml	H_2O
Condition	1.5 ml	SB 3M HNO_3
Load	200µl	SB 3M HNO_3
Wash in	200µl	SB 3M HNO_3
Elute	2.5ml	SB 3M HNO_3
Collect	1.5ml	H_2O

Procedure for separation of Pb on Anion Exchange columns

1. Take columns out of storage and rinse with ELGA water
2. Place columns in rack – add 5-10 drops of AG1x8 resin with a rinsed 1ml pipette – final column should be ~8mm.
3. Fill column above brim and pass through: 6M HCl-water-6M HCl-water
4. ¾ fill column with 1M HBr and allow to pass through
5. Rinse pipette with water (3x) and 1M HBr – including bulb of pipette
6. Place clean scint vial under column to collect column waste (for Nd and Sr analysis)
7. Take up supernatant sample solution, and load onto column
8. Pass 3x ¾ fill of 1M HBr through the column
9. Place rinsed Pb pot under the column
10. Add 2Ml 6M HCl to the column
11. Add 3 drops conc. HNO_3 to the pot, and evaporate to dryness
12. Rinse out columns with ELGA water and replace in same position in rack
13. Add 5mm AG1x8 resin to column
14. Add 1ml of 1M HBr to Pb residue – cap and place on hotplate for 20 minutes, then allow to cool
15. Repeat steps 3 and 4
16. Pour sample HBr carefully onto columns
17. Pass 3x ¾ fill of 1M HBr through the column
18. Place water rinsed Pb pot under column
19. Add 2Ml 6M HCl to the column
20. Add 2 drops of 0.05M H_3PO_4 to pot and evaporate to dryness

TIMS Filament Loading Procedures

Samples are loaded onto the centre of the filament to avoid spillage or excessive spreading. The centre of the ribbon experiences the highest temperatures, and is the optimum position for efficient ionisation. Samples which are excessively spread may ionise weakly.

All single-use loading capillaries and pipettes are thoroughly cleaned in ultra pure nitric acid prior to loading. Application of excessive current to the sample is avoided, as it may result in sample material 'burning off' before the analysis, and can also warp the filament. Current is gradually increased to prevent bubbling and uneven drying, and to prevent the sample from spreading across the filament.

Nd is loaded in a small droplet (~1.5µl) of ultra pure 0.5M HNO_3. The dried sample residue is thoroughly mixed into the acid and dissolved prior to loading. The Nd sample is added incrementally between drying, keeping filament currents below 1.5A.

Sr residue is loaded in weak HCl (~1.5µl), and is accompanied by 1µl of Ta activator solution. Half of the Ta activator is loaded onto the filament and dried down. When dry, the other half of the solution is added, followed by the sample, which is thoroughly mixed in to ensure ionisation is efficient. The sample is kept within the bounds of the Ta activator residue during drying at~0.8A .The filament temperature is then increased until a dull red glow is visible at the centre.

Pb loading is complex, as each sample is divided into two portions, one of which is natural (just sample), and the other which is mixed with a Pb double spike. Pb loading is aided by a drop of phosphoric acid, added at the end of the column collection stage. This droplet provides several functions. Firstly, it acts as a marker, allowing easy identification of the dried sample material in the bottom of the pot. This precludes the possibility of human error in failing to find the sample material if it has dried in an unusual position inside the vessel. Secondly, phosphoric acid is thought to displace other anion species, yielding a

more uniform salt composition on the filament. Thirdly, phosphoric acid appears to destroy organic residues such as ultra-fine ion exchange resin, which may disrupt ionisation. The phosphoric acid also serves to “glue” the residue to the filament.

~1.9µlof weak HCl is added to the sample residue in the pot, dissolving the residue into the acid. ~0.63µl of Si gel is loaded onto the filament, and dried down, then another ~0.63µl of Si gel is added, onto which the sample is loaded. Si gel is heated on a hotplate prior to use to ensure it is thoroughly stirred and no separation has occurred.

For the natural sample run, 1.3µl of the sample is loaded incrementally onto the filament, allowing the residue to dry between loads. Spiked runs contain ~0.38 of sample, and ~1.0µl of spike. To load procedural blanks, ~1.0µl of blank is loaded onto Si gel, followed by ~1.0µl of a 50ppb ^{206}Pb spike solution. In all cases, filaments are turned up gradually to ~2A whilst loading, allowing the filament to glow gently.

APPENDIX 3

Major Element Compositions – M2 Type Basalts, 13°19'N

Sample ID	Latitude	Longitude	SiO_2 (wt%)	TiO_2	Al_2O^3	Fe_2O_3	MnO	MgO	CaO	K_2O	Na_2O	P_2O_5	SO_3	LOI %	Total	Total+ LOI
D05-1	13.30	44.96	49.25	1.35	14.78	10.36	0.17	8.47	11.11	0.39	2.23	0.16	0.10	1.43	98.37	99.80
D05-1.2	13.30	44.96	49.24	1.24	14.16	10.08	0.17	11.38	10.83	0.35	2.15	0.15	0.08	0.10	99.83	99.93
D05-1.3	13.30	44.96	49.84	1.36	15.66	10.17	0.17	8.39	11.12	0.40	2.39	0.16	0.11	-0.04	99.76	99.72
D05-1.4	13.30	44.96	49.70	1.33	15.63	10.08	0.17	8.67	11.17	0.36	2.35	0.16	0.12	-0.01	99.72	99.71
D05-1A	13.30	44.96	49.40	1.38	14.83	10.24	0.17	8.22	11.14	0.38	2.28	0.17	0.06	2.46	98.28	100.73
D05-2.6	13.30	44.96	48.46	1.78	14.22	9.71	0.15	9.97	10.92	0.74	2.58	0.31	0.15	0.63	99.00	99.63
D05-2.7	13.30	44.96	49.62	1.38	15.57	10.16	0.17	7.32	11.49	0.38	2.34	0.16	0.07	1.66	98.66	100.32
D05-4.1	13.30	44.96	49.64	1.26	15.07	10.15	0.18	8.18	11.51	0.08	2.51	0.13	0.08	1.35	98.79	100.14
D05-5.4	13.30	44.96	50.77	1.43	15.13	10.28	0.17	7.38	11.69	0.34	2.43	0.16	0.12	0.86	99.89	100.74
D06-3.1	13.30	44.96	50.00	1.50	14.72	10.97	0.18	8.08	11.12	0.37	2.41	0.19	0.21	0.01	99.76	99.77
D06-6	13.30	44.96	50.39	1.44	14.69	10.70	0.18	8.17	10.94	0.35	2.41	0.19	0.20	0.34	99.64	99.98
D06-7.3	13.30	44.96	50.35	1.45	14.67	10.78	0.18	8.65	10.83	0.42	2.43	0.19	0.12	0.15	100.06	100.21
D06-7.4	13.30	44.96	50.87	1.40	14.89	11.07	0.19	7.88	11.15	0.32	2.45	0.16	0.26	0.41	100.64	101.04
D12-2.2	13.30	44.78	48.90	1.02	19.53	7.87	0.13	5.79	12.96	0.21	2.28	0.11	0.08	0.19	98.88	99.07
D12-3.4	13.30	44.78	48.88	1.25	15.48	10.25	0.17	7.64	12.04	0.21	2.15	0.15	0.17	2.01	98.39	100.40
D12-5	13.30	44.78	48.54	1.97	13.71	11.17	0.21	9.69	10.18	0.83	2.77	0.37	0.28	1.14	99.72	100.86
D12-8	13.30	44.78	48.79	1.07	17.01	9.16	0.15	7.36	12.34	0.18	2.12	0.10	0.14	1.70	98.41	100.10
D06-7.6	13.30	44.96	51.19	1.48	14.85	10.86	0.18	8.33	10.99	0.40	2.41	0.19	0.26	0.23	101.13	101.35
D06-9	13.30	44.96	50.67	1.46	14.63	10.76	0.18	8.44	10.91	0.41	2.42	0.19	0.21	0.24	100.28	100.52

Major Element Compositions – M1 Type Basalts, 13°19'N

Sample ID	Latitude	Longitude	SiO_2 (wt%)	TiO_2	Al_2O_3	Fe_2O_3	MnO	MgO	CaO	K_2O	Na_2O	P_2O_5	SO_3	LOI %	Total	Total + LOI
D12-1.2	13.30	44.78	48.90	1.02	19.53	7.87	0.13	5.79	12.96	0.21	2.28	0.11	0.08	0.94	98.58	99.82
D05-5.2	13.30	44.96	48.60	1.81	14.71	9.90	0.16	8.06	11.45	0.69	2.59	0.33	0.13	1.52	98.42	99.94
D05-5.3	13.30	44.96	49.32	1.85	15.23	9.84	0.16	7.91	11.61	0.72	2.74	0.33	0.14	0.65	99.83	100.48
D05-8.7	13.30	44.96	49.16	1.78	14.70	10.33	0.16	8.95	10.93	0.66	2.60	0.31	0.12	-0.43	99.69	99.27
D06-1.10	13.30	44.96	48.97	2.44	14.28	11.44	0.16	7.54	10.21	0.79	3.02	0.48	0.08	1.01	99.39	100.40
D05-16	13.30	44.96	49.09	1.77	14.77	10.14	0.16	8.76	10.97	0.65	2.65	0.32	0.17	-0.09	99.44	99.35
D05-2.1	13.30	44.96	47.79	1.95	13.87	10.40	0.16	10.49	10.58	0.83	2.64	0.36	0.12	0.20	99.19	99.39
D05-2.2	13.30	44.96	49.18	2.08	15.03	10.07	0.15	8.76	11.19	0.87	2.79	0.38	0.13	0.28	100.62	100.90
D12-6.2G	13.30	44.78	48.41	1.96	13.68	10.96	0.17	9.63	10.23	0.82	2.79	0.37	0.19	1.51	99.20	100.71
D12-12	13.30	44.78	50.30	1.19	15.16	10.26	0.17	8.22	11.60	0.18	2.45	0.13	0.26	1.29	99.91	101.20
D12-1.2R	13.30	44.78	47.81	1.96	13.51	11.19	0.19	9.52	10.42	0.80	2.60	0.36	0.21	0.94	98.58	99.52
D12-1.4	13.30	44.78	47.99	1.96	13.56	11.08	0.18	9.62	10.30	0.80	2.61	0.36	0.08	0.90	98.53	99.43

Major Element Compositions – On-Axis Basalts, ~12°60' -14°N

Sample ID	Latitude	Longitude	SiO_2 (wt%)	TiO_2	Al_2O_3	Fe_2O_3	MnO	MgO	CaO	K_2O	Na_2O	P_2O_5	SO_3	LOI %	Total	Total + LOI
D07-18	13.30	44.93	48.01	1.50	13.35	10.24	0.16	9.23	12.40	0.19	2.17	0.19	0.09	2.64	97.51	100.16
D07-20	13.30	44.93	49.54	0.98	18.07	8.42	0.14	6.63	12.51	0.04	2.07	0.09	0.07	1.07	98.56	99.63
D07-21	13.30	44.93	49.80	1.11	15.25	9.58	0.17	8.28	12.23	0.04	2.49	0.10	0.00	0.44	99.05	99.48
D09-11.8	13.32	44.93	49.33	1.10	14.42	10.44	0.19	8.50	11.87	0.03	2.25	0.09	0.06	1.63	98.27	99.90
D09-3.5	13.32	44.93	48.32	1.49	15.02	10.33	0.16	7.98	11.55	0.23	2.33	0.18	-0.02	2.54	97.56	100.10
D09-8.2	13.32	44.93	50.71	1.50	15.21	10.75	0.17	7.08	11.37	0.34	2.46	0.17	0.25	0.38	100.01	100.39
D10-18	13.34	44.89	49.04	1.50	14.93	10.49	0.19	7.47	11.36	0.33	2.56	0.19	0.09	1.25	98.14	99.39
D10-28	13.34	44.89	50.14	1.39	15.06	10.42	0.17	7.80	11.44	0.44	2.30	0.18	0.09	1.98	99.42	101.40
D10-30.2	13.34	44.89	49.62	1.50	15.13	10.76	0.17	7.20	11.28	0.15	2.53	0.17	0.01	1.67	98.50	100.17
D10-37	13.34	44.89	49.57	1.39	14.83	10.28	0.17	7.62	11.49	0.44	2.41	0.18	0.28	0.42	98.67	99.09

Sample ID	Latitude	Longitude	SiO_2 (wt%)	TiO_2	Al_2O_3	Fe_2O_3	MnO	MgO	CaO	K_2O	Na_2O	P_2O_5	SO_3	LOI %	Total	Total + LOI
D10-38.1	13.34	44.89	49.49	1.33	14.90	10.22	0.17	7.76	11.95	0.08	1.90	0.13	-0.02	2.07	97.90	99.97
D10-38.2	13.34	44.89	49.50	1.16	14.60	10.04	0.16	7.84	12.45	0.05	2.30	0.11	0.00	1.44	98.18	99.62
D10-9	13.34	44.89	48.51	1.10	19.01	8.00	0.13	6.57	12.34	0.34	2.29	0.14	0.06	0.80	98.50	99.30
D11-11	13.27	44.87	48.17	1.03	15.98	10.18	0.17	8.46	11.76	0.19	2.21	0.11	0.14	2.62	98.40	101.02
D11-2	13.27	44.87	49.13	1.31	15.29	10.16	0.15	7.27	12.13	0.18	2.45	0.13	-0.03	1.46	98.17	99.63
D11-3	13.27	44.87	48.16	1.05	15.92	10.59	0.18	8.45	11.96	0.22	2.26	0.13	0.05	1.63	98.96	100.59
D11-5	13.27	44.87	47.65	0.67	16.73	10.01	0.17	9.45	12.19	0.10	1.92	0.06	0.26	0.52	99.20	99.71
D11-8	13.27	44.87	51.28	1.51	14.95	10.29	0.17	7.95	10.76	0.55	2.68	0.22	0.23	0.29	100.60	100.89
D13-12	13.32	44.89	49.72	1.34	14.99	9.86	0.16	7.91	11.83	0.41	2.36	0.18	0.06	0.31	98.81	99.12
D13-2	13.32	44.89	49.75	1.45	14.48	11.10	0.16	7.56	10.46	0.04	2.83	0.16	-0.03	2.16	97.97	100.12
D13-9	13.32	44.89	48.12	1.49	14.79	10.51	0.21	7.86	10.82	0.04	3.25	0.16	-0.03	2.22	97.22	99.44
D14-1.1	13.33	44.86	49.79	0.97	15.58	11.08	0.18	8.79	10.70	0.31	2.26	0.11	0.13	-0.42	99.90	99.48
D14-1.15	13.33	44.86	50.09	1.26	14.45	10.87	0.18	8.09	11.56	0.31	2.15	0.15	0.13	-0.13	99.24	99.11
D14-1.2	13.33	44.86	50.18	1.25	14.53	10.87	0.19	8.07	11.42	0.34	2.17	0.15	0.16	0.20	99.33	99.52
D14-1.5	13.33	44.86	50.26	1.25	14.52	10.81	0.18	8.03	11.38	0.33	2.19	0.15	0.18	0.19	99.28	99.46
D14-1.6	13.33	44.86	49.50	0.97	15.46	11.15	0.18	8.65	10.70	0.26	2.25	0.12	0.17	0.15	99.40	99.55
D14-1.7	13.33	44.86	50.51	1.26	14.58	10.84	0.18	8.10	11.53	0.26	2.18	0.15	0.18	0.37	99.76	100.13
D15-1	13.07	44.09	50.27	1.44	14.56	10.20	0.17	8.38	10.67	0.51	2.61	0.21	0.25	0.55	99.26	99.81
D15-12	13.07	44.09	47.40	0.72	16.34	11.09	0.18	9.38	12.17	0.15	1.87	0.07	0.18	0.69	99.54	100.23
D15-13	13.07	44.09	50.77	1.43	14.75	10.22	0.17	8.43	10.55	0.58	2.53	0.21	0.36	-0.27	100.00	99.72
D15-14	13.07	44.09	50.43	1.42	14.62	10.45	0.17	8.47	10.51	0.60	2.49	0.21	0.12	-1.24	99.48	98.24
D15-15	13.07	44.09	50.81	1.43	14.72	10.31	0.17	8.42	10.60	0.61	2.52	0.21	0.28	0.09	100.08	100.17
D16-11	13.03	44.84	50.41	1.48	14.40	11.01	0.18	8.25	10.59	0.32	2.48	0.20	0.22	0.18	99.52	99.70
D16-12	13.03	44.84	50.47	1.48	14.47	11.16	0.18	8.28	10.66	0.29	2.57	0.20	0.30	1.01	100.05	101.05
D16-13	13.03	44.84	48.77	0.67	16.99	10.14	0.17	9.33	12.17	0.10	1.96	0.06	0.20	0.26	100.55	100.80
D16-14	13.03	44.84	50.51	1.49	14.40	11.19	0.18	8.26	10.60	0.30	2.58	0.20	0.38	0.13	100.07	100.20
D16-17	13.03	44.84	50.95	1.50	14.54	10.95	0.18	8.27	10.69	0.29	2.58	0.20	0.35	0.34	100.50	100.84

Sample ID	Latitude	Longitude	SiO_2 (wt%)	TiO_2	Al_2O_3	Fe_2O_3	MnO	MgO	CaO	K_2O	Na_2O	P_2O_5	SO_3	LOI %	Total	Total + LOI
D19-1.3	12.78	44.84	50.45	1.22	17.70	9.03	0.15	6.90	12.13	0.23	2.41	0.15	0.16	0.22	100.53	100.75
D19-1.7	12.78	44.84	48.90	1.17	17.52	9.03	0.16	6.77	12.08	0.23	2.32	0.14	0.22	2.32	98.54	100.85
D19-2	12.78	44.84	50.23	1.27	14.98	10.03	0.17	8.86	11.13	0.33	2.31	0.15	0.27	0.38	99.74	100.12
D19-3	12.78	44.84	48.78	1.01	19.89	7.67	0.12	6.05	12.72	0.19	2.26	0.12	0.12	0.96	98.93	99.89
D19-4.2	12.78	44.84	49.73	1.31	14.93	10.01	0.18	7.52	11.63	0.45	2.36	0.17	0.25	3.06	98.54	101.59
D19-5	12.78	44.84	50.61	1.51	14.53	11.30	0.18	8.02	10.78	0.38	2.54	0.21	0.32	0.23	100.38	100.60
D19-6	12.78	44.84	49.38	1.13	18.59	8.78	0.19	6.61	12.32	0.23	2.30	0.14	0.17	0.74	99.82	100.56
D20-18	12.99	44.93	49.93	1.33	15.18	10.44	0.17	6.92	11.82	0.30	2.51	0.13	0.09	0.61	98.82	99.42
D20-32	12.99	44.93	49.13	1.31	16.03	10.07	0.18	6.93	12.21	0.15	2.47	0.14	0.15	0.45	98.77	99.22
D23-11	13.51	44.90	49.28	1.66	14.63	11.96	0.19	6.46	10.65	0.44	2.48	0.22	0.09	2.60	98.07	100.66
D23-13	13.51	44.90	50.75	1.62	14.23	11.83	0.19	6.73	10.48	0.55	2.60	0.22	0.35	0.87	99.55	100.42
D23-14	13.51	44.90	49.26	1.65	14.82	11.05	0.20	7.16	10.70	0.60	2.46	0.28	0.28	2.85	98.46	101.31
D23-27	13.51	44.90	50.83	1.63	14.35	11.69	0.19	6.61	10.66	0.59	2.51	0.22	0.31	0.61	99.59	100.20
D23-32	13.51	44.90	49.77	1.65	14.40	11.70	0.19	6.64	10.50	0.47	2.47	0.21	0.20	0.86	98.20	99.06
D24-1	13.35	44.90	50.41	1.35	14.90	10.99	0.18	8.14	10.94	0.44	2.36	0.18	0.19	0.39	100.08	100.47
D24-1.2	13.35	44.90	49.80	1.36	14.75	11.02	0.18	8.18	10.88	0.39	2.37	0.18	0.31	-0.39	99.42	99.02
D24-1.3	13.35	44.90	50.55	1.38	15.10	11.17	0.18	8.27	11.11	0.40	2.46	0.19	0.35	-0.38	101.14	100.76
D24-1.4	13.35	44.90	50.06	1.36	14.75	10.98	0.18	8.23	10.93	0.39	2.40	0.19	0.35	-0.34	99.82	99.48
D24-5	13.35	44.90	49.35	1.35	14.67	11.10	0.19	8.04	10.96	0.38	2.37	0.18	0.29	0.96	98.89	99.85
D24-6	13.35	44.90	50.32	1.40	14.67	11.27	0.20	7.99	10.82	0.40	2.40	0.19	0.29	0.87	99.97	100.83
D24-7	13.35	44.90	50.43	1.23	17.31	9.25	0.15	6.92	11.77	0.45	2.48	0.16	0.23	0.02	100.37	100.40
D24-9	13.35	44.90	50.20	1.36	14.73	11.02	0.18	8.13	11.03	0.39	2.42	0.18	0.28	0.86	99.93	100.79
D25-1.1	13.40	44.89	50.89	1.53	14.81	11.27	0.18	7.76	10.99	0.38	2.56	0.21	0.19	0.49	100.78	101.27
D25-1.3	13.40	44.89	49.87	1.51	14.55	11.37	0.18	7.98	10.68	0.37	2.49	0.20	0.34	0.19	99.55	99.73
D25-1.4	13.40	44.89	50.02	1.51	14.57	11.26	0.18	7.97	10.83	0.38	2.50	0.20	0.36	0.11	99.77	99.88
D25-2.3	13.40	44.89	51.60	1.49	15.03	9.54	0.15	8.50	10.16	0.57	2.69	0.25	0.22	0.57	100.18	100.74
D25-3.1	13.40	44.89	48.27	0.64	17.29	9.88	0.18	9.31	12.28	0.09	1.92	0.06	0.26	-0.57	100.18	99.61

Sample ID	Latitude	Longitude	SiO_2 (wt%)	TiO_2	Al_2O_3	Fe_2O_3	MnO	MgO	CaO	K_2O	Na_2O	P_2O_5	SO_3	LOI %	Total	Total + LOI
D25-3.2	13.40	44.89	49.95	1.51	14.57	11.27	0.18	7.93	10.75	0.38	2.50	0.20	0.35	NO DATA	99.58	99.58
D25-3.3	13.40	44.89	50.00	1.51	14.53	11.28	0.18	8.03	10.80	0.38	2.59	0.20	0.35	0.16	99.84	100.00
D25-5.1	13.40	44.89	49.98	1.49	14.57	11.11	0.18	7.90	10.58	0.43	2.46	0.21	0.29	-2.04	99.20	97.15
D25-5.2	13.40	44.89	50.49	1.50	14.64	11.31	0.18	8.02	10.68	0.40	2.51	0.21	0.20	0.17	100.13	100.30
D26-1	13.66	44.97	47.46	0.73	16.66	10.90	0.20	9.51	12.30	0.13	1.92	0.08	0.09	1.37	99.98	101.35
D26-2	13.66	44.97	47.58	0.75	16.35	10.63	0.18	9.45	12.37	0.17	1.84	0.07	0.23	-0.38	99.62	99.25
D26-3	13.66	44.97	48.66	0.72	16.94	10.84	0.18	9.52	12.43	0.16	1.91	0.08	0.20	0.31	101.66	101.97
D26-4.2	13.66	44.97	46.85	0.71	16.41	10.58	0.18	9.53	12.30	0.15	1.94	0.08	0.11	0.54	98.84	99.37
D26-4.4	13.66	44.97	46.53	0.72	16.27	10.71	0.18	9.48	12.33	0.14	1.89	0.08	0.10	1.52	98.44	99.96
D26-5	13.66	44.97	47.27	0.73	16.44	10.82	0.18	9.53	12.46	0.15	1.83	0.07	0.16	0.87	99.65	100.51
D26-6	13.66	44.97	47.52	0.74	16.44	10.74	0.18	9.41	12.20	0.17	1.83	0.08	0.22	1.22	99.52	100.74
D26-7	13.66	44.97	48.47	0.73	16.79	10.73	0.18	9.59	12.34	0.15	1.90	0.07	0.15	-0.37	101.10	100.74
D26-9	13.66	44.97	46.38	0.68	16.52	10.48	0.17	9.84	12.13	0.15	1.81	0.07	0.12	1.17	98.34	99.51
D27-1	13.80	44.96	49.26	2.70	13.22	12.34	0.18	7.23	11.15	0.53	2.25	0.26	0.05	2.21	99.17	101.37
D27-2	13.80	44.96	47.97	0.72	16.58	10.73	0.18	9.48	12.30	0.16	1.85	0.07	0.12	0.48	100.14	100.62
D27-3	13.80	44.96	48.06	0.74	16.40	10.78	0.18	9.48	12.30	0.17	1.88	0.08	0.23	-0.04	100.31	100.27
D28-12	13.84	44.94	51.52	1.65	14.56	11.76	0.19	6.59	10.66	0.59	2.48	0.22	0.19	NO DATA	100.41	100.41
D29-1	13.90	45.03	49.93	1.36	14.98	10.04	0.17	8.78	11.09	0.50	2.46	0.19	0.30	0.77	99.80	100.56
D29-15	13.90	45.03	49.29	1.34	14.83	10.00	0.17	9.13	11.08	0.49	2.39	0.18	0.26	0.67	99.15	99.82
D29-16	13.90	45.03	49.26	1.37	14.58	10.13	0.17	9.11	11.09	0.51	2.39	0.19	0.22	0.14	99.02	99.16
D29-17	13.90	45.03	50.67	1.48	14.98	10.36	0.17	7.80	11.10	0.56	2.57	0.20	0.19	-0.31	100.08	99.77
D29-4	13.90	45.03	50.38	1.43	15.13	10.13	0.17	7.99	11.18	0.51	2.54	0.20	0.23	NO DATA	99.88	99.88
D29-5	13.90	45.03	49.05	1.30	14.23	10.01	0.16	10.00	10.82	0.48	2.32	0.18	0.25	0.52	98.79	99.31
D29-9	13.90	45.03	50.00	1.10	15.27	9.67	0.16	7.77	12.21	0.41	2.34	0.12	0.17	0.04	99.21	99.24
D30-2.1	14.09	45.02	48.50	1.07	17.45	8.71	0.14	7.02	12.21	0.35	2.27	0.14	0.21	2.27	98.08	100.35
D30-2.3	14.09	45.02	49.74	1.12	17.51	8.83	0.14	7.13	12.41	0.38	2.39	0.14	0.28	0.19	100.08	100.26
D30-2.4	14.09	45.02	49.10	1.07	17.83	8.61	0.14	6.81	12.44	0.34	2.32	0.14	0.24	1.52	99.04	100.55

Sample ID	Latitude	Longitude	SiO_2 (wt%)	TiO_2	Al_2O_3	Fe_2O_3	MnO	MgO	CaO	K_2O	Na_2O	P_2O_5	SO_3	LOI %	Total	Total + LOI
D30-2.6	14.09	45.02	49.25	1.08	18.02	8.60	0.14	6.97	12.40	0.36	2.34	0.14	0.24	0.54	99.54	100.08
D30-5	14.09	45.02	51.24	1.69	15.23	10.40	0.17	6.54	10.42	0.75	2.92	0.27	0.23	0.68	99.86	100.54

Trace Element Compositions – M2 Type Basalts, 13°19'N

Sample ID	Latitude	Longitude	Li	Sc	Rb	Sr	Y	Zr	Nb	Cs	Ba	La	Ce	Pr
D05-1	13.30	44.96	3.09	23.72	4.35	102.20	27.56	81.97	10.28	0.09	60.09	6.45	15.68	2.29
D05-1.2	13.30	44.96	3.91	31.66	5.52	120.10	24.75	79.74	8.16	0.10	52.11	5.67	13.62	2.03
D05-1.3	13.30	44.96	3.89	26.36	5.66	122.60	23.42	82.33	8.41	0.14	53.11	5.74	14.00	2.10
D05-1.4	13.30	44.96	4.01	34.70	5.66	163.80	26.69	84.58	8.74	0.11	55.24	6.07	14.47	2.15
D05-1A	13.30	44.96	4.14	35.13	6.88	149.60	30.45	96.17	10.61	0.13	64.86	6.85	16.42	2.39
D05-2.7	13.30	44.96	3.43	26.71	5.04	132.30	27.13	92.95	10.15	0.10	57.44	6.49	15.57	2.30
D05-3.1	13.30	44.96	8.23	44.41	1.60	120.70	24.79	56.79	2.62	0.03	18.96	2.53	7.18	1.24
D05-4.1	13.30	44.96	6.82	30.74	0.58	142.70	25.35	75.20	6.24	0.04	17.23	4.45	11.02	1.68
D05-5.4	13.30	44.96	4.35	34.92	4.80	151.00	31.12	104.20	9.28	0.07	56.65	6.65	16.54	2.45
D06-3.1	13.30	44.96	4.97	30.62	5.93	148.70	26.68	101.40	11.09	0.06	73.60	7.62	18.30	2.67
D06-6	13.30	44.96	4.12	15.59	2.56	122.00	26.50	98.57	9.81	0.02	65.30	7.13	17.10	2.52
D06-7.3	13.30	44.96	4.59	23.35	4.90	135.00	21.62	100.00	10.91	0.05	71.50	7.10	17.09	2.47
D06-7.4	13.30	44.96	5.17	24.95	5.75	142.60	21.57	102.50	11.24	0.06	73.96	7.31	17.40	2.51
D12-2.1	13.30	44.78	7.06	38.95	2.74	227.20	30.06	94.72	6.42	0.03	39.94	6.92	18.61	2.42
D12-2.2	13.30	44.78	3.54	26.49	2.98	152.40	20.44	62.18	4.40	0.08	23.88	3.55	9.19	1.45
D12-3.1	13.30	44.78	8.00	33.51	3.82	138.20	23.80	69.49	4.60	0.33	23.73	4.29	11.02	1.69
D12-3.4	13.30	44.78	5.18	31.95	3.34	93.50	26.72	71.25	4.73	0.08	38.75	5.09	12.58	1.93
D12-5	13.30	44.78	7.54	43.34	3.06	224.60	30.87	87.67	6.22	0.04	33.40	5.09	13.14	2.00
D12-8	13.30	44.78	6.18	33.74	2.86	84.54	24.15	63.13	4.76	0.06	35.01	3.81	9.89	1.58
D06-7.6	13.30	44.96	4.95	23.69	3.84	120.30	21.60	103.90	8.03	0.04	51.51	5.74	14.36	2.19
D06-9	13.30	44.96	5.78	35.49	6.42	146.50	28.10	100.90	10.92	0.07	76.81	7.39	17.73	2.60

Sample ID	Sm	Eu	Gd	Tb	Dy	Ho	Er	Tm	Yb	Lu	Hf	Ta	Pb	Th	U
D05-1	3.33	1.16	4.16	0.72	4.53	0.95	2.71	0.39	2.60	0.39	1.94	0.75	0.68	0.47	0.20
D05-1.2	2.94	1.03	3.68	0.65	4.22	0.89	2.57	0.38	2.47	0.37	2.07	0.54	0.63	0.49	0.20
D05-1.3	2.99	1.09	3.77	0.66	4.29	0.91	2.60	0.38	2.51	0.38	2.17	0.56	0.52	0.46	0.18
D05-1.4	3.09	1.11	3.95	0.69	4.44	0.93	2.68	0.40	2.60	0.39	2.16	0.49	0.64	0.51	0.18
D05-1A	3.38	1.19	4.19	0.74	4.66	1.02	2.80	0.42	2.71	0.41	2.16	0.78	0.64	0.53	0.26
D05-2.7	3.27	1.18	4.11	0.72	4.62	0.95	2.77	0.40	2.66	0.39	2.25	0.77	0.65	0.48	0.21
D05-3.1	2.31	0.91	3.29	0.60	4.00	0.87	2.54	0.38	2.53	0.38	1.56	0.19	0.64	0.15	0.25
D05-4.1	2.77	1.04	3.69	0.66	4.28	0.90	2.57	0.38	2.46	0.36	1.98	0.33	0.34	0.35	0.17
D05-5.4	3.52	1.28	4.54	0.77	4.97	1.05	3.03	0.45	2.87	0.42	2.40	0.47	0.66	0.47	0.19
D06-3.1	3.57	1.25	4.38	0.76	4.90	1.03	2.94	0.43	2.82	0.42	2.58	0.73	0.92	0.64	0.25
D06-6	3.46	1.19	4.19	0.73	4.71	0.99	2.81	0.41	2.69	0.40	2.52	0.63	0.65	0.59	0.21
D06-7.3	3.30	1.14	3.97	0.69	4.43	0.93	2.65	0.39	2.50	0.37	2.50	0.75	0.76	0.50	0.21
D06-7.4	3.35	1.16	4.09	0.70	4.52	0.95	2.70	0.40	2.54	0.38	2.54	0.80	0.72	0.50	0.21
D12-2.1	3.42	1.23	4.19	0.74	4.73	0.98	2.82	0.42	2.68	0.40	2.18	0.34	3.42	0.57	0.19
D12-2.2	2.35	0.90	3.04	0.54	3.54	0.75	2.17	0.32	2.11	0.31	1.63	0.30	0.41	0.26	0.11
D12-3.1	2.62	0.96	3.39	0.60	3.95	0.83	2.38	0.35	2.29	0.34	1.79	0.25	0.83	0.31	0.13
D12-3.4	2.89	1.04	3.76	0.67	4.30	0.90	2.62	0.39	2.46	0.38	1.71	0.37	0.57	0.39	0.14
D12-5	3.16	1.17	4.03	0.71	4.60	0.97	2.79	0.41	2.68	0.40	2.03	0.34	0.92	0.36	0.14
D12-8	2.62	0.98	3.38	0.60	4.06	0.84	2.46	0.36	2.31	0.35	1.61	0.33	0.53	0.25	0.10
D06-7.6	3.23	1.13	4.05	0.72	4.66	0.98	2.82	0.41	2.65	0.39	2.65	0.55	0.72	0.36	0.17
D06-9	3.53	1.23	4.29	0.75	4.83	1.02	2.91	0.43	2.83	0.42	2.56	0.78	0.66	0.68	0.22

Trace Element Compositions – M1 Type Basalts, 13°19'N

Sample ID	Latitude	Longitude	Li	Sc	Rb	Sr	Y	Zr	Nb	Cs	Ba	La	Ce	Pr
D12-1.2	13.30	44.78	5.41	30.77	16.68	358.30	29.37	172.60	38.00	0.16	226.00	20.73	42.89	5.24
D05-5.2	13.30	44.96	3.19	29.86	10.45	319.30	26.56	144.00	30.78	0.15	153.10	17.61	35.72	4.45
D05-5.3	13.30	44.96	3.95	33.89	11.96	334.70	26.01	145.90	29.06	0.23	162.70	17.42	35.55	4.44
D12-4	13.30	44.78	9.26	43.68	15.31	388.60	37.77	206.40	26.37	0.27	198.70	19.34	41.20	5.32
D05-8.7	13.30	44.96	3.18	12.29	5.83	244.00	12.49	136.20	24.53	0.06	139.90	14.60	29.96	3.82
D06-1.10	13.30	44.96	5.74	25.74	12.53	483.20	24.85	184.20	33.38	0.24	173.10	20.16	44.13	5.88
D05-16	13.30	44.96	4.29	25.87	9.97	295.40	22.79	155.00	27.75	0.10	156.20	16.53	33.99	4.27
D05-2.1	13.30	44.96	3.26	28.97	10.62	356.70	24.78	155.80	32.63	0.24	186.50	19.90	40.25	4.98
D05-2.2	13.30	44.96	2.75	20.20	10.81	357.00	14.38	153.20	35.50	0.18	181.10	18.90	38.15	4.73
D12-6.2G	13.30	44.78				318.41	28.10	164.95	30.79	0.17	194.93	16.53	38.31	4.32
D12-12	13.30	44.78	7.52	44.17	22.05	461.50	37.89	225.70	41.77	0.22	285.10	26.79	56.60	6.78
D12-1.2R	13.30	44.78	5.41	30.77	16.68	358.30	29.37	172.60	38.00	0.16	226.00	20.73	42.89	5.24
D12-1.4	13.30	44.78	4.87	23.32	13.28	324.50	27.75	157.10	34.27	0.11	218.70	20.14	42.00	5.14

Sample ID	Nd	Sm	Eu	Gd	Tb	Dy	Ho	Er	Tm	Yb	Lu	Hf	Ta	Pb	Th	U
D12-1.2	22.02	5.17	1.75	5.30	0.84	4.99	0.94	2.58	0.35	2.27	0.34	3.52	2.95	1.93	1.98	0.60
D05-5.2	18.73	4.51	1.55	4.89	0.78	4.50	0.90	2.38	0.32	2.05	0.30	3.01	2.15	1.06	1.63	0.55
D05-5.3	18.59	4.54	1.59	4.94	0.79	4.67	0.91	2.46	0.35	2.18	0.31	3.30	1.71	1.09	1.79	0.69
D12-4	22.92	5.85	2.01	6.45	1.04	6.19	1.21	3.28	0.46	2.89	0.42	4.30	0.35	2.12	1.76	0.54
D05-8.7	15.86	3.73	1.26	3.90	0.62	3.66	0.71	1.89	0.26	1.56	0.22	3.28	1.55	1.21	0.83	0.53
D06-1.10	25.72	6.28	2.16	6.18	0.89	4.83	0.87	2.18	0.29	1.72	0.24	4.16	1.99	1.01	1.58	0.56
D05-16	17.82	4.34	1.51	4.68	0.75	4.43	0.87	2.33	0.33	2.05	0.30	3.58	1.90	1.05	1.69	0.53
D05-2.1	20.73	4.87	1.68	5.10	0.80	4.65	0.88	2.34	0.32	2.01	0.29	3.55	1.62	1.19	2.08	0.67
D05-2.2	19.43	4.34	1.46	4.34	0.68	3.92	0.75	1.97	0.27	1.61	0.23	3.54	2.42	1.26	1.17	0.77
D12-6.2G	18.89	4.16	1.56	4.59	0.77	4.30	0.88	2.36	0.31	1.94	0.29	3.37	1.97	1.03	1.85	0.57

Sample ID	Nd	Sm	Eu	Gd	Tb	Dy	Ho	Er	Tm	Yb	Lu	Hf	Ta	Pb	Th	U
D12-12	27.96	6.59	2.18	6.92	1.07	6.28	1.22	3.28	0.46	2.87	0.42	4.45	0.91	3.60	2.55	0.77
D12-1.2R	22.02	5.17	1.75	5.30	0.84	4.99	0.94	2.58	0.35	2.27	0.34	3.52	2.95	1.93	1.98	0.60
D12-1.4	21.42	5.06	1.67	5.48	0.83	4.86	0.93	2.57	0.36	2.25	0.32	3.26	1.92	1.87	1.82	0.62

Trace Element Compositions – On-Axis Basalts, ~12°60’ -14°N

Sample ID	Latitude	Longitude	Li	Sc	Rb	Sr	Y	Zr	Nb	Cs	Ba	La	Ce	Pr
D07-15	13.30	44.93	6.60	38.45	0.29	196.90	25.07	41.65	9.73	0.01	18.98	6.78	16.13	2.35
D07-18	13.30	44.93	10.11	42.57	1.37	206.90	25.54	76.13	14.89	0.01	46.03	9.25	20.23	2.77
D07-19	13.30	44.93	4.12	38.02	7.36	179.20	26.63	92.43	11.78	0.13	75.69	7.64	17.64	2.52
D07-20	13.30	44.93	2.29	15.14	0.26	100.40	11.43	45.61	2.88	0.01	14.12	2.28	6.26	1.04
D07-21	13.30	44.93	2.12	38.50	0.40	133.20	25.58	68.07	3.86	0.02	12.55	3.33	9.15	1.50
D09-11.8	13.32	44.93	2.62	41.46	0.19	106.60	24.53	44.96	2.96	0.01	13.70	2.72	7.61	1.29
D09-3.5	13.32	44.93	5.42	39.70	2.72	180.10	28.03	83.05	11.60	0.01	30.14	8.13	18.64	2.64
D09-8.2	13.32	44.93	6.65	38.74	4.87	152.70	32.63	97.35	9.40	0.08	55.40	6.67	16.25	2.44
D10-18	13.34	44.89	11.42	29.10	5.20	120.00	26.74	90.69	8.52	0.20	34.44	6.29	15.20	2.28
D10-28	13.34	44.89	8.60	14.99	5.83	182.90	14.58	88.57	14.18	0.41	52.74	8.63	19.02	2.61
D10-30.3	13.34	44.89	4.57	31.31	4.43	257.90	19.68	87.91	13.46	0.02	48.72	8.47	18.37	2.47
D10-30.5	13.34	44.89	9.53	24.97	0.38	148.30	20.53	69.27	7.89	0.01	20.28	4.77	11.06	1.61
D10-37	13.34	44.89	4.13	38.43	7.43	180.30	27.10	96.18	12.22	0.13	81.46	7.82	18.08	2.54
D10-38.1	13.34	44.89	4.79	33.58	0.76	121.30	25.64	75.16	6.96	0.05	20.88	4.93	12.31	1.87
D10-38.2	13.34	44.89	2.64	29.79	0.15	97.89	25.38	64.35	3.50	0.00	10.98	3.08	8.61	1.43
D10-9	13.34	44.89	3.47	25.67	4.87	202.30	20.69	72.96	8.63	0.11	52.71	5.77	13.45	1.91
D11-1	13.27	44.87	4.38	61.28	2.51	196.10	22.43	49.09	4.47	0.04	28.74	3.10	7.39	1.12
D11-11	13.27	44.87	9.24	46.24	3.47	146.20	25.44	74.48	5.78	0.09	36.13	5.20	12.29	1.84
D11-2	13.27	44.87	20.84	44.63	3.40	167.10	31.42	85.71	4.75	0.21	33.03	4.19	11.20	1.83
D11-3	13.27	44.87	15.27	60.79	5.14	217.50	34.01	96.16	10.62	0.13	45.43	7.06	16.46	2.38

Sample ID	Latitude	Longitude	Li	Sc	Rb	Sr	Y	Zr	Nb	Cs	Ba	La	Ce	Pr
D11-4	13.27	44.87	3.53	45.88	2.09	129.70	17.29	41.99	3.41	0.02	25.80	2.78	6.68	0.97
D11-5	13.27	44.87				101.93	16.20	31.41	2.72	0.03	18.47	1.82	4.64	0.73
D11-8	13.27	44.87	6.70	54.78	4.45	223.50	35.06	105.40	6.53	0.05	52.27	6.10	15.37	2.35
D13-12	13.32	44.89	3.63	38.65	6.93	175.80	27.51	99.40	12.92	0.10	76.47	8.22	18.64	2.60
D13-2	13.32	44.89	3.36	28.30	0.16	113.40	26.84	83.92	7.10	0.00	17.89	4.94	12.18	1.92
D13-9	13.32	44.89	4.13	29.50	0.14	135.80	30.75	80.23	7.31	0.00	18.18	5.67	13.21	2.04
D14-1.15	13.33	44.86	4.28	26.73	3.40	108.50	22.79	88.88	6.86	0.04	54.18	5.43	13.08	1.94
D14-1.2	13.33	44.86	4.50	24.62	3.70	111.00	19.71	80.48	7.75	0.04	54.86	5.51	13.39	1.98
D14-1.5	13.33	44.86	4.70	52.15	2.68	107.40	45.49	93.56	7.18	0.03	58.56	6.26	15.20	2.27
D14-1.6	13.33	44.86	2.45	14.66	2.17	111.70	8.86	51.34	6.71	0.02	42.57	3.88	9.06	1.29
D14-1.7	13.33	44.86	5.21	38.88	4.76	119.20	26.34	86.01	7.98	0.05	57.42	5.59	13.39	1.99
D15-1	13.07	44.09				142.32	37.74	113.79	10.20	0.07	65.86	6.99	17.31	2.48
D15-10	13.07	44.09	4.93	34.88	10.01	234.60	25.55	127.90	16.00	0.11	115.30	10.98	24.40	3.28
D15-12	13.07	44.09	5.74	50.64	12.99	333.10	37.63	164.00	21.49	0.17	150.60	14.78	32.74	4.43
D15-13	13.07	44.09	3.85	20.96	6.86	168.50	21.41	132.20	16.03	0.07	109.50	10.22	23.17	3.14
D15-15	13.07	44.09	5.17	33.78	10.41	192.50	25.58	147.80	17.42	0.11	120.60	10.88	24.16	3.30
D16-11	13.03	44.84	4.05	19.59	3.43	114.70	24.24	124.90	9.68	0.03	70.26	7.19	17.37	2.50
D16-12	13.03	44.84	8.10	53.65	8.02	239.40	43.92	157.10	15.33	0.08	92.03	10.22	24.17	3.47
D16-13	13.03	44.84	5.77	37.93	5.80	170.30	30.93	105.40	10.53	0.06	68.63	7.60	18.08	2.60
D16-14	13.03	44.84	5.72	37.96	5.83	170.10	30.93	108.60	10.46	0.06	68.37	7.51	17.79	2.60
D16-17	13.03	44.84				182.64	26.26	113.78	13.86	0.11	101.24	8.68	21.41	2.71
D19-1.1	12.78	44.84	3.88	27.52	3.40	193.80	20.79	68.95	6.49	0.04	44.02	4.53	10.98	1.64
D19-1.3	12.78	44.84				135.45	25.66	79.81	6.05	0.05	43.86	4.29	11.37	1.60
D19-1.7	12.78	44.84	4.66	33.66	4.55	165.90	25.66	95.38	6.75	0.06	53.70	5.80	14.47	2.06
D19-2	12.78	44.84	5.22	35.43	4.22	135.90	26.51	87.10	7.46	0.04	51.74	5.54	13.84	2.11
D19-3	12.78	44.84	4.03	30.24	3.56	178.80	22.78	74.28	7.08	0.05	44.91	5.04	12.27	1.82
D19-4.1	12.78	44.84	4.92	55.08	10.38	321.10	34.91	135.30	16.82	0.15	120.60	11.83	27.47	3.66

Sample ID	Latitude	Longitude	Li	Sc	Rb	Sr	Y	Zr	Nb	Cs	Ba	La	Ce	Pr
D19-4.2	12.78	44.84	3.69	40.74	8.44	200.70	26.28	103.50	11.98	0.13	98.57	9.44	21.59	2.89
D19-5	12.78	44.84	3.36	29.33	3.41	189.90	21.78	69.12	6.30	0.05	41.90	4.66	11.64	1.70
D19-6	12.78	44.84	5.53	43.13	5.23	263.00	32.77	109.50	9.74	0.07	61.04	7.21	18.45	2.54
D20-18	12.99	44.93	5.39	36.55	6.11	127.50	31.39	82.28	4.18	0.33	26.81	3.85	10.52	1.75
D20-32	12.99	44.93	4.91	40.07	1.85	167.40	29.43	72.71	5.61	0.03	30.94	5.28	12.46	2.07
D23-11	13.51	44.90	4.88	35.61	6.43	221.80	29.24	103.50	15.56	0.10	95.59	9.74	21.50	3.00
D23-13	13.51	44.90	4.85	38.53	9.09	211.80	29.84	108.30	15.42	0.10	113.10	10.03	22.25	3.04
D23-14	13.51	44.90	5.69	28.93	8.54	208.00	29.77	135.60	18.99	0.09	131.80	13.36	29.12	3.89
D23-16	13.51	44.90	7.31	35.05	10.61	214.80	29.61	140.60	20.94	0.12	133.30	12.72	27.91	3.73
D23-18	13.51	44.90	4.06	36.02	11.96	245.90	29.26	136.70	22.00	0.14	140.40	13.15	28.51	3.78
D23-27	13.51	44.90	4.59	37.15	9.59	209.10	29.13	105.60	15.23	0.16	109.60	10.00	22.04	3.04
D23-32	13.51	44.90	5.67	40.19	7.96	225.80	29.67	111.40	16.25	0.11	106.10	9.75	21.67	2.99
D24-1	13.35	44.90	4.75	26.52	6.98	148.50	18.93	102.90	12.23	0.07	89.33	7.88	17.93	2.52
D24-1.3	13.35	44.90	5.04	28.46	7.11	149.40	21.88	93.84	12.33	0.07	89.84	8.02	18.26	2.57
D24-1.4	13.35	44.90	4.42	25.42	6.26	143.60	21.90	92.30	11.60	0.06	86.93	7.87	18.02	2.55
D24-5	13.35	44.90	4.90	39.82	7.25	191.20	26.55	95.55	11.58	0.08	87.79	8.21	18.83	2.58
D24-6	13.35	44.90	7.42	56.90	11.07	257.80	39.60	143.20	16.64	0.11	124.30	11.89	27.16	3.64
D24-7	13.35	44.90	8.20	56.50	12.16	268.40	41.91	155.70	17.15	0.12	137.40	12.96	28.98	3.95
D24-9	13.35	44.90				157.05	29.13	96.87	10.39	0.09	78.51	6.95	18.07	2.24
D25-1.1	13.40	44.89				148.60	32.08	105.09	11.31	0.09	78.82	6.92	17.29	2.38
D25-1.2	13.40	44.89	6.79	42.85	8.79	175.30	34.58	124.70	14.78	0.09	102.60	9.71	22.22	3.14
D25-1.3	13.40	44.89	3.10	45.36	2.85	119.50	19.24	45.54	5.82	0.04	37.26	3.79	8.62	1.24
D25-1.4	13.40	44.89	5.62	38.00	7.47	183.10	30.64	105.80	13.19	0.07	89.86	8.49	19.53	2.76
D25-2.3	13.40	44.89	5.72	39.14	14.83	401.20	27.98	157.10	22.44	0.15	172.50	14.47	30.88	4.05
D25-3.1	13.40	44.89	5.92	52.02	13.33	315.90	30.94	151.80	25.03	0.16	170.80	14.61	32.11	4.24
D25-3.2	13.40	44.89	6.33	42.28	8.56	172.00	34.22	124.40	14.28	0.08	99.83	9.62	21.87	3.07
D25-3.3	13.40	44.89	5.94	39.86	8.04	158.90	32.20	115.70	14.52	0.08	92.81	9.00	20.43	2.86

Sample ID	Latitude	Longitude	Li	Sc	Rb	Sr	Y	Zr	Nb	Cs	Ba	La	Ce	Pr
D25-5.1	13.40	44.89	5.16	24.75	6.12	136.70	22.44	102.40	12.55	0.06	86.53	7.97	18.50	2.64
D25-5.2	13.40	44.89	5.93	36.00	7.57	147.40	30.03	117.90	11.97	0.07	90.55	8.41	19.44	2.81
D26-1	13.66	44.97	3.80	60.94	3.19	189.10	25.82	55.42	7.71	0.04	45.43	5.08	11.37	1.62
D26-2	13.66	44.97	3.38	46.50	3.93	124.50	20.15	49.97	6.78	0.04	46.84	4.19	9.58	1.35
D26-3	13.66	44.97				102.72	18.41	39.84	4.45	0.04	33.65	2.79	6.96	1.00
D26-4.2	13.66	44.97	2.83	43.40	2.61	135.00	18.31	42.20	5.52	0.04	35.25	3.56	8.14	1.17
D26-4.4	13.66	44.97	3.15	49.01	2.81	125.40	21.02	48.24	6.29	0.04	38.31	4.23	9.47	1.36
D26-4.5	13.66	44.97	4.03	62.19	4.43	195.00	26.20	65.59	6.93	0.05	53.00	5.31	12.08	1.69
D26-5	13.66	44.97	3.12	45.05	3.15	117.00	19.12	44.33	6.05	0.04	40.01	3.86	8.82	1.24
D26-6	13.66	44.97	3.51	45.89	3.77	122.70	19.96	49.12	6.02	0.04	47.33	4.18	9.50	1.34
D26-7	13.66	44.97	3.75	60.23	3.95	187.80	25.33	58.16	7.60	0.05	49.14	4.69	10.80	1.52
D26-9	13.66	44.97	3.05	41.44	2.77	115.10	17.54	47.32	5.45	0.04	35.22	3.50	7.96	1.14
D27-1	13.80	44.96	3.75	59.80	3.89	182.00	25.02	60.99	7.57	0.04	48.22	4.62	10.58	1.51
D27-2	13.80	44.96				100.28	17.95	39.37	4.45	0.04	31.18	2.68	6.80	0.96
D27-3	13.80	44.96	4.17	59.78	4.72	190.10	25.67	64.78	8.36	0.05	56.82	5.02	11.54	1.62
D28-12	13.84	44.94	4.30	37.22	9.58	215.20	29.94	109.20	15.68	0.14	111.60	10.14	22.53	3.08
D29-1	13.90	45.03	5.41	49.19	12.71	293.00	28.86	132.10	21.04	0.14	155.30	13.37	29.14	3.83
D29-10	13.90	45.03				208.03	18.62	72.73	11.22	0.10	96.21	6.70	15.76	2.02
D29-11	13.90	45.03	5.40	39.98	13.58	248.80	26.43	114.50	20.85	0.14	160.90	13.06	27.61	3.58
D29-15	13.90	45.03	4.37	36.67	10.48	232.20	22.05	106.10	13.06	0.12	130.00	11.09	24.19	3.21
D29-16	13.90	45.03	4.29	38.69	10.56	237.80	23.11	109.80	12.83	0.12	131.50	11.56	25.14	3.33
D29-17	13.90	45.03	2.90	17.29	7.03	185.80	9.64	99.40	16.38	0.07	118.20	9.84	21.74	2.87
D29-4	13.90	45.03	4.19	32.38	8.48	252.10	23.16	116.50	18.02	0.10	135.70	11.30	25.00	3.32
D29-5	13.90	45.03	4.62	40.29	11.03	245.90	23.48	113.00	18.59	0.12	136.40	11.73	25.50	3.37
D29-6	13.90	45.03	4.06	34.97	9.38	220.40	21.21	97.26	15.01	0.11	120.80	10.32	22.69	3.01
D29-9	13.90	45.03	3.04	37.42	7.33	251.10	17.99	68.15	9.98	0.08	99.14	7.47	16.37	2.21
D30-2.1	14.09	45.02	4.06	36.16	8.10	271.40	20.80	109.40	11.33	0.09	109.10	8.77	18.68	2.52

Sample ID	Latitude	Longitude	Li	Sc	Rb	Sr	Y	Zr	Nb	Cs	Ba	La	Ce	Pr
D30-2.2	14.09	45.02	3.36	30.73	6.72	240.60	17.41	68.08	11.46	0.07	90.30	7.29	15.81	2.16
D30-2.3	14.09	45.02	4.02	35.70	8.18	254.30	20.32	82.28	13.69	0.09	104.00	8.55	18.51	2.50
D30-2.4	14.09	45.02	3.57	32.85	6.80	251.10	18.38	83.49	11.80	0.08	92.81	7.46	16.27	2.21
D30-2.5	14.09	45.02	4.29	35.87	8.42	270.50	20.49	85.01	13.63	0.09	107.50	8.73	18.97	2.57
D30-2.6	14.09	45.02	3.86	34.20	7.79	257.90	19.66	80.73	9.68	0.08	99.71	8.38	17.87	2.43
D30-3	14.09	45.02	5.05	48.01	12.09	341.60	29.67	122.40	20.95	0.13	153.10	12.44	27.09	3.63
D30-4	14.09	45.02	4.10	45.12	8.77	334.80	23.92	96.12	15.63	0.10	114.90	9.26	20.22	2.72
D30-5	14.09	45.02				224.35	27.82	141.12	21.65	0.17	161.63	12.81	30.29	3.58

Sample ID	Nd	Sm	Eu	Gd	Tb	Dy	Ho	Er	Tm	Yb	Lu	Hf	Ta	Pb	Th	U
D07-15	10.97	3.17	1.32	3.90	0.67	4.25	0.88	2.48	0.36	2.32	0.34	1.34	0.61	0.17	0.40	0.11
D07-18	12.49	3.56	1.26	4.27	0.73	4.50	0.91	2.52	0.36	2.26	0.33	2.19	0.91	0.35	0.65	0.22
D07-19	11.63	3.31	1.15	4.01	0.70	4.51	0.94	2.70	0.40	2.61	0.39	2.31	0.62	0.64	0.71	0.27
D07-20	5.40	1.80	0.67	2.36	0.43	2.79	0.59	1.70	0.25	1.57	0.23	1.31	0.21	0.26	0.10	0.07
D07-21	7.79	2.65	1.01	3.56	0.64	4.20	0.90	2.60	0.39	2.55	0.38	1.82	0.26	0.14	0.23	0.09
D09-11.8	6.84	2.44	0.93	3.36	0.61	4.03	0.85	2.47	0.36	2.36	0.35	1.42	0.13	0.24	0.13	0.06
D09-3.5	12.21	3.52	1.24	4.33	0.75	4.76	0.99	2.76	0.40	2.58	0.38	2.29	0.74	0.30	0.51	0.23
D09-8.2	11.73	3.60	1.25	4.67	0.82	5.34	1.13	3.28	0.49	3.20	0.48	2.52	0.54	0.63	0.56	0.32
D10-18	10.83	3.24	1.13	4.09	0.72	4.65	0.99	2.85	0.42	2.73	0.41	2.32	0.48	0.56	0.53	0.25
D10-28	11.56	3.00	1.06	3.38	0.56	3.48	0.71	1.96	0.28	1.78	0.26	2.23	1.01	0.39	0.57	0.39
D10-30.3	11.14	3.20	1.23	3.72	0.61	3.63	0.70	1.86	0.26	1.62	0.23	2.28	0.61	0.51	0.72	0.24
D10-30.5	7.82	2.65	1.09	3.59	0.61	3.73	0.73	1.95	0.27	1.65	0.23	1.92	0.49	0.39	0.38	0.17
D10-37	11.72	3.34	1.16	4.11	0.71	4.54	0.95	2.72	0.40	2.64	0.40	2.38	0.69	0.67	0.72	0.29
D10-38.1	9.22	2.88	1.05	3.75	0.67	4.35	0.92	2.64	0.39	2.56	0.38	2.01	0.32	0.30	0.39	0.15
D10-38.2	7.53	2.64	0.96	3.56	0.64	4.22	0.90	2.59	0.39	2.53	0.38	1.78	0.18	0.39	0.20	0.09
D10-9	8.81	2.57	0.95	3.16	0.55	3.49	0.73	2.09	0.31	2.02	0.30	1.81	0.51	0.62	0.50	0.16

Sample ID	Nd	Sm	Eu	Gd	Tb	Dy	Ho	Er	Tm	Yb	Lu	Hf	Ta	Pb	Th	U
D11-1	5.53	1.85	0.81	2.61	0.49	3.31	0.73	2.13	0.32	2.10	0.32	1.17	0.23	0.36	0.25	0.11
D11-11	8.81	2.70	1.02	3.58	0.64	4.19	0.90	2.61	0.39	2.53	0.38	1.87	0.15	0.51	0.44	0.13
D11-2	9.43	3.17	1.17	4.34	0.77	5.11	1.10	3.18	0.47	3.08	0.47	2.29	0.31	0.51	0.30	0.19
D11-3	11.15	3.33	1.23	4.25	0.76	5.05	1.09	3.15	0.47	3.09	0.47	2.14	0.56	0.83	0.58	0.20
D11-4	4.77	1.56	0.68	2.24	0.42	2.80	0.62	1.83	0.27	1.82	0.27	1.11	0.12	0.59	0.26	0.10
D11-5	3.78	1.29	0.60	1.90	0.37	2.53	0.57	1.64	0.23	1.59	0.23	0.89	0.23	0.17	0.21	0.07
D11-8	11.52	3.62	1.34	4.62	0.82	5.32	1.12	3.23	0.48	3.12	0.47	2.37	0.24	0.73	0.44	0.17
D13-12	11.91	3.41	1.18	4.09	0.70	4.40	0.92	2.55	0.38	2.36	0.36	2.25	0.88	1.10	0.70	0.31
D13-2	9.61	3.17	1.26	4.26	0.76	4.95	1.04	2.97	0.43	2.78	0.41	2.35	0.46	0.41	0.33	0.18
D13-9	10.09	3.37	1.27	4.49	0.80	5.18	1.08	3.04	0.44	2.84	0.41	2.29	0.38	0.87	0.37	0.20
D14-1.15	9.38	2.87	1.02	3.67	0.65	4.26	0.91	2.63	0.39	2.54	0.38	2.32	0.25	0.58	0.44	0.19
D14-1.2	9.44	2.85	1.01	3.60	0.64	4.14	0.88	2.53	0.37	2.41	0.36	2.17	0.52	0.81	0.41	0.19
D14-1.5	11.02	3.52	1.28	4.68	0.84	5.50	1.17	3.43	0.52	3.56	0.55	2.47	0.36	0.54	0.91	0.18
D14-1.6	6.11	1.81	0.71	2.29	0.41	2.69	0.57	1.61	0.23	1.43	0.21	1.39	0.44	0.56	0.19	0.16
D14-1.7	9.54	2.92	1.04	3.79	0.67	4.36	0.93	2.70	0.40	2.66	0.40	2.23	0.53	0.54	0.52	0.17
D15-1	12.01	3.54	1.36	4.46	0.83	5.48	1.20	3.08	0.43	2.91	0.45	2.92	0.72	0.59	0.72	0.21
D15-10	14.39	3.70	1.24	4.19	0.70	4.39	0.91	2.58	0.38	2.48	0.37	3.01	0.83	1.32	1.14	0.37
D15-12	19.31	5.03	1.69	5.66	0.94	5.87	1.20	3.40	0.50	3.22	0.48	3.43	0.91	1.20	1.36	0.46
D15-13	13.79	3.57	1.19	3.95	0.67	4.18	0.86	2.45	0.36	2.30	0.35	3.18	0.92	0.88	0.91	0.36
D15-15	14.45	3.74	1.25	4.26	0.71	4.45	0.93	2.63	0.39	2.53	0.38	3.51	1.29	0.85	1.14	0.37
D16-11	11.81	3.44	1.19	4.25	0.75	4.82	1.02	2.91	0.43	2.75	0.41	3.10	0.52	0.66	0.51	0.23
D16-12	16.33	4.82	1.65	5.87	1.03	6.62	1.39	3.99	0.59	3.83	0.57	3.38	0.73	1.10	0.82	0.26
D16-13	12.28	3.63	1.25	4.55	0.79	5.13	1.08	3.11	0.46	3.01	0.46	2.59	0.60	0.77	0.68	0.21
D16-14	12.25	3.61	1.26	4.51	0.79	5.13	1.08	3.10	0.46	3.02	0.45	2.67	0.60	0.66	0.67	0.21
D16-17	12.18	3.24	1.20	3.72	0.67	4.00	0.83	2.26	0.32	2.15	0.33	2.51	0.88	0.64	1.00	0.31
D19-1.1	7.87	2.43	0.92	3.06	0.54	3.46	0.73	2.07	0.31	2.02	0.30	1.72	0.42	0.46	0.37	0.13
D19-1.3	8.58	2.62	1.07	3.38	0.64	3.93	0.85	2.25	0.32	2.06	0.32	2.02	0.37	0.42	0.44	0.15

Sample ID	Nd	Sm	Eu	Gd	Tb	Dy	Ho	Er	Tm	Yb	Lu	Hf	Ta	Pb	Th	U
D19-1.7	9.94	3.00	1.10	3.87	0.67	4.31	0.91	2.60	0.38	2.50	0.37	2.38	0.27	1.09	0.52	0.17
D19-2	10.14	3.12	1.11	3.97	0.69	4.52	0.96	2.76	0.41	2.70	0.41	2.23	0.57	0.58	0.48	0.15
D19-3	8.80	2.70	1.03	3.46	0.60	3.81	0.82	2.31	0.34	2.20	0.33	1.86	0.44	0.64	0.45	0.14
D19-4.1	16.28	4.35	1.53	5.05	0.86	5.42	1.12	3.19	0.47	3.03	0.45	2.89	0.63	1.77	1.06	0.35
D19-4.2	12.96	3.49	1.24	4.16	0.70	4.46	0.93	2.66	0.39	2.54	0.38	2.48	0.45	1.35	0.92	0.27
D19-5	8.21	2.54	0.95	3.19	0.56	3.63	0.76	2.17	0.32	2.09	0.31	1.74	0.32	0.64	0.39	0.14
D19-6	12.07	3.62	1.32	4.51	0.79	5.04	1.05	2.98	0.44	2.82	0.42	2.43	0.56	1.97	0.62	0.22
D20-18	9.20	3.14	1.17	4.27	0.78	5.14	1.09	3.18	0.47	3.09	0.46	2.21	0.24	0.63	0.28	0.14
D20-32	10.45	3.30	1.22	4.32	0.76	4.91	1.03	2.96	0.44	2.83	0.43	2.04	0.33	1.89	0.39	0.31
D23-11	13.66	3.74	1.32	4.51	0.77	4.93	1.03	2.94	0.44	2.83	0.43	2.64	0.84	2.38	1.00	0.46
D23-13	13.76	3.76	1.31	4.55	0.78	5.02	1.05	3.02	0.45	2.92	0.44	2.70	0.82	0.89	0.98	0.40
D23-14	17.02	4.31	1.44	4.91	0.82	5.14	1.06	2.99	0.44	2.86	0.43	3.18	0.78	1.85	1.28	0.46
D23-16	16.37	4.24	1.41	4.81	0.81	5.07	1.04	2.97	0.44	2.83	0.43	3.28	1.17	5.29	1.31	0.67
D23-18	16.49	4.16	1.40	4.79	0.80	4.99	1.03	2.89	0.43	2.77	0.42	3.19	1.37	3.79	1.35	0.48
D23-27	13.64	3.72	1.29	4.50	0.77	4.96	1.04	2.97	0.44	2.86	0.43	2.65	0.78	1.09	0.97	0.44
D23-32	13.54	3.72	1.31	4.52	0.78	4.97	1.04	2.97	0.44	2.90	0.43	2.76	0.98	5.45	1.02	0.47
D24-1	11.46	3.15	1.08	3.70	0.65	4.14	0.87	2.49	0.36	2.36	0.35	2.60	0.71	0.69	0.59	0.27
D24-1.3	11.73	3.27	1.14	3.88	0.68	4.34	0.91	2.61	0.38	2.51	0.38	2.39	0.85	0.71	0.69	0.26
D24-1.4	11.56	3.24	1.12	3.85	0.67	4.29	0.90	2.57	0.38	2.46	0.37	2.35	0.57	0.68	0.66	0.26
D24-5	11.83	3.27	1.15	3.98	0.69	4.45	0.94	2.68	0.40	2.59	0.39	2.37	0.43	0.98	0.81	0.25
D24-6	16.24	4.55	1.54	5.43	0.93	5.91	1.24	3.55	0.53	3.41	0.51	3.05	0.73	1.85	1.05	0.33
D24-7	17.88	4.93	1.68	5.88	1.01	6.43	1.34	3.84	0.57	3.68	0.55	3.38	0.59	1.80	1.16	0.36
D24-9	10.72	2.82	1.12	3.77	0.71	4.21	0.94	2.52	0.34	2.32	0.35	2.28	0.73	0.62	0.76	0.25
D25-1.1	11.89	3.32	1.25	4.35	0.79	4.79	1.05	2.81	0.38	2.66	0.43	2.59	0.76	0.49	0.77	0.26
D25-1.2	14.60	4.21	1.45	5.24	0.90	5.75	1.22	3.48	0.52	3.37	0.51	3.05	0.76	0.79	0.92	0.28
D25-1.3	5.76	1.75	0.71	2.39	0.45	3.02	0.67	2.02	0.31	2.07	0.32	1.18	0.32	0.48	0.36	0.17
D25-1.4	12.74	3.70	1.27	4.56	0.79	5.07	1.06	3.07	0.46	2.97	0.45	2.60	0.80	0.67	0.79	0.25

Sample ID	Nd	Sm	Eu	Gd	Tb	Dy	Ho	Er	Tm	Yb	Lu	Hf	Ta	Pb	Th	U
D25-2.3	17.81	4.59	1.66	4.94	0.79	4.61	0.90	2.40	0.34	2.12	0.31	3.17	0.29	1.03	1.33	0.45
D25-3.1	18.24	4.55	1.57	4.95	0.80	4.92	1.00	2.79	0.41	2.62	0.39	3.11	1.37	1.04	1.34	0.42
D25-3.2	14.22	4.07	1.40	5.08	0.88	5.61	1.20	3.43	0.51	3.29	0.50	3.03	0.58	0.80	0.91	0.27
D25-3.3	13.33	3.80	1.31	4.73	0.82	5.28	1.12	3.22	0.48	3.07	0.47	2.81	0.84	0.76	0.86	0.25
D25-5.1	12.34	3.50	1.19	4.19	0.73	4.70	0.99	2.83	0.42	2.69	0.40	2.63	0.76	0.68	0.57	0.26
D25-5.2	12.98	3.70	1.29	4.58	0.80	5.11	1.08	3.12	0.46	3.03	0.46	2.96	0.67	0.69	0.83	0.27
D26-1	7.50	2.23	0.89	3.01	0.56	3.76	0.82	2.45	0.37	2.47	0.38	1.28	0.43	0.91	0.43	0.19
D26-2	6.32	1.89	0.76	2.58	0.47	3.19	0.71	2.12	0.32	2.14	0.33	1.27	0.40	0.34	0.39	0.12
D26-3	4.91	1.46	0.65	2.07	0.41	2.75	0.61	1.70	0.26	1.73	0.28	1.04	0.33	0.10	0.33	0.10
D26-4.2	5.41	1.66	0.67	2.28	0.42	2.88	0.64	1.90	0.29	1.96	0.30	1.08	0.35	0.32	0.33	0.17
D26-4.4	6.30	1.90	0.76	2.63	0.49	3.33	0.74	2.17	0.33	2.21	0.34	1.25	0.36	0.50	0.39	0.19
D26-4.5	7.79	2.29	0.92	3.06	0.56	3.80	0.83	2.47	0.38	2.49	0.38	1.47	0.26	1.08	0.45	0.18
D26-5	5.80	1.71	0.71	2.39	0.45	3.05	0.68	2.03	0.31	2.04	0.32	1.15	0.38	0.50	0.36	0.14
D26-6	6.27	1.86	0.75	2.55	0.46	3.19	0.71	2.11	0.32	2.13	0.33	1.25	0.31	0.57	0.40	0.13
D26-7	7.10	2.13	0.88	2.92	0.54	3.69	0.81	2.41	0.37	2.44	0.38	1.35	0.43	0.40	0.40	0.19
D26-9	5.28	1.60	0.65	2.20	0.41	2.79	0.62	1.84	0.28	1.89	0.29	1.21	0.29	0.37	0.33	0.14
D27-1	7.00	2.08	0.86	2.90	0.53	3.62	0.80	2.39	0.36	2.42	0.37	1.38	0.42	0.52	0.39	0.16
D27-2	4.70	1.44	0.67	1.96	0.39	2.63	0.65	1.72	0.25	1.73	0.27	0.97	0.31	0.17	0.30	0.10
D27-3	7.49	2.21	0.89	2.97	0.55	3.71	0.81	2.42	0.37	2.47	0.38	1.46	0.49	0.43	0.43	0.14
D28-12	13.90	3.82	1.31	4.58	0.79	5.04	1.05	3.01	0.45	2.93	0.44	2.71	0.78	1.32	0.99	0.41
D29-1	16.54	4.13	1.43	4.50	0.74	4.51	0.92	2.56	0.37	2.40	0.36	2.67	0.88	1.20	1.20	0.37
D29-10	9.92	2.65	1.01	2.88	0.52	3.19	0.68	1.77	0.26	1.59	0.26	1.77	0.76	0.53	0.75	0.24
D29-11	15.41	3.80	1.33	4.28	0.72	4.43	0.93	2.63	0.38	2.52	0.38	2.70	1.38	0.92	1.31	0.40
D29-15	13.79	3.46	1.20	3.81	0.62	3.82	0.78	2.18	0.32	2.06	0.31	2.45	0.68	0.93	1.12	0.34
D29-16	14.45	3.60	1.26	4.04	0.66	4.02	0.82	2.32	0.34	2.16	0.33	2.54	0.56	1.01	1.17	0.35
D29-17	12.37	2.92	0.97	3.03	0.49	3.00	0.61	1.69	0.24	1.47	0.21	2.36	0.98	0.84	0.43	0.34
D29-4	14.31	3.57	1.24	3.87	0.64	3.90	0.79	2.20	0.33	2.09	0.31	2.56	1.17	0.89	1.10	0.35

Sample ID	Nd	Sm	Eu	Gd	Tb	Dy	Ho	Er	Tm	Yb	Lu	Hf	Ta	Pb	Th	U
D29-5	14.60	3.66	1.26	4.05	0.66	4.04	0.83	2.31	0.34	2.18	0.33	2.63	1.11	1.04	1.19	0.35
D29-6	13.14	3.30	1.16	3.62	0.60	3.68	0.75	2.11	0.31	1.98	0.30	2.28	0.61	1.05	1.04	0.33
D29-9	9.74	2.56	0.95	2.95	0.50	3.10	0.64	1.80	0.27	1.73	0.26	1.68	0.44	0.72	0.73	0.24
D30-2.1	11.16	2.96	1.09	3.41	0.56	3.54	0.74	2.10	0.31	1.97	0.30	2.60	0.31	0.84	0.90	0.34
D30-2.2	9.48	2.47	0.94	2.85	0.48	3.02	0.62	1.75	0.26	1.69	0.25	1.67	0.63	0.64	0.73	0.29
D30-2.3	10.99	2.87	1.07	3.30	0.56	3.47	0.73	2.03	0.30	1.94	0.29	1.99	0.71	0.69	0.87	0.29
D30-2.4	9.76	2.60	0.98	2.99	0.51	3.17	0.65	1.84	0.27	1.77	0.26	2.00	0.69	0.73	0.75	0.31
D30-2.5	11.34	2.94	1.10	3.40	0.57	3.55	0.74	2.07	0.31	1.96	0.29	2.05	0.73	0.73	0.89	0.32
D30-2.6	10.71	2.77	1.05	3.21	0.54	3.38	0.71	1.96	0.29	1.87	0.28	1.93	0.35	0.74	0.85	0.31
D30-3	15.72	4.05	1.46	4.51	0.76	4.70	0.96	2.68	0.39	2.53	0.38	2.62	1.08	0.89	1.15	0.36
D30-4	11.96	3.11	1.19	3.60	0.60	3.73	0.76	2.14	0.31	2.01	0.30	2.04	0.88	0.77	0.84	0.28
D30-5	16.72	3.75	1.39	4.42	0.75	4.48	0.92	2.35	0.33	2.31	0.34	2.98	1.44	0.94	1.51	0.49

Pb Isotope Compositions of Basalt - ~12°60' -14°N

Sample ID	Latitude	Longitude	$^{206}Pb/^{204}Pb$	2SD(*10^{-6})	$^{207}Pb/^{204}Pb$	2SD(*10^{-6})	$^{208}Pb/^{204}Pb$	2SD(*10^{-6})	Q	d7-4	d8-4	208*/206*
D05-1.2	13.2962	44.9575	18.6379	55.0580	15.5135	51.1409	38.0947	158.6568	0.0658	0.2099	-6.5553	0.9238
D05-1A	13.2962	44.9575	18.6280	57.8929	15.4978	53.7513	38.0892	166.3412	0.0315	-1.2497	-5.9003	0.9242
D05-2.6	13.2962	44.9575	19.2811	14.9079	15.6118	13.4676	38.7393	42.0542	0.2833	3.0759	-19.8531	0.9288
D05-2.7	13.2962	44.9575	18.6418	61.9428	15.5168	57.5304	38.1318	177.9530	0.1011	0.5015	-3.3128	0.9274
D06-1.12	13.2962	44.9583	19.4570	20.3252	15.6028	18.1836	38.7380	56.8007	0.2303	0.2712	-41.2501	0.9126
D06-7.4	13.2962	44.9583	18.6912	31.9746	15.5213	29.6198	38.2098	91.7277	0.1583	0.4203	-1.4831	0.9308
D12-2.2	13.3045	44.7822	18.4985	42.6886	15.5026	39.9227	38.0155	123.2582	0.0973	0.6331	2.3809	0.9292
D12-3.1	13.3045	44.7822	18.5106	22.7061	15.5365	21.2617	38.0727	65.5565	0.0472	3.8948	6.6381	0.9342
D12-5	13.3045	44.7822	18.4759	30.2721	15.4911	28.3331	37.9905	87.5449	0.0517	-0.2640	2.6159	0.9287

Sample ID	Latitude	Longitude	$^{206}Pb/^{204}Pb$	2SD(*10^{-6})	$^{207}Pb/^{204}Pb$	2SD(*10^{-6})	$^{208}Pb/^{204}Pb$	2SD(*10^{-6})	Q	d7-4	d8-4	208*/206*
D12-8	13.3045	44.7822	18.4529	12.6198	15.5004	11.8277	37.9680	36.4626	0.0702	0.9066	3.1494	0.9286
D12-1.2	13.3045	44.7822	19.2454	32.0225	15.6068	28.9706	38.7402	90.4783	0.1953	2.9641	-15.4545	0.9323
D05-5.2	13.2962	44.9575	19.2790	18.2641	15.6117	16.4983	38.7373	51.4954	0.1614	3.0816	-19.8028	0.9288
D05-5.3	13.2962	44.9575	19.2708	45.0586	15.6043	40.7051	38.7162	127.0759	0.2000	2.4346	-20.9146	0.9275
D06-1.10	13.2962	44.9583	19.4554	37.4125	15.6004	33.4724	38.7311	104.5906	0.1836	0.0419	-41.7455	0.9121
D12-6.2G	13.3045	44.7822	19.2501		15.5958		38.7219			1.8117	-17.8546	0.9300
D09-11.8	13.3192	44.9343	18.4554	34.6159	15.5023	32.4328	37.9549	99.8659	0.0772	1.0716	1.5245	0.9269
D09-8.2	13.3192	44.9343	18.6203	26.4310	15.5020	24.5519	38.1431	76.0307	0.0414	-0.7470	0.4141	0.9307
D10-38.2	13.3428	44.8903	18.4251	15.3567	15.5021	14.4125	37.9269	44.3527	0.0957	1.3789	2.3930	0.9269
D11-1	13.2732	44.8718	18.8328	109.0865	15.4956	100.1761	38.2830	311.7038	0.0170	-3.6866	-11.2889	0.9246
D11-5	13.2732	44.8718	18.8447		15.4986		38.2942			-3.5149	-11.6130	0.9247
D13-12	13.3188	44.8871	18.7776	25.9568	15.5261	23.9461	38.2300	74.2046	0.0331	-0.0365	-9.9125	0.9244
D14-1.10	13.3257	44.8592	19.2074	13.5791	15.5919	12.2949	38.8741	38.5490	0.0586	1.8823	2.5369	0.9494
D14-1.4	13.3257	44.8592	18.7496	34.7300	15.5269	32.0866	38.2774	99.5298	0.0726	0.3403	-1.7915	0.9322
D15-1	13.0697	44.0888	19.0291		15.5612		38.6409			0.7480	0.7680	0.9428
D15-10	13.0697	44.0888	19.0510	33.4866	15.5887	30.5574	38.7307	95.4382	0.1119	3.2592	7.1088	0.9499
D16-13	13.0270	44.8388	18.6869	25.8238	15.5356	23.9486	38.1896	74.0508	0.1176	1.8941	-2.9877	0.9291
D16-17	13.0270	44.8388	18.6823		15.5302		38.1732			1.4053	-4.0644	0.9278
D19-1.1	12.7808	44.8385	18.5880	18.5331	15.5261	17.2685	38.0462	53.2306	0.0966	2.0147	-5.3747	0.9235
D19-5	12.7808	44.8385	18.5847	18.1466	15.5217	16.9125	38.0551	52.2021	0.1243	1.6081	-4.0876	0.9248
D20-18	12.9863	44.9318	18.2570	8.2134	15.4816	7.7711	37.7054	23.8207	0.0536	1.1496	0.5640	0.9196
D23-11	13.5097	44.8988	18.9487	60.7756	15.5368	55.6137	38.4837	173.4582	0.1951	-0.8196	-5.2309	0.9343
D23-13	13.5097	44.8988	18.9723	42.6724	15.5538	39.0396	38.5227	121.7343	0.1651	0.6246	-4.1748	0.9361
D24-9	13.3532	44.9023	18.8891		15.5405		38.4222			0.1930	-4.1732	0.9337
D25-1.1	13.4010	44.8855	18.8587		15.5688		38.3932			3.3482	-3.3986	0.9337
D25-3.1	13.4010	44.8855	18.8725	25.6118	15.5346	23.5182	38.3264	72.9950	0.0294	-0.2186	-11.7471	0.9253
D26-3	13.6595	44.9660	19.1436		15.5922		38.7913			2.6051	1.9781	0.9471

Sample ID	Latitude	Longitude	$^{206}Pb/^{204}Pb$	2SD(*10^{-6})	$^{207}Pb/^{204}Pb$	2SD(*10^{-6})	$^{208}Pb/^{204}Pb$	2SD(*10^{-6})	Q	d7-4	d8-4	208*/206*
D27-1	13.8030	44.9647	19.2257	46.1474	15.5789	41.7260	38.8427	130.9577	0.0216	0.3820	-2.8189	0.9444
D27-2	13.8030	44.9647	19.2161		15.5801		38.8299			0.6084	-2.9357	0.9441
D28-12	13.8430	44.9378	18.8803	35.8460	15.5525	32.9476	38.3771	102.3339	0.0975	1.4838	-7.6252	0.9299
D29-10	13.9025	45.0305	19.2178		15.5517		38.8979			-2.2456	3.6670	0.9508
D30-5	14.0853	45.0207	19.1305	29.5698	15.5627	26.8323	38.7639	84.0606	0.0645	-0.2024	0.8063	0.9456

Nd Isotope Compositions of Basalt - ~12°60' -14°N

Sample ID	Latitude	Longitude	$^{146}Nd/^{144}Nd$	2SD (*10^{-6})	ITR	$^{143}Nd/^{144}Nd$	2SD(*10^{-6})	Iterations	End Voltage	Sm Detected (ppm)
D05-1.2	13.2962	44.9575	0.72187	71	153	0.51306	15	149		1111
D05-1.3	13.2962	44.9575	0.72344	74	37	0.51309	33	37	0.17	37
D05-2.6	13.2962	44.9575	0.72233	316	11	0.51293	186	10		46
D12-2.1	13.3045	44.7822	0.72323	21	189	0.51313	8	191	0.47	65
D12-5	13.3045	44.7822	0.72300	24	140	0.51313	5	142	0.72	2
D12-1.2	13.3045	44.7822	0.72271	82	159	0.51299	15	154		92
D05-5.2	13.2962	44.9575	0.72335	176	78	0.51301	22	76		30
D05-5.3	13.2962	44.9575	0.72381	53	33	0.51297	44	35	0.16	11
D06-1.10	13.2962	44.9583	0.72343	23	36	0.51291	137	38	0.16	96
D05-2.1	13.2962	44.9575	0.72293	71	10	0.51306	49	10	0.36	27
D12-6.2G	13.3045	44.7822	0.72159	19	150	0.51303	7	147	1.11	19
D12-12	13.3045	44.7822	0.72375	427	20	0.51305	46	20	0.35	13
D07-3	13.3007	44.9312	0.72291	169	50	0.51303	9	47	0.82	4
D09-8.2	13.3192	44.9343	0.72332	165	110	0.51311	15	113	0.40	130
D11-1	13.2732	44.8718	0.72480	382	57	0.51304	139	56	0.07	13
D11-5	13.2732	44.8718	0.72278	74	150	0.51305	7	145	0.78	1
D14-1.10	13.3257	44.8592	0.72404	119	82	0.51310	15	87	0.40	0
D15-1	13.0697	44.0888	0.72229	27	150	0.51302	8	146	0.71	10

Sample ID	Latitude	Longitude	$^{146}Nd/^{144}Nd$	2SD (*10^{-6})	ITR	$^{143}Nd/^{144}Nd$	2SD(*10^{-6})	Iterations	End Voltage	Sm Detected (ppm)
D16-12	13.0270	44.8388	0.72362	248	29	0.51311	44	28	0.87	No Data
D16-13	13.0270	44.8388	0.72414	196	39	0.51309	27	39	0.36	21
D16-17	13.0270	44.8388	0.72333	40	80	0.51311	13	76	0.55	3
D19-1.1	12.7808	44.8385	0.72354	35	77	0.51314	13	74	0.85	3
D19-5	12.7808	44.8385	0.72350	38	140	0.51313	5	143	1.19	7
D20-18	12.9863	44.9318	0.72341	51	114	0.51320	8	112	0.80	1
D20-32	12.9863	44.9318	0.72309	9	194	0.51314	8	190	0.60	8
D23-13	13.5097	44.8988	0.72328	17	95	0.51304	9	96	1.03	1
D25-1.1	13.4010	44.8855	0.72257	131	150	0.51306	6	148	1.04	1
D25-1.4	13.4010	44.8855	0.72306	205	48	0.51310	11	47	0.94	4
D25-3.1	13.4010	44.8855	0.72256	42	145	0.51308	6	143	0.95	56
D26-3	13.6595	44.9660	0.72217	74	150	0.51302	10	144	0.74	156
D26-5	13.6595	44.9660	0.72352	34	140	0.51303	8	141	0.89	17
D28-12	13.8430	44.9378	0.72303	17	140	0.51308	5	140	1.46	3
D29-15	13.9025	45.0305	0.72380	174	56	0.51308	28	57	0.39	27
D30-5	14.0853	45.0207	0.72161	67	150	0.51299	7	142	0.80	22

Sr Isotope Compositions of Basalt - ~12°60’ -14°N

Sample ID	Latitude	Longitude	$^{87}Sr/^{86}Sr$	ppm Rb	2SD	Iterations
D05-1.2	13.2962	44.9575	0.70266	9	1.26E-05	142
D05-2.6	13.2962	44.9575	0.70286	14	1.97E-05	118
D05-2.7	13.2962	44.9575	0.70265	8	1.12E-05	147
D05-3.1	13.2962	44.9575	0.70253	14	1.97E-05	90
D05-4.1	13.2962	44.9575	0.70267	25	3.51E-05	38
D12-2.1	13.3045	44.7822	0.70256	8	1.12E-05	145
D12-2.2	13.3045	44.7822	0.70264	12	1.69E-05	125

Sample ID	Latitude	Longitude	$^{87}Sr/^{86}Sr$	ppm Rb	2SD	Iterations
D12-5	13.3045	44.7822	0.70259	9	1.26E-05	144
D12-8	13.3045	44.7822	0.70254	49	6.88E-05	10
D12-1.2	13.3045	44.7822	0.70290	15	2.11E-05	76
D05-5.2	13.2962	44.9575	0.70290	12	1.69E-05	48
D05-5.3	13.2962	44.9575	0.70288	9	1.27E-05	142
D12-4	13.3045	44.7822	0.70285	12	1.69E-05	118
D05-2.1	13.2962	44.9575	0.70287	19	2.67E-05	38
D12-6.2G	13.3045	44.7822	0.70288	14	1.97E-05	118
D12-12	13.3045	44.7822	0.70299	31	4.36E-05	120
D07-3	13.3007	44.9312	0.70284	11	1.56E-05	141
D11-8	13.2732	44.8718	0.70258	9	1.26E-05	150
D14-1.10	13.3257	44.8592	0.70272	8	1.12E-05	143
D15-1	13.0697	44.0888	0.70278	12	1.69E-05	124
D15-10	13.0697	44.0888	0.70281	10	1.41E-05	142
D16-13	13.0270	44.8388	0.70264	8	1.12E-05	146
D19-1.3	12.7808	44.8385	0.70270	27	3.79E-05	90
D19-5	12.7808	44.8385	0.70262	10	1.41E-05	148
D20-32	12.9863	44.9318	0.70254	10	1.41E-05	144
D23-13	13.5097	44.8988	0.70283	8	1.12E-05	140
D24-1.4	13.3532	44.9023	0.70273	8	1.12E-05	146
D24-9	13.3532	44.9023	0.70276	9	1.26E-05	115
D25-1.1	13.4010	44.8855	0.70271	13	1.83E-05	56
D25-1.4	13.4010	44.8855	0.70273	8	1.12E-05	146
D26-5	13.6595	44.9660	0.70282	7	9.84E-06	143
D27-1	13.8030	44.9647	0.70279	9	1.27E-05	150
D27-2	13.8030	44.9647	0.70284	12	1.69E-05	78
D29-10	13.9025	45.0305	0.70295	14	1.97E-05	85

Sample ID	Latitude	Longitude	$^{87}Sr/^{86}Sr$	ppm Rb	2SD	Iterations
D29-15	13.9025	45.0305	0.70277	10	1.41E-05	170
D30-2.3	14.0853	45.0207	0.70283	15	2.11E-05	138
D30-5	14.0853	45.0207	0.70280	9	1.27E-05	143

Water Concentrations of Basaltic Glass (FTIR)- ~12°60' -14°N

Sample ID	Latitude	Longitude	Chip Thickness (M)	Abs. Intensity (Peak 3550 $^{cm-1}$)	Av. Conc. H_2O (3 Shot Average)	1SD
D05-10.1	13.2962	44.9575	0.00015	0.413	0.289	0.011
D05-16	13.2962	44.9575	0.00033	1.166	0.358	0.005
D05-8.1	13.2962	44.9575	0.00015	0.771	0.525	0.010
D05-8.3	13.2962	44.9575	0.00025	1.630	0.666	0.006
D05-8.4	13.2962	44.9575	0.00018	0.704	0.409	0.009
D06-6	13.3033	44.9583	0.00030	0.821	0.279	0.001
D06-7.1	13.3033	44.9583	0.00017	1.623	0.993	0.017
D06-7.3	13.3033	44.9583	0.00022	0.709	0.329	0.001
D06-7.4	13.3033	44.9583	0.00014	0.356	0.260	0.001
D06-9	13.3033	44.9583	0.00016	0.387	0.248	0.003
D11-13	13.2732	44.8718	0.00022	0.532	0.248	0.002
D11-5	13.2732	44.8718	0.00024	0.295	0.125	0.002
D12-1.8	13.3045	44.7822	0.00021	1.804	0.883	0.005
D12-6.2	13.3045	44.7822	0.00029	2.692	0.938	0.015
D12-7	13.3045	44.7822	0.00024	0.533	0.233	0.009
D12-7A	13.3045	44.7822	0.00026	0.812	0.319	0.000
D12-7B	13.3045	44.7822	0.00021	0.761	0.373	0.005
D12-ARC2	13.3045	44.7822	0.00019	0.472	0.256	0.002
D14-1.1	13.3257	44.8592	0.00015	0.253	0.173	0.001
D14-1.13	13.3257	44.8592	0.00017	0.406	0.241	0.019

Sample ID	Latitude	Longitude	Chip Thickness (M)	Abs. Intensity (Peak 3550 $^{cm-1}$)	Av. Conc. H_2O (3 Shot Average)	1SD
D14-1.15	13.3257	44.8592	0.00013	0.347	0.270	0.011
D14-1.2	13.3257	44.8592	0.00020	0.434	0.222	0.000
D14-1.6	13.3257	44.8592	0.00017	0.261	0.151	0.008
D14-1.7	13.3257	44.8592	0.00014	0.402	0.304	0.015
D14-3	13.3257	44.8592	0.00026	0.771	0.304	0.009
D15-1	13.0697	44.0888	0.00023	1.234	0.535	0.011
D15-13	13.0697	44.0888	0.00016	0.763	0.502	0.013
D15-14	13.0697	44.0888	0.00011	0.300	0.266	0.012
D15-15	13.0697	44.0888	0.00011	0.615	0.558	0.026
D16-10A	13.0270	44.8388	0.00021	0.633	0.308	0.001
D16-10B	13.0270	44.8388	0.00020	0.665	0.345	0.010
D16-11	13.0270	44.8388	0.00011	0.368	0.341	0.002
D16-11A	13.0270	44.8388	0.00023	0.745	0.333	0.002
D16-11B	13.0270	44.8388	0.00026	0.880	0.353	0.006
D16-11C	13.0270	44.8388	0.00024	0.815	0.345	0.003
D16-11D	13.0270	44.8388	0.00020	0.694	0.352	0.004
D16-15	13.0270	44.8388	0.00023	1.229	0.526	0.017
D16-16A	13.0270	44.8388	0.00020	1.334	0.673	0.012
D16-16B	13.0270	44.8388	0.00020	0.614	0.319	0.005
D16-18	13.0270	44.8388	0.00025	0.797	0.329	0.003
D16-7A	13.0270	44.8388	0.00027	0.933	0.354	0.001
D16-7B	13.0270	44.8388	0.00021	0.682	0.324	N/A
D19-1.1	12.7808	44.8385	0.00019	0.595	0.310	0.001
D19-1.3	12.7808	44.8385	0.00017	0.462	0.278	0.002
D19-2A	12.7808	44.8385	0.00027	0.691	0.261	0.000
D19-2B	12.7808	44.8385	0.00026	0.713	0.280	0.000
D19-2BX	12.7808	44.8385	0.00026	0.672	0.263	0.001

Sample ID	Latitude	Longitude	Chip Thickness (M)	Abs. Intensity (Peak 3550 $^{cm-1}$)	Av. Conc. H_2O (3 Shot Average)	1SD
D19-2C	12.7808	44.8385	0.00037	0.575	0.159	0.000
D19-7.16	12.7808	44.8385	0.00020	0.592	0.303	0.000
D24-1	13.3532	44.9023	0.00008	0.590	0.738	0.029
D24-16	13.3532	44.9023	0.00020	0.674	0.343	0.001
D24-1A	13.3532	44.9023	0.00020	0.757	0.384	0.003
D24-2A	13.3532	44.9023	0.00022	0.863	0.406	0.007
D24-2B	13.3532	44.9023	0.00025	0.919	0.391	0.020
D24-7A	13.3532	44.9023	0.00026	1.045	0.410	0.001
D24-7B	13.3532	44.9023	0.00019	0.767	0.401	0.000
D24-7C	13.3532	44.9023	0.00021	0.848	0.414	0.001
D24-9	13.3532	44.9023	0.00015	0.523	0.360	0.006
D25-1.1	13.4010	44.8855	0.00017	0.724	0.439	0.008
D25-1.2	13.4010	44.8855	0.00026	0.341	0.128	0.005
D25-1.2B	13.4010	44.8855	0.00022	0.306	0.150	0.007
D25-1.3	13.4010	44.8855	0.00022	0.841	0.399	0.012
D25-1.4A	13.4010	44.8855	0.00022	0.892	0.412	0.002
D25-1.4B	13.4010	44.8855	0.00025	0.979	0.405	0.007
D25-3.2A	13.4010	44.8855	0.00027	0.956	0.354	0.004
D25-3.2B	13.4010	44.8855	0.00023	0.897	0.396	0.004
D25-3.3	13.4010	44.8855	0.00023	0.851	0.389	0.015
D25-3.5	13.4010	44.8855	0.00020	0.786	0.396	0.010
D25-5.1	13.4010	44.8855	0.00012	0.451	0.397	0.011
D25-5.1A	13.4010	44.8855	0.00019	0.638	0.366	0.032
D25-5.1B	13.4010	44.8855	0.00021	0.777	0.375	0.004
D25-5.2	13.4010	44.8855	0.00008	0.358	0.458	0.001
D25-5.2B	13.4010	44.8855	0.00018	0.684	0.396	0.007
D25-5.2C	13.4010	44.8855	0.00025	0.685	0.374	0.005

Sample ID	Latitude	Longitude	Chip Thickness (M)	Abs. Intensity (Peak 3550 $^{cm-1}$)	Av. Conc. H_2O (3 Shot Average)	1SD
D25-5.2D	13.4010	44.8855	0.00023	0.855	0.387	0.007
D25-5.2E	13.4010	44.8855	0.00024	0.919	0.383	0.011
D26-11A	13.6595	44.9660	0.00025	0.456	0.174	0.011
D26-11AX	13.6595	44.9660	0.00020	0.783	0.398	0.002
D26-11B	13.6595	44.9660	0.00022	0.331	0.155	0.002
D26-11BX	13.6595	44.9660	0.00021	0.424	0.198	N/A
D26-1A	13.6595	44.9660	0.00023	0.325	0.148	0.003
D26-1AX	13.6595	44.9660	0.00023	0.904	0.403	0.003
D26-6A	13.6595	44.9660	0.00019	0.203	0.165	0.000
D27-4	13.8030	44.9647	0.00020	0.385	0.192	0.009
D29-1	13.9025	45.0305	0.00023	1.406	0.619	0.011
D29-10	13.9025	45.0305	0.00015	0.598	0.422	0.020
D29-11B	13.9025	45.0305	0.00020	1.222	0.578	0.012
D29-12	13.9025	45.0305	0.00021	1.113	0.541	0.001
D29-14	13.9025	45.0305	0.00025	0.923	0.377	0.002
D29-15A	13.9025	45.0305	0.00024	1.427	0.604	0.010
D29-15B	13.9025	45.0305	0.00022	1.272	0.591	0.000
D29-17	13.9025	45.0305	0.00011	0.587	0.540	0.005
D29-17A	13.9025	45.0305	0.00027	1.056	0.397	0.003
D29-17B	13.9025	45.0305	0.00023	1.276	0.567	0.000
D29-2	13.9025	45.0305	0.00023	1.262	0.558	0.002
D29-6B	13.9025	45.0305	0.00022	1.215	0.568	0.004
D29-7	13.9025	45.0305	0.00024	1.460	0.618	0.004
D30-1	14.0853	45.0207	0.00023	1.678	0.752	0.007
D30-2A	14.0853	45.0207	0.00024	1.676	0.712	0.003
D30-2C	14.0853	45.0207	0.00021	1.219	0.565	0.030

Major Element Concentrations of Dolerite Dykes ~12°60' -14°N

Sample ID	Latitude	Longitude	SiO_2 (wt%)	TiO_2	Al_2O_3	Fe_2O_3	MnO	MgO	CaO	K_2O	Na_2O	P_2O_5	SO_3	LOI %	Total	Total + LOI
D05-6.1	13.30	44.96	49.46	1.09	15.05	9.79	0.16	8.37	12.01	0.14	2.23	0.12	0.14	-0.11	98.54	98.43
D05-6.2	13.30	44.96	49.56	1.09	14.86	9.58	0.16	8.09	12.79	0.14	2.20	0.11	0.03	-0.02	98.60	98.57
D09-3.2	13.32	44.93	50.00	1.29	13.68	10.40	0.18	8.11	12.17	0.22	2.33	0.12	0.13	0.54	98.62	99.16
D09-3.4	13.32	44.93	48.61	1.11	14.75	10.40	0.22	8.64	11.83	0.04	2.40	0.10	0.10	1.35	98.21	99.56
D09-3.6	13.32	44.93	50.12	1.28	14.04	10.36	0.17	7.77	11.97	0.17	2.35	0.11	0.16	0.70	98.49	99.19
D09-3.7	13.32	44.93	48.73	1.40	14.71	9.70	0.15	7.71	11.28	0.20	3.04	0.19	0.04	2.39	97.15	99.54
D13-26	13.32	44.89	49.22	1.60	15.03	9.64	0.19	8.32	10.16	0.03	2.70	0.19	0.02	1.99	97.09	99.08
D13-36	13.32	44.89	45.87	1.07	15.27	9.43	0.29	9.75	13.10	0.03	1.62	0.10	0.02	2.38	96.54	98.92
D20-28	12.99	44.93	47.98	1.36	14.68	11.33	0.14	8.41	8.86	0.06	3.15	0.14	0.06	2.54	96.17	98.71

Trace Element Concentrations of Dolerite Dykes ~12°60' -14°N

Sample ID	Latitude	Longitude	Li (ppm)	Rb	Sr	Y	Zr	Nb	Cs	Ba	La	Ce	Pr	Nd
D05-6.1	13.30	44.96	3.78	1.99	122.90	26.64	72.17	5.03	0.02	30.94	3.92	10.19	1.60	8.20
D05-6.2	13.30	44.96	10.61	1.89	137.90	29.84	76.79	5.55	0.05	33.48	4.19	11.10	1.77	9.14
D09-3.2	13.32	44.93	4.28	8.44	126.80	31.10	72.16	6.13	0.87	20.82	4.80	12.45	1.96	10.11
D09-3.4	13.32	44.93	4.41	0.27	108.80	26.59	46.40	3.44	0.01	16.17	3.02	8.60	1.43	7.64
D09-3.6	13.32	44.93	4.03	5.98	123.20	29.02	76.61	5.65	0.62	20.70	4.36	11.47	1.80	9.23
D09-3.7	13.32	44.93	7.78	2.61	222.20	29.67	93.09	11.41	0.01	23.78	8.39	19.20	2.74	12.83
D13-26	13.32	44.89	3.36	0.15	219.10	22.52	60.02	12.32	0.00	28.31	7.43	16.24	2.22	10.50
D13-36	13.32	44.89	2.78	0.17	109.00	25.35	38.44	5.30	0.00	11.00	3.87	10.36	1.64	8.38
D20-28	12.99	44.93	20.38	0.74	124.60	37.45	97.51	3.62	0.06	13.54	3.59	11.11	1.94	10.50

Sample ID	Sm	Eu	Gd	Tb	Dy	Ho	Er	Tm	Yb	Lu	Hf	Ta	Pb	Th	U
D05-6.1	2.69	1.01	3.50	0.64	4.28	0.93	2.69	0.41	2.57	0.39	1.91	0.33	0.33	0.31	0.10
D05-6.2	3.08	1.16	3.72	0.72	4.86	1.05	3.01	0.46	2.90	0.43	2.08	0.40	0.29	0.33	0.35
D09-3.2	3.32	1.20	4.13	0.78	5.22	1.12	3.19	0.48	3.04	0.45	2.10	0.44	0.41	0.33	0.15
D09-3.4	2.64	1.05	3.49	0.65	4.38	0.94	2.69	0.41	2.57	0.38	1.48	0.23	0.42	0.17	0.07
D09-3.6	3.03	1.15	3.87	0.72	4.75	1.03	2.94	0.44	2.81	0.42	2.12	0.39	0.48	0.32	0.15
D09-3.7	3.67	1.41	4.37	0.77	4.97	1.05	2.95	0.44	2.77	0.40	2.45	0.70	1.04	0.61	0.26
D13-26	3.21	1.23	3.86	0.67	4.07	0.80	2.11	0.30	1.79	0.25	1.87	0.74	0.16	0.60	0.17
D13-36	2.74	1.16	3.32	0.64	4.23	0.90	2.54	0.38	2.37	0.35	1.31	0.37	0.34	0.21	0.07
D20-28	3.67	1.26	4.65	0.89	6.00	1.30	3.75	0.57	3.60	0.54	2.56	0.26	0.44	0.20	0.23

Major Element Concentrations of Gabbro and Plagiogranite Samples ~12°60' -14°N

Sample ID	Lithology	Latitude	Longitude	SiO_2 (wt%)	TiO_2	Al_2O_3	Fe_2O_3	MnO	MgO	CaO	K_2O	Na_2O	P_2O_5	SO_3	LOI %	Total	Total+ LOI
D16-3	Gabbro	13.0270	44.8388	45.13	2.33	15.82	16.19	0.22	5.25	7.75	0.18	3.45	0.84	0.22	1.56	97.37	98.92
D20-20	Gabbro	12.9863	44.9318	49.66	1.53	12.66	10.83	0.43	9.66	8.53	0.16	3.35	0.04	0.06	2.23	96.91	99.13
D28-16	Plagiogranite	13.8430	44.9378	58.81	0.16	19.72	1.95	0.07	5.51	1.27	0.17	8.12	0.01	0.05	2.61	95.84	98.46
D28-16B	Plagiogranite	13.8430	44.9378	58.36	0.16	19.58	1.93	0.07	5.44	1.25	0.17	8.08	0.01	0.02	2.61	95.08	97.69
D28-3	Plagiogranite	13.8430	44.9378	74.59	0.11	12.61	1.39	0.05	1.52	0.50	0.06	6.06	0.02	0.06	1.05	96.96	98.01
D28-36	Plagiogranite	13.8430	44.9378	66.75	0.07	18.78	0.35	0.01	0.72	0.70	0.06	9.98	0.01	0.00	0.56	97.41	97.97
D28-39	Plagiogranite	13.8430	44.9378	60.75	0.25	17.77	10.34	0.04	1.73	0.05	3.35	0.32	0.04	0.08	3.85	94.71	98.56
D28-59	Plagiogranite	13.8430	44.9378	72.75	0.11	14.50	1.21	0.06	1.66	0.59	0.07	6.98	0.02	0.02	1.10	97.96	99.06

Trace Element Concentrations of Gabbro and Plagiogranite Samples ~12°60' -14°N

Sample ID	Latitude	Longitude	Li	Rb	Sr	Y	Zr	Nb	Cs	Ba	La	Ce	Pr	Nd
D16-3	13.0270	44.8388	13.01	4.30	255.90	57.94	30.70	15.35	0.19	132.00	10.98	29.72	4.82	25.70
D20-20	12.9863	44.9318	5.50	0.92	163.10	23.00	38.16	2.71	0.01	20.20	2.08	5.60	0.94	5.17
D28-16	13.8430	44.9378	9.96	1.29	231.20	7.27	4.07	17.58	0.01	854.10	28.81	48.27	4.71	15.54
D28-16B	13.8430	44.9378	9.96	1.29	231.20	7.27	4.07	17.58	0.01	854.10	28.81	48.27	4.71	15.54
D28-3	13.8430	44.9378	3.48	0.56	63.77	77.21	7.41	76.93	0.01	139.40	46.69	99.96	11.18	41.81
D28-36	13.8430	44.9378	1.95	0.15	184.90	118.30	11.11	139.60	0.00	94.28	9.22	22.07	3.13	13.99
D28-39	13.8430	44.9378	2.14	39.59	7.07	68.13	9.25	114.00	0.02	1,317.00	89.16	170.00	19.80	73.48
D28-41	13.8430	44.9378	0.90	57.65	29.42	57.10	4.69	78.91	0.13	407.90	47.00	98.59	10.46	35.70
D28-59	13.8430	44.9378	3.55	0.53	72.33	78.18	7.35	75.24	0.01	120.50	56.57	119.40	13.43	49.48

Sample ID	Sm	Eu	Gd	Tb	Dy	Ho	Er	Tm	Yb	Lu	Hf	Ta	Pb	Th	U
D16-3	7.84	3.25	9.47	1.59	9.93	2.05	5.52	0.78	4.67	0.68	1.06	0.92	0.63	0.11	0.13
D20-20	1.99	1.17	2.65	0.53	3.71	0.82	2.37	0.36	2.35	0.36	1.15	0.21	0.43	0.07	0.07
D28-16	2.19	2.37	1.72	0.23	1.24	0.24	0.66	0.09	0.57	0.08	0.20	1.27	1.23	10.22	0.18
D28-16B	2.19	2.37	1.72	0.23	1.24	0.24	0.66	0.09	0.57	0.08	0.20	1.27	1.23	10.22	0.18
D28-3	9.30	1.12	9.24	1.68	11.09	2.38	7.17	1.17	7.50	1.07	0.47	6.28	1.50	8.47	2.38
D28-36	6.06	0.35	8.46	2.15	16.38	3.83	11.97	1.92	11.48	1.48	0.79	9.23	0.34	12.11	4.60
D28-39	13.92	0.65	11.53	1.71	10.35	2.22	6.69	1.05	6.56	0.95	0.41	7.28	0.03	13.25	5.17
D28-41	7.19	0.85	6.95	1.25	8.18	1.77	5.40	0.89	5.91	0.87	0.30	5.93	1.90	12.66	3.52
D28-59	10.65	1.36	10.17	1.82	11.77	2.50	7.34	1.18	7.39	1.04	0.37	4.63	1.47	9.19	2.39

APPENDIX 4

BULK KDs (From: McKenzie and O'Nions, 1991)															
	La	**Ce**	**Pr**	**Nd**	**Sm**	**Eu**	**Gd**	**Tb**	**Dy**	**Ho**	**Er**	**Tm**	**Yb**	**Lu**	**Hf**
Spinel Assemblage	0.008	0.013	0.020	0.028	0.035	0.042	0.041	0.043	0.047	0.045	0.045	0.047	0.048	0.051	0.036
Garnet Assemblage	0.006	0.012	0.019	0.028	0.048	0.064	0.084	0.115	0.153	0.206	0.260	0.376	0.496	0.667	0.052

Please note: The Ce value (highlighted) is arbitrary, having been modified from the original value to improve smoothness of the model output.